JAERI-M
85-106

TWO-DIMENSIONAL THERMAL-HYDRAULIC BEHAVIOR IN CORE IN SCTF CORE-II COLD LEG INJECTION TESTS (RADIAL POWER PROFILE TEST RESULTS)

July 1985

Takamichi IWAMURA, Makoto SOBAJIMA
Tsutomu OKUBO, Akira OHNUKI
Yutaka ABE and Hiromichi ADACHI

日本原子力研究所
Japan Atomic Energy Research Institute

JAERI-M レポートは，日本原子力研究所が不定期に公刊している研究報告書です。
入手の問合わせは，日本原子力研究所技術情報部情報資料課（〒319-11茨城県那珂郡東海村）あて，お申しこしください。なお，このほかに財団法人原子力弘済会資料センター（〒319-11 茨城県那珂郡東海村日本原子力研究所内）で複写による実費頒布をおこなっております。

JAERI-M reports are issued irregularly.
Inquiries about availability of the reports should be addressed to Information Division Department of Technical Information, Japan Atomic Energy Research Institute, Tokai-mura, Naka-gun, Ibaraki-ken 319-11, Japan.

©Japan Atomic Energy Research Institute, 1985

編集兼発行　日本原子力研究所
印　　刷　いばらき印刷㈱

Two-dimensional Thermal-hydraulic Behavior in Core in SCTF Core-II Cold Leg Injection Tests (Radial Power Profile Test Results)

Takamichi IWAMURA, Makoto SOBAJIMA, Tsutomu OKUBO
Akira OHNUKI, Yutaka ABE and Hiromichi ADACHI

Department of Reactor Safety Research,
Tokai Research Establishment, JAERI

(Received June 27, 1985)

Major purpose of the Slab Core Test Program is to investigate the two-dimensional thermal-hydraulic behavior in the core during the reflood phase in a PWR-LOCA. In order to investigate the effects of radial power profile, three cold leg injection tests with different radial power profiles under the same total heating power and core stored energy were performed by using the Slab Core Test Facility (SCTF) Core-II. It was revealed by comparing these three tests that the heat transfer was enhanced in the higher power bundles and degraded in the lower power bundles in the non-uniform radial power profile tests. The turnaround temperature in the high power bundles were evaluated to be reduced by about 40 to 120 K. On the other hand, a two-dimensional flow in the core was also induced by the non-uniform water accumulation in the upper plenum and the quench was delayed resultantly in the bundles corresponding to the peripheral bundles of a PWR. However, the effect of the non-uniform upper plenum water accumulation on the turnaround temperature was small because the effect dominated after the turnaround of the cladding temperature.

The work was performed under contract with the Atomic Energy Bureau of Science and Technology Agency of Japan.

Selected data from Tests S2-SH1, S2-SH2 and S2-06 are also presented in this report. Some data from Tests S2-SH1 and S2-SH2 were compared with TRAC post-test calculations performed by the Los Alamos National Laboratory.

Keywords: Reflood, LOCA, ECCS, PWR, Reactor Safety, Two-Phase Flow, Chimney Effect, Cross Flow, Quench, Heat Transfer

SCTF第2次炉心コールドレグ注入試験における炉心内2次元熱水力挙動
（半径方向出力分布試験結果）

日本原子力研究所東海研究所原子炉安全工学部
岩村　公道・傍島　　真・大久保　努・大貫　　晃
阿部　　豊・安達　公道

（1985年6月受理）

平板炉心試験計画の主目的は，PWR－LOCA時再冠水過程における炉心内2次元熱水力挙動を調べることである。半径方向出力分布の効果を調べるため，平板炉心試験装置（SCTF）第2次炉心を用いて，同一総発熱量かつ同一炉心蓄積熱条件下で半径方向出力分布の異なる3回のコールドレグ注入試験を行ない，比較評価した結果，半径方向出力分布が存在する場合には，高出力バンドルでは熱伝達が促進され，低出力バンドルでは熱伝達が悪化することが明らかとなった。高出力バンドルにおける最高温度の低下量は，急峻出力分布試験において約40～120K と評価された。一方，上部プレナム内の不均一蓄水によっても炉心内2次元流れが生じ，その結果PWRの外周バンドルに相当するバンドルではクエンチが遅れた。しかしながら，上部プレナム蓄水分布が顕著となるのは，炉心が最高温度に達した後なので，炉心最高温度に及ぼす影響は小さかった。

なお，試験S2－SH1，S2－SH2およびS2－06のデータの一部も本報告書に収録する。

また，試験S2－SH1とS2－SH2の一部データと，ロスアラモス国立研究所で実施されたTRAC試験後計算結果との比較も行った。

本報告書は，電源開発促進対策特別会計法に基づき，科学技術庁からの受託によって行なった研究の成果である。

Contents

1. Introduction 1
2. Test Description 3
2.1 Test Facility 3
2.2 Test Conditions 3
2.3 Test Procedure 4
3. Test Results and Discussions 6
3.1 Fluid Behavior in Pressure Vessel and Primary Loops 6
3.1.1 Boundary Conditions for Fluid Behavior in Loops 6
3.1.2 Fluid Behavior in Upper Plenum and around End Box Tie Plate 6
3.1.3 Water Accumulation Behavior in Core and Downcommer ... 7
3.1.4 Steam Generation Rate in Core 7
3.1.5 Fluid Behavior in Primary Loops 8
3.2 Two-Dimensional Hydraulic Behavior 8
3.2.1 Absolute Pressure Behavior 8
3.2.2 Void Fraction Distribution 10
3.2.3 Horizontal Differential Pressure 10
3.3 Two-Dimensional Thermal Behavior 12
3.3.1 Heater Rod Temperature 12
3.3.2 Relation between Quench Front Propagation and Non-uniform Water Accumulation in Upper Plenum 12
3.3.3 Heat Transfer Characteristics 13
3.3.4 Evaluation of Core Cooling Enhancement due to Two-dimensional Effects 14
4. Conclusions 18
Acknowledgement 19
References 19

Appendix A Slab Core Test Facility Core-II 63
A.1 Test Facility..... 63
A.2 Instrumentation..... 67
A.3 Mass Balance Calculation..... 68
A.4 Calculation Method of Steam Generation rate..... 69
A.5 Calculation Method of Horizontal Differential Pressure..... 72
Appendix B Selected Data of Test S2-SH1 114

Appendix C Selected Data of Test S2-SH2 129
Appendix D Selected Data of Test S2-06 144
Appendix E Comparison between TRAC Post-Test Analysis and Test Data of Test S2-SH1 159
Appendix F Comparison between TRAC Post-Test Analysis and Test Data of Test S2-SH2 197

目　　次

1. 緒言 …… 1
2. 試験 …… 3
2.1 試験装置 …… 3
2.2 試験条件 …… 3
2.3 試験手順 …… 4
3. 試験結果と検討 …… 6
3.1 圧力容器と1次系内の流体挙動 …… 6
3.1.1 ループ内流体挙動の境界条件 …… 6
3.1.2 上部プレナム及びエンドボックス内流体挙動 …… 6
3.1.3 炉心及びダウンカマ内蓄水挙動 …… 7
3.1.4 炉心内蒸気発生量 …… 7
3.1.5 1次系内流体挙動 …… 8
3.2 2次元流体挙動 …… 8
3.2.1 絶対圧力分布 …… 8
3.2.2 ボイド率分布 …… 10
3.2.3 水平差圧 …… 10
3.3 2次元熱的挙動 …… 12
3.3.1 ヒーターロッド温度 …… 12
3.3.2 クエンチフロント進行と上部プレナム不均一蓄水との関係 …… 12
3.3.3 熱伝達特性 …… 13
3.3.4 2次元効果による炉心冷却促進の評価 …… 14
4. 結論 …… 18
謝辞 …… 19
参考文献 …… 19
付録A 平板炉心試験装置第2次炉心 …… 63
A.1 試験装置 …… 63
A.2 計測 …… 67

A.3　質量バランス計算方法 …… 68
A.4　蒸気発生量計算方法 …… 69
A.5　水平差圧計算方法 …… 72
付録B　試験S2－SH1のデータ …… 114
〃 C　試験S2－SH2のデータ …… 129
〃 D　試験S2－06のデータ …… 144
〃 E　TRAC試験後解析と試験S2－SH1データとの比較 …… 159
〃 F　TRAC試験後解析と試験S2－SH2データとの比較 …… 197

List of Tables

Table 2-1 Test Conditions for Tests S2-SH1, S2-SH2 and S2-06

Table 2-2 Chronologies of major events for Tests S2-SH1, S2-SH2 and S2-06

List of Figures

Fig. 2-1 Schematic diagram of SCTF

Fig. 2-2 Vertical cross section of pressure vessel

Fig. 3-1 ECC water injection rate

Fig. 3-2 Comparison of core inlet water temperature

Fig. 3-3 Comparison of pressures at core center and containment tank II

Fig. 3-4 Comparison of core heating power

Fig. 3-5 Comparison of core inlet mass flow rate and ECC water injection rate

Fig. 3-6 Comparison of liquid levels in upper plenum

Fig. 3-7 Comparison of differential pressures across end box tie plate

Fig. 3-8 Comparison of core full height differential pressures

Fig. 3-9 Comparison of differential pressures in downcomer

Fig. 3-10 Comparison between steam generation rate in core obtained by heat balance method and steam outflow rate through hot leg obtained by mass balance method in Test S2-06

Fig. 3-11 Comparison of steam generation rates in core

Fig. 3-12 Mass flow rates and void fractions in 4 regions of hot leg in Test S2-06

Fig. 3-13 Comparison of differential pressures across hot leg

Fig. 3-14 Comparison of differential pressures across intact cold leg

Fig. 3-15 Comparison of differential pressures across broken cold leg steam/water separator side

Fig. 3-16 Comparison of differential pressures across broken cold leg pressure vessel side

Fig. 3-17 (a) through (e)
Comparison of equal pressure lines in core and bottom

quench front distribution

Fig. 3-18 Comparison of absolute pressure distribution at core outlet

Fig. 3-19 (a) through (c)
Comparison of void fractions at 6 elevations in core

Fig. 3-20 Comparison of horizontal differential pressures at 1.905, 3.235 and 3.821 m between Bundles 1 and 4

Fig. 3-21 Comparison of horizontal differential pressures at 1.905, 3.235 and 3.821 m between Bundles 4 and 8

Fig. 3-22 Magnitude of horizontal differential pressure and direction of cross flow at 1.905, 3.235 and 3.821 m at 50, 100, 200 and 400 s in Test S2-06

Fig. 3-23 Comparison of heater rod surface temperatures in Bundles 2, 4, 6 and 8 at 1.905, 2.33 and 2.76 m (Test S2-SH2)

Fig. 3-24 Comparison of heater rod surface temperatures in Bundles 2, 4, 6 and 8 at 1.905, 2.33 and 2.76 m (Test S2-06)

Fig. 3-25 Radial distribution of turnaround temperature and temperature rise at 1.905 and 2.76 m for Tests S2-SH2 and S2-06

Fig. 3-26 Comparison of bottom quench front distribution

Fig. 3-27 Difference in water accumulation level in upper plenum vs. bottom quench front eeevation in Bundle 8

Fig. 3-28 Comparison of heat transfer coefficients in Bundles 2, 4, 6 and 8 at 2.76 m

Fig. 3-29 Heat transfer coefficient vs. distance from quench front in Bundles 2, 4 and 8 at 1.905 and 2.76 m for Tests S2-06 and S2-SH2

Fig. 3-30 Liquid fraction vs. distance from quench front in Bundles 2, 4 and 8 at 1.905 and 2.76 m for Tests S2-06 and S2-SH2

Fig. 3-31 Heat transfer coefficient vs. liquid fraction in Bundles 2, 4, and 8 at 1.905 and 2.76 m for Tests S2-06 and S2-SH2

Fig. 3-32 Axial power profile, cross section of heater rod and average heat capacity

Fig. 3-33 Comparison of temperatures calculated from heat transfer coefficients in Tests S2-SH2 and S2-06 at 1.905, 2.33, 2.76 and 3.19 m in Bundle 4 using initial temperatures and power transients in Test S2-06

Fig. 3-34 Radial distributions of differences in temperatures

calculated from heat transfer coefficients in Tests S2-SH2 and S2-06 at 2.33 m at 50, 100, 150, 200, 250 and 300 s

Fig. 3-35 Radial distributions of differences in turnaround temperatures calculated from heat transfer coefficients in Test S2-SH2 and in Test S2-06 at 1.38, 1.905, 2.33, 2.76 and 3.19 m

1. Introduction

The thermo-hydrodynamic behavior during the reflood phase of a postulated loss of coolant accident (LOCA) in a pressurized water reactor (PWR) has been investigated by using Slab Core Test Facility (SCTF). The SCTF program is a part of the large scale reflood test program under contract with Atomic Energy Bureau of Science and Technology Agency of Japan together with the Cylindical Core Test Facility (CCTF) program. One of the major objectives of the SCTF program is to investigate the two-dimensional thermo-hydrodynamic behavior in the core(5)-(11). In order to meet the above objective, SCTF simulates a full radius slab section of a PWR with 8 bundles arranged in a row and the heating power for each bundle can be independently controlled. Therefore, the effects of radial core power profile can be investigated with SCTF.

In the SCTF Core-I forced feed flooding tests, it was found that the steep radial power profile gave the higher heat transfer coefficients in the higher power bundles under the same total core power(1) and a significant cross flow between rod bundles was established even for the flat radial power profile test(2). However, the core inlet flow rate in these tests was much higher than a typical flooding rate observed in the CCTF tests(11). In addition, the emergency core cooling (ECC) water is injected into the cold legs in an actual PWR instead of the lower plenum in these tests.

In order to investigate the effects of two-dimensionality on the core cooling under more realistic conditions of feed mode and core inlet flow, three tests: S2-SH1, S2-SH2 and S2-06 were performed under the modified cold leg injection condition in the SCTF Core-II test series with the base case, flat and steep radial core power profiles, respectively.

The present report describes the effects of the radial power profile and the distribution of upper plenum water level on the two-dimensional behavior in the core.

Presented in Appendix A are a brief description of SCTF Core-II and calculation methods of mass balance, steam generation rate and additional horizontal differential pressures. Some selected data obtained in Tests S2-SH1, S2-SH2 and S2-06 are presented in Appendixes B, C and D, respectively. Additionally, in order to evaluate the

predictability of the two-dimensional behavior observed in the SCTF tests by the Transient Reactor Analysis Code (TRAC)[13], some data from Tests S2-SH1 and S2-SH2 were compared with TRAC post-test calculations performed by the Los Alamos National Laboratory in Appendixes E and F with some comments.

2. Test Description

2.1 Test Facility

A schematic diagram of SCTF is shown in Fig. 2-1. The primary coolant loops consist of a hot leg equivalent to four actual hot legs, a steam/water separator corresponding to four actual steam generators, an intact cold leg equivalent to three intact cold legs, a broken cold leg on the pressure vessel side, and a broken cold leg on the steam/water separator side. These two broken cold legs are connected to two containment tanks one by one which are connected to each other by the pressure equalizing pipe.

The flow area scaling ratio is 1/21 of a 1,100 MWe PWR, whereas the heights of each component are preserved.

The emergency core cooling system (ECCS) consists of an accumulator (Acc) system and a low pressure coolant injection (LPCI) system. The injection ports for the Acc and LPCI systems are the lower plenum and the intact cold leg, respectively.

Figure 2-2 shows a vertical cross section of the pressure vessel. The pressure vessel includes a simulated core, an upper plenum with internals, a lower plenum, a core baffle and a downcomer. The SCTF pressure vessel simulates a full radius slab section of a 1,100 MWe PWR.

The simulated core consists of 8 bundles arranged in a row with full radial width. Each bundle consists of 234 heater rods and 22 non-heated rods arranged in 16x16 array. The outer diameter and the heated length of the heater rod are 10.7 mm and 3660 mm, respectively. The dimensions and arrangement pitch of the rods are based on those for a 15x15 fuel rod bundle of a Westinghouse type PWR.

The core and the upper plenum are enveloped by honeycomb thermal insulators with wall plates to minimize the wall thermal effects.

More detailed information on SCTF is available in references (3) and (4) and a brief description is pressented in Appendix A.

2.2 Test Conditions

The tests referred to in this report are Test S2-SH1 (base case), Test S2-SH2 (flat radial power profile) and Test S2-06 (steep radial

power profile). Major test conditions for these three tests are listed in Table 2-1. The BOCREC (bottom of core recovery) in Table 2-1 represents the time when the ECC water reaches the bottom of heated part.

These three tests were performed under almost the same conditions as each other except the radial power profile. The radial power profile in Test S2-SH1 (base case) was based on the radial power profile in a 1,100 MWe Westinghouse initial loading core. The radial power profile was changed to steep (Test S2-06) or flat (Test S2-SH2) but the total heating power was unchanged from the base case test. The initial stored energy in the core was also set to be almost the same for these three tests.

The test conditions common to these three tests have been selected to reasonably represent the situation of reflood phase of a PWR-LOCA. However, the Acc injection rate was reduced and the injection period was extended from the scaled injection rate and period because a significant U-tube oscillation occurred during the Acc injection period under the scaled injection conditions. The Acc injection water temperature was determined so as to give the same core inlet water temperature as in a typical CCTF test. The LPCI flow rate was based on the scaled value of a 1,100 MWe Westinghouse type PWR. The Acc and LPCI flow rates were 19.3 and 5.41 kg/s, respectively, which correspond to about 5.71 and 1.59 cm/s of nominal flooding velocities. The intended system pressure in the containment tanks was 0.2 MPa.

2.3 Test Procedure

The test procedure for these three tests is as follows. After setting the initial pressure and temperature conditions, core heating was initiated. In order to make the initial stored energy the same, when four cladding temperatures exceeded 1053 K, 1013 K and 1137 K for Tests S2-SH1, S2-SH2 and S2-06, respectively, the accumulator injection into the lower plenum was initiated. The initial saturation water level in the lower plenum was 0.14 m below the bottom of heated part. After keeping the core power constant for 40 s from accumulator injection initiation, the core power decay simulation started simulating the reactor transient from 40 s after shutdown. The decay curve

was based on the 1.02 x (ANS standard+Actinides). The injection location was switched from the lower plenum to the intact cold leg at 55 s after accumulator injection initiation. At this time, accumulator injection was terminated and LPCI injection was initiated. At 900 s after the initiation of LPCI, the test was terminated.

The chronologies of major events for these three tests are summarized in Table 2-2.

3. Test Results and Discussions

3.1 Fluid Behavior in Pressure Vessel and Primary Loops

3.1.1 Boundary Conditions for Fluid Behavior in Core

As shown in Figs. 3-1, 3-2 and 3-3, the accumulator and LPCI injection rates, the core inlet water temperatures and the pressure transients at the core center and the containment tank-II are in good agreement with each other for Tests S2-SH1, S2-SH2 and S2-06.

Figure 3-4 shows the core heating power transients in Bundles 2, 4, 6 and 8 for these three tests. The normalized radial power factors in Bundles 1&2, 3&4, 5&6 and 7&8 are 1.001, 1.065, 1.015 and 0.919, for Test S2-SH1, 1.0, 1.0, 1.0, and 1.0 for Test S2-SH2 and 1.0, 1.2, 1.0 and 0.8 for Test S2-06, respectively, under the same total heating power in these three tests.

Figure 3-5 shows the estimated core inlet mass flow rate obtained by a mass balance method together with the ECC injection rate in Test S2-06. The procedure of mass balance calculation is explained in Appendix A.3. As shown in this figure, the core inlet mass flow rate during the accumulator injection period is about 12 kg/s. The estimated core inlet mass flow rate is almost in agreement with the LPCI flow rate during the LPCI period. Approximately the same core inlet mass flow rate was obtained in Tests S2-SH1 and S2-SH2 as in Test S2-06.

3.1.2 Fluid Behavior in Upper Plenum and around End Box Tie Plate

Figure 3-6 shows the comparison of liquid level in the upper plenum above Bundles 2, 4, 6 and 8 in these three tests. The liquid level in the upper plenum increases gradually after about 200 s and rapidly after about 450 s and remains at almost constant after 500 s. The liquid level is higher above the Bundle 8 side and lower above the Bundle 1 side especially after 450 s. The above-mentioned water accumulation behavior in the upper plenum is almost similar to each other in these three tests except the relatively lower liquid level above Bundle 8 in Test S2-06 than in the other two tests before 450 s.

Figure 3-7 shows the differential pressures across the end box

tie plate above Bundles 2, 4, 6 and 8 in these three tests. The differential pressure is much lower above Bundle 8 than above the other Bundles in Tests S2-SH1 and S2-SH2, suggesting the lower steam up-flow rate above the Bundle 8 side. On the other hand, the differential pressure is larger above Bundle 8 before 260 s in Test S2-06, suggesting that the steam up-flow rate is higher above the Bundle 8 side during the initial 260 s for the steep power profile test. After about 300 s, the differential pressure above Bundle 8 becomes much lower than those above the other bundles even for Test S2-06. The negative differential pressure across the end box tie plate at the later period indicates the water fall back into the core through the end box tie plate holes.

3.1.3 Water Accumulation Behavior in Core and Downcomer

Figure 3-8 shows the differential pressures across the core full height in Bundles 2, 4, 6 and 8 in Tests S2-SH2 and S2-06. As shown in this figure, the total water accumulation behavior in the core is almost flat even for the steep power profile test and no significant difference is observed between these two tests.

The differential pressure in downcomer is also in good agreement with each other in these three tests as shown in Fig. 3-9.

3.1.4 Steam Generation Rate in Core

The steam flow rate in the hot leg can be estimated by two independent methods. One is the steam generation rate obtained by a heat balance calculation in the core as described in Appendix A.4 and the other is the steam outflow rate obtained by a mass balance calculation. Figure 3-10 shows the comparison of these two methods for Test S2-06. As shown in this figure, the steam generation rate is in good agreement with the steam outflow rate after 80 s. However, during the initial 80 s, the steam generation rate in the core is higher than the steam outflow rate. The reason of this discrepancy may be attributed to the following two reasons. On reason is that some amount of the generated steam contributed to the pressurization of the system as shown in Fig. 3-3. Also some amount of the generated steam is considered to be condensed because the temperature of the

structure could not be in equilibrium with the saturation temperature during the rapid pressurization period.

Figure 3-11 shows the comparison of steam generation rate for Tests S2-SH1, S2-SH2 and S2-06. The steam generation rates for Tests S2-SH1, S2-SH2 and S2-06 are almost in agreement with each other because the total core heating power and the initial core stored energy are almost the same for these three tests.

Although the steam outflow rate could not be obtained for Tests S2-SH1 and S2-SH2 due to the malfunction of venturi flow meter in the intact cold leg, it is reasonably suggested from Figs. 3-10 and 3-11 that the steam outflow rates for these three tests are also in good agreement with each other as well as the steam generation rates.

3.1.5 Fluid Behavior in Primary Loops

Figure 3-12 shows the comparisons of mass flow rates and void fractions in 4 regions of the hot leg. The top region comprises the upper 31 % of the pipe cross-sectional area, the second region comprises the next lower 27 %, the third region comprises the next lower 26 %, and the bottom region comprises the bottom 16 %. As shown in Fig. 3-12, after 160 s, the mass flow rate in the bottom region is negative and the void fraction in the bottom region is almost 0.0, indicating the flow reversal at the bottom part of the hot leg after 160 s. The flow reversal in the hot leg enhances the water accumulation above the Bundle 8 side and therefore contributes to the development of non-uniform exit head effect as will be discussed in section 3.2.1.

Figures 3-13 through 3-16 show the comparisons of differential pressures across the hot leg, the intact cold leg, the broken cold leg steam/water separator side and the broken cold leg pressure vessel side, respectively. As shown in these figures, the transients of differential pressures agree well with each other, indicating that the fluid behaviors in these primary loops are quite similar for these three tests.

3.2 Two-Dimensional Hydraulic Behavior

3.2.1 Absolute Pressure Distribution

In order to investigate the two-dimensional hydraulic behavior in the core, vertical and horizontal differential pressures were measured at various locations in the core. By combining the measured horizontal and/or vertical differential pressures, horizontal differential pressures at other locations could be obtained. The calculation method of additional horizontal differential pressures in the core is described in Appendix A.5. The absolute pressures at various points in the core were also obtained by combining the measured absolute pressure with the measured or calculated differential pressures. By vertically interpolating these calculated absolute pressures, equal pressure lines were obtained. Figures 3-17(a) through (e) show the comparisons of equal pressure lines in the core between Tests S2-SH2 and S2-06 at 100, 200, 300, 400 and 500 s, respectively. The distribution of bottom quench front along the center rods in all bundles is also shown in these figures.

Before 300 s, the pressure in the Bundle 8 side is lower than the pressure in the Bundle 1 side at the middle elevation of the core in Test S2-06, indicating the steam flow towards the Bundle 8 side while almost flat pressure distribution is observed in Test S2-SH2. The two-dimensional flow caused by the radial power profile is called the power profile-induced convection effect. The quench front profile is also almost flat in Test S2-SH2 and the quench front is lowest in Bundles 3 and 4 and highest in Bundles 7 and 8 in Test S2-06 corresponding to the radial power profiles for these two test, respectively.

On the other hand, after 300 s, the pressure in the Bundle 8 side becomes higher than the pressure in the Bundle 1 side especially at the upper part of core indicating the cross flow from the Bundle 8 side to the Bundle 1 side. At 500 s, the core pressure distribution for Test S2-06 is almost similar to that for Test S2-SH2. The inclined pressure distribution in the core is considered to be caused by the non-uniform upper plenum water level shown in Fig. 3-6. Figure 3-18 shows the comparison of absolute pressure distribution below the end box tie plate (3.821 m from the bottom of core). As shown in this figure, the pressure in the Bundle 8 side becomes higher with time for both tests. The inclined pressure distribution in the core shown in Fig. 3-17 is in accordance with the developing of the inclined pressure distribution at the outlet of core shown in Fig. 3-18.

Therefore, the two-dimensional flow caused by the non-uniform water accumulation in the upper plenum is called the non-uniform exit head effect.

The quench front propagation in the Bundle 8 side is suppressed after 300 s and the quench front becomes lower in the Bundle 8 side for these two tests due to the non-uniform exit head effect in the later period.

3.2.2 Void Fraction Distribution

Figure 3-19 shows the comparison of void fractions in Bundles 2, 4 and 8 at 6 elevations for Tests S2-SH2 and S2-06. These void fractions were calculated from the measured vertical differential pressures by neglecting the effects of frictional and accelerational pressure drops.

In the lower half of the core, no significant difference in the void fractions between bundles is observed in Test S2-SH2. In Test S2-06, on the contrary, the void fraction in Bundle 8 becomes lower after the quench front reaches the bottom of measurement section because the quench front propagates faster in the Bundle 8 side at the lower half of the core and the steam generation rate is lower in the Bundle 8 side due to the radial power profile.

In the upper half of the core the void fraction in Bundle 8 is higher than in the other bundles for these two tests.

The increase of void fraction at the bottom elevation after about 450 s in these two tests is due to the flashing caused by the depressurization at this time as shown in Fig. 3-3.

3.2.3 Horizontal Differential Pressure

Figures 3-20 and 3-21 show the horizontal differential pressures between Bundles 1 and 4 and between Bundles 4 and 8, respectively, for Tests S2-SH1, S2-SH2 and S2-06. In these figures, the horizontal differential pressures at 1.905 and 3.235 m were directly measured values while those at 3.821 m were calculated from the measured vertical and horizontal differential pressures as described in Appendix A.5.

As shown in Fig. 3-20, the pressure in Bundles 4 is slightly

higher than the pressure in Bundle 1 during the first 80 s at 1.905 m and the pressure in Bundle 1 is slightly higher than the pressure in Bundle 4 before 300 s at 3.821 m for all of these three tests. However, it is generally concluded that the horizontal differential pressure between Bundles 1 and 4 is almost zero at all elevations before about 350 s and after that time the pressure in Bundle 4 is higher than the pressure in Bundle 1 at all elevations. No significant difference in these characteristics is observed among these three tests.

On the other hand, it is observed in Fig. 3-21 that the pressure in Bundle 4 is higher than the pressure in Bundle 8 for about initial 260 s (S2-SH2) or 400 s (S2-06) at 1.905 m. The positive horizontal differential pressure is the largest in Test S2-06 and the smallest in Test S2-SH2, indicating that the steeper radial power profile induces the higher cross flow from Bundle 4 to Bundle 8 at the middle elevation of core. Since the non-uniform exit head effect becomes dominant with time, the horizontal differential pressure between Bundles 4 and 8 becomes negative and the negative differential pressure is larger at the higher elevation. At 3.821 m, the pressure in Bundle 8 is always higher than the pressure in Bundle 4 during the test period, indicating the cross flow from Bundle 8 to Bundle 4. Also the pressure difference between Bundle 4 and 8 is the largest in Test S2-06 and the smallest in Test S2-SH2 at this elevation.

Figure 3-22 shows the magnitude of the horizontal differential pressure and the direction of the cross flow at elevations of 1.905, 3.235 and 3.821 m at 50, 100, 200, and 400 s in Test S2-06. The bottom quench front is also shown in this figure. At 50 s, the cross flow direction at the middle elevation is from Bundle 4 to Bundle 1 and from Bundle 4 to Bundle 8 indicating the divergent flow from the higher power bundle to the lower power bundle. At 100 and 200 s, it is suggested that the cross flow direction is from Bndle 4 to Bundle 8 at 1.905 m and from Bundle 8 to Bundle 4 at 3.821 m. As disccussed in Section 3.1.2, the differential pressure across the end box tie plate is higher above Bundle 8 than above the other bundles. Therefore, it is suggested that the generated steam in the core tends to flow toward the Bundle 8 side due to the power profile-induced convection effect and the steam up-flow rate at the end box tie plate is larger in the Bundle 8 side. As the bottom quench front proceeds upward, the cross

flow direction above the quench front is from the Bundle 8 side to the Bundle 1 side due to the non-uniform exit head effect.

3.3 Two-Dimensional Thermal Behavior

3.3.1 Heater Rod Temperature

Figures 3-23 and 3-24 show the comparisons of heater rod surface temperatures in Bundles 2, 4, 6 and 8 at elevations of 1.905, 2.33 and 2.76 m from the bottom of heated part in Tests S2-SH2 and S2-06 respectively. These temperatures were measured at the center rods at each bundle.

As shown in Fig. 3-23, in the flat radial power profile test, the heater rod temperature becomes higher in the Bundle 8 side than in the Bundle 2 side after the turnaround time especially at the higher elevation. In addition, both the turnaround time and the quench time tend to be delayed in Bundle 8.

In the steep radial power profile test, the turnaround time and the quench time in Bundle 8 are also delayed at the higher elevation as shown in Fig. 3-24 though the heating power is the lowest in this bundle.

Figure 3-25 shows the radial distribution of the turnaround temperature and the temperature rise from the BOCREC to the turnaround at elevations of 1.905 and 2.76 m in Tests S2-SH2 and S2-06. The turnaround temperature is higher in Bundles 3 and 4 than in the other bundles in Test S2-06 because the core heating power is the highest in these bundles. However, in Test S2-06, the turnaround temperature in Bundle 8 is higher especially at elevation of 2.76 m though the heating power is the lowest in Bundles 7 and 8. The temperature rise is also remarkably higher in the Bundle 8 side at the higher elevation in this test. On the other hand, the radial distribution of the turnaround temperature and the temperature rise is almost flat in Test S2-SH2.

3.3.2 Relation between Quench Front Propagation and Non-uniform water Accumulation in Upper Plenum

Figure 3-26 shows the comparisons of bottom quench front profile

for Tests S2-SH1, S2-SH2 and S2-06. Before the quench front reaches the middle of the core, the bottom quench front profile is corresponding to the radial power profile. That is, the quench propagation speed is higher in the lower power bundles and lower in the higher power bundles in the non-uniform radial power profile tests and the quench propagates at almost the same speed over 8 bundles in the flat radial power profile test. At the later period, however, the quench propagation is suppressed in the Bundle 8 side in these three tests.

As shown in Fig. 3-6, the water accumulation level in the upper plenum is higher above the Bundle 8 side and lower above the Bundle 1 side and the difference increases with time. In order to investigate the relation between the non-uniform water accumulation in the upper plenum and the progression of the bottom quench front, the difference of water accumulation level between above Bundle 8 and above Bundle 1 is plotted against the bottom quench front elevation in Bundle 8 in Fig. 3-27 for Tests S2-SH1, S2-SH2 and S2-06. As shown in this figure, with respect to the quench front elevation, the difference of water accumulation level in the upper plenum is larger in Test S2-SH2 than in Test S2-06. This is corresponding to the fact that the steam up-flow rate is larger in the Bundle 8 side in Test S2-06 and smaller in the Bundle 8 side in Test S2-SH2 as indicated by the differential pressure across the end box tie plate shown in Fig. 3-7.

The non-uniform water accumulation in the upper plenum becomes significant as the quench front proceeds upwards in the upper half of the core, corresponding to the fact that the quench in the upper part of the core was delayed in the Bundle 8 side as mentioned before. In addition, since the turnaround temperature appears before the difference in the upper plenum water accumulation level becomes significant, the non-uniform water accumulation in the upper plenum has little effect on the turnaround temperature.

3.3.3 Heat Transfer Characteristics

Figure 3-28 shows the comparisons of heat transfer coefficients at 2.33 m among Bundles 2, 4, 6 and 8 in Tests S2-SH2 and S2-06. These heat transfer coefficients were calculated from the transient of average temperature in each bundle. In Test S2-06, the heat transfer

coefficient is highest in Bundle 4 and lowest in Bundle 8 due to the power profile-induced convection effect. In Test S2-SH2, on the other hand, there exists no clear difference in the heat transfer coefficients among these bundles.

In order to clarify the heat transfer characteristics, the heat transfer coefficients in Bundles 2, 4 and 8 at elevations of 2.76 m and 1.905 m are plotted against the distance from the bottom quench front for Tests S2-SH2 and S2-06 in Fig. 3-29. As shown in this figure, the difference of heat transfer coefficients between bundles is larger in Test S2-06 than in Test S2-SH2 and the band of heat transfer coefficients for Test S2-SH2 is included in that for Test S2-06. Therefore, it is indicated that the effect of radial power profile on the two-dimensional heat transfer characteristics is more dominant than the effect of non-uniform upper plenum water accumulation.

The local liquid fractions at elevations of 2.76 and 1.905 m for these two tests are plotted against the distance from the quench front in Fig. 3-30. The local liquid fraction is obtained by the differential pressures in 6 sections of the core. As the quench front aproaches the elevation of 2.76 m, the local liquid fraction becomes higher in Bundle 2 in these two tests at this elevation, indicating the water concentration in the Bundle 1 side due to the non-uniform upper plenum water accumulation. On the other hand, no significant difference is observed among bundles and also between these two tests at the elevation of 1.905 m.

Figure 3-31 shows the relation between the heat transfer coefficient and the local liquid fraction at these elevations for these two tests. It is noted by comparing Fig. 3-31 with Fig. 3-29 that the differnce of heat transfer coefficient in Test S2-06 between bundles 4 and 8 is slightly smaller with respect to the local liquid fraction than with respect to the distance from the quench front. It is therefore suggested that the heat transfer coefficient is affected not only by the distance from the quench front and the local water fraction but also by other parameters such as the local vapor or water velocity.

3.3.4 Evaluation of Core Cooling Enhancement due to Two-Dimensional Effects

As discussed before, the heat transfer is enhanced in the higher power bundles and degraded in the lower power bundles due to the power profile-induced convection effect. However, the actual decrease of cladding temperature due to the effect of radial power profile can not be evaluated by directly comparing the measured cladding temperature in the flat radial power profile test with that in the steep radial power profile test because the initial temperature and the power were different for each test.

In order to quantitatively evaluate the effect of radial power profile on the cladding temperature, hypothetical temperature transients were calculated by applying the experimentally obtained heat transfer coefficients from the flat radial power profile test (Test S2-SH2) and the steep radial power profile test (Test S2-06) to the conditions with the same initial temperature and power transient given in the latter test. The calculation was made by solving a heat balance equation per unit length by assuming a lumped heat capacity for a heater rod. A cross section of the heater rod and the calculation method of the average heat capacity are shown in Fig. 3-32.

By using the lumped approximation for a heater rod, the heat balance equation per unit length is written as:

$$\frac{\pi}{4} D^2 (C_p \rho)_a \frac{T_w(t+1) - T_w(t)}{\Delta t} = \frac{Q(t) f_z}{N_{rod} L} - \pi D h (T_w(t) - T_{sat}(t)) \qquad (1)$$

where $(C_p)_a$ = Average heat capacity of a heater rod

D = Heater rod diameter

$T_w(t+1)$ = Cladding temperature at time (t+1)

$T_w(t)$ = Cladding temperature at time (t)

t = Time interval

$Q(t)$ = Bundle power at time (t)

f_z = Axial peaking factor

N_{rod} = Number of heater rods in a bundle

L = Heated length

h = Heat transfer coefficient

$T_{sat}(t)$ = Saturation temperature at time (t)

The initial temperature is the temperature at the beginning of bottom reflood in the steep radial power profile test (Test S2-06). The bundle power transient is also given in this test.

Although the cladding temperature affects the heat transfer coefficient, especially for the radiation heat transfer coefficient, the effect of the difference in cladding temperature on the heat transfer coefficient was not considered in the calculation for Test S2-SH2. Therefore, the calculated cladding temperature using the heat transfer coefficient of Test S2-SH2 indicates a hypothetical temperature transient. In spite of this error involved in the calculation, the difference between these two calculated temperatures is considered to be induced by the effect of two-dimensional flow due to the radial power profile.

Figure 3-33 shows the comparisons between the two temperature transients at four elevations in Bundle 4 calculated with eq.(1) under the initial temperature and power transient in Tests S2-06 using the heat transfer coefficients obtained for the particular locations in Test S2-SH2 and in Test S2-06. As shown in this figure, the turnaround time is delayed and resultantly the turnaround temperature is higher in the temperature transients calculated from the heat transfer coefficients in Test S2-SH2 (Case 1) than in those from the heat transfer coefficients in Test S2-06 (Case 2).

Figure 3-34 shows the horizontal distributions of the temperature differences between Case 1 and Case 2 at 2.33 m from the bottom of heated part at 50, 100, 150, 200, 250 and 300 s. As shown in this figure, the temperature difference is positive in Bundles 1 through 6, indicating that the heat transfer was enhanced not only in the higher power bundles (Bundles 3 and 4) but also in the average power bundles (Bundles 1, 2, 5 and 6) in the steep radial power profile test. On the contrary, the negative temperature difference in the lower power bundles (Bundles 7 and 8) implys that the heat transfer was degraded in these bundles in the steep radial power profile test. However, since the initial cladding temperature was lower in these bundles because of the lower heating power, the heat transfer degradation in these bundles did not affect the maximum temperature in the core.

The difference in the turnaround temperatures between the two cases is plotted against the bundle number at five elevations in Fig. 3-35. In general, the turnaround temperature tends to be decreased in

the higher and average power bundles and increased in the lower power bundles in Test S2-06. The degree of increase and decrease in turnaround temperature is more significant at elevations of 2.76 and 3.19 m than at elevations of 1.905 and 2.33 m where the maximum cladding temperature was observed. As shown in Fig. 3-35, the turnaround temperatures in Bundles 2 through 6 at elevations of 2.33, 2.76 and 3.19 m are evaluated to be reduced by about 40 to 120 K. These reductions are considered to be due to the power profile-induced convection effect.

4. Conclusions

The effects of radial power profile and non-uniform water accumulation in the upper plenum on the two-dimensional thermal-hydraulic behavior in the core were investigated under relatively low flooding rates and resultantly low heat transfer conditions in the SCTF Core II cold leg injection test series and the following conclusions were obtained.

1) Two-dimensional flow in the core was induced by the radial power distribution in the core and the non-uniform water accumulation in the upper plenum.

2) Heat transfer was enhanced for the higher and average power bundles and degraded for the peripheral lower power bundles and resultantly the turnaround temperature was reduced for the former bundles and increased for the latter bundles in the test with a steep radial power profile as compared with the test with a flat radial power profile under the same total heating power and initial core stored energy.

3) The turnaround temperatures in the higher and average power bundles at the upper elevations were evaluated to be reduced by about 40 to 120 K due to the two-dimensional flow effect.

4) The collapsed water level in the upper plenum was higher in the hot leg side than in the other side and the difference increased with time due to the water concentration in the hot leg side and the flow reversal in the hot leg. The variation of radial power profile has little effect on the non-uniform water accumulation behavior in the upper plenum.

5) The turnaround temperature was not much affected by the non-uniform water accumulation in the upper plenum because the effect dominated after the turnaround of the cladding temperature.

6) The quench in the upper half of the core was delayed in the bundles corresponding to the peripheral bundles of a PWR core. This is considered to be caused by the lower upward flow trend in those bundles than the other bundles due to the non-uniform water accumulation in the upper plenum.

Acknowledgement

The authors are much indebted to Dr. K. Hirano and Dr. Y. Murao for their guidance and encouragement for this program.

They would like to express their appreciation to Messrs. T. Iguchi, K. Okabe, J. Sugimoto and Dr. H. Akimoto for their useful discussions.

References

(1) T. Iwamura et al., Effects of Radial Core Power Profile on Core Thermo-Hydraulic Behavior during Reflood Phase in PWR-LOCA, J. Nucl. Sci. Tech., vol. 20, No. 9, pp. 743-751, (1983).

(2) T. Iwamura and H. Adachi, Evaluation of Cross Flow Velocity across Rod Bundles during Reflood Phase in SCTF Core-I Forced-Feed Flooding Tests, Private comunication.

(3) H. Adachi et al., Design of Slab Core Test Facility (SCTF) in Large Scale Reflood Test Program, Part I: Core I, JAERI-M 83-080, (1983).

(4) M. Sobajima et al., Design of Slab Core Test Facility (SCTF) in Large Scale Reflood Test Program, Part II: JAERI-M, to be published.

(5) H. Adachi et al., System Pressure Effects on Reflooding Phenomena Observed in the SCTF Core I Forced Flooding Tests, JAERI-M 83-079, (1983).

(6) Y. Sudo et al., Effect of Upper Plenum Water Accumulation on Reflooding Phenomena under Forced Flooding in SCTF Core I Test, JAERI-M 83-114, (1983).

(7) T. Iwamura et al., Effects of Core Inlet Water Subcooling on Reflooding Phenomena -SCTF Core I Forced Feed Floding Test-, JAERI-M 83-122, (1983).

(8) M. Sobajima et al., Examination of Repeatability in Reflood Phenomena under Forced Flooding in SCTF Core I Tests, JAERI-M 83-237, (1984).

(9) T. Iwamura et al., Effects of Upper Plenum Injection on Thermo-Hydrodynamic Behavior under Refill and Reflood Phases, JAERI-M 84-221, (1984).

Acknowledgement

The authors are much indebted to Dr. K. Hirano and Dr. Y. Murao for their guidance and encouragement for this program.

They would like to express their appreciation to Messrs. T. Iguchi, K. Okabe, J. Sugimoto and Dr. H. Akimoto for their useful discussions.

References

(1) T. Iwamura et al., Effects of Radial Core Power Profile on Core Thermo-Hydraulic Behavior during Reflood Phase in PWR-LOCA, J. Nucl. Sci. Tech., vol. 20, No. 9, pp. 743-751, (1983).

(2) T. Iwamura and H. Adachi, Evaluation of Cross Flow Velocity across Rod Bundles during Reflood Phase in SCTF Core-I Forced-Feed Flooding Tests, Private comunication.

(3) H. Adachi et al., Design of Slab Core Test Facility (SCTF) in Large Scale Reflood Test Program, Part I: Core I, JAERI-M 83-080, (1983).

(4) M. Sobajima et al., Design of Slab Core Test Facility (SCTF) in Large Scale Reflood Test Program, Part II: JAERI-M, to be published.

(5) H. Adachi et al., System Pressure Effects on Reflooding Phenomena Observed in the SCTF Core I Forced Flooding Tests, JAERI-M 83-079, (1983).

(6) Y. Sudo et al., Effect of Upper Plenum Water Accumulation on Reflooding Phenomena under Forced Flooding in SCTF Core I Test, JAERI-M 83-114, (1983).

(7) T. Iwamura et al., Effects of Core Inlet Water Subcooling on Reflooding Phenomena -SCTF Core I Forced Feed Floding Test-, JAERI-M 83-122, (1983).

(8) M. Sobajima et al., Examination of Repeatability in Reflood Phenomena under Forced Flooding in SCTF Core I Tests, JAERI-M 83-237, (1984).

(9) T. Iwamura et al., Effects of Upper Plenum Injection on Thermo-Hydrodynamic Behavior under Refill and Reflood Phases, JAERI-M 84-221, (1984).

(10) M. Sobajima et al., Characteristics of Lower Plenum Injection Reflood Tests in SCTF Core I, JAERI-M 84-223, (1984).

(11) Y. Murao et al., Analytical Study of Thermo-Hydrodynamic Behavior of Reflood-Phase during LOCA, J. Nucl. Sci. Tech. vol.16, No. 11, pp802-817 (1979).

(12) M. Osakabe and Y. Sudo., Heat Transfer Calculation of Simulated Heater Rods throughout Reflood Phase in Postulated PWR-LOCA Experiments, J. Nucl. Sci. Tech vol. 20, No.7, pp 559-570 (1983).

(13) D. Liles et al., TRAC-PF1/Model An Advanced Best-Estimate Computer Program for Pressurized Water Reactor Thermal-Hydraulic Analysis, NUREG/CR-3567, (1984).

Table 2-1 Test conditions for Tests S2-SH1, S2-SH2 and S2-06

	Test S2-SH1 (base case)	Test S2-SH2 (flat power)	Test S2-06 (steep power)
Test type	modified cold leg injection		
Initial system pressure	0.2MPa	0.2MPa	0.2MPa
Initial total power	7.12MW	7.12MW	7.12MW
Maximum rod temperature at BOCREC			
Bundles 1 & 2	1039K	1012K	1060K
" 3 & 4	1076K	1022K	1163K
" 5 & 6	1061K	1040K	1072K
" 7 & 8	1019K	1035K	955K
Acc injection condition			
Flow rate	18.9 kg/s	19.3 kg/s	19.1 kg/s
Temperature	363K	364K	362K
Time	55s	55s	55s
LPCI injection condition			
Flow rate	5.41 kg/s	5.41 kg/s	5.41 kg/s
Temperature	350K	350K	350K
Radial power ratio			
Bundles 1 & 2	1.001	1.0	1.0
" 3 & 4	1.065	1.0	1.2
" 5 & 6	1.015	1.0	1.0
" 7 & 8	0.919	1.0	0.8
Decay curve	1.02 × (ANS + Actinides)		

Table 2-2 Chronologies of major events for Tests S2-SH1, S2-SH2 and S2-06

(1) Test S2-SH1	Time after BOCREC (s)
Core power "ON"	- 146
Acc injection initiation	- 3
BOCREC	0
Maximum containment tank-II pressure (0.22 MPa)	29
Core power decay initiation	37
Switching of ECC from lower plenum to cold leg and from Acc to LPCI	52
Maximum core pressure (0.266 MPa)	54
Maximum core temperature (1166K)	105.5
Whole core quenched	492.5

(2) Test S2-SH2	Time after BOCREC (s)
Core power "ON"	- 139
Acc injection initiation	- 2.5
BOCREC	0
Maximum containment tank-II pressure (0.217 MPa)	32.5
Core power decay initiation	37.5
Maximum core pressure (0.266 MPa)	53.5
Switching of ECC from lower plenum to cold leg and From Acc to LPCI	55
Maximum core temperature (1142K)	145
Whole core quenched	473.5

(3) Test S2-06	Time after BOCREC (s)
Core power "ON"	- 150
Acc injection initiation	- 3.5
BOCREC	0
Maximum containment tank-II pressure (0.217 MPa)	29
Core power decay initiation	36.5
Maximum core temperature (1244K)	42
Switching of ECC from lower plenum to cold leg and from Acc to LPCI	54
Maximum core pressure (0.274 MPa)	59
Whole core quenched	475.5

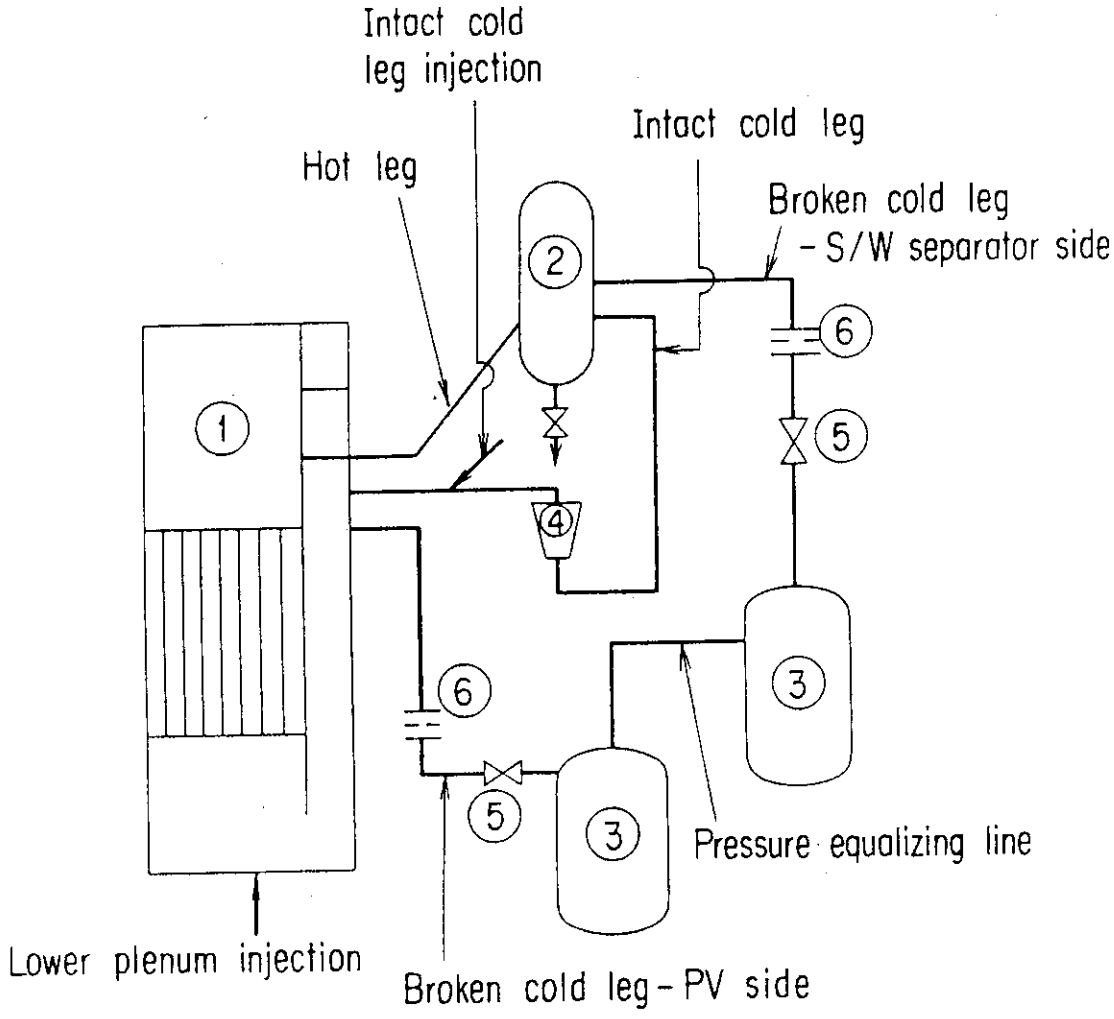

① Pressure vesel
② Steam / water separator
③ Containment tanks
④ Pump simulator
⑤ Break valves
⑥ Flow resistance simulators

Fig. 2-1 Schematic diagram of SCTF

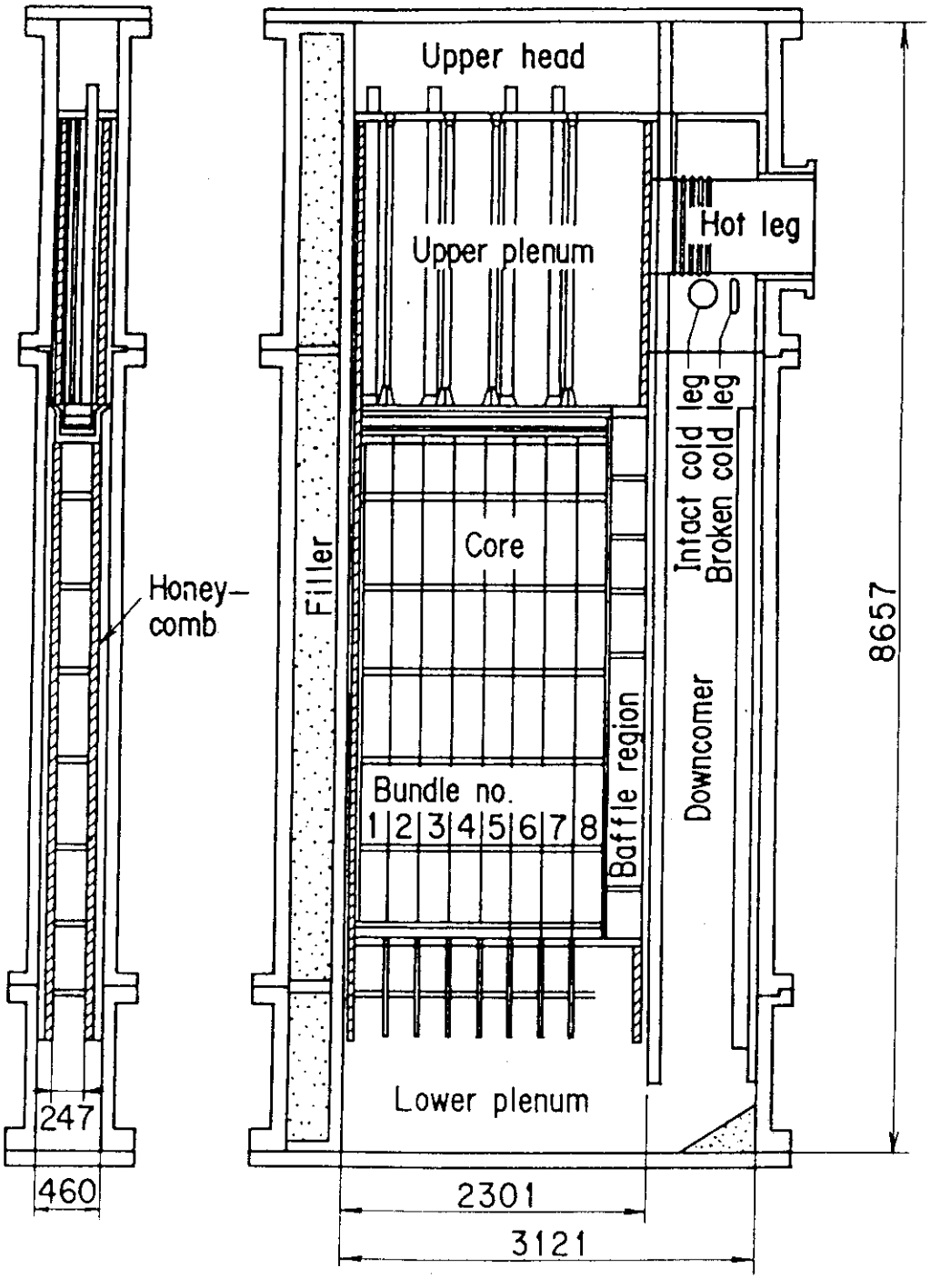

Fig. 2-2 Vertical cross section of pressure vessel

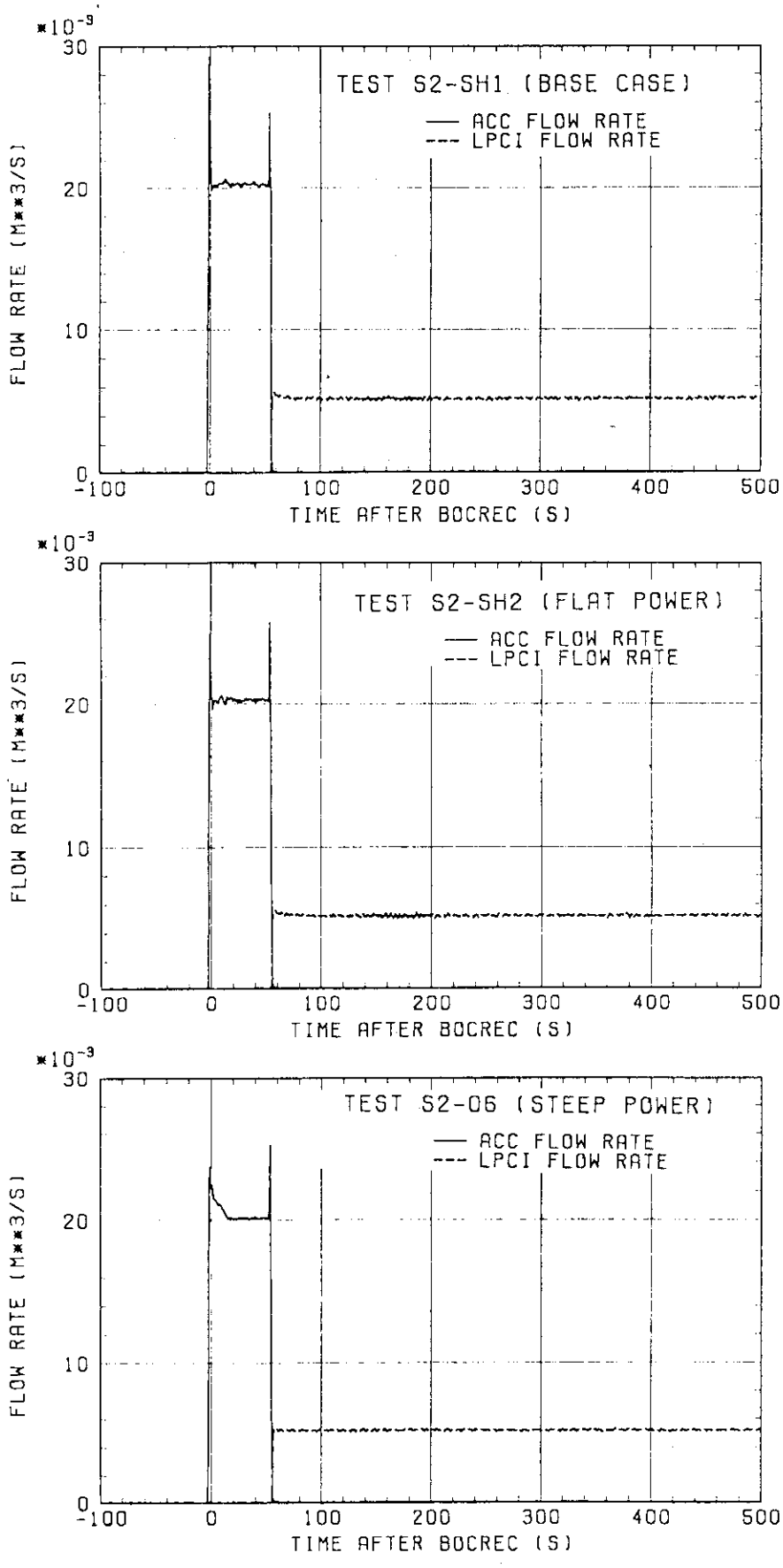

Fig. 3-1 ECC water injection rate

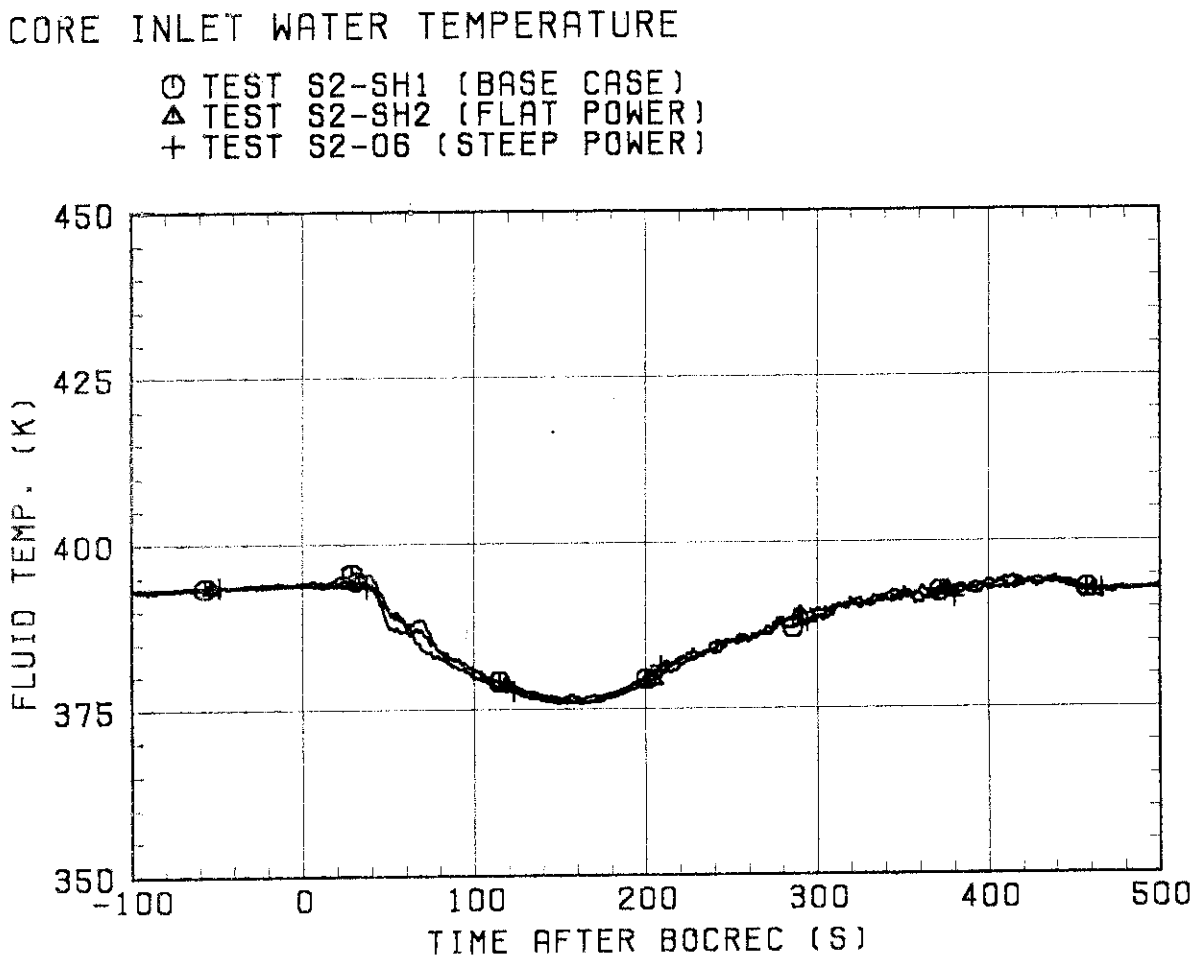

Fig. 3-2 Comparison of core inlet water temperature

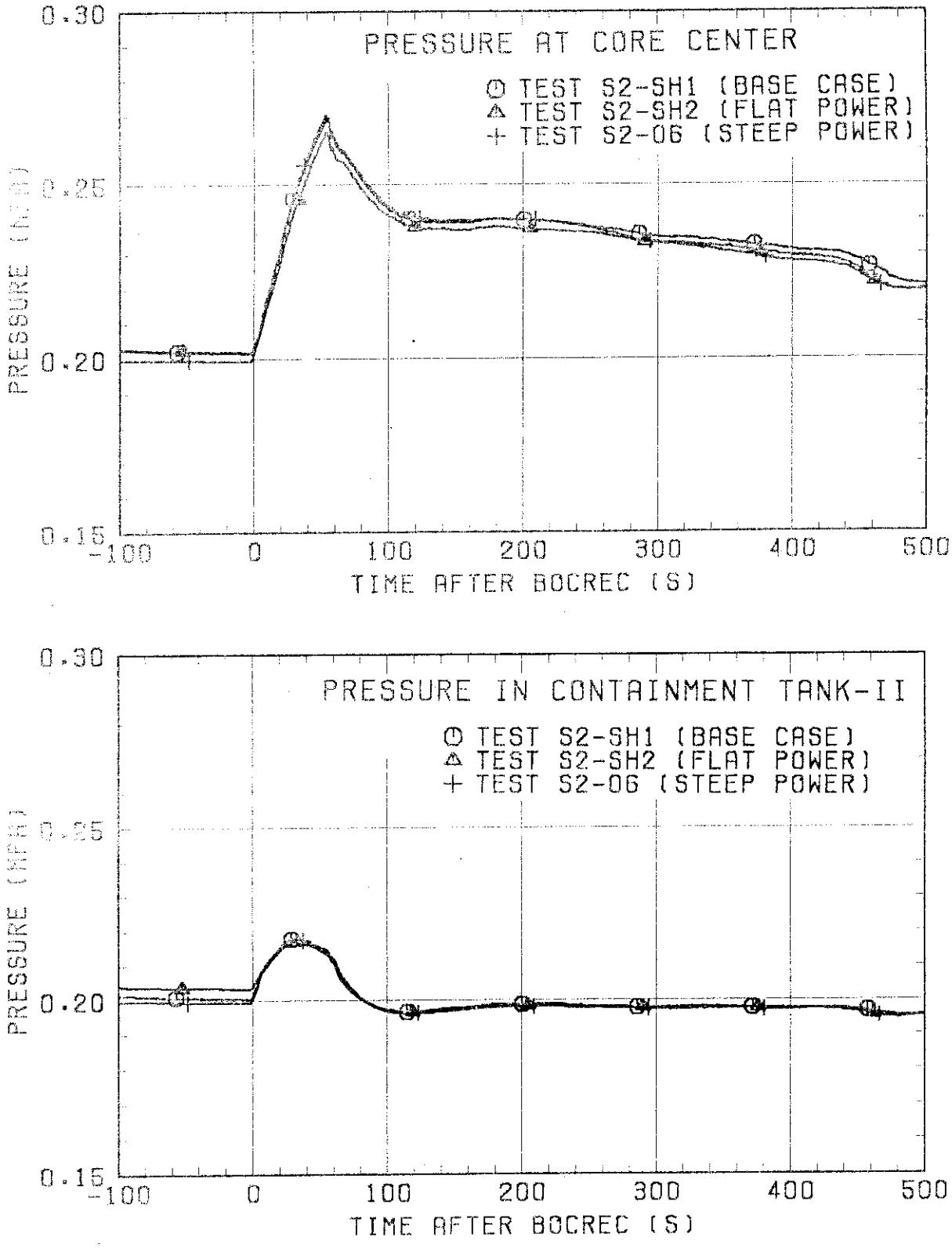

Fig. 3-3 Comparison of pressures at core center and containment tank II

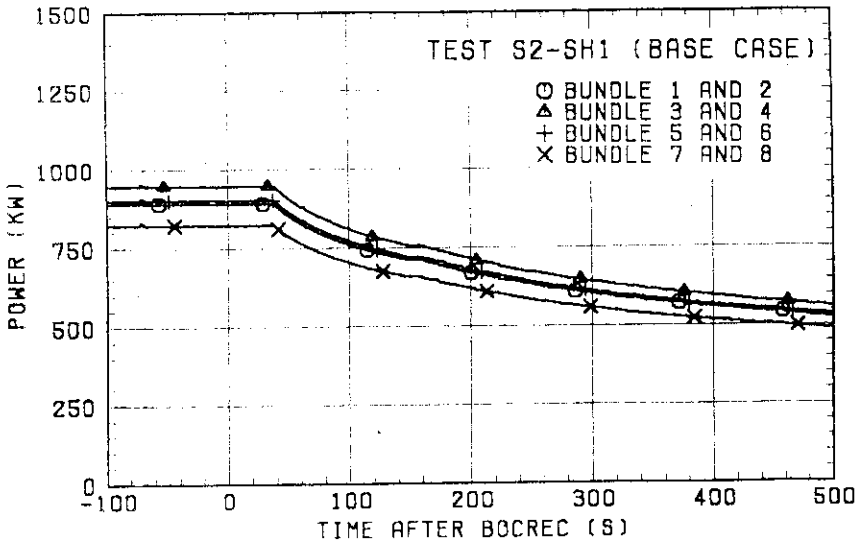

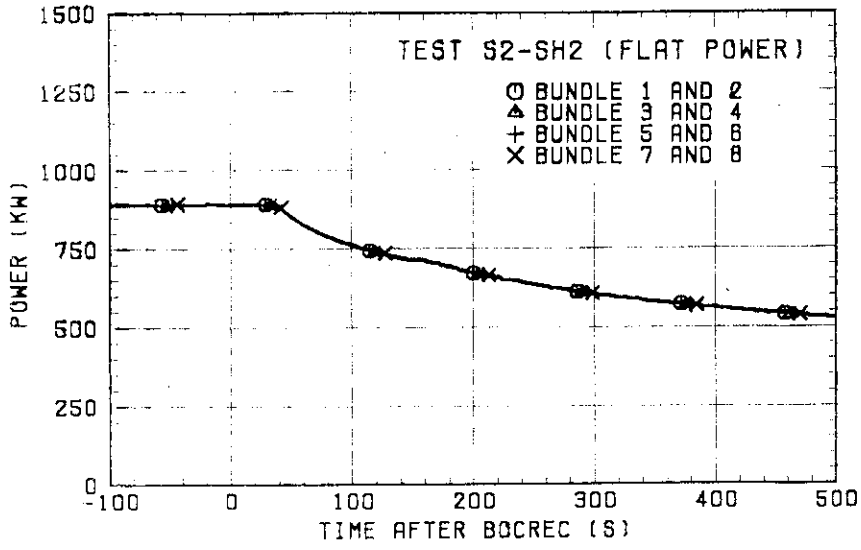

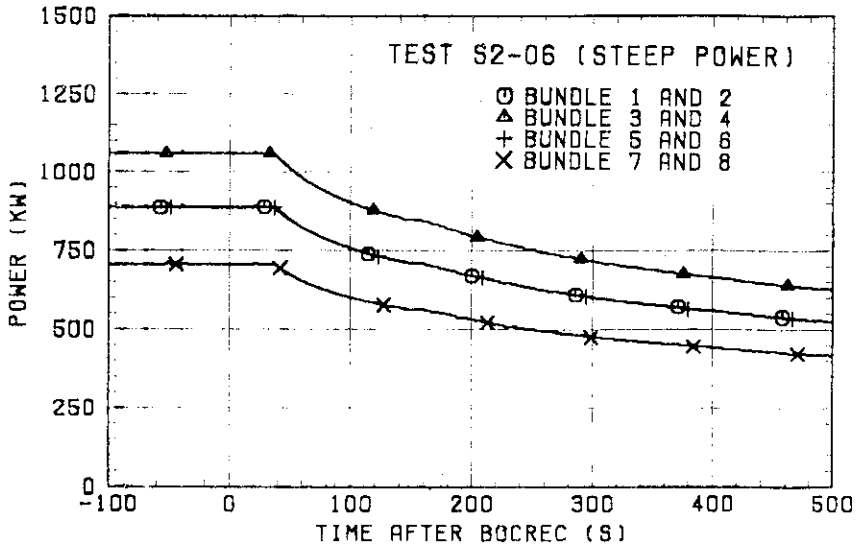

Fig. 3-4 Comparison of core heating power

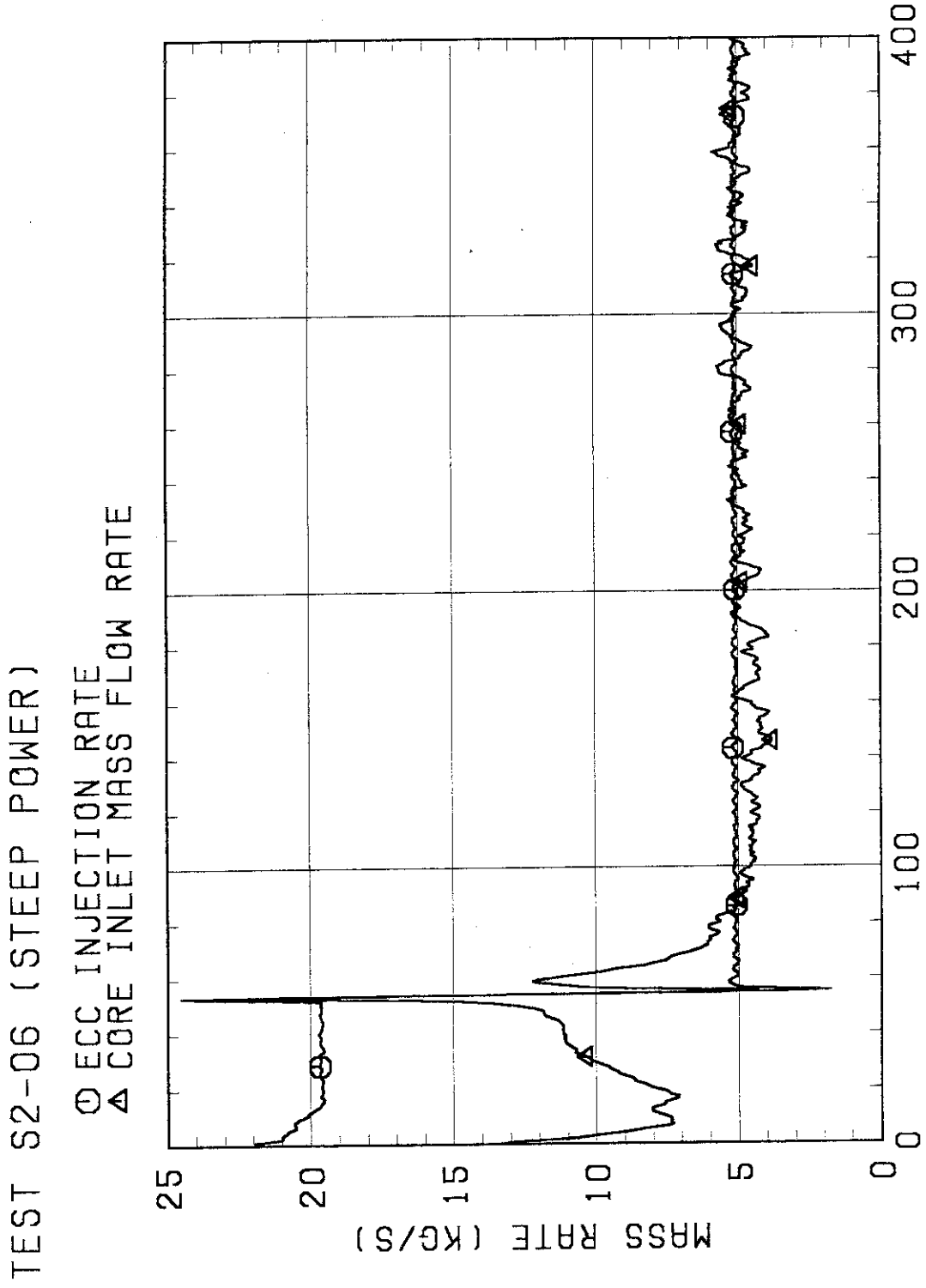

Fig. 3-5 Comparison of core inlet mass flow rate and Ecc water injection rate

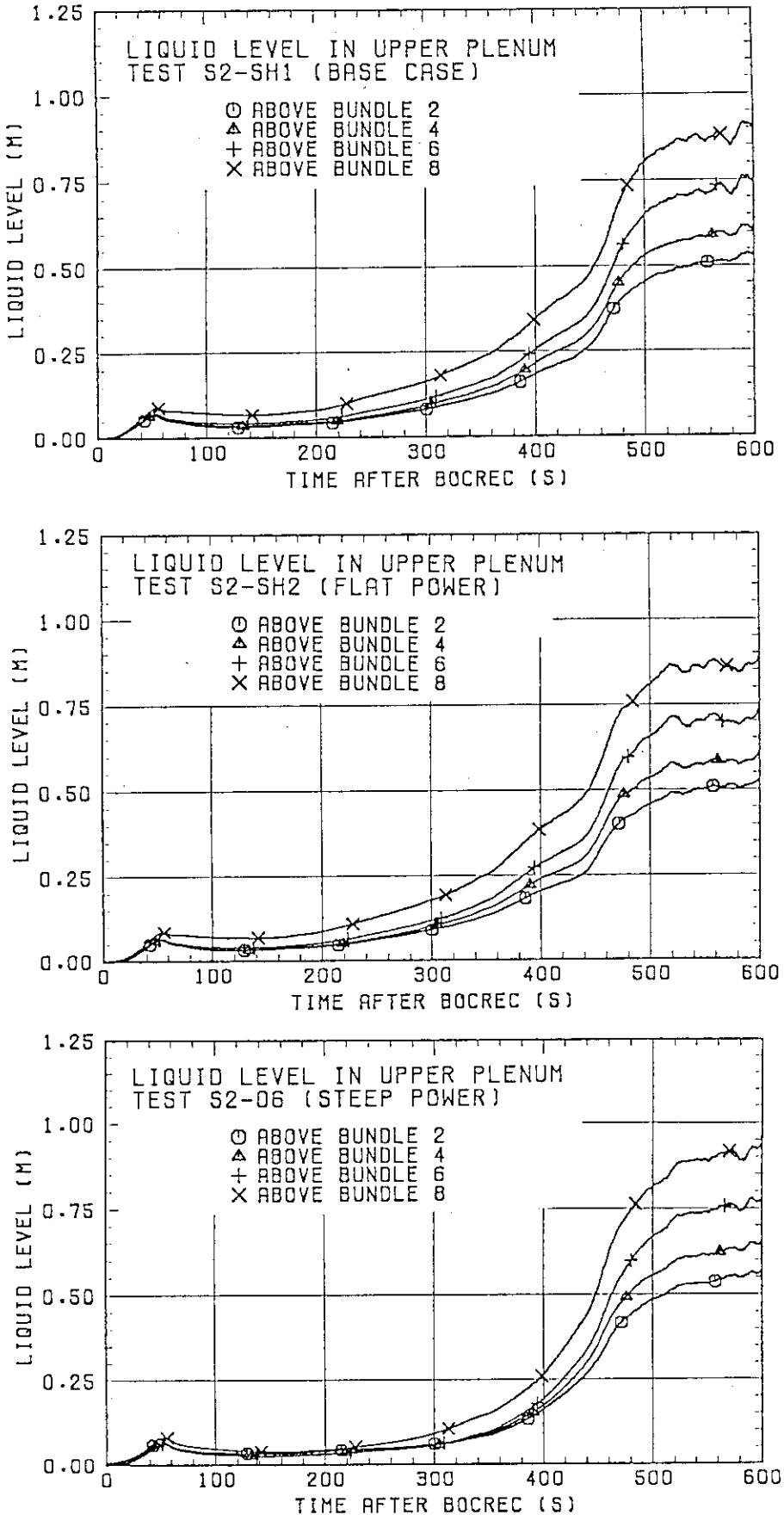

Fig. 3-6 Comparison of liquid levels in upper plenum

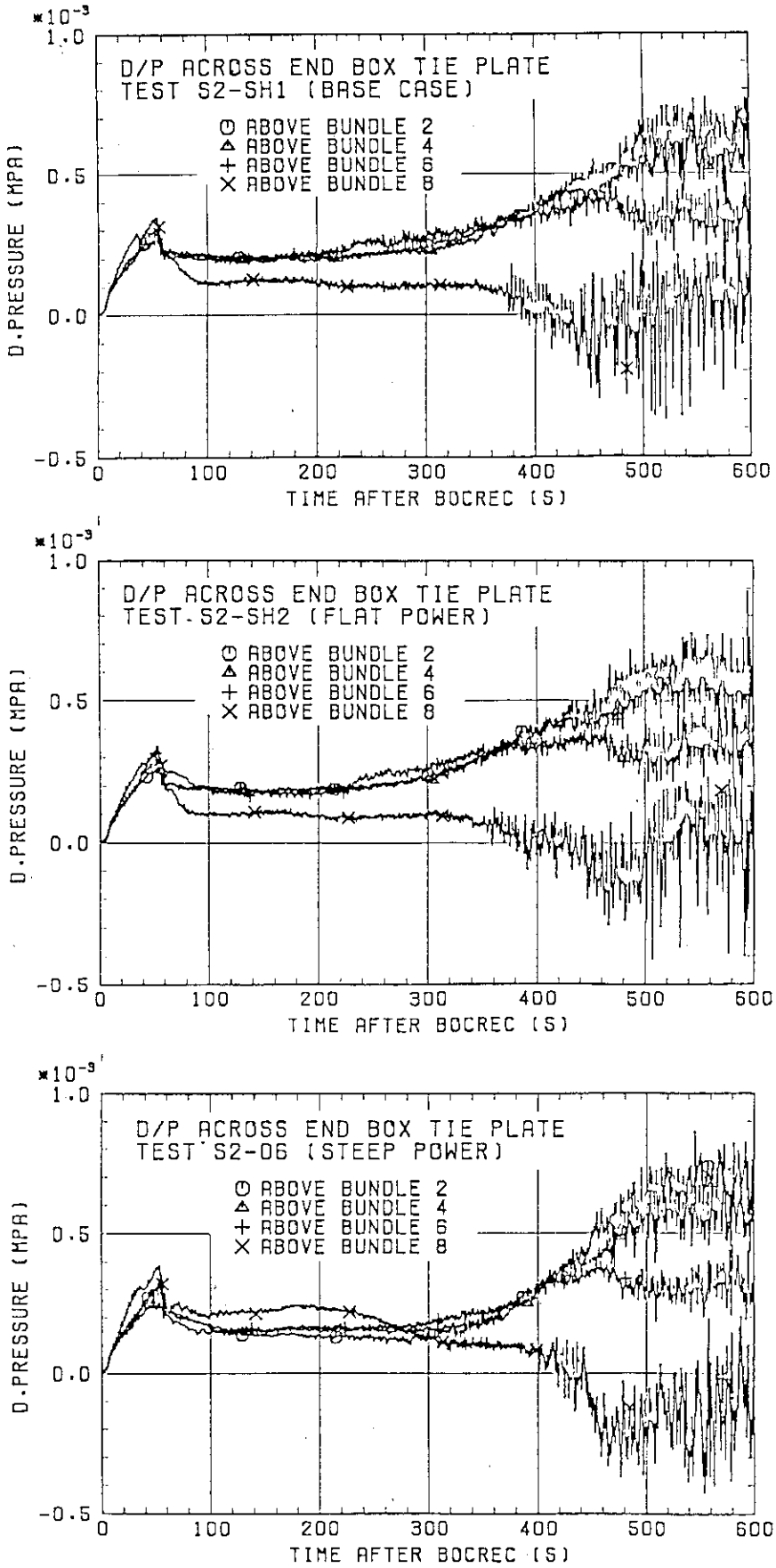

Fig. 3-7 Comparison of differential pressures across end box tie plate

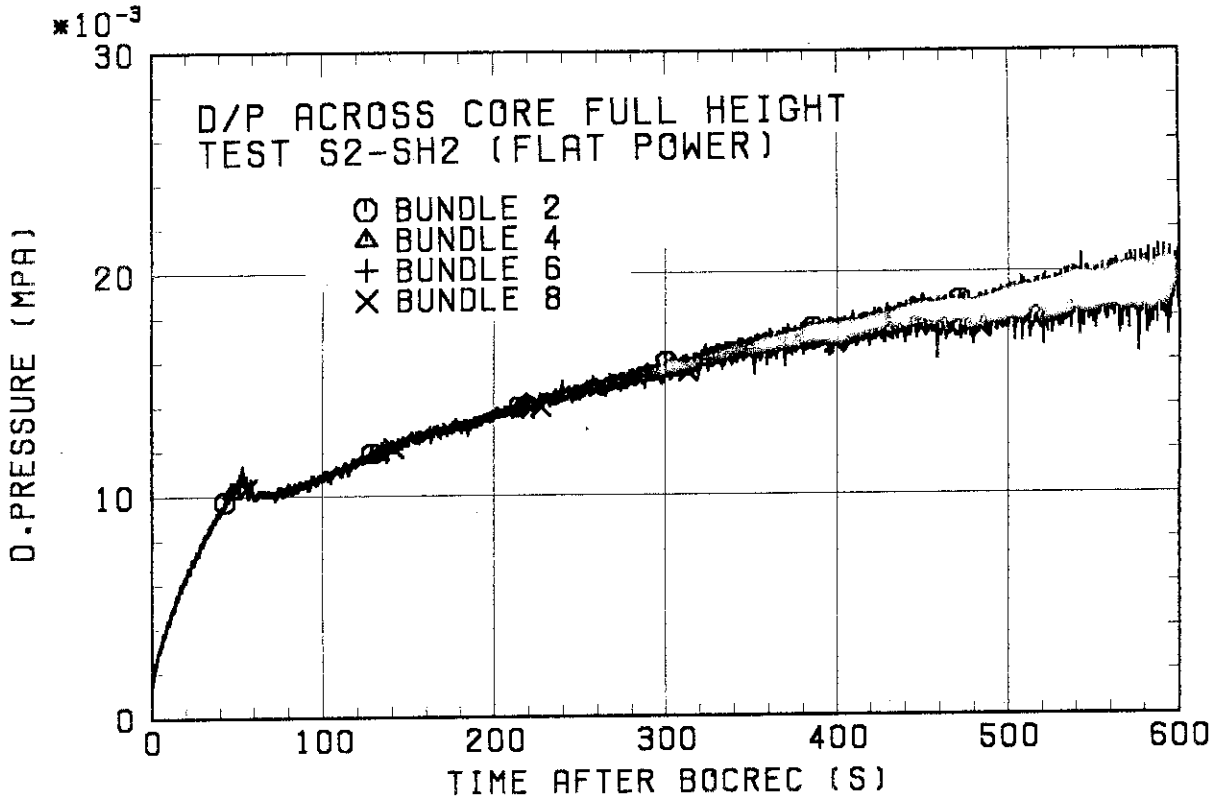

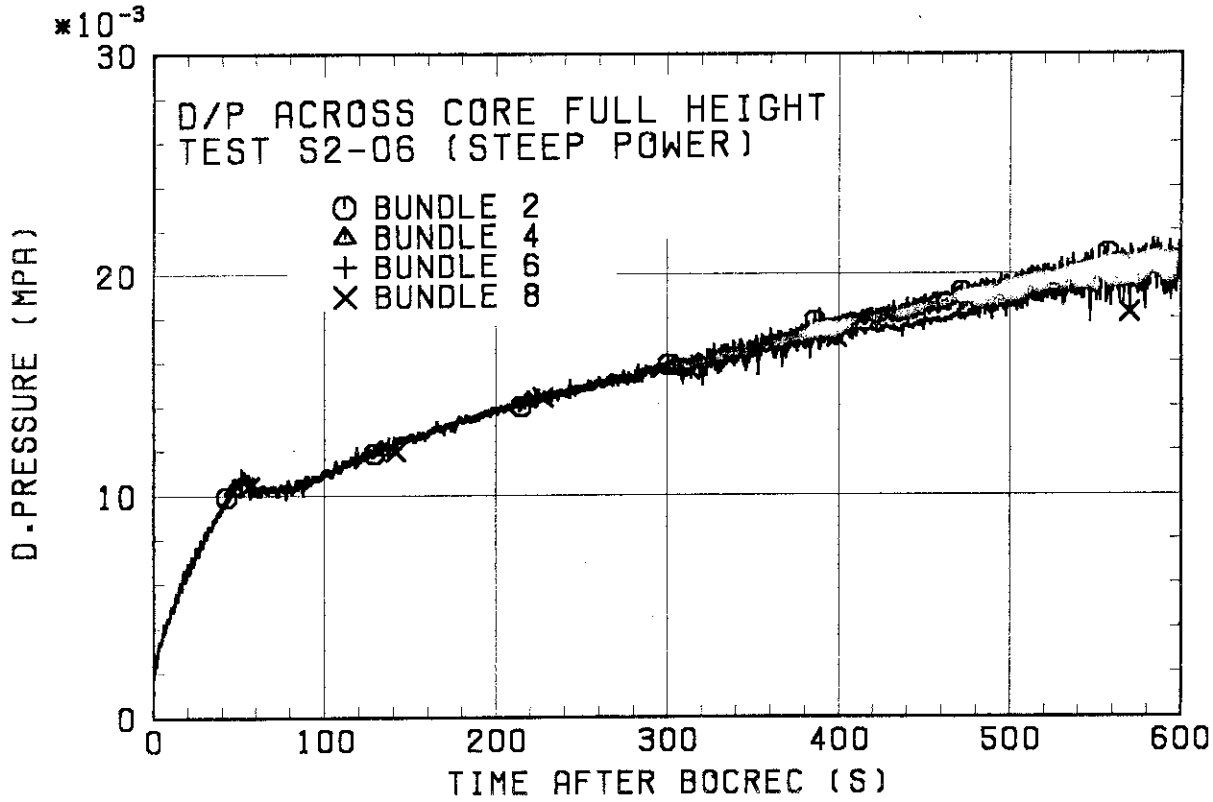

Fig. 3-8 Comparison of core full height differential pressures

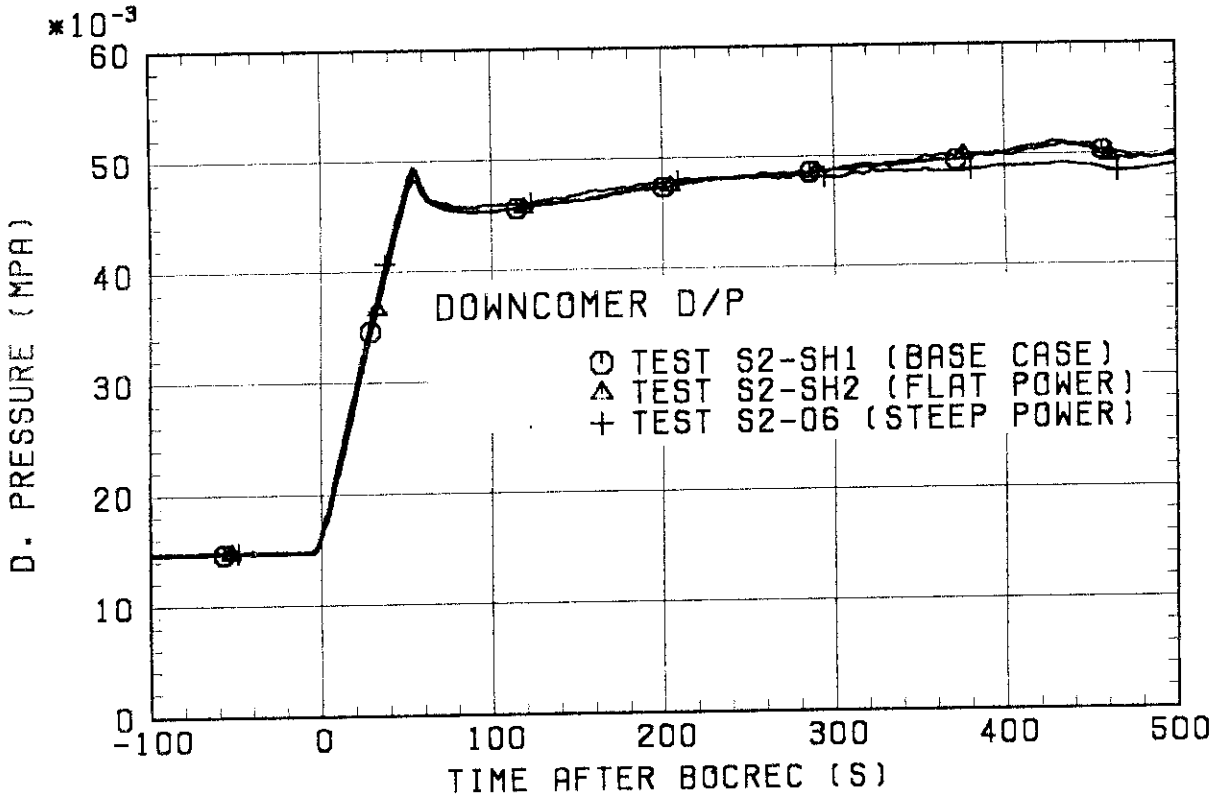

Fig. 3-9 Comparison of differential pressures in downcomer

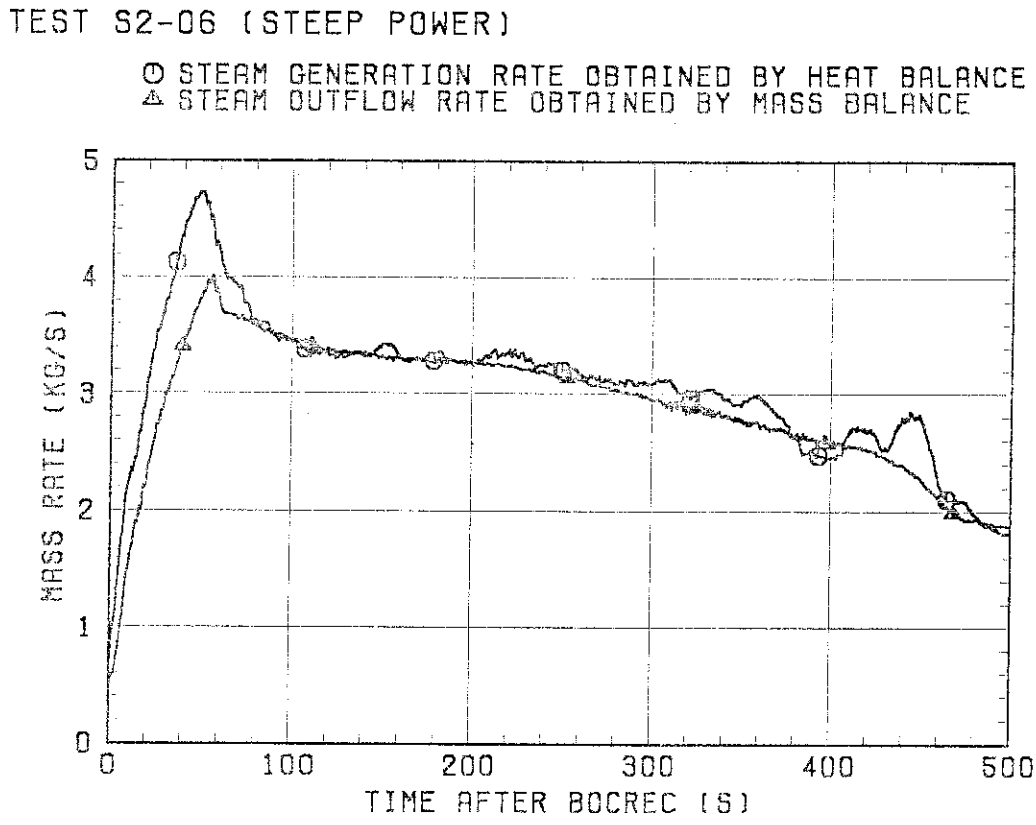

Fig. 3-10 Comparison between steam generation rate in core obtained by heat balance method and steam outflow rate through hot leg obtained by mass balance method in Test S2-06

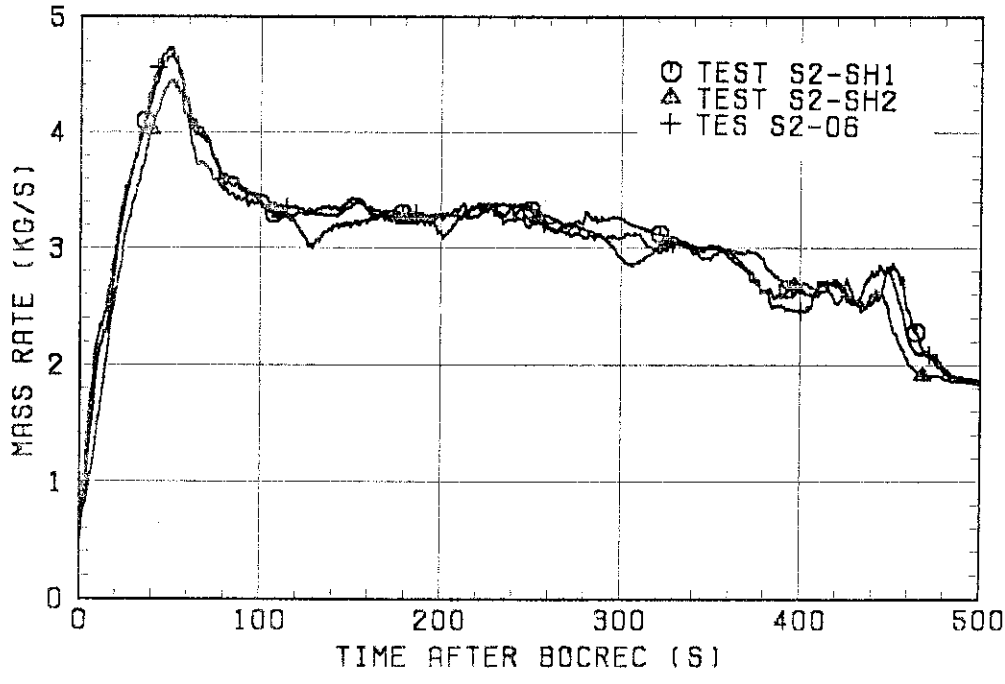

Fig. 3-11 Comparison of steam generation rates in core

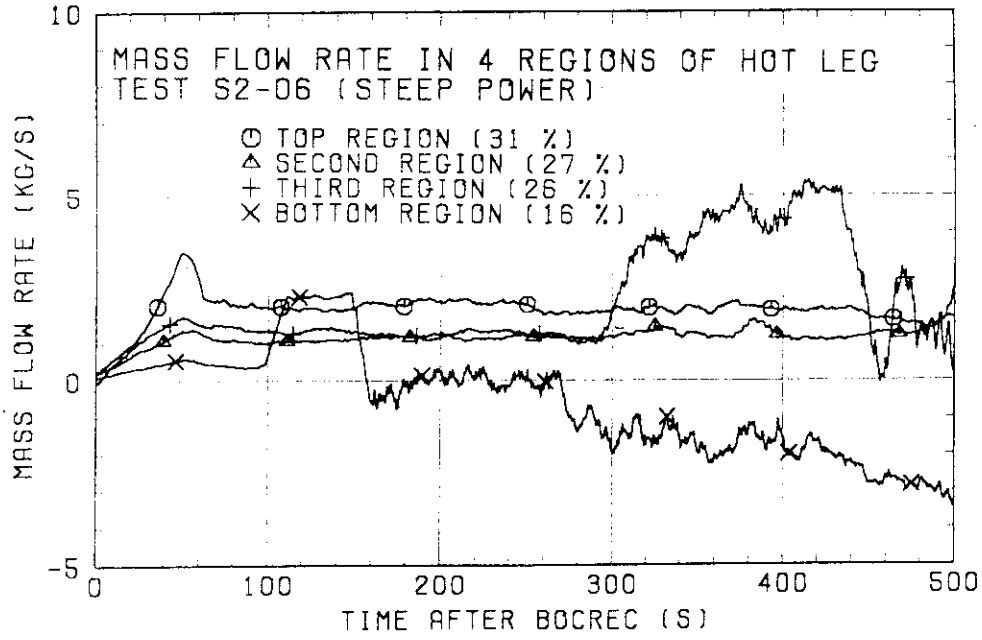

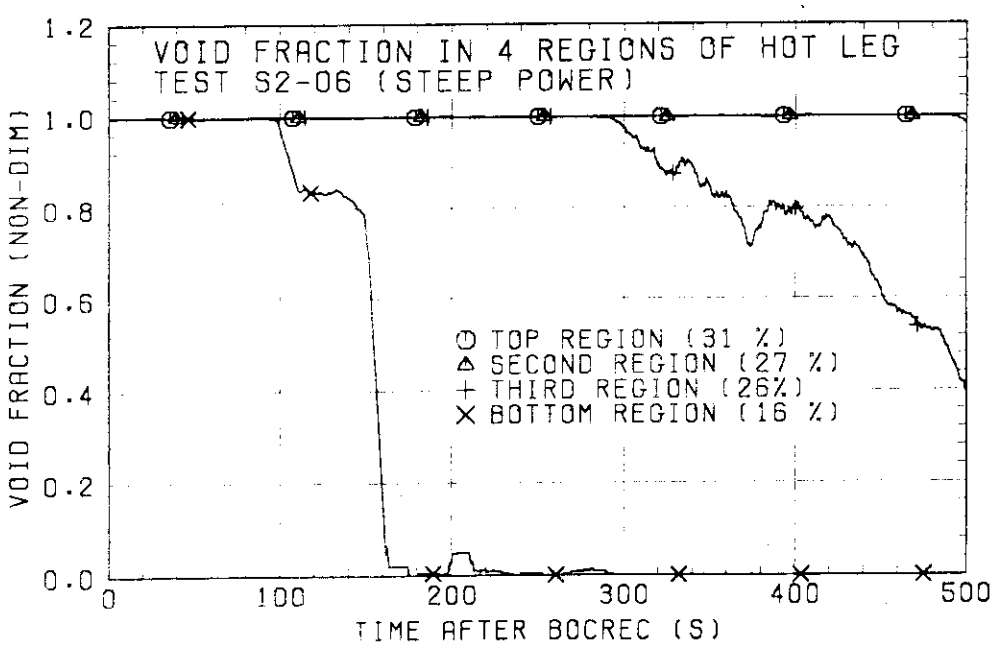

Fig. 3-12 Mass flow rates and void fractions in 4 regions of hot leg in Test S2-06

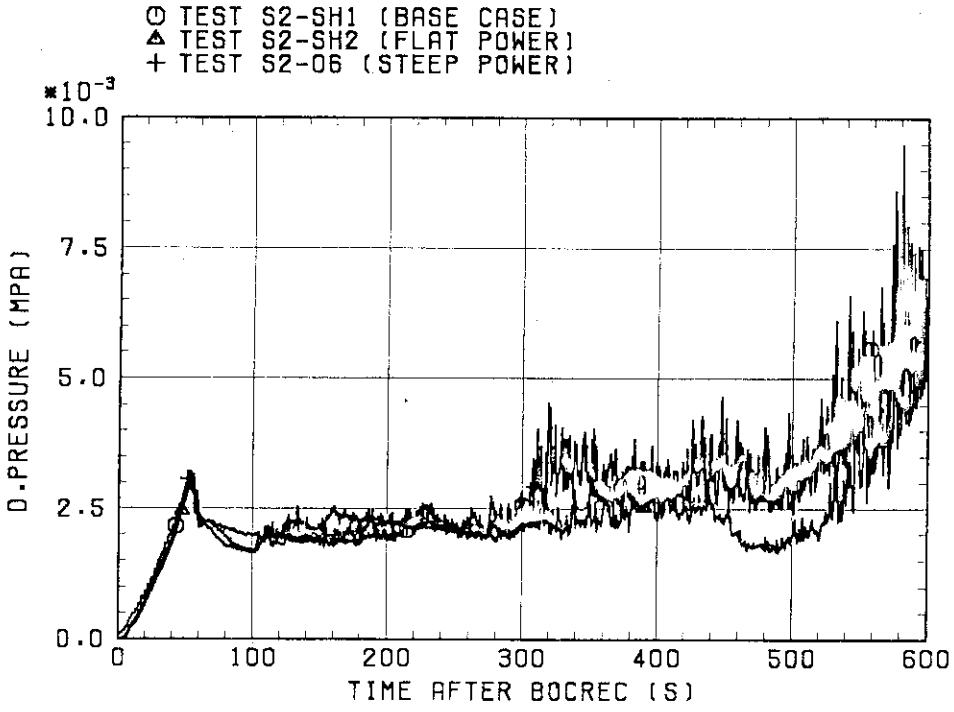

Fig. 3-13 Comparison of differential pressures across hot leg

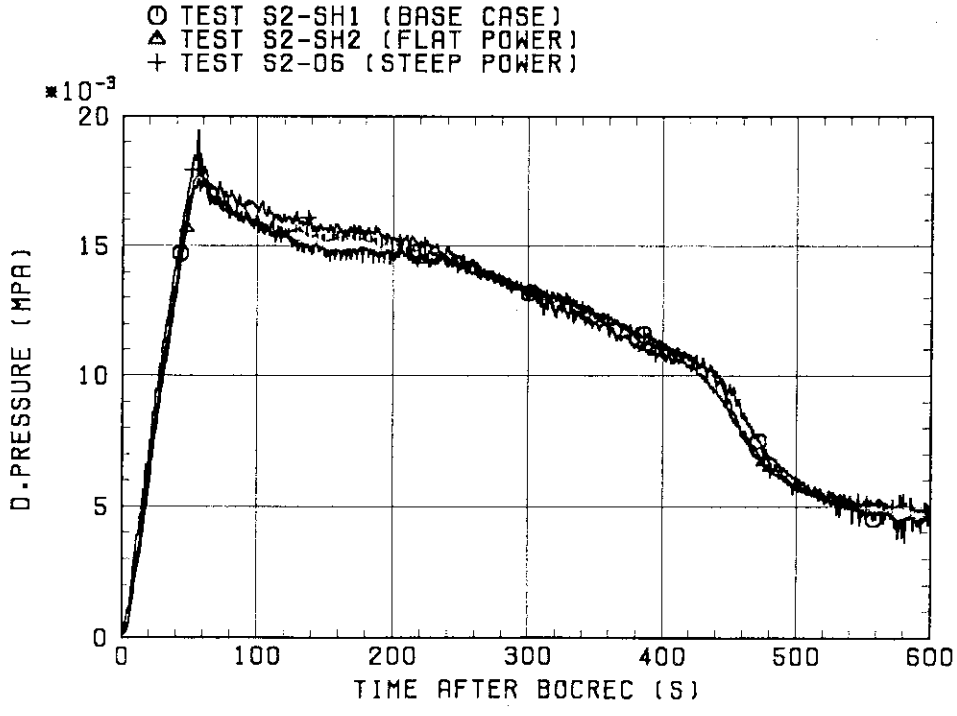

Fig. 3-14 Comparion of diffrential pressures across intact cold leg

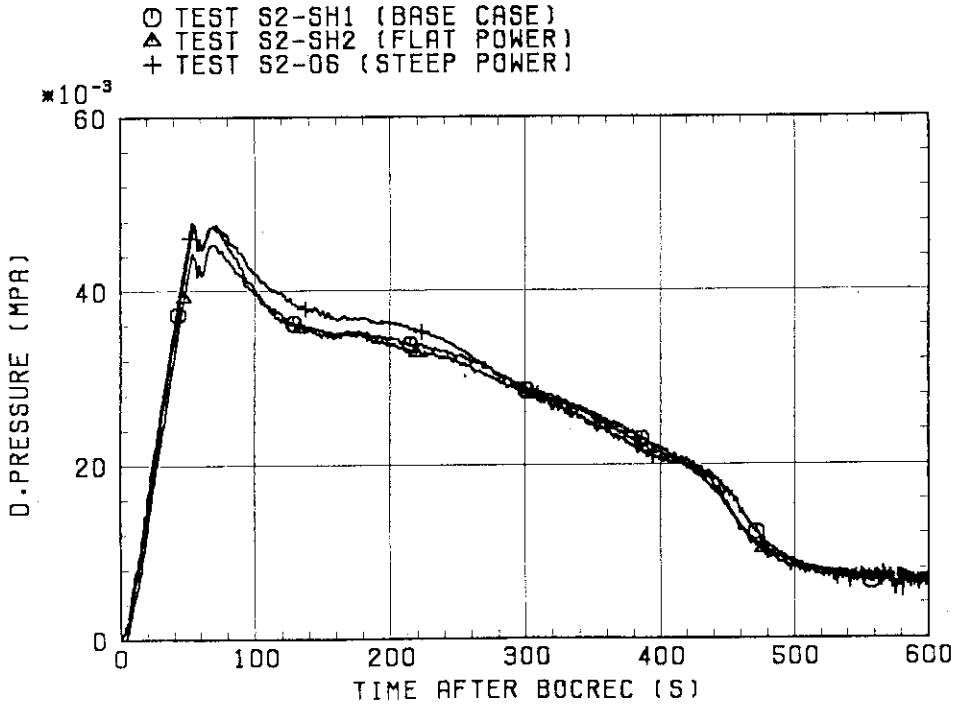

Fig. 3-15 Comparison of differential pressures across broken cold leg steam/water separator side

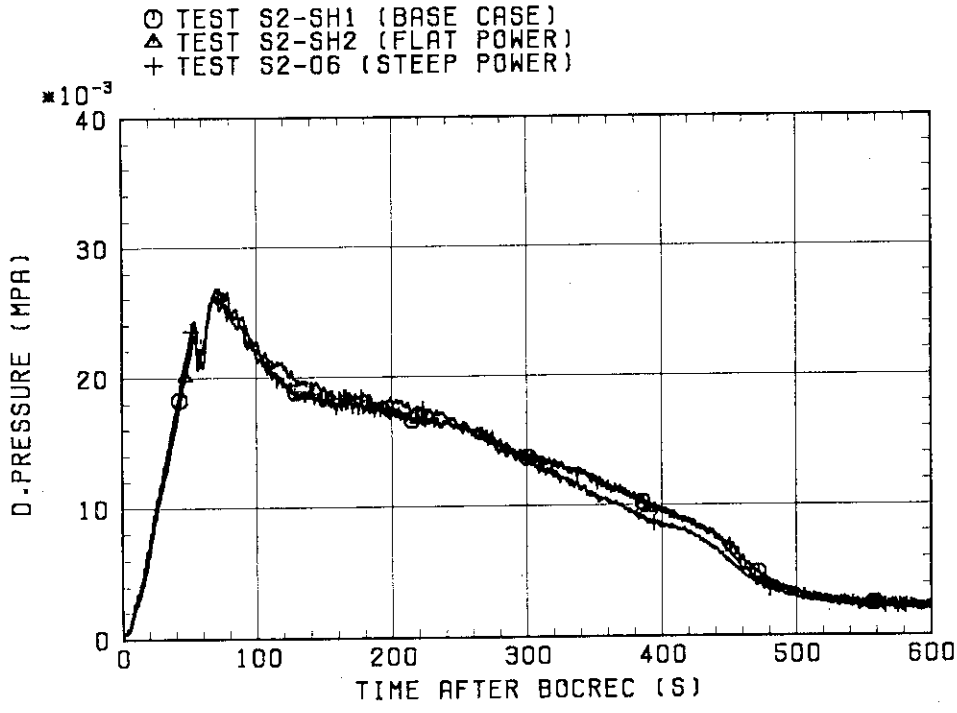

Fig. 3-16 Comparison of differential pressures across broken cold leg pressure vessel side

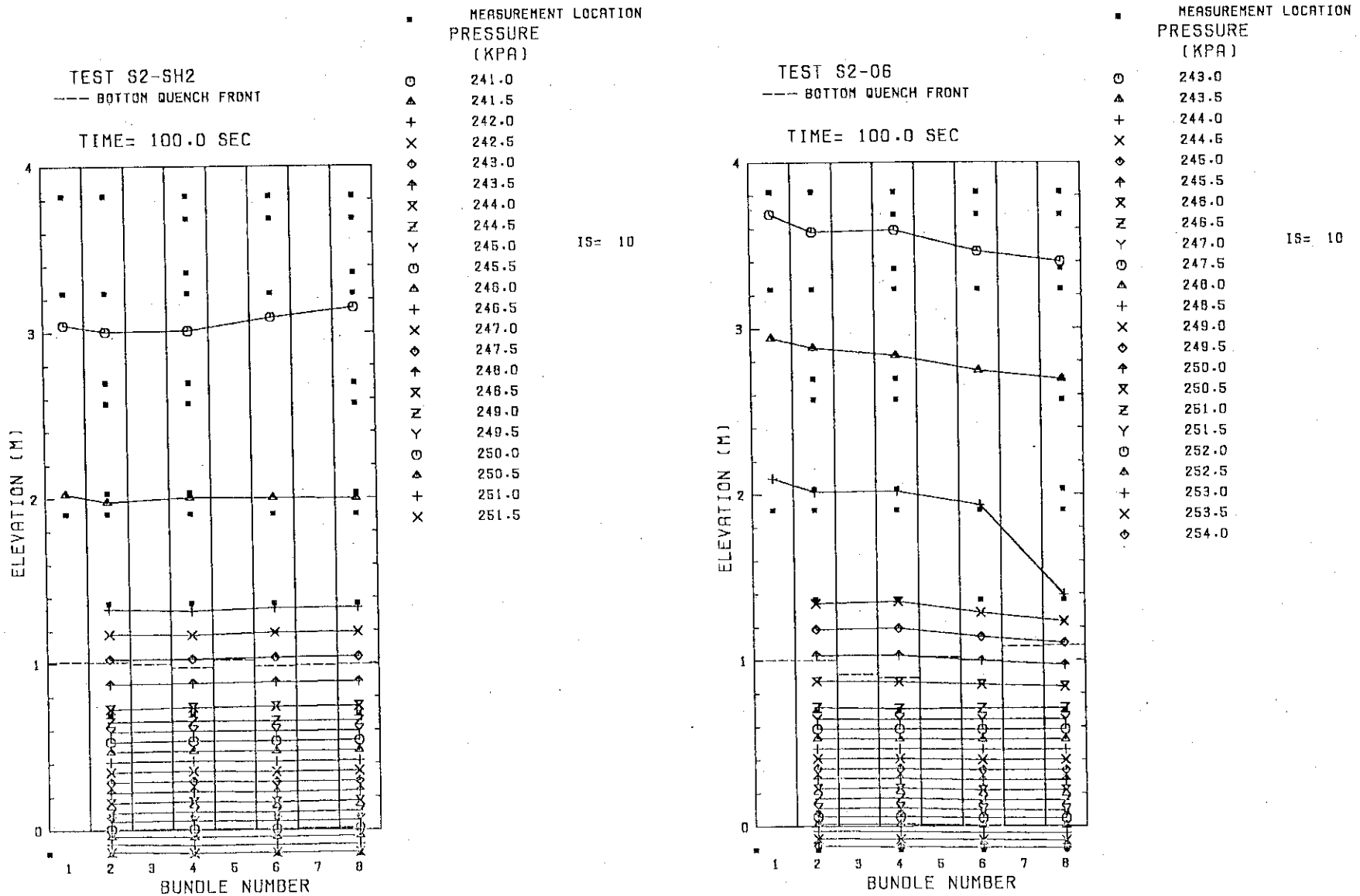

Fig.3-17(a) Comparison of equal pressure lines in core and bottom quench front distribution (100 s)

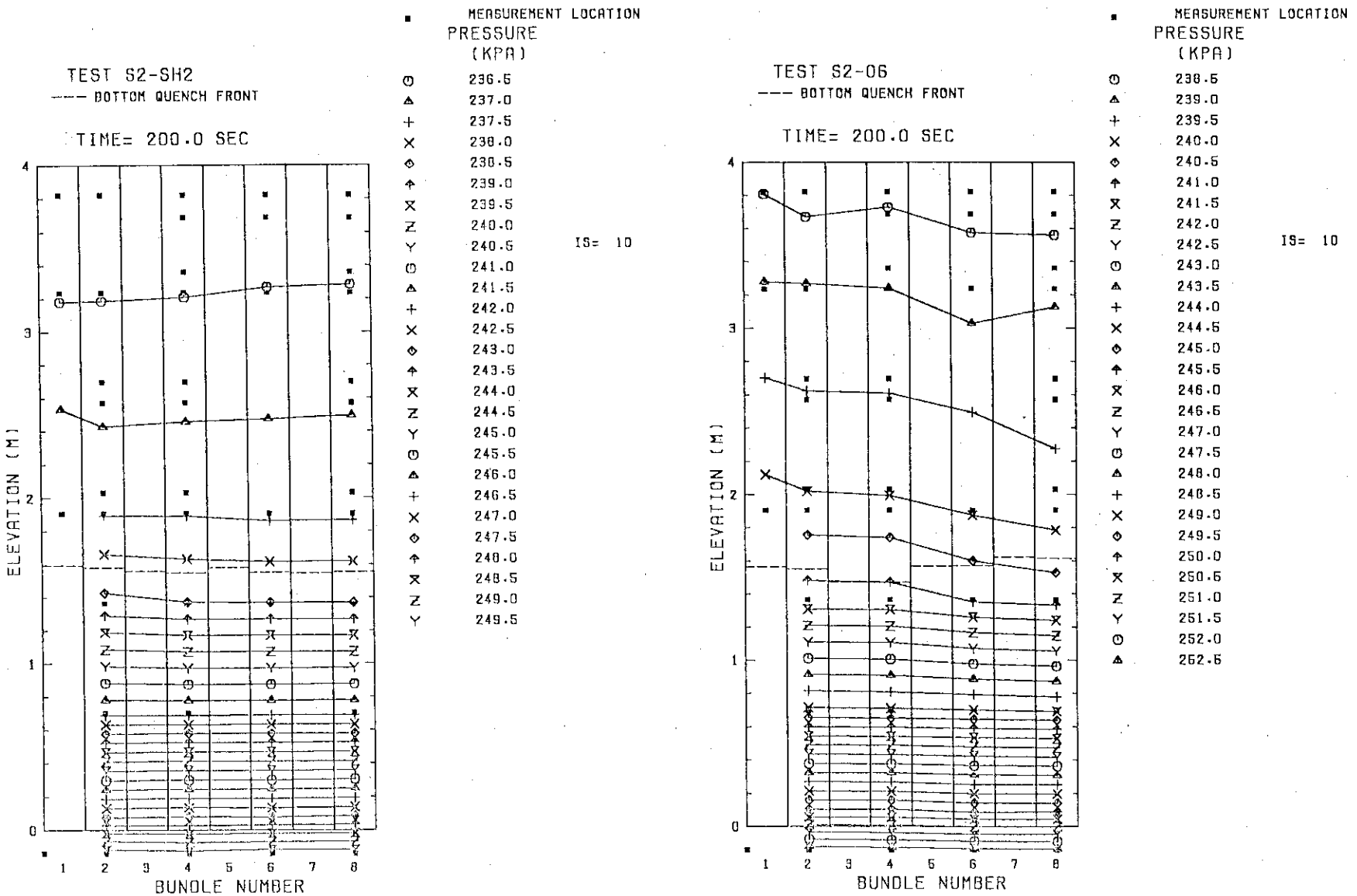

Fig.3-17(b) Comparison of equal pressure lines in core and bottom quench front distribution (200 s)

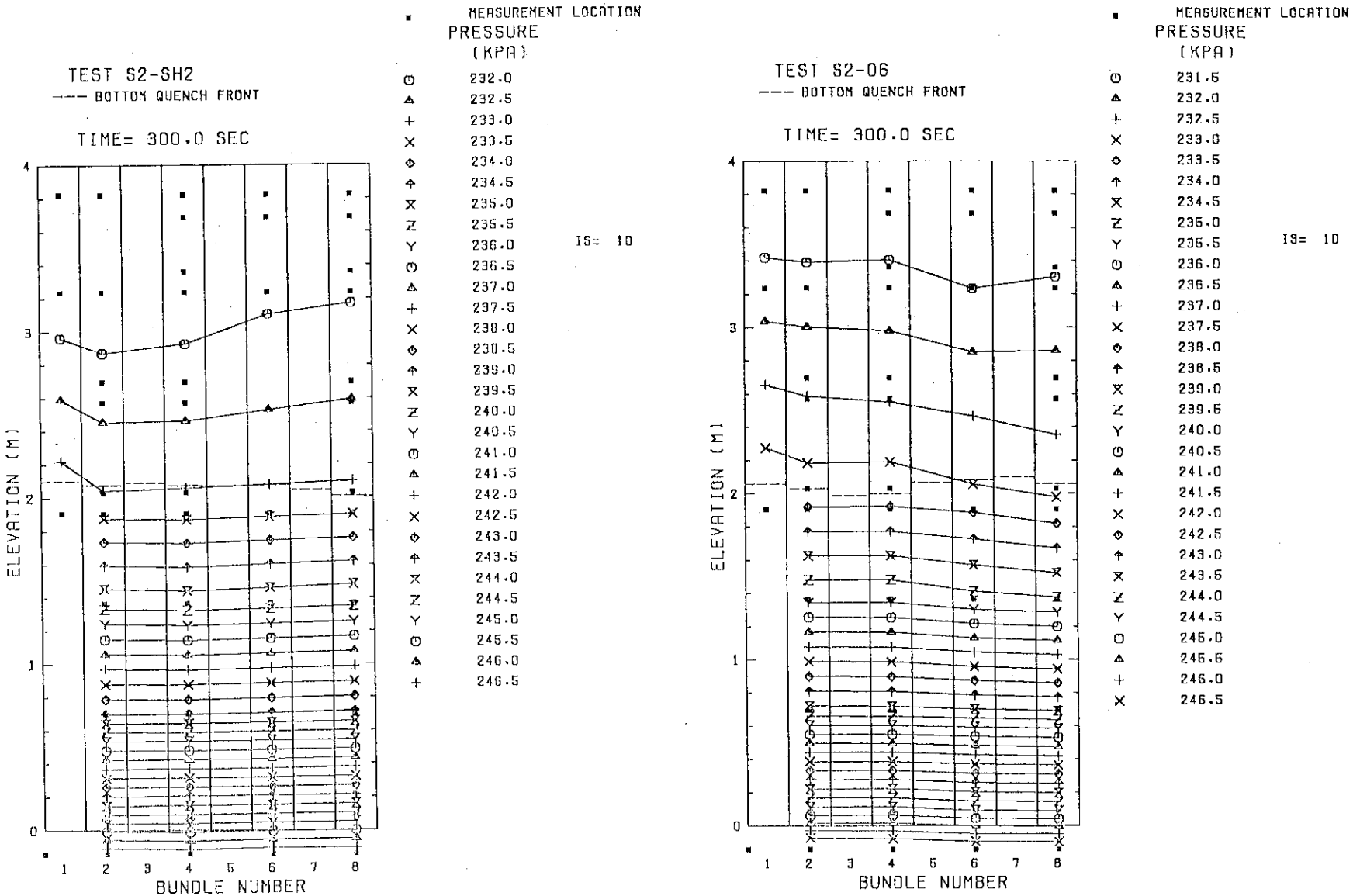

Fig.3-17(c) Comparison of equal pressure lines in core and bottom quench front distribution (300 s)

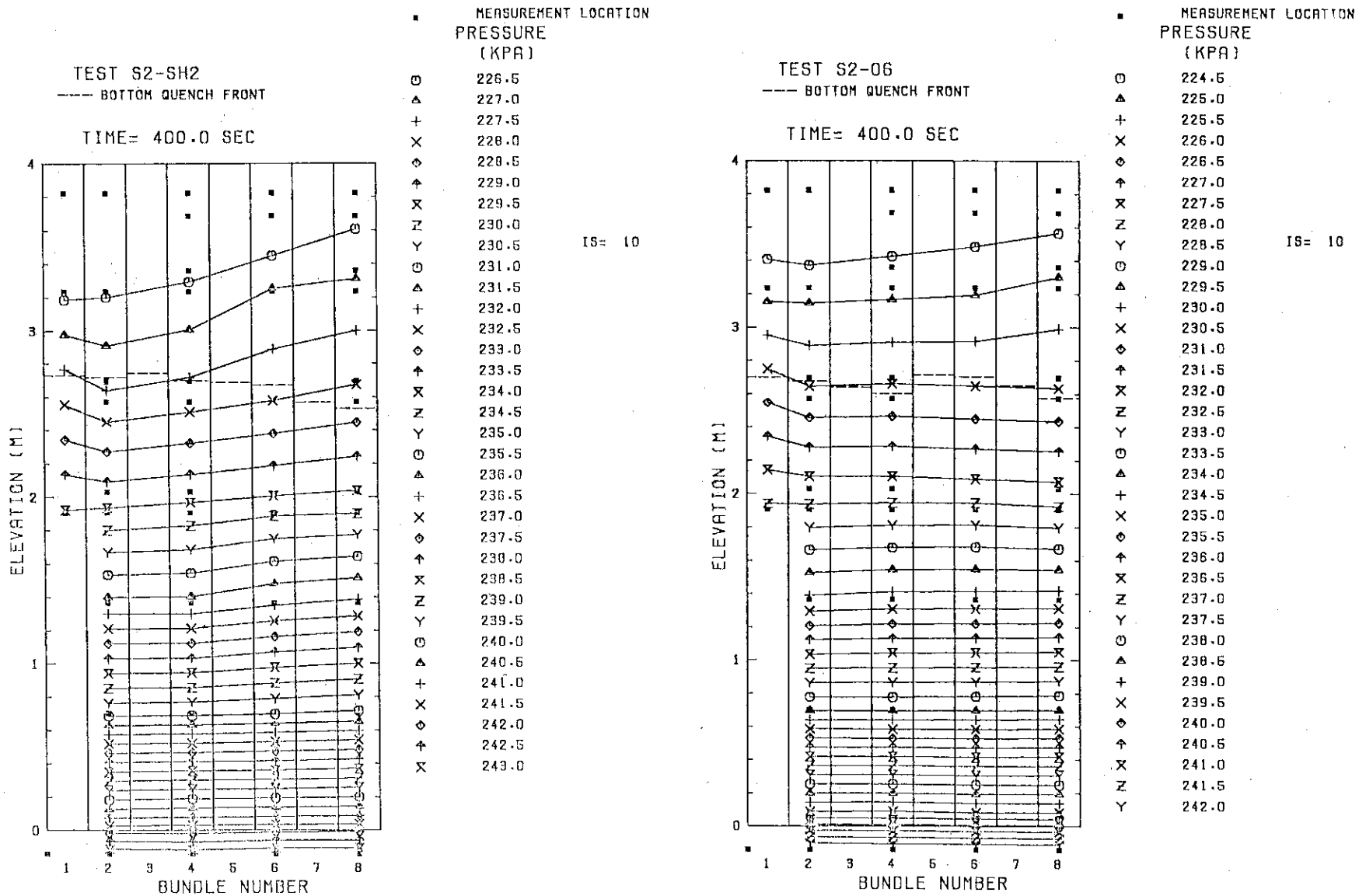

Fig.3-17(d) Comparison of equal pressure lines in core and bottom quench front distribution (400 s)

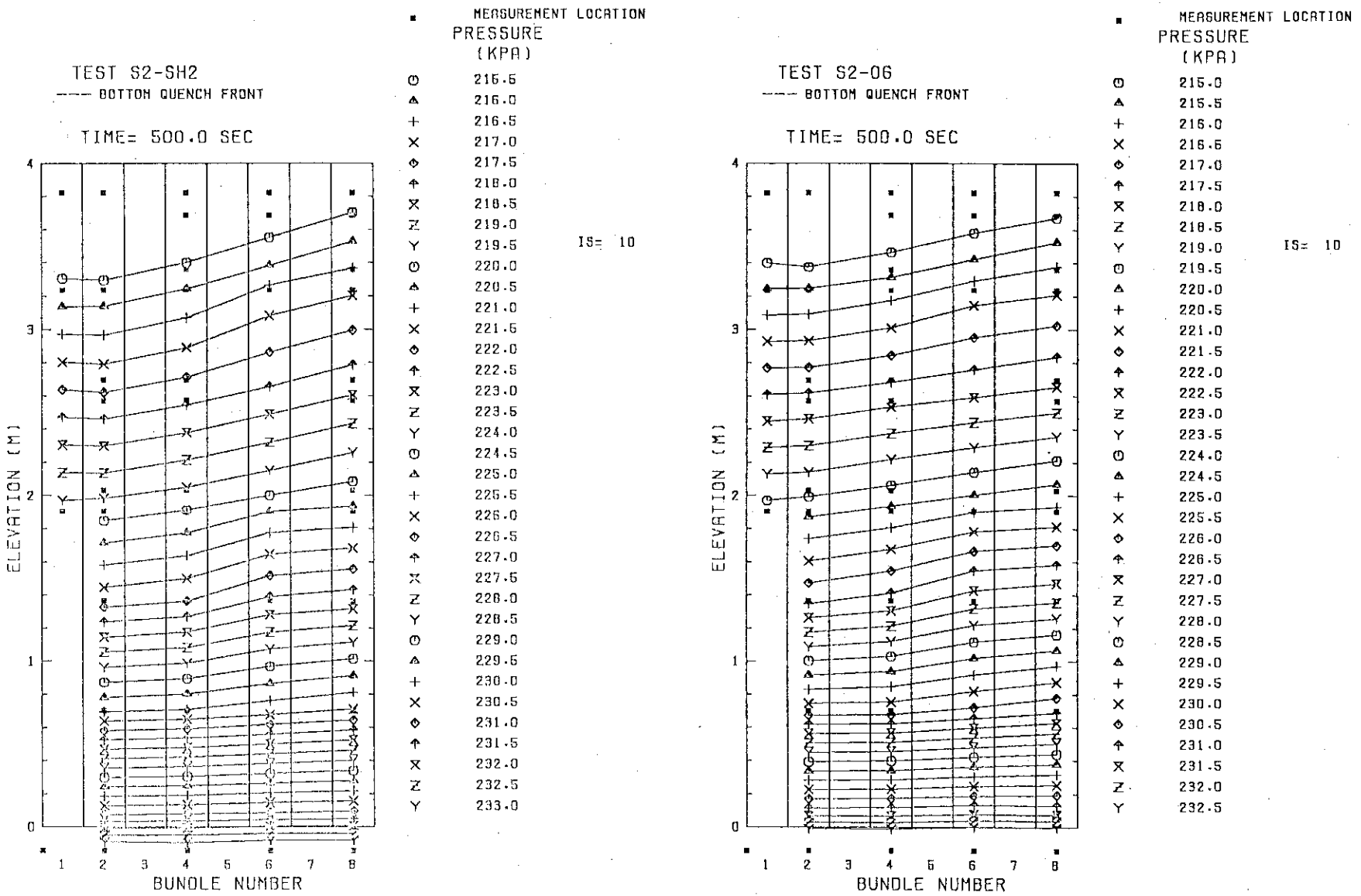

Fig.3-17(e) Comparison of equal pressure lines in core and bottom quench front distribution (500 s)

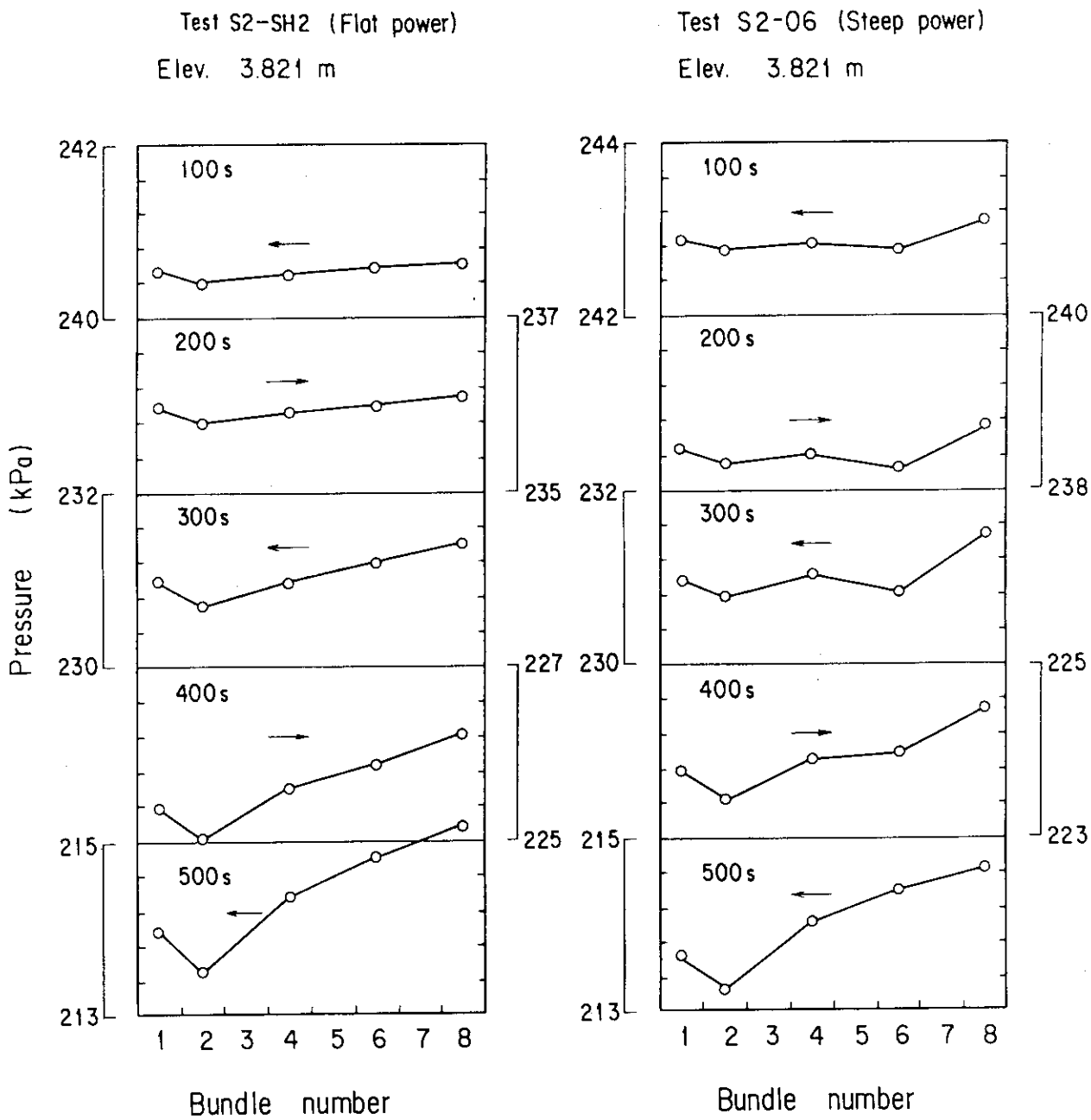

Fig. 3-18 Comparison of absolute pressure distribution at core outlet

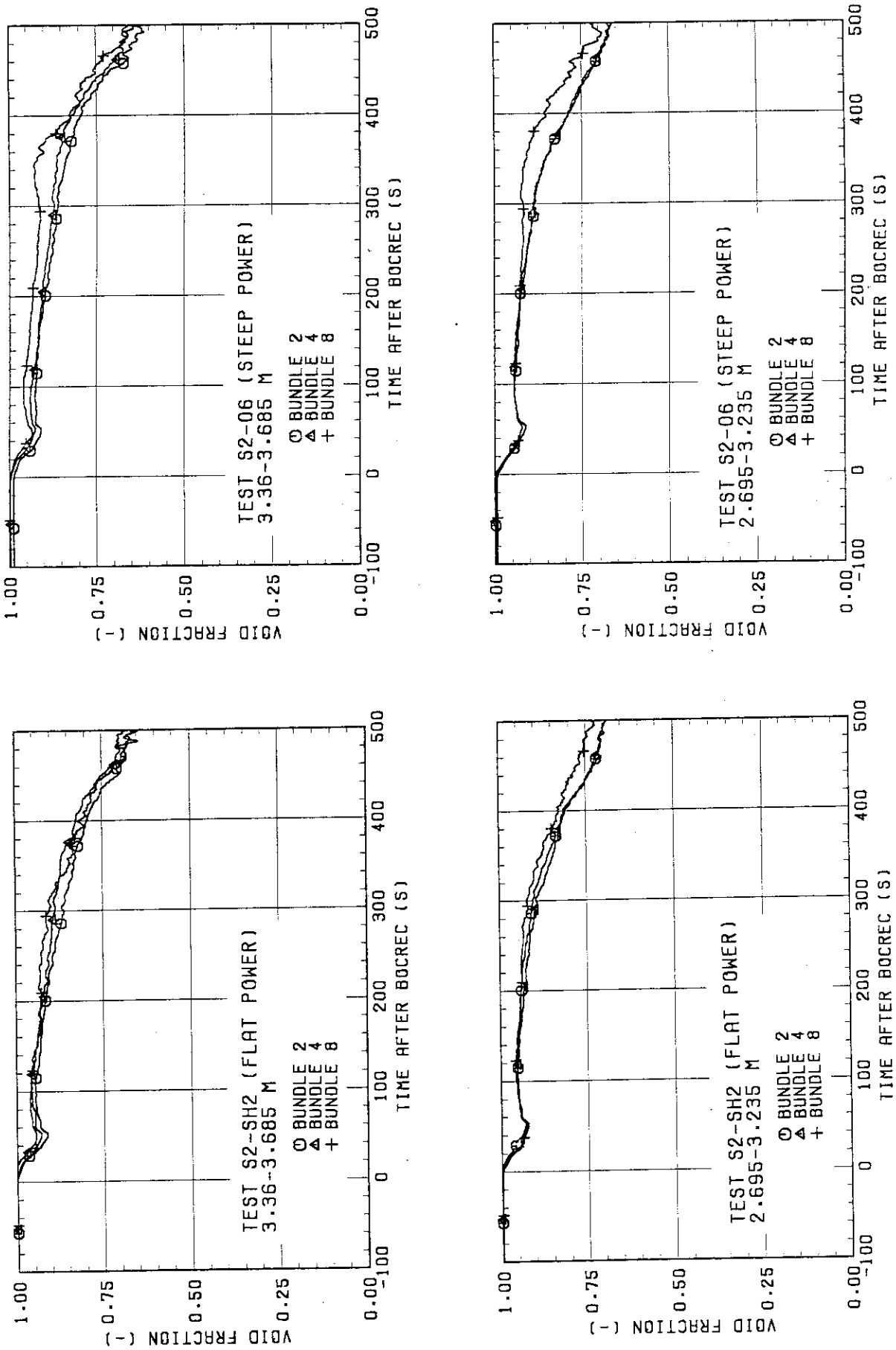

Fig. 3-19 Comparison of void fractions at 6 elevations in core

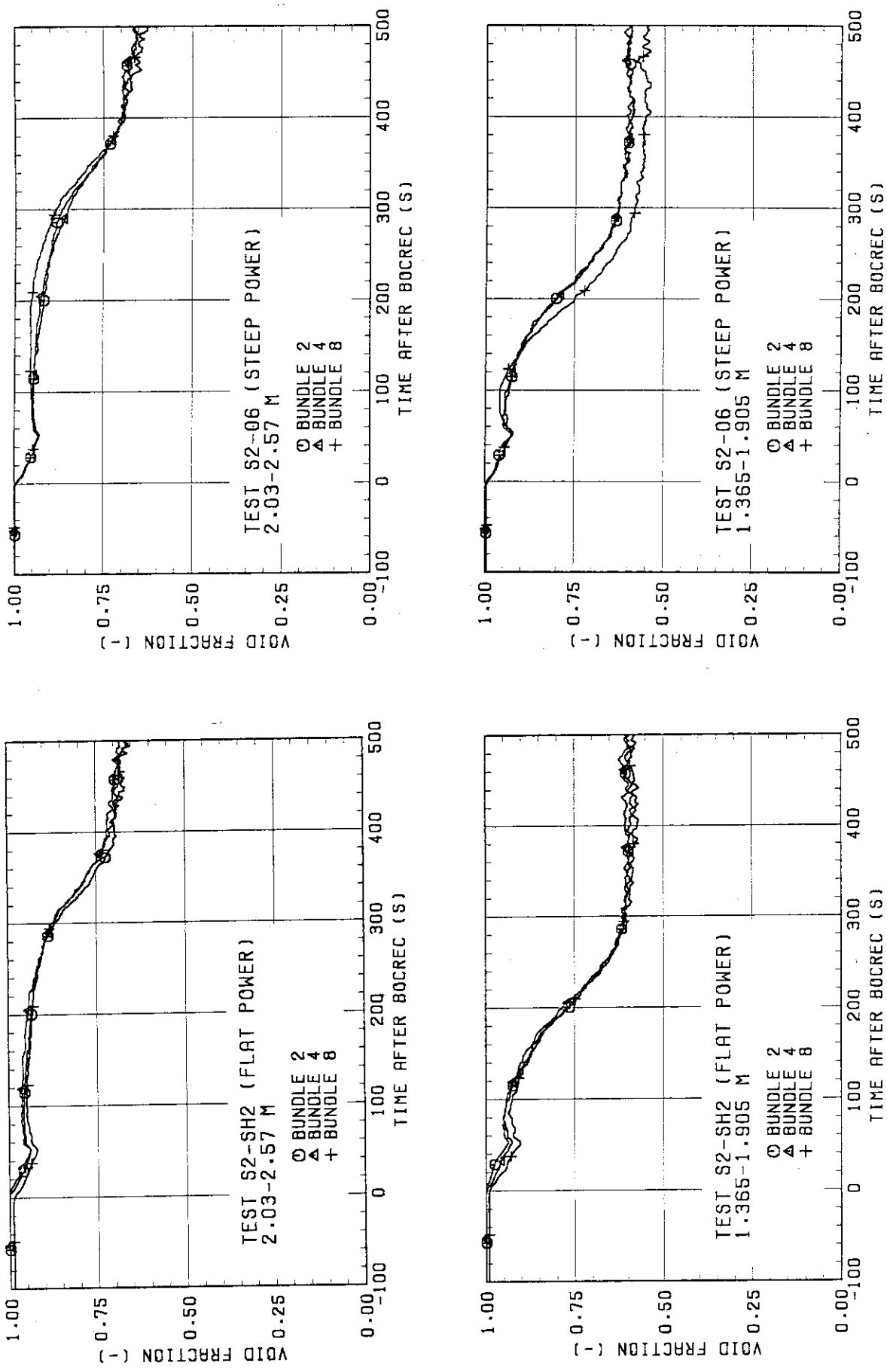
TEST S2-06 (STEEP POWER)
2.03-2.57 M
BUNDLE 2
BUNDLE 4
BUNDLE 8
TEST S2-06 (STEEP POWER)
1.365-1.905 M
BUNDLE 2
BUNDLE 4
BUNDLE 8
TEST S2-SH2 (FLAT POWER)
2.03-2.57 M
BUNDLE 2
BUNDLE 4
BUNDLE 8
TEST S2-SH2 (FLAT POWER)
1.365-1.905 M
BUNDLE 2
BUNDLE 4
BUNDLE 8
VOID FRACTION (-)
TIME AFTER BOCREC (S)
1.00
0.75
0.50
0.25
0.00
-100
0
100
200
300
400
500

Fig.3-19(b)

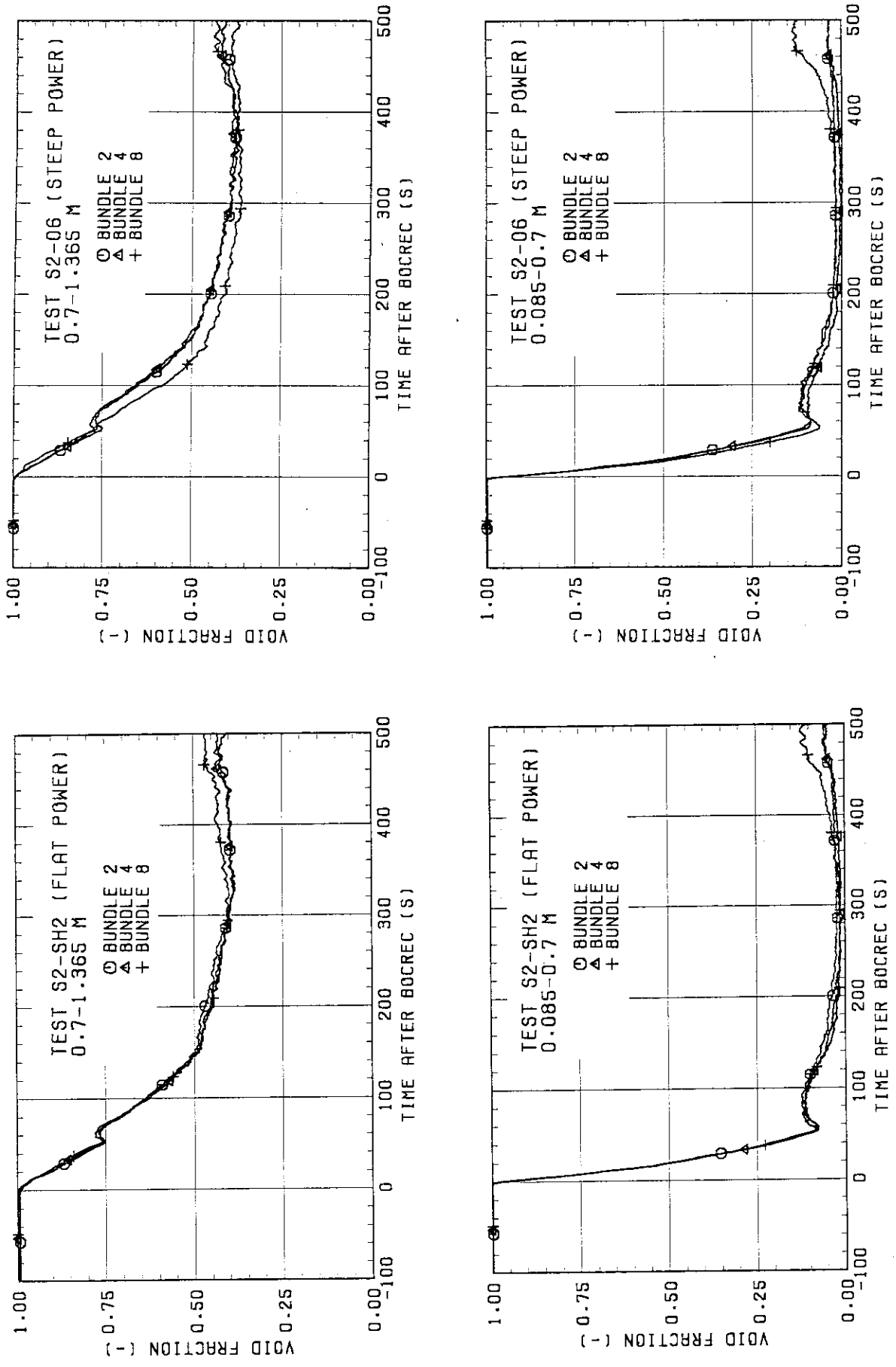
TEST S2-06 (STEEP POWER)
0.7-1.365 M
BUNDLE 2
BUNDLE 4
BUNDLE 8
TEST S2-06 (STEEP POWER)
0.085-0.7 M
BUNDLE 2
BUNDLE 4
BUNDLE 8
TEST S2-SH2 (FLAT POWER)
0.7-1.365 M
BUNDLE 2
BUNDLE 4
BUNDLE 8
TEST S2-SH2 (FLAT POWER)
0.085-0.7 M
BUNDLE 2
BUNDLE 4
BUNDLE 8
VOID FRACTION (-)
TIME AFTER BOCREC (S)
1.00
0.75
0.50
0.25
0.00
-100
0
100
200
300
400
500

Fig.3-19(c)

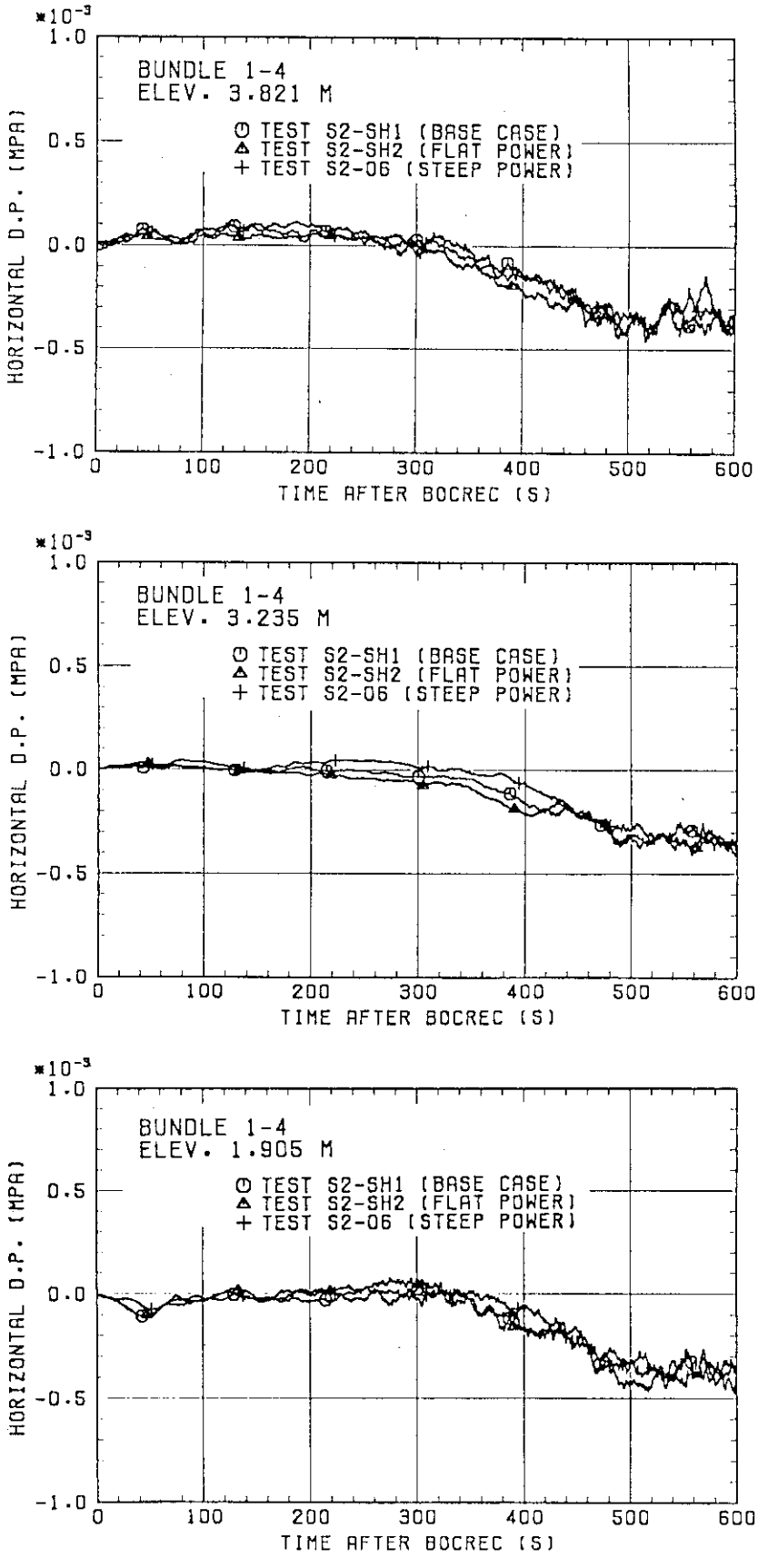

Fig. 3-20 Comparison of horizontal differential pressures at 1.905, 3.235 and 3.821 m between Bundles 1 and 4

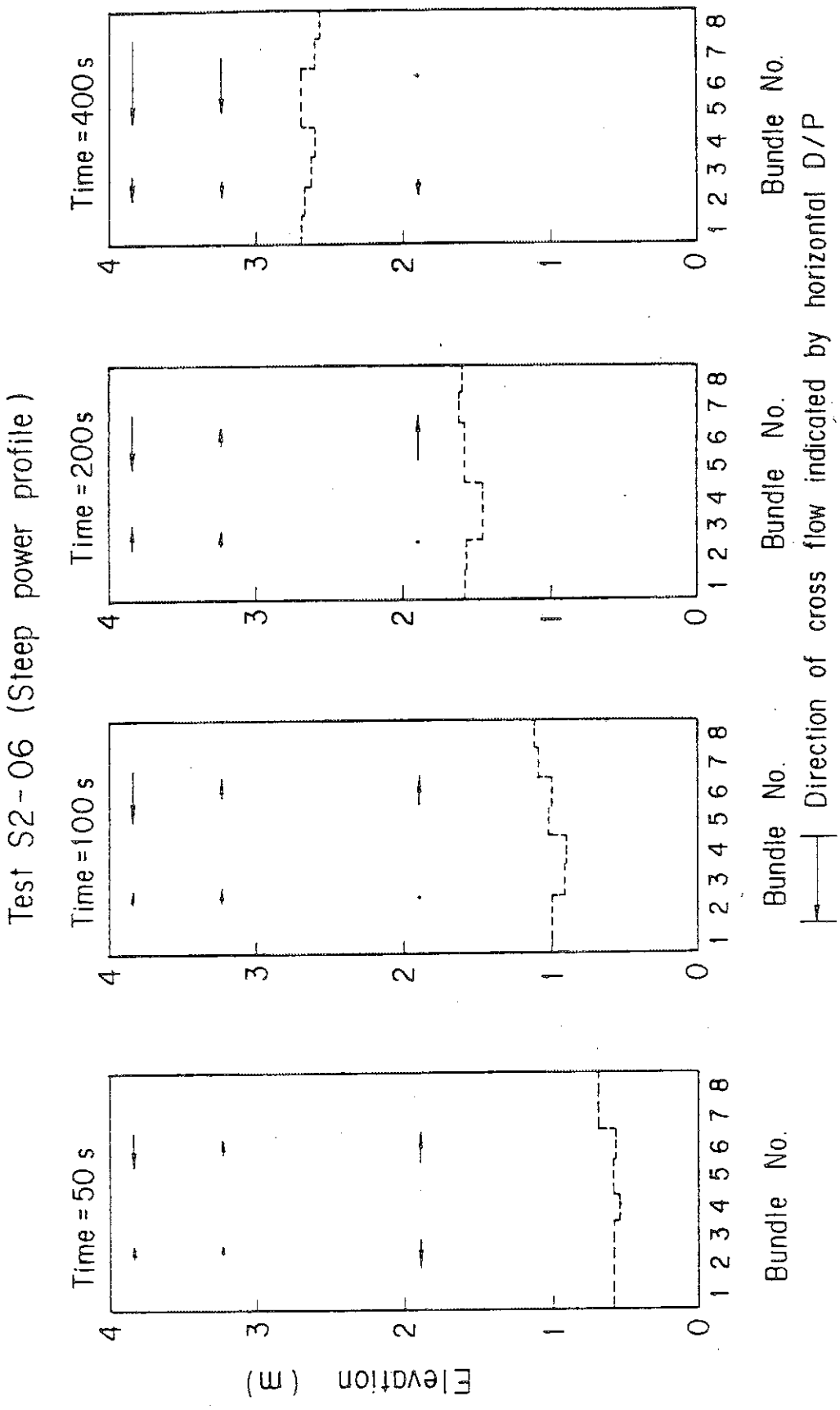

Fig. 3-22 Magnitude of horizontal differential pressure and direction of cross flow at 1.905, 3.235 and 3.821 m at 50, 100, 200 and 400 s in Test S2-06

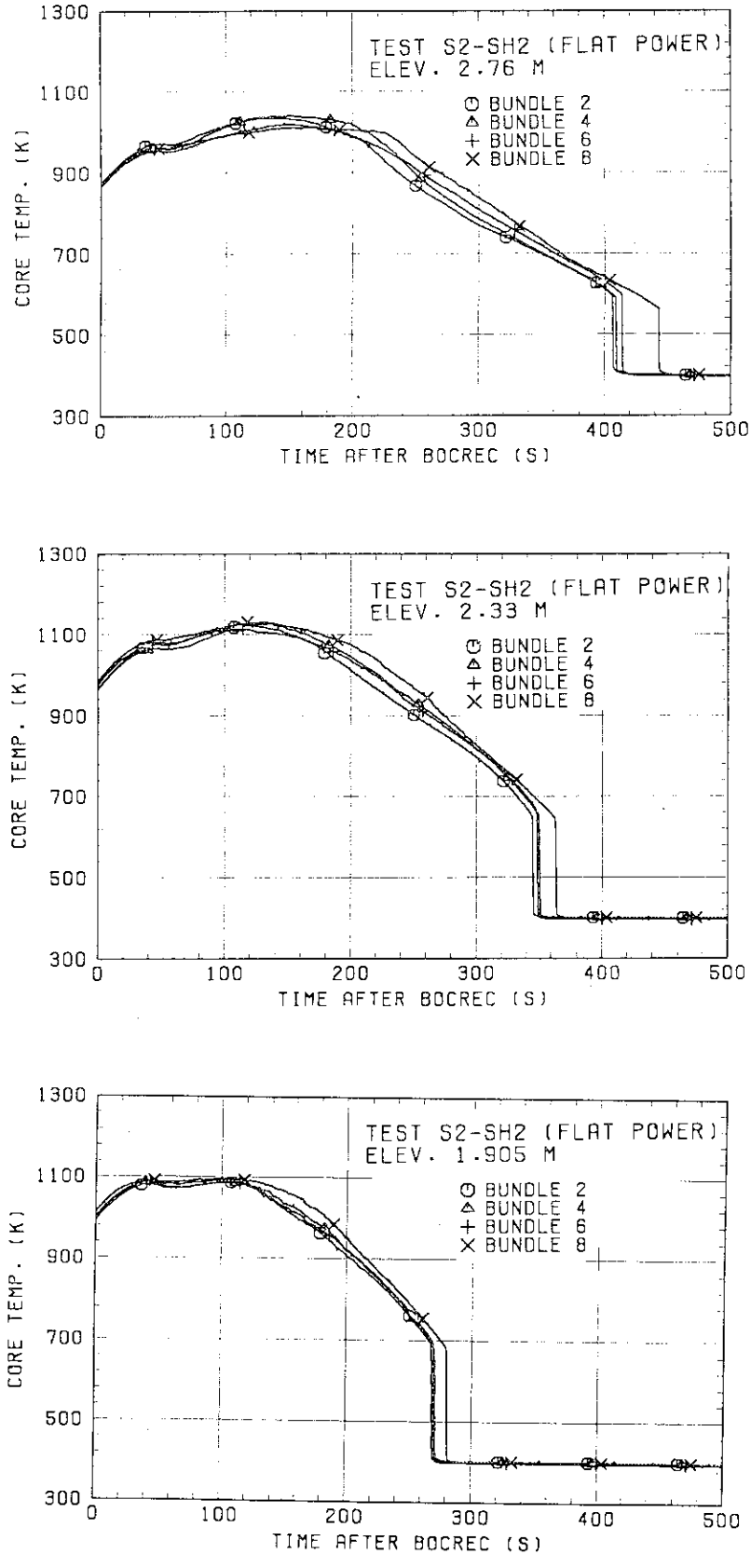

Fig. 3-23 Comparison of heater rod surface temperatures in Bundles 2, 4, 6 and 8 at 1.905, 2.33 and 2.76 m (Test S2-SH2)

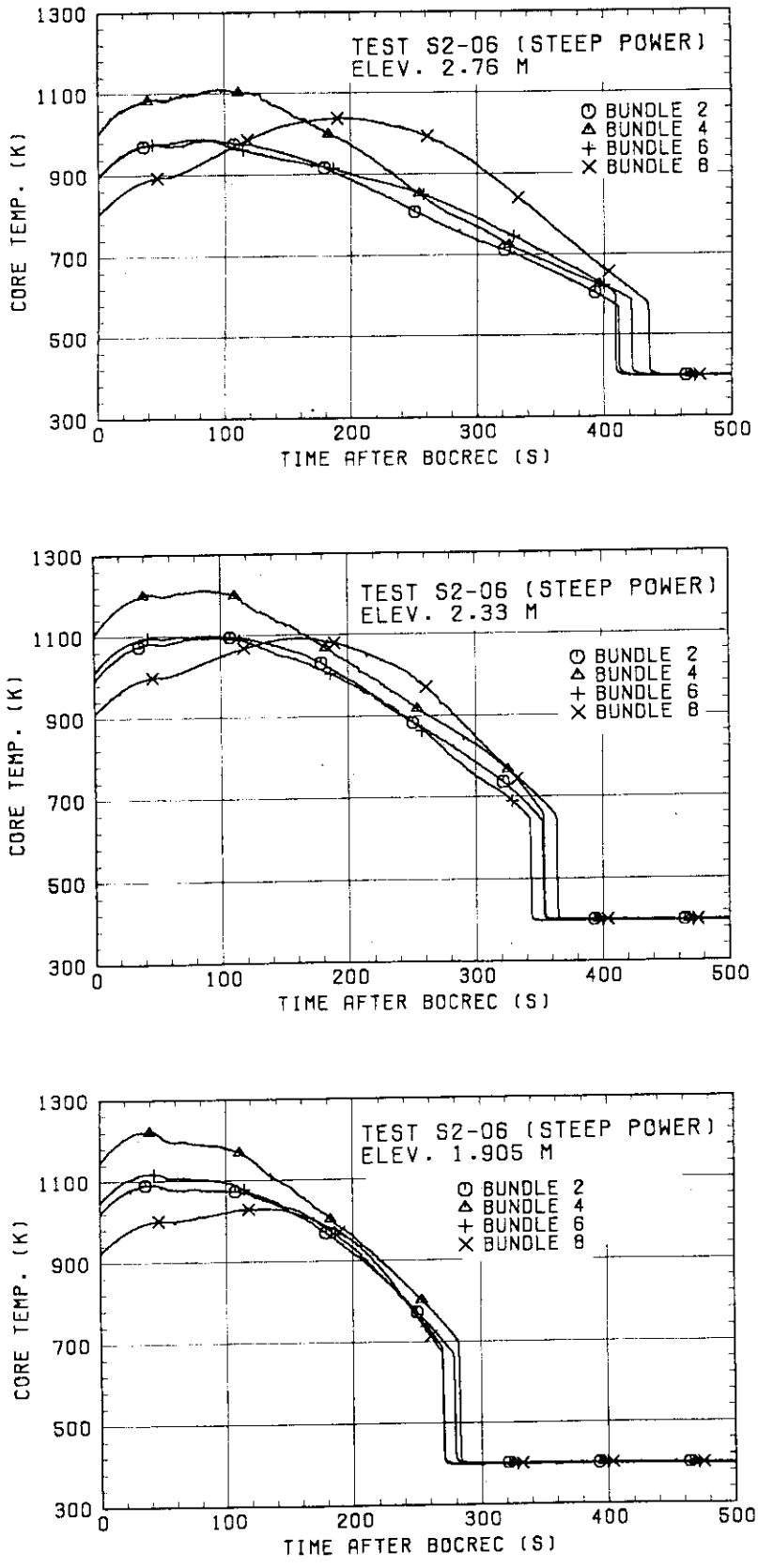

Fig. 3-24 Comparison of heater rod surface temperatures in Bundles 2, 4, 6 and 8 at 1.905, 2.33 and 2.76 m (Test S2-06)

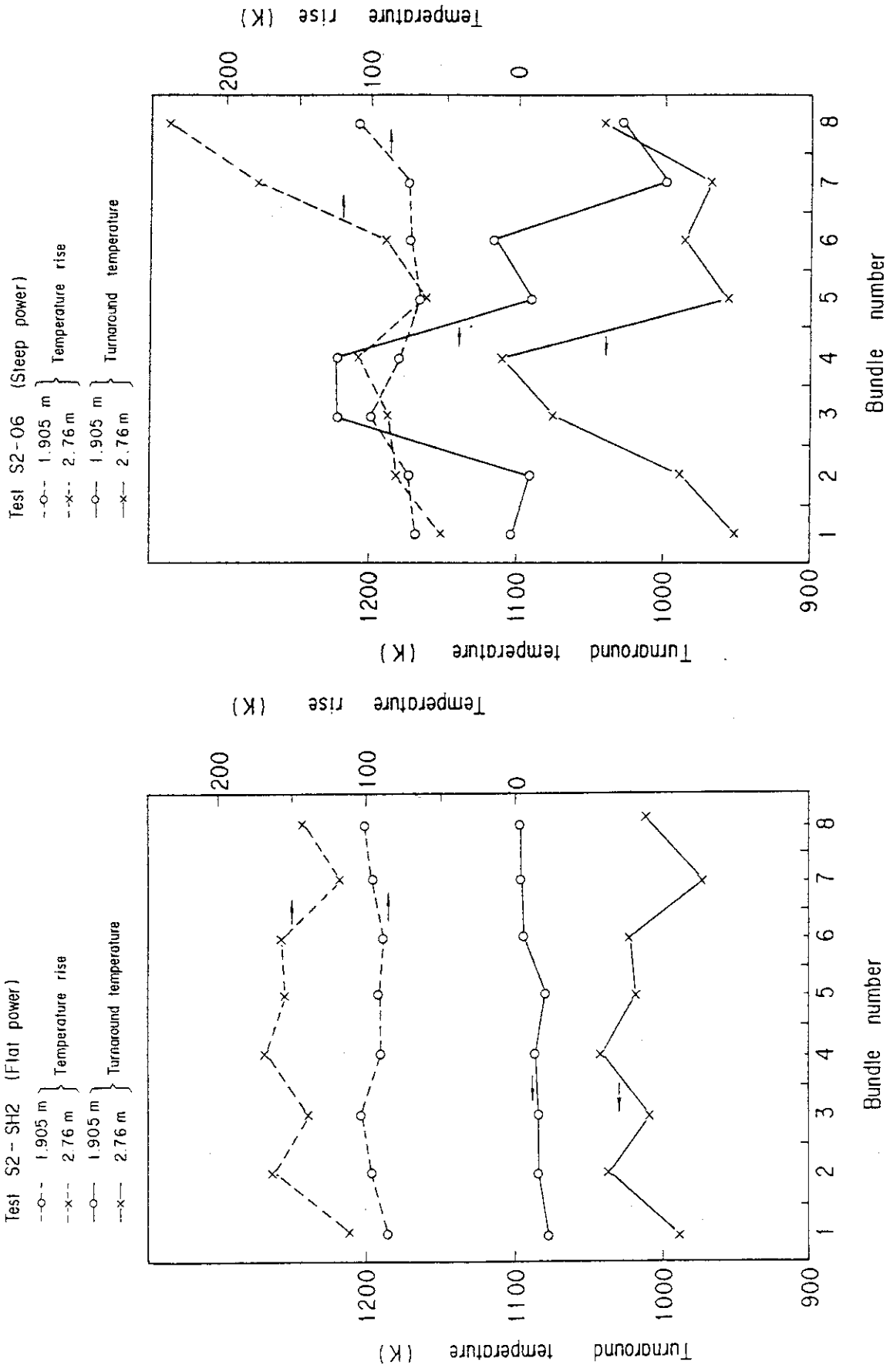

Fig. 3-25 Radial distribution of turnaround temperature and temperature rise at 1.905 and 2.76 m for Tests S2-SH2 and S2-06

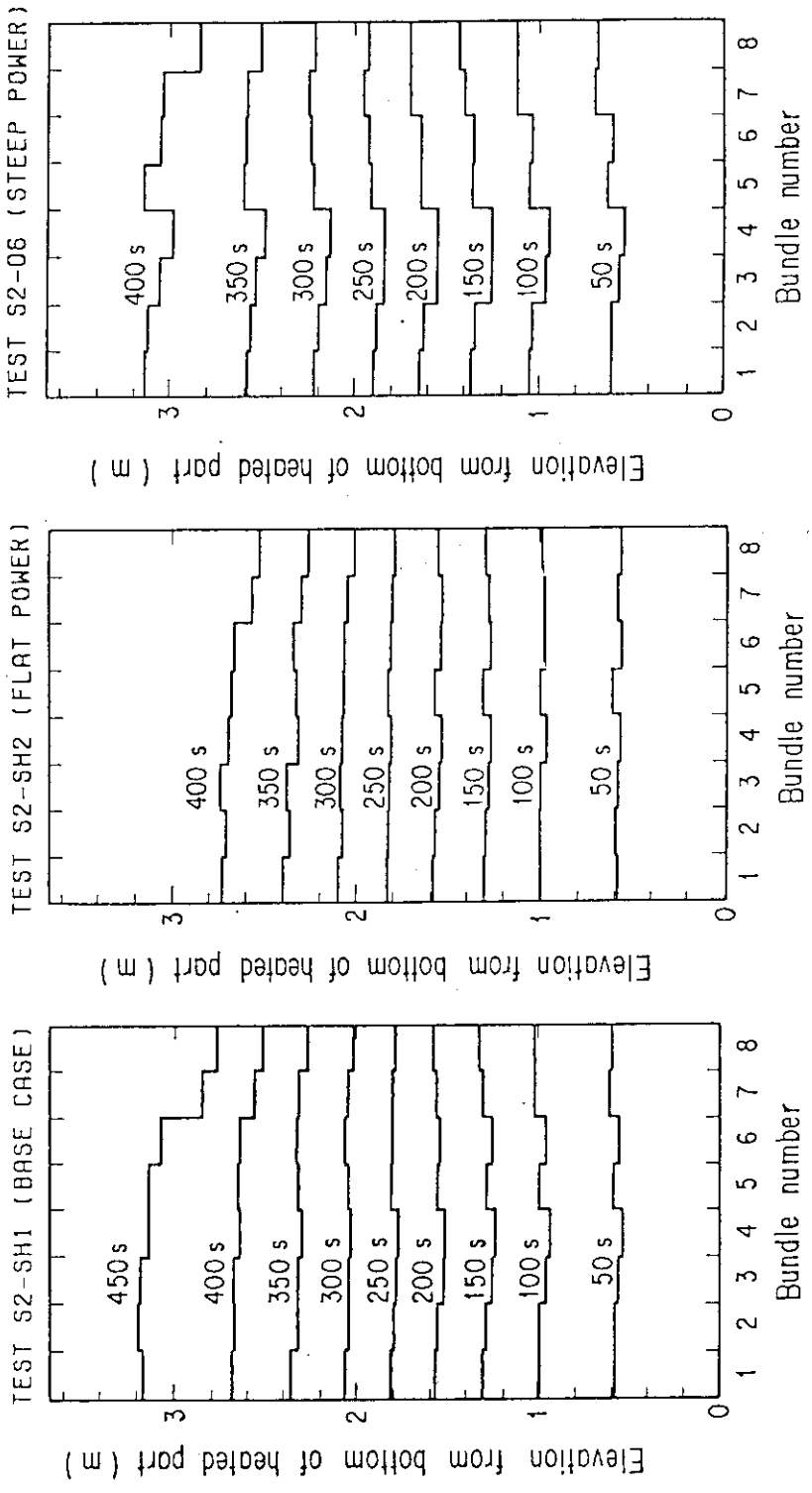

Fig. 3-26 Comparison of bottom quench front distribution

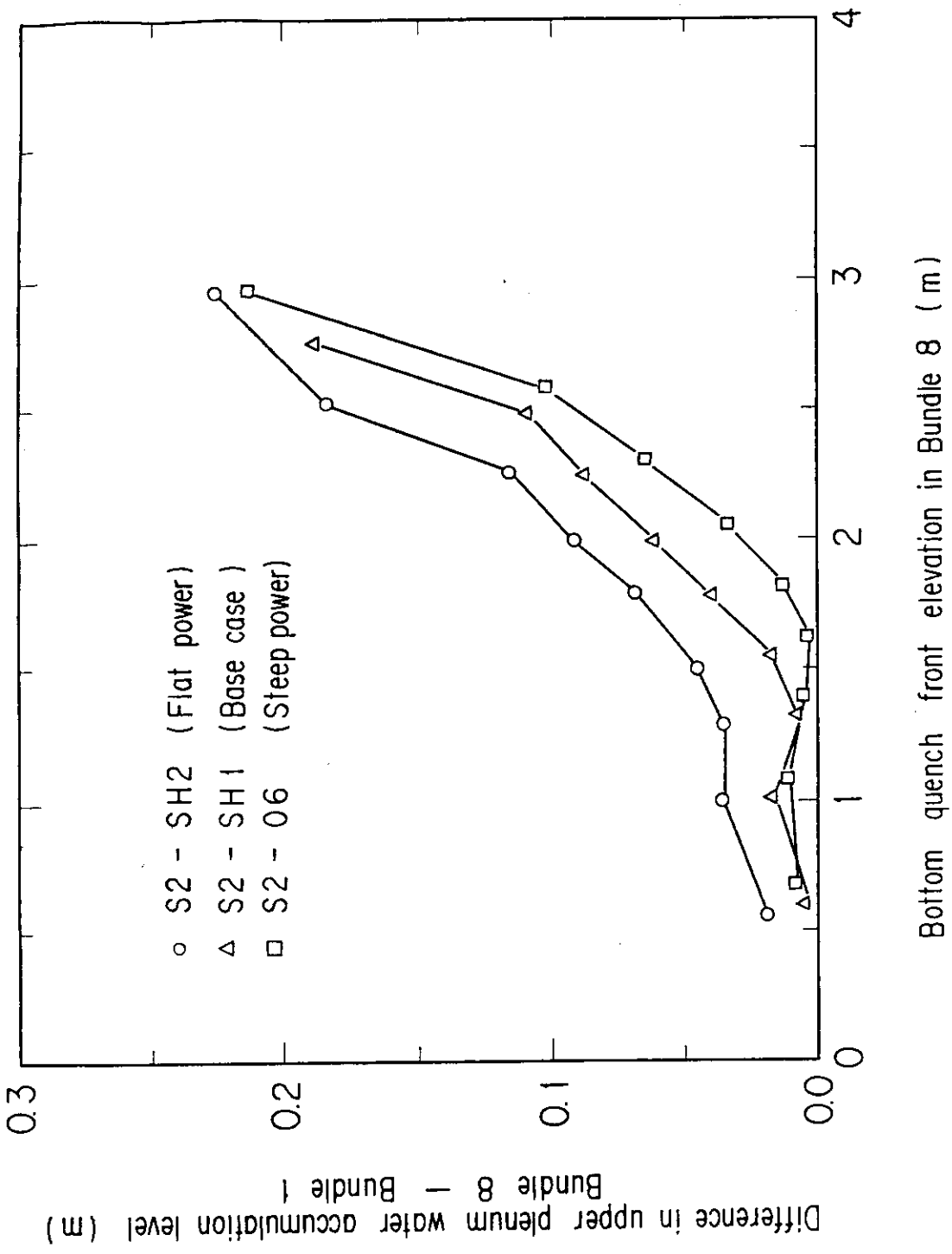

Fig. 3-27 Difference in water accumulation level in upper plenum vs. bottom quench front eeevation in Bundle 8

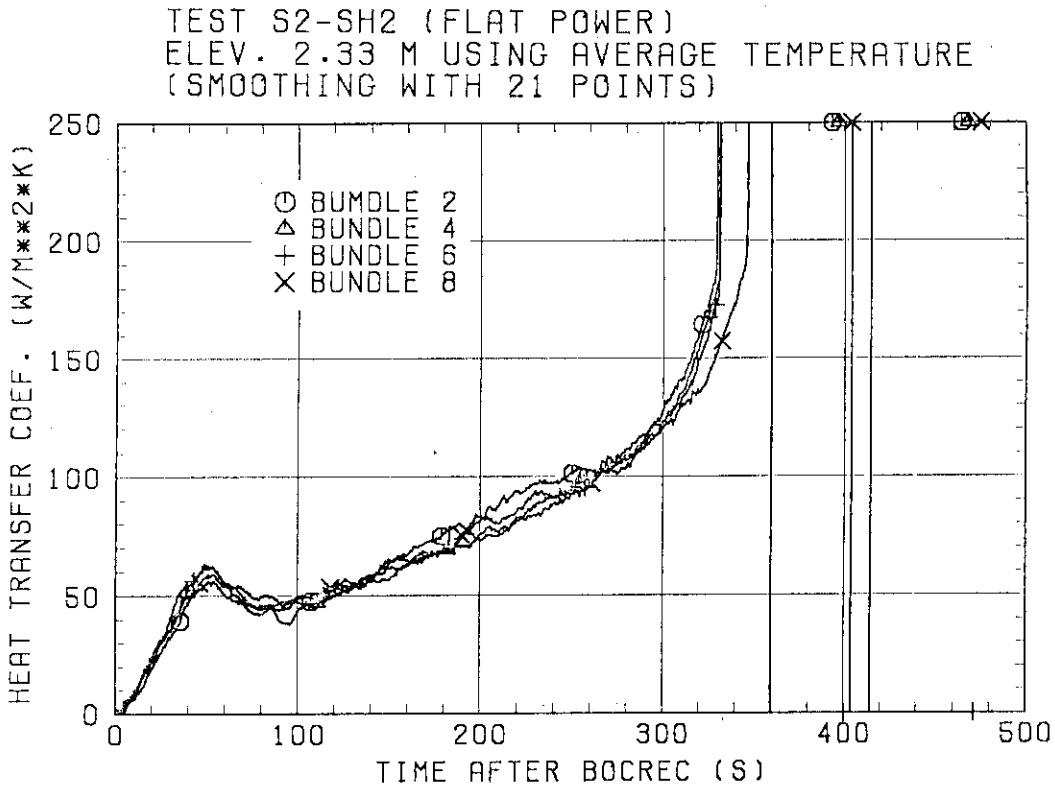

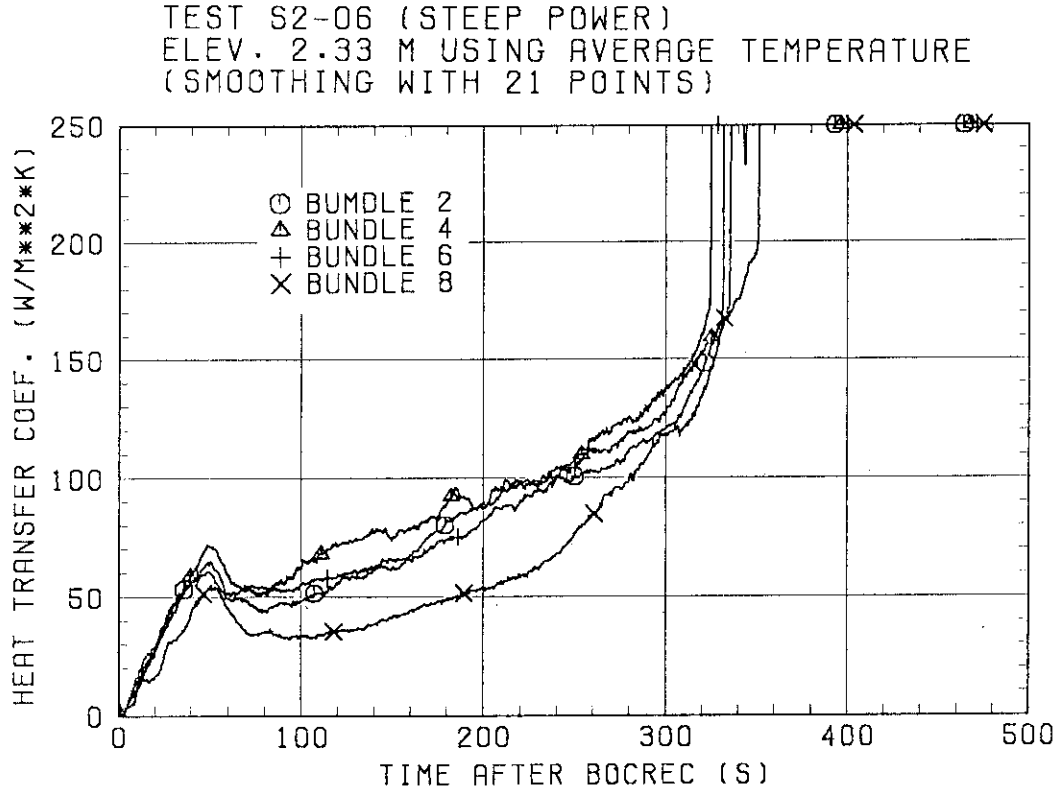

Fig. 3-28 Comparison of heat transfer coefficients in Bundles 2, 4, 6 and 8 at 2.76 m

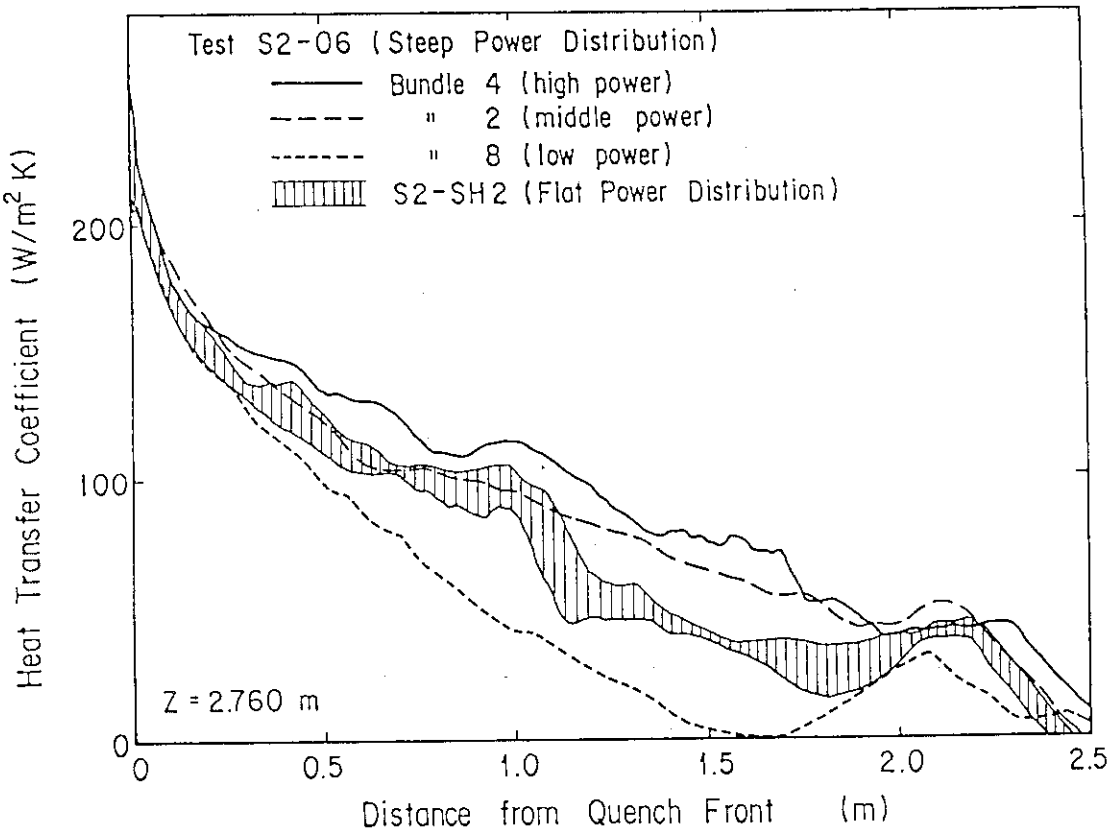

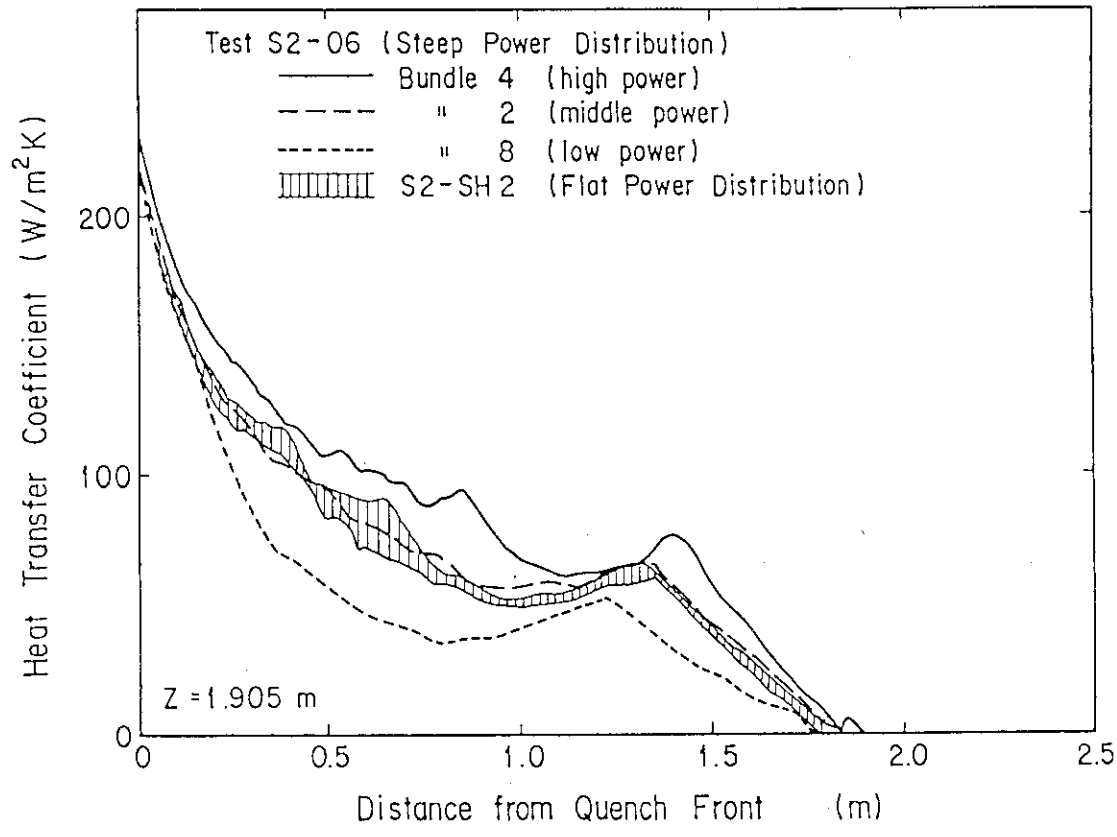

Fig. 3-29 Heat transfer coefficient vs. distance from quench front in Bundles 2, 4 and 8 at 1.905 and 2.76 m for Tests S2-06 and S2-SH2

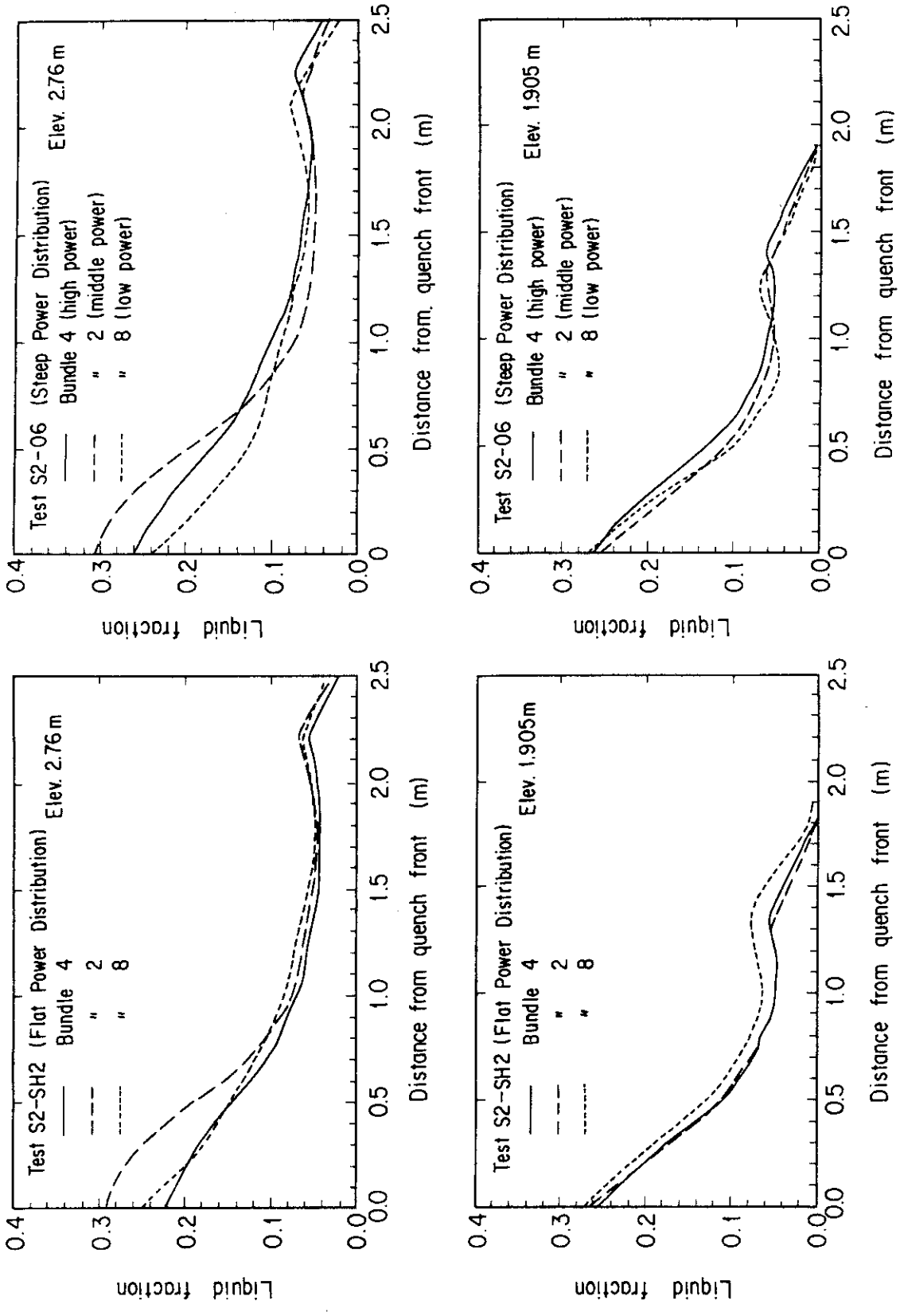

Fig. 3-30 Liquid fraction vs. distance from quench front in Bundles 2, 4 and 8 at 1.905 and 2.76 m for Tests S2-06 and S2-SH2

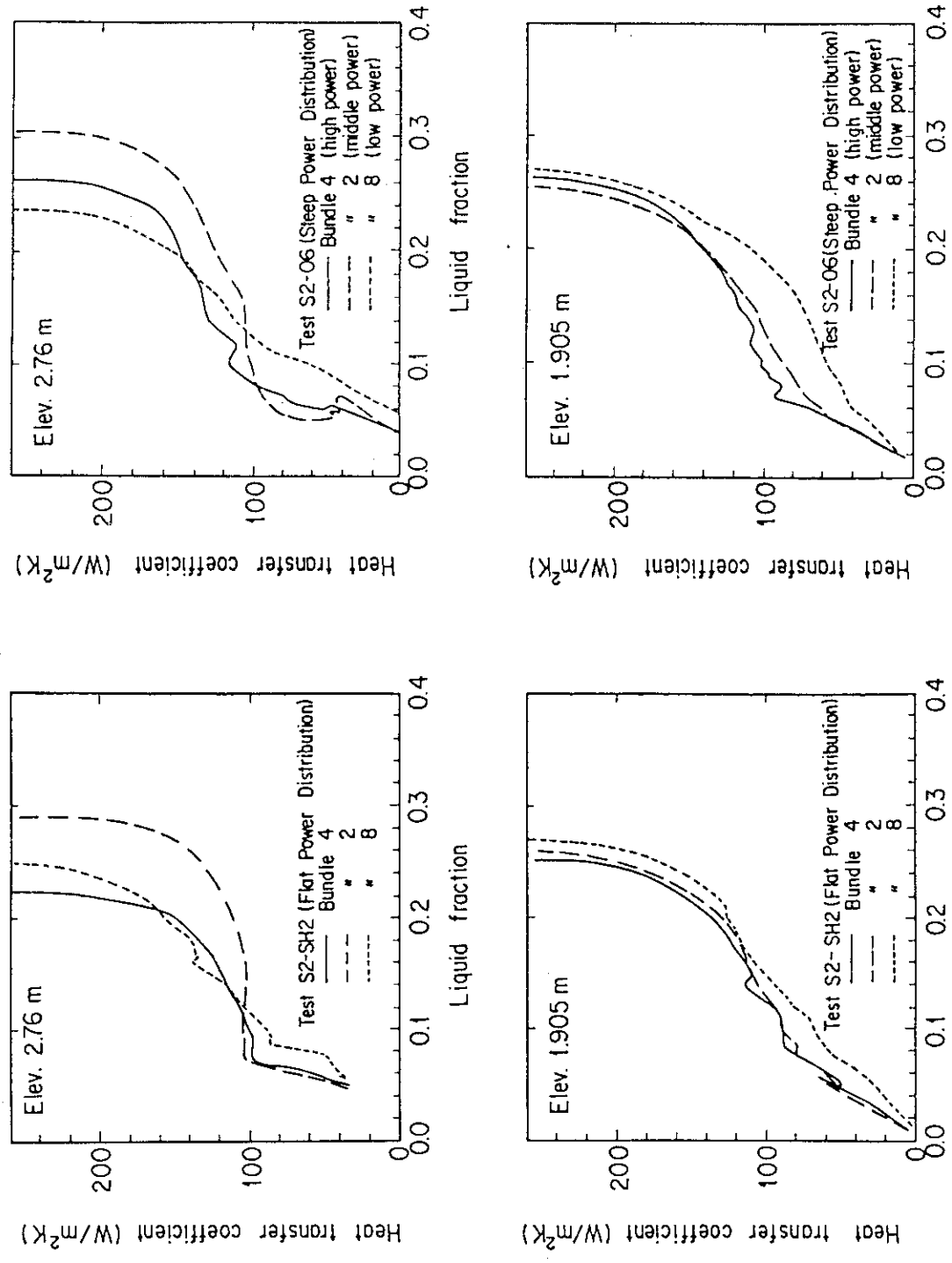

Fig. 3-31 Heat transfer coefficient vs. liquid fraction in Bundles 2, 4, and 8 at 1.905 and 2.76 m for Tests S2-06 and S2-SH2

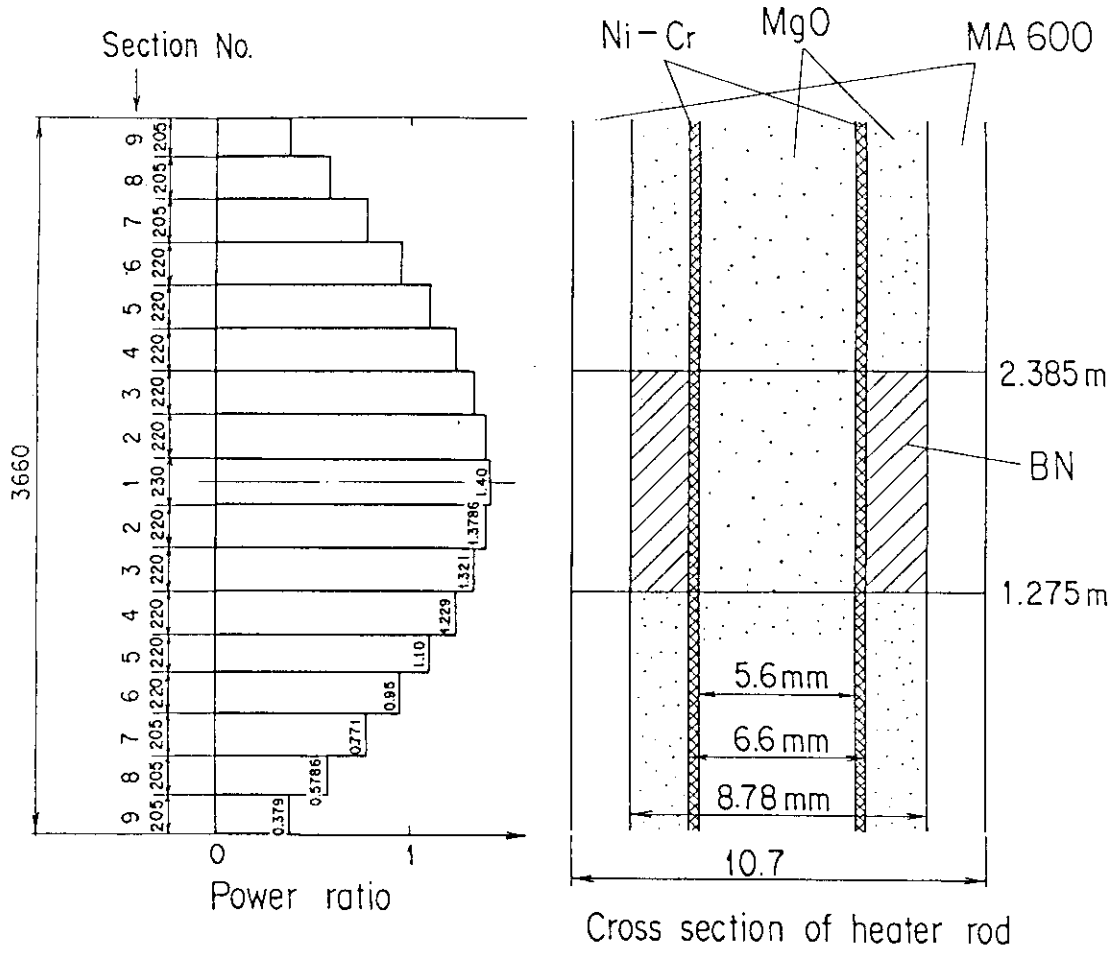

Material properties

	Specific heat (Kcal/kg)	Density (kg/m^3)
MgO	$C_{P1} = 0.1665\ T^{0.09}$	$\rho_1 = 2520.0$
Ni－Cr	$C_{P2} = 5.83 \times 10^{-5} T + 0.105$	$\rho_2 = 8410.0$
BN	$C_{P3} = 0.0526\ T^{0.311}$	$\rho_3 = 1840.0$
MA 600	$C_{P4} = 5 \times 10^{-5} T + 0.105$	$\rho_4 = 8430.0$

Elev. 1.275 ~ 2.385 m

$$(C_P \rho)_a = (0.2739\ C_{P1}\rho_1 + 0.1066\ C_{P2}\rho_2 + 0.2929\ C_{P3}\rho_3 + 0.3266\ C_{P4}\rho_4) \times 4186.8\ \mathrm{J/m^3K}$$

Elev. 0 ~ 1.275 m , 2.385 ~ 3.66 m

$$(C_P \rho)_a = (0.2739\ C_{P1}\rho_1 + 0.1066\ C_{P2}\rho_2 + 0.2929\ C_{P1}\rho_1 + 0.3266\ C_{P4}\rho_4) \times 4186.8\ \mathrm{J/m^3K}$$

Fig. 3-32 Axial power profile, cross section of heater rod and average heat capacity

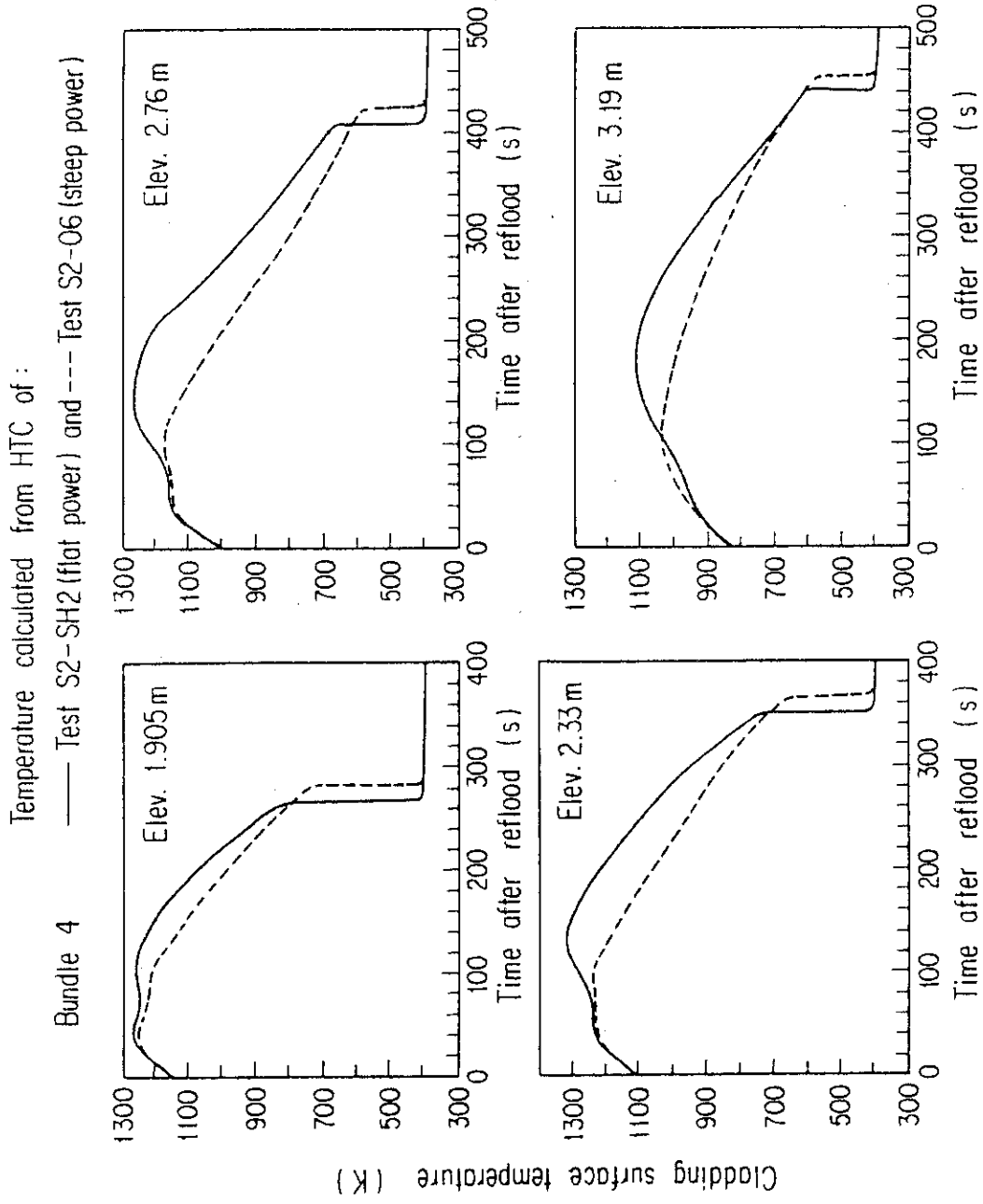

Fig. 3-33 Comparison of temperatures calculated from heat transfer coefficients in Tests S2-SH2 and S2-06 at 1.905, 2.33, 2.76 and 3.19 m in Bundle 4 using initial temperatures and power transients in Test S2-06

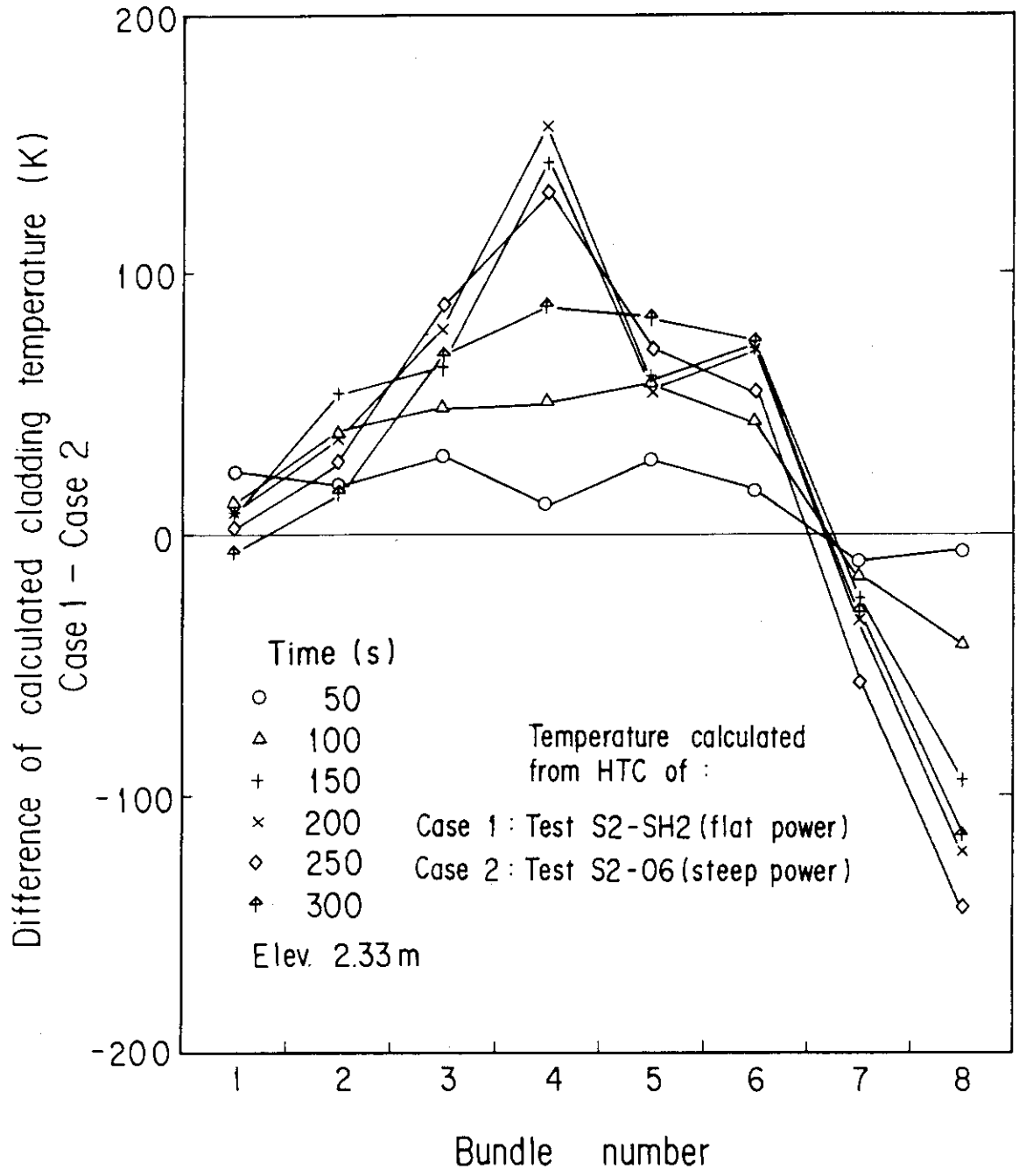

Fig. 3-34 Radial distributions of differences in temperatures calculated from heat transfer coefficients in Tests S2-SH2 and S2-06 at 2.33 m at 50, 100, 150, 200, 250 and 300 s

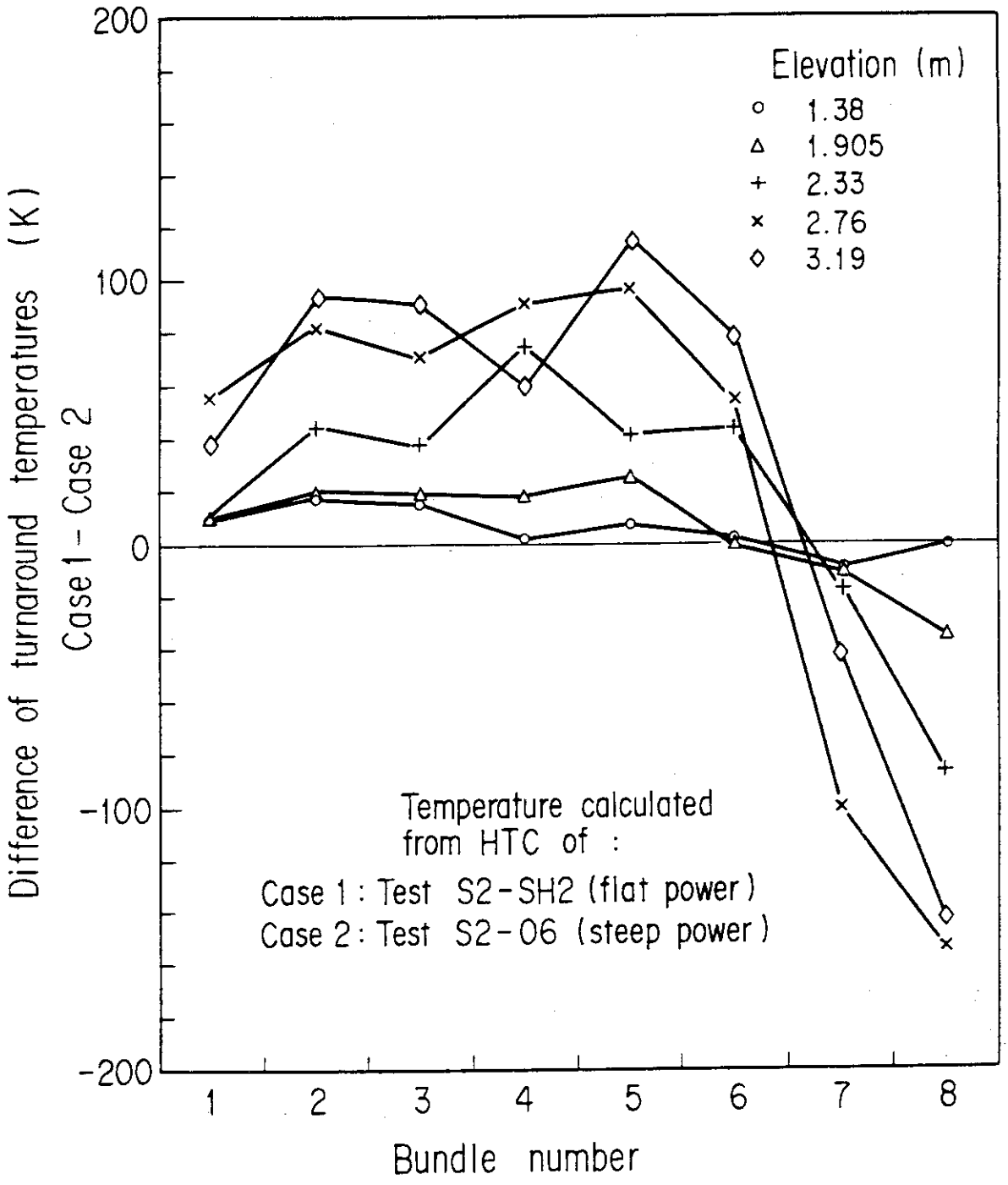

Fig. 3-35 Radial distributions of differences in turnaround temperatures calculated from heat transfer coefficients in Test S2-SH2 and in Test S2-06 at 1.38, 1.905, 2.33, 2.76 and 3.19 m

Appendix A Slab Core Test Facility (SCTF) Core-II

A.1 Test Facility

The Slab Core Test Facility is designed under the following design philosophy and design criteria:

a. Design Philosophy

(1) The facility should provide the capability to study the two-dimensional thermohydraulic behavior in a reactor pressure vessel especially due to the radial power distribution during the end of blowdown, refill and reflood pahses of a postulated LOCA in a PWR.

(2) To properly simulate the core heat transfer and hydrodynamics, a special emphasis is put on the proper simulation of the components in the pressure vessel. Provided as the components in the pressure vessel are the simulated core, downcomer, core baffle region, lower plenum, upper plenum and upper head. On the other hand, simplified primary coolant loops are also provided. Provided as the primary coolant loop components are a hot leg, an intact cold leg, broken cold legs and a steam/water separator which is to simulate single steam phase flow downstream of a steam generator and to measure the flow rate of carryover water coming from the upper plenum.

b. Design Criteria

(1) The reference reactor to be simulated in SCTF is the Trojan reactor in the United States which is a four-loop 3300 MWt PWR. The Ooi reactor etc. in Japan are also referred which are of the similar type to the Trojan reactor except the provision of UHI system.

(2) A full scale radial and axial section of core with single bundle width of the pressurized water reactor is provided as the simulated core of SCTF.

(3) The simulated core consists of 8 bundles arranged in a row. Each bundle has electrically heated rods simulating fuel rods and non-heated rods with 16×16 array, with the diameter and the pitch for Trojan which has 15×15 rod array.

(4) The flow area and fluid volume of components are scaled down based on the nominal core flow area scaling, 1/21.

(5) To properly simulate the flow behavior of carryover water or entrainment, the elevations of hot leg and cold legs are designed

to be the same as the PWR as much as possible.

(6) A honeycomb structure is used for side walls with surface plates which accomodates the slab core, the upper plenum and the upper part of lower plenum, so as to minimize the effect of walls on the core heat transfer and hydrodynamics.

(7) To investigate the effect of flow resistance in the primary loop are provided the orifices of which dimension is changeable.

(8) The maximum allowable temperature of the simulated fuel rods is 900°C (1173 K) and the maximum allowable pressure of the facility is 0.6 MPa.

(9) The facility is equipped with the hot leg equivalent to four hot legs connecting the upper plenum and the steam/water separator, the intact cold leg equivalent to three intact cold legs connecting the steam/water separator and the downcomer and the two broken cold legs, one is for the steam/water separator side and another for the pressure vessel side.

(10) The ECCS consists of an accumulator (Acc), a low pressure coolant injection (LPCI) system and a combined injection system.

(11) ECC water injection ports are at the cold leg, the hot leg, the upper plenum, the downcomer, the lower plenum and above the upper core support plate. These ports are to be chosen according to the objective of the test.

(12) For better simulation of lower plenum flow resistance, simulated fuel rods do not penetrate through the bottom plate of the lower plenum but terminate at below the bottom of the core.

(13) For measurements in the pressure vessel including core, the feature of the slab geometry of the pressure vessel is utilized as much as possible. Design and arrangement of the instruments are done so as to be able to carry out installation, calibration and removal of the instruments.

(14) View windows are provided where flow pattern recognition is important. Their locations are the interface between the core and the upper plenum, the hot leg, the pressure vessel side broken cold leg and the downcomer.

(15) Blocked bundle test is carried out in Core-I in order to investigate the effect of ballooned fuel rods and unblocked normal bundle test follows in the Core-II and -III.

(16) Types of break simulated are cold leg break and hot leg break.

(17) The components and systems such as the containment tanks and ECC water supply system in CCTF are shared with SCTF to the maximum extent.

The overall schematic diagram of SCTF is shown in Fig. A-1. The principal dimensions of the facility is shown in Table A-1, and the comparison of dimensions between SCTF and the reference PWR is shown in Fig. A-2.

A.1.1 Pressure Vessel and Internals

The pressure vessel is of slab geometry as shown in Fig. A-3. The height of the components in the pressure vessel is almost the same as the reference reactor's, and the flow area and the fluid volume of each component are scaled down based on the nominal core flow area scaling, 1/21.

The core consists of 8 bundles arranged in a row and each bundle includes heater rods and non-heated rods with 16×16 array. The core is enveloped by the honeycomb thermal insulator which is attached on the back surface of core wall plate.

The downcomer is located at one end of the pressure vessel which corresponds to the periphery of the actual reactor pressure vessel. The core baffle region located between the core and the downcomer is basically isolated for Core-II to minimize uncertainty in actual core flow. However, some leak holes are still existing. For better understanding, the cross section of the pressure vessel at the elevation of midplance of the core is shown in Fig. A-4.

The design of upper plenum internals is based on that for the new Westinghouse 17×17 array fuel assemblies. The internals consist of control rod guide tubes, support columns and orifice plates which are attached to the upper core support plate (UCSP). The UCSP has some open holes without internals. Those arrangement is shown in Fig. A-5. The radius of each internal is scaled down based on the factor of 8/15 of an actual reactor. Baffle plates are inserted in the guide tubes. The elevation and the configuration of baffle plates are shown in Figs. A-6 and A-7.

The heights of the hot leg and cold legs are designed as close to the reference PWR as possible. However, in order to avoid the interference of the nozzles in the downcomer, the heights of nozzles for the

broken cold leg and the intact cold leg are shifted down compared to that of the hot leg as shown in Fig. A-3.

A.1.2 Simulated Core

The simulated core for the SCTF Core-II consists of 8 heater rod bundles arranged in a row. Each bundle has 234 electrically heated rods and 22 non-heated rods. The dimensions of the heater rods are based on 15×15 fuel rods bundle for a PWR and the heated length and the outer diameter of each heater rod are 3.66 m and 10.7 mm, respectively. A heater rod consists of a nichrome heater element, boron nitride (BN) or magnesium oxide (MgO) depending on elevation in the heated zone and Nichrofer 7216 (equivalent to Inconel 600) sheath. The sheath thickness is about 1.0 mm and is thicker than the actual fuel cladding because of the requirements for thermocouple installation. The heater element is a helical coil and has a 17 step chopped cosine axial power profile as shown in Fig. A-8. The peaking factor is 1.4.

Non-heated rods are either pipes or solid rods of stainless steel with 13.8 mm O.D. The heater rods and non-heated rods are fixed at the top of the core allowing downward expansion. In Fig. A-9, relative elevation of rods and spacers is shown.

For better simulation of flow resistance in the lower plenum the simulated fuel rods end in the lower plenum and do not penetrate through the bottom plate of the lower plenum as shown in Fig. A-9.

A.1.3 Primary Loops and ECCS

Primary loops consist of a hot leg equivalent to four hot legs in area, a steam/water separator for simulating single steam phase flow downstream of the steam generator and for measuring flow rate of carry over water, an intact cold leg equivalent to three intact loops, a broken cold leg on the pressure vessel side and a broken cold leg on the steam/water separator side. These two broken cold legs are connected to two containment tanks through break valves, respectively. The arrangement of the primary loops is shown in Fig. A-10. The flow area of each loop is scaled down based on the core flow area scaling, 1/21. It should be emphasized that the cross section of the hot leg is an elongated circle with an actual height to realize proper flow pattern in the hot leg. The steam/water separator has a steam generator inlet

plenum simulator to correctly simulate the flow characteristics of carryover water into the U-tubes. The cross section of the hot leg and the configuration of the steam genrator inlet plenum simulator are shown in Fig. A-11.

A pump simulator and a loop seal part are provided for the intact cold leg. The arangement of the intact cold leg is shown in Fig. A-12. The pump simulator consists of the casing and duct simulators and an orifice plate as shown in Fig. A-13. The loop resistance is adjusted with the orifice plates attached to the intact cold leg, the steam/water separator side and pressure vessel side broken cold legs and the pump simulator.

ECCS consists of the Acc and an LPCI systems. Injection ports are located as already described in the design criteria section. Besides, the UCSP water extraction system and the UCSP water injection system are provided for combined injection tests.

A.1.4 Containment Tanks and Auxiliary System

Two containment tanks are provided to SCTF. The containment tank-I is connected with the downcomer through the pressure vessel side broken cold leg and the containment tank-II is connected with the steam/water separator through the steam/water separator side broken cold leg. Especially in the containment tank-I, carryover water from the downcomer is measured by the differentiation of the liquid level. These containment tanks and auxiliary system such as a pressurizer for injecting water from the Acc tanks, etc. are shared with CCTF.

A.2 Instrumentation

The instrumentation in SCTF has been provided both by JAERI and USNRC. The JAERI-provided instrumentation includes the measurement of temperatures, pressures, differential pressures, liquid levels, flow velocities, and heating powers. USNRC has provided film probes, impedance probes, string probes, liquid level detectors (LLDs), fluid distribution grids (FDGs), turbine meters, drag disks, densitometers, spool pieces and video optical probes. Location of each instrument is shown in Figs. A-14 through A-32.

Appendix A.3 Mass Balance Calculation

The mass flow rate at the core inlet, $\dot{m}_F$ shown in Fig. A-33, was estimated by the mass balance in the SCTF system assuming the quasi-steady state conditions. The following mass accumulation rates in various parts, $\dot{m}_K$, were estimated by the time differentiation of the measured differential pressure ΔP_K:

$$\dot{m}_K = \frac{1}{g} \cdot \frac{d}{dt} (\Delta P_K) \; S_K \; ,$$

where K = Ci (core, i = 1 ~ 8),
Ui (upper plenum, i = 1 ~ 8),
Ei (end box, i = 1 ~ 8),
B (baffle region),
UB (upper plenum above baffle region),
L (lower plenum),
D (downcomer),
H (hot leg),
CI (containment tank-I) and
SW (steam/water separator).

The total steam flow rate generated in the core was estimated by the sum of mass flow rates at intact cold leg, $\dot{m}_I$, and at broken cold leg (steam/water separator side), $\dot{m}_{BS}$, measured by the ventury flow meters assuming single-phase steam flow conditions, which was confirmed by the differential pressure along the vertical direction in those pipings. Condensation due to the subcooled ECC water at intact cold leg was estimated by the difference between $\dot{m}_I$ and $\dot{m}_{I\,II}$, where $\dot{m}_{I\,II}$ is the mass flow rate from the containment tank I to the containment tank-II measured by the orifice flow meter.

The core inlet mass flow rate $\dot{m}_F$ can then be expressed considering the upstream mass balance from the core inlet as

$$\dot{m}_F = \dot{m}_{SL} + \dot{m}_{SI} + \dot{m}_I - \dot{m}_{I\,II} - \dot{m}_L - \dot{m}_D - \dot{m}_{CI} \; ,$$

where $\dot{m}_{SL}$ and $\dot{m}_{SI}$ are the supplied ECC water mass flow rate into the lower plenum and the intact cold leg, respectively. The core inlet mass flow rate can also be estimated considering the downstream mass balance from the core inlet as

$$\dot{m}_F' = \sum_{i=1}^{8} (\dot{m}_{ci} + \dot{m}_{ui} + \dot{m}_{Ei}) + \dot{m}_B + \dot{m}_{UB} + \dot{m}_H + \dot{m}_{SW} + \dot{m}_{OW}$$

$$+ \dot{m}_I + \dot{m}_{SB} ,$$

where $\dot{m}_{OW}$ is the overflowing water mass flow rate from the steam/water separator.

A.4 Calculation Method of Steam Generation Rate

The steam generation rate in the core was calculated with a heat balance calculation code "STEAM". The heat flux at the surface of heater rods was calculated with a heat transfer calculation code "HEATT"[12] developed for the SCTF test analysis. The temperature dependence of physical properties is considered but the axial heat conduction is neglected in this code.

The following assumptions were made in the calculation.

(1) The heat flux from the heater rods is totally absorbed in the fluid.

(2) The core inlet flow rate is equally divided into each of 8 bundles.

(3) The steam and water mixture is always saturated.

The core is divided into 8 bundles and 10 elevations.

The steam generation rate in each of 80 cells is calculated by

$$S_{ij} = \frac{1}{h_{fg}} \{q_{ij}A - m_i C_{p\ell} \Delta T_{sub}^{i}\} \qquad \text{(A3-1)}$$

where i = Bundle i

j = elevation j

S_{ij} = steam generation rate in this cell

q_{ij} = heat flux

A = $234\pi D \cdot \Delta H_j$ (Heat transfer area)

D = heater rod diameter

ΔH_j = height of this cell

m_i = core inlet mass flow rate in Bundle i

$C_{p\ell}$ = specific heat capacity of saturated water at the pressure in the lower plenum (PT01A11)

ΔT_{sub}^{i} = subcooling of core inlet water in Bundle i

h_{fg} = latent heat of evaporation at the pressure in the core center (PT01D11)

The core inlet mass flow rate is assumed to be equally distributed in each bundle and given by

$$m_i = \frac{1}{8} W_{in} \tag{A3-2}$$

where the W_{in} is the total core inlet mass flow rate obtained by the mass balance calculation described in A.3.

The ΔT_{sub}^{i} is obtained by using the following Data:

$$\Delta T_{sub}^{i} = T_{sat} - (TW01i11 + TW01i41)/2 \tag{A3-3}$$

where T_{sat} = saturation temperature at the pressure in the lower plenum (PT01A11)

TW01i11 and TOW1i41 are the fluid temperature at the bottom of heated part in Bundle i

The heat flux, q_{ij}, is calculated from the transient of heater rod surface temperature. In the STEAM code, two kinds of temperature transients can be selected. One is the temperature at the center of each bundle (TEji1C in Fig. A-14, j = 01 ~ 10, i = 1 ~ 8). Another is the average temperature in each bundle at the same elevation. Figure A-34 shows a comparison of total steam generation rate obtained by these two methods in Test S2-06. As shown in this figure, the difference of these two method is less than about 8 %. If not specially commented, the average temperature transient is used in the steam generation calculation.

Two kinds of vertical nording models are involved in the STEAM code. One is a even division between two adjacent thermocouple locations ("Even" division). Another type of division is made so that the heat flux in each cell accuratelly represent the average heat flux of the cell by considering the stepwise axial power profile shown in Fig. A-8 ("Step" division). Figure A-35 shows the vertical nording models of these two division methods. The difference of the total steam generation rates obtained by these two methods is less than about 8 % as shown in Fig. A-36. If not specially commented, the "Step"

division method is used in the steam generation calculation. The "Even" division method is mainly used for the evaluation of steam flow rate at each elevation.

Since the heat flux shows a very high peak value when the thermocouple is quenched, the heat flux is averaged for the calculation of steam generation rate when the quench front exists in the cell. The averaging method is classified into two cases.

(1) In case of: $t_{j-1} < t_q < t_j$ or $t_j < t_q < t_{j-1}$

where t_q = quench time at thermocouple location

t_{j-1} = quench time at the bottom of cell j

t_j = quench time at the top of cell j

$$q\,A = \sum_{k=0}^{m} q(t_m) \cdot 234\pi D\Delta H_j/(m+1) \qquad \text{(A3-4)}$$

where $m = |t_j - t_{j-1}|/\Delta t$, $\Delta t = 0.5$ s

$$t_m = t + 0.5\left(\frac{\Delta H_j^{\,2}}{\Delta H_j^{\,1} + \Delta H_j^{\,2}}\, m - k\right)$$

$\Delta H_j^{\,1}$ = distance between thermocouple elevation and bottom of cell

$\Delta H_j^{\,2}$ = distance between thermocouple elevation and top of cell

When t is between t_{j-1} and t_j, eq. (A3-4) is used in eq. (A3-1).

(2) In case of: $t_j<t_{j-1}<t_q$, $t_{j-1}<t_j<t_q$, $t_q<t_j<t_{j-1}$ or $t_q<t_{j-1}<t_j$

$$qA = \sum_{k=0}^{m} q(t_m) \cdot 234\pi D\Delta H_j/(m+1) \qquad \text{(A3-5)}$$

where $m = |t_j - t_{j-1}|/\Delta t$, $\Delta t = 0.5$ s

$t_m = t + 0.5(m - k)$

When t is between t_{j-1} and t_j, eq. (A3-5) is used in eq. (A3-1). For the other time, eq. (A3-4) is used in eq. (A3-1).

The quench time at the bottom of the core is set to the initiation time of bottom reflooding. The quench time at the top of the core is obtained by extraporating the quench times at elevations 10 and 9.

A.5 Calculation Method of Horizontal Differential Pressure

The measurement locations of the horizontal differential pressures in the core are shown in Fig. A-26. In addition, the vertical differential pressures were measured at various locations as shown in Fig. A-25. The horizontal differential pressures which were not measured directly can be obtained by combining these measured horizontal and vertical differential pressures. Figure A-37 shows the locations and Tag ID's of calculated horizontal differential pressures together with the locations of measured horizontal and vertical differential pressures. The calculation method for the additional horizontal differential pressures is shown in Table A-3. The Tag ID's used in this table are explained in Figs. A-25, A-26 and A-37.

Table A-1 Principal Dimensions of Test Facility

1. Core Dimension

(1)	Quantity of Bundle	8 Bundles
(2)	Bundle Array	1×8
(3)	Bundle Pitch	230 mm
(4)	Rod Array in a Bundle	16×16
(5)	Rod Pitch in a Bundle	14.3 mm
(6)	Quantity of Heater Rod in a Bundle	234 rods
(7)	Quantity of Non-Heated Rod in a Bundle	22 rods
(8)	Total Quantity of Heater Rods	234×8=1872 rods
(9)	Total Quantity of Non-Heated Rods	22×8=176 rods
(10)	Effective Heated Length of Heater Rod	3660 mm
(11)	Diameter of Heater Rod	10.7 mm
(12)	Diameter of Non-Heated Rod	13.8 mm

2. Flow Area & Fluid Volume

(1)	Core Flow Area (Nominal)	0.227 m^2
(2)	Core Fluid Volume	0.92 m^3
(3)	Baffle Region Flow Area	0.10 m^2
(4)	Baffle Region Fluid Volume (Nominal)	0.36 m^3
(5)	Effective Core Flow Area Based on the Measured Level-Volume Relationship Shown in Fig. 4-7 Including Gap between Core Barrel and Pressure Vessel Wall and Various Penetration Holes	0.35 m^2
(6)	Downcmomer Flow Area	0.121 m^2
(7)	Upper Annulus Flow Area	0.158 m^2
(8)	Upper Plenum Horizontal Flow Area	0.525 m^2
(9)	Upper Plenum Fluid Volume	1.16 m^3
(10)	Upper Head Fluid Volume	0.86 m^3
(11)	Lower Plenum Fluid Volume	1.38 m^3
(12)	Steam Generator Inlet Plenum Simulator Flow Area	0.626 m^2
(13)	Steam Generator Inlet Plenum Simulator Fluid Volume	0.931 m^3
(14)	Steam Water Separator Fluid Volume	5.3 m^3
(15)	Flow Area at the Top Plate of Steam Generator Inlet Plenum Simulator	0.195 m^2
(16)	Hot Leg Flow Area	0.0826m^2
(17)	Intact Cold Leg Flow Area (Diameter = 297.9 mm)	0.9697m^2
(18)	Broken Cold Leg Flow Area (Diameter = 151.0 mm)	0.0179m^2

Table A-1 (Continued)

(19)	Containment Tank-I Fluid Volume	30	m^3
(20)	Containment Tank-II Fluid Volume	50	m^3
(21)	Flow Area of Exhausted Steam Line from Containment Tank-II to the Atmosphere	see Ref. (1)	

3. Elevation & Height

(1)	Top Surface of Upper Core Support Plate (UCSP)	0	mm
(2)	Bottom Surface of UCSP	- 76	mm
(3)	Top of the Effective Heated Length of Heater Rod	- 393	mm
(4)	Bottom of the Skirt in the Lower Plenum	-5270	mm
(5)	Bottom of Intact Cold Leg	+ 724	mm
(6)	Bottom of Hot Leg	+1050	mm
(7)	Top of Upper Plenum	+2200	mm
(8)	Bottom of Steam Generator Inlet Plenum Simulator	+1933	mm
(9)	Centerline of Loop Seal Bottom	-2281	mm
(10)	Bottom Surface of End Box	- 185.1	mm
(11)	Top of the Upper Annulus of Downcomer	+2234	mm
(12)	Height of Steam Generator Inlet Plenum Simulator	1595	mm
(13)	Height of Loop Seal	3140	mm
(14)	Inner Height of Hot Leg Pipe	737	mm
(15)	Bottom of Lower Plenum	-5770	mm
(16)	Top of Upper Head	+2887	mm

Table A-2 Total, lower and upper heights of each cell for calculation of steam generation rate

(a) "Even"division method

Elev. No.	ΔH_j (m)	ΔH_j^1 (m)	ΔH_j^2 (m)
10	0.255	0.215	0.04
9	0.430	0.215	0.215
8	0.430	0.215	0.215
7	0.4275	0.2125	0.215
6	0.2975	0.085	0.2125
5	0.2625	0.1775	0.085
4	0.3925	0.215	0.1775
3	0.430	0.215	0.215
2	0.420	0.205	0.215
1	0.315	0.110	0.205

(b) "Step" division method

Elev. No.	ΔH_j (m)	ΔH_j^1 (m)	ΔH_j^2 (m)
10	0.205	0.165	0.04
9	0.630	0.365	0.265
8	0.220	0.155	0.065
7	0.660	0.385	0.275
6	0.115	0.075	0.040
5	0.115	0.020	0.095
4	0.660	0.325	0.335
3	0.220	0.115	0.105
2	0.630	0.315	0.315
1	0.205	0.110	0.095

ΔH_j = total height of each cell (elev. No. j)

ΔH_j^1 = distance between thermocouple elevation and bottom of cell (elev. No. j)

ΔH_j^2 = distance between thermocouple elevation and top of cell (elev. No. j)

Table A-3 Calculation method for additional horizontal differential pressures using measured horizontal and vertical differential pressures

(1) elev.1 (-0.142 m) for Run 601 ~ 619

HD01C11 = DT01D11 + HD05C11 - DT01D21

HD01C21 = DT01D21 + HD05C21 - DT01D41

HD01C12 = HD01C11 + HD01C21

HD01C41 = DT01D41 + DT04D41 - DT01D61

HD01C61 = DT01D61 + HD05C61 - DT01D81

HD01C42 = HD01C41 + HD01C61

(1)' elev.1 (-0.142 m) for Run 620 ~ 625

HD01C11 = DT01D11 + HD05C11 - DT01D21

HD01C21 = DT00D11 - HD01C11

HD01C12 = DT00D11

HD01C41 = DT00D41

HD01C61 = DT00D42 - DT00D41

HD01C42 = DT00D42

(2) elev.2 (0.085 m)

HD02C21 = DT01S21 + HD03C21 - DT01S41

HD02C41 = DT01S41 + DT02S41 + HD04C41 - DT01S61

HD02C61 = DT01S61 + HD04C61 - DT02S81 - DT01S81

HD02C42 = HD02C41 + HD02C61

(3) elev.3 (0.7 m) for Run 601 ~ 619

HD03C21 = DT02S21 + DT03D22 - DT02S41

HD03C42 = DT02S41 + HD04C42 - DT02S81

(3)' elev.3 (0.7 m) for Run 620 ~ 625

HD03C21 = DT02D22

HD03C42 = DT02D42

(4) elev.4 (1.365 m)

HD04C21 = DT03D22

HD04C41 = DT03S41 + DT04D41 - DT02S61

HD04C61 = DT02S61 + HD05C61 - DT03S81

HD04C42 = HD04C41 + HD04C61

(5) elev.5 (1.905 m)

HD05C11 = DT04D11 - HD05C21

HD05C21 = DT03D22 + DT03S41 - DT03S21

HD05C12 = DT04D11

HD05C41 = DT04D42

HD05C61 = DT04D41 - DT04D42

HD05C42 = DT04D41

(6) elev.6 (2.03 m)

HD06C21 = DT04S21 + DT05D21 - DT04S41

HD06C42 = DT04S41 + HD07C42 - DT04S81

(7) elev.7 (2.57 m)

HD07C21 = DT05D21

HD07C42 = DT05G41 + HD08C42 - DT05G81

(8) elev.8 (2.695 m)

HD08C21 = DT05D21 + DT05G41 - DT05G21

HD08C42 = DT05S41 + DT06D41 - DT05S81

(9) elev.9 (3.235 m)

HD09C11 = DT06D11 - HD09C21

HD09C21 = HD08C21 + DT05S41 - DT05S21

HD09C12 = DT06D11

HD09C41 = DT04D41 + DT03S61 - DT05S41 - DT05G41 - DT04S41 - DT04G41

HD09C61 = DT06D41 - HD09C41

HD09C42 = DT06D41

(10) elev.10 (3.36 m)

HD10C42 = DT06S41 + HD11C42 - DT06S81

(11) elev.11 (3.685 m)

HD11C41 = HD09C41 + DT04S61 - DT06S41 - DT06G41

HD11C61 = HD11C42 - HD11C41

HD11C42 = DT07G41 + HD12C42 - DT07G81

(12) elev.12 (3.821 m)

HD12C11 = HD05C11 + DT02D21 - DT02D11

HD12C21 = HD05C21 + DT02C41 - DT02D21

HD12C12 = HD12C11 + HD12C21

HD12C41 = DT04D41 + DT02D61 - DT02D41

HD12C61 = HD05C61 + DT02D81 - DT02D61

HD12C42 = HD12C41 + HD12C61

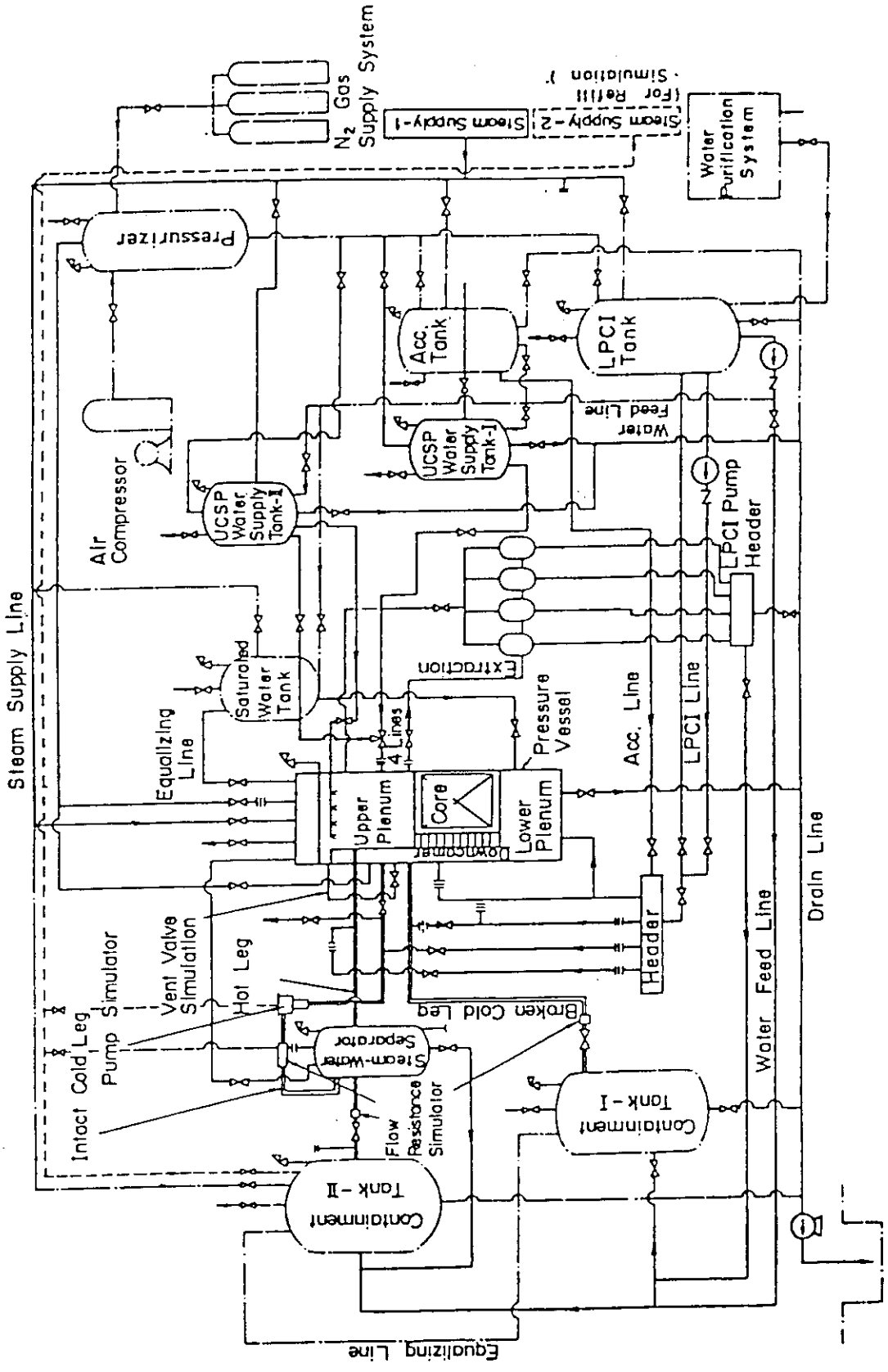

Fig. A-1 Schematic Diagram of Slab Core Test Facility

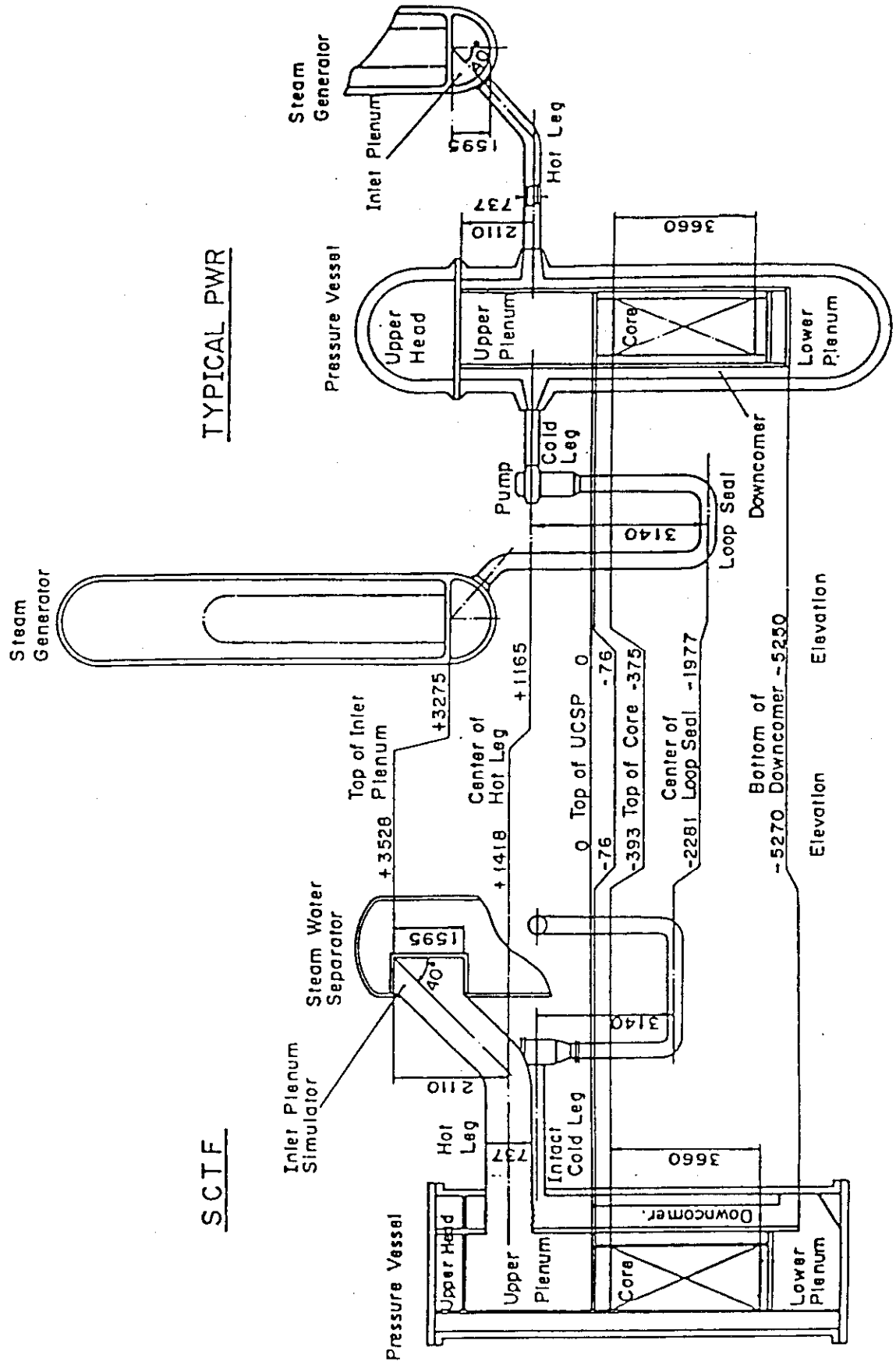

Fig. A-2 Comparison of Dimensions between SCTF and a Reference PWR

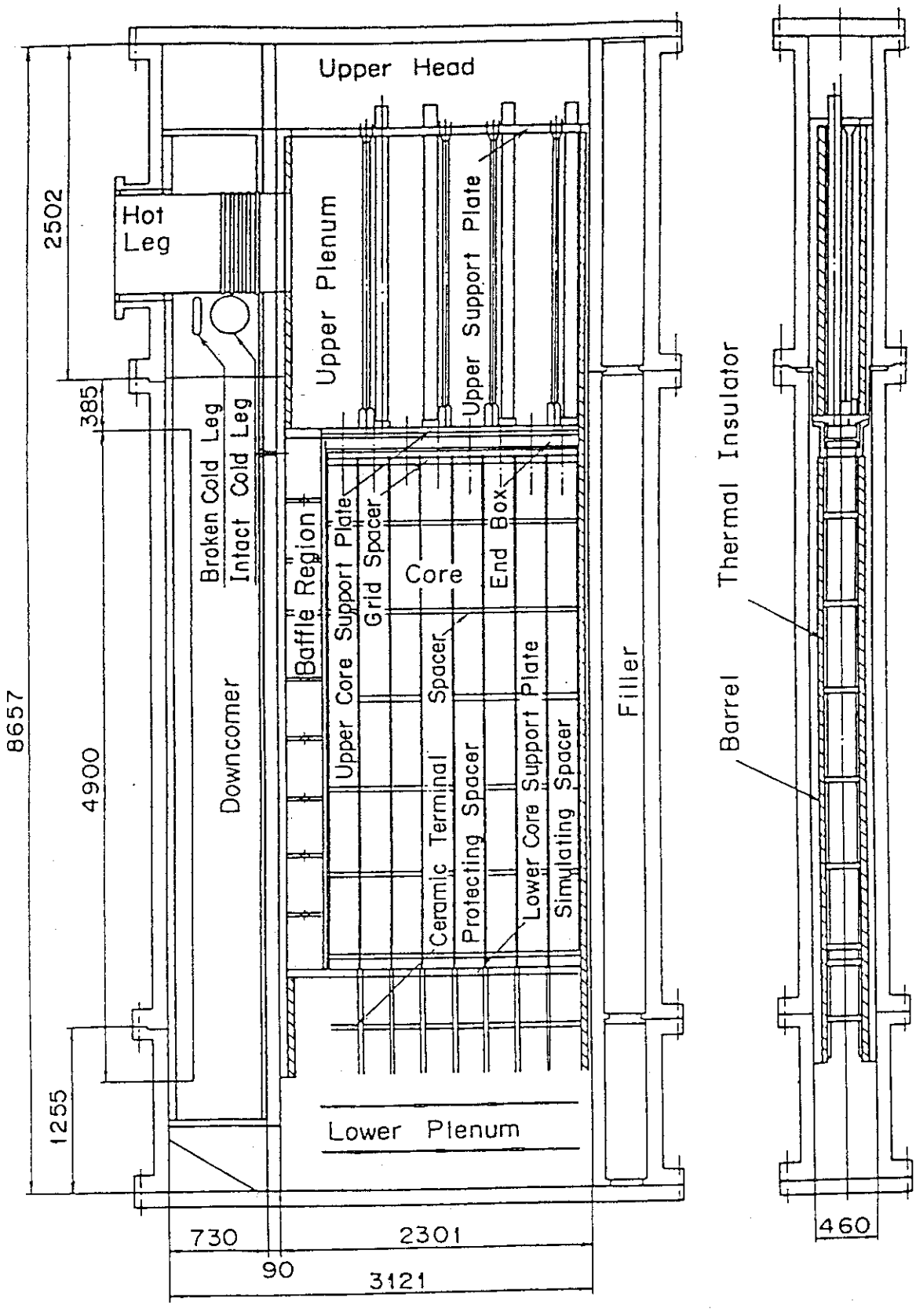

Fig. A-3 Vertical Cross Section of the Pressure Vessel

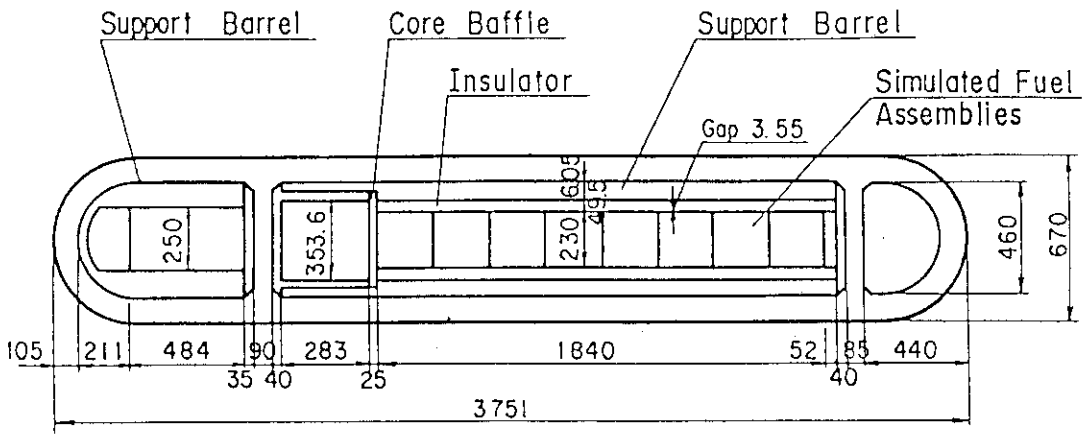

Fig. A-4 Horizontal Cross Section of the Pressure Vessel (1)

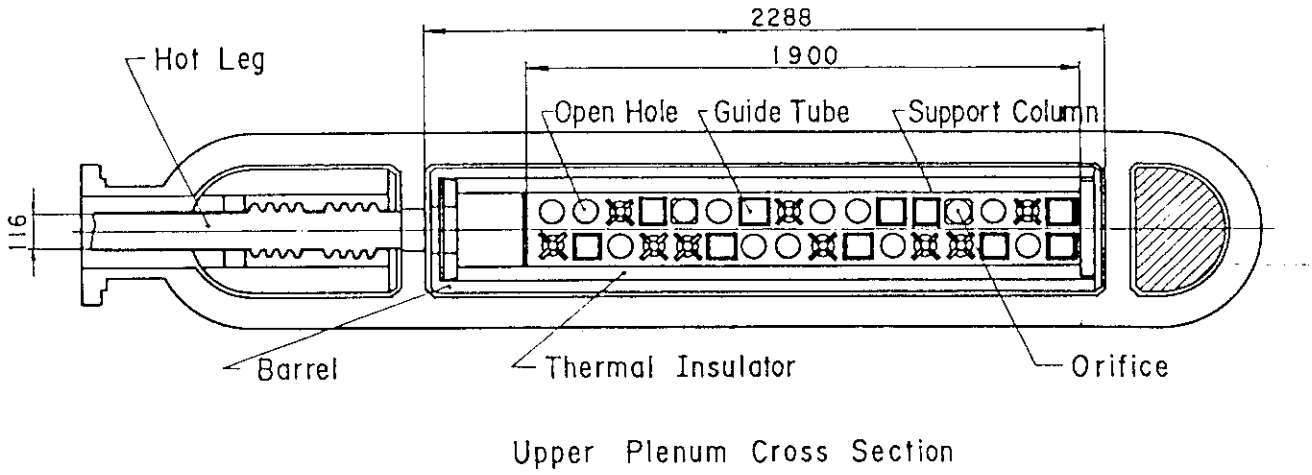

Fig. A-5 Horizontal Cross Section of the Pressure Vessel (2)

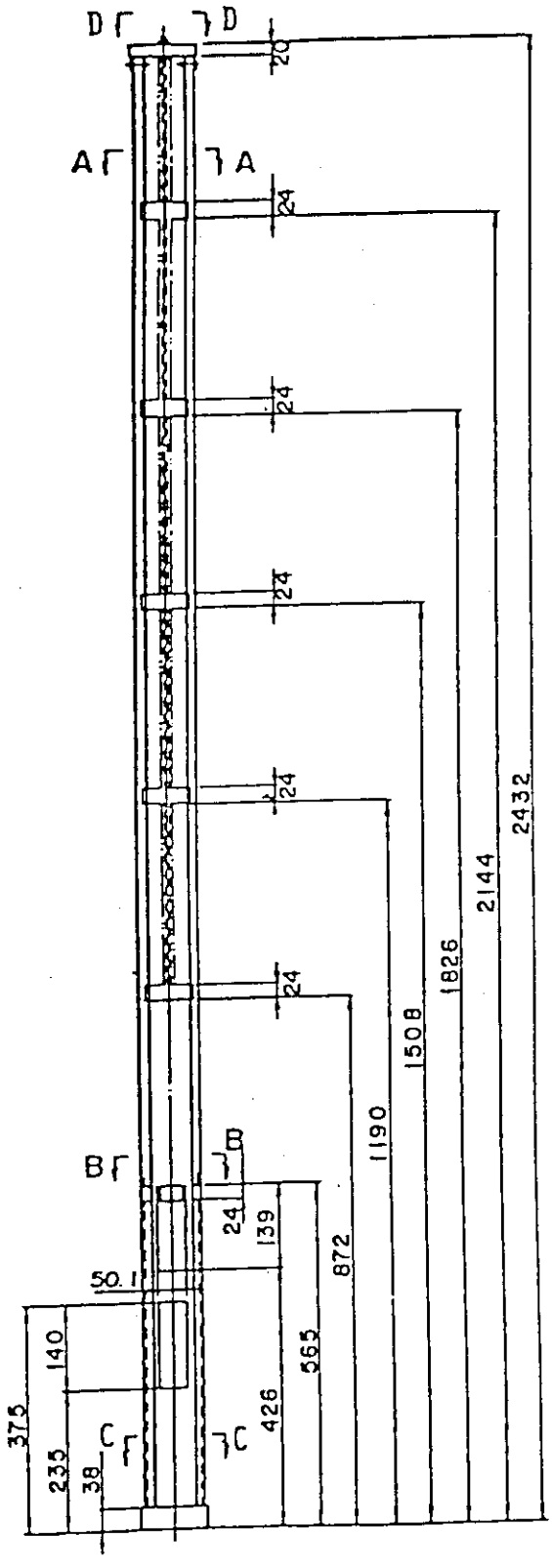

Fig. A-6 Dimension of Guide Tube (1)

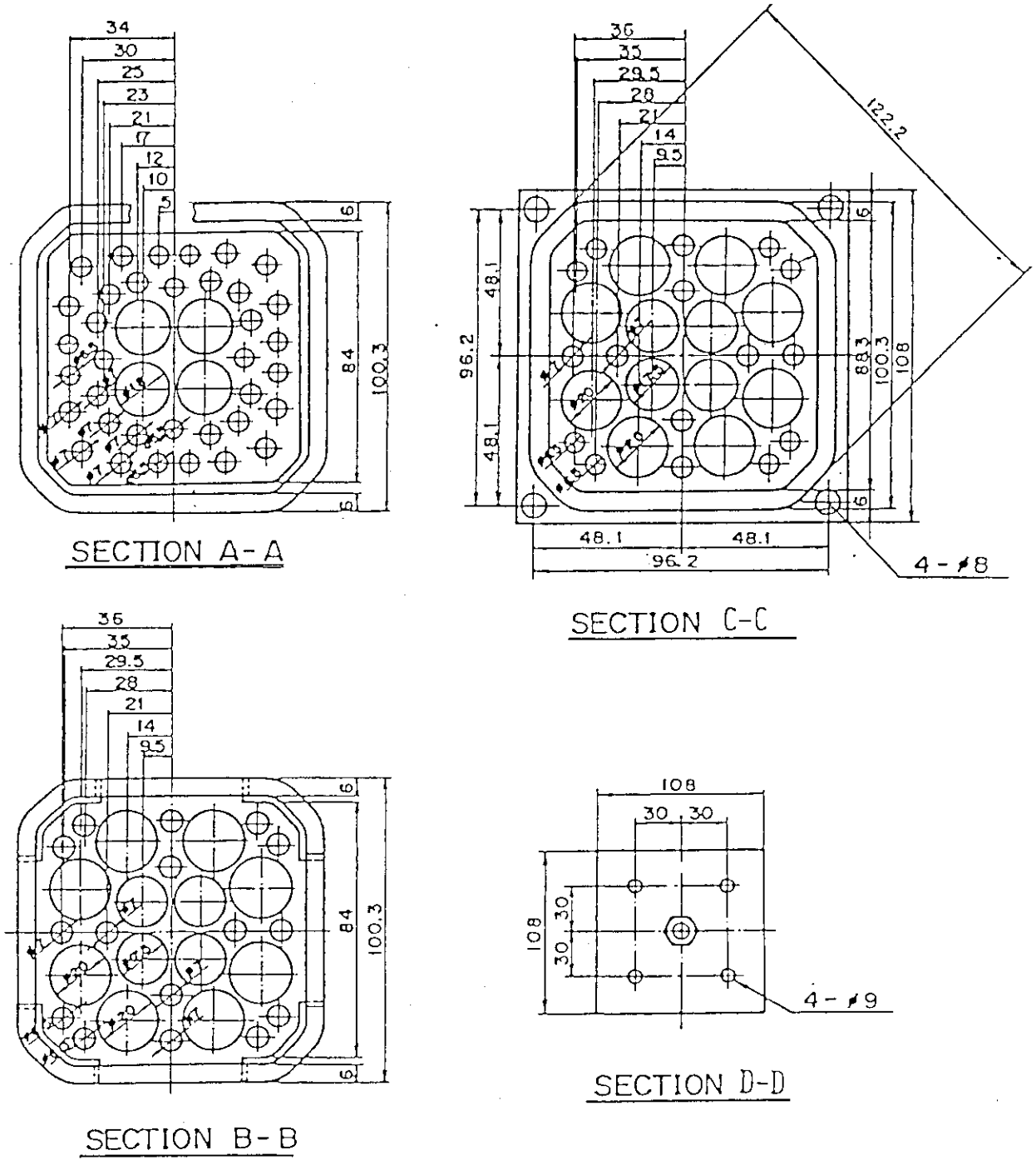

Fig. A-7 Dimension of Guide Tube (2)

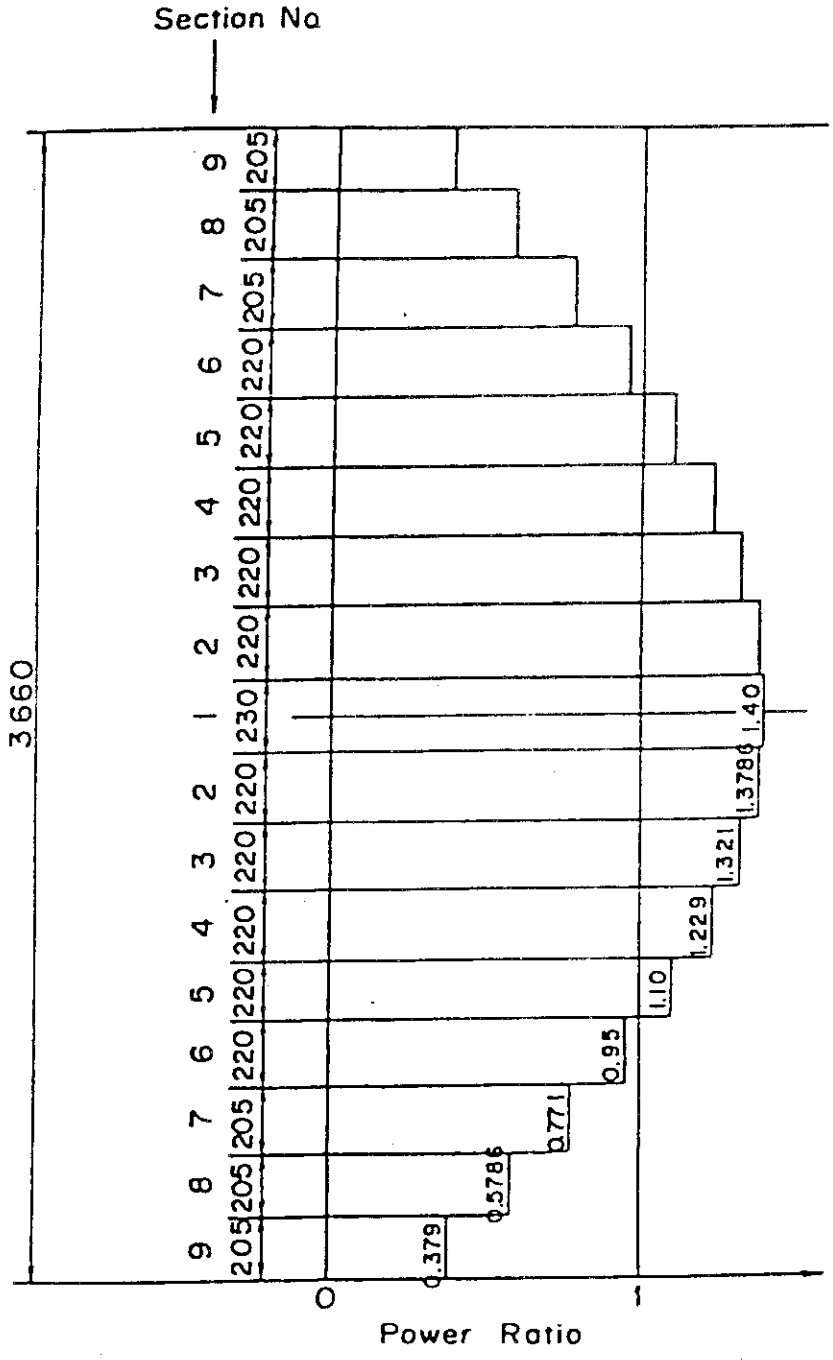

Fig. A-8 Axial Power Distribution of Heater Rod

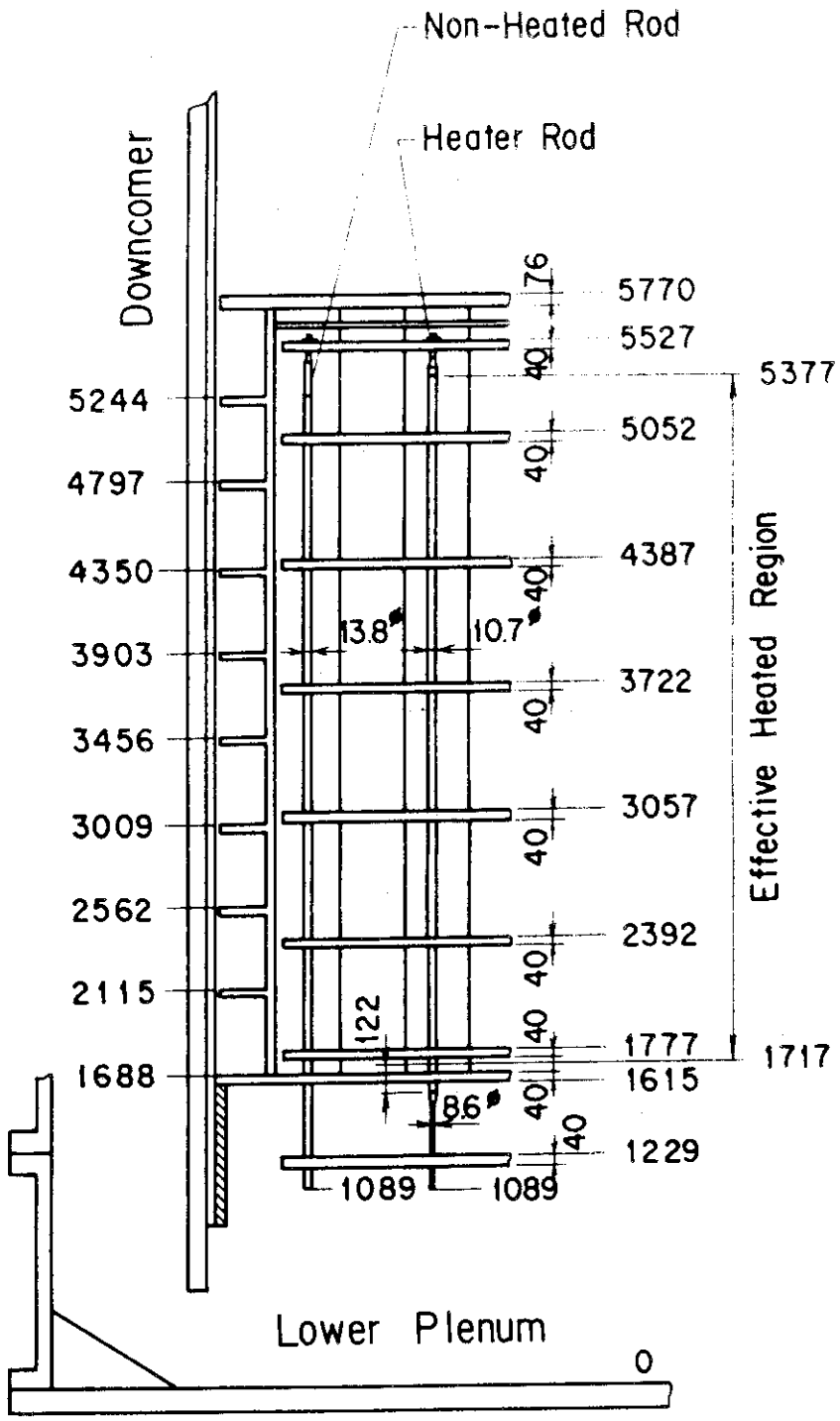

Fig. A-9 Relative Elevation and Dimension of the Core in SCTF

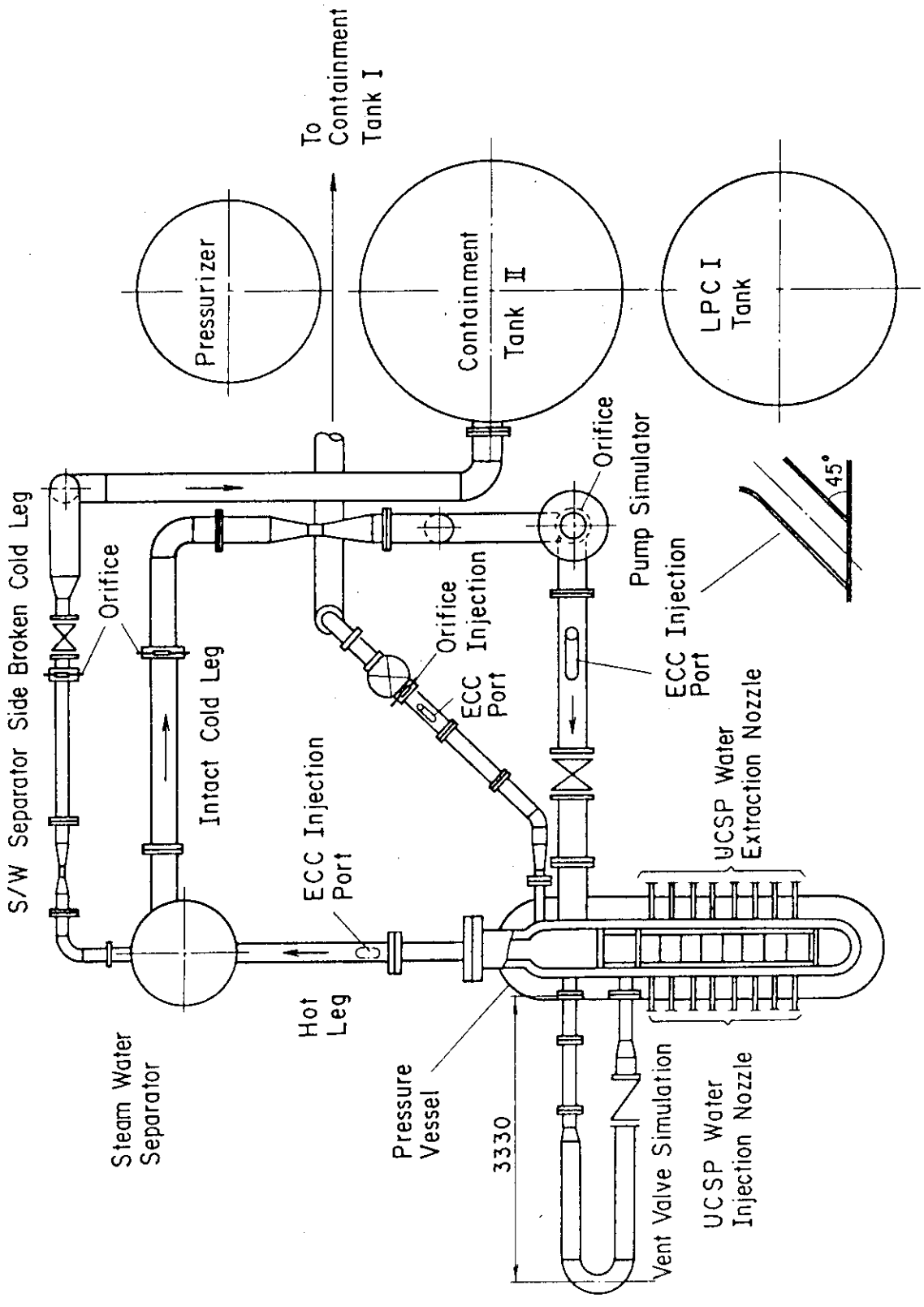

Fig. A-10 Overview of the Arrangements of the SCTF

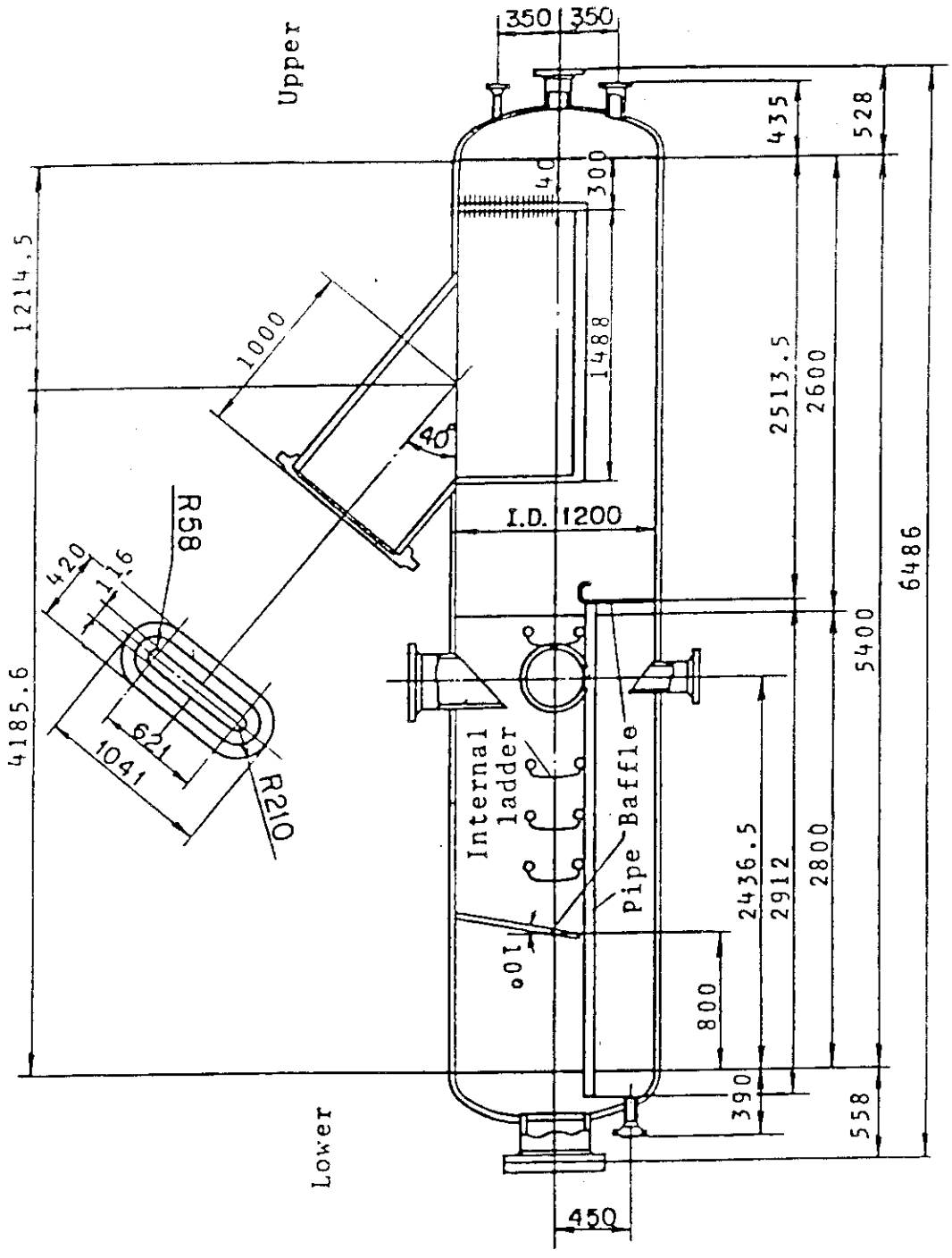

Fig. A-11 Steam/Water Separator

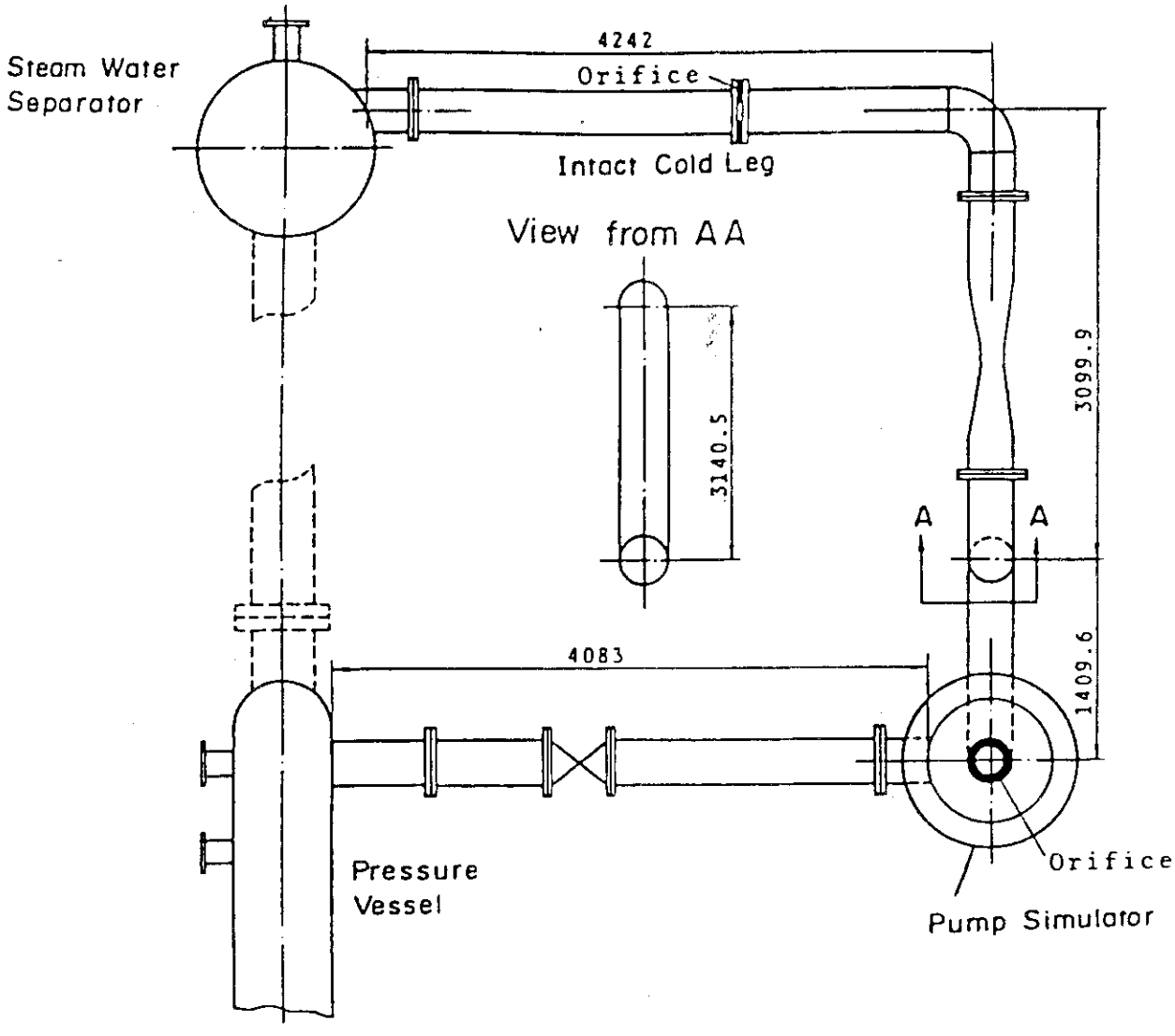

Fig. A-12 Arrangement of Intact Cold Leg

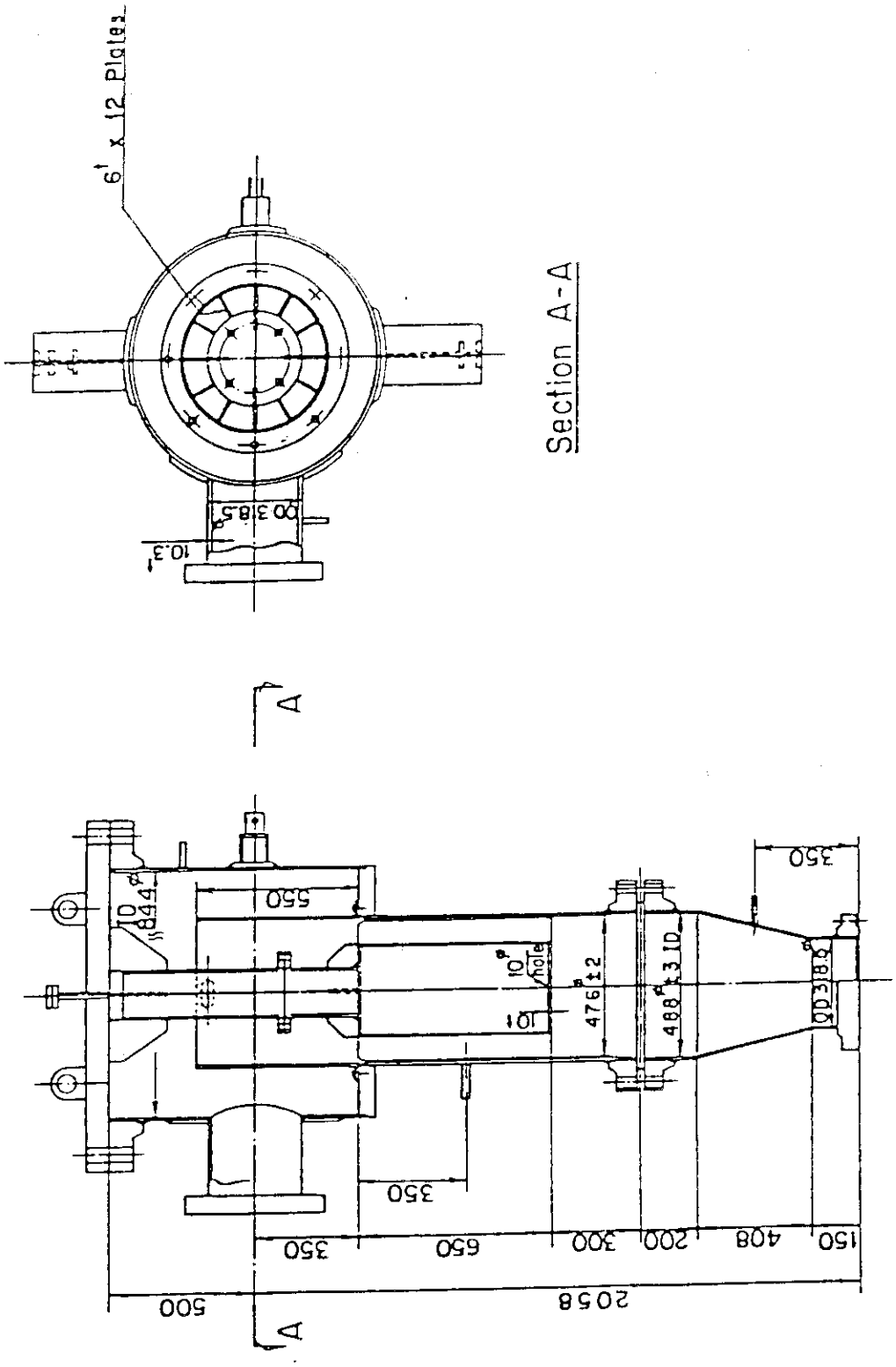

Fig. A-13 Configuration and Dimension of Pump Simulator

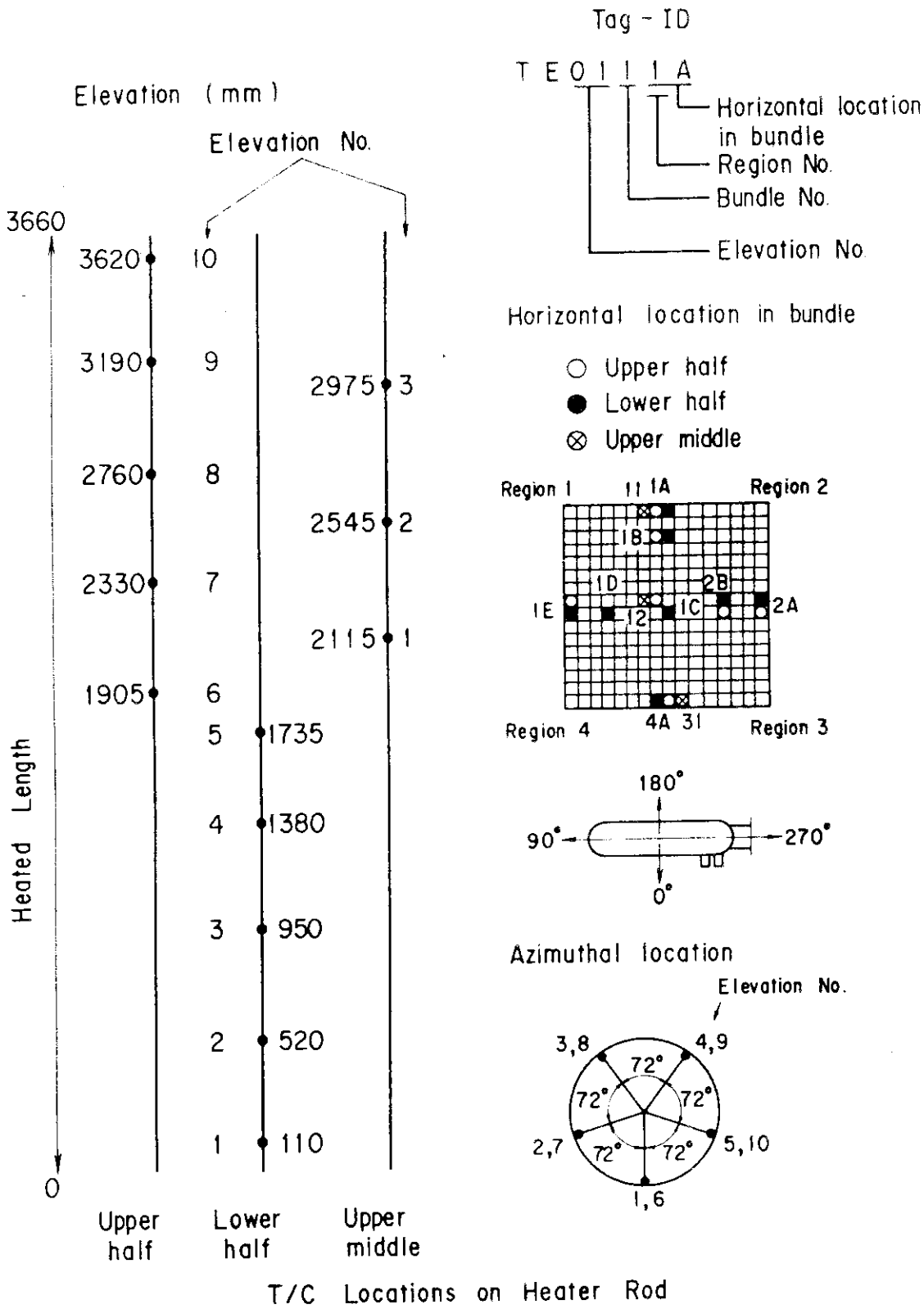

Fig. A-14 Thermocouple Locations of Heater Rod Surface Temperature Measurements

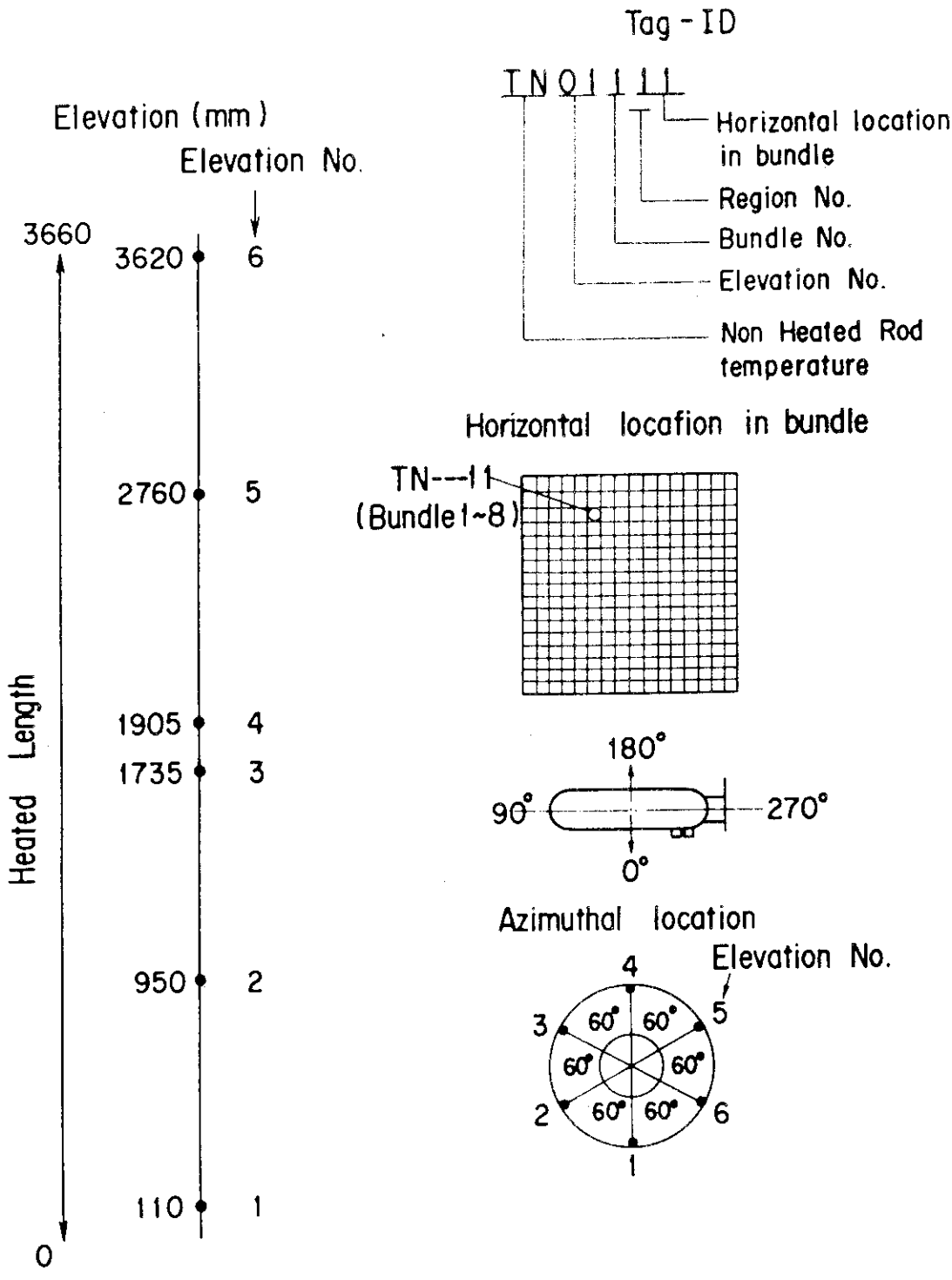

Fig. A-15 Thermocouple Locations of Non-Heated Rod Surface Temperature Measurements

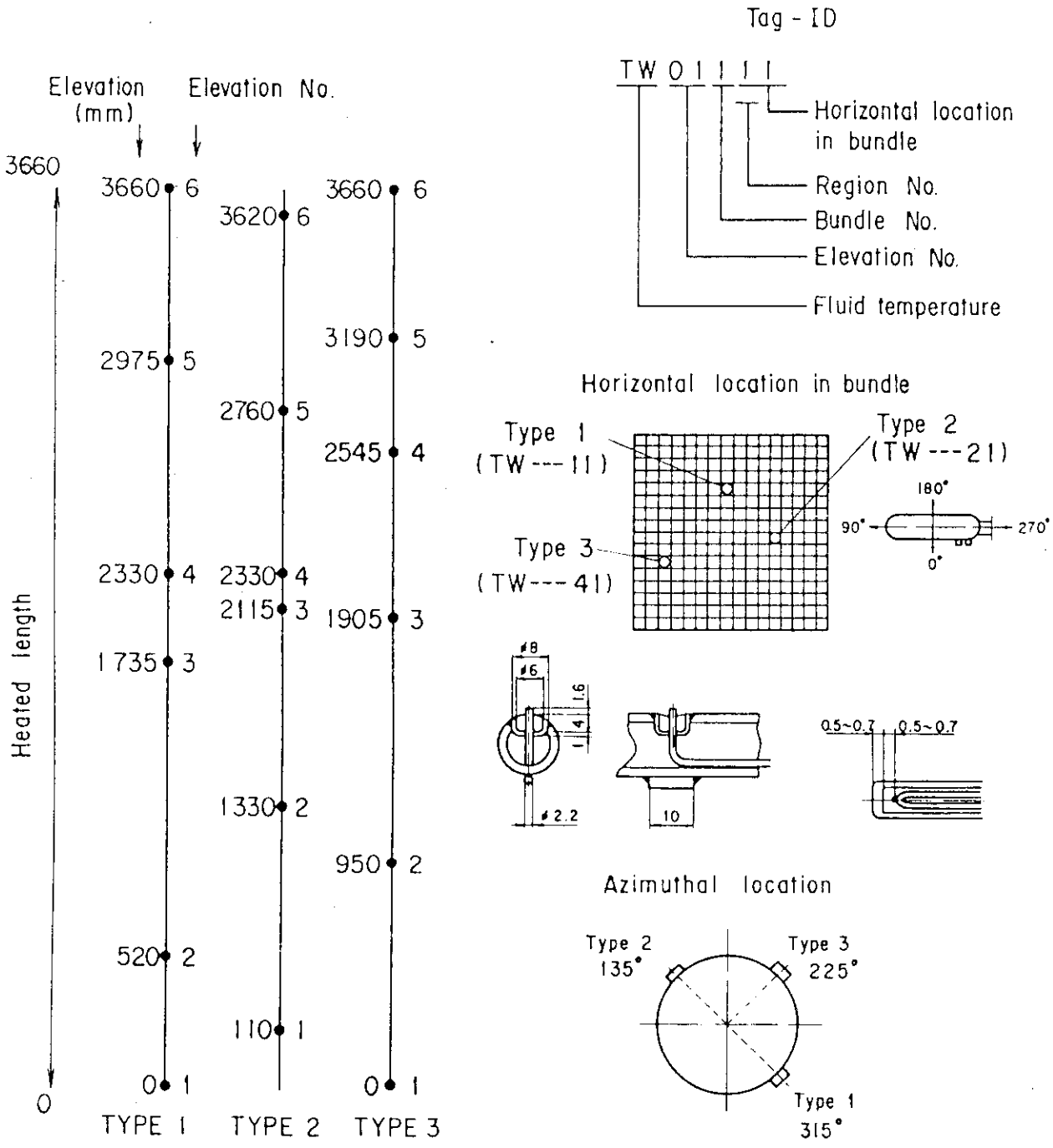

Fig. A-16 Thermocouple Locations of Fluid Temperature (Sputtering) Measurements in Core

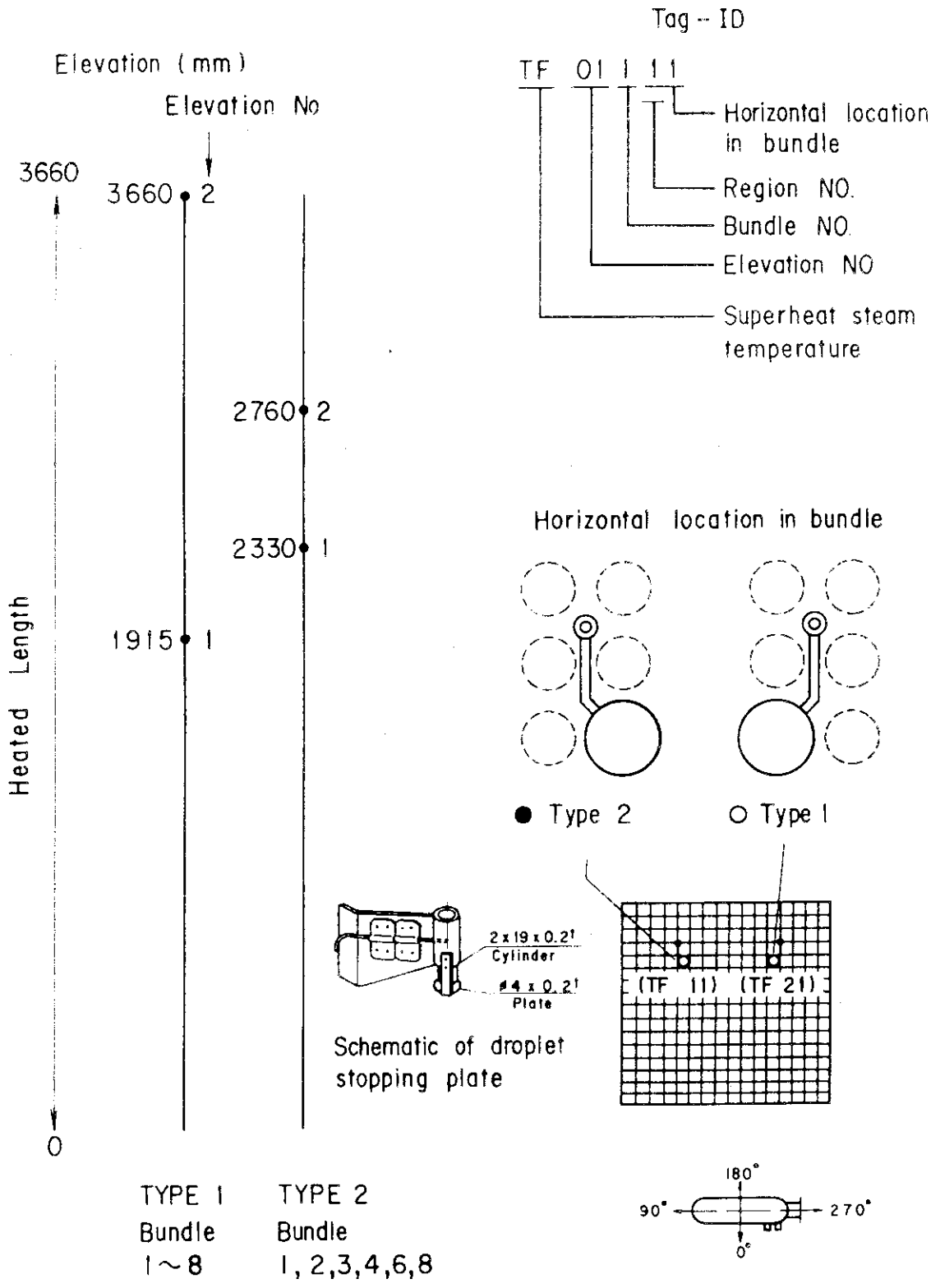

Fig. A-17 Thermocouple Locations of Steam Temperature Measurements in Core

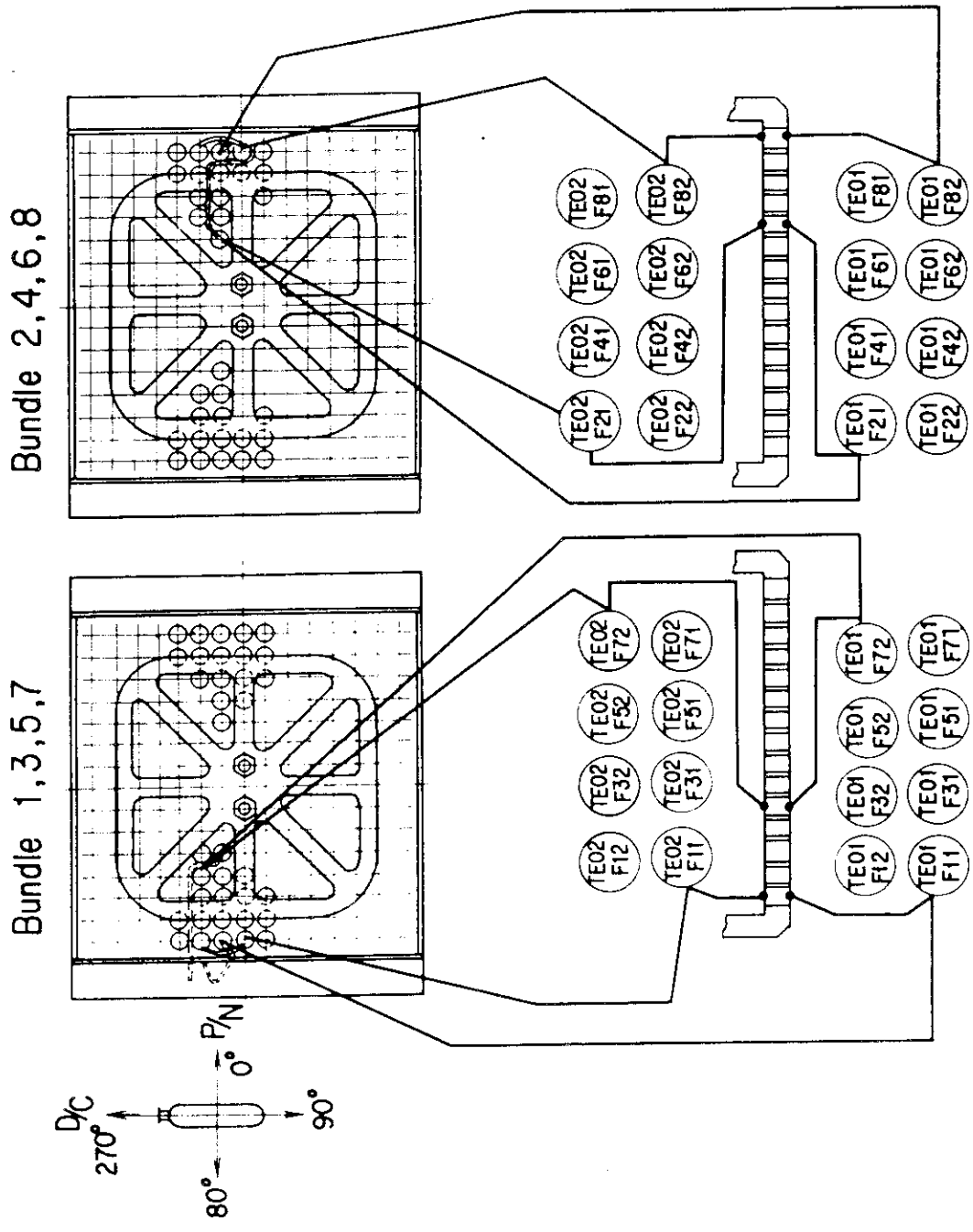

Fig. A-18 Thermocouple Locations of Fluid Temperature Measurement just above and below End Box Tie Plate

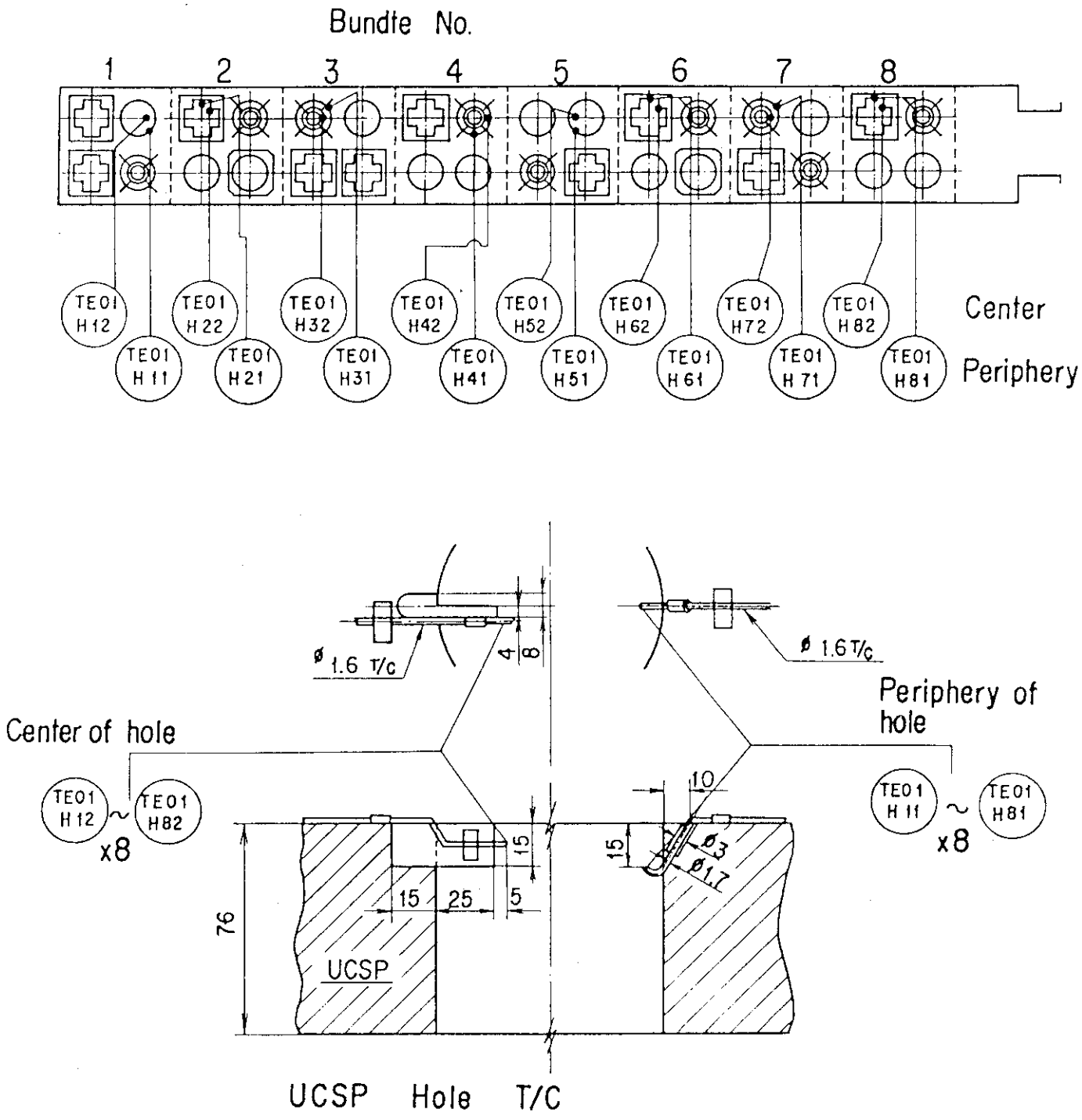

Fig. A-19 Thermocouple Locations of Fluid Temperature Measurements at Center and Periphery of UCSP Holes

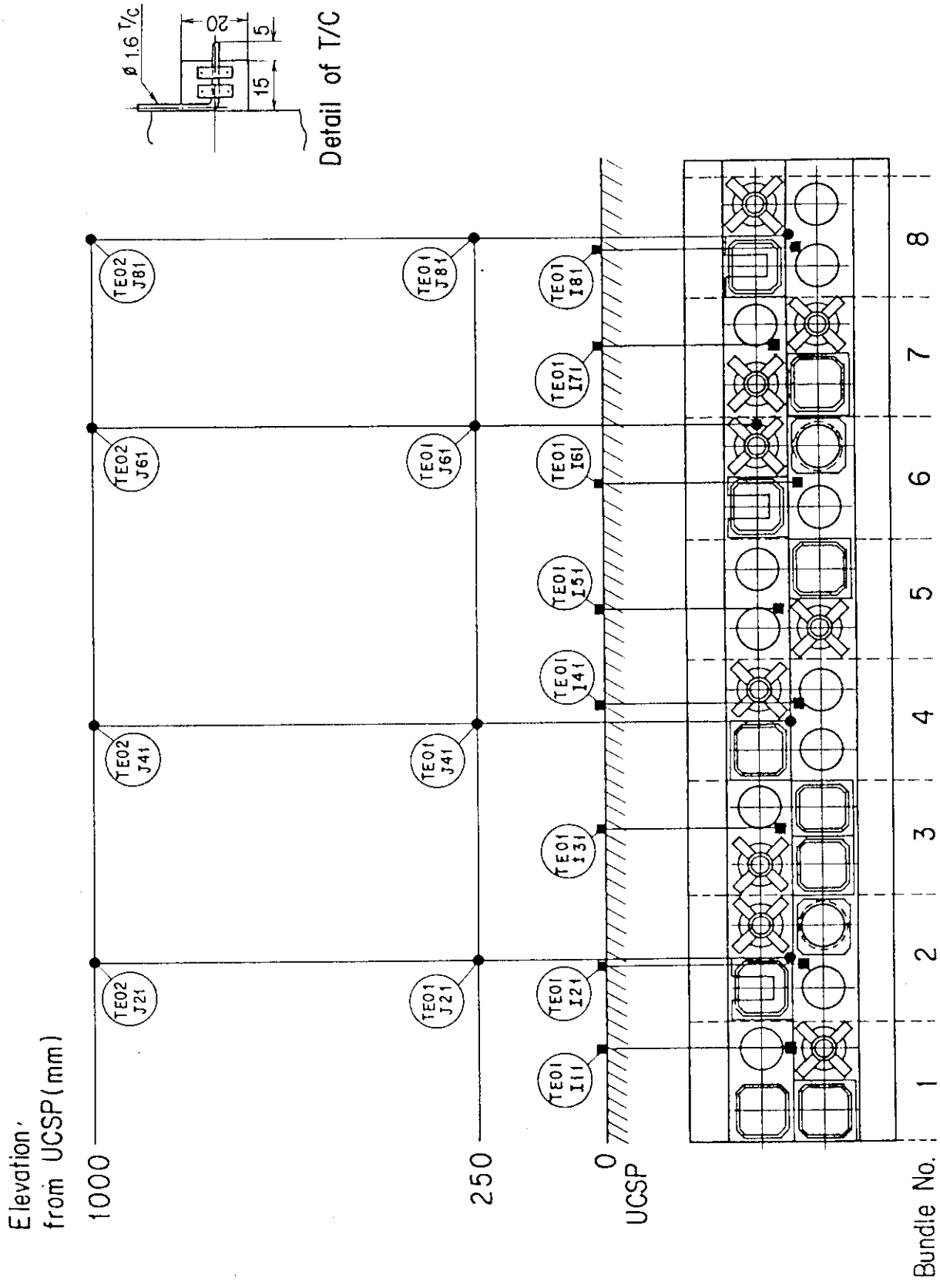

Fig. A-20 Thermocouple Locations of Fluid Temperature Measurements on and above UCSP

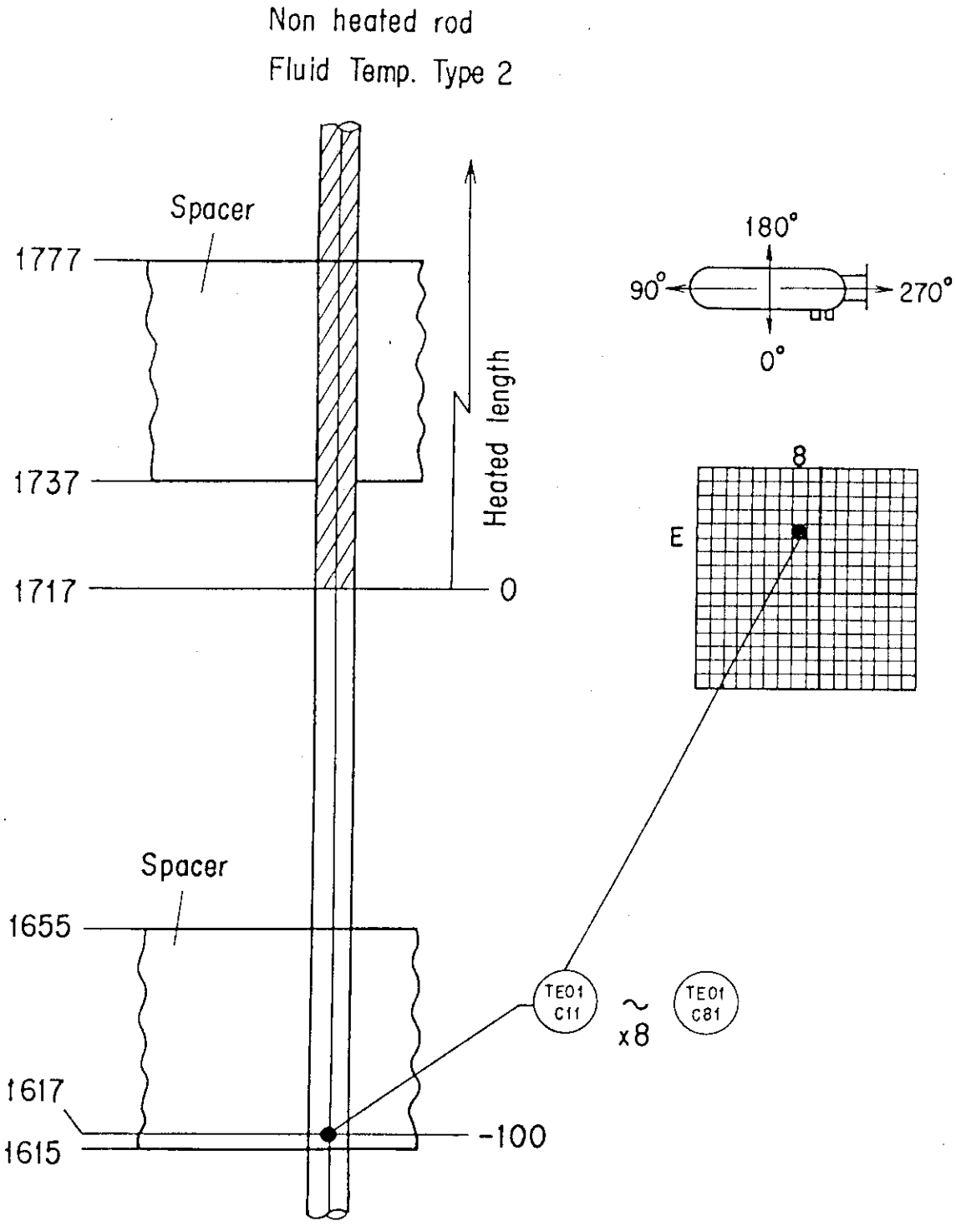

Fig. A-21 Thermocouple Locations of Fluid Temperature Measurements at Core Inlet

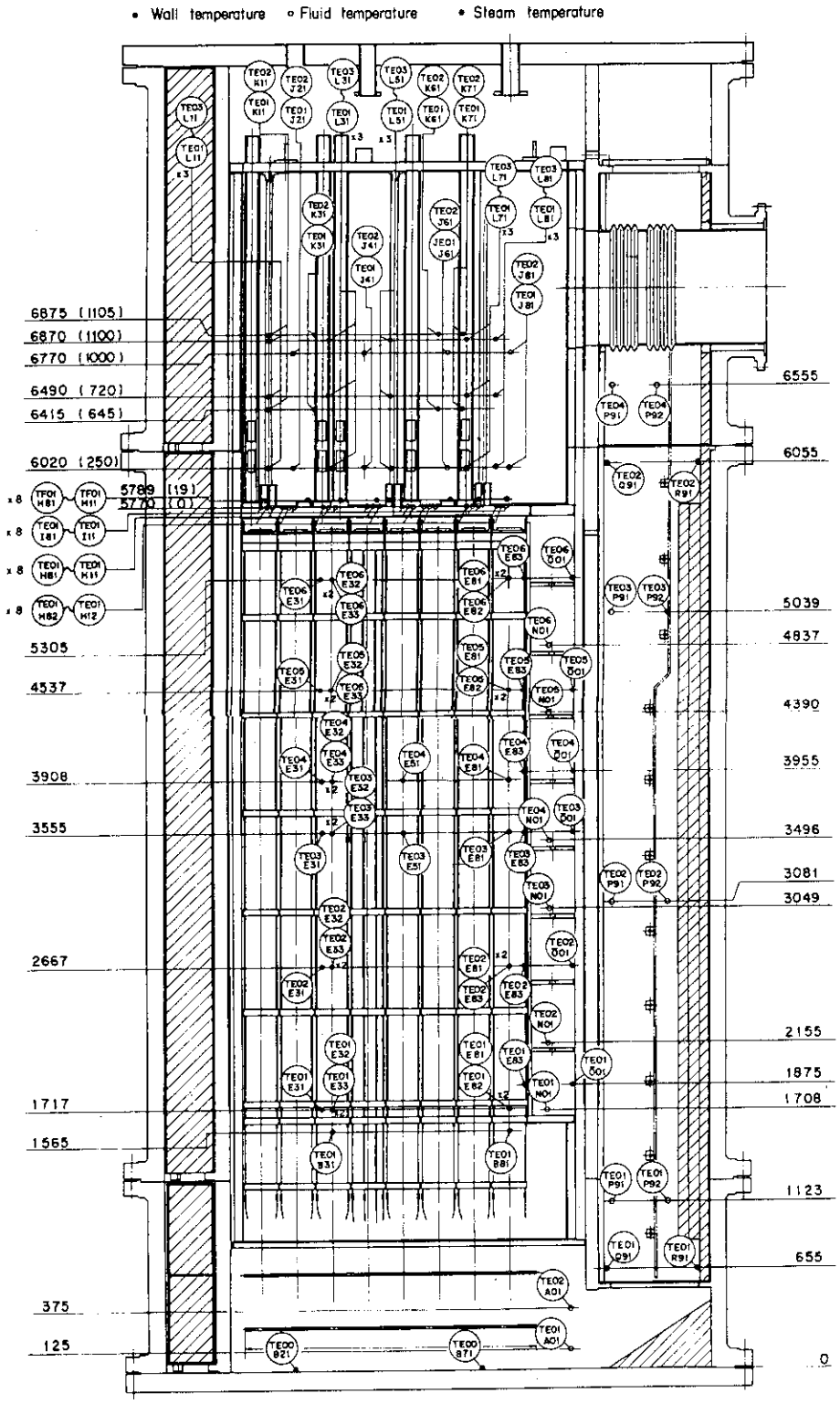

Fig. A-22 Thermocouple Locations of Temperature Measurements in Pressure Vessel except Core Region

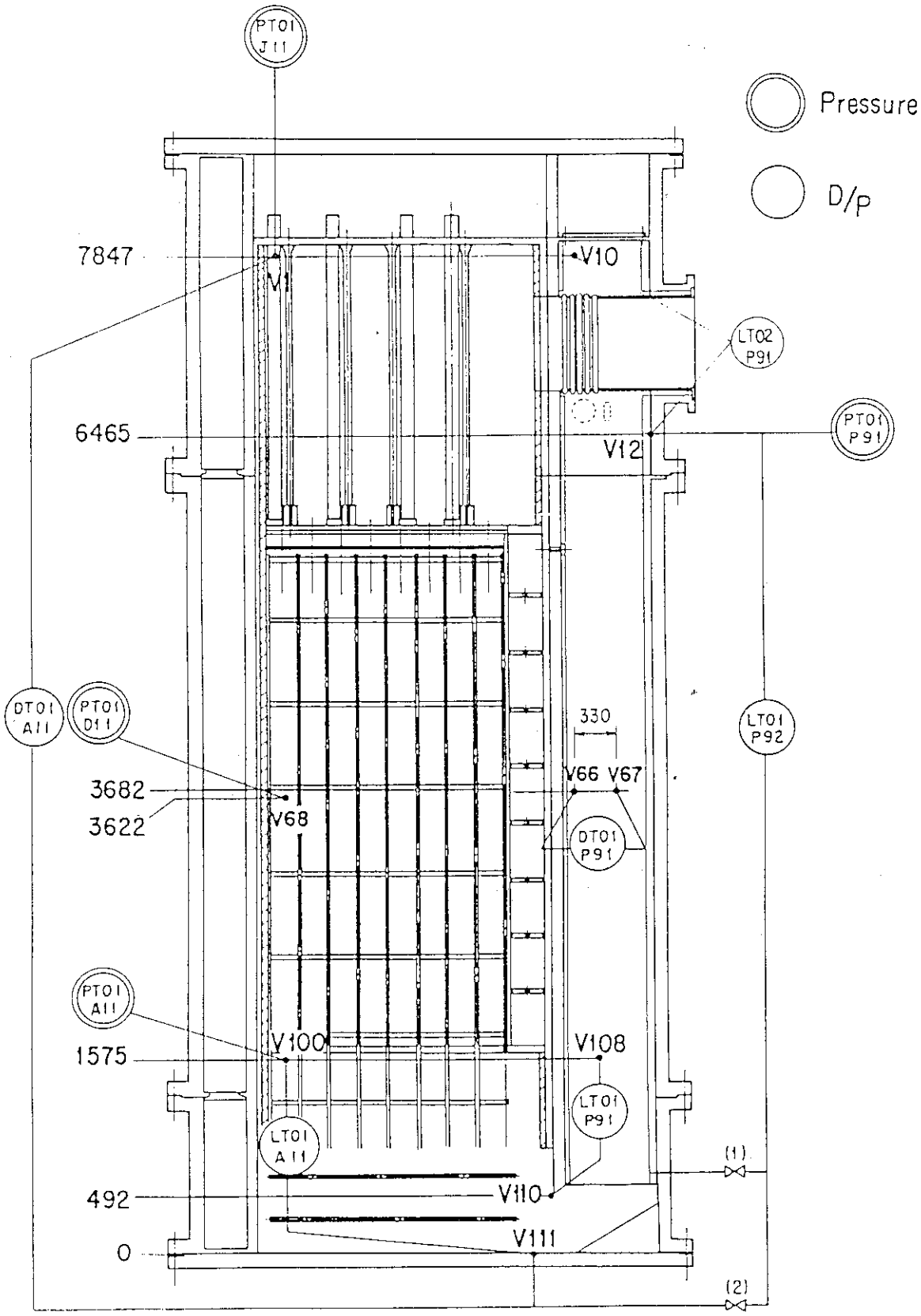

Fig. A-23 Location of Pressure Measurements in Pressure Vessel, Differential Pressure Measurements between Upper and Lower Plenums and Liquid Level Measurements in Downcomer and Lower Plenum

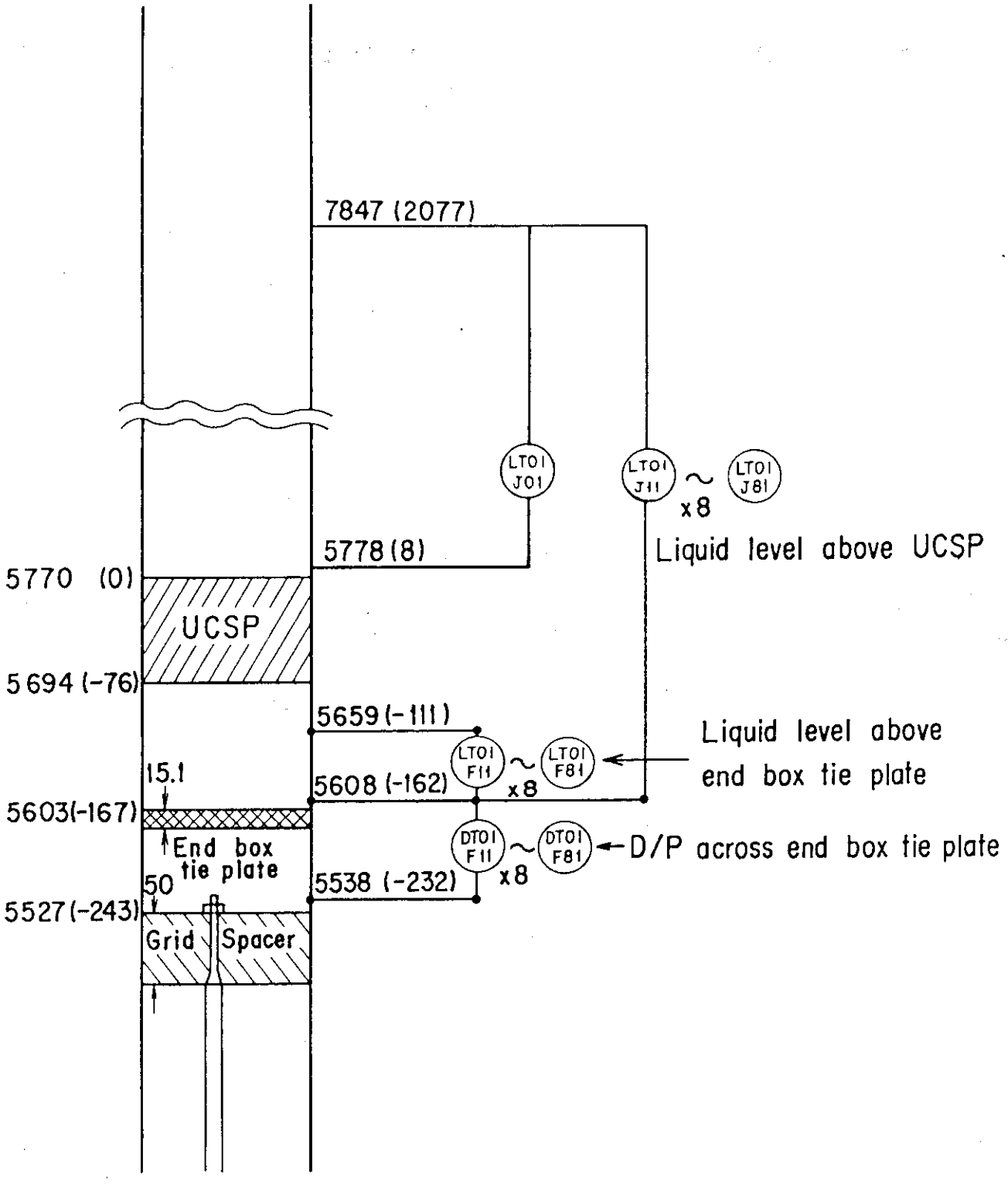

Fig. A-24 Locations of Differential Pressure Measurements across End Box Tie Plate and Liquid Level Measurements above UCSP and End Box Tie Plate

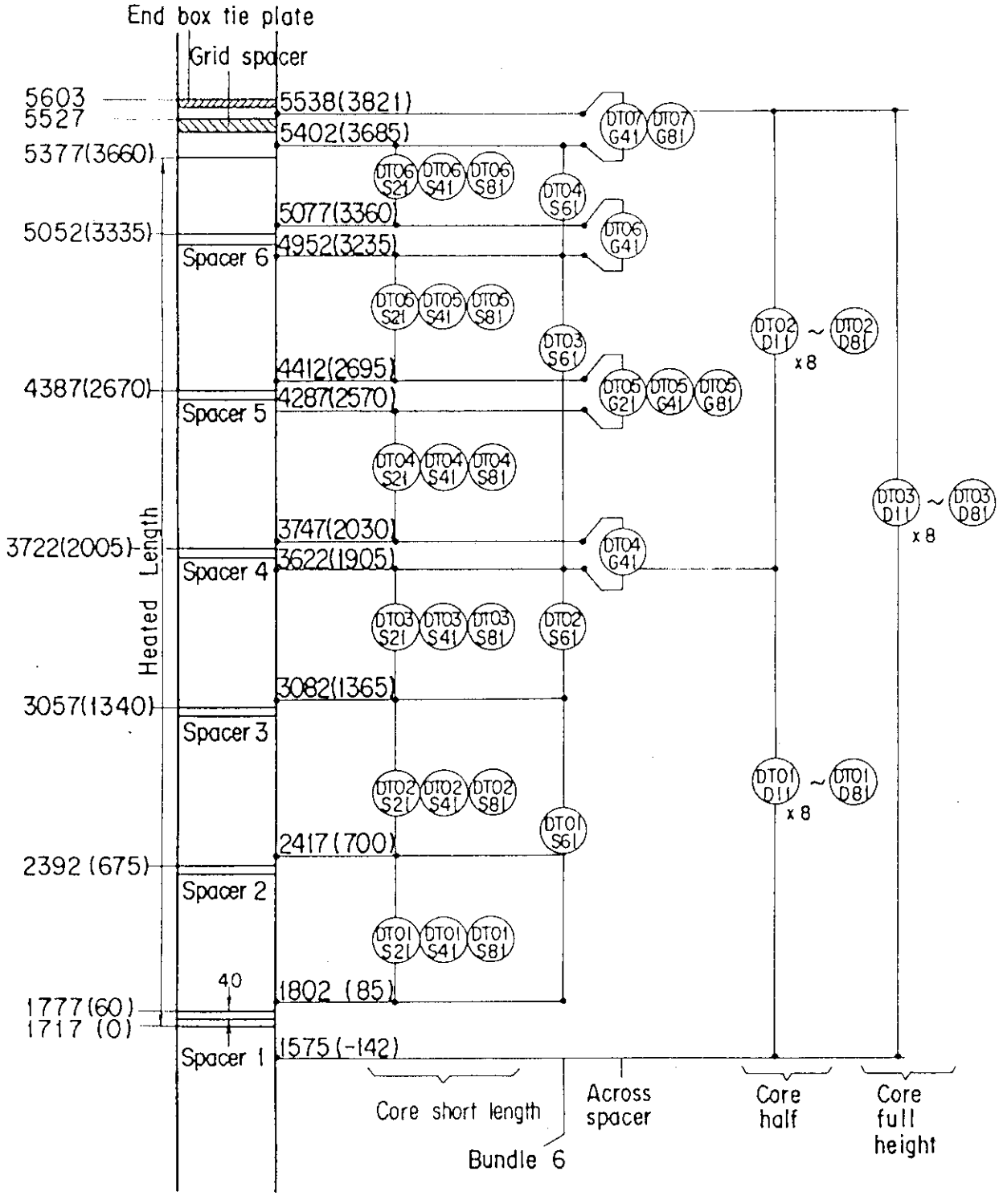

Fig. A-25 Locations of Vertical Differential Pressure Measurements in Core

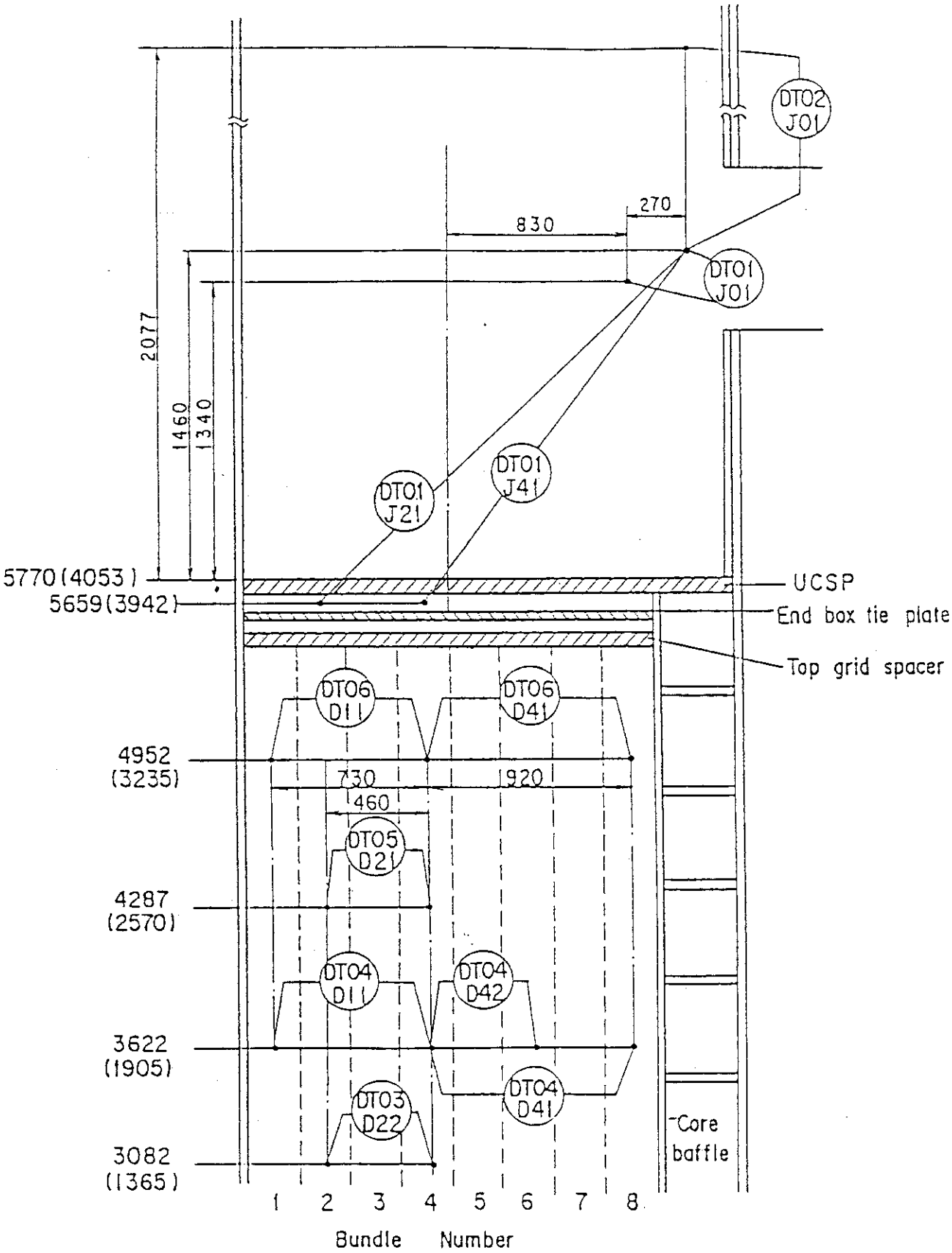

Fig. A-26 Measurement Locations of Horizontal Differential Pressures in Core and Differential Pressures in Upper Plenum

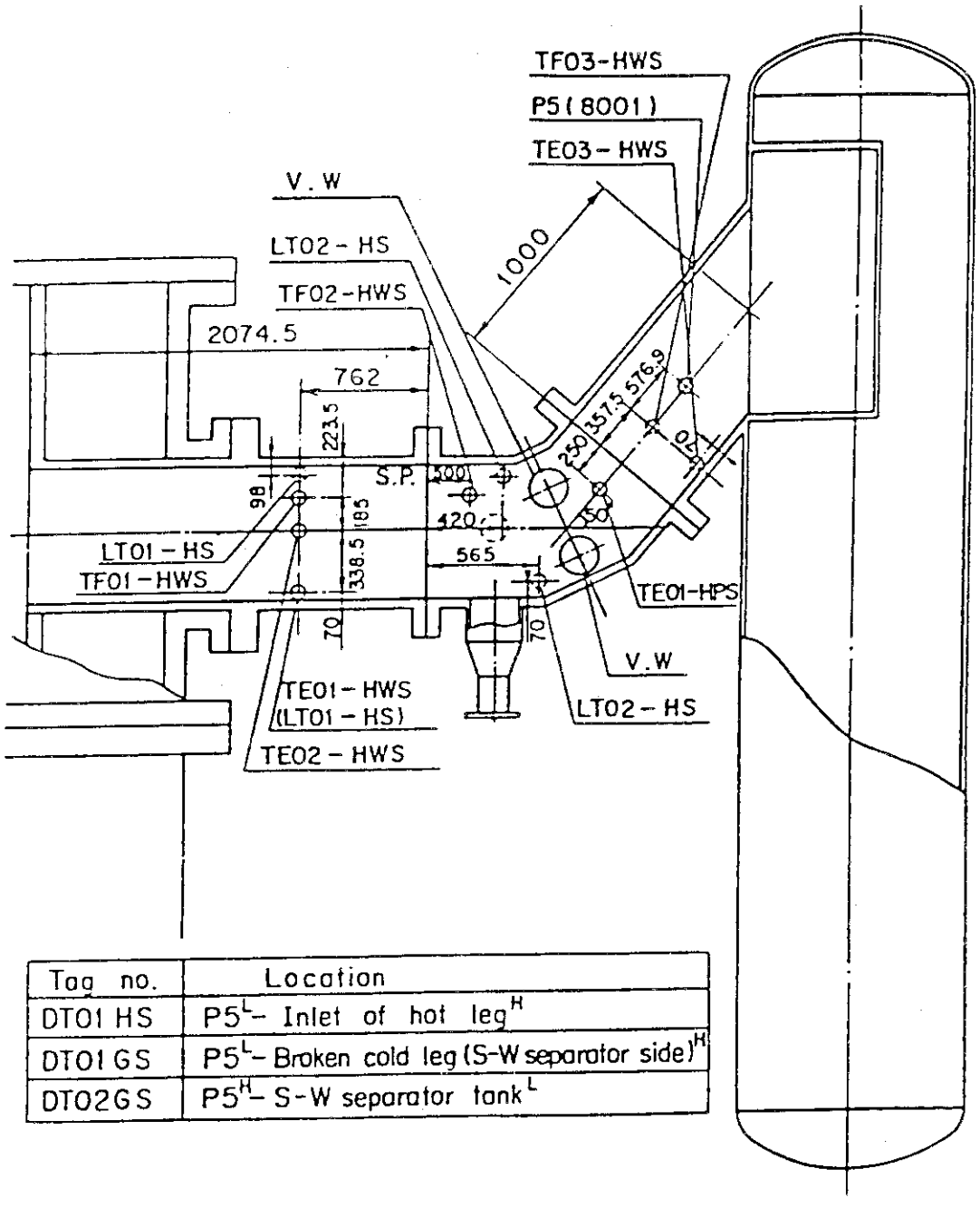

Tag no.	Location
DT01 HS	P5[L]- Inlet of hot leg[H]
DT01 GS	P5[L]- Broken cold leg (S-W separator side)[H]
DT02GS	P5[H]- S-W separator tank[L]

Fig. A-27 Locations of Hot Leg Instrumentation

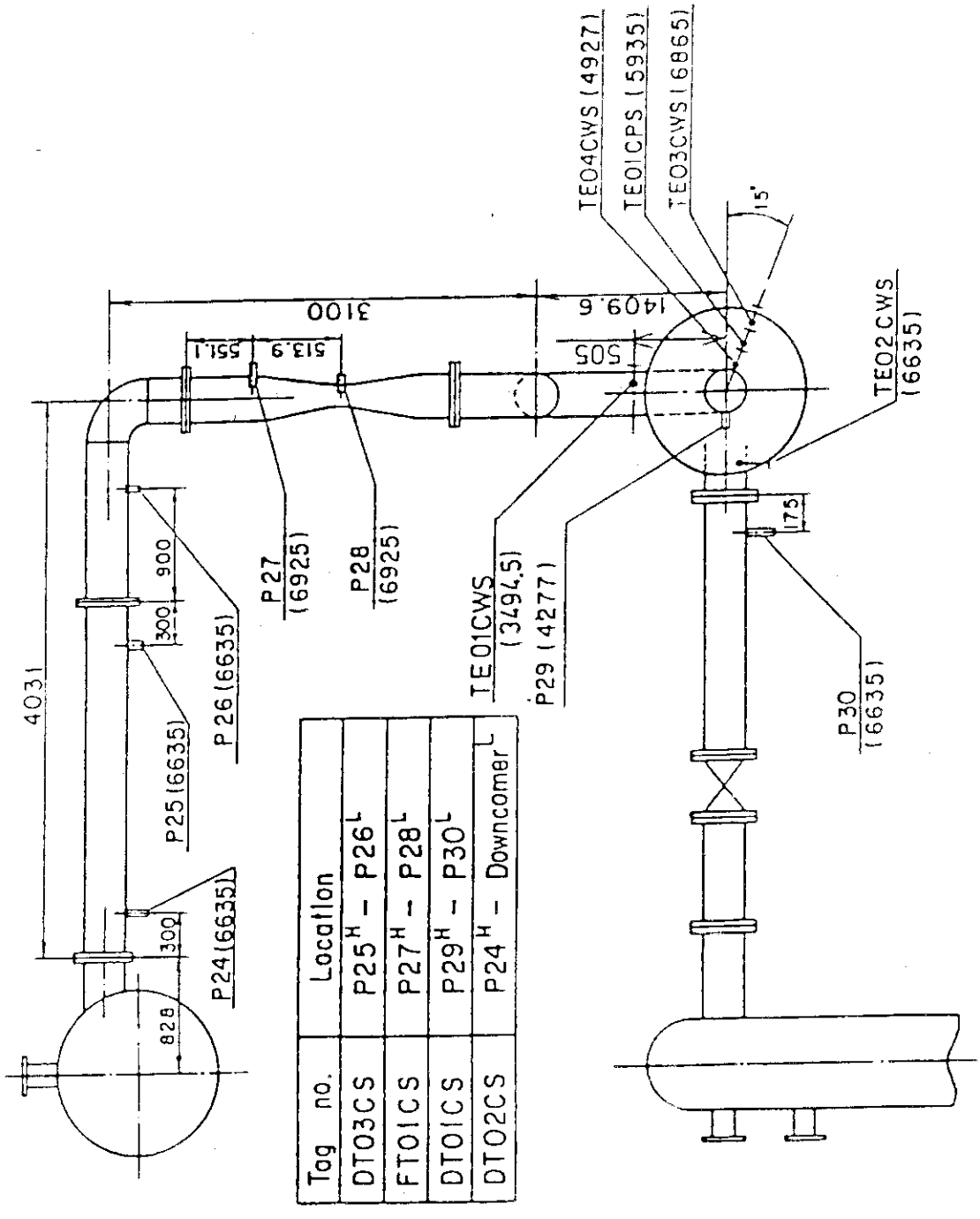

Fig. A-28 Locations of Intact Cold Leg Instrumentation

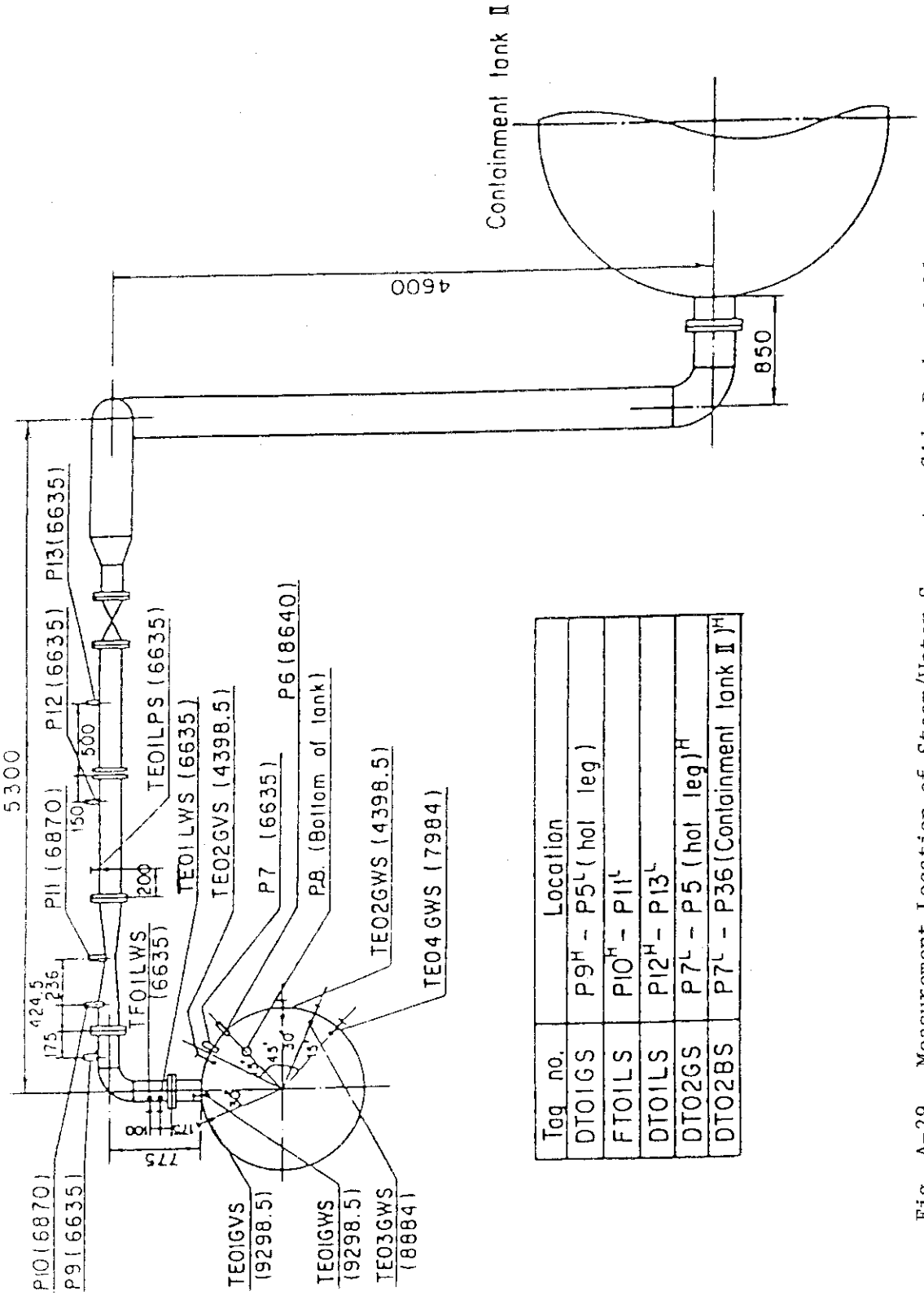

Tag no.	Location
DT01GS	$P9^H$ - $P5^L$ (hot leg)
FT01LS	$P10^H$ - $P11^L$
DT01LS	$P12^H$ - $P13^L$
DT02GS	$P7^L$ - P5 (hot leg)^H
DT02BS	$P7^L$ - P36 (Containment tank II)^H

Fig. A-29 Measurement Location of Steam/Water Separator Side Broken Cold Leg

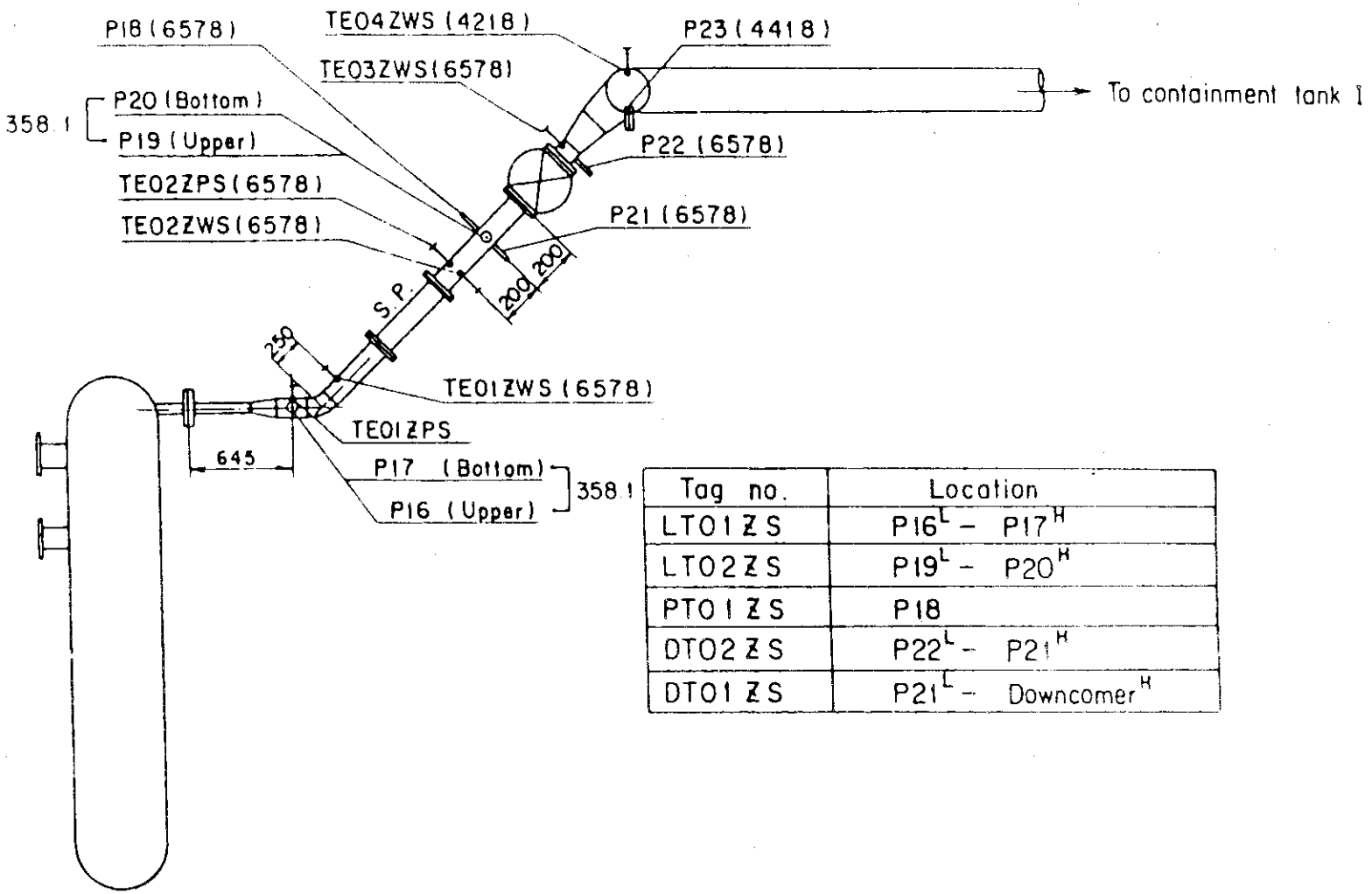

Tag no.	Location
LT01ZS	$P16^L$ – $P17^H$
LT02ZS	$P19^L$ – $P20^H$
PT01ZS	P18
DT02ZS	$P22^L$ – $P21^H$
DT01ZS	$P21^L$ – $Downcomer^H$

Fig. A-30 Measurement Location of Pressure Vessel Side Broken Cold Leg

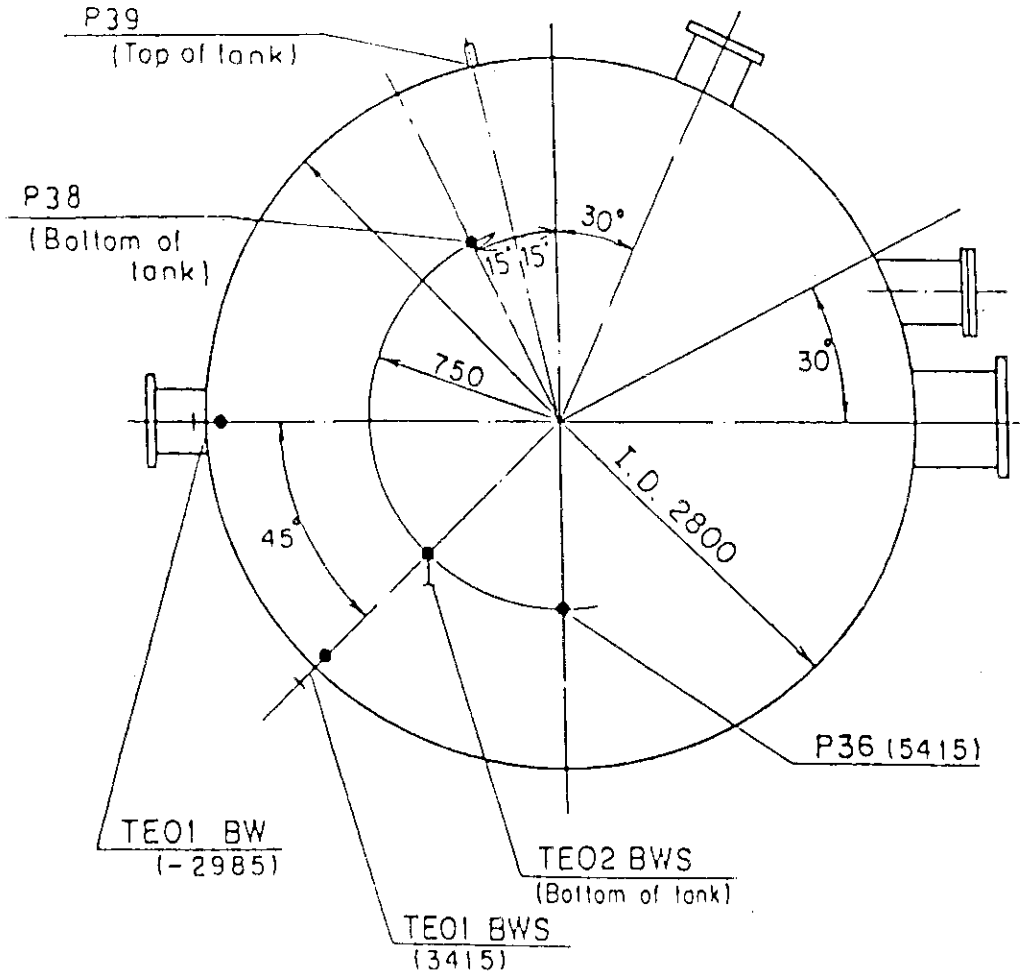

Tag no.	Location
DT01 BS	$P36^{H}$ – Upper plenum^{L}
DT02 BS	$P36^{H}$ – S-W Separator^{L}
DT01 E	$P36^{L}$ – P35 (C.T.I)^{H}
PT01 B	P36
LT01 1B	$P38^{H}$ – $P39^{L}$

Fig. A-31 Locations of Containment Tank-II Instrumentation

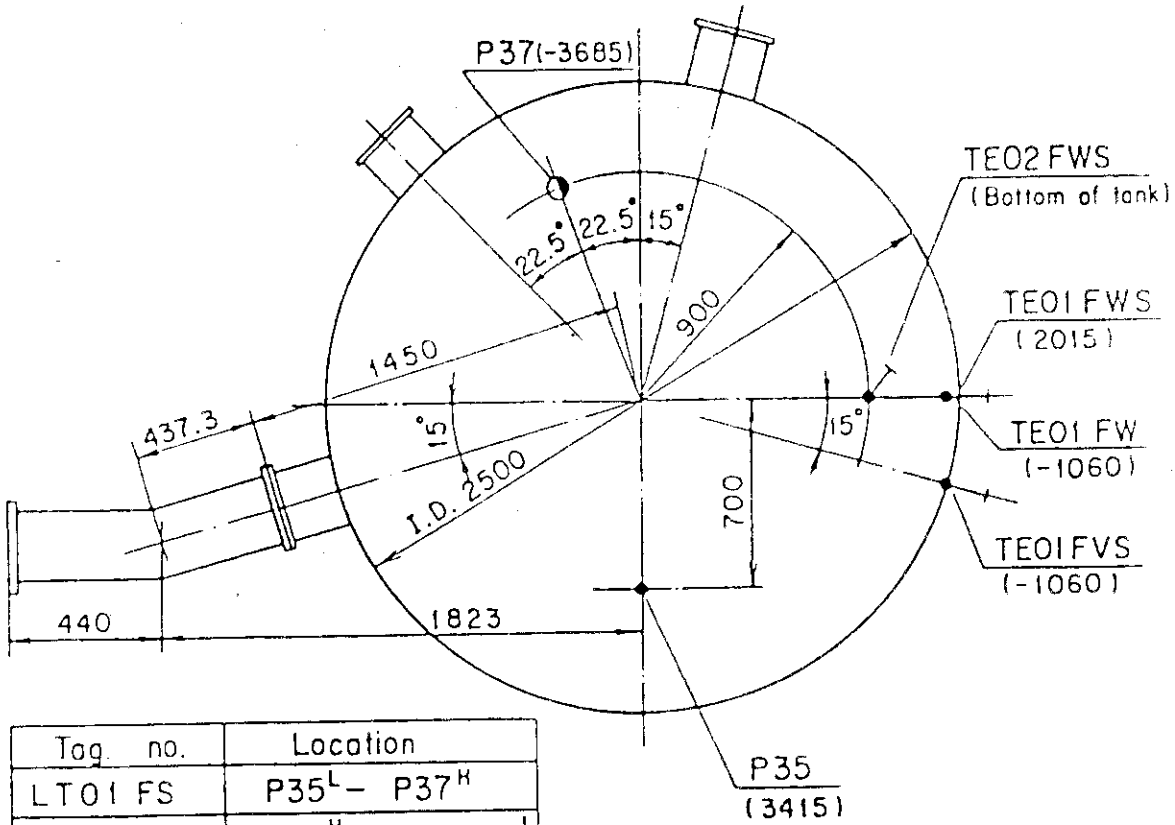

Tag. no.	Location
LT01 FS	$P35^{L}$ – $P37^{H}$
DT01 FS	$P35^{H}$ – $Downcomer^{L}$
DT01 E	$P35^{H}$ – P36(C.T. II)^{H}
PT01 F	P35

Fig. A-32 Locations of Containment Tank-I Instrumentation

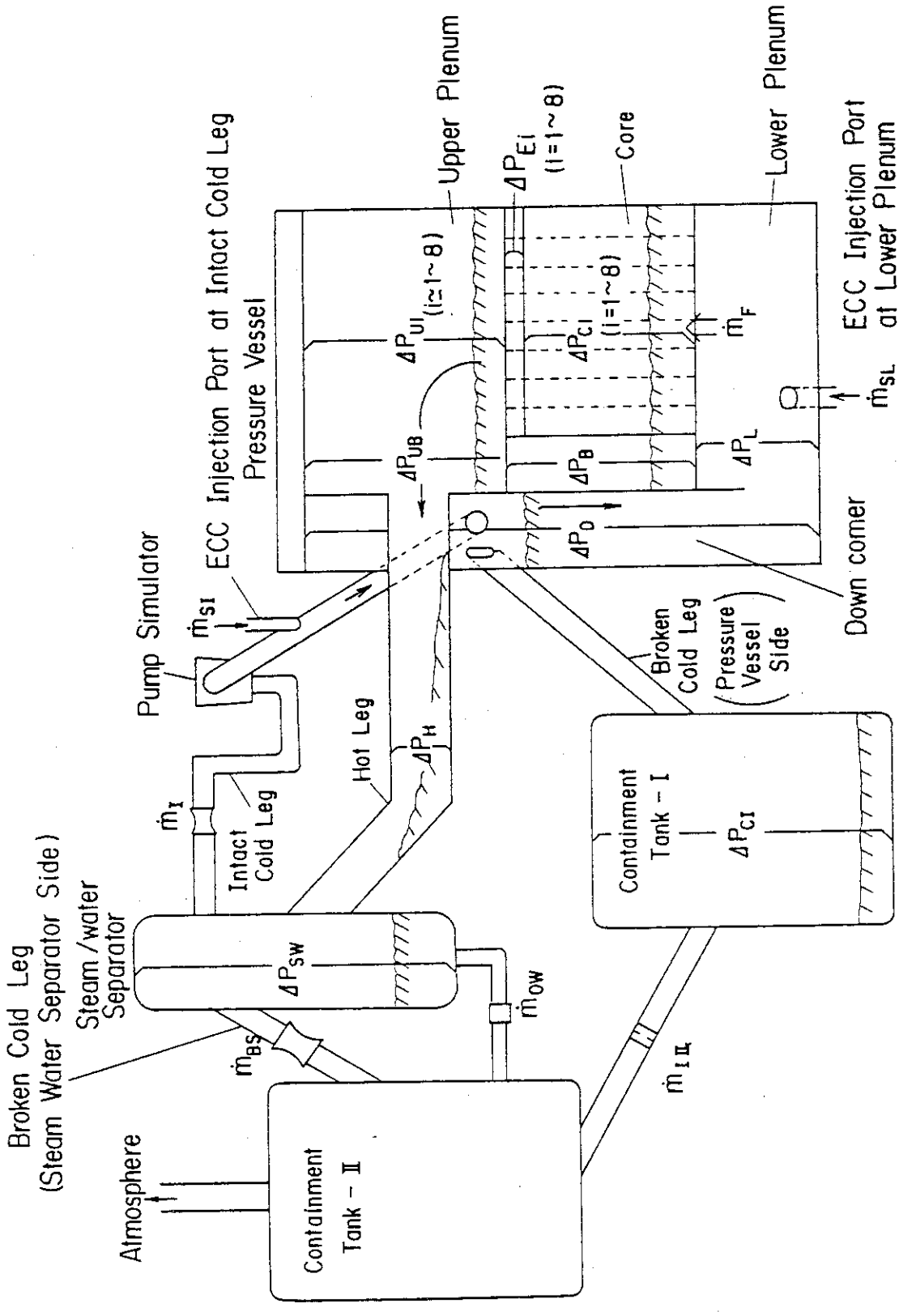

Fig.A-33 Schematic of SCTF and locations of differential pressure and mass flow rate measurements

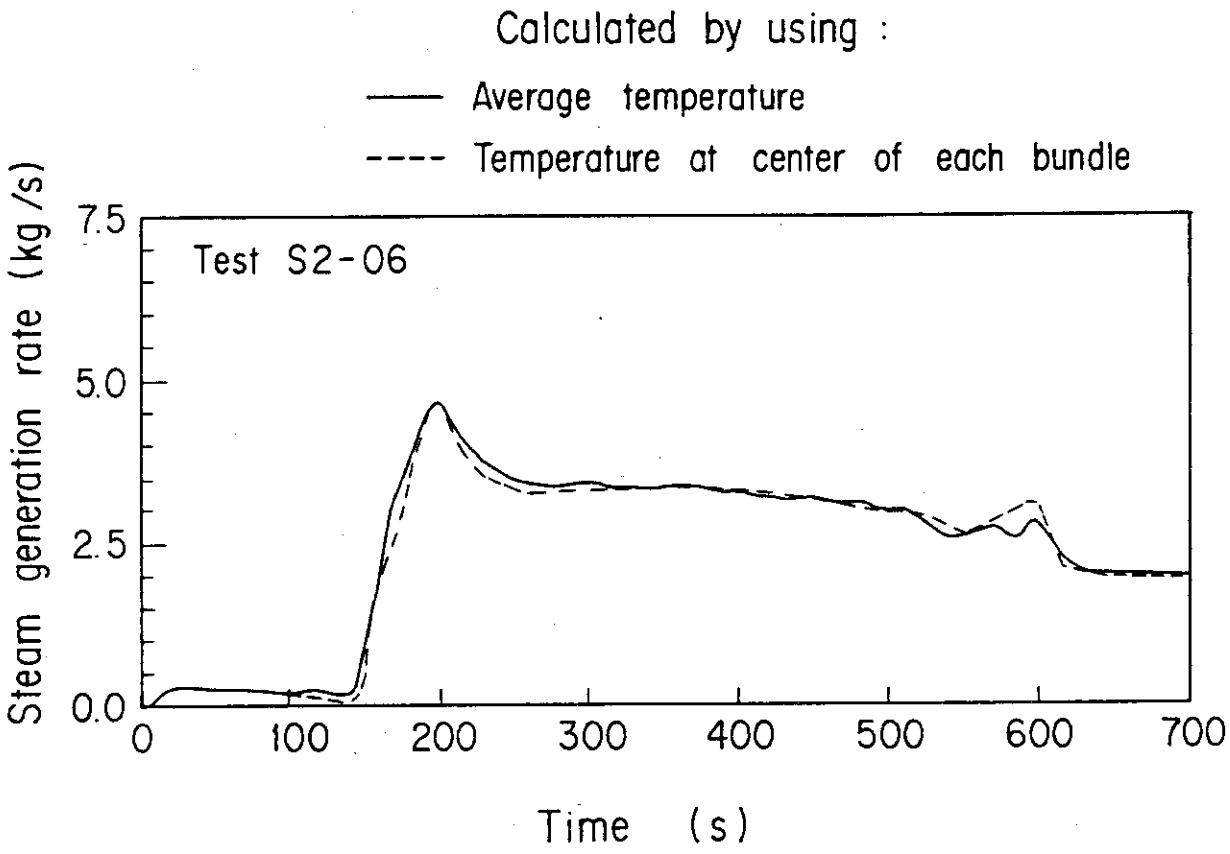

Fig. A-34 Effect of temperature data on steam generation calculation

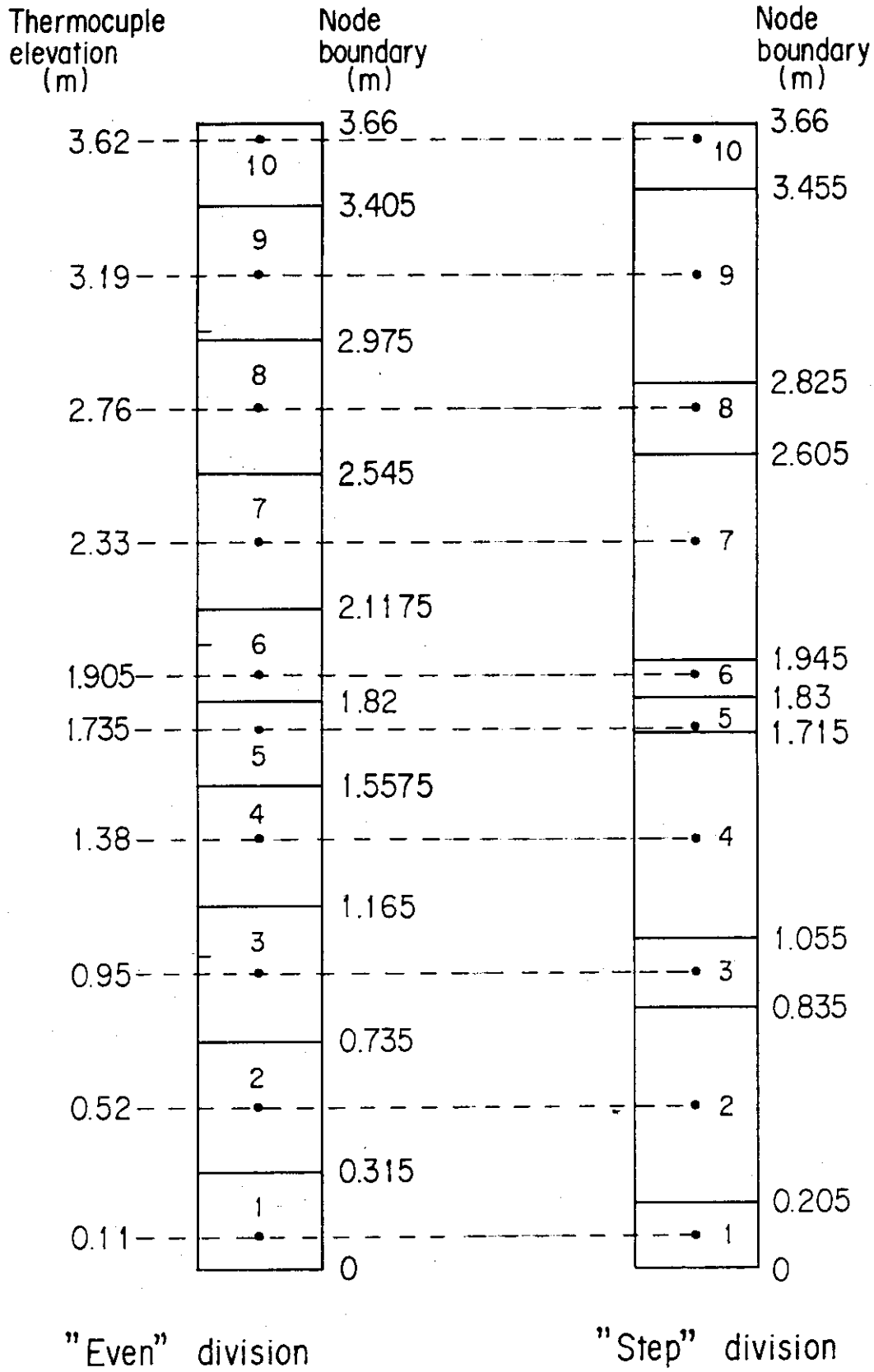

Fig. A-35 Two kinds of vertical noding models for steam generation calculation

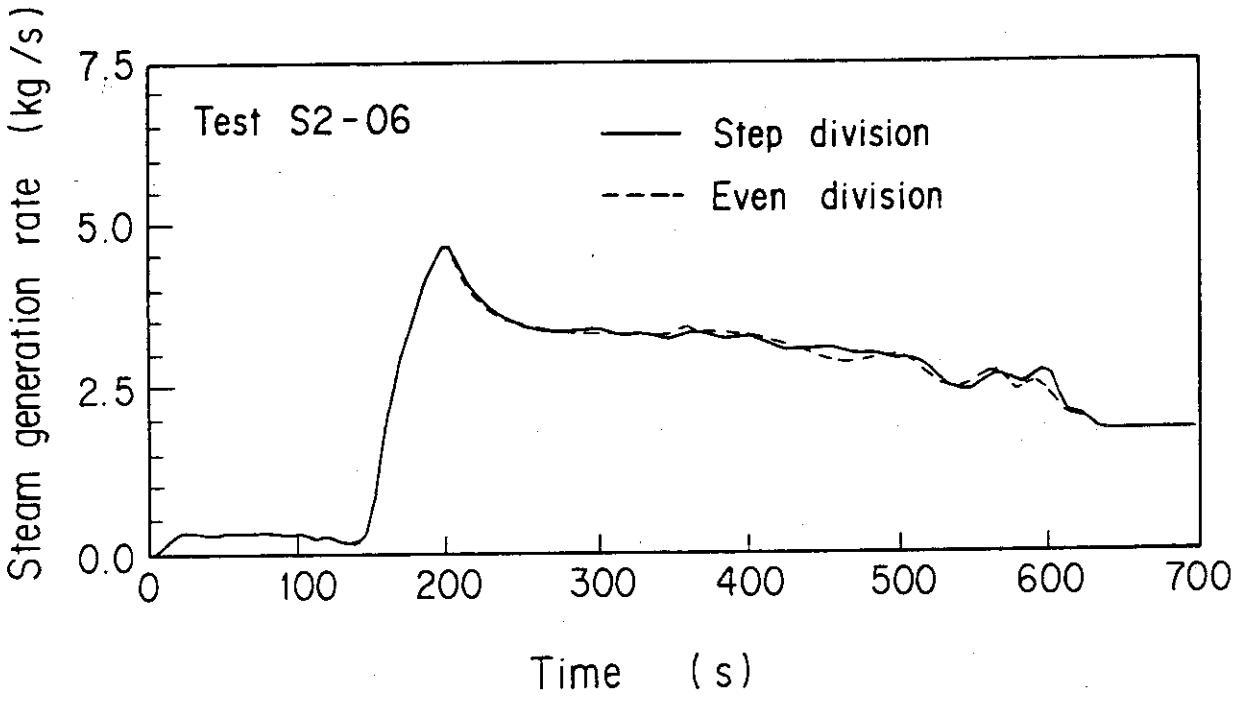

Fig. A-36 Effect of vertical noding models on steam generation calculation

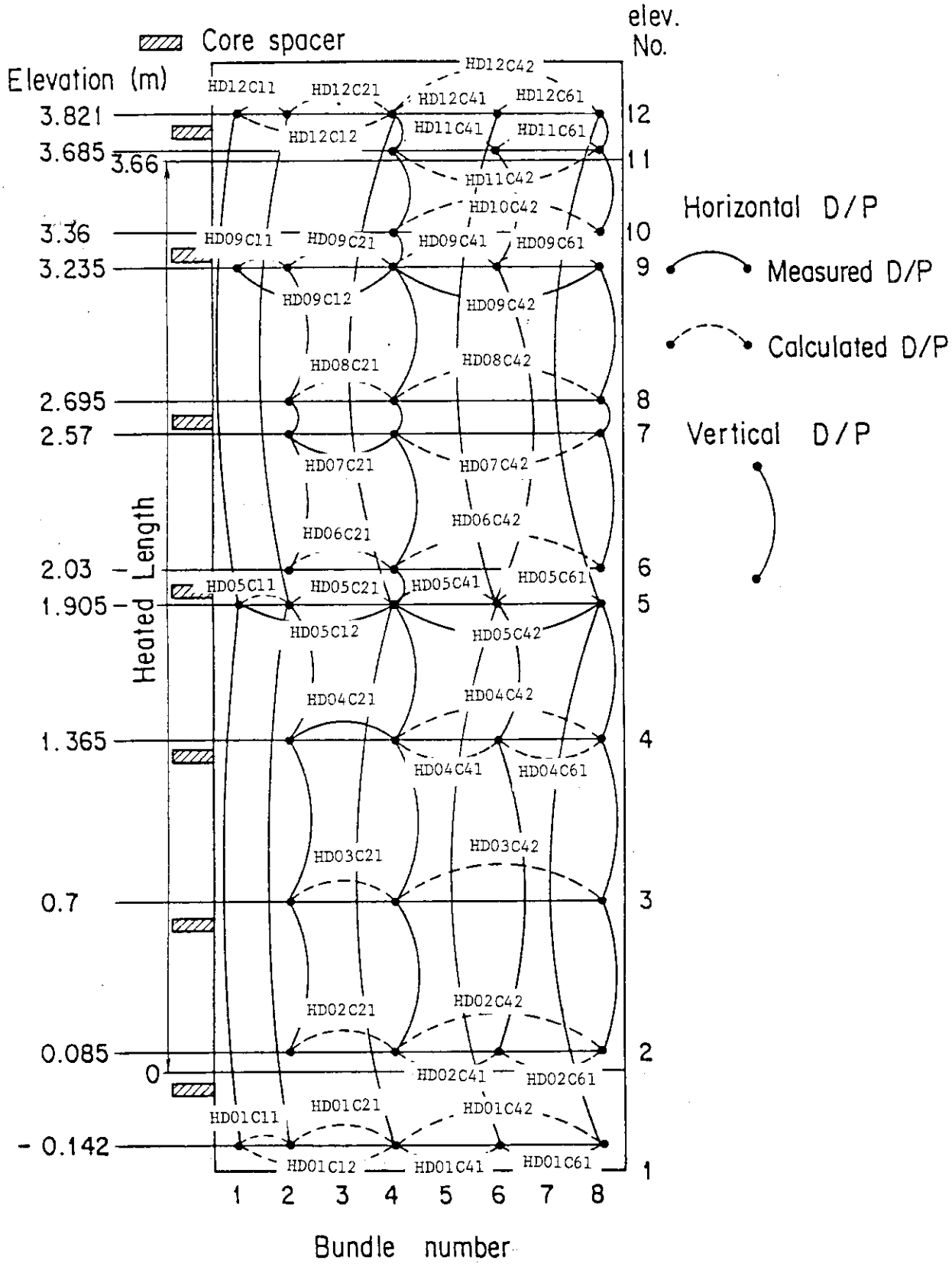

Fig. A-37 Locations of calculated horizontal differential pressures

Appendix B Selected Data of Test S2-SH1

Fig. B-1 ∿ B-16	Heater rod temperatures
Fig. B-17 ∿ B-20	Non-heated rod temperatures
Fig. B-21 ∿ B-24	Steam temperatures
Fig. B-25 ∿ B-26	Fluid temperatures just above end box tie plate
Fig. B-27 ∿ B-28	Fluid temperatures at core inlet
Fig. B-29 ∿ B-32	Fluid temperatures in core
Fig. B-33 ∿ B-34	Liquid levels above end box tie plate
Fig. B-35 ∿ B-36	Liquid levels above UCSP
Fig. B-37	Liquid levels in hot leg
Fig. B-38 ∿ B-39	Differential pressures across core full height
Fig. B-40 ∿ B-41	Differential pressures across end box tie plate
Fig. B-42 ∿ B-45	Horizontal differential pressures in core
Fig. B-46 ∿ B-50	Differential pressures in primary loops
Fig. B-51 ∿ B-52	Pressures in pressure vessel and containment tanks
Fig. B-53 ∿ B-54	Bundle powers
Fig. B-55	ECC flow rates

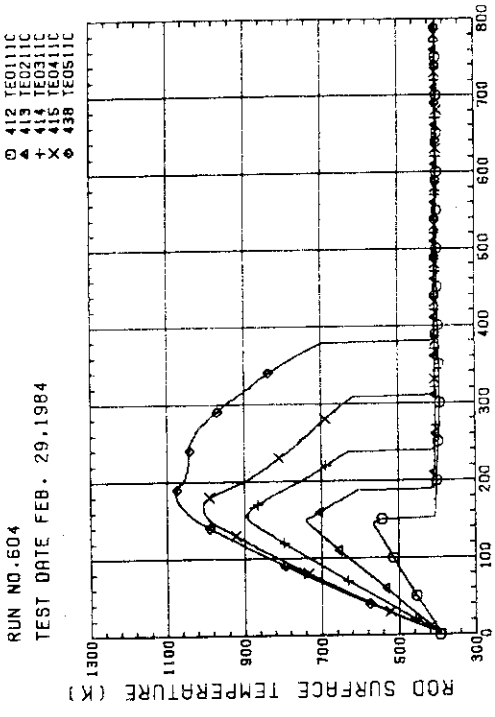

Fig. B- 1 HEATER ROD TEMPERATURE (BUNDLE 1-1C, LOWER HALF)

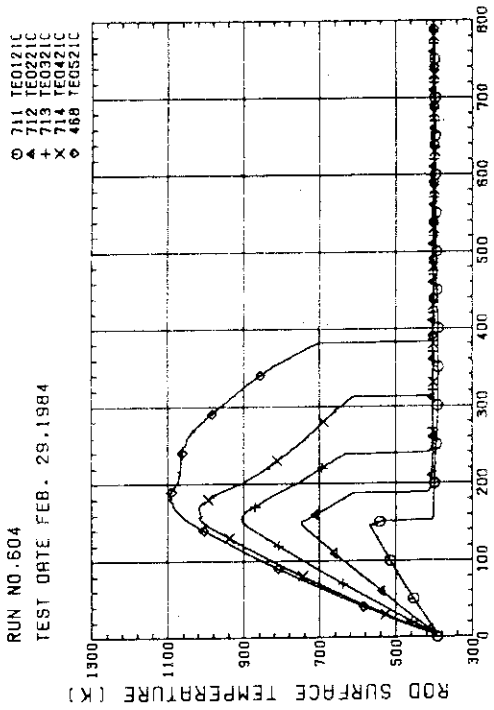

Fig. B- 3 HEATER ROD TEMPERATURE (BUNDLE 2-1C, LOWER HALF)

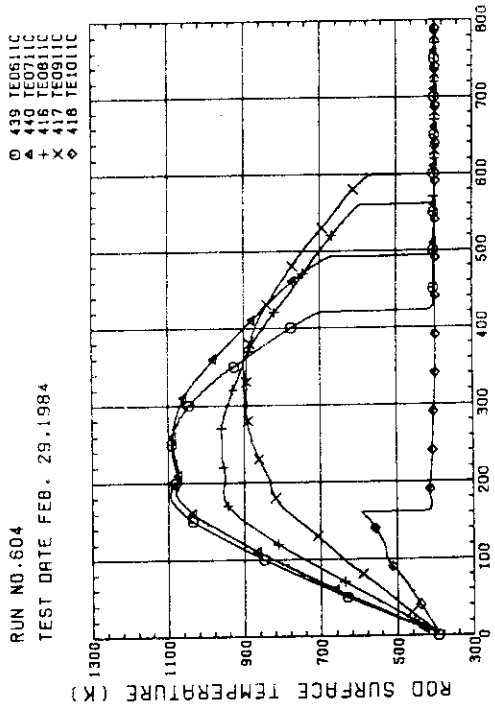

Fig. B- 2 HEATER ROD TEMPERATURE (BUNDLE 1-1C, UPPER HALF)

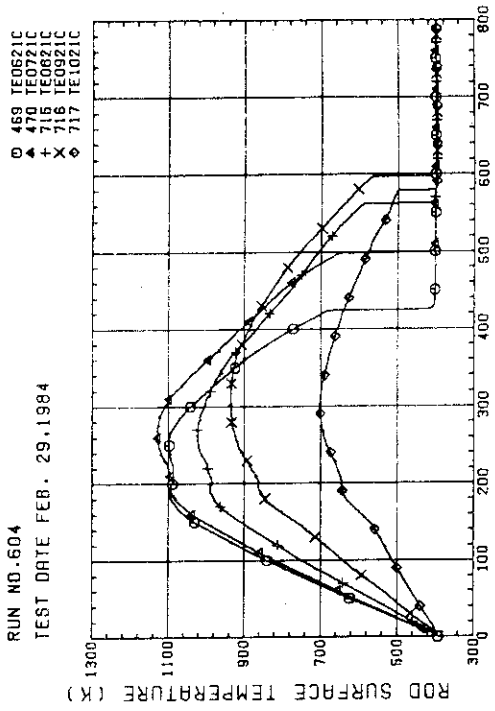

Fig. B- 4 HEATER ROD TEMPERATURE (BUNDLE 2-1C, UPPER HALF)

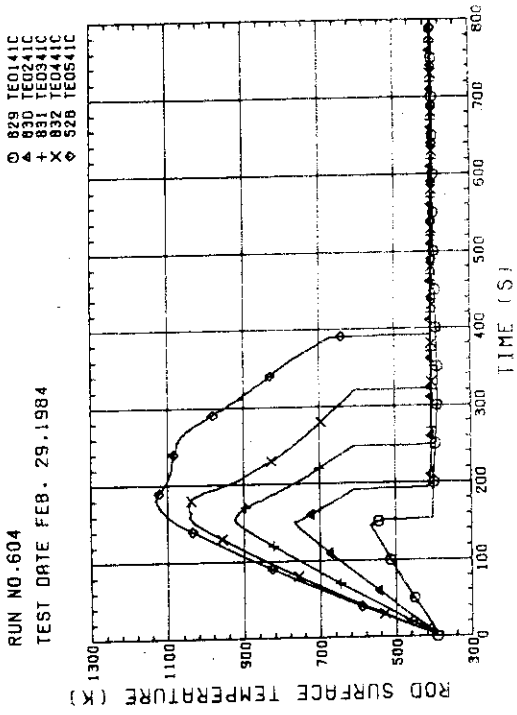

Fig. B- 7 HEATER ROD TEMPERATURE (BUNDLE 4-1C, LOWER HALF)

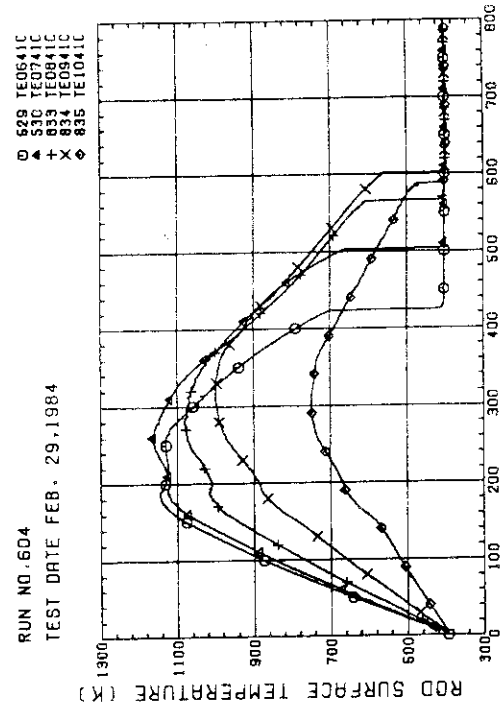

Fig. B- 8 HEATER ROD TEMPERATURE (BUNDLE 4-1C, UPPER HALF)

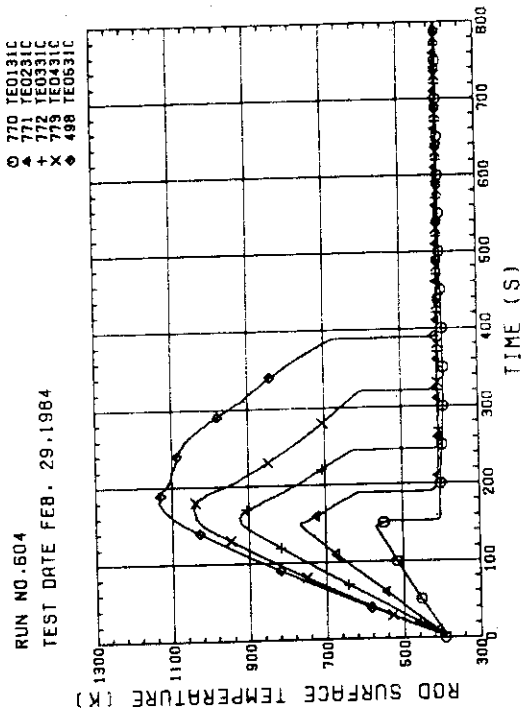

Fig. B- 5 HEATER ROD TEMPERATURE (BUNDLE 3-1C, LOWER HALF)

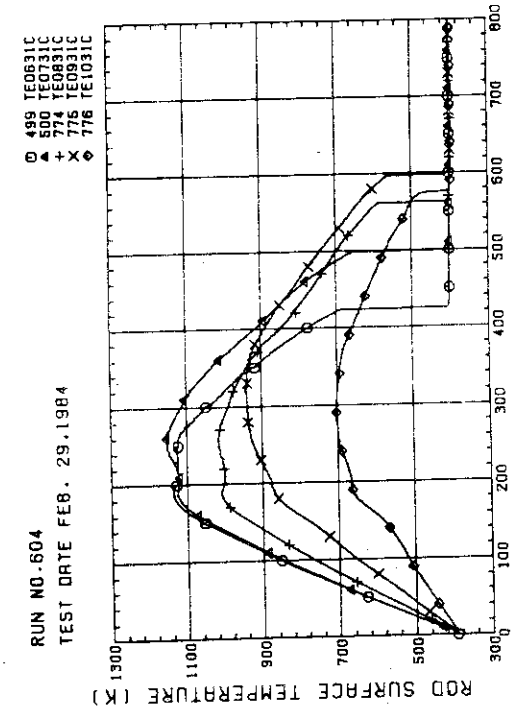

Fig. B- 6 HEATER ROD TEMPERATURE (BUNDLE 3-1C, UPPER HALF)

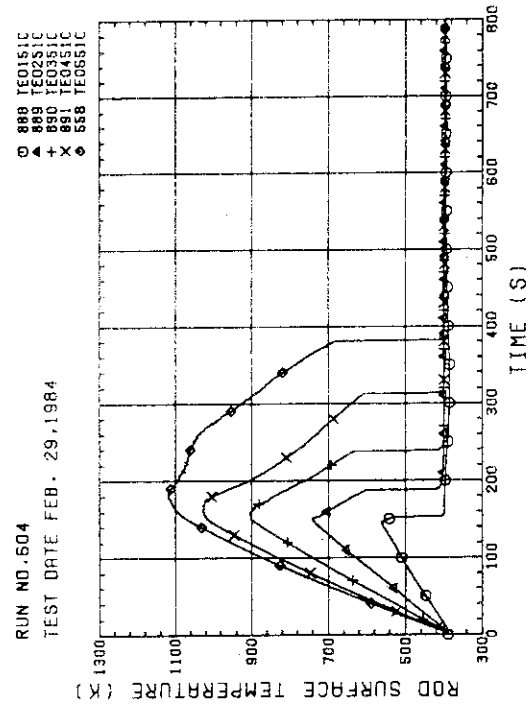

Fig. B- 9 HEATER ROD TEMPERATURE (BUNDLE 5-IC, LOWER HALF)

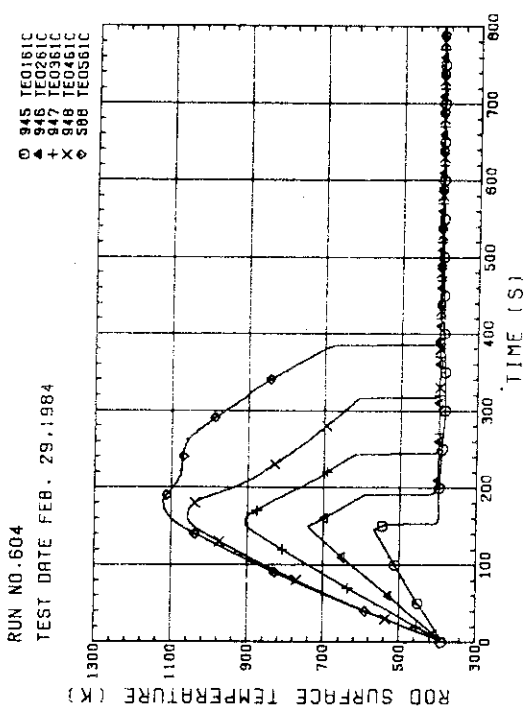

Fig. B-11 HEATER ROD TEMPERATURE (BUNDLE 6-IC, LOWER HALF)

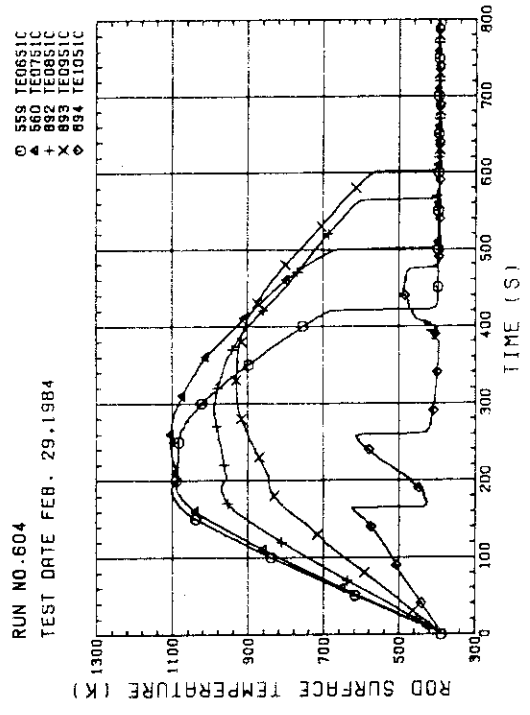

Fig. B-10 HEATER ROD TEMPERATURE (BUNDLE 5-IC, UPPER HALF)

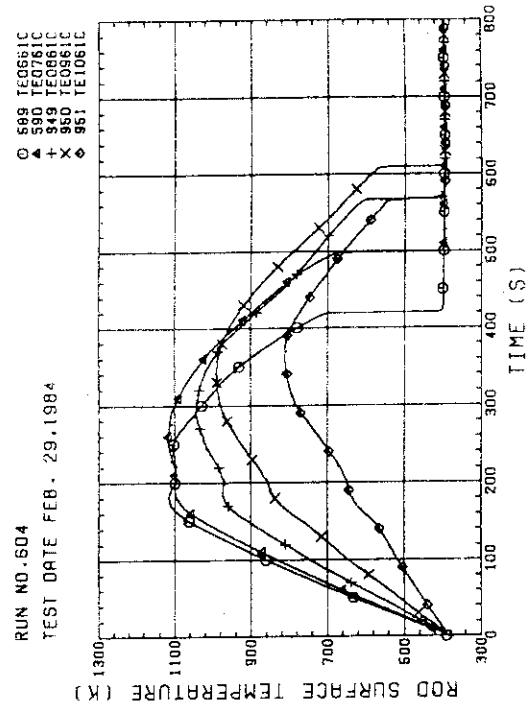

Fig. B-12 HEATER ROD TEMPERATURE (BUNDLE 6-IC, UPPER HALF)

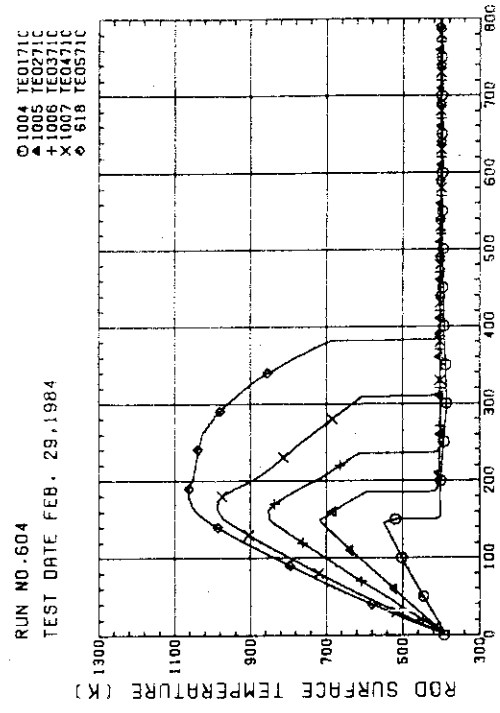

Fig. B-13 HEATER ROD TEMPERATURE (BUNDLE 7-IC, LOWER HALF)

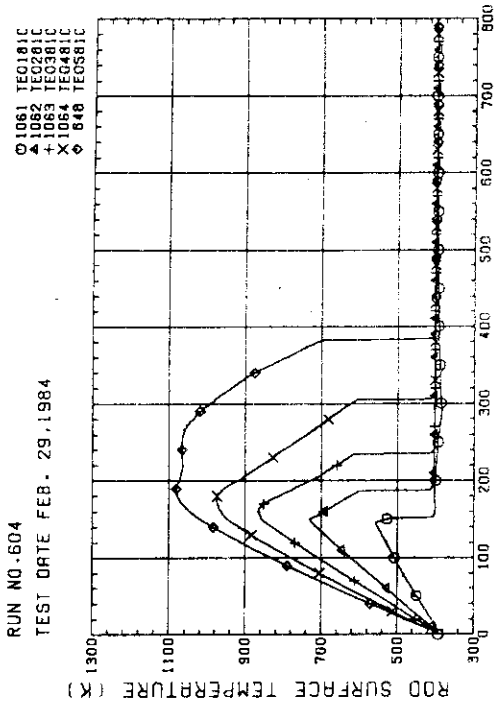

Fig. B-15 HEATER ROD TEMPERATURE (BUNDLE 8-IC, LOWER HALF)

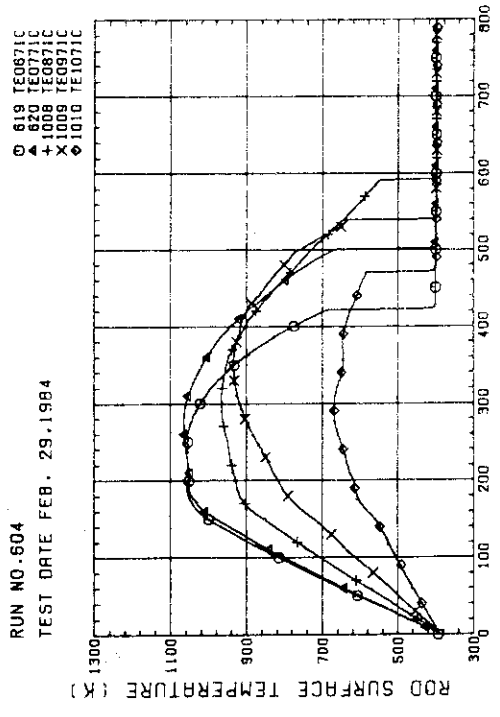

Fig. B-14 HEATER ROD TEMPERATURE (BUNDLE 7-IC, UPPER HALF)

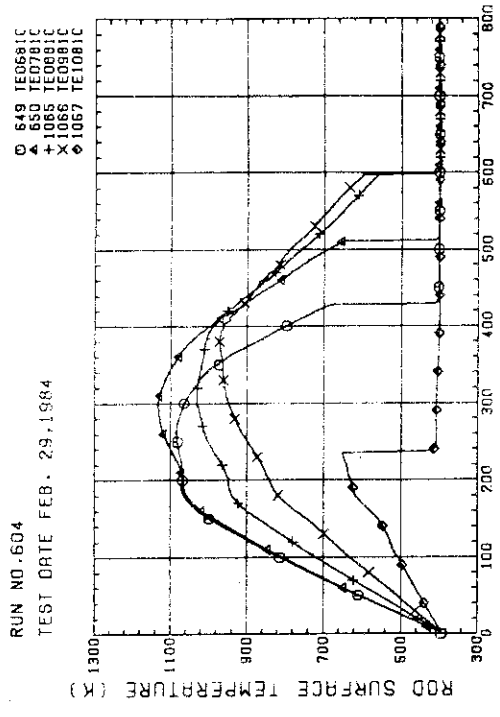

Fig. B-16 HEATER ROD TEMPERATURE (BUNDLE 8-IC, UPPER HALF)

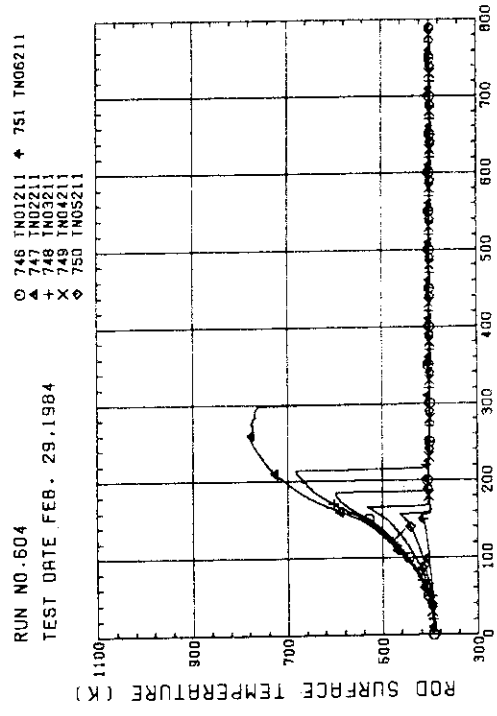

Fig. B-17 NON-HEATED ROD TEMPERATURE (BUNDLE 2-1)

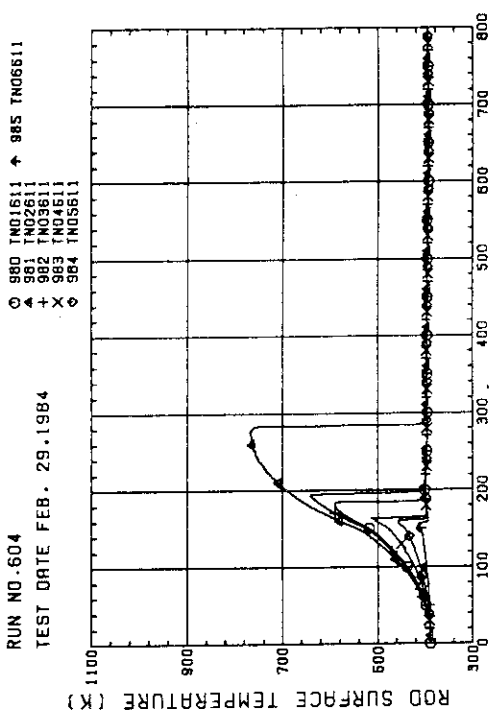

Fig. B-19 NON-HEATED ROD TEMPERATURE (BUNDLE 6-1)

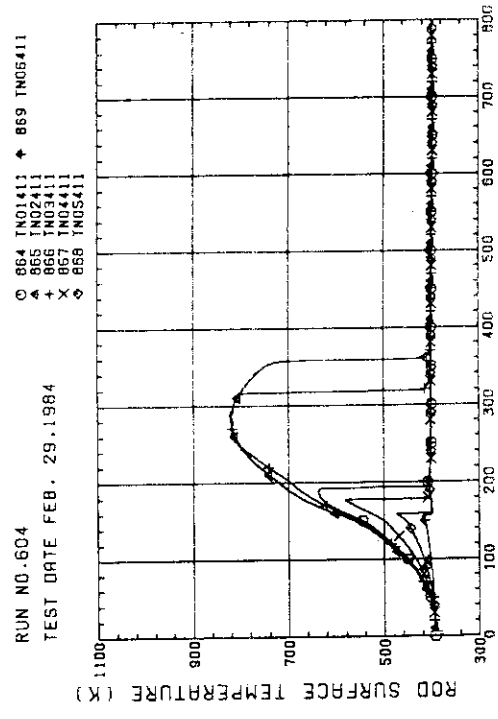

Fig. B-18 NON-HEATED ROD TEMPERATURE (BUNDLE 4-1)

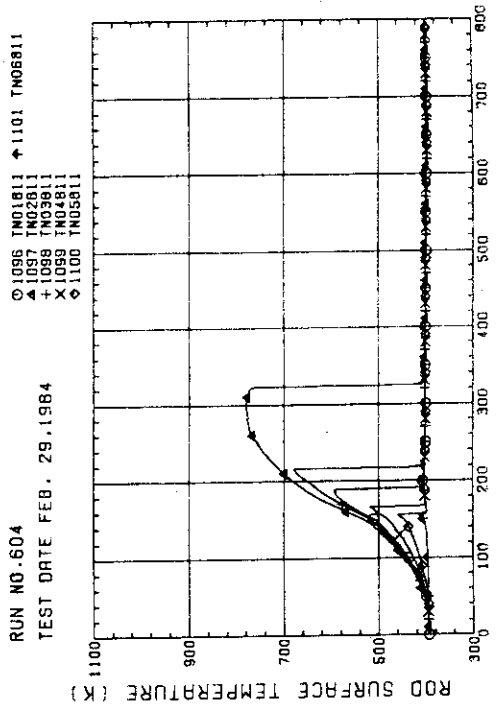

Fig. B-20 NON-HEATED ROD TEMPERATURE (BUNDLE 8-1)

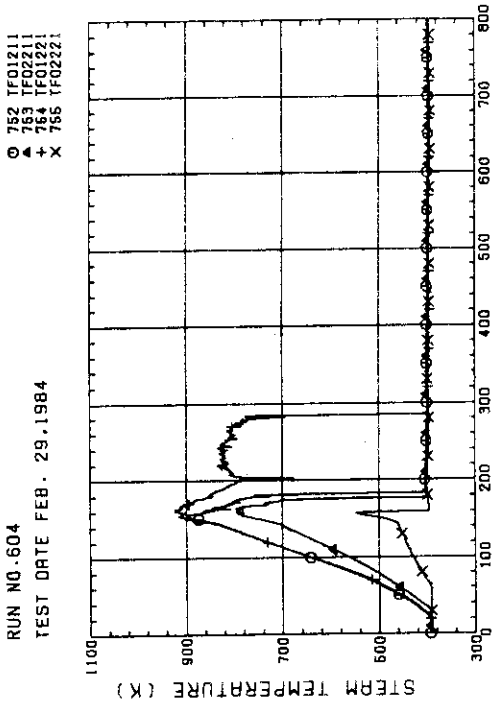

Fig. B-21 STEAM TEMPERATURE IN CORE, BUNDLE 2 (01211-1.735M, 02211-1.875M, 01221-1.38M, 02221-1.915M)

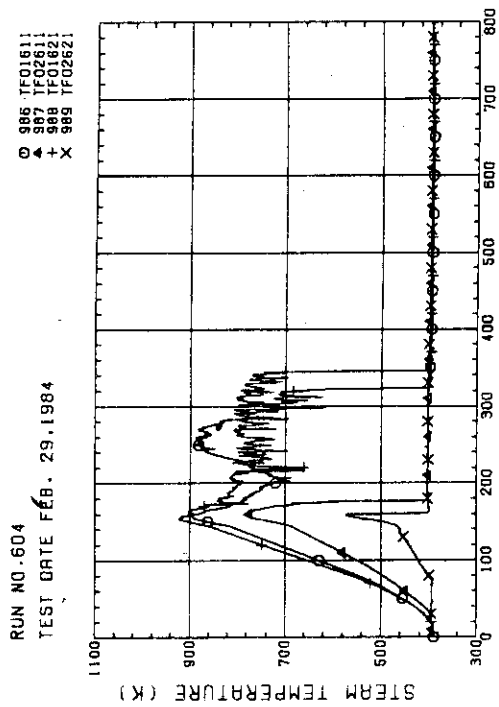

Fig. B-23 STEAM TEMPERATURE IN CORE, BUNDLE 6

Fig. B-22 STEAM TEMPERATURE IN CORE, BUNDLE 4 (01411-1.735M, 02411-1.875M, 01421-1.38M, 02421-1.915M)

Fig. B-24 STEAM TEMPERATURE IN CORE, BUNDLE 8

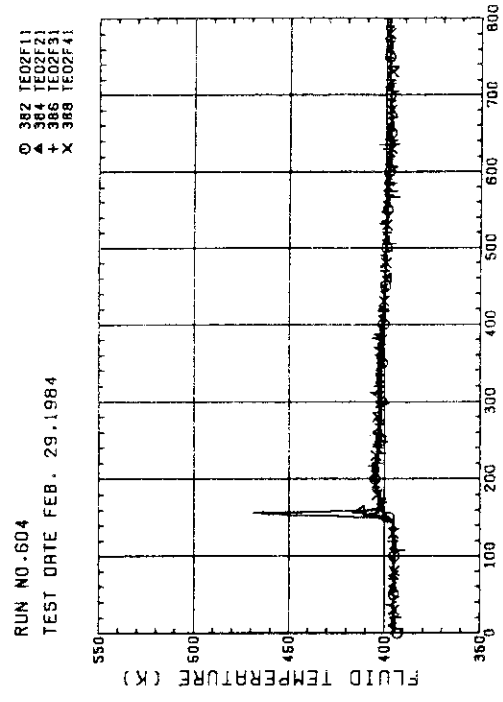

Fig. B-25 FLUID TEMPERATURE JUST ABOVE END BOX TIE PLATE (BUNDLE 1.2.3.4. OPPOSITE SIDE OF COLD LEG)

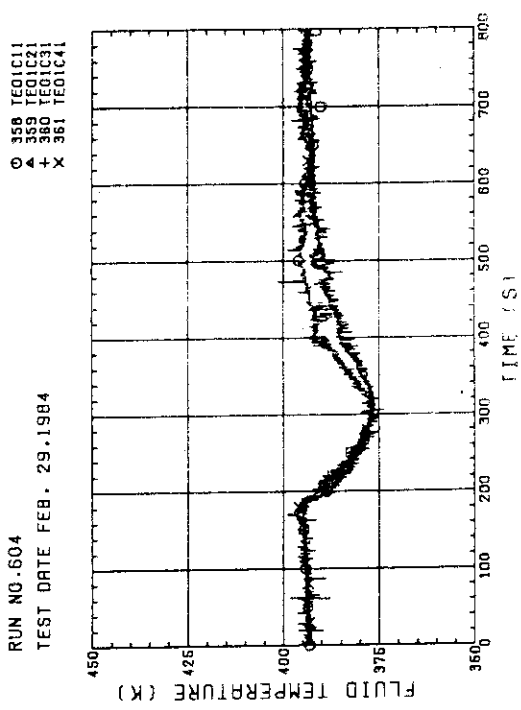

Fig. B-27 FLUID TEMPERATURE AT CORE INLET (BUNDLE 1.2.3.4. 100MM BELOW HEATED PART)

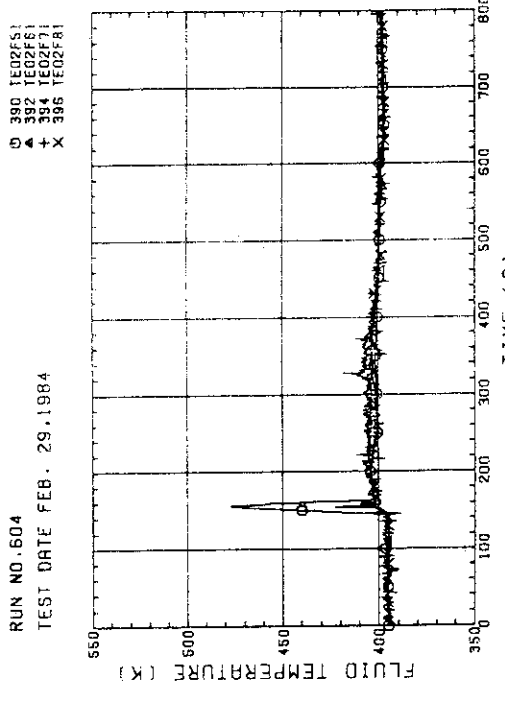

Fig. B-26 FLUID TEMPERATURE JUST ABOVE END BOX TIE PLATE (BUNDLE 5.6.7.8. OPPOSITE SIDE OF COLD LEG)

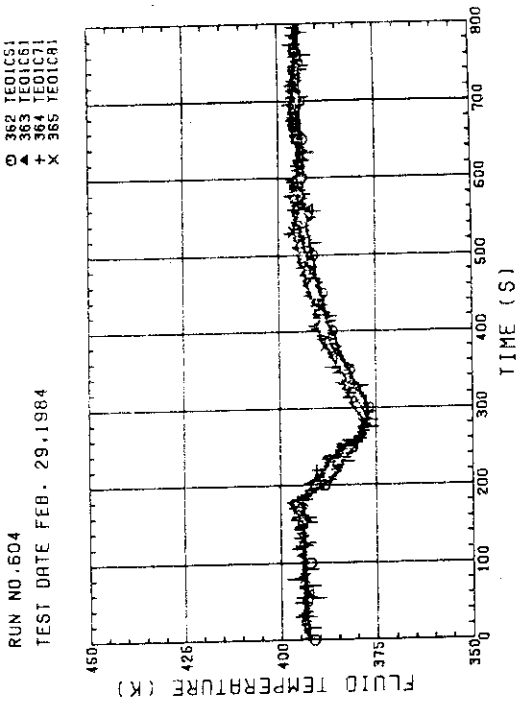

Fig. B-28 FLUID TEMPERATURE AT CORE INLET (BUNDLE 5.6.7.8. 100MM BELOW HEATED PART)

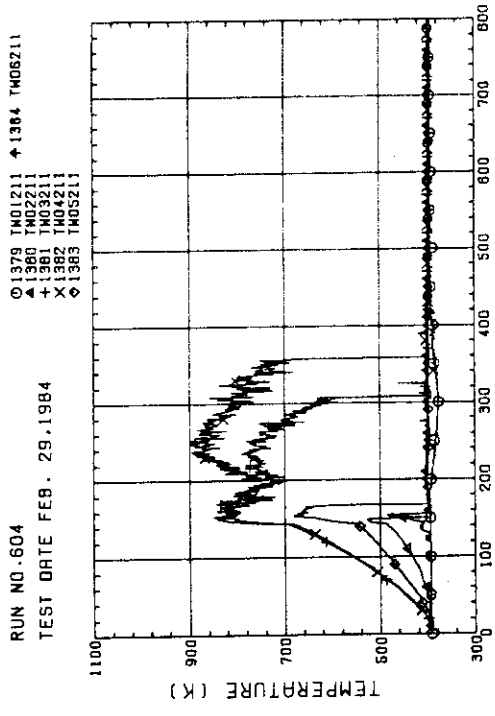

Fig. B-29 TEMPERATURE FOR SPUTTERING DETECTION BUNDLE 2 , REGION 1 , TYPE 1

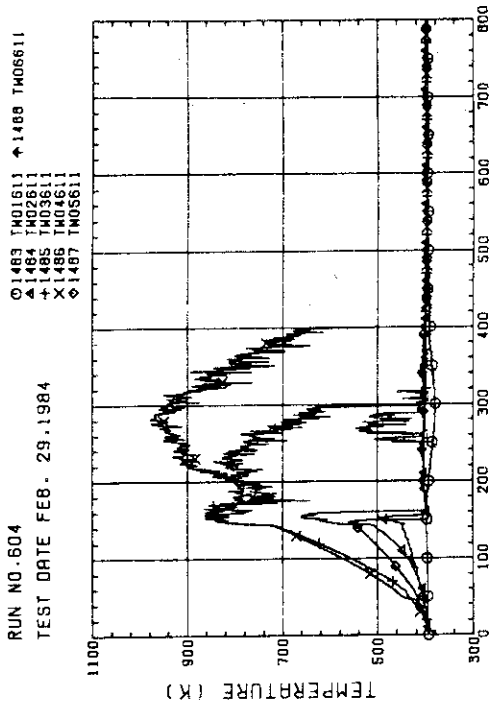

Fig. B-31 TEMPERATURE FOR SPUTTERING DETECTION BUNDLE 6 , REGION 1 , TYPE 1

Fig. B-30 TEMPERATURE FOR SPUTTERING DETECTION BUNDLE 4 , REGION 1 , TYPE 1

Fig. B-32 TEMPERATURE FOR SPUTTERING DETECTION BUNDLE 8 , REGION 1 , TYPE 1

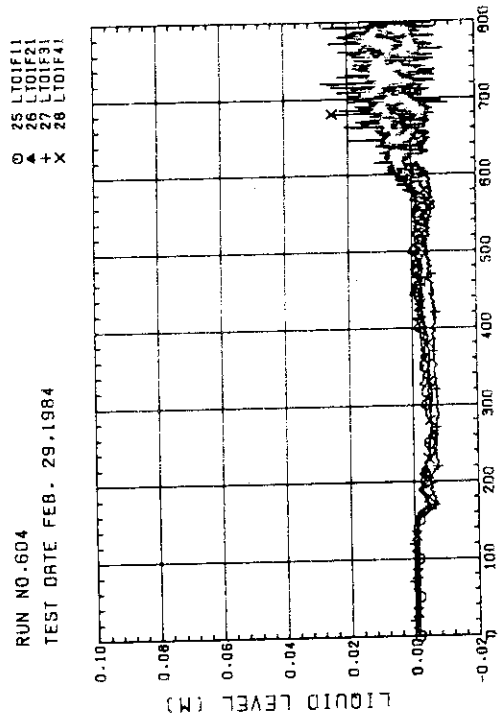

Fig. B-33 LIQUID LEVEL ABOVE END BOX TIE PLATE (BUNDLE 1,2,3,4)

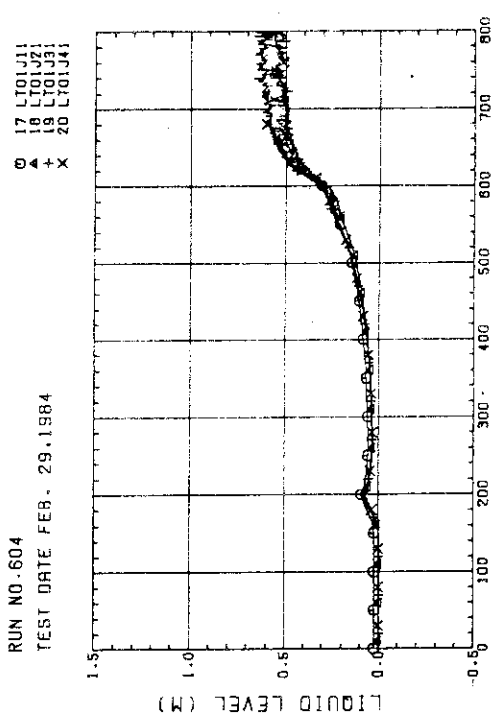

Fig. B-35 LIQUID LEVEL ABOVE UCSP (BUNDLE 1,2,3,4)

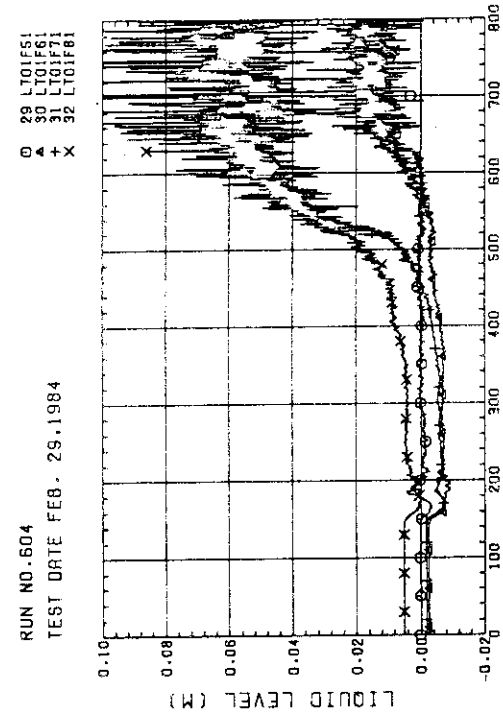

Fig. B-34 LIQUID LEVEL ABOVE END BOX TIE PLATE (BUNDLE 5,6,7,8)

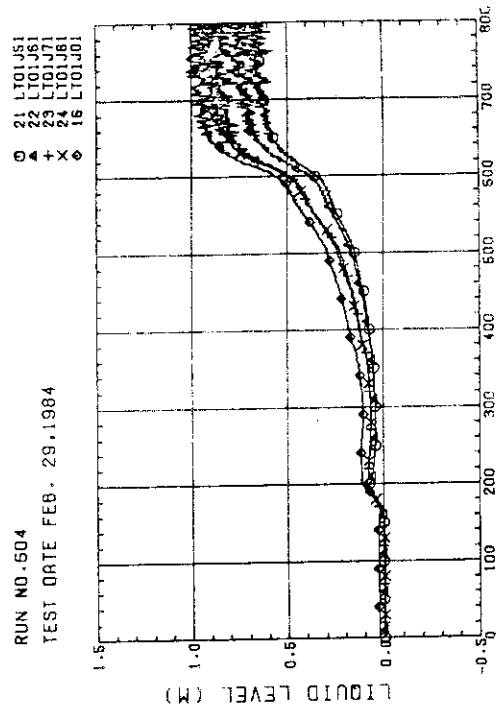

Fig. B-36 LIQUID LEVEL ABOVE UCSP (BUNDLE 5,6,7,8 AND CORE BAFFLE)

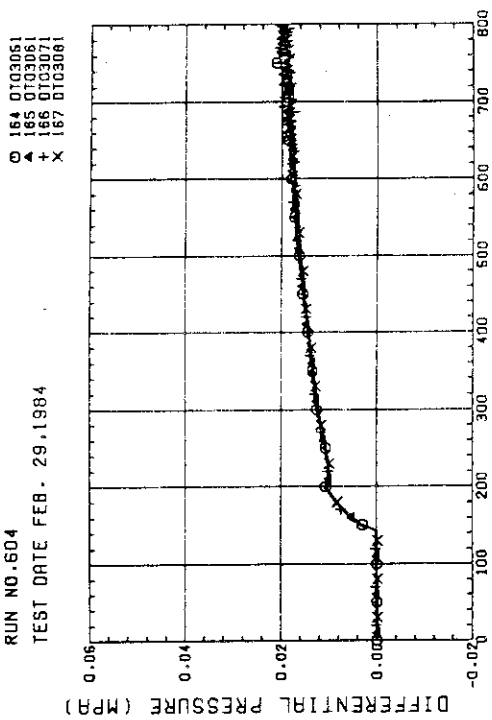

Fig. B-39 DIFFERENTIAL PRESSURE OF CORE FULL HEIGHT (BUNDLE 5,6,7,8)

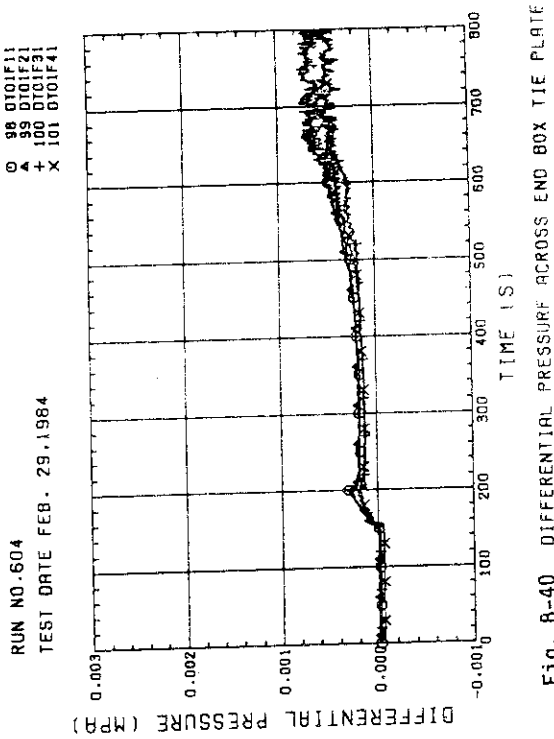

Fig. B-40 DIFFERENTIAL PRESSURE ACROSS END BOX TIE PLATE (BUNDLE 1,2,3,4)

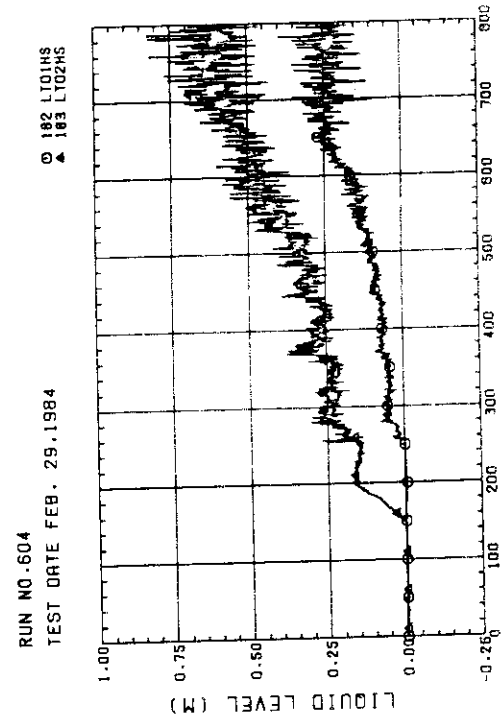

Fig. B-37 LIQUID LEVEL IN HOT LEG (01HS - PV SIDE, 02HS - STEAM/WATER SEPARATOR SIDE)

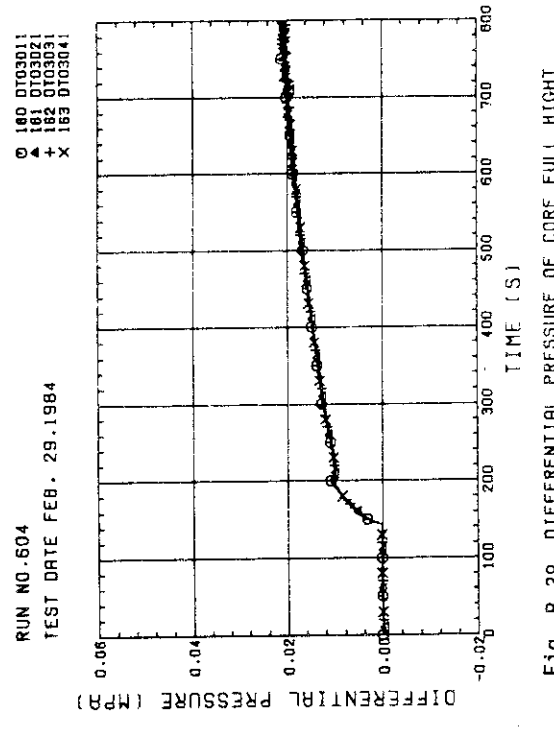

Fig. B-38 DIFFERENTIAL PRESSURE OF CORE FULL HIGHT (BUNDLE 1,2,3,4)

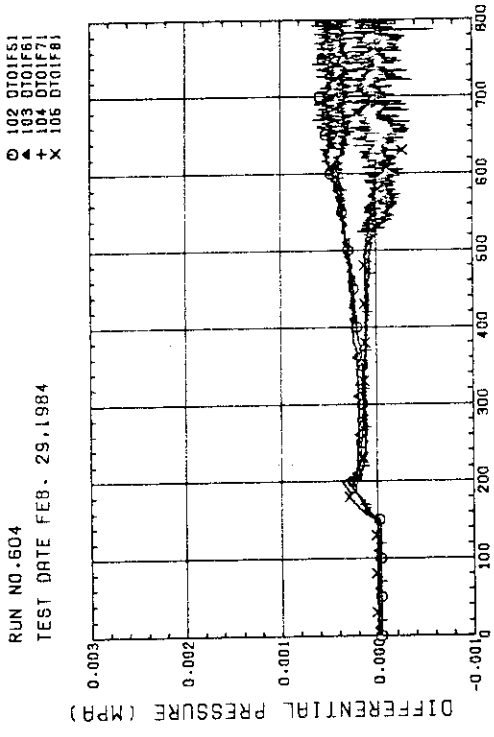

Fig. B-41 DIFFERENTIAL PRESSURE ACROSS END BOX TIE PLATE (BUNDLE 5,6,7,8)

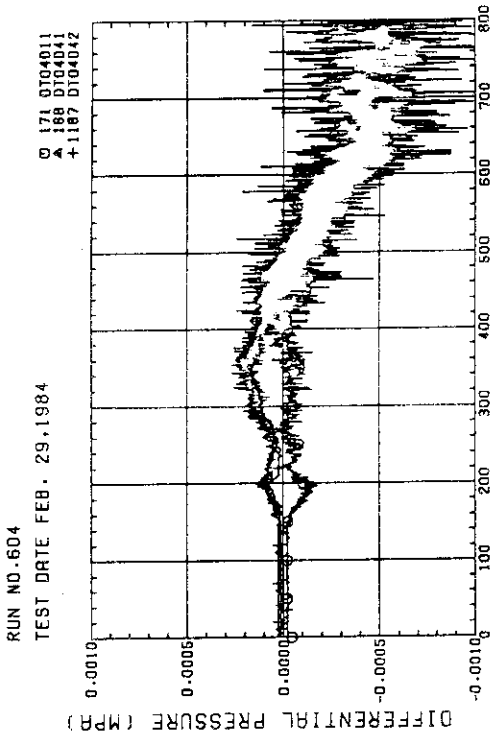

Fig. B-43 DIFFERENTIAL PRESSURE, HORIZONTAL AT 1905 MM (11-BUNDLE 1-4, 41-BUNDLE 4-8, 42-BUNDLE 4-6)

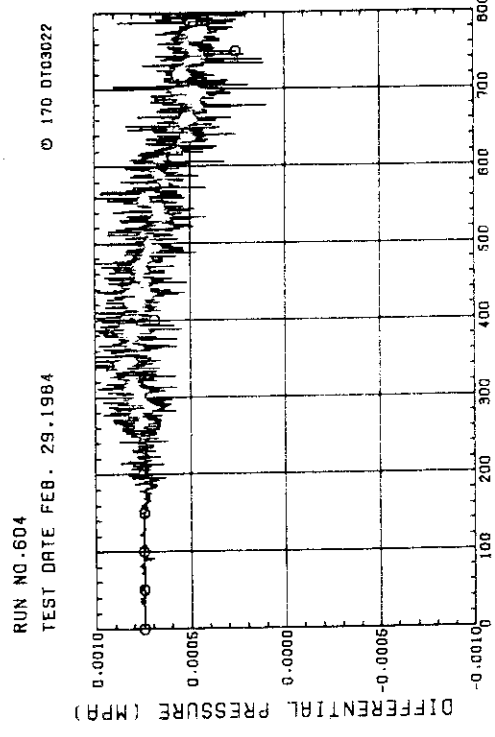

Fig. B-42 DIFFERENTIAL PRESSURE, HORIZONTAL AT 1365 MM (BUNDLE 2-4)

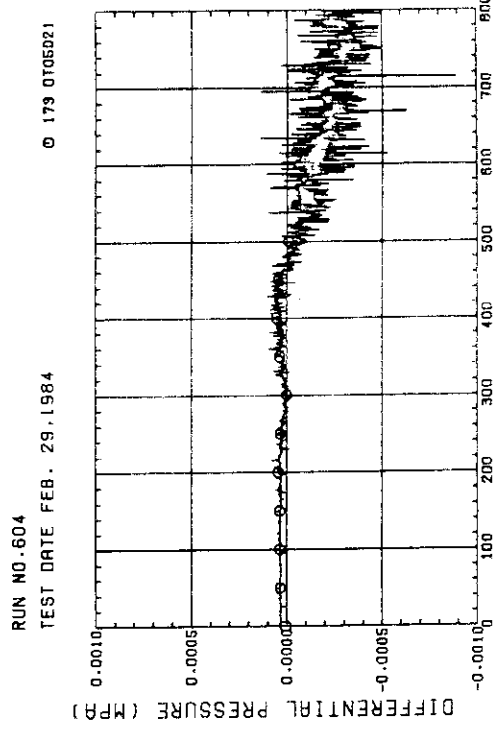

Fig. B-44 DIFFERENTIAL PRESSURE, HORIZONTAL AT 2570 MM (BUNDLE 2-4)

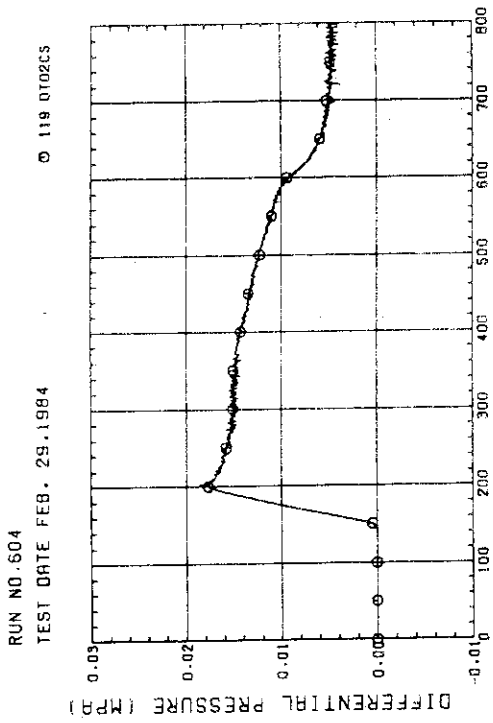

Fig. B-47 DIFFERENTIAL PRESSURE OF INTACT COLD LEG

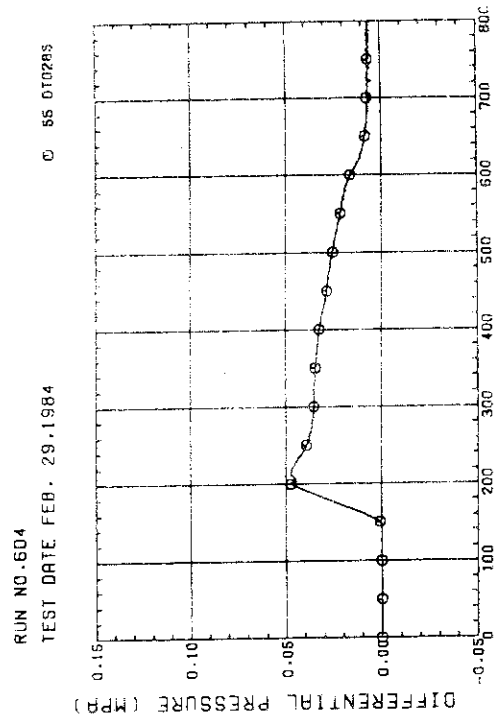

Fig. B-48 DIFFERENTIAL PRESSURE, STEAM/WATER SEPARATOR - CONTAINMENT TANK-II

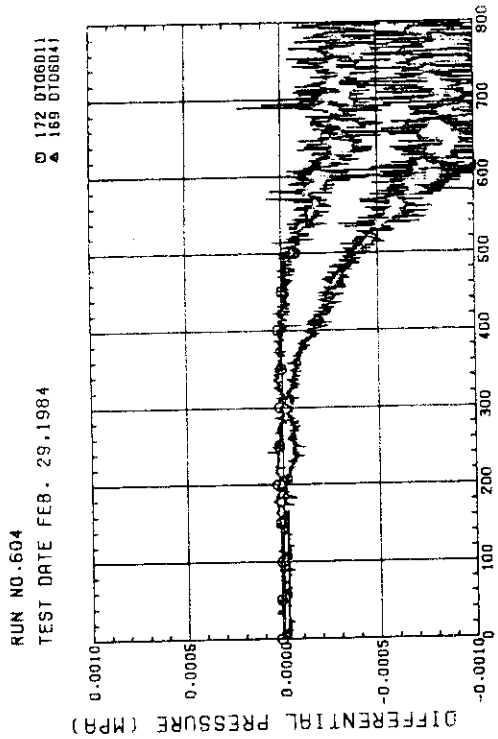

Fig. B-45 DIFFERENTIAL PRESSURE, HORIZONTAL AT 3235 MM (11-BUNDLE 1-4, 41-BUNDLE 4-8)

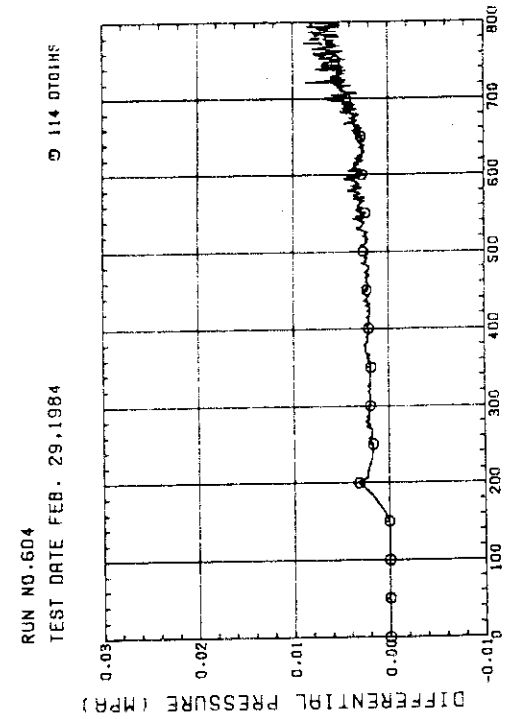

Fig. B-46 DIFFERENTIAL PRESSURE OF HOT LEG, HOT LEG INLET - STEAM/WATER SEPARATOR INLET

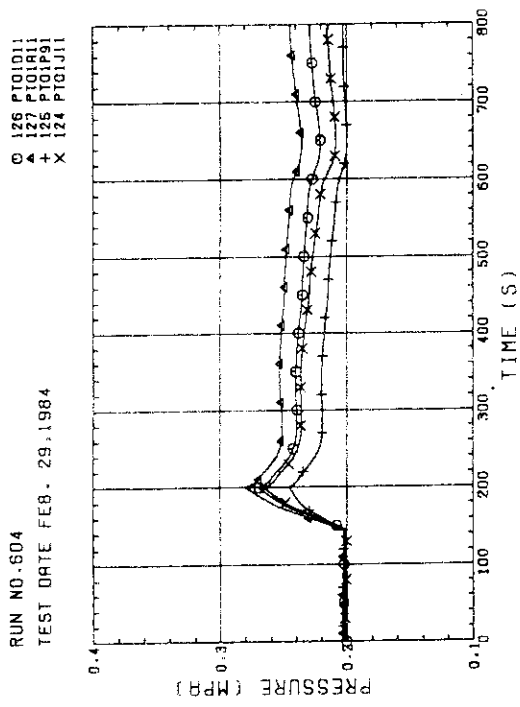

Fig. B-51 PRESSURE IN PV (J - TOP OF PV, D - CORE CENTER, A - CORE INLET, P - BELOW COLD LEG NOZZLE IN DOWNCOMER)

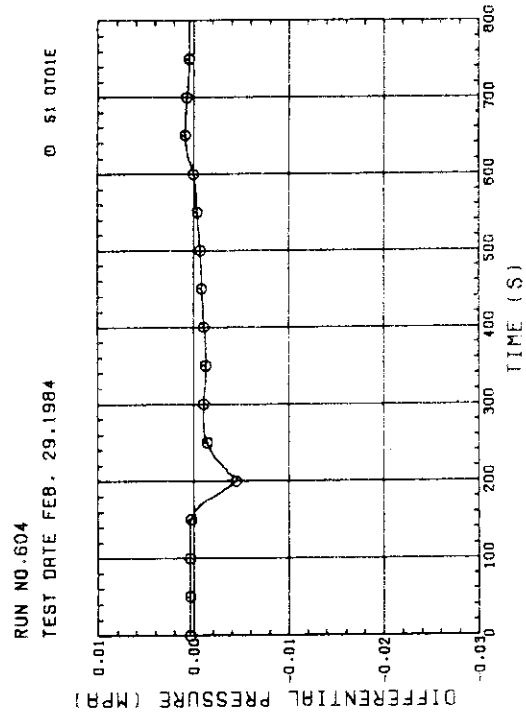

Fig. B-49 DIFFERENTIAL PRESSURE, CONTAINMENT TANK-II - CONTAINMENT TANK-I

Fig. B-52 PRESSURE AT TOP OF CONTAINMENT TANK-I AND CONTAINMENT TANK-II (F-CONTAINMENT TANK-I, B-CONTAINMENT TANK-II)

Fig. B-50 DIFFERENTIAL PRESSURE OF BROKEN COLD LEG - PV SIDE, DOWNCOMER - CONTAINMENT TANK-I

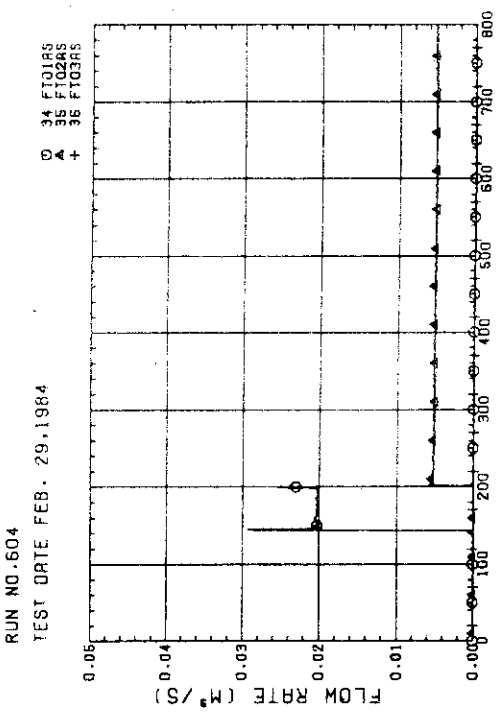

Fig. B-55 FLOW RATE OF ECC WATER (01-LOWER PLENUM. 02-INTACT COLD LEG, 03-BROKEN COLD LEG)

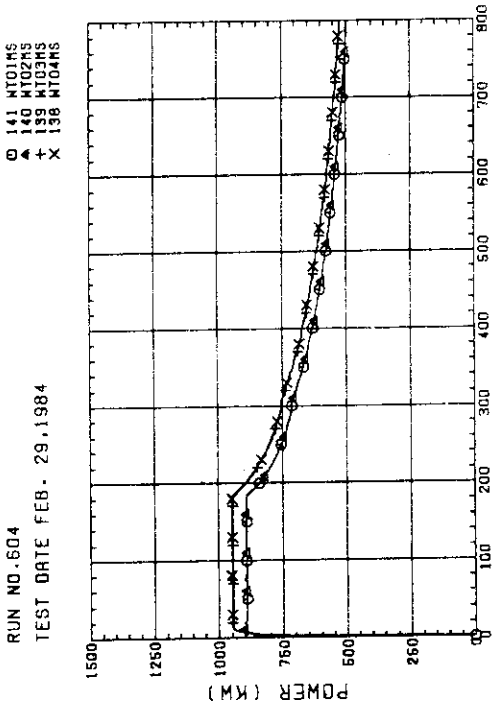

Fig. B-53 BUNDLE POWER (BUNDLE 1,2,3,4)

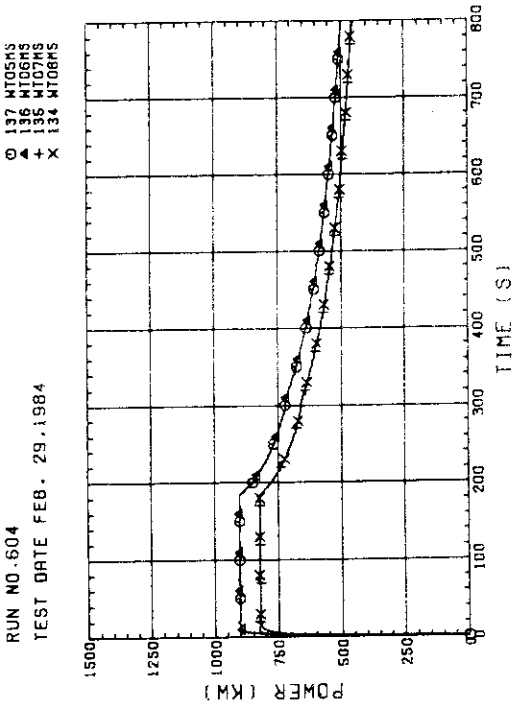

Fig. B-54 BUNDLE POWER (BUNDLE 5,6,7,8)

Appendix C Selected Data of Test S2-SH2

Fig. C-1 ∿ C-16	Heater rod temperatures
Fig. C-17 ∿ C-20	Non-heated rod temperatures
Fig. C-21 ∿ C-24	Steam temperatures
Fig. C-25 ∿ C-26	Fluid temperatures just above end box tie plate
Fig. C-27 ∿ C-28	Fluid temperatures at core inlet
Fig. C-29 ∿ C-32	Fluid temperatures in core
Fig. C-33 ∿ C-34	Liquid levels above end box tie plate
Fig. C-35 ∿ C-36	Liquid levels above UCSP
Fig. C-37	Liquid levels in hot leg
Fig. C-38 ∿ C-39	Differential pressures across core full height
Fig. C-40 ∿ C-41	Differential pressures across end box tie plate
Fig. C-42 ∿ C-45	Horizontal differential pressures in core
Fig. C-46 ∿ C-50	Differential pressures in primary loops
Fig. C-51 ∿ C-52	Pressures in pressure vessel and containment tanks
Fig. C-53 ∿ C-54	Bundle powers
Fig. C-55	ECC flow rates

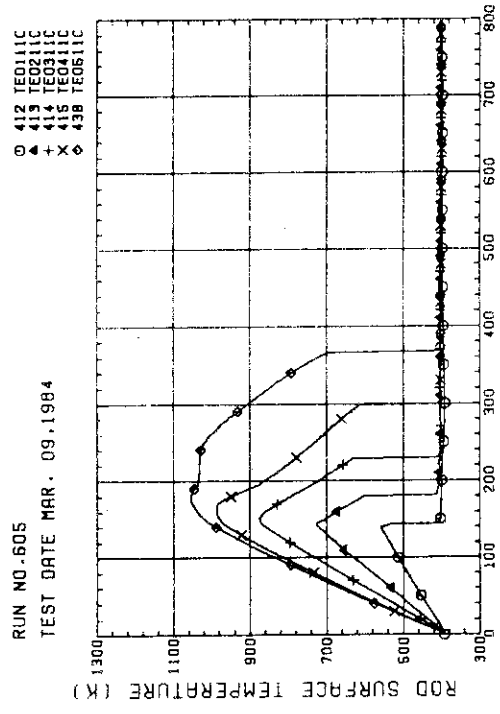

Fig. C- 1 HEATER ROD TEMPERATURE (BUNDLE 1-1C, LOWER HALF)

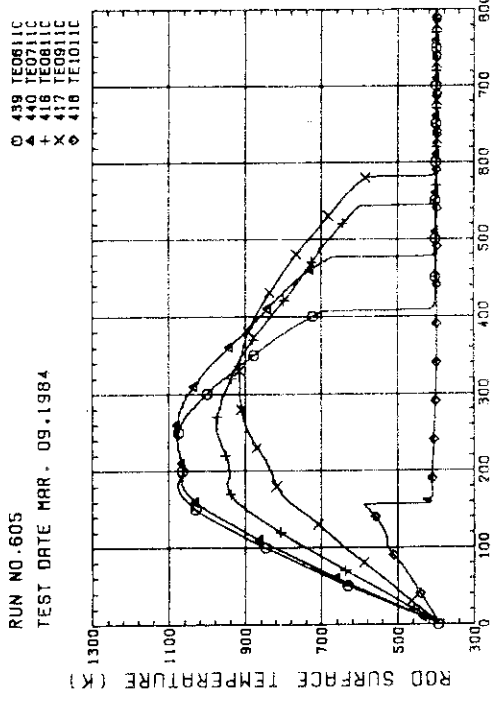

Fig. C- 2 HEATER ROD TEMPERATURE (BUNDLE 1-1C, UPPER HALF)

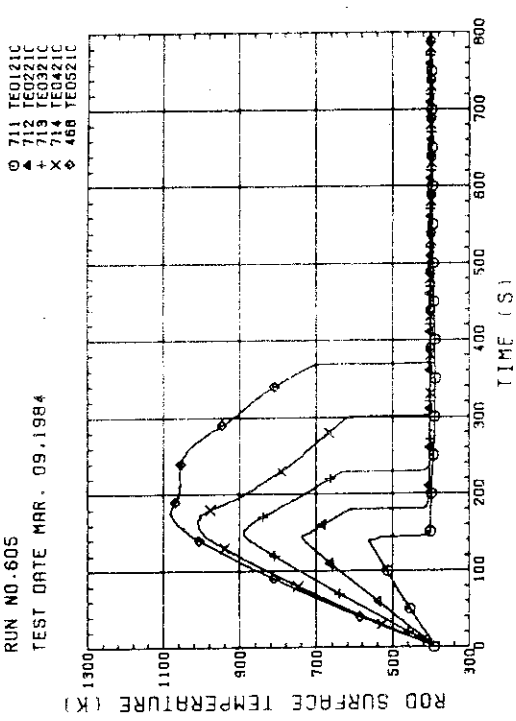

Fig. C- 3 HEATER ROD TEMPERATURE (BUNDLE 2-1C, LOWER HALF)

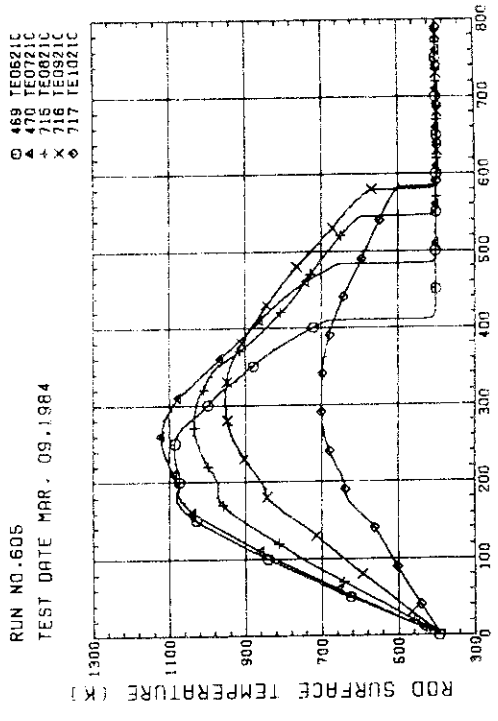

Fig. C- 4 HEATER ROD TEMPERATURE (BUNDLE 2-1C, UPPER HALF)

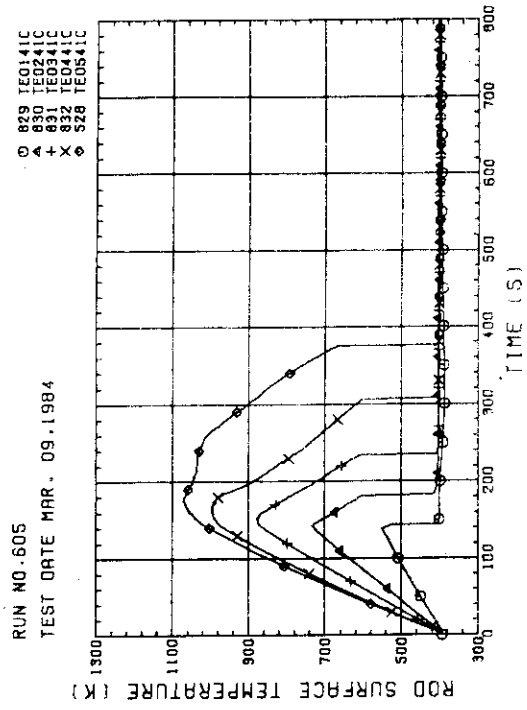

Fig. C- 7 HEATER ROD TEMPERATURE (BUNDLE 4-1C, LOWER HALF)

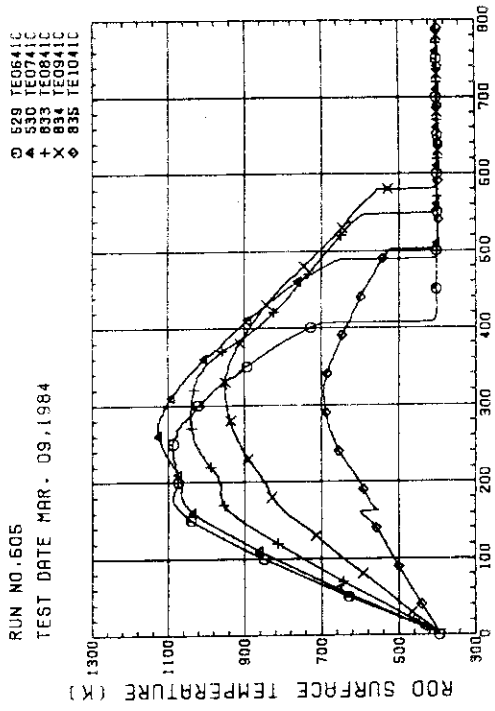

Fig. C- 8 HEATER ROD TEMPERATURE (BUNDLE 4-1C, UPPER HALF)

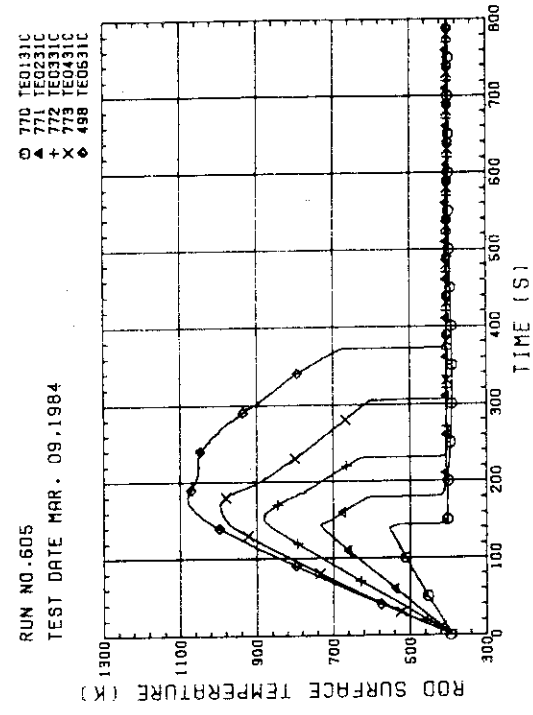

Fig. C- 5 HEATER ROD TEMPERATURE (BUNDLE 3-1C, LOWER HALF)

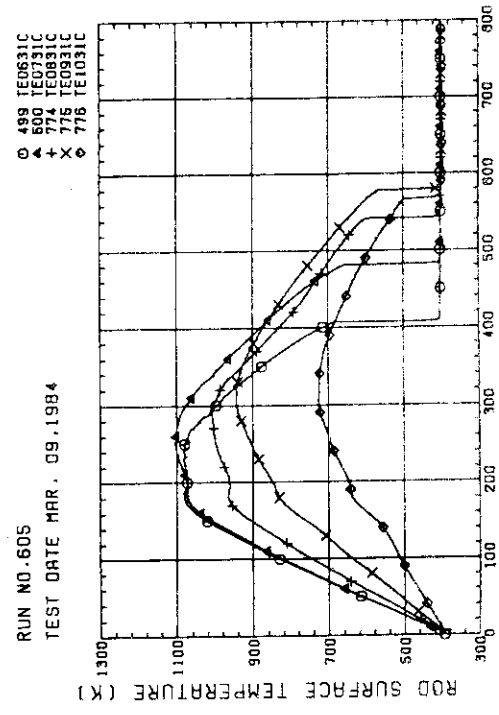

Fig. C- 6 HEATER ROD TEMPERATURE (BUNDLE 3-1C, UPPER HALF)

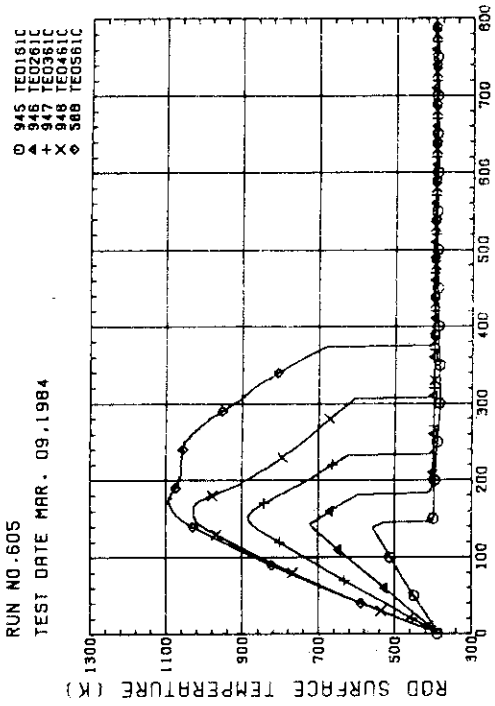

Fig. C-11 HEATER ROD TEMPERATURE (BUNDLE 6-1C, LOWER HALF)

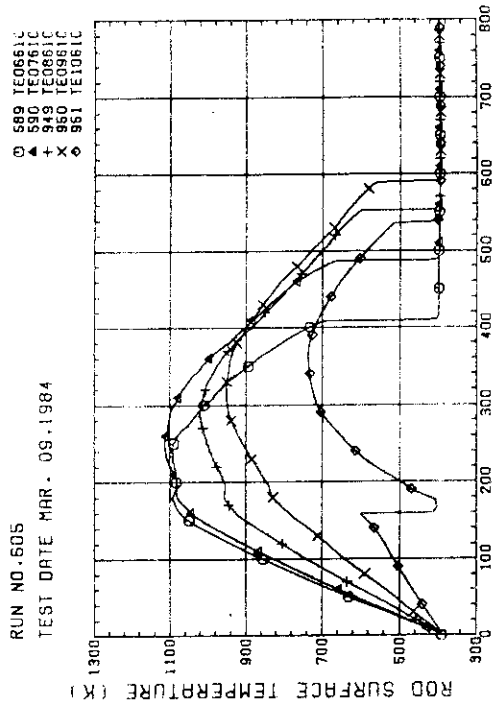

Fig. C-12 HEATER ROD TEMPERATURE (BUNDLE 6-1C, UPPER HALF)

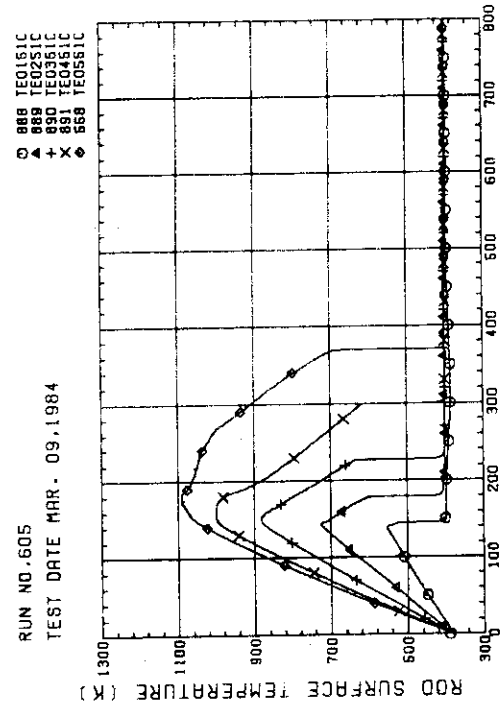

Fig. C- 9 HEATER ROD TEMPERATURE (BUNDLE 5-1C, LOWER HALF)

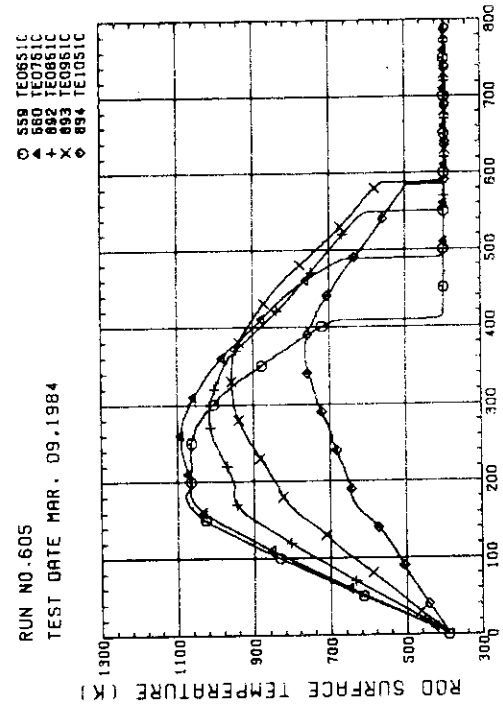

Fig. C-10 HEATER ROD TEMPERATURE (BUNDLE 5-1C, UPPER HALF)

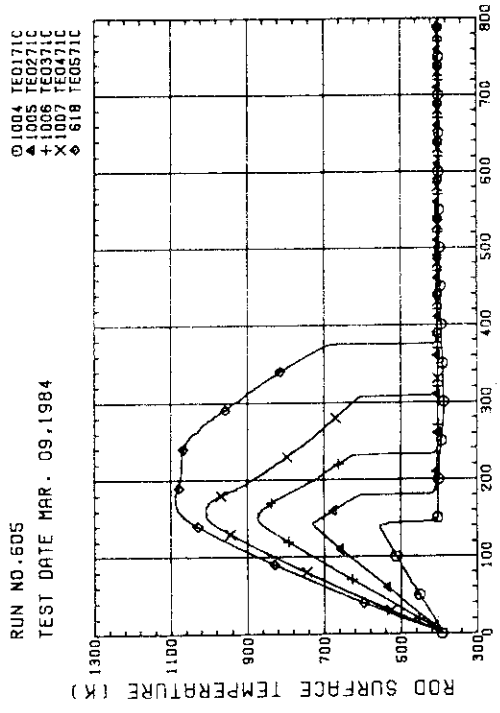

Fig. C-13 HEATER ROD TEMPERATURE (BUNDLE 7-1C, LOWER HALF)

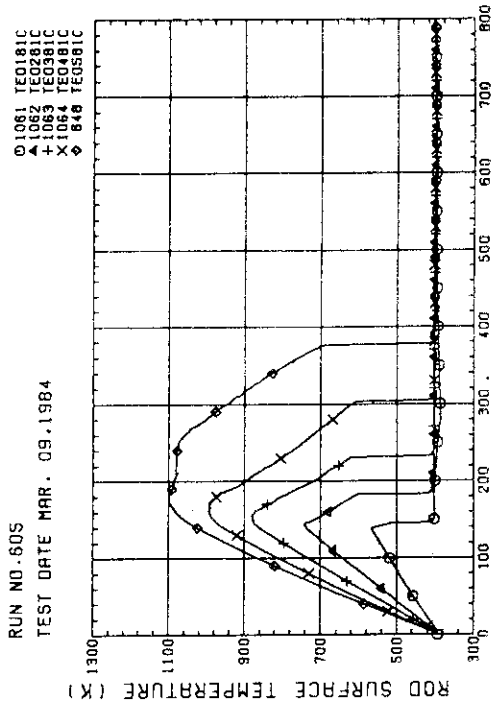

Fig. C-15 HEATER ROD TEMPERATURE (BUNDLE 8-1C, LOWER HALF)

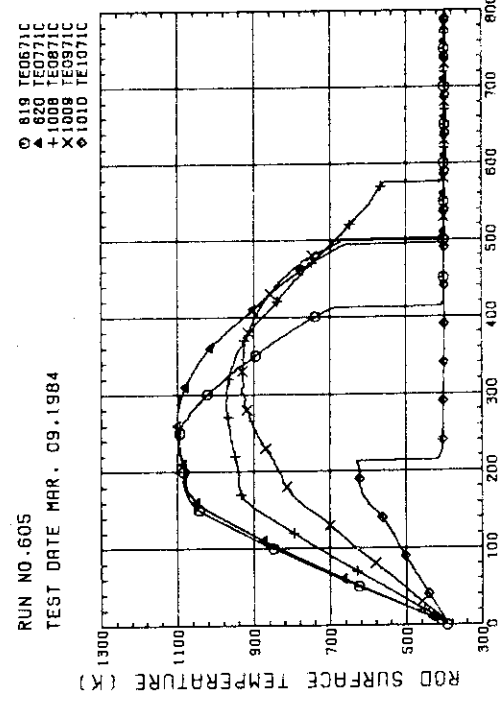

Fig. C-14 HEATER ROD TEMPERATURE (BUNDLE 7-1C, UPPER HALF)

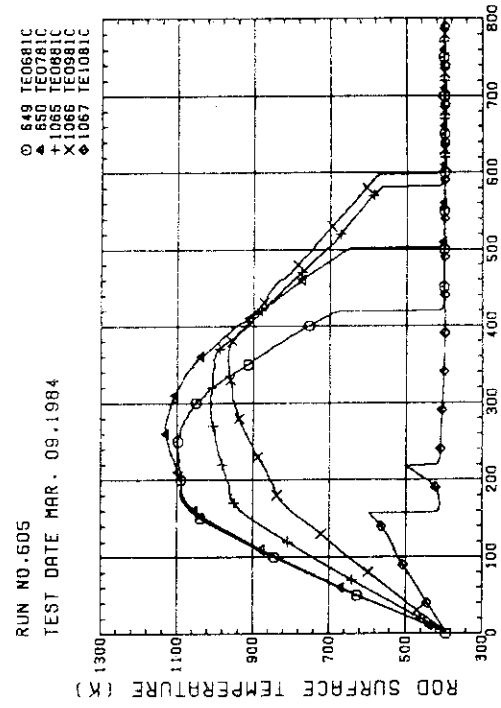

Fig. C-16 HEATER ROD TEMPERATURE (BUNDLE 8-1C, UPPER HALF)

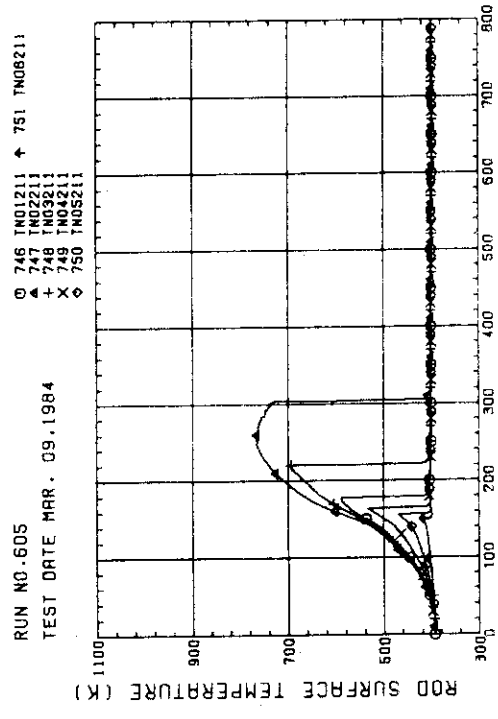

Fig. C-17 NON-HEATED ROD TEMPERATURE (BUNDLE 2-1)

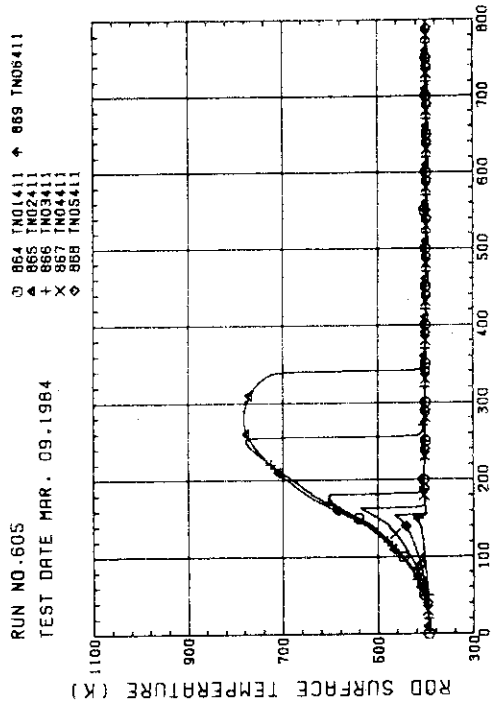

Fig. C-18 NON-HEATED ROD TEMPERATURE (BUNDLE 4-1)

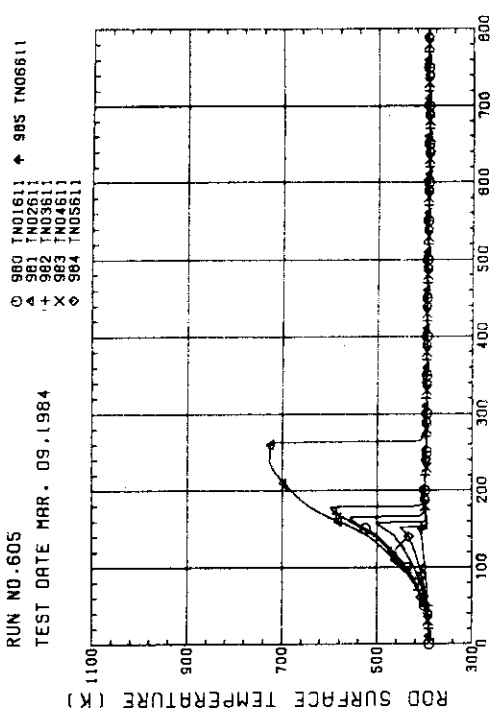

Fig. C-19 NON-HEATED ROD TEMPERATURE (BUNDLE 6-1)

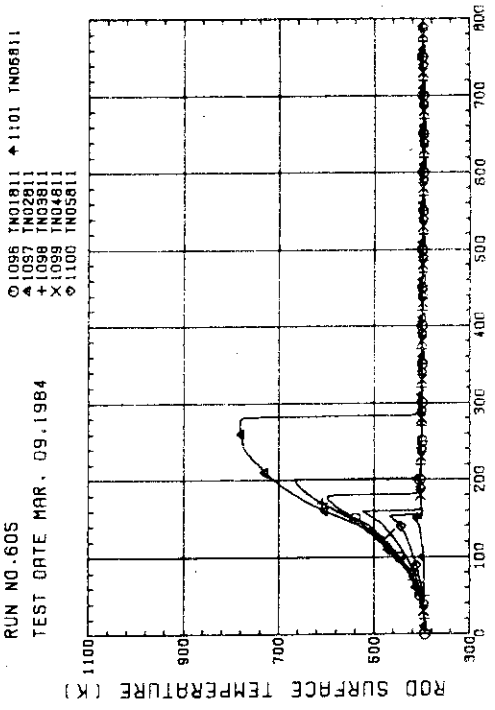

Fig. C-20 NON-HEATED ROD TEMPERATURE (BUNDLE 8-1)

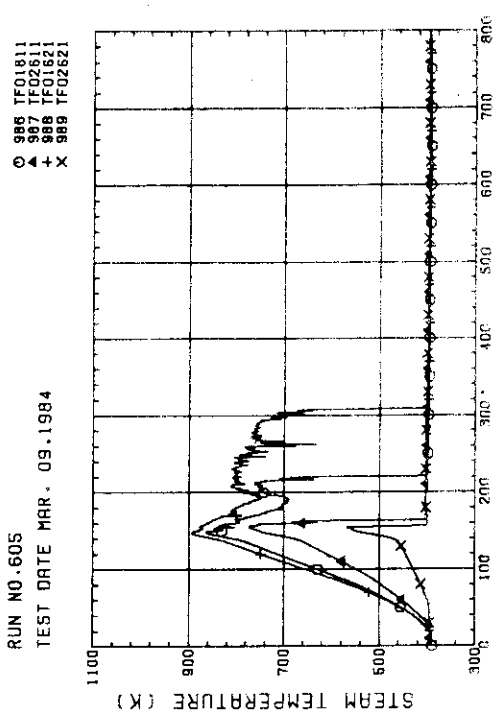

Fig. C-21 STEAM TEMPERATURE IN CORE, BUNDLE 2 (01211-1.735M, 02211-1.875M, 01221-1.38M, 02221-1.915M)

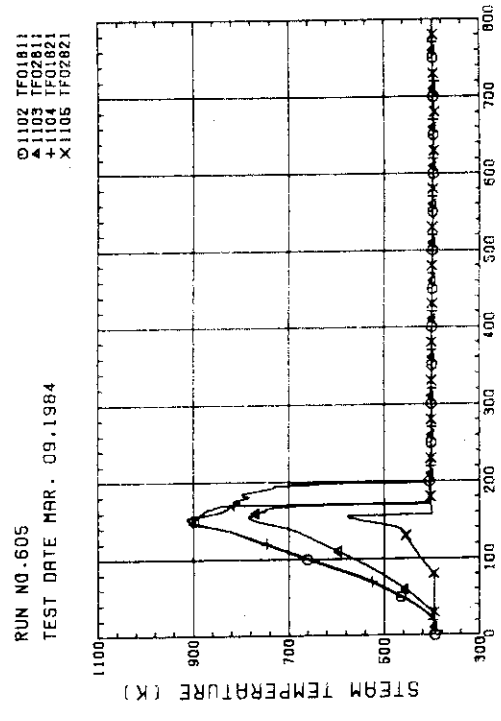

Fig. C-22 STEAM TEMPERATURE IN CORE, BUNDLE 4 (01411-1.735M, 02411-1.875M, 01421-1.38M, 02421-1.915M)

Fig. C-23 STEAM TEMPERATURE IN CORE, BUNDLE 6

Fig. C-24 STEAM TEMPERATURE IN CORE, BUNDLE 8

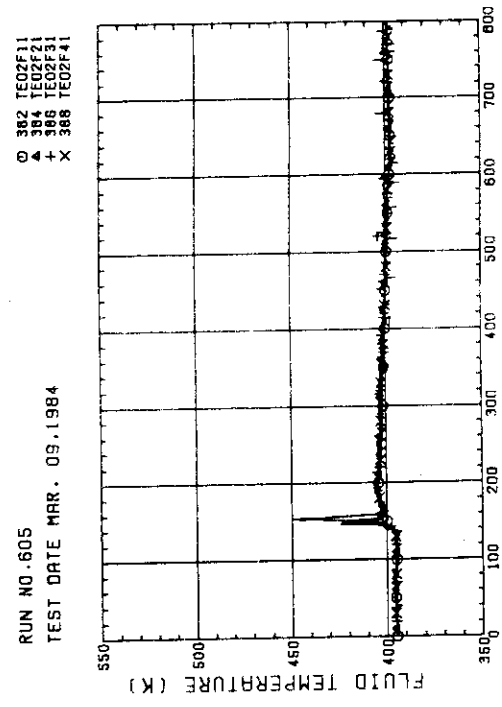

Fig. C-25 FLUID TEMPERATURE JUST ABOVE END BOX TIE PLATE (BUNDLE 1,2,3,4, OPPOSITE SIDE OF COLD LEG)

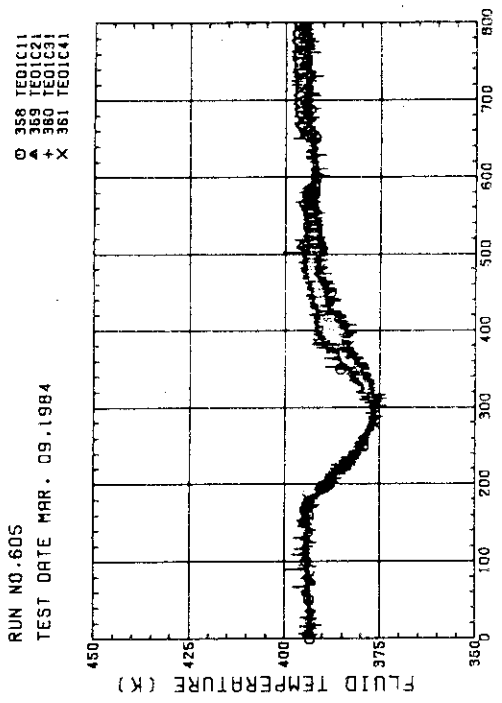

Fig. C-27 FLUID TEMPERATURE AT CORE INLET (BUNDLE 1,2,3,4, 100MM BELOW HEATED PART)

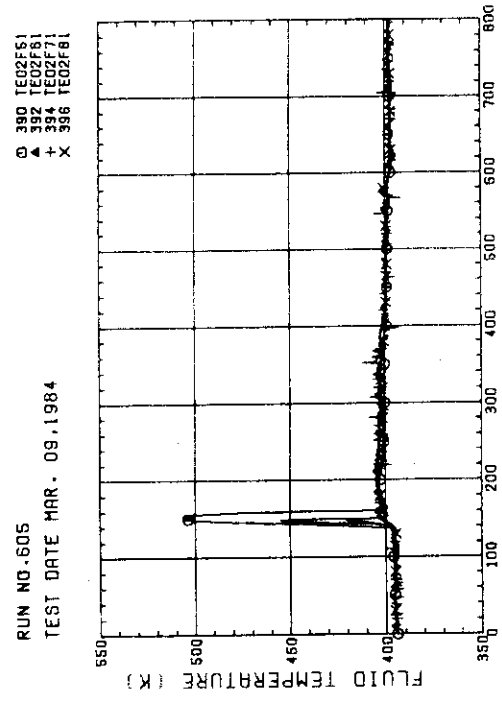

Fig. C-26 FLUID TEMPERATURE JUST ABOVE END BOX TIE PLATE (BUNDLE 5,6,7,8, OPPOSITE SIDE OF COLD LEG)

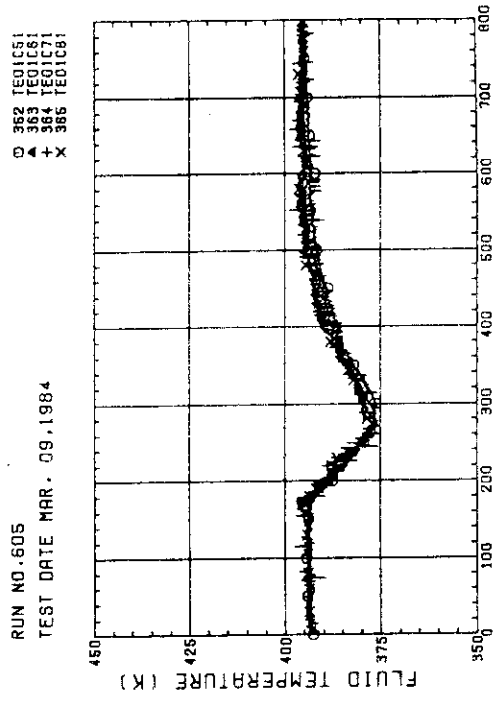

Fig. C-28 FLUID TEMPERATURE AT CORE INLET (BUNDLE 5,6,7,8, 100MM BELOW HEATED PART)

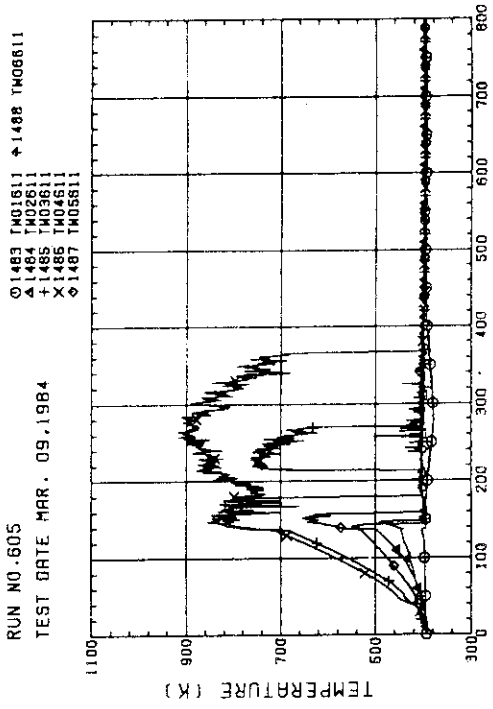

Fig. C-31 TEMPERATURE FOR SPUTTERING DETECTION BUNDLE 6 , REGION 1 , TYPE 1

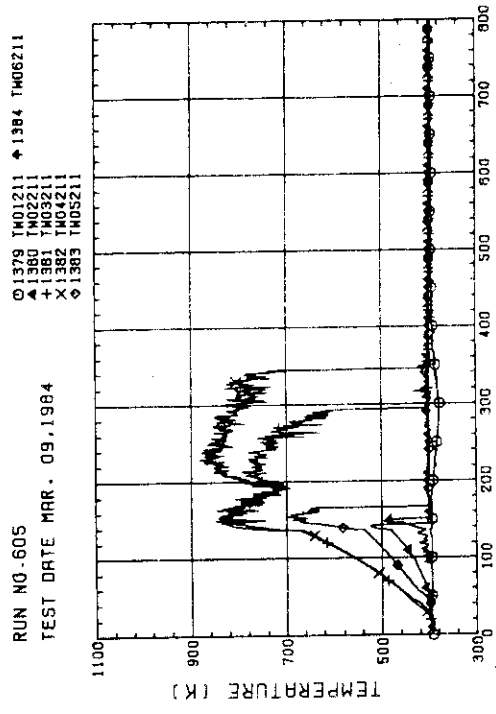

Fig. C-29 TEMPERATURE FOR SPUTTERING DETECTION BUNDLE 2 , REGION 1 , TYPE 1

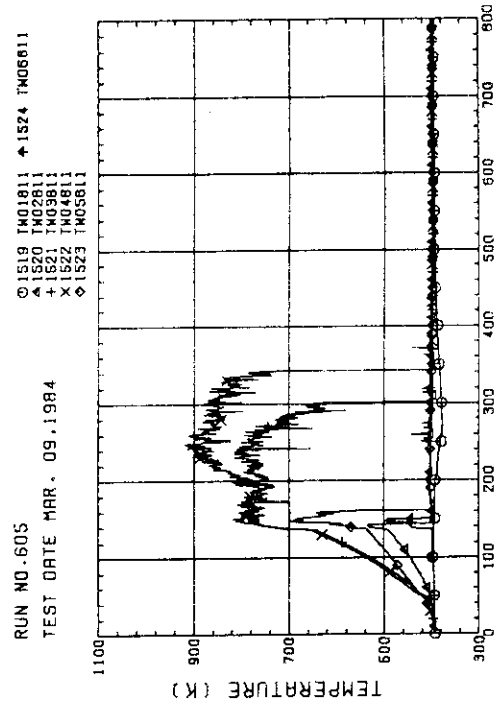

Fig. C-32 TEMPERATURE FOR SPUTTERING DETECTION BUNDLE 8 , REGION 1 , TYPE 1

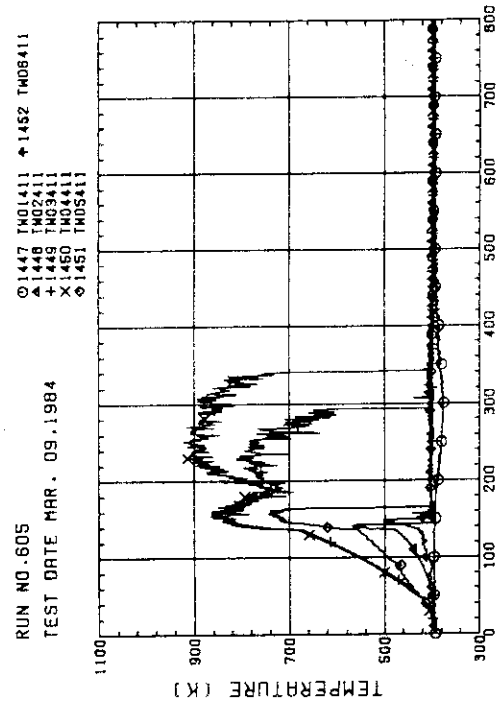

Fig. C-30 TEMPERATURE FOR SPUTTERING DETECTION BUNDLE 4 , REGION 1 , TYPE 1

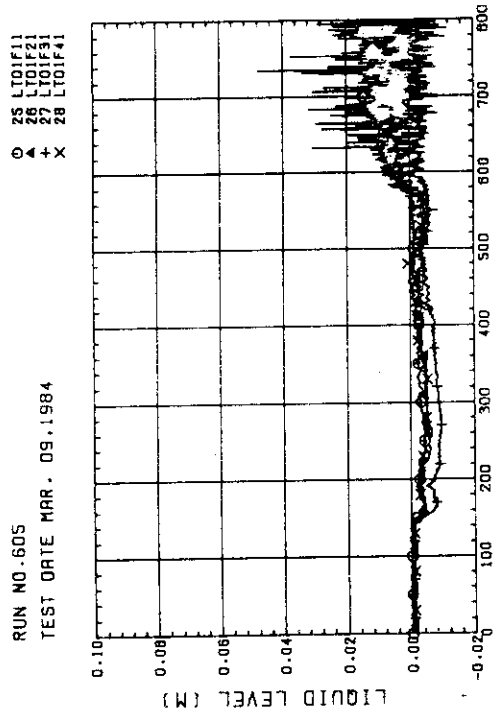

Fig. C-33 LIQUID LEVEL ABOVE END BOX TIE PLATE (BUNDLE 1,2,3,4)

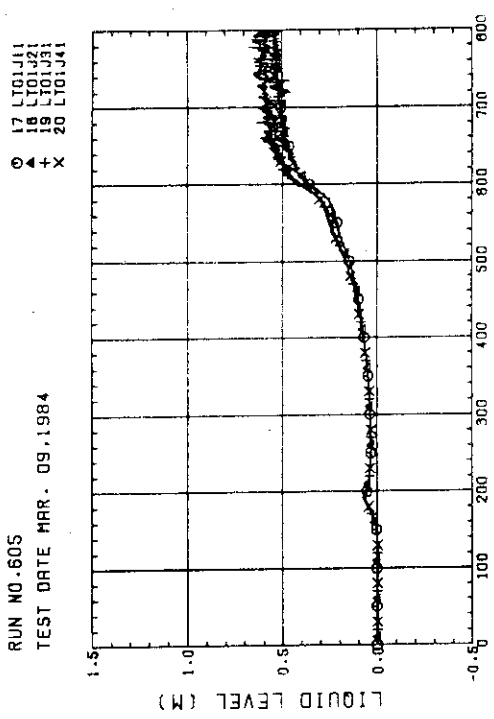

Fig. C-35 LIQUID LEVEL ABOVE UCSP (BUNDLE 1,2,3,4)

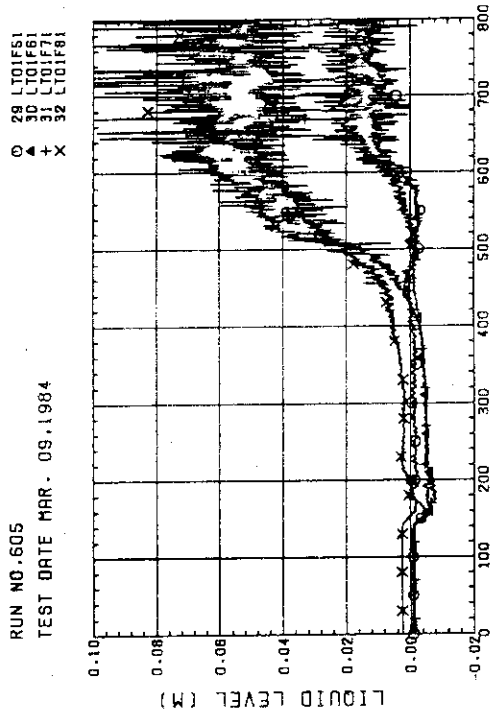

Fig. C-34 LIQUID LEVEL ABOVE END BOX TIE PLATE (BUNDLE 5,6,7,8)

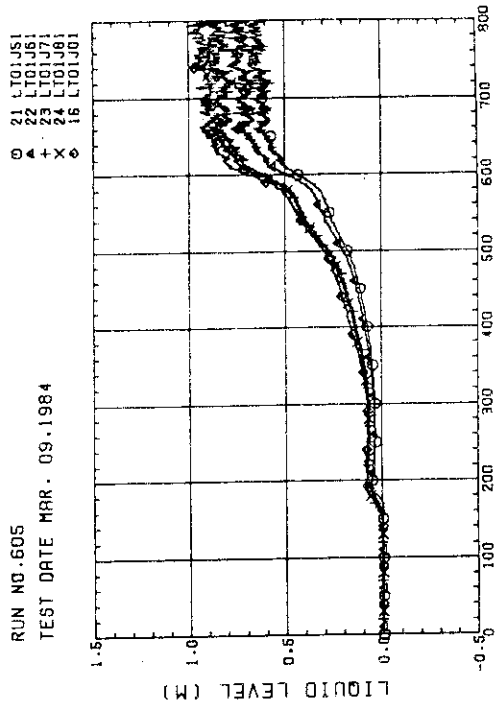

Fig. C-36 LIQUID LEVEL ABOVE UCSP (BUNDLE 5,6,7,8 AND CORE BAFFLE)

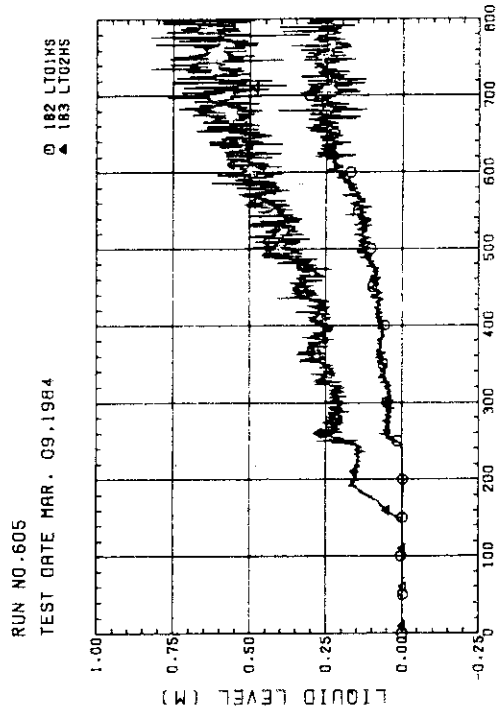

Fig. C-37 LIQUID LEVEL IN HOT LEG (01HS - PV SIDE, 02HS - STEAM/WATER SEPARATOR SIDE)

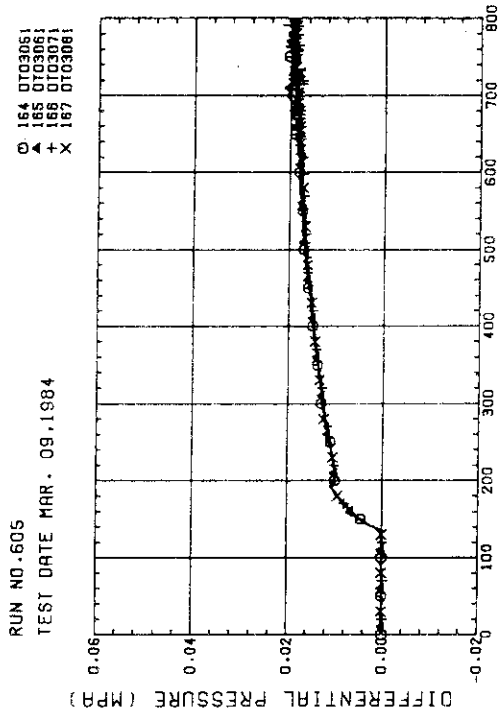

Fig. C-38 DIFFERENTIAL PRESSURE OF CORE FULL HIGHT (BUNDLE 1,2,3,4)

Fig. C-39 DIFFERENTIAL PRESSURE OF CORE FULL HEIGHT (BUNDLE 5,6,7,8)

FIG. C-40 DIFFERENTIAL PRESSURE ACROSS END BOX TIE PLATE (BUNDLE 1,2,3,4)

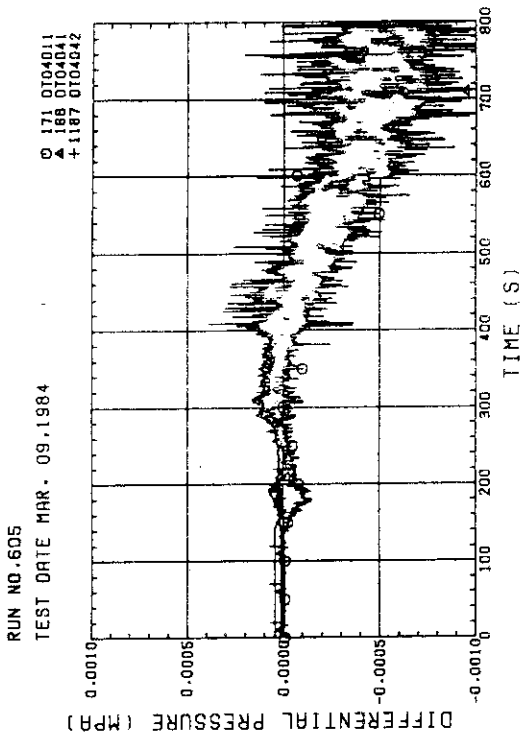

Fig. C-43 DIFFERENTIAL PRESSURE, HORIZONTAL AT 1905 MM (11-BUNDLE 1-4, 41-BUNDLE 4-8, 42-BUNDLE 4-6)

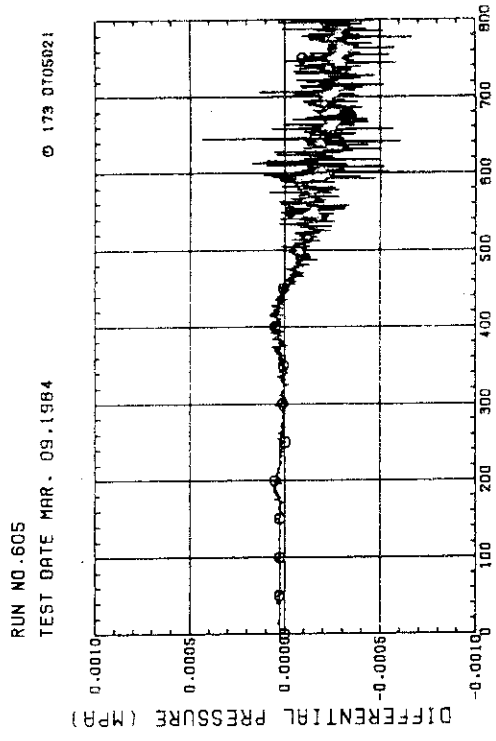

Fig. C-44 DIFFERENTIAL PRESSURE, HORIZONTAL AT 2570 MM (BUNDLE 2-4)

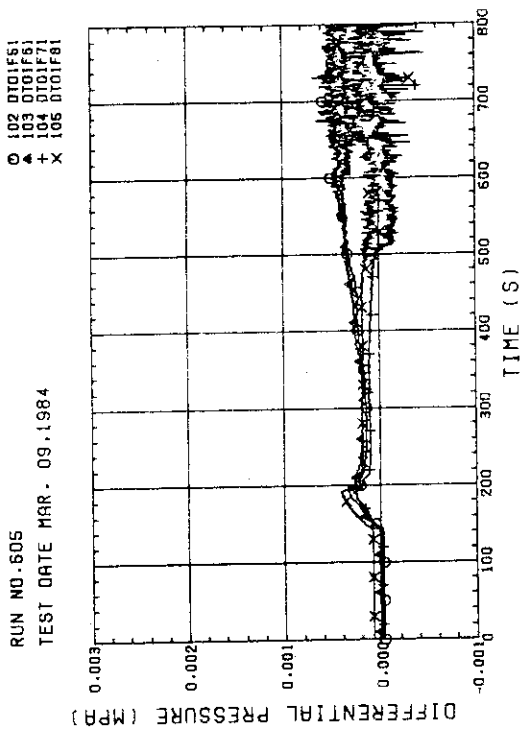

Fig. C-41 DIFFERENTIAL PRESSURE ACROSS END BOX TIE PLATE (BUNDLE 5,6,7,8)

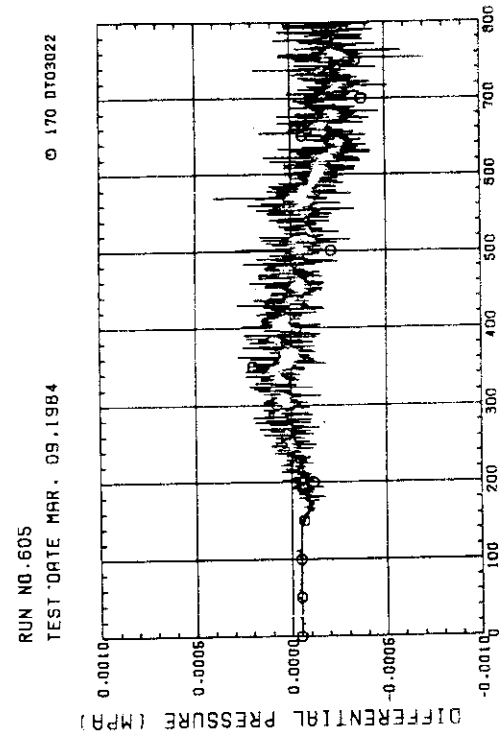

Fig. C-42 DIFFERENTIAL PRESSURE, HORIZONTAL AT 1365 MM (BUNDLE 2-4)

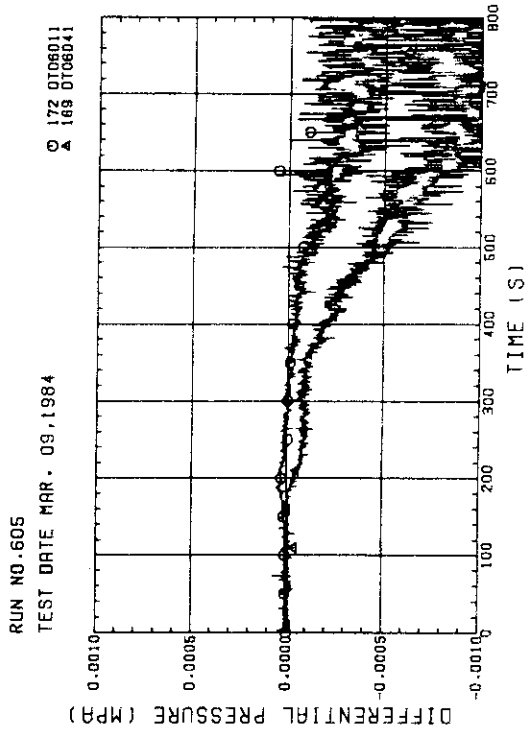

Fig. C-45 DIFFERENTIAL PRESSURE, HORIZONTAL AT 3235 MM (11-BUNDLE 1-4, 41-BUNDLE 4-8)

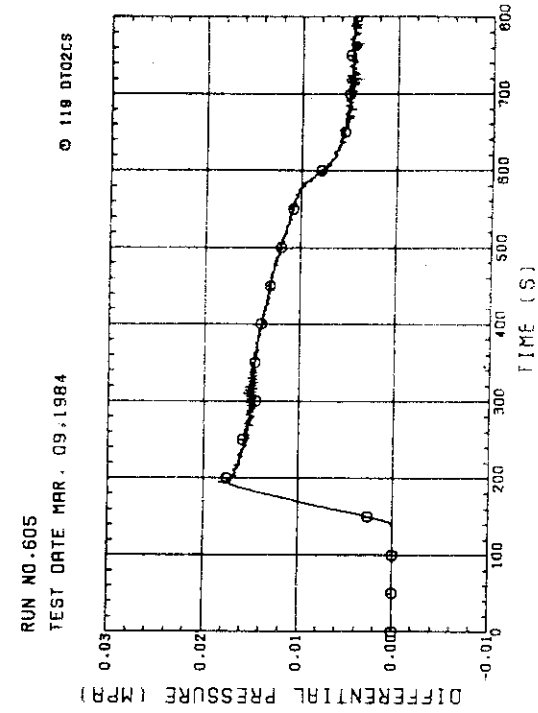

Fig. C-47 DIFFERENTIAL PRESSURE OF INTACT COLD LEG

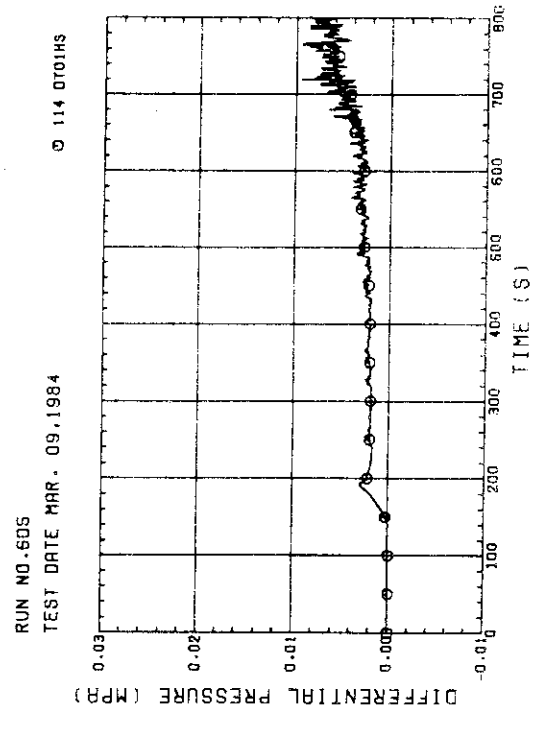

Fig. C-46 DIFFERENTIAL PRESSURE OF HOT LEG, HOT LEG INLET - STEAM/WATER SEPARATOR INLET

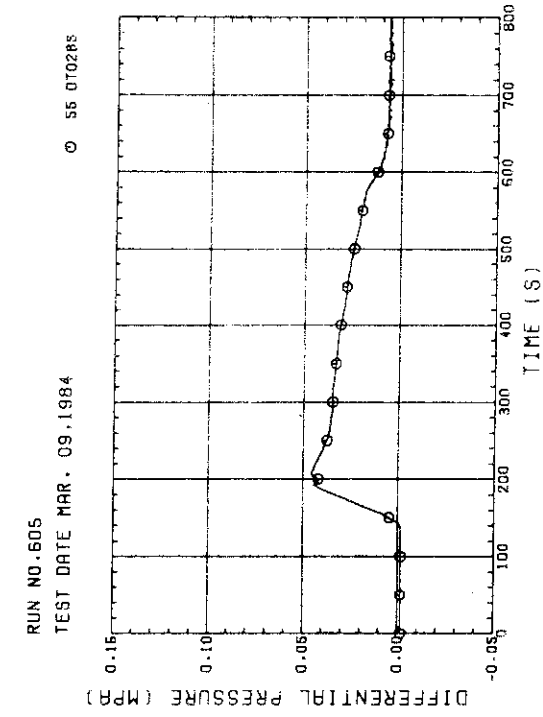

Fig. C-48 DIFFERENTIAL PRESSURE, STEAM/WATER SEPARATOR - CONTAINMENT TANK-T1

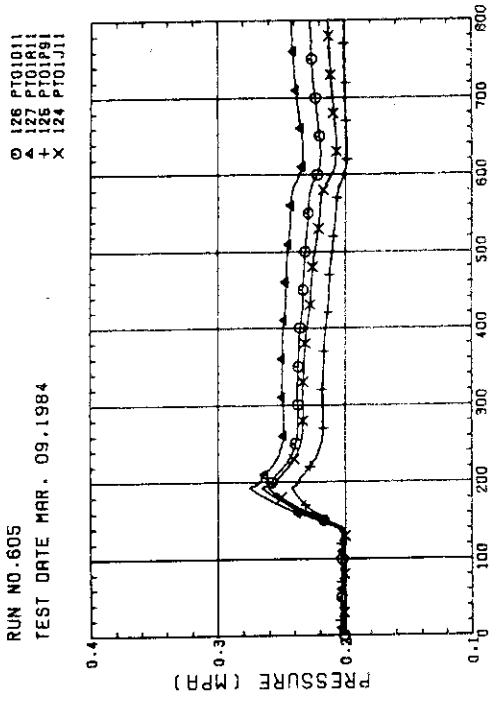

Fig. C-51 PRESSURE IN PV (J - TOP OF PV, O - CORE CENTER, A - CORE INLET, P - BELOW COLD LEG NOZZLE IN DOWNCOMER)

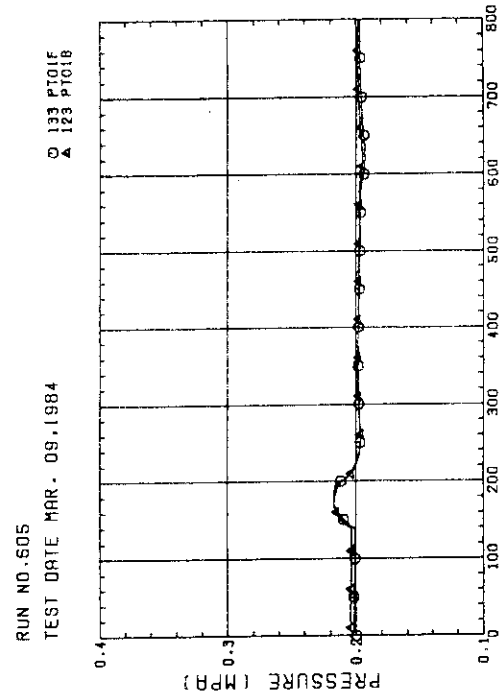

Fig. C-52 PRESSURE AT TOP OF CONTAINMENT TANK-I AND CONTAINMENT TANK-II (F-CONTAINMENT TANK-I, B-CONTAINMENT TANK-II)

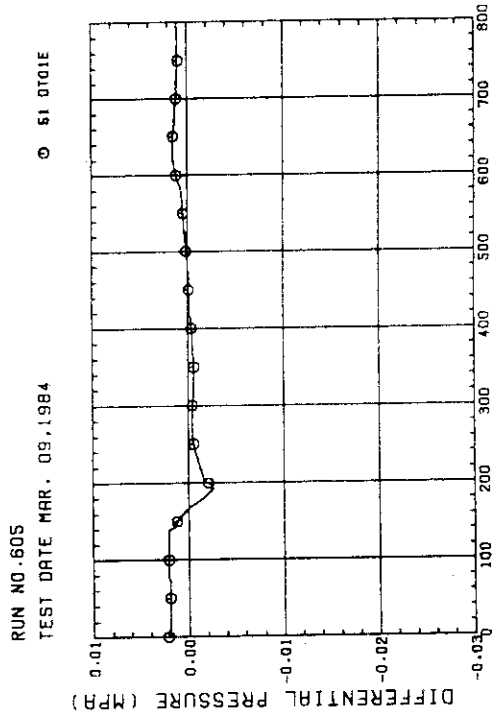

Fig. C-49 DIFFERENTIAL PRESSURE. CONTAINMENT TANK-II - CONTAINMENT TANK-I

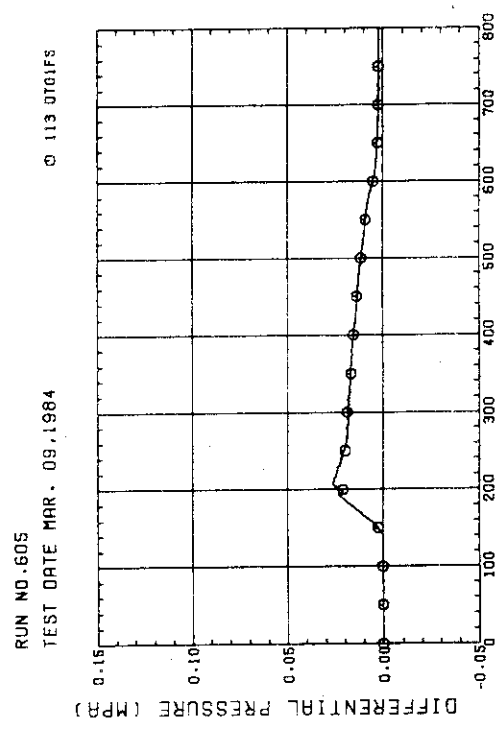

Fig. C-50 DIFFERENTIAL PRESSURE OF BROKEN COLD LEG - PV SIDE. DOWNCOMER - CONTAINMENT TANK-I

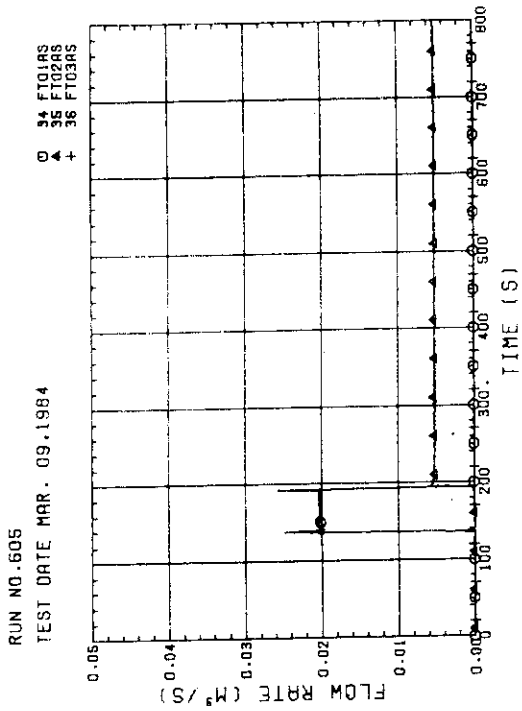

Fig. C-55 FLOW RATE OF ECC WATER (01-LOWER PLENUM. 02-INTACT COLD LEG. 03-BROKEN COLD LEG)

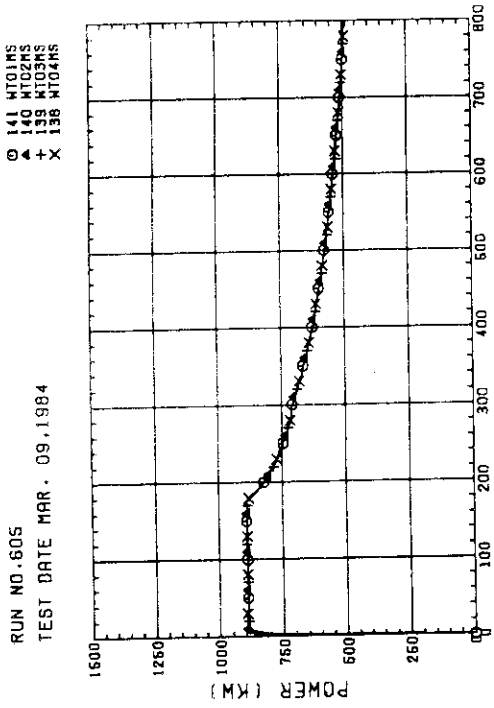

Fig. C-53 BUNDLE POWER (BUNDLE 1,2,3,4)

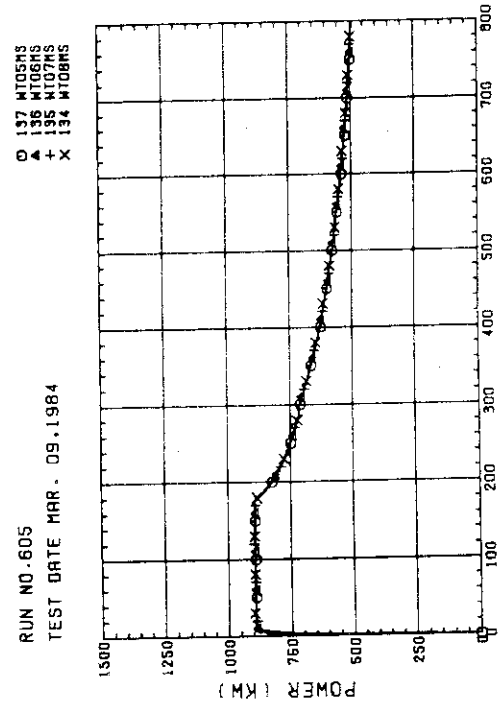

Fig. C-54 BUNDLE POWER (BUNDLE 5,6,7,8)

Appendix D Selected Data of Test S2-06

Fig. D-1 ∿ D-16	Heater rod temperatures
Fig. D-17 ∿ D-20	Non-heated rod temperatures
Fig. D-21 ∿ D-24	Steam temperatures
Fig. D-25 ∿ D-26	Fluid temperatures just above end box tie plate
Fig. D-27 ∿ D-28	Fluid temperatures at core inlet
Fig. D-29 ∿ D-32	Fluid temperatures in core
Fig. D-33 ∿ D-34	Liquid levels above end box tie plate
Fig. D-35 ∿ D-36	Liquid levels above UCSP
Fig. D-37	Liquid levels in hot leg
Fig. D-38 ∿ D-39	Differential pressures across core full height
Fig. D-40 ∿ D-41	Differential pressures across end box tie plate
Fig. D-42 ∿ D-45	Horizontal differential pressures in core
Fig. D-46 ∿ D-50	Differential pressures in primary loops
Fig. D-51 ∿ D-52	Pressures in pressure vessel and containment tanks
Fig. D-53 ∿ D-54	Bundle powers
Fig. D-55	ECC flow rates

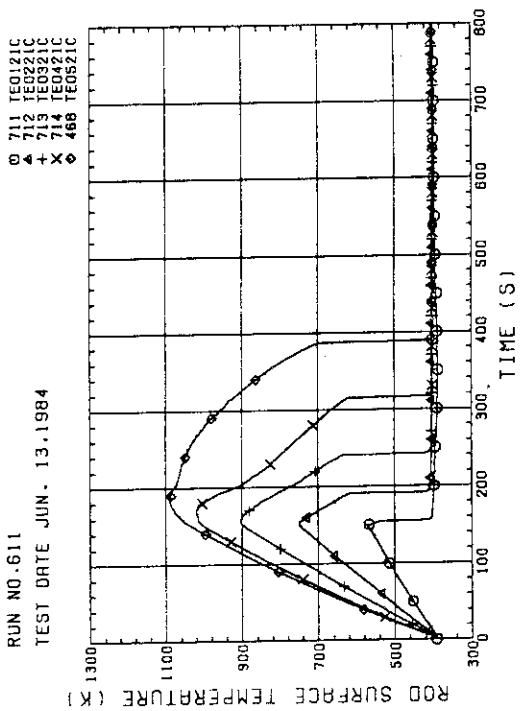

Fig. D- 3 HEATER ROD TEMPERATURE (BUNDLE 2-1C, LOWER HALF)

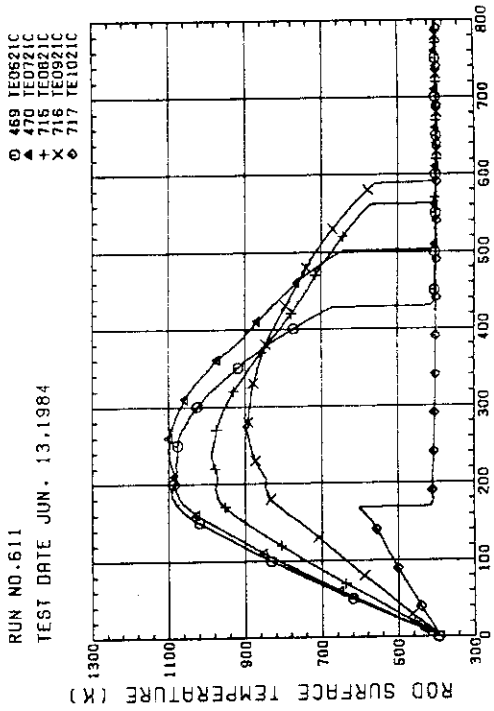

Fig. D- 4 HEATER ROD TEMPERATURE (BUNDLE 2-1C, UPPER HALF)

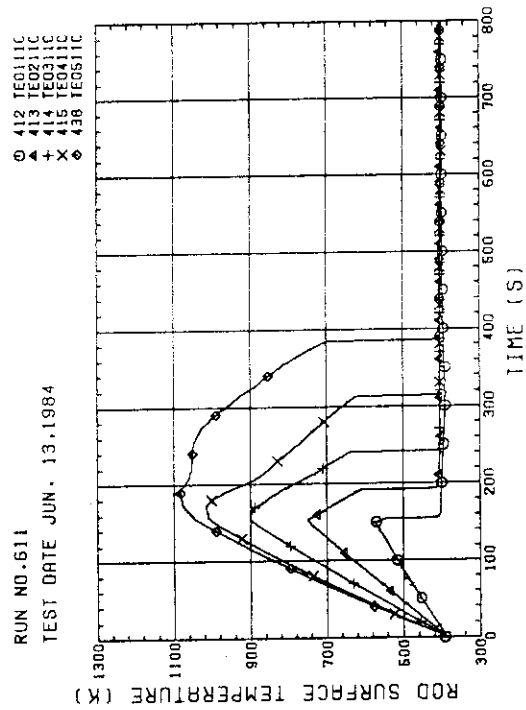

Fig. D- 1 HEATER ROD TEMPERATURE (BUNDLE 1-1C, LOWER HALF)

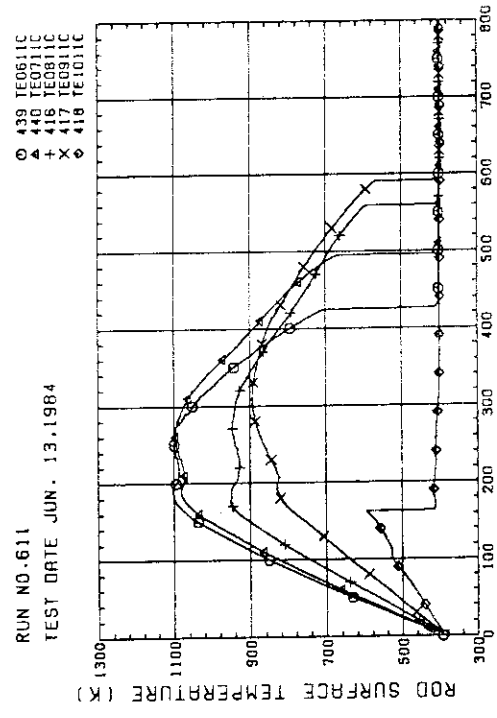

Fig. D- 2 HEATER ROD TEMPERATURE (BUNDLE 1-1C, UPPER HALF)

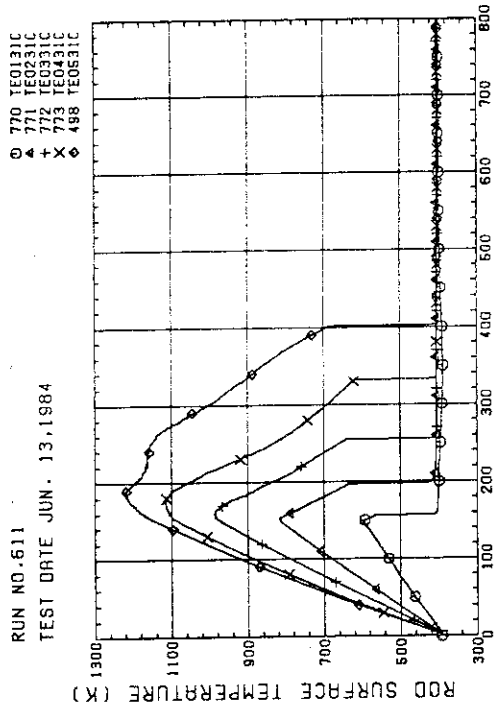

Fig. D- 5 HEATER ROD TEMPERATURE (BUNDLE 3-1C, LOWER HALF)

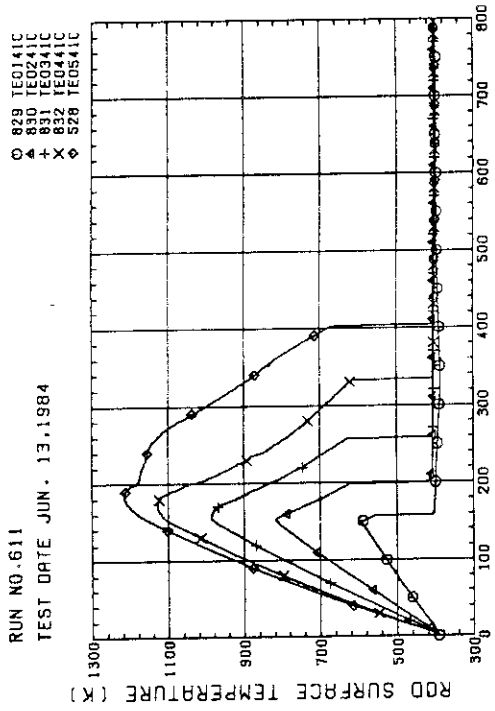

Fig. D- 7 HEATER ROD TEMPERATURE (BUNDLE 4-1C, LOWER HALF)

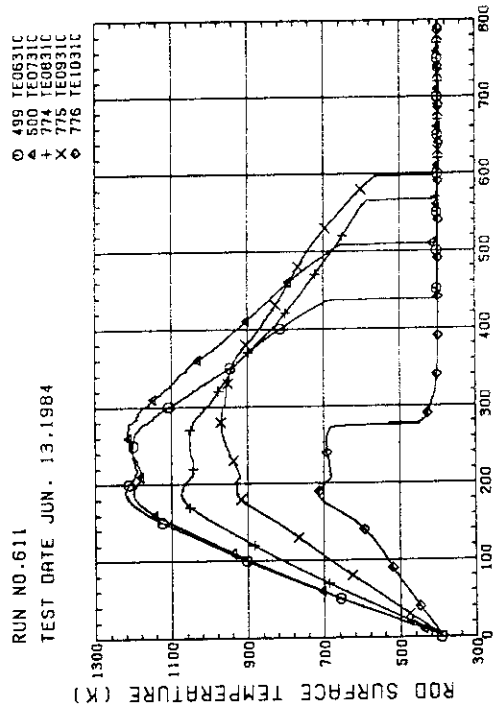

Fig. D- 6 HEATER ROD TEMPERATURE (BUNDLE 3-1C, UPPER HALF)

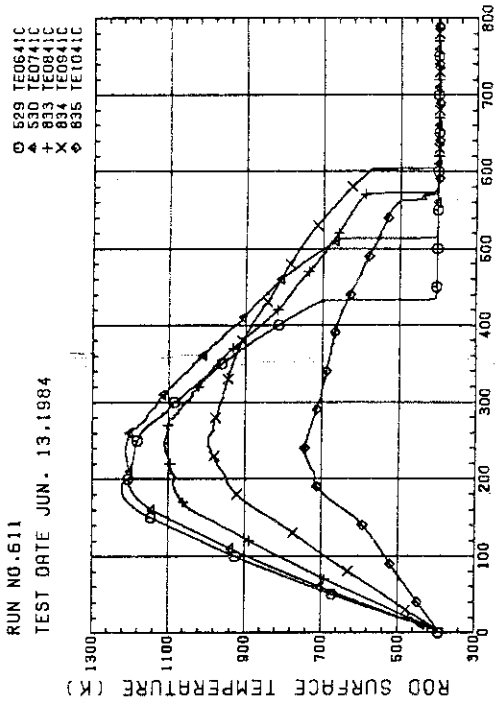

Fig. D- 8 HEATER ROD TEMPERATURE (BUNDLE 4-1C, UPPER HALF)

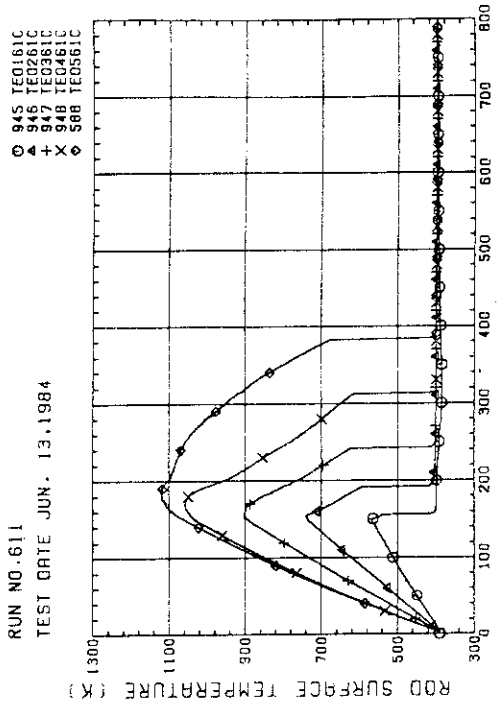

Fig. D-11 HEATER ROD TEMPERATURE (BUNDLE 6-1C, LOWER HALF)

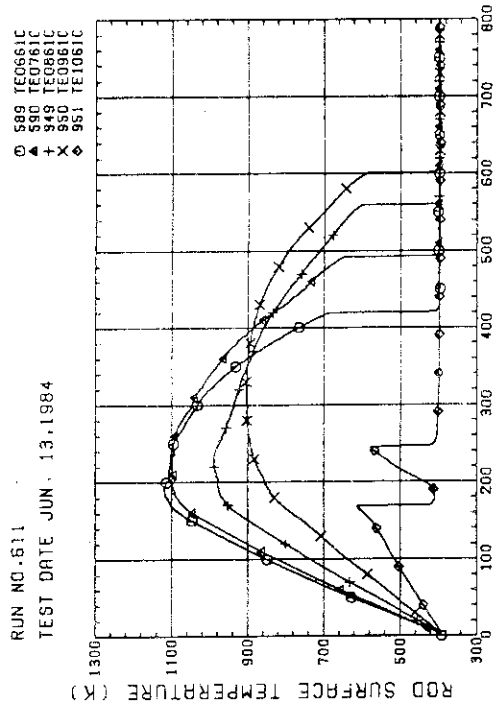

Fig. D-12 HEATER ROD TEMPERATURE (BUNDLE 6-1C, UPPER HALF)

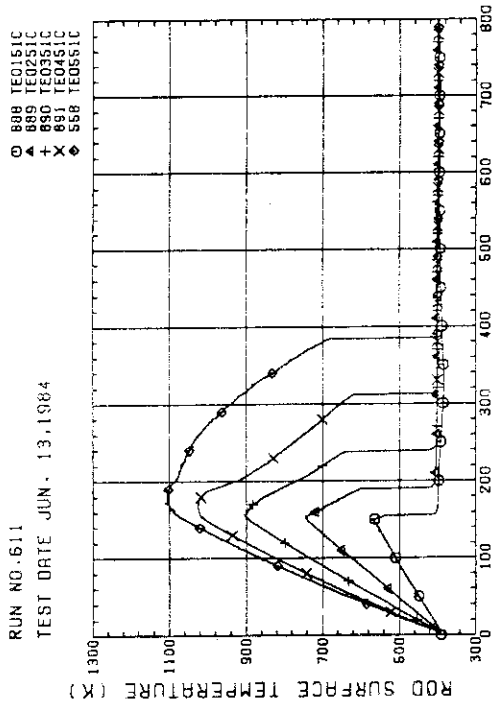

Fig. D- 9 HEATER ROD TEMPERATURE (BUNDLE 5-1C, LOWER HALF)

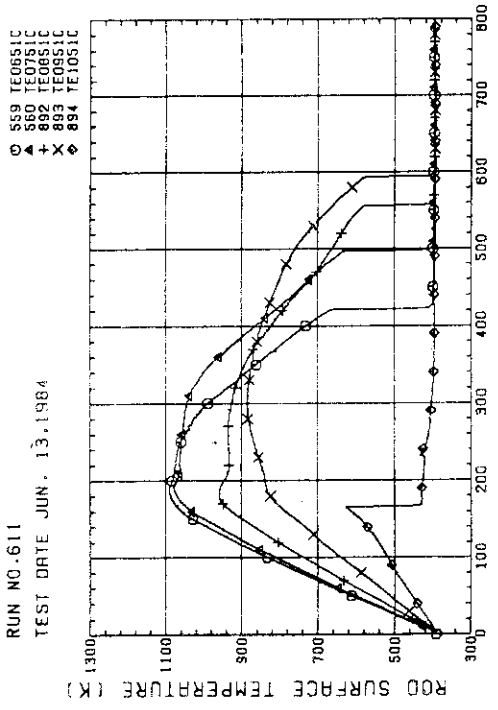

Fig. D-10 HEATER ROD TEMPERATURE (BUNDLE 5-1C, UPPER HALF)

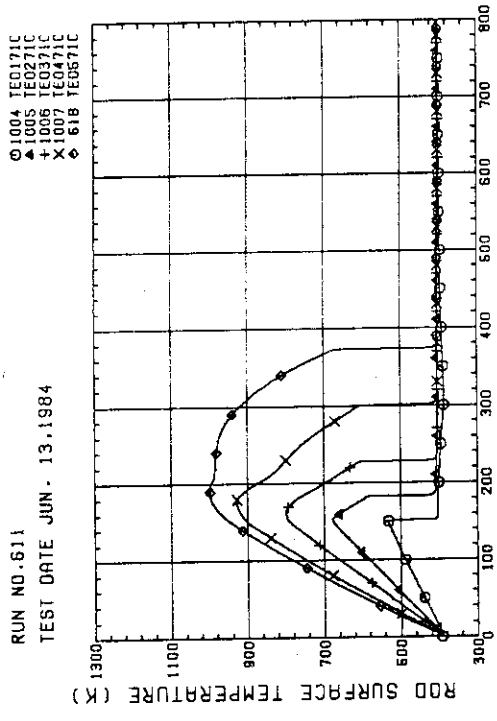

Fig. D-13 HEATER ROD TEMPERATURE (BUNDLE 7-1C, LOWER HALF)

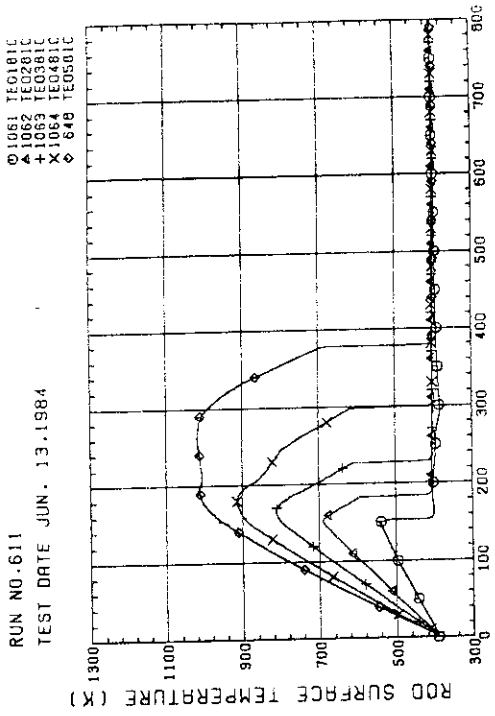

Fig. D-15 HEATER ROD TEMPERATURE (BUNDLE 8-1C, LOWER HALF)

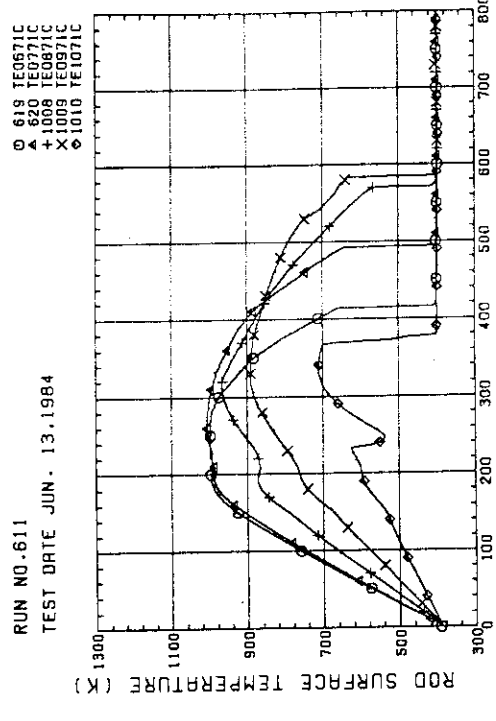

Fig. D-14 HEATER ROD TEMPERATURE (BUNDLE 7-1C, UPPER HALF)

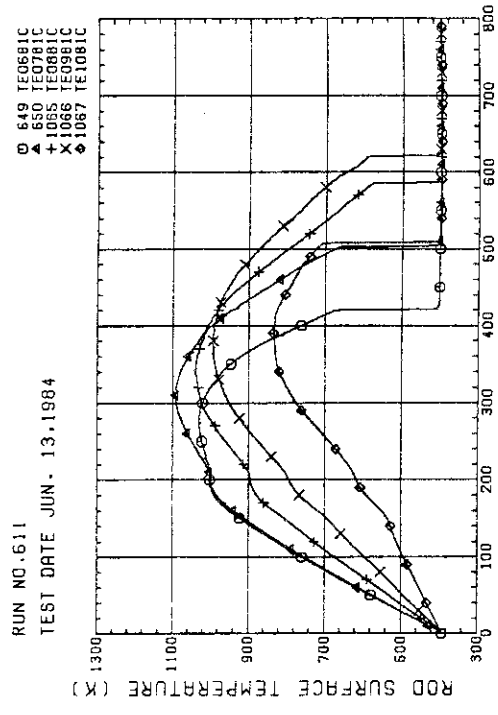

Fig. D-16 HEATER ROD TEMPERATURE (BUNDLE 8-1C, UPPER HALF)

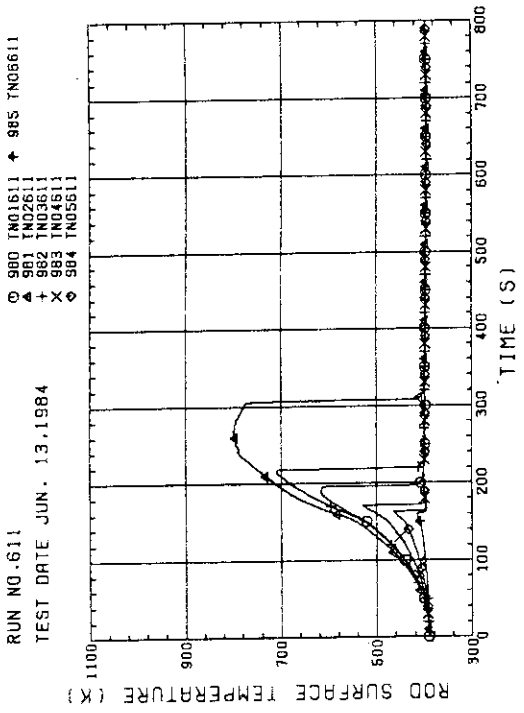

Fig. D-19 NON-HEATED ROD TEMPERATURE (BUNDLE 6-1)

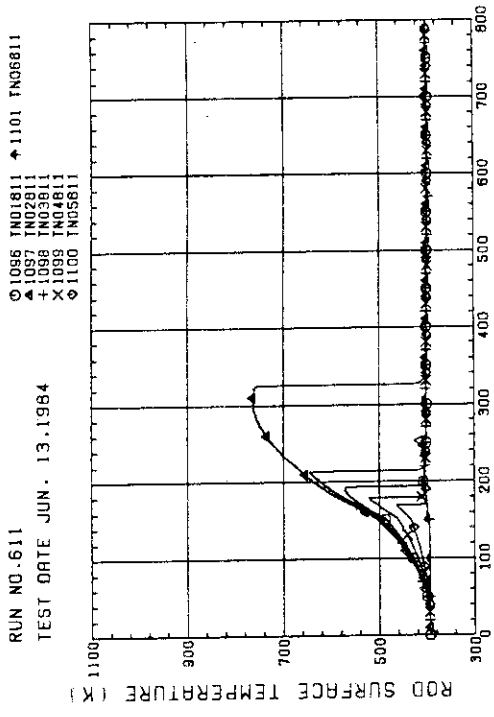

Fig. D-20 NON-HEATED ROD TEMPERATURE (BUNDLE 8-1)

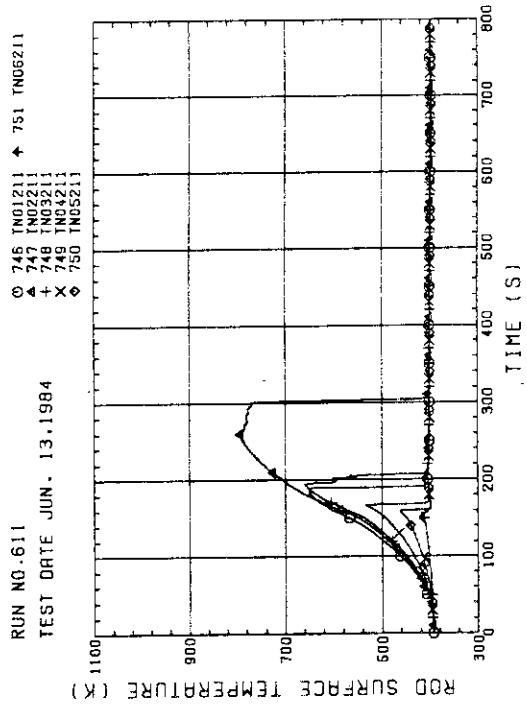

Fig. D-17 NON-HEATED ROD TEMPERATURE (BUNDLE 2-1)

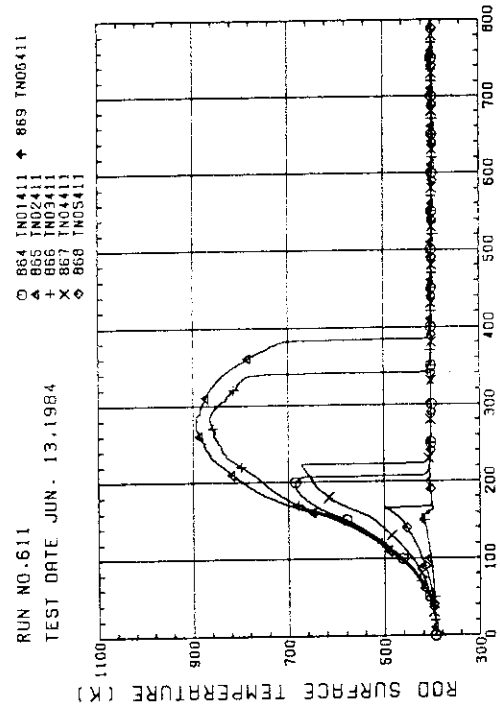

Fig. D-18 NON-HEATED ROD TEMPERATURE (BUNDLE 4-1)

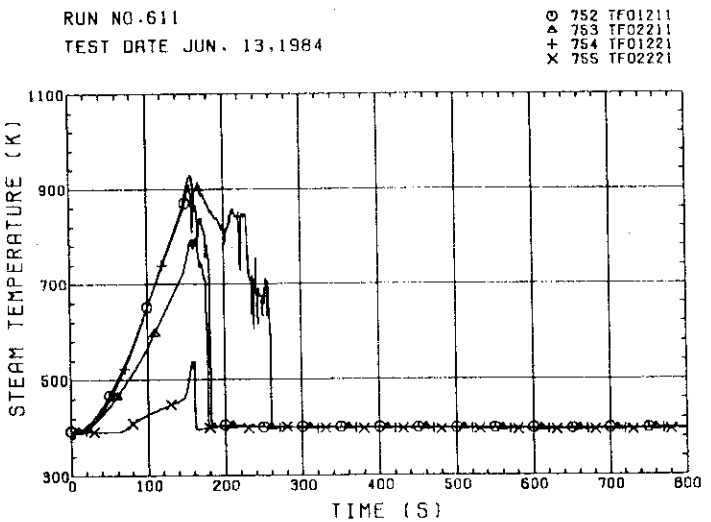

Fig. D-21 STEAM TEMPERATURE IN CORE, BUNDLE 2 (01211-1.735M, 02211-1.875M, 01221-1.38M, 02221-1.915M)

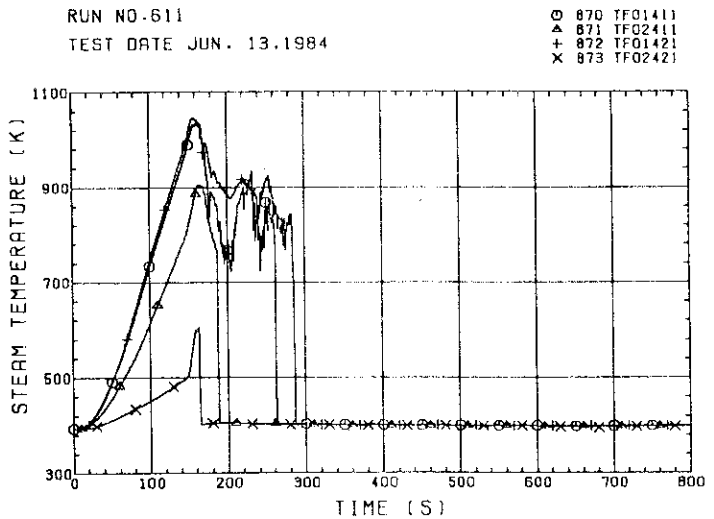

Fig. D-22 STEAM TEMPERATURE IN CORE, BUNDLE 4 (01411-1.735M, 02411-1.875M, 01421-1.38M, 02421-1.915M)

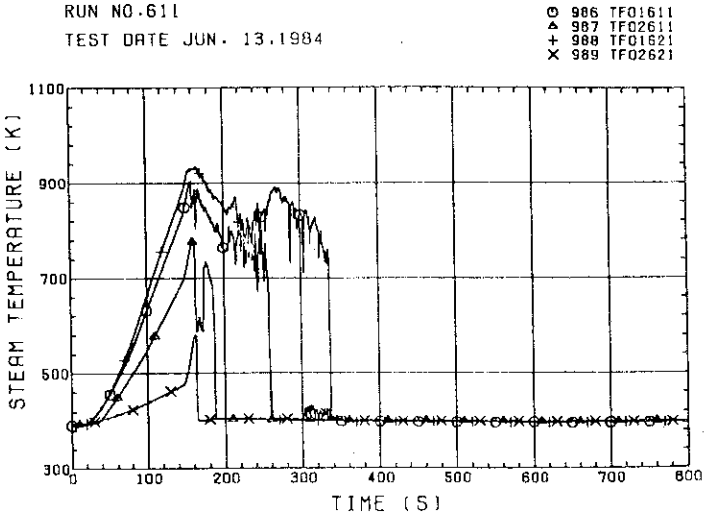

Fig. D-23 STEAM TEMPERATURE IN CORE, BUNDLE 6

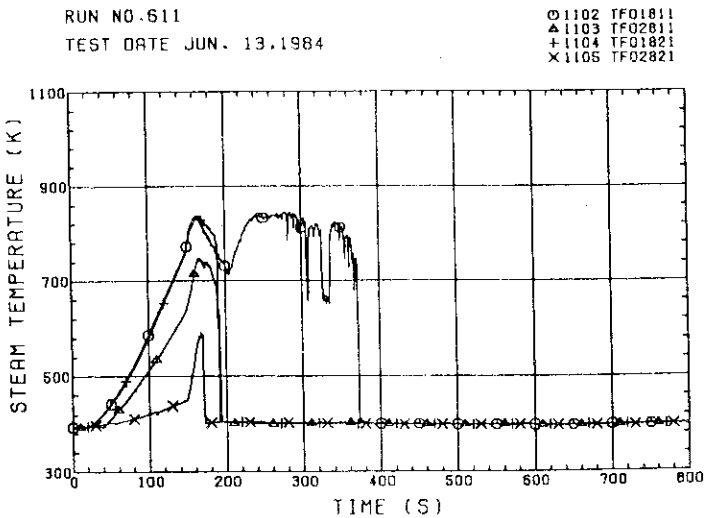

Fig. D-24 STEAM TEMPERATURE IN CORE, BUNDLE 8

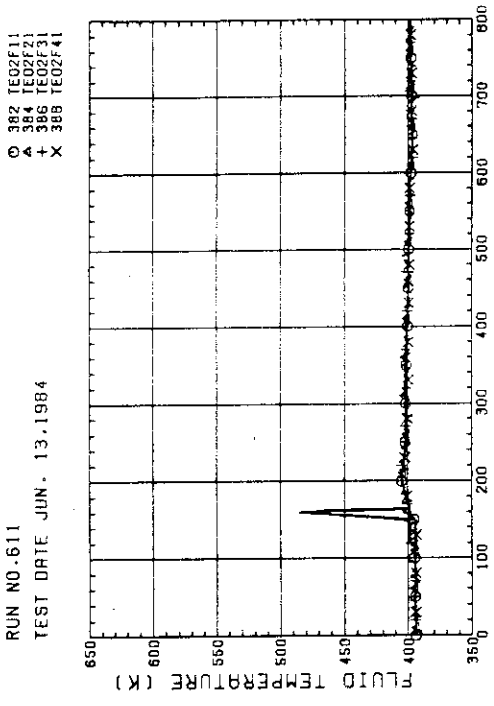

Fig. D-25 FLUID TEMPERATURE JUST ABOVE END BOX TIE PLATE (BUNDLE 1,2,3,4, OPPOSITE SIDE OF COLD LEG)

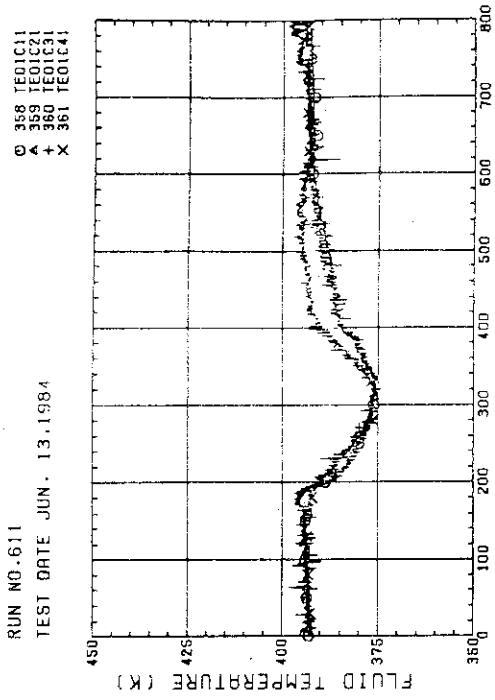

Fig. D-27 FLUID TEMPERATURE AT CORE INLET (BUNDLE 1,2,3,4, 100MM BELOW HEATED PART)

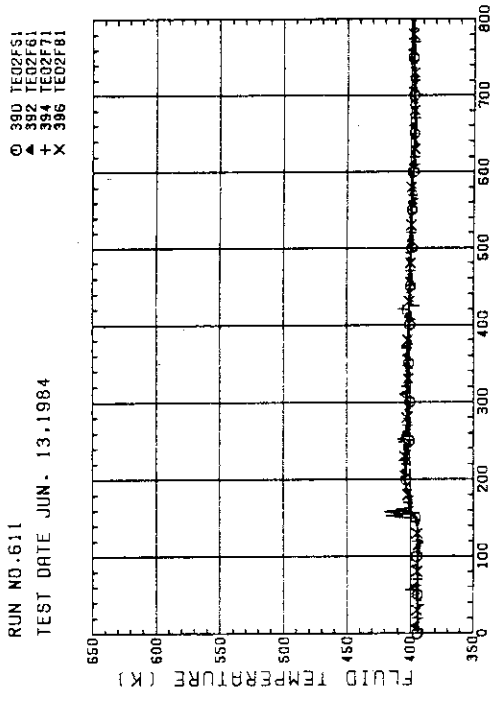

Fig. D-26 FLUID TEMPERATURE JUST ABOVE END BOX TIE PLATE (BUNDLE 5,6,7,8, OPPOSITE SIDE OF COLD LEG)

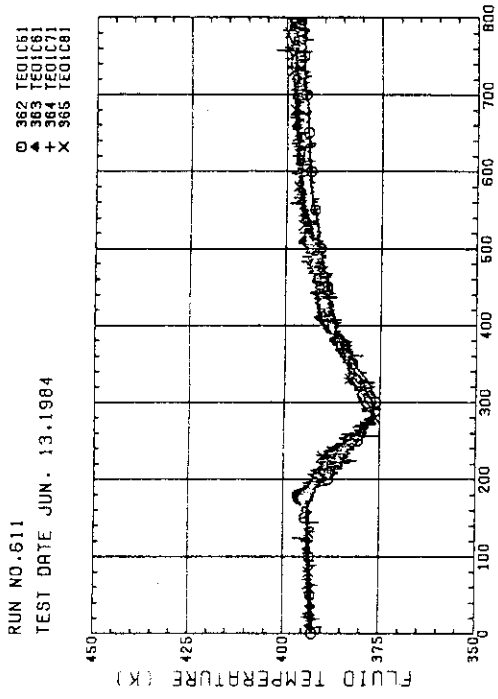

Fig. D-28 FLUID TEMPERATURE AT CORE INLET (BUNDLE 5,6,7,8, 100MM BELOW HEATED PART)

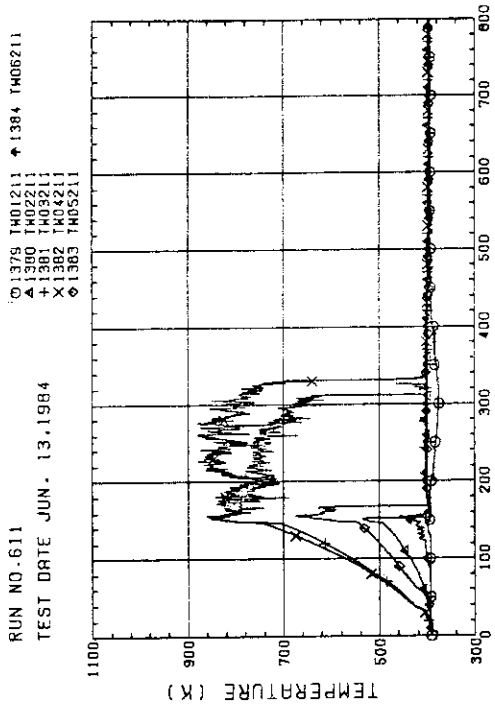

Fig. D-29 TEMPERATURE FOR SPUTTERING DETECTION
BUNDLE 2 , REGION 1 , TYPE 1

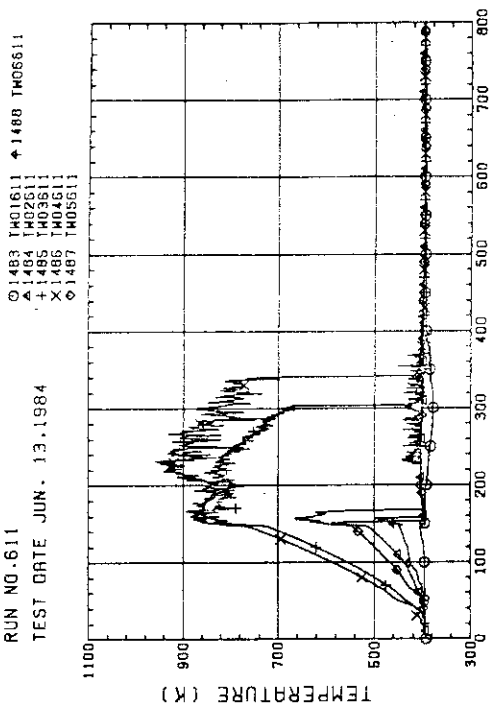

Fig. D-31 TEMPERATURE FOR SPUTTERING DETECTION
BUNDLE 6 , REGION 1 , TYPE 1

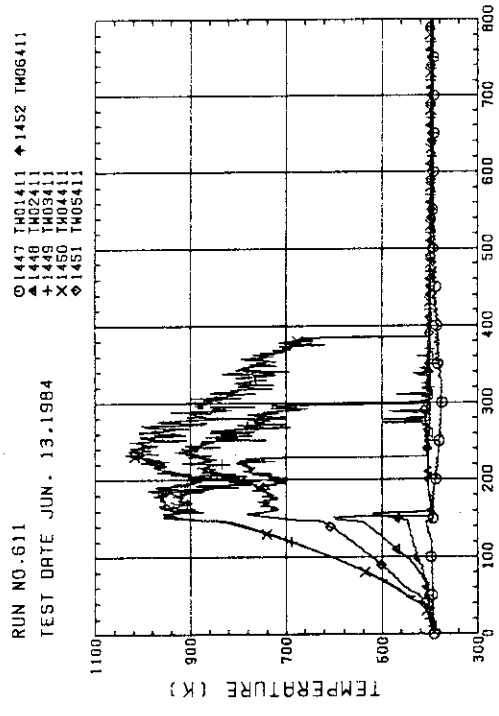

Fig. D-30 TEMPERATURE FOR SPUTTERING DETECTION
BUNDLE 4 , REGION 1 , TYPE 1

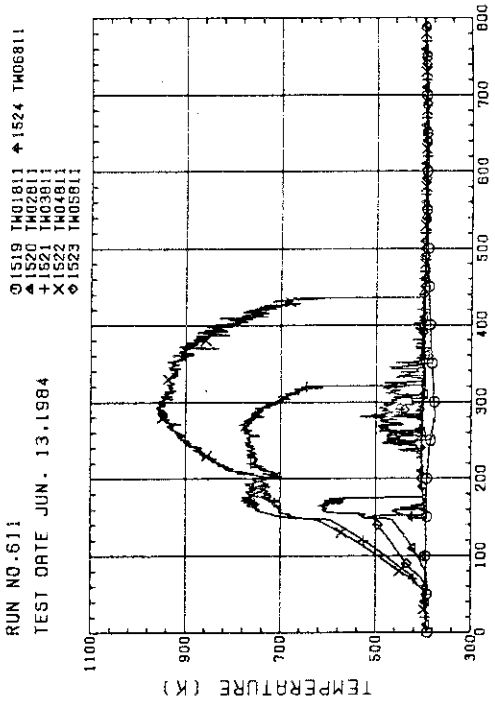

Fig. D-32 TEMPERATURE FOR SPUTTERING DETECTION
BUNDLE 8 , REGION 1 , TYPE 1

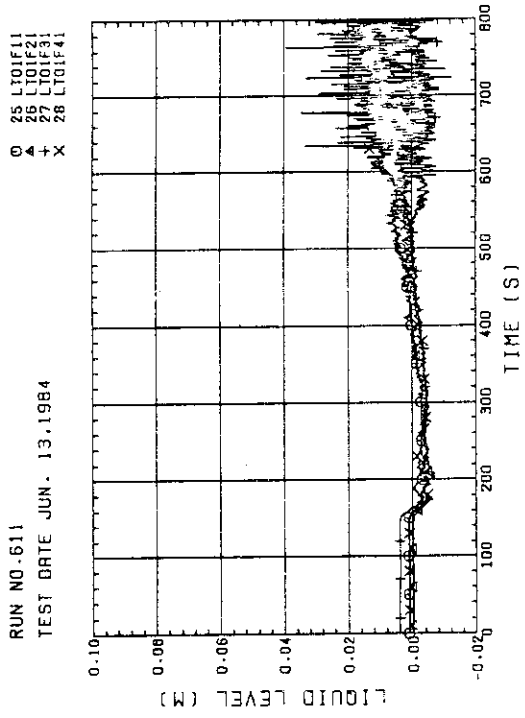

Fig. D-33 LIQUID LEVEL ABOVE END BOX TIE PLATE (BUNDLE 1,2,3,4)

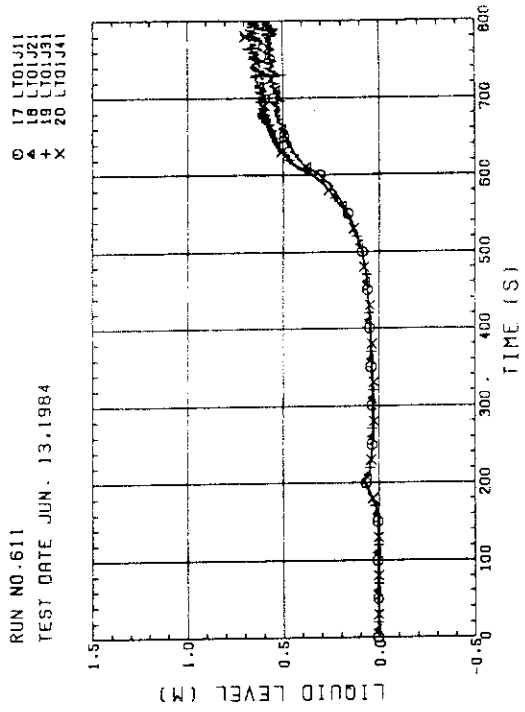

Fig. D-35 LIQUID LEVEL ABOVE UCSP (BUNDLE 1,2,3,4)

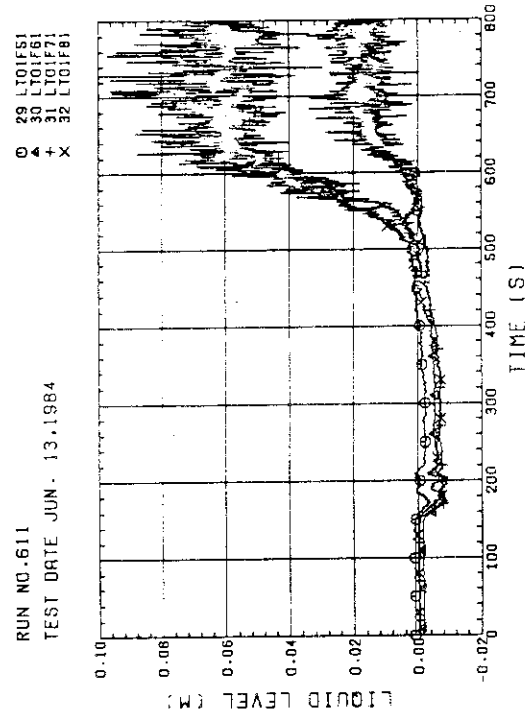

Fig. D-34 LIQUID LEVEL ABOVE END BOX TIE PLATE (BUNDLE 5,6,7,8)

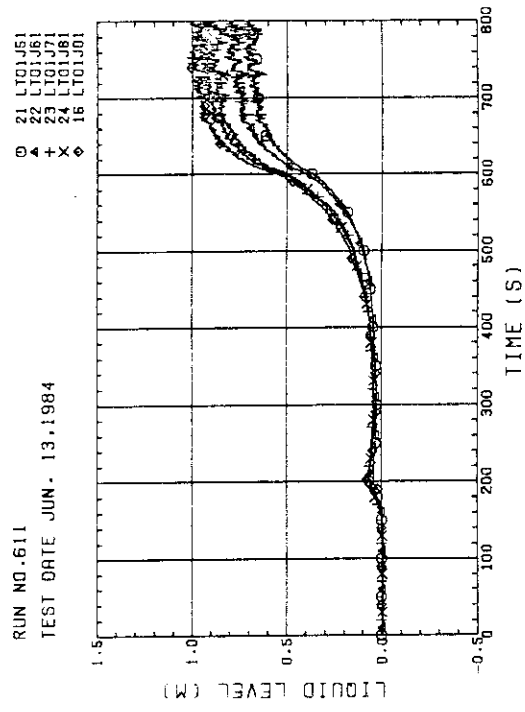

Fig. D-36 LIQUID LEVEL ABOVE UCSP (BUNDLE 5,6,7,8 AND CORE BAFFLE)

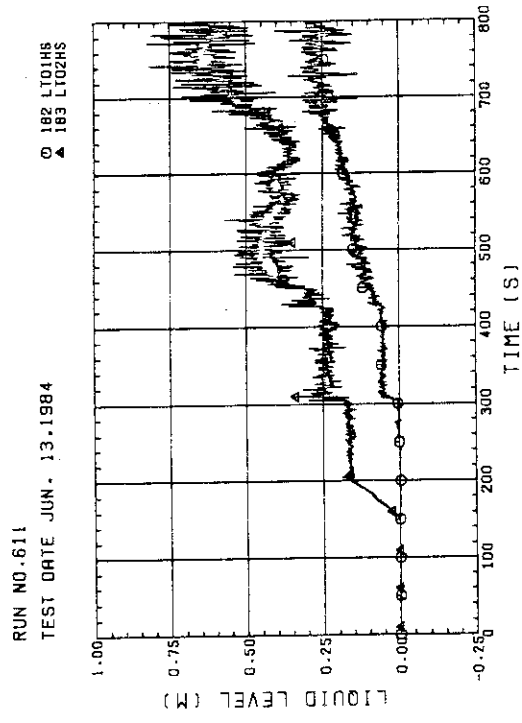

Fig. D-37 LIQUID LEVEL IN HOT LEG (O1HS - PV SIDE, O2HS - STEAM/WATER SEPARATOR SIDE)

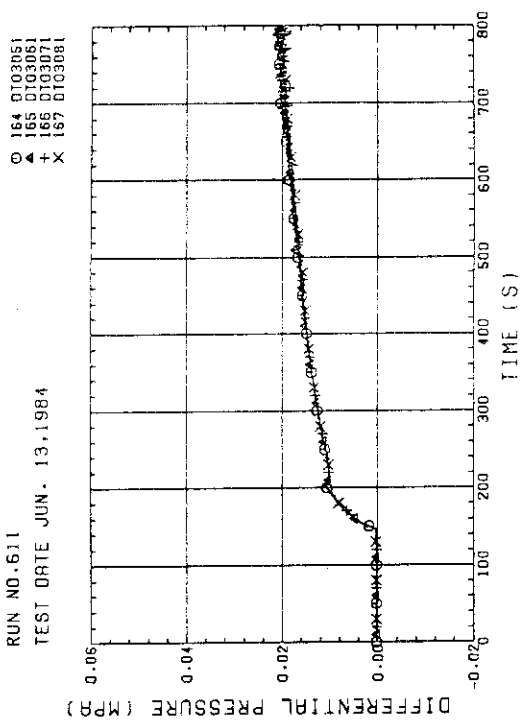

Fig. D-39 DIFFERENTIAL PRESSURE OF CORE FULL HEIGHT (BUNDLE 5,6,7,8)

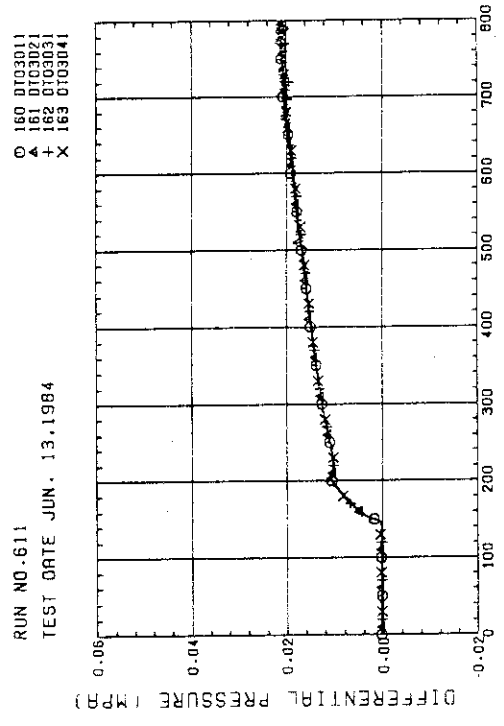

Fig. D-38 DIFFERENTIAL PRESSURE OF CORE FULL HIGHT (BUNDLE 1,2,3,4)

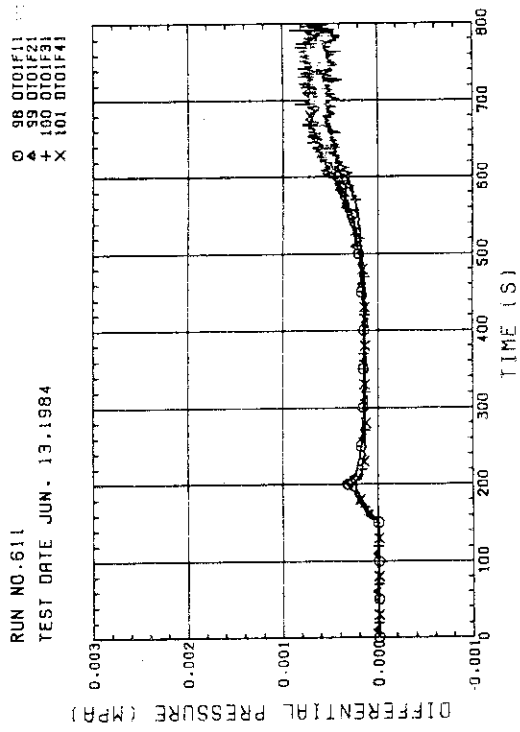

Fig. D-40 DIFFERENTIAL PRESSURE ACROSS END BOX TIE PLATE (BUNDLE 1,2,3,4)

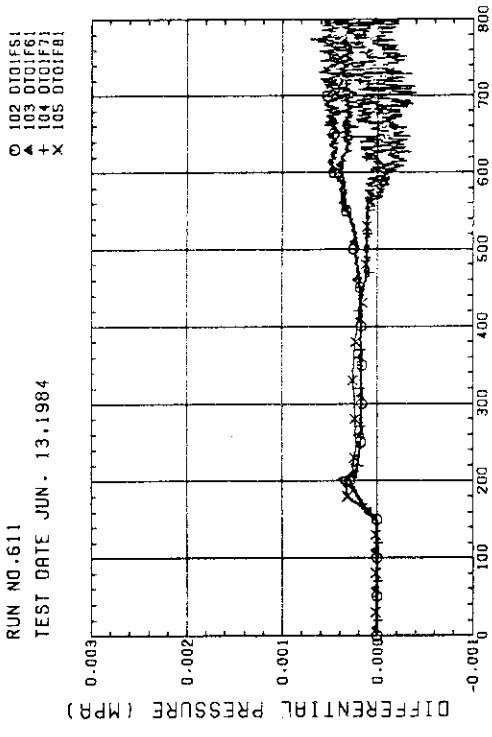

Fig. D-41 DIFFERENTIAL PRESSURE ACROSS END BOX TIE PLATE (BUNDLE 5,6,7,8)

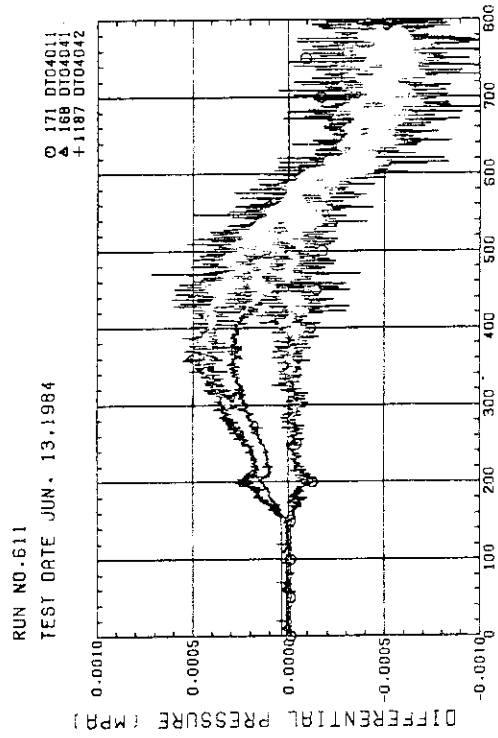

Fig. D-43 DIFFERENTIAL PRESSURE, HORIZONTAL AT 1905 MM (11-BUNDLE 1-4, 41-BUNDLE 4-8, 42-BUNDLE 4-6)

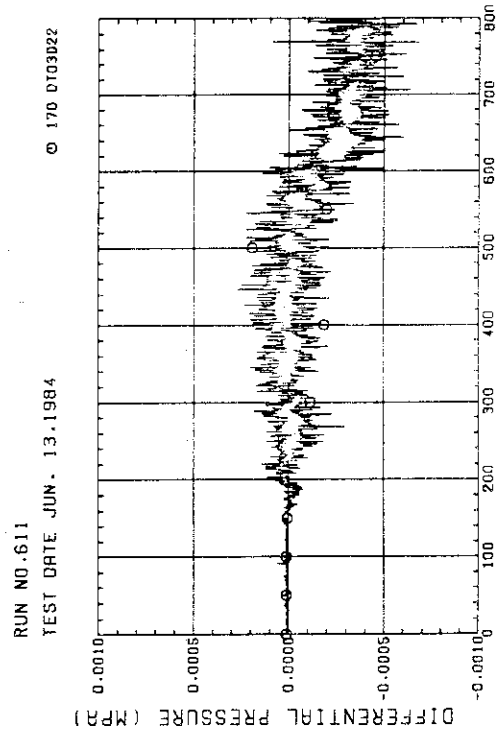

Fig. D-42 DIFFERENTIAL PRESSURE, HORIZONTAL AT 1365 MM (BUNDLE 2-4)

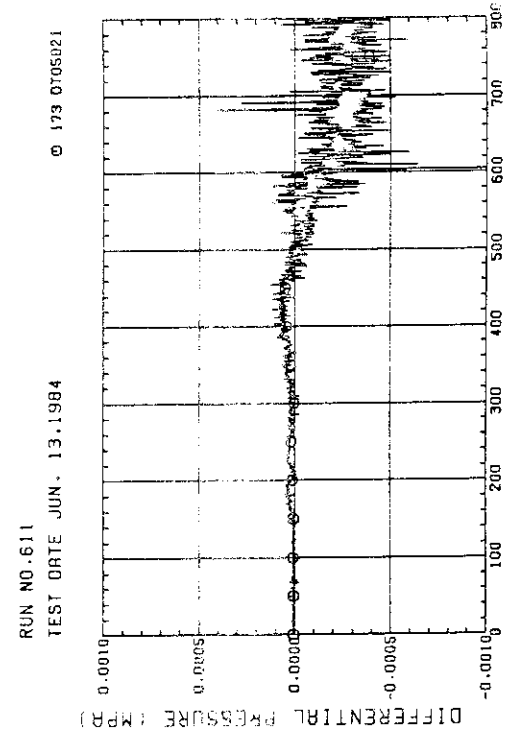

Fig. D-44 DIFFERENTIAL PRESSURE, HORIZONTAL AT 2570 MM (BUNDLE 2-4)

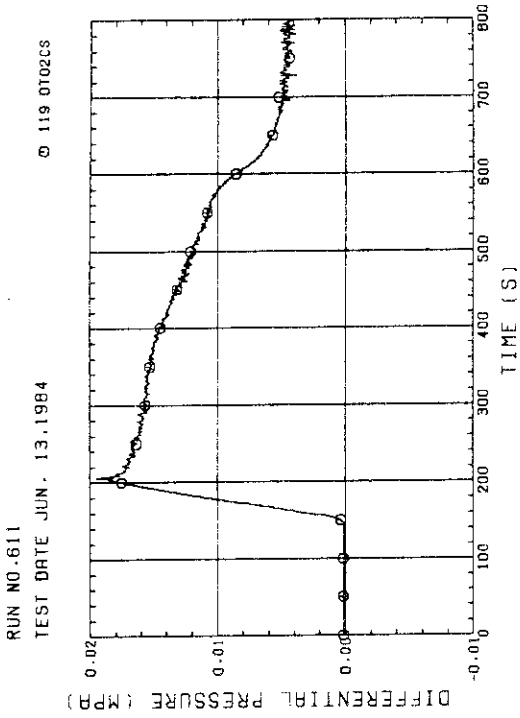

Fig. D-47 DIFFERENTIAL PRESSURE OF INTACT COLD LEG

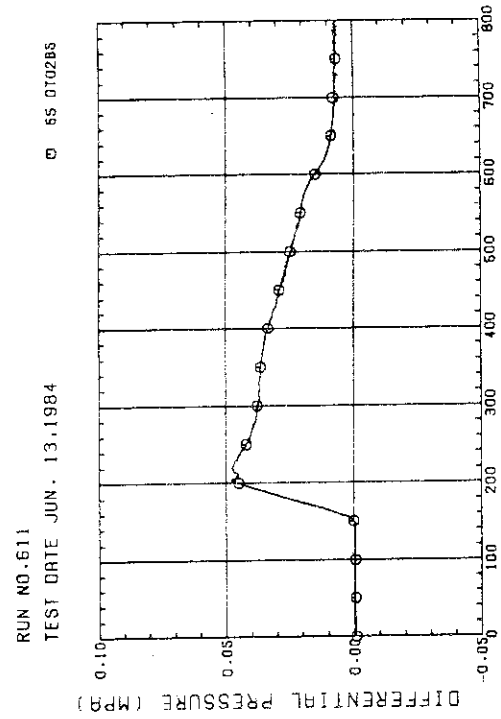

Fig. D-48 DIFFERENTIAL PRESSURE, STEAM/WATER SEPARATOR - CONTAINMENT TANK-II

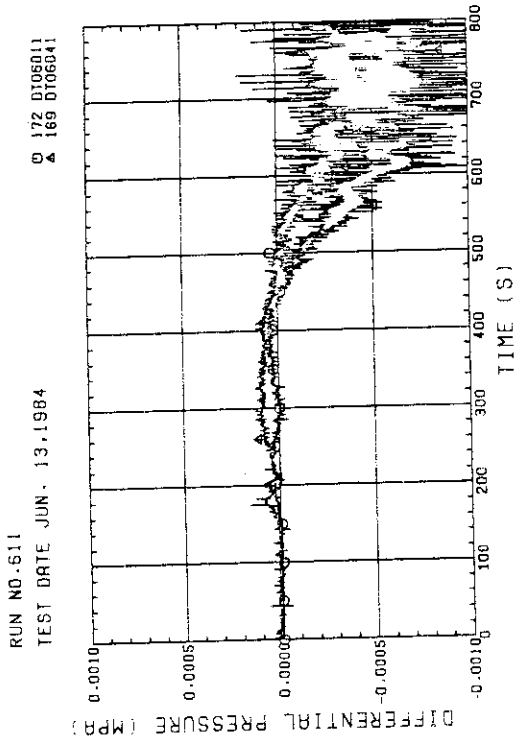

Fig. D-45 DIFFERENTIAL PRESSURE, HORIZONTAL AT 3235 MM (11-BUNDLE 1-4, 41-BUNDLE 4-8)

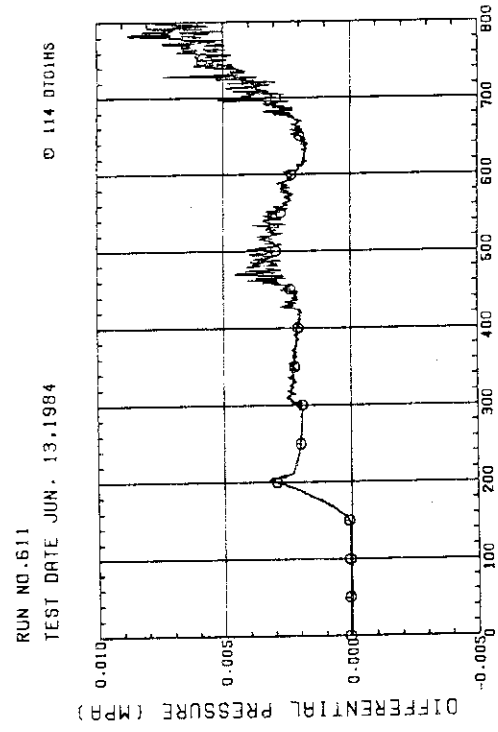

Fig. D-46 DIFFERENTIAL PRESSURE OF HOT LEG, HOT LEG INLET - STEAM/WATER SEPARATOR INLET

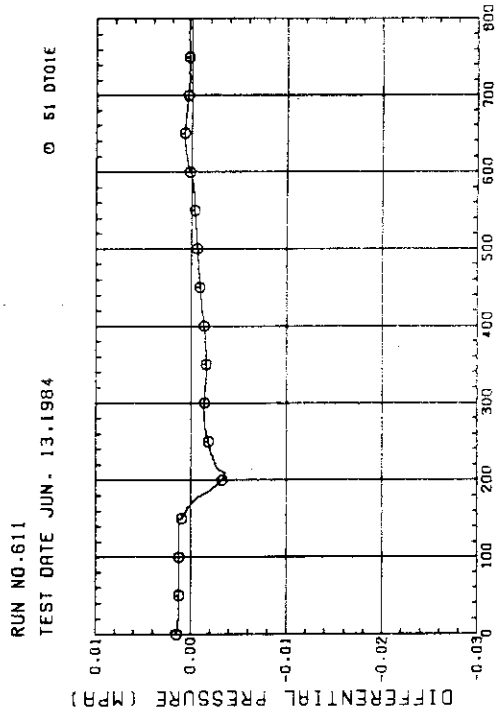

Fig. D-49 DIFFERENTIAL PRESSURE, CONTAINMENT TANK-II - CONTAINMENT TANK-I

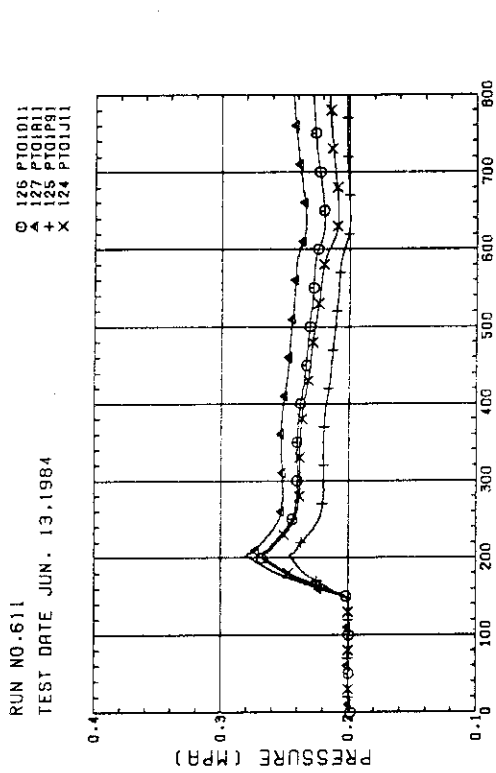

Fig. D-51 PRESSURE IN PV (J - TOP OF PV, D - CORE CENTER, A - CORE INLET, P - BELOW COLD LEG NOZZLE IN DOWNCOMER)

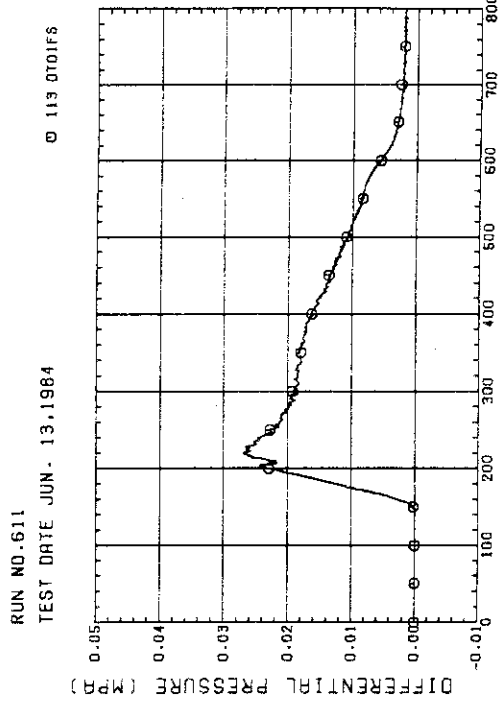

Fig. D-50 DIFFERENTIAL PRESSURE OF BROKEN COLD LEG - PV SIDE, DOWNCOMER - CONTAINMENT TANK-I

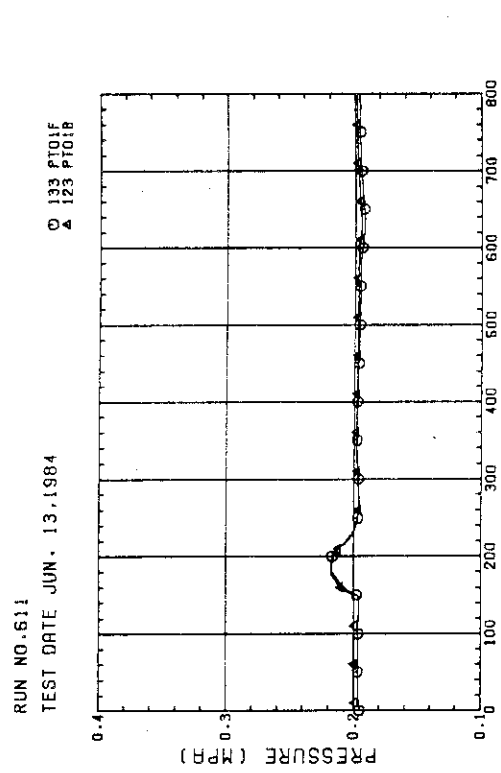

Fig. D-52 PRESSURE AT TOP OF CONTAINMENT TANK-I AND CONTAINMENT TANK-II (F-CONTAINMENT TANK-I, B-CONTAINMENT TANK-II)

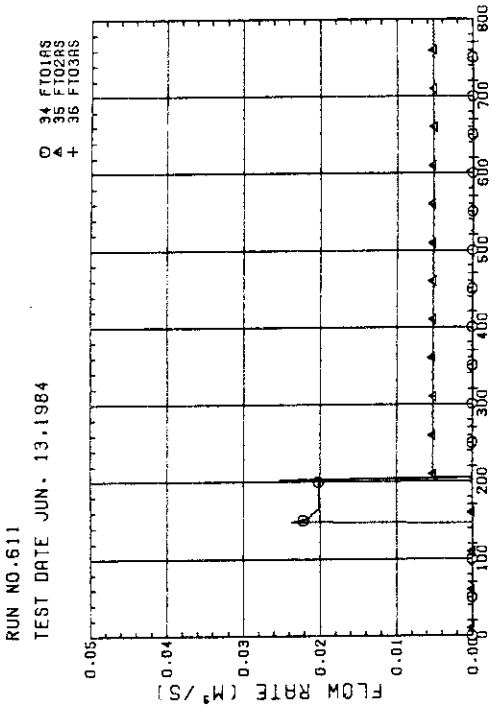

Fig. D-55 FLOW RATE OF ECC WATER (01-LOWER PLENUM, 02-INTACT COLD LEG, 03-BROKEN COLD LEG)

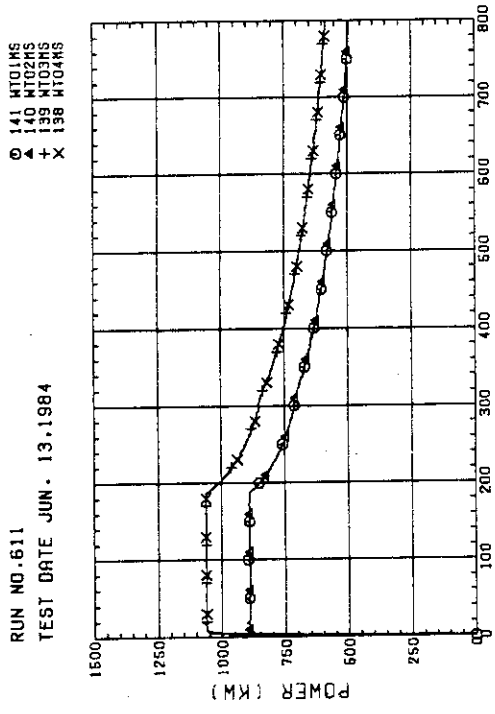

Fig. D-53 BUNDLE POWER (BUNDLE 1,2,3,4)

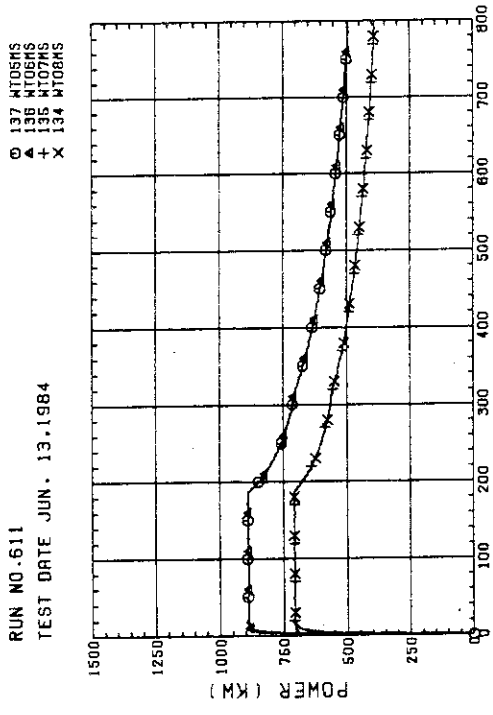

Fig. D-54 BUNDLE POWER (BUNDLE 5,6,7,8)

Appendix E Comparison between TRAC Post-test Analysis and Test Data of Test S2-SH1

List of figures in Appendix E

Fig. E-1 - E-40	Heater rod temperatures
Fig. E-41 - E-64	Water temperatures in core
Fig. E-65 - E-72	Steam temperature in core
Fig. E-73 - E-76	Vertical differential pressures across core lower half
Fig. E-77 - E-80	Vertical differential pressures across core upper half
Fig. E-81 - E-84	Vertical differential pressures across core full height
Fig. E-85 - E-102	Void fractions in core
Fig. E-103	Liquid level in core baffle
Fig. E-104 - E-111	Liquid levels in upper plenum
Fig. E-112	Liquid level in lower plenum
Fig. E-113 - E-116	Pressures in pressure vessel
Fig. E-117	Liquid level in downcomer
Fig. E-118 - E-121	Differential pressures in primary loops
Fig. E-122 - E-125	Mass flow rates in primary loops
Fig. E-126 - E-127	Pressures in containment tanks
Fig. E-128	Liquid level in S/W separator
Fig. E-129 - E-133	Horizontal differential pressures in core

TRAC-PF1 post-test analysis results obtained by the Los Alamos National Laboratory (LANL) based on the 2D/3D Agreement are compared with the test results of Test S2-SH1. For the comparison plots in this Appendix, the TRAC results are identified by circle symbols and the SCTF results by triangular symbols. Comments on the comparison results are presented as follows :

(1) Heater rod temperature (Figs. E-1 - E-40)

The heater rod temperatures predicted by TRAC qualitatively agree with the SCTF results except at the upper part of the core. TRAC overpredicts the turnaround temperature at the lower half of the core and

at the top of the core except in Bundle 6 while underpredicts at elevations from 3622 to 4907 mm from the bottom of pressure vessel (1905 to 3190 mm from the bottom of heated part) in all bundles. The calculated quench time is longer than the test data at almost all elevations. The top quench sometimes observed in the test results is not predicted by TRAC. The beginning of heat up is delayed by about 20 to 40 s in Bundle 6 probably due to an error in the input data.

(2) Water temperatures in core (Figs. E-41 - E-64)

The water temperatures in the core predicted by TRAC exhibit the saturation temperature, while the measured temperatures are affected by the superheated steam temperatures except at the bottom of heated part. At the later period, the measured water temperatures wall agree with the calculated temperatures.

(3) Steam temperatures in core (Fig. E-65 - E-72)

The measured steam temperature sometimes shows much lower temperature than the calculated temperature as shown in Figs. E-66 and E-68 and the measured temperature decreases to the saturation temperature at much earlier time than the calculated temperature. These are due to the fact that the superheated steam probes used for the steam temperature measurement might be wetted by water droplets. Superheat data before the quench of the probes show almost reasonable agreement with the TRAC calculattion as shown in Figs. E-65, E-67 and E-70.

(4) Vertical differential pressures in core (Figs. E-73 - E-84)

TRAC overpredicts the differential pressure across the lower half of the core and underpredicts the differential pressure across the upper half of the core. The differential pressure across the core full height is slightly overpredicted by TRAC except during the initial 60 s after the beginning of bottom reflood. During that period, TRAC underpredicts the differential pressure. In general, the calculated vertical differential pressures in the core show oscillatory behavior, whereas no significant oscillations are observed in the SCTF results.

(5) Void fractions in core (Figs. E-85 - E-102)

The calculated void fraction remains almost unity before the occurrence of quench and then decreases repidly, while the measured void fraction gradually decreases with time from the beginning of reflood.

(6) Liquid level in core baffle (Fig. E-103)

The initial increasing of the liquid level in the core baffle is well predicted by TRAC. Thereafter, TRAC slightly overpredicts the

liquid level.

(7) Liquid levels in upper plenum (Figs. E-104 - E-111)

TRAC underpredicts the liquid level in the upper plenum above all bundles. The measured liquid levels in the upper plenum begin to increase just after the beginning of reflood, while the predicted values indicate no increases until about 280 s after the beginning of reflood. In addition, the measured liquid level in the upper plenum is higher at the Bundle 8 side than at the Bundle 1 side at the later period. However, TRAC cannot predict the nonuniform water accumulation in the upper plenum.

(8) Liquid level in lower plenum (Fig. E-112)

The initial liquid level in the TRAC calculation is lower than the measured initial value. There may be an input error for the initial liquid level in the caculation.

(9) Pressures in presure vessel (Fig. E-113 - E-116)

TRAC slightly underestimates the pressure in the core, the upper plenum, the lower plenum and the downcomer during the initial 60 s after the beginning of reflood. After that time, the predicted pressures well agree with the test data.

(10) Liquid level in downcomer (Fig. E-117)

The initial liquid level in the TRAC calculation is shifted lower. If the shift of the initial liquid level is corrected, the calculated result well agrees with the test data.

(11) Differential pressures in primary loop (Fig. E-118 - E-121)

The differential pressure between the upper plenum and the steam/water separator predicted by TRAC is much smaller than the SCTF result especially at the later period. The differential pressure between the steam/water separator and the downcomer is also underpredicted by TRAC until 600s. The differential pressure between the downcomer and the containment tank-I is well predicted by TRAC. However, the calculated differential pressure between the steam/water separator and the containment tank-II is much lower than the test result.

(12) Mass flow rate in primary loops (Fig. E-122 - E-125)

The mass flow rates in the hot leg and the intact cold leg were not measured correctly and the comparison has no meaning in Figs. E-122 and E-123. The measured mass flow rate in the steam/water separator side broken cold leg well agrees with the TRAC result if correcting the initial shifting in the measured value. TRAC overpredicts the mass flow

rate in the pressure vessel side broken cold leg.

(13) Pressures in containment tanks (Figs. E-126 and E-127)

Since the measured pressure transients in the containment tank-I were used in the TRAC analysis as the boundary condition, the TRAC and SCTF results agree well with each other.

(14) Liquid level in steam/water separator (Fig. E-128)

TRAC underpredicts the increasing rate of the liquid level in the steam/water separator.

(15) Horizontal differential pressures in core (Figs. E-129 - E-133)

The average values of the horizontal differential pressures calculated by TRAC are almost zero while the measured horizontal differential pressures become negative at the later period. Therefore TRAC cannot correctly predict the two-dimensional flow behavior in the core.

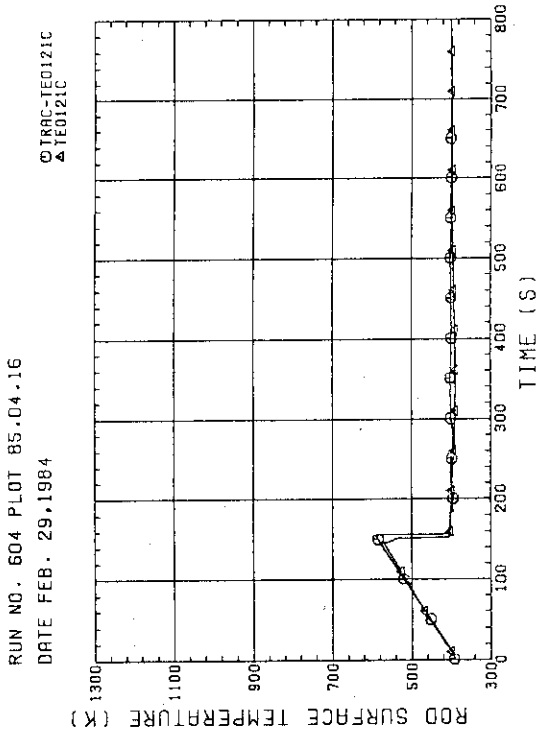

Fig. E-1 HEATER ROD TEMPERATURE (BUNDLE 2 H=1827MM)

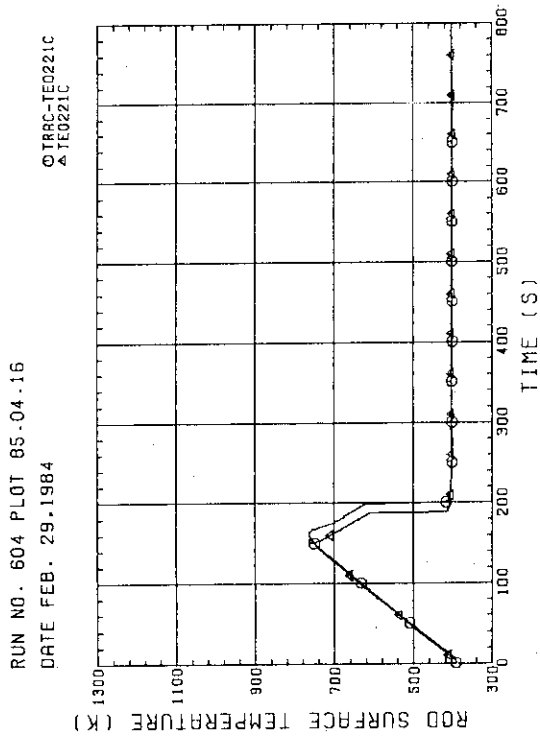

Fig. E-2 HEATER ROD TEMPERATURE (BUNDLE 2 H=2237MM)

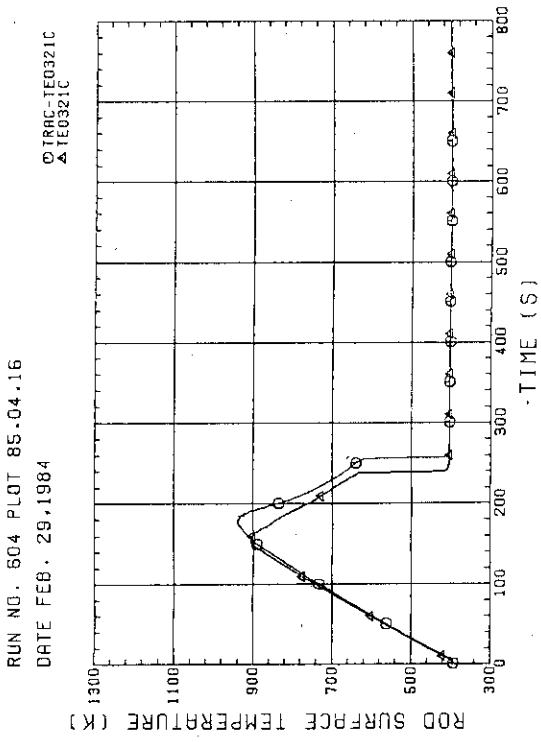

Fig. E-3 HEATER ROD TEMPERATURE (BUNDLE 2 H=2667MM)

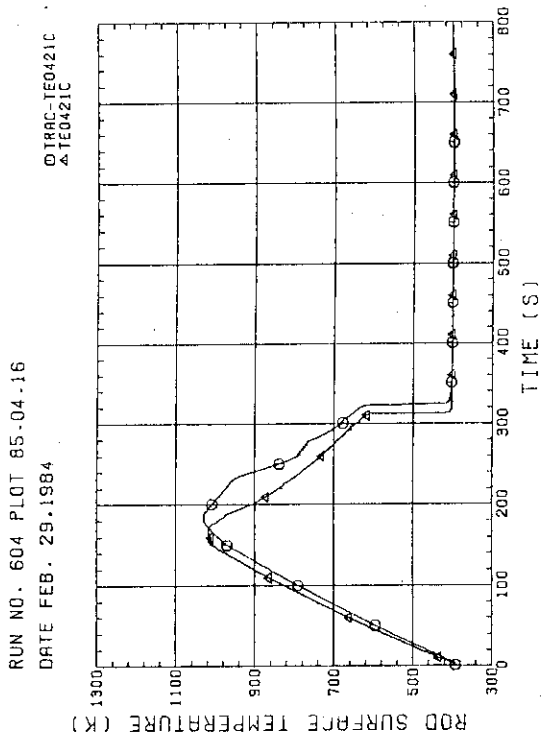

Fig. E-4 HEATER ROD TEMPERATURE (BUNDLE 2 H=3097MM)

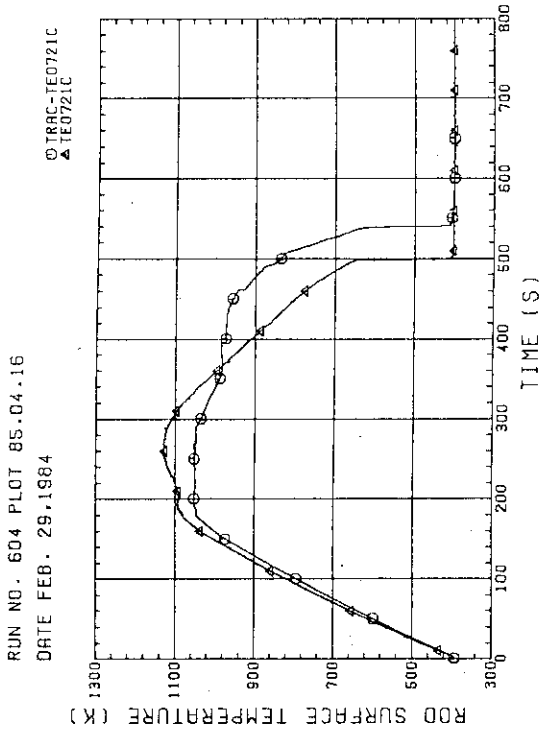

Fig. E-7 HEATER ROD TEMPERATURE (BUNDLE 2 H=4047MM)

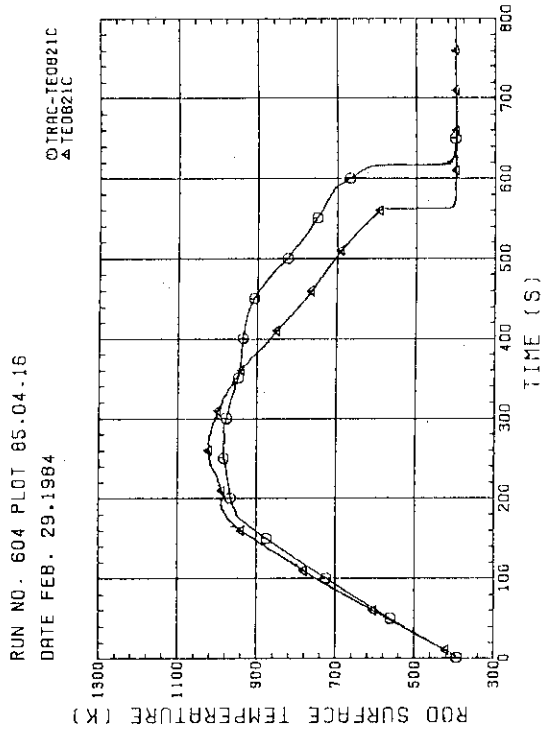

Fig. E-8 HEATER ROD TEMPERATURE (BUNDLE 2 H=4477MM)

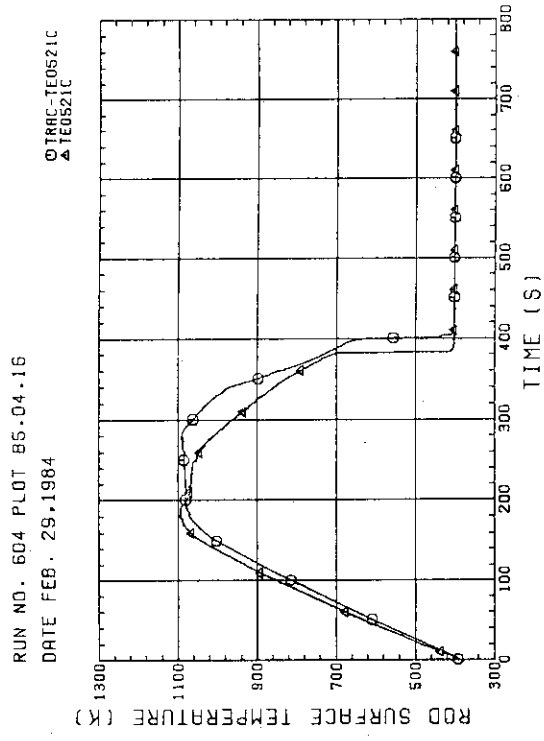

Fig. E-5 HEATER ROD TEMPERATURE (BUNDLE 2 H=3452MM)

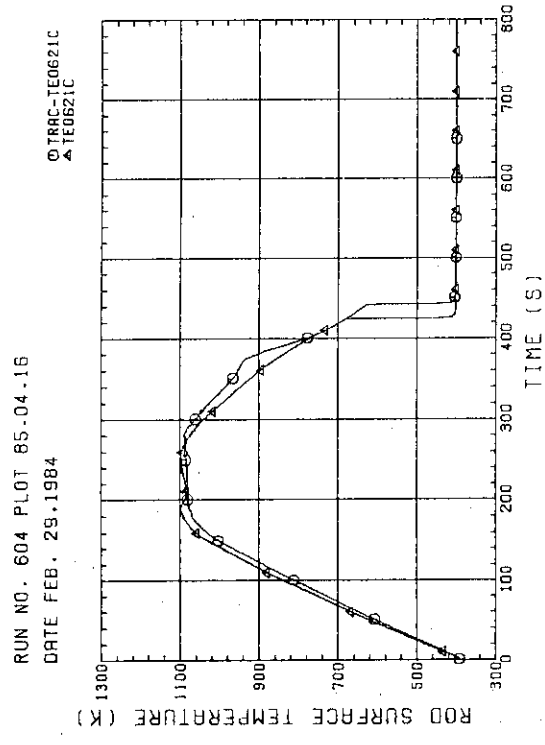

Fig. E-6 HEATER ROD TEMPERATURE (BUNDLE 2 H=3622MM)

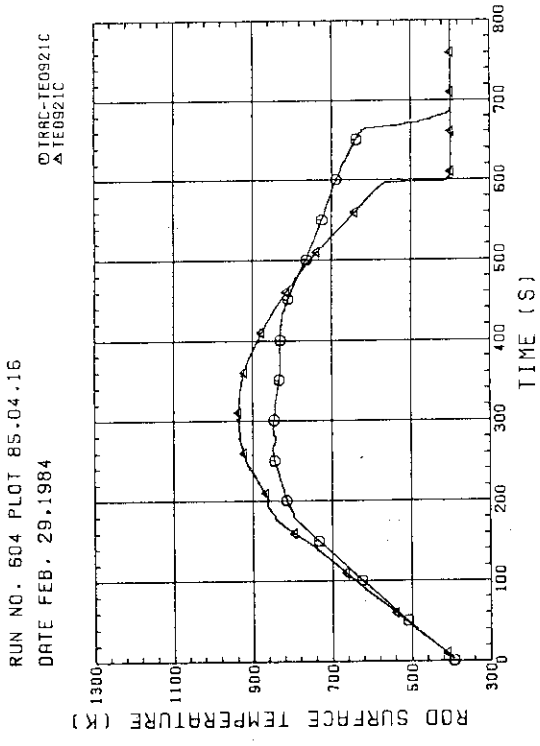

Fig. E-9 HEATER ROD TEMPERATURE (BUNDLE 2 H=4907MM)

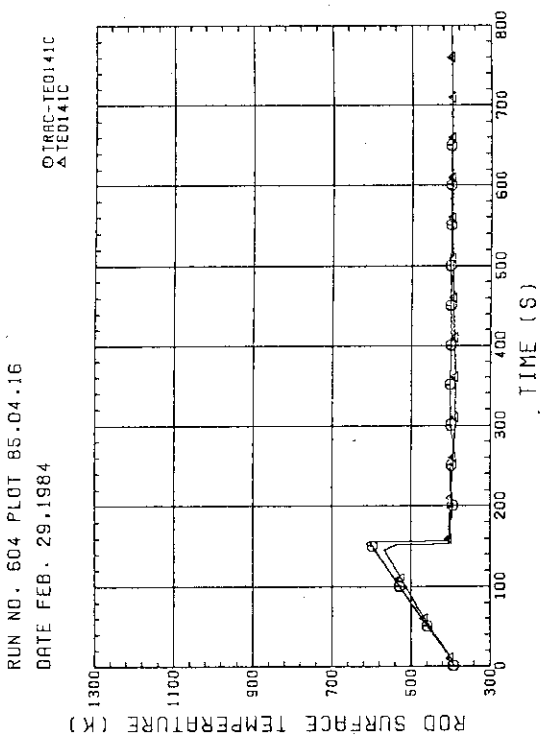

Fig. E-11 HEATER ROD TEMPERATURE (BUNDLE 4 H=1827MM)

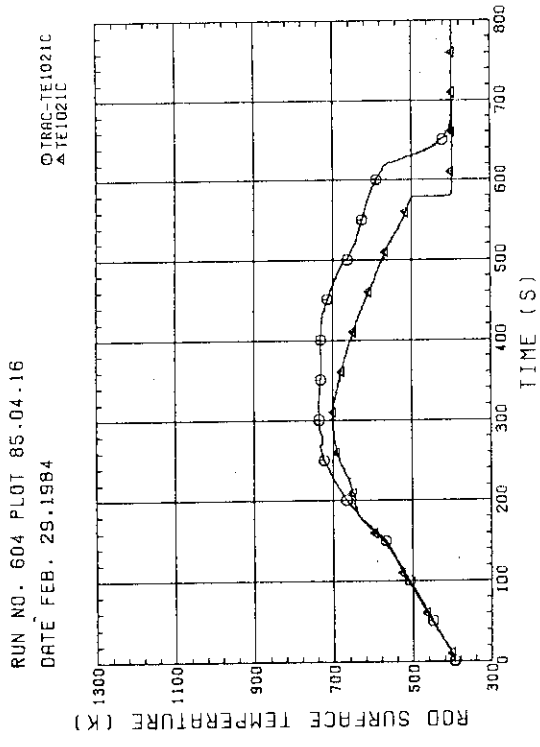

Fig. E-10 HEATER ROD TEMPERATURE (BUNDLE 2 H=5337MM)

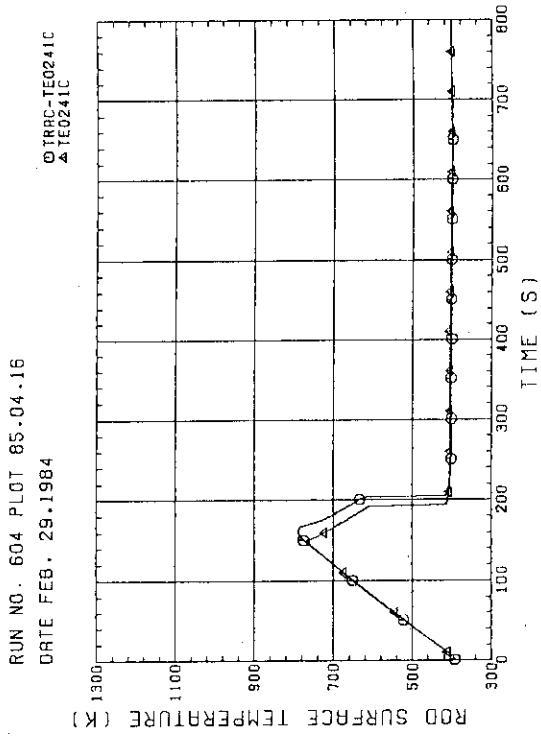

Fig. E-12 HEATER ROD TEMPERATURE (BUNDLE 4 H=2237MM)

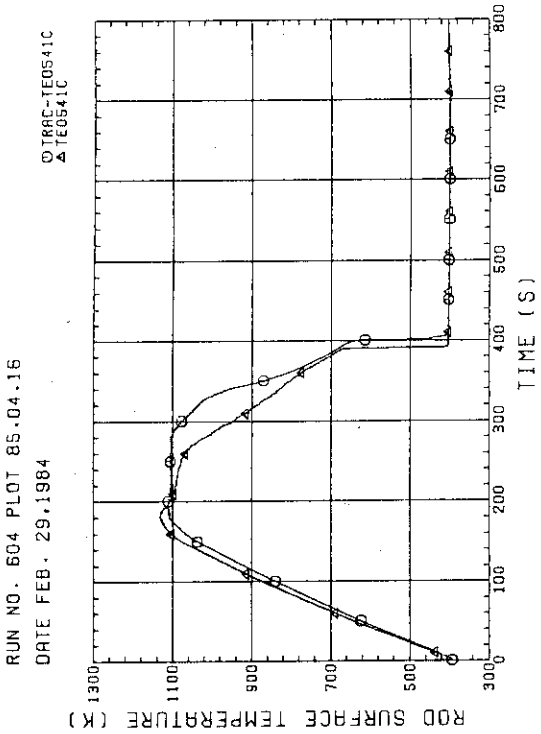

Fig. E-15 HEATER ROD TEMPERATURE (BUNDLE 4 H=3452MM)

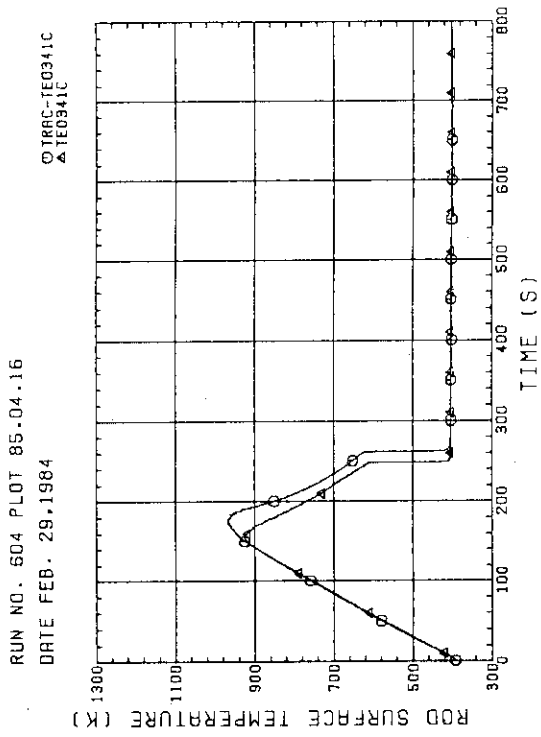

Fig. E-13 HEATER ROD TEMPERATURE (BUNDLE 4 H=2667MM)

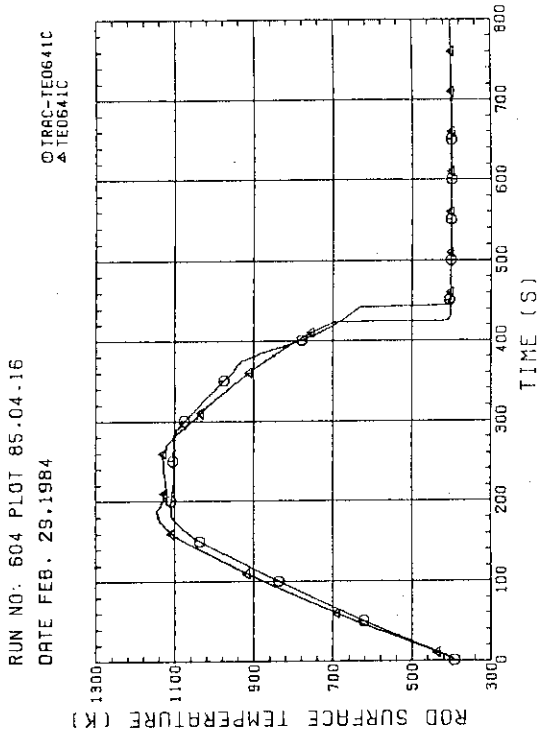

Fig. E-16 HEATER ROD TEMPERATURE (BUNDLE 4 H=3622MM)

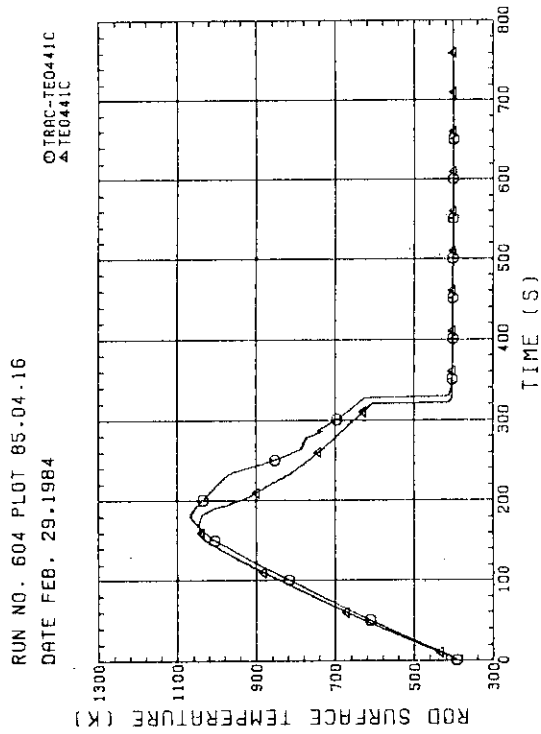

Fig. E-14 HEATER ROD TEMPERATURE (BUNDLE 4 H=3097MM)

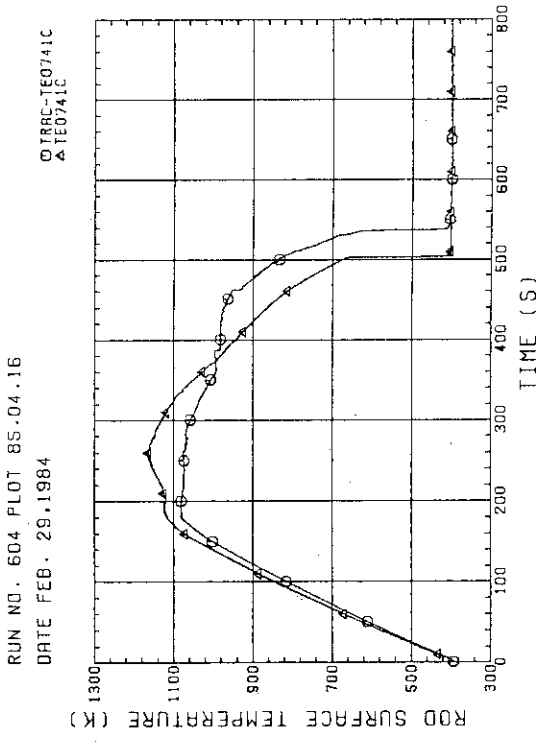

Fig. E-17 HEATER ROD TEMPERATURE (BUNDLE 4 H=4047MM)

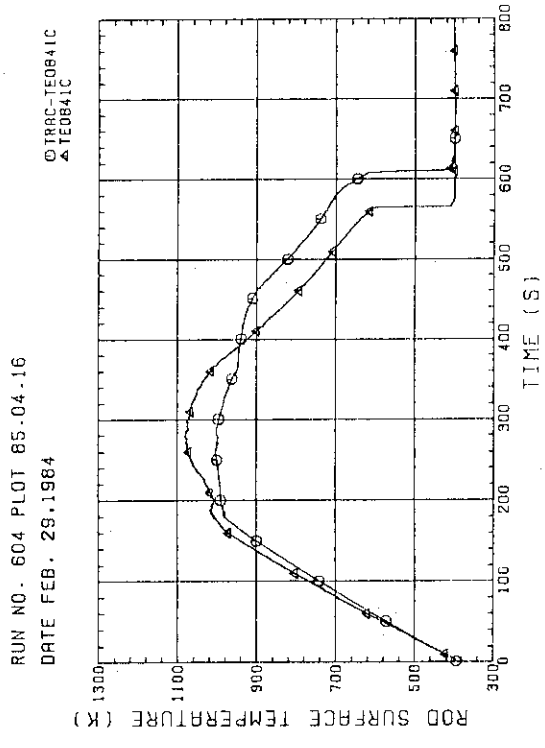

Fig. E-18 HEATER ROD TEMPERATURE (BUNDLE 4 H=4477MM)

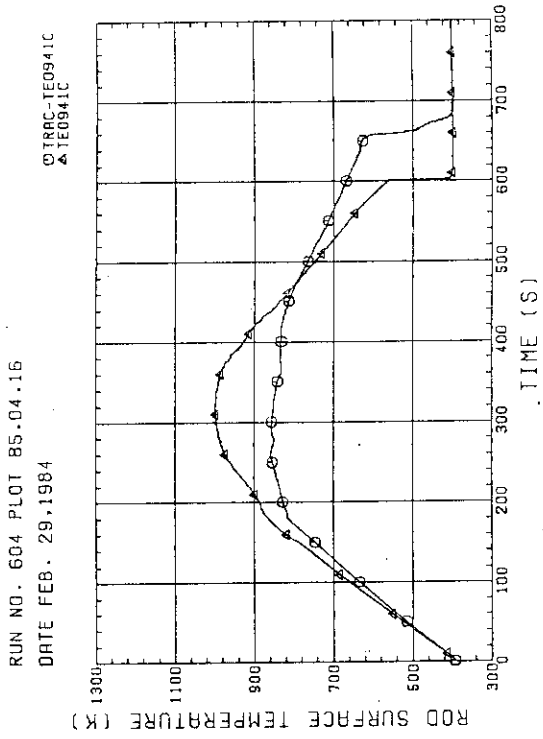

Fig. E-19 HEATER ROD TEMPERATURE (BUNDLE 4 H=4907MM)

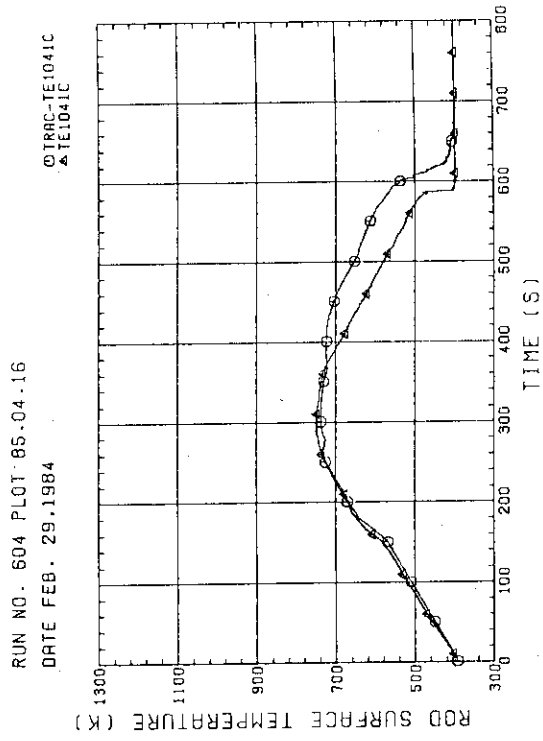

Fig. E-20 HEATER ROD TEMPERATURE (BUNDLE 4 H=5337MM)

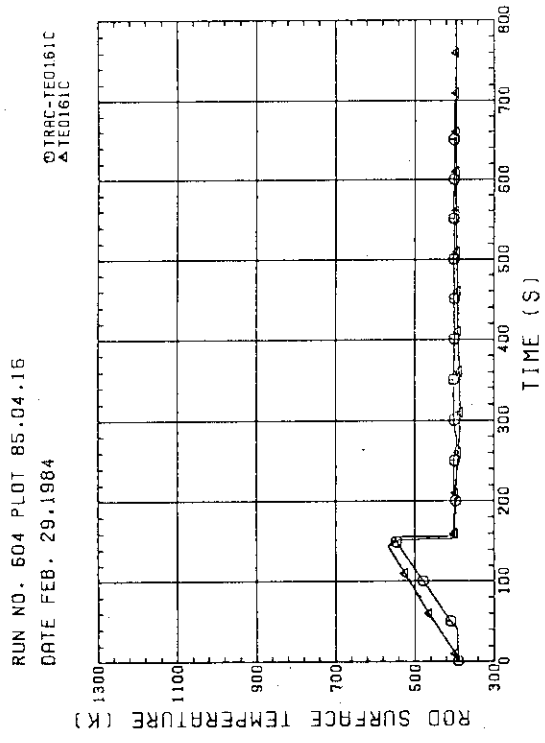

Fig. E-21 HEATER ROD TEMPERATURE (BUNDLE 6 H=1827MM)

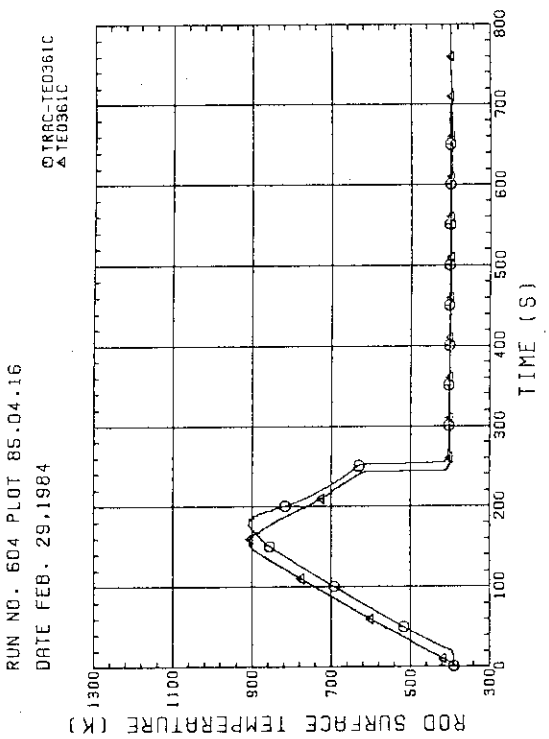

Fig. E-23 HEATER ROD TEMPERATURE (BUNDLE 6 H=2607MM)

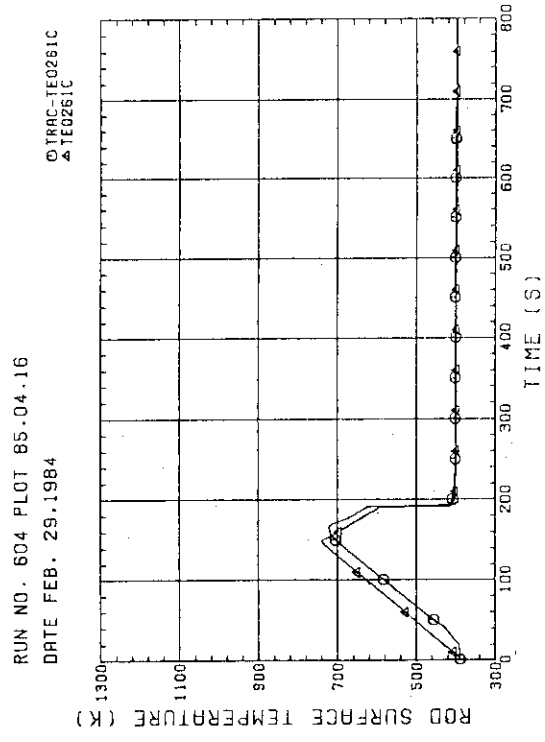

Fig. E-22 HEATER ROD TEMPERATURE (BUNDLE 6 H=2237MM)

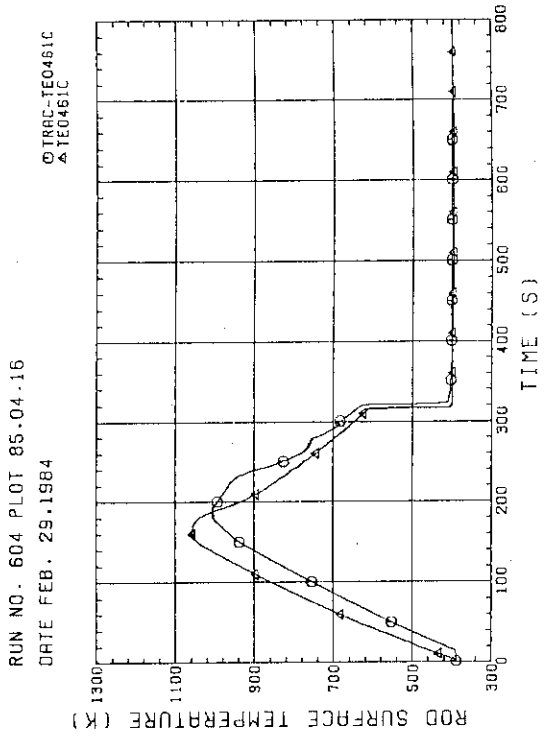

Fig. E-24 HEATER ROD TEMPERATURE (BUNDLE 6 H=3097MM)

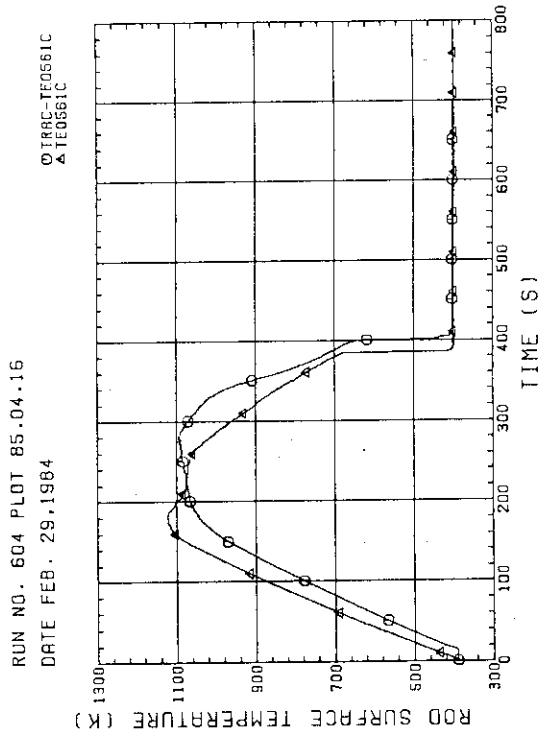

Fig. E-25 HEATER ROD TEMPERATURE (BUNDLE 6 H=3452MM)

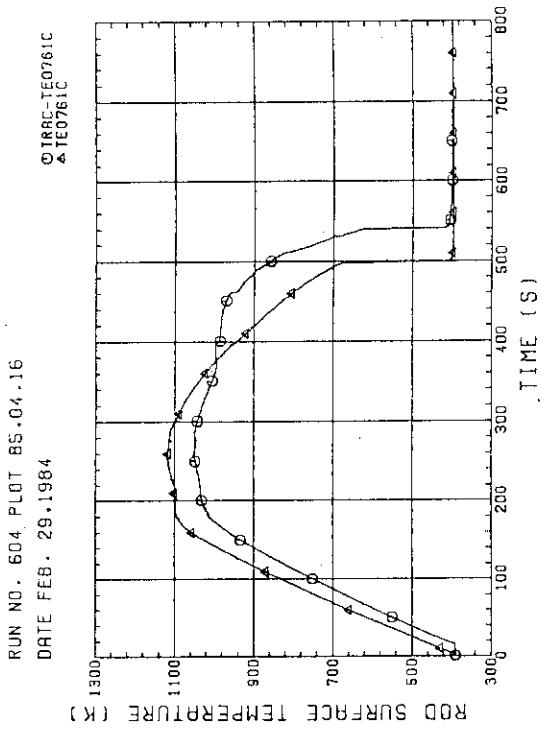

Fig. E-27 HEATER ROD TEMPERATURE (BUNDLE 6 H=4047MM)

Fig. E-26 HEATER ROD TEMPERATURE (BUNDLE 6 H=3622MM)

Fig. E-28 HEATER ROD TEMPERATURE (BUNDLE 6 H=4477MM)

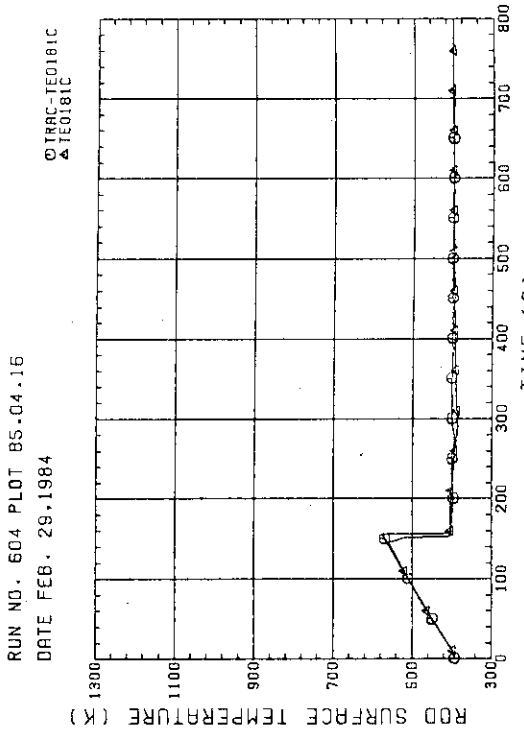

Fig. E-31 HEATER ROD TEMPERATURE (BUNDLE 8 H=1827MM)

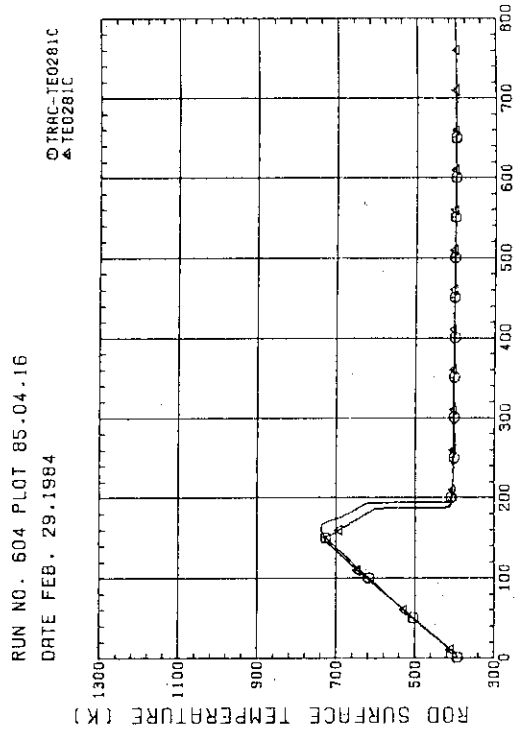

Fig. E-32 HEATER ROD TEMPERATURE (BUNDLE 8 H=2297MM)

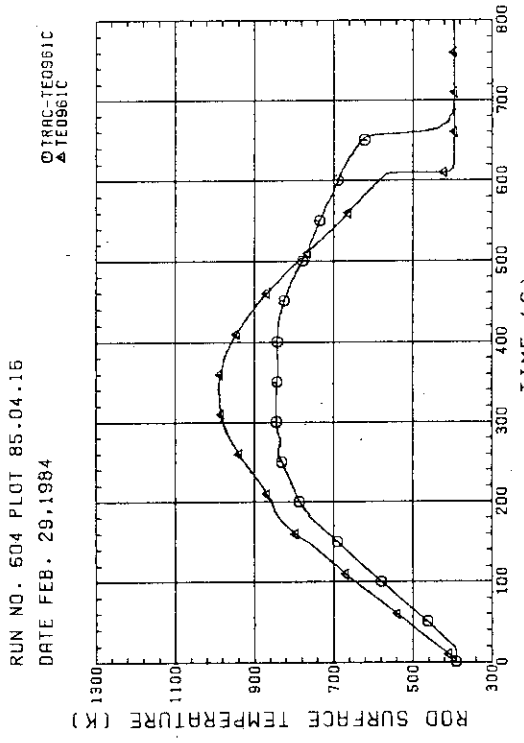

Fig. E-29 HEATER ROD TEMPERATURE (BUNDLE 6 H=4907MM)

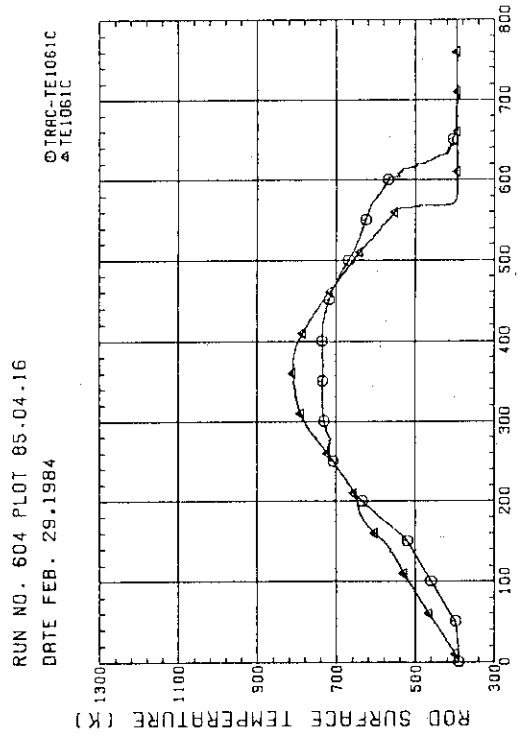

Fig. E-30 HEATER ROD TEMPERATURE (BUNDLE 6 H=5337MM)

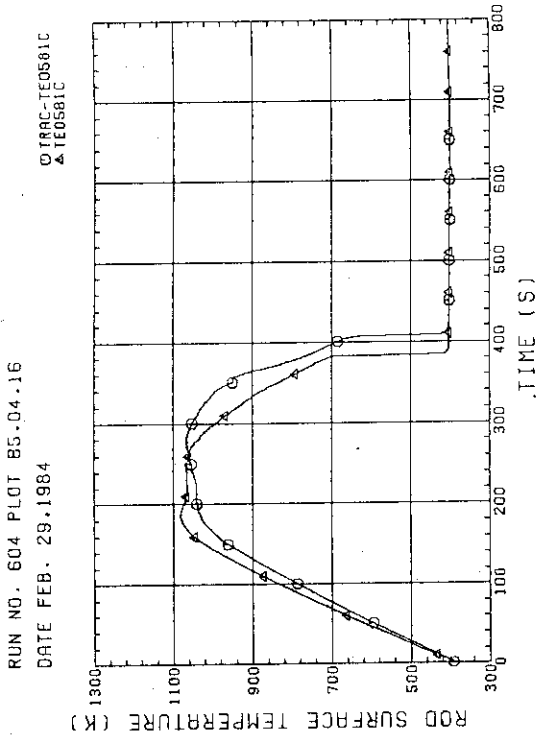

Fig. E-35 HEATER ROD TEMPERATURE (BUNDLE 8 H=3452MM)

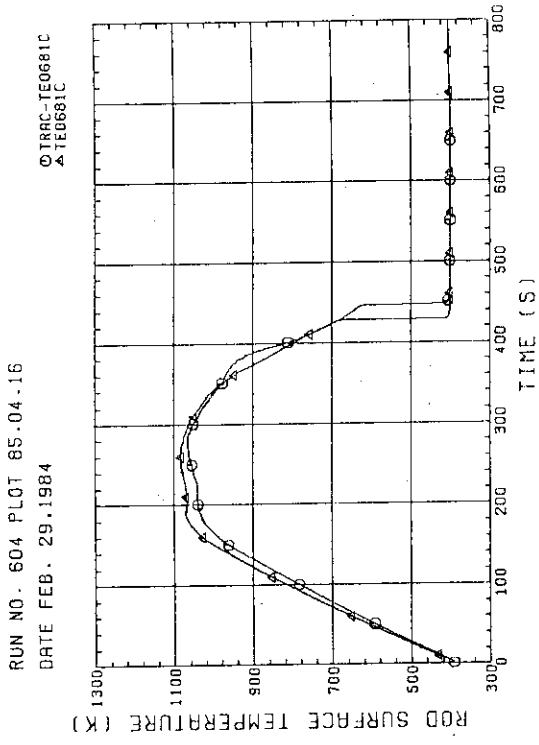

Fig. E-36 HEATER ROD TEMPERATURE (BUNDLE 8 H=3622MM)

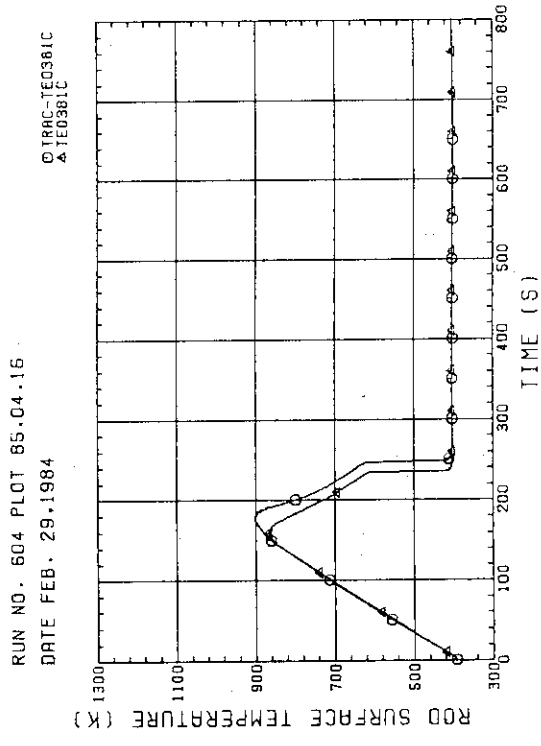

Fig. E-33 HEATER ROD TEMPERATURE (BUNDLE 8 H=2667MM)

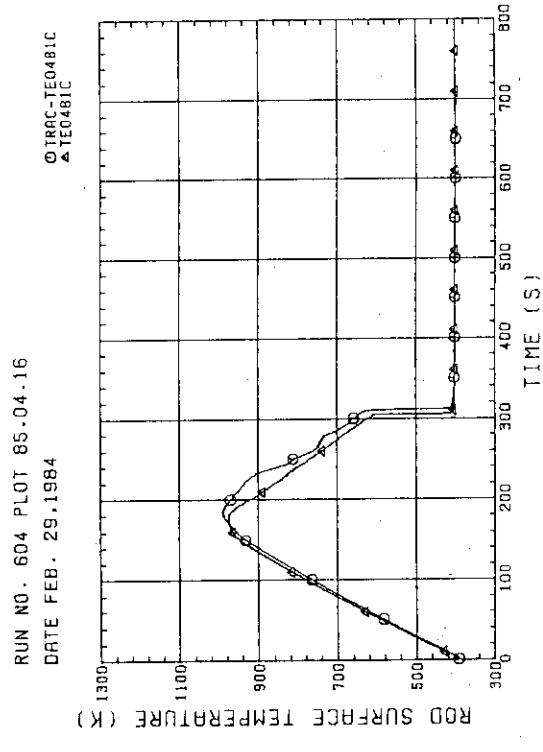

Fig. E-34 HEATER ROD TEMPERATURE (BUNDLE 8 H=3097MM)

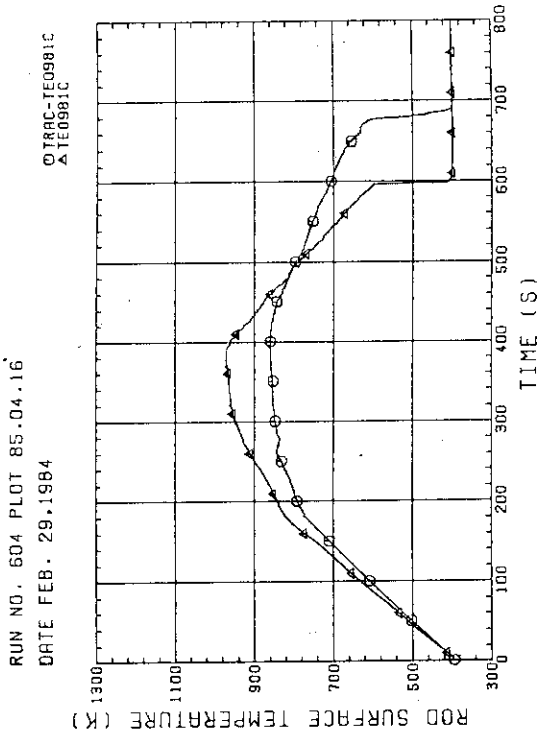

Fig. E-39 HEATER ROD TEMPERATURE (BUNDLE 8 H=4907MM)

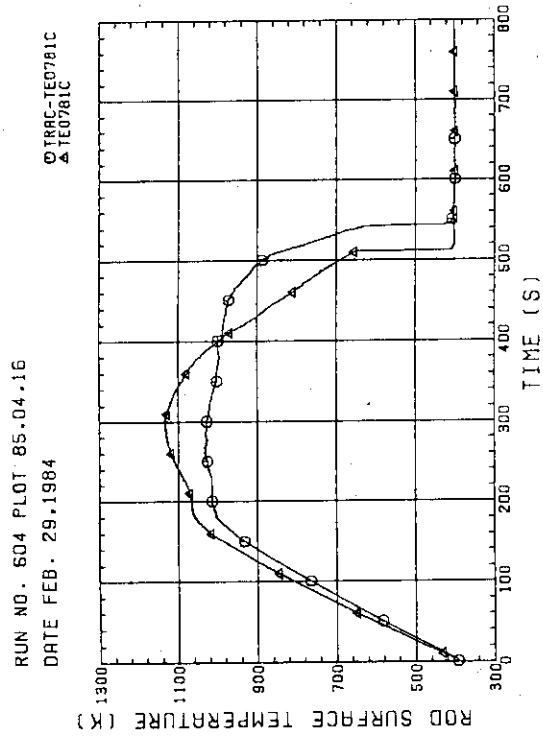

Fig. E-37 HEATER ROD TEMPERATURE (BUNDLE 8 H=4047MM)

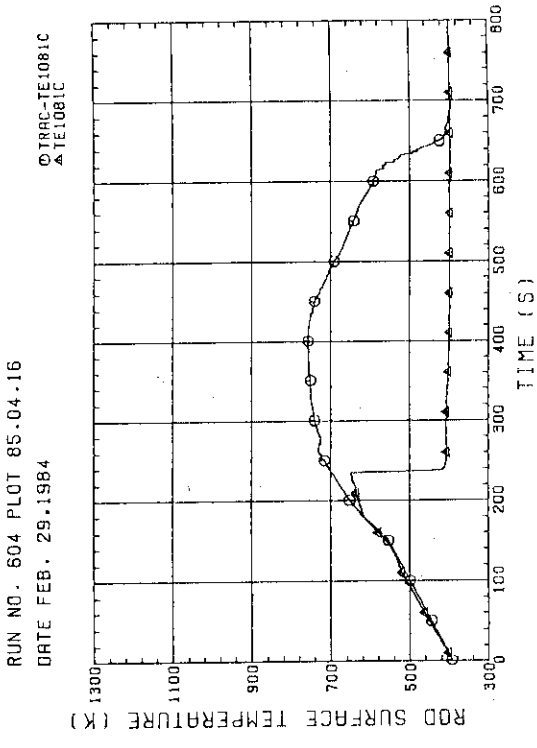

Fig. E-40 HEATER ROD TEMPERATURE (BUNDLE 8 H=5337MM)

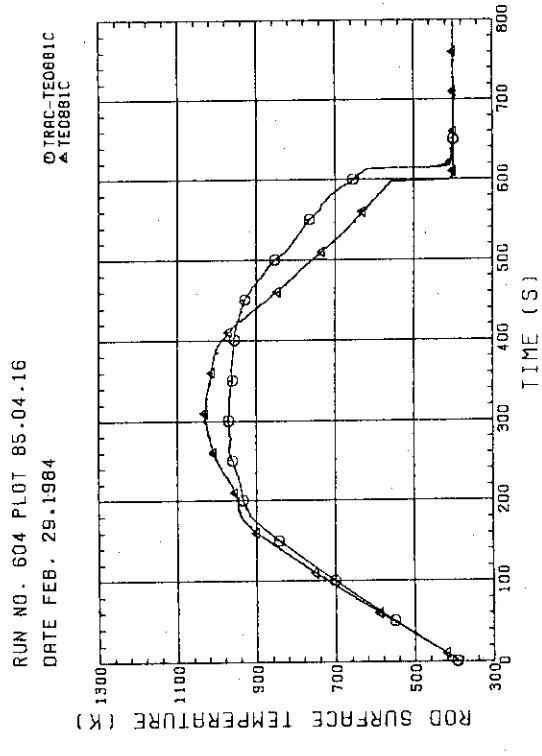

Fig. E-38 HEATER ROD TEMPERATURE (BUNDLE 8 H=4477MM)

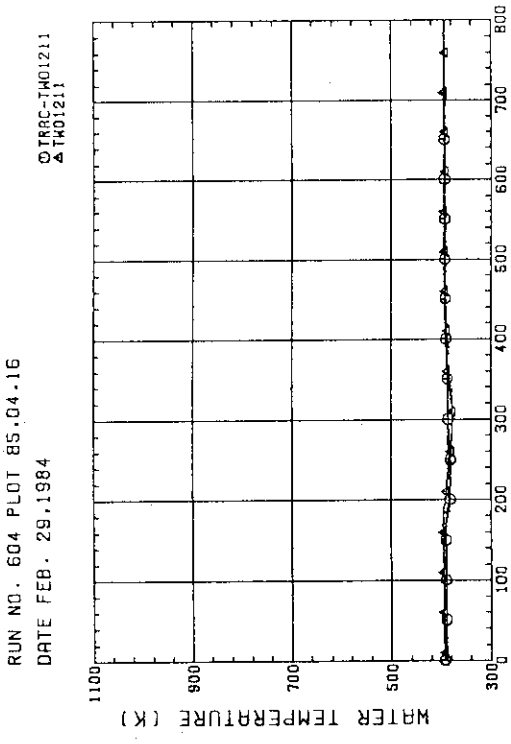

Fig. E-41 WATER TEMPERATURE (BUNDLE 2 H= 0MM)

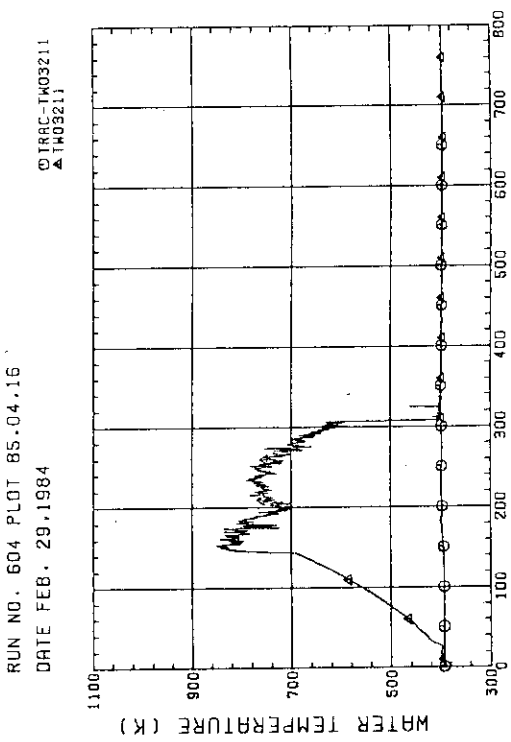

Fig. E-43 WATER TEMPERATURE (BUNDLE 2 H=1735MM)

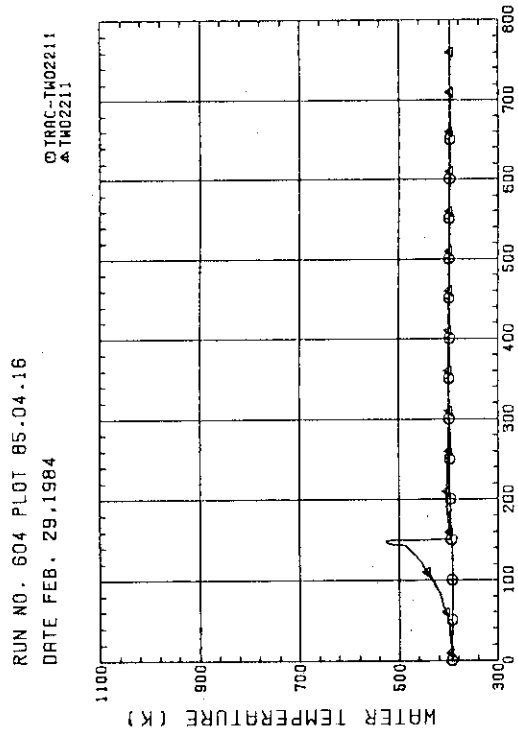

Fig. E-42 WATER TEMPERATURE (BUNDLE 2 H= 950MM)

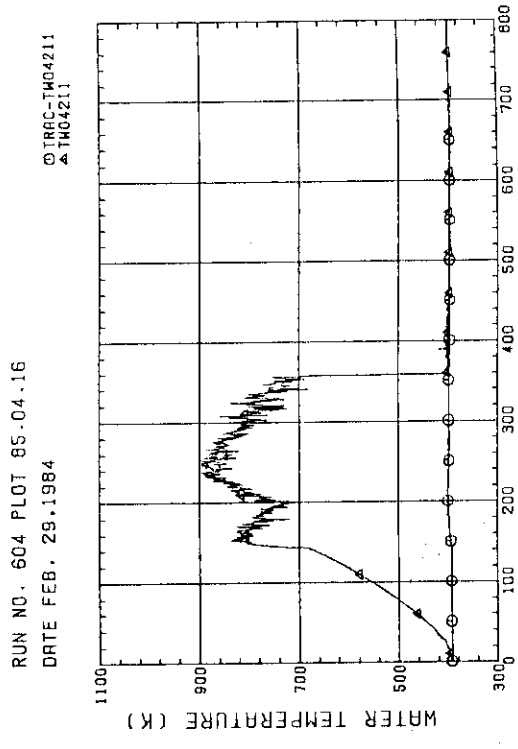

Fig. E-44 WATER TEMPERATURE (BUNDLE 2 H=1905MM)

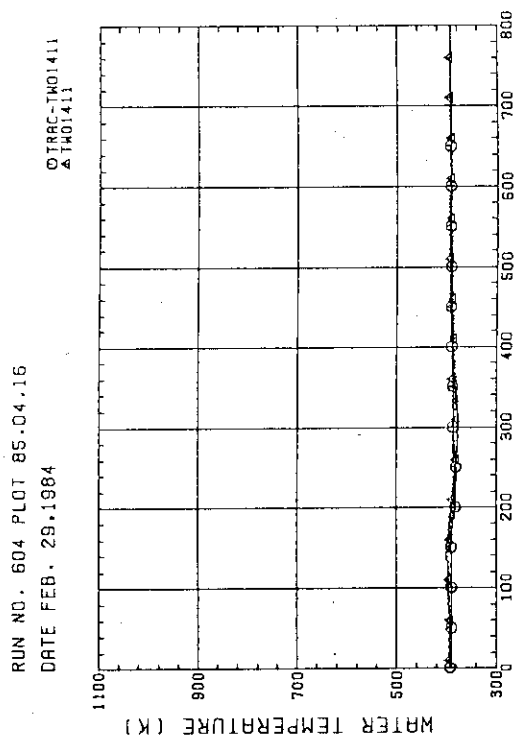

Fig. E-45 WATER TEMPERATURE (BUNDLE 2 H=2760MM)

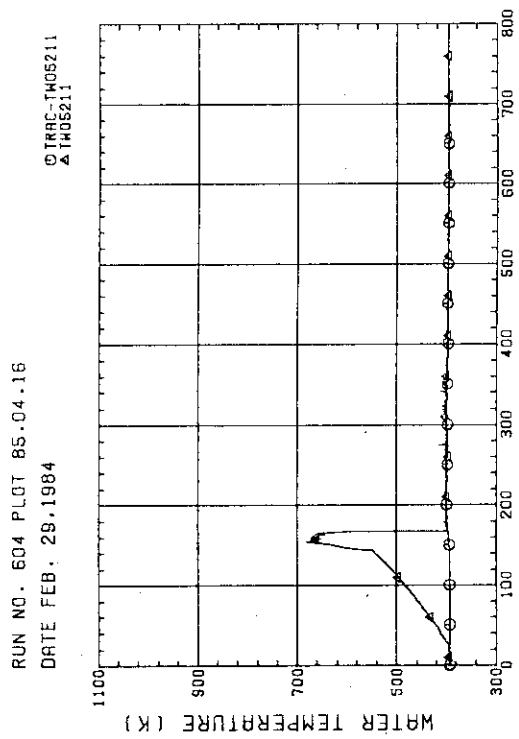

Fig. E-46 WATER TEMPERATURE (BUNDLE 2 H=3660MM)

Fig. E-47 WATER TEMPERATURE (BUNDLE 4 H= 0MM)

Fig. E-48 WATER TEMPERATURE (BUNDLE 4 H= 950MM)

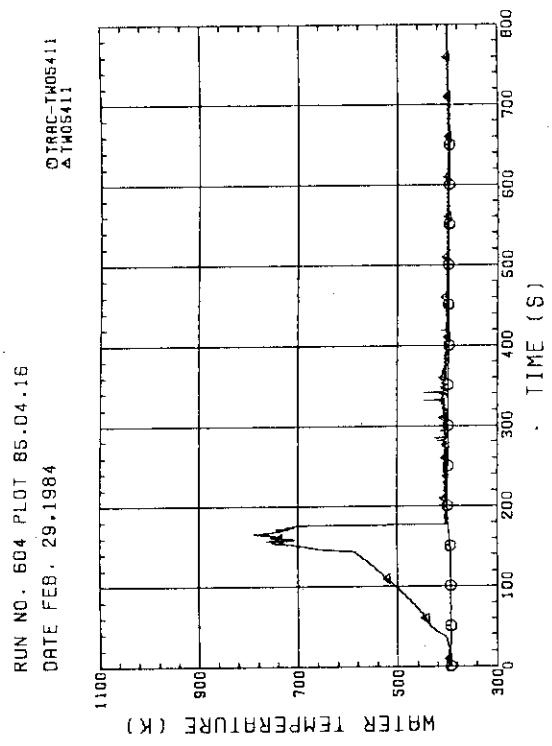

Fig. E-49 WATER TEMPERATURE (BUNDLE 4 H=1735MM)

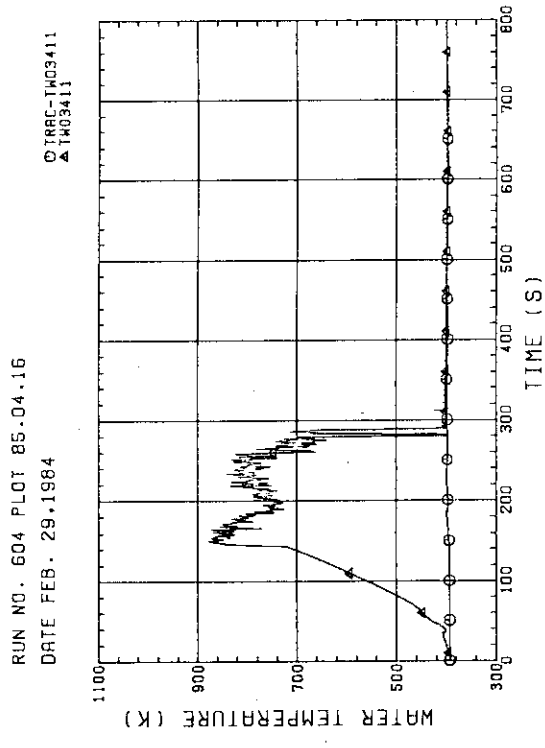

Fig. E-50 WATER TEMPERATURE (BUNDLE 4 H=1905MM)

Fig. E-51 WATER TEMPERATURE (BUNDLE 4 H=2760MM)

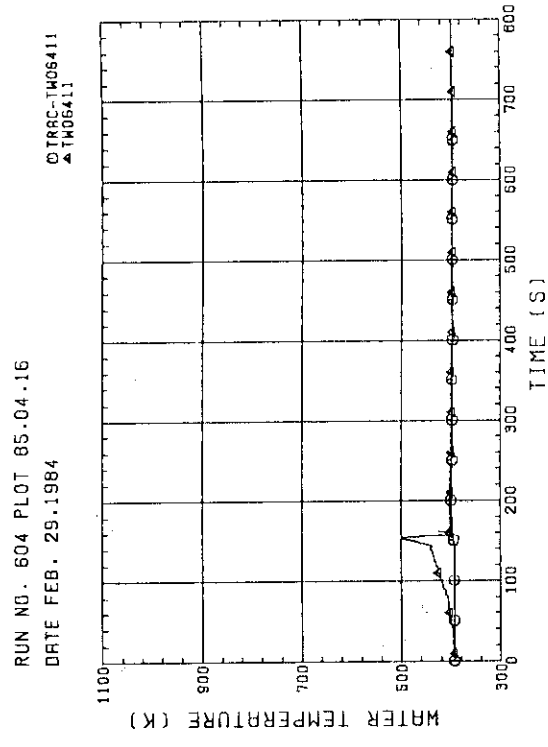

Fig. E-52 WATER TEMPERATURE (BUNDLE 4 H=3660MM)

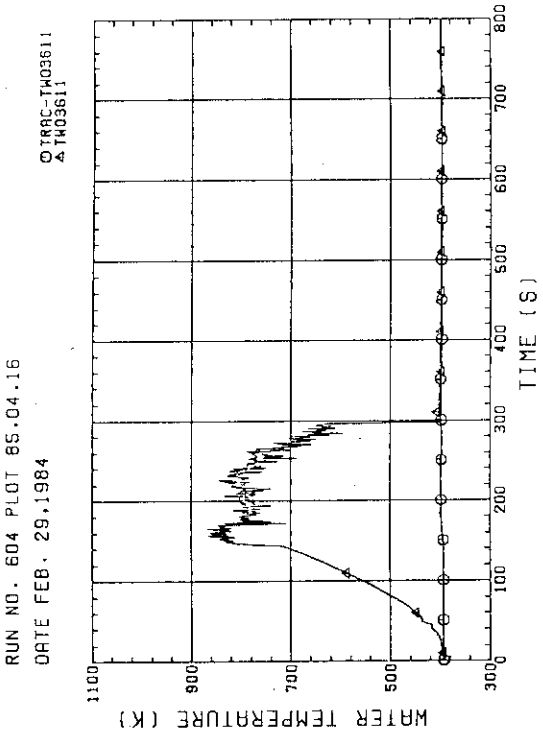

Fig. E-55 WATER TEMPERATURE (BUNDLE 6 H=1735MM)

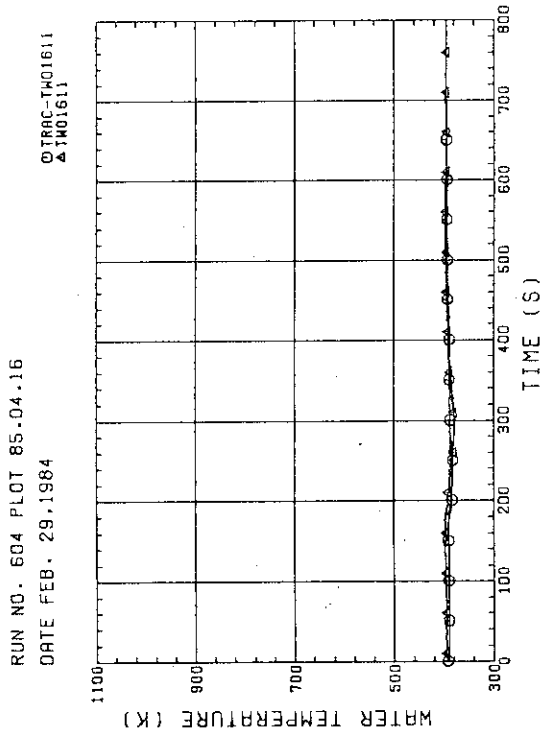

Fig. E-53 WATER TEMPERATURE (BUNDLE 6 H= 0MM)

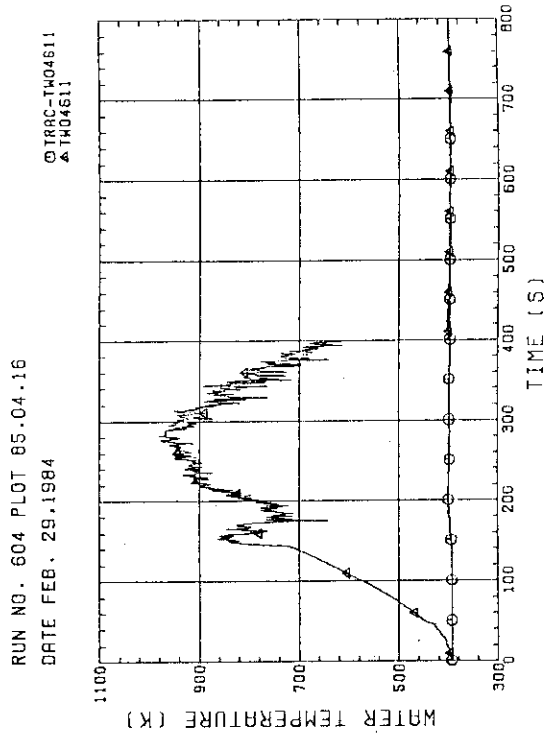

Fig. E-56 WATER TEMPERATURE (BUNDLE 6 H=1905MM)

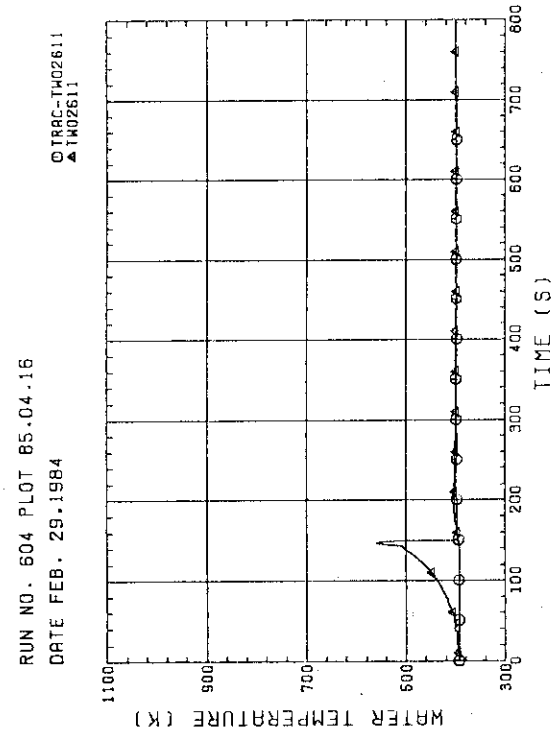

Fig. E-54 WATER TEMPERATURE (BUNDLE 6 H= 950MM)

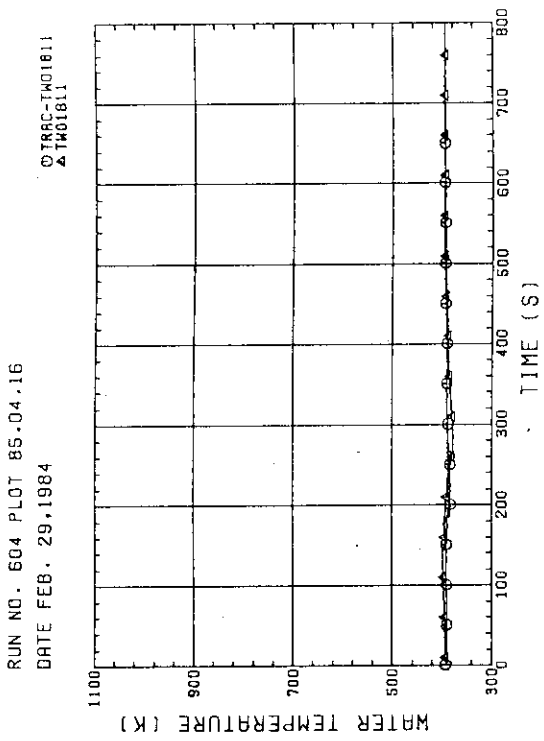

Fig. E-57 WATER TEMPERATURE (BUNDLE 6 H=2760MM)

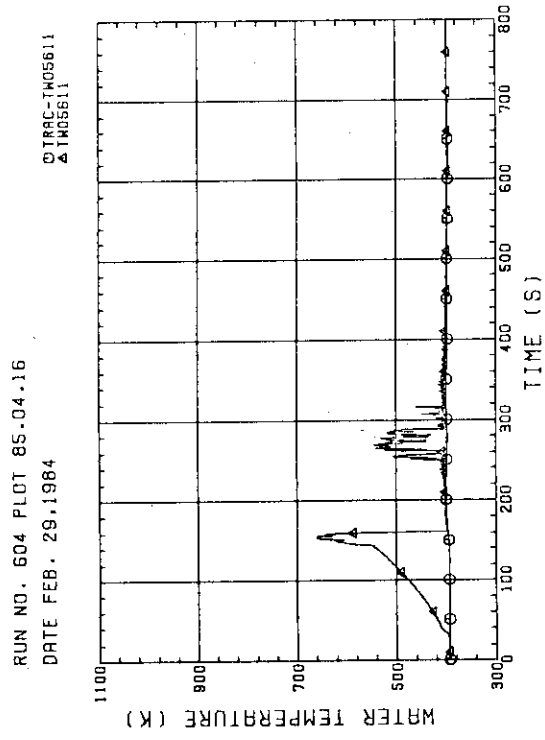

Fig. E-58 WATER TEMPERATURE (BUNDLE 6 H=3660MM)

Fig. E-59 WATER TEMPERATURE (BUNDLE 8 H= 0MM)

Fig. E-60 WATER TEMPERATURE (BUNDLE 8 H= 950MM)

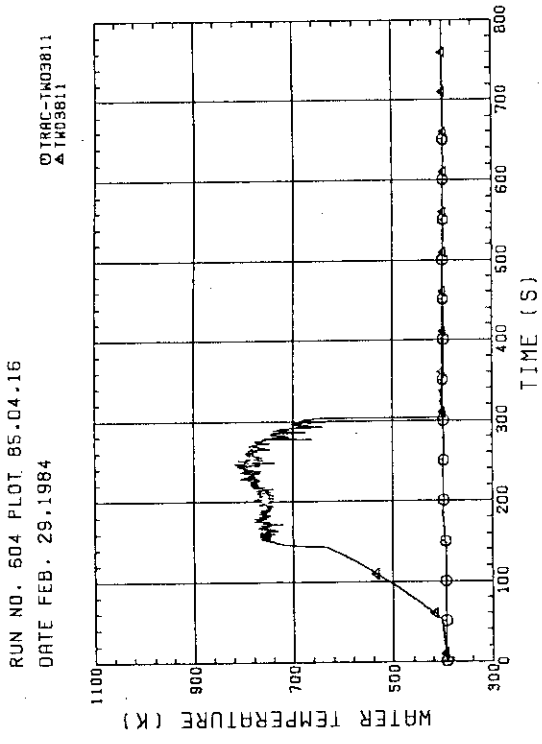

Fig. E-61 WATER TEMPERATURE (BUNDLE 8 H=1735MM)

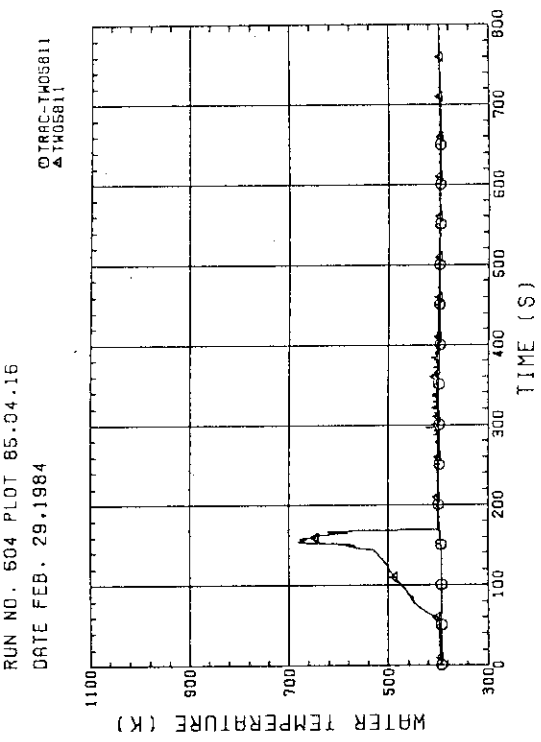

Fig. E-63 WATER TEMPERATURE (BUNDLE 8 H=2760MM)

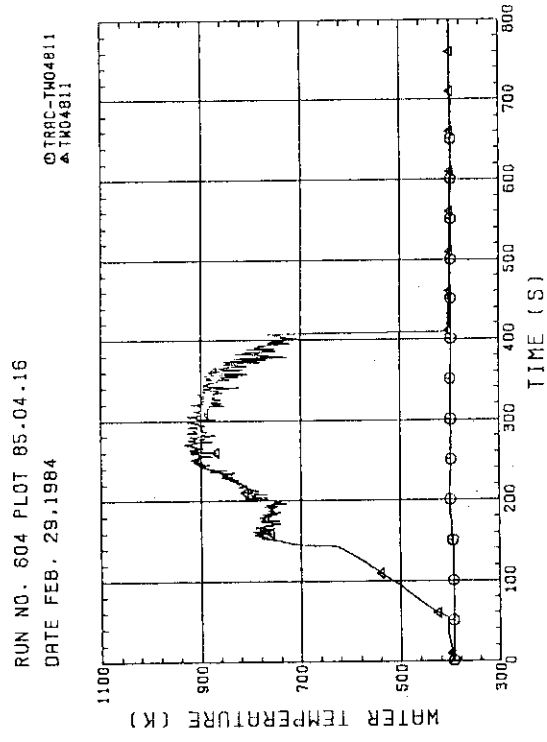

Fig. E-62 WATER TEMPERATURE (BUNDLE 8 H=1905MM)

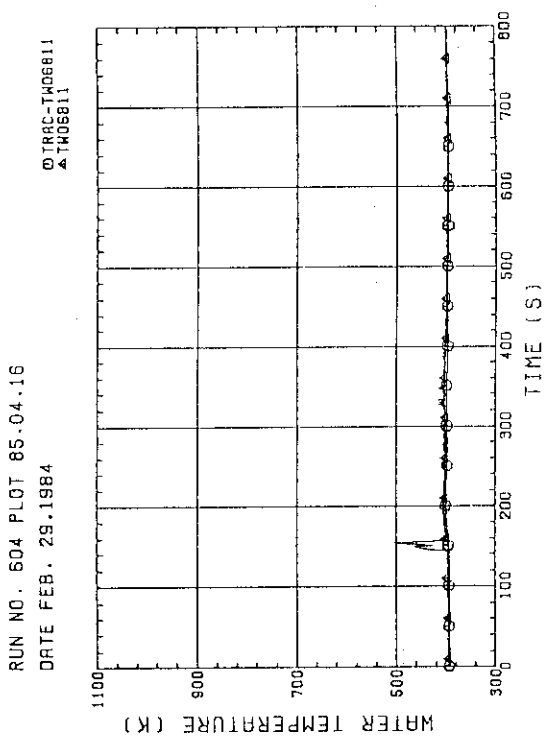

Fig. E-64 WATER TEMPERATURE (BUNDLE 8 H=3660MM)

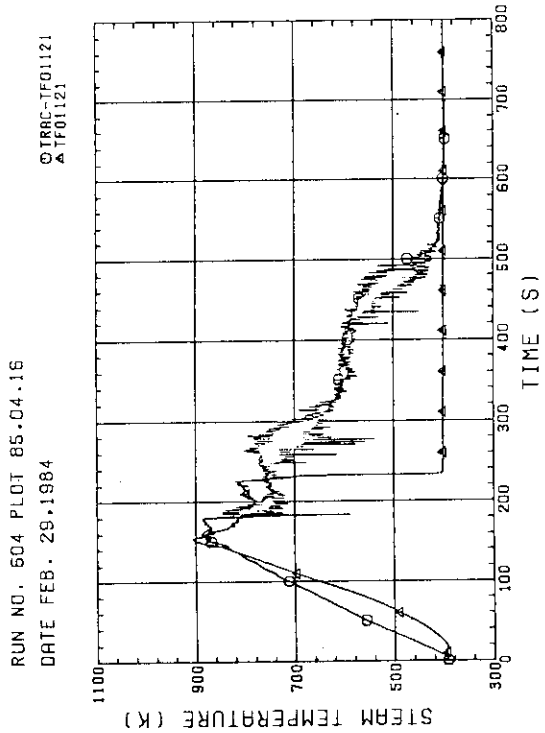

Fig. E-65 STEAM TEMPERATURE (BUNDLE 1 H=1915MM)

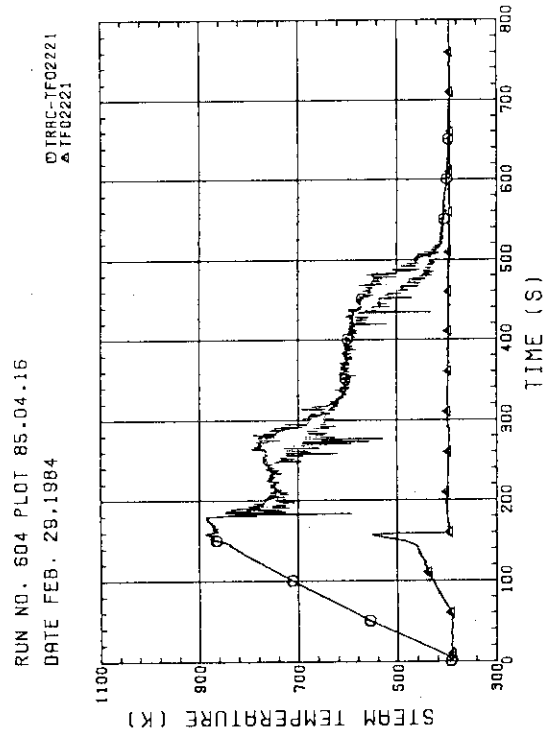

Fig. E-66 STEAM TEMPERATURE (BUNDLE 2 H=1915MM)

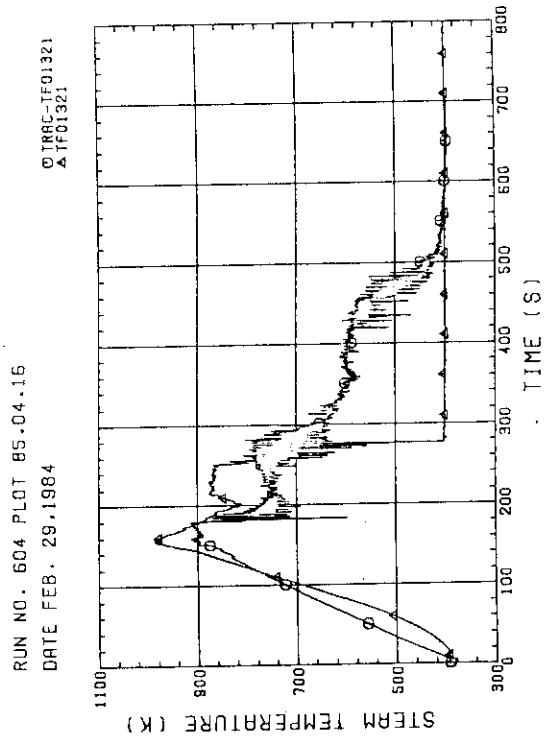

Fig. E-67 STEAM TEMPERATURE (BUNDLE 3 H=1915MM)

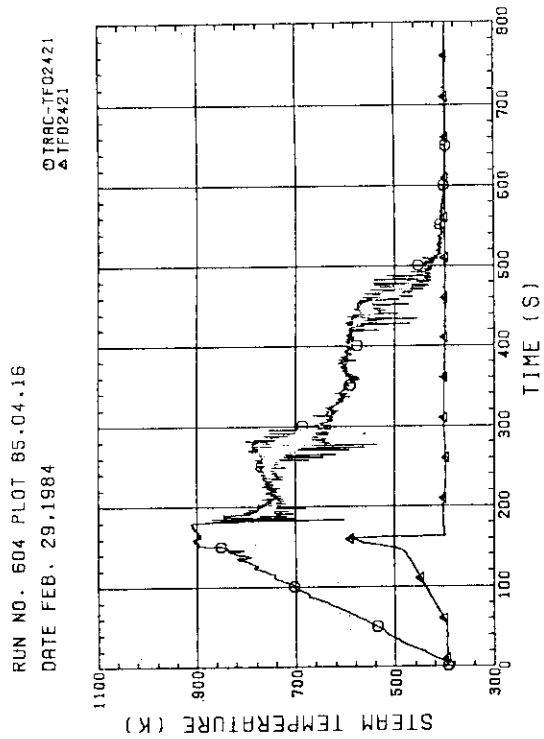

Fig. E-68 STEAM TEMPERATURE (BUNDLE 4 H=1915MM)

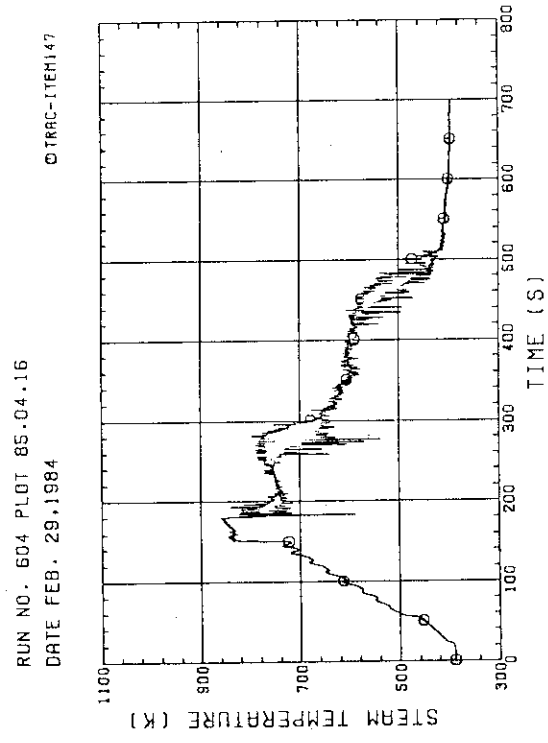

Fig. E-69 STEAM TEMPERATURE (BUNDLE 5 H=1915MM)

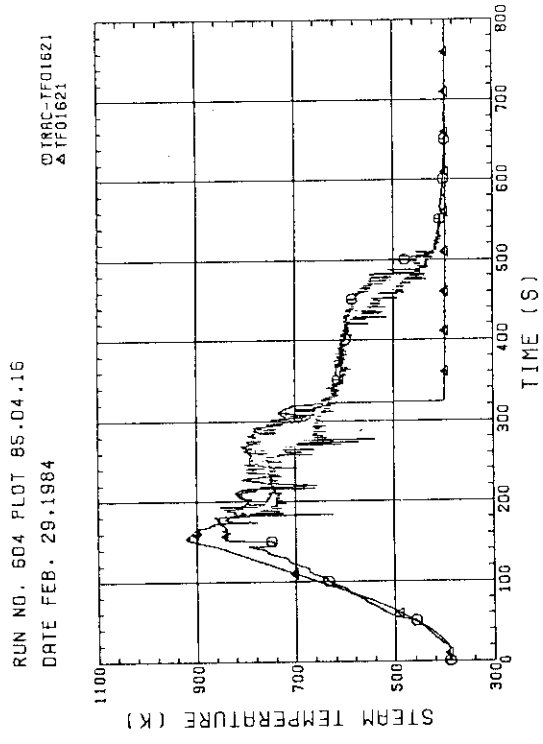

Fig. E-70 STEAM TEMPERATURE (BUNDLE 6 H=1915MM)

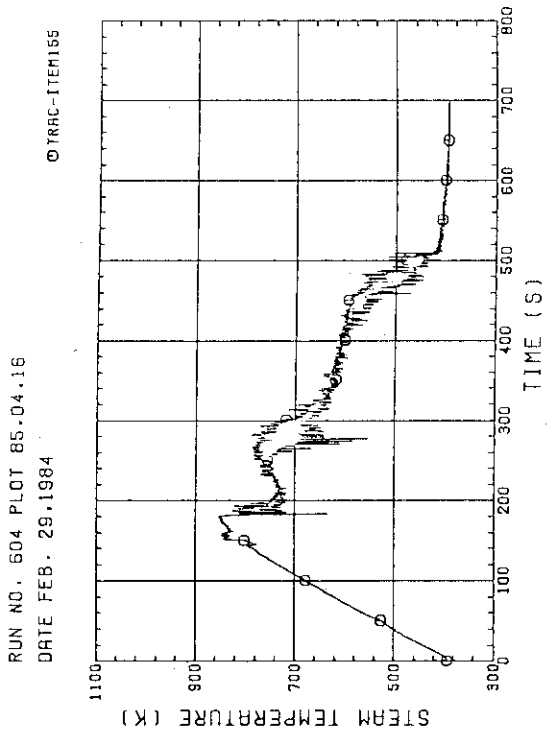

Fig. E-71 STEAM TEMPERATURE (BUNDLE 7 H=1915MM)

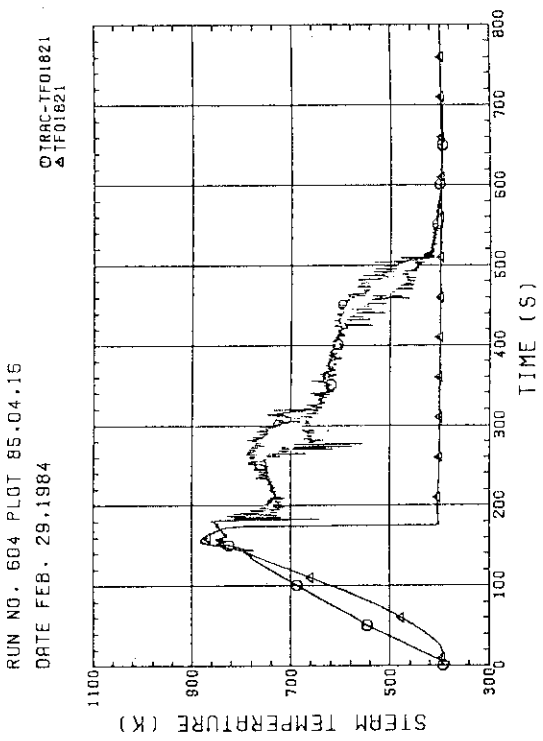

Fig. E-72 STEAM TEMPERATURE (BUNDLE 8 H=1915MM)

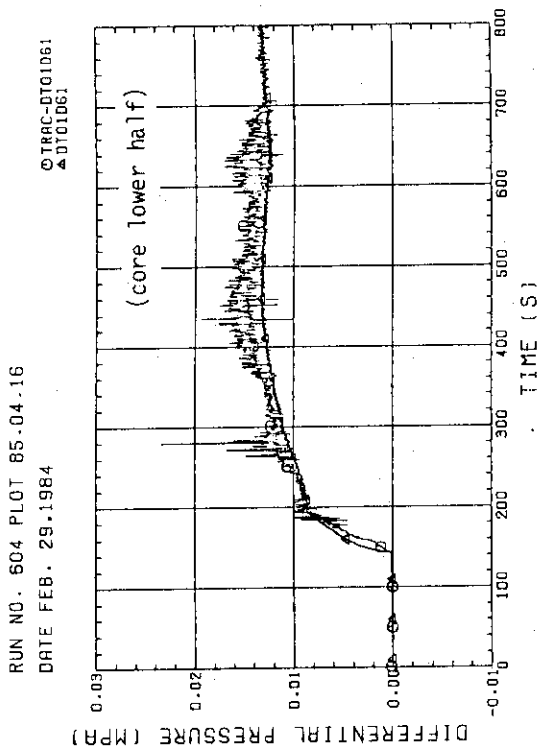

Fig. E-75 VERTICAL DIFFERENTIAL PRESSURE (BUNDLE 6)

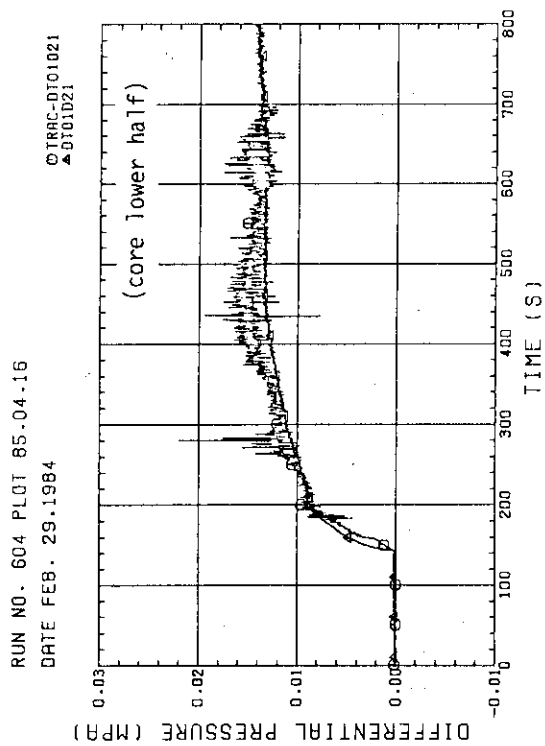

Fig. E-73 VERTICAL DIFFERENTIAL PRESSURE (BUNDLE 2)

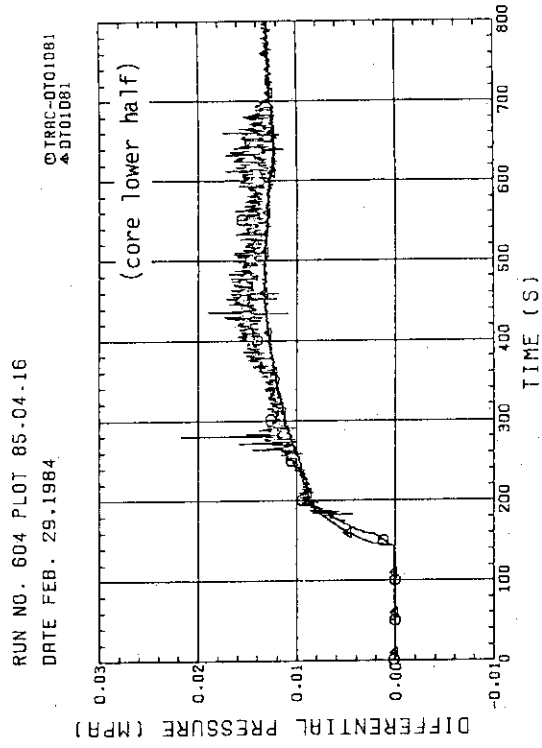

Fig. E-76 VERTICAL DIFFERENTIAL PRESSURE (BUNDLE 8)

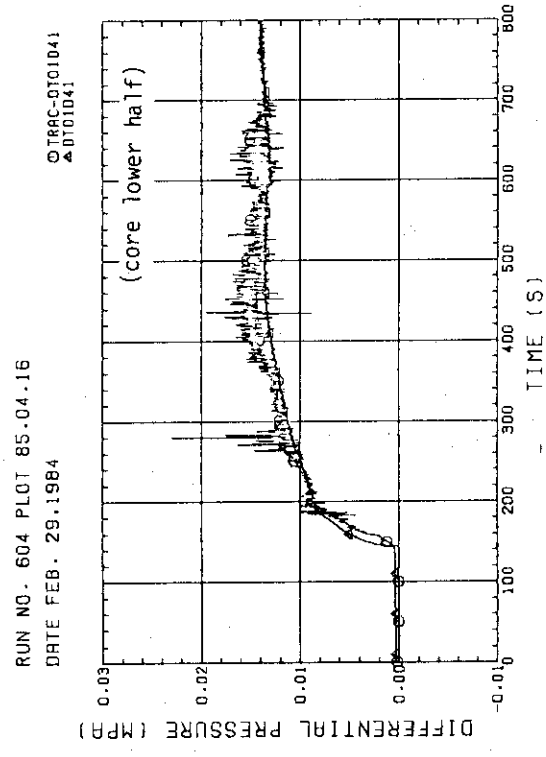

Fig. E-74 VERTICAL DIFFERENTIAL PRESSURE (BUNDLE 4)

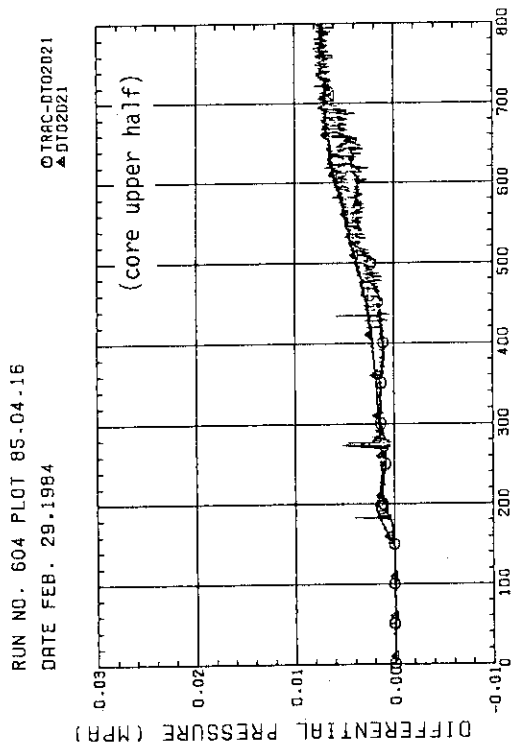

Fig. E-77 VERTICAL DIFFERENTIAL PRESSURE (BUNDLE 2)

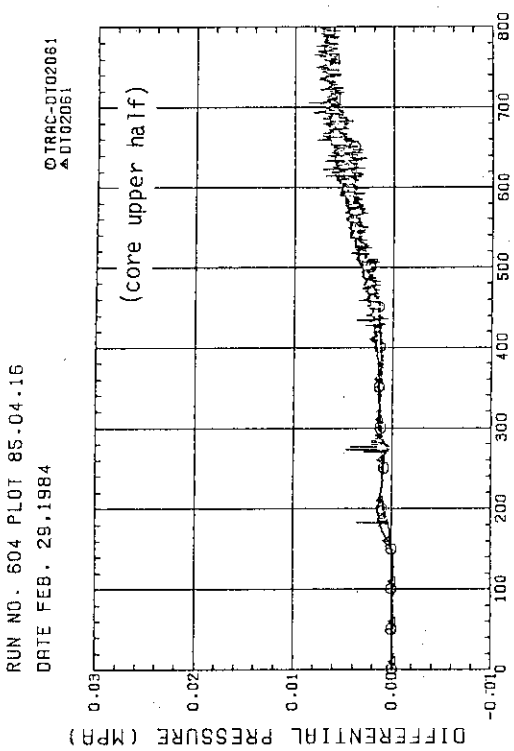

Fig. E-79 VERTICAL DIFFERENTIAL PRESSURE (BUNDLE 6)

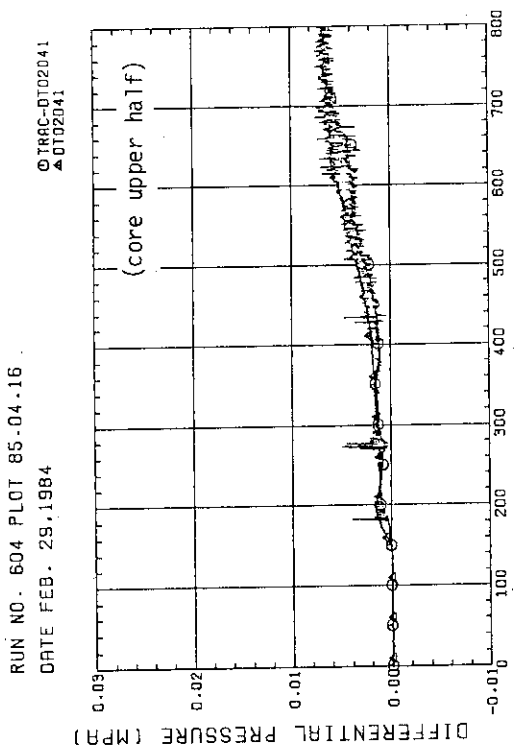

Fig. E-78 VERTICAL DIFFERENTIAL PRESSURE (BUNDLE 4)

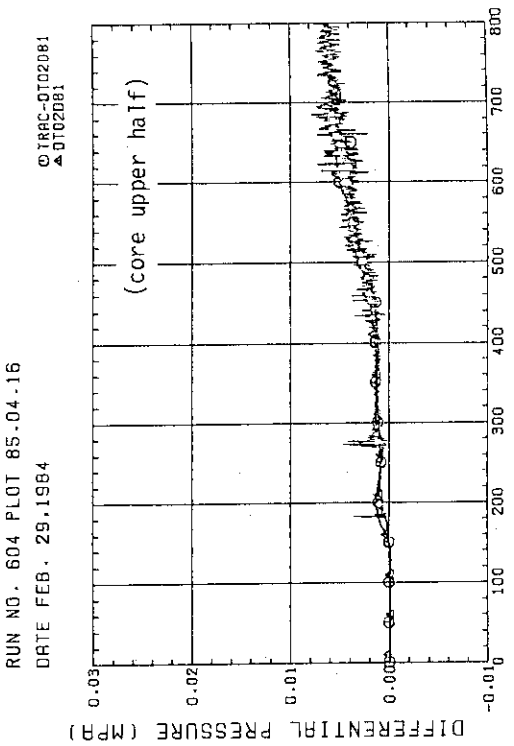

Fig. E-80 VERTICAL DIFFERENTIAL PRESSURE (BUNDLE 8)

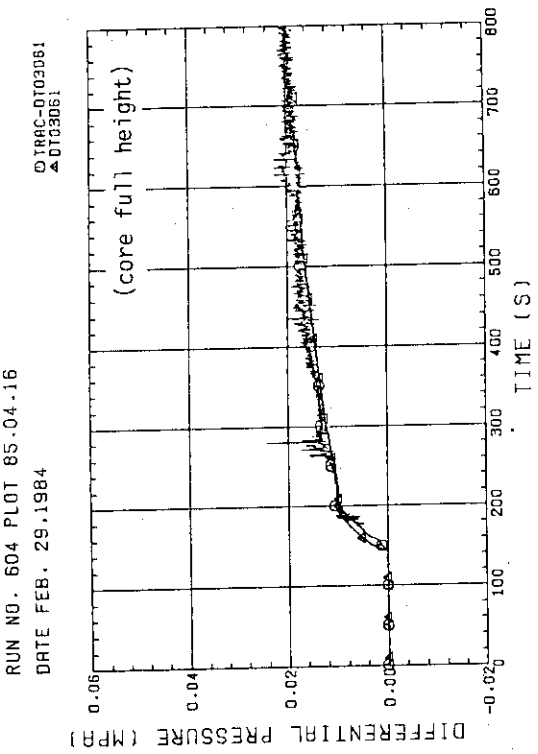

Fig. E-81 VERTICAL DIFFERENTIAL PRESSURE (BUNDLE 2)

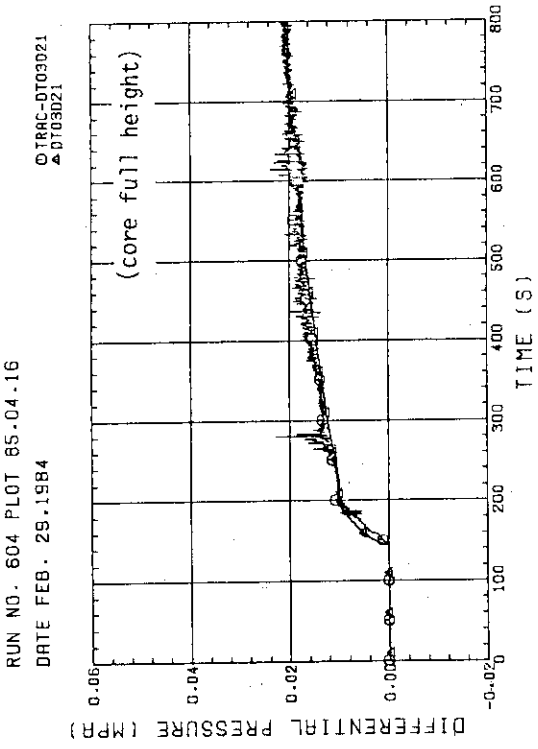

Fig. E-83 VERTICAL DIFFERENTIAL PRESSURE (BUNDLE 6)

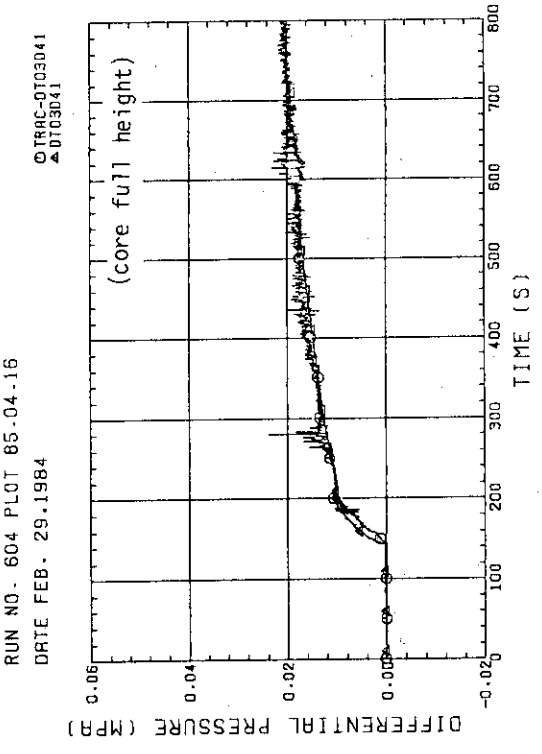

Fig. E-82 VERTICAL DIFFERENTIAL PRESSURE (BUNDLE 4)

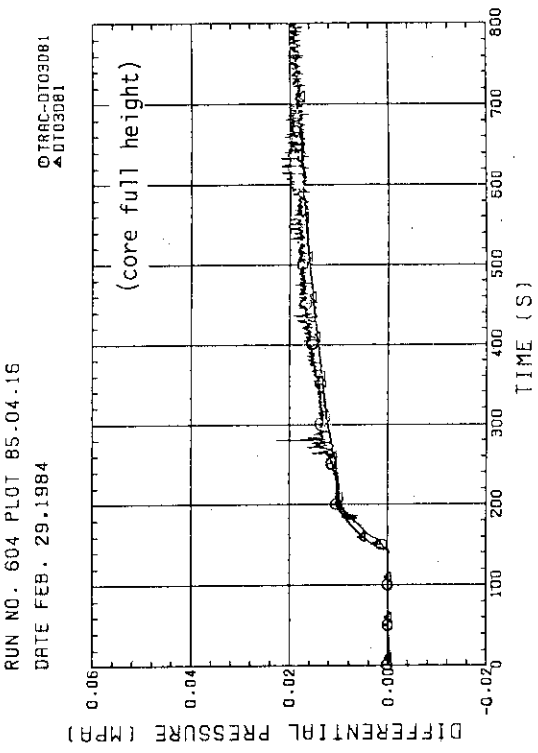

Fig. E-84 VERTICAL DIFFERENTIAL PRESSURE (BUNDLE 8)

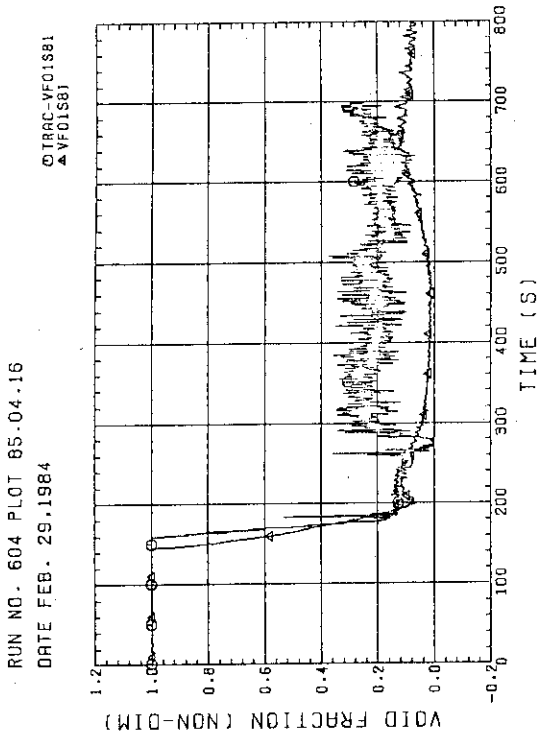

Fig. E-85 VOID FRACTION (BUNDLE 2)

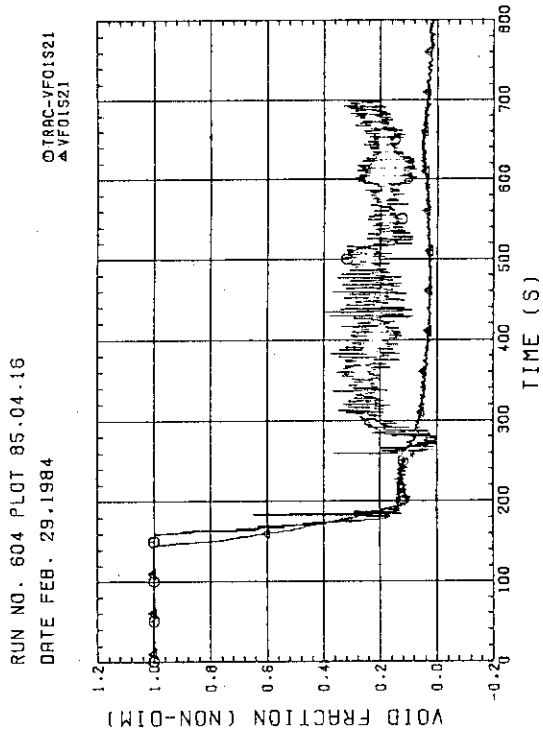

Fig. E-86 VOID FRACTION (BUNDLE 4)

Fig. E-87 VOID FRACTION (BUNDLE 8)

Fig. E-88 VOID FRACTION (BUNDLE 2)

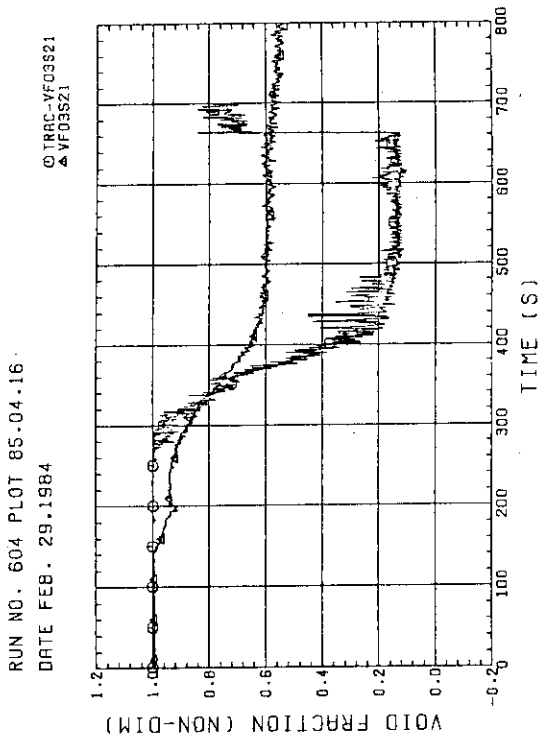

Fig. E-91 VOID FRACTION (BUNDLE 2)

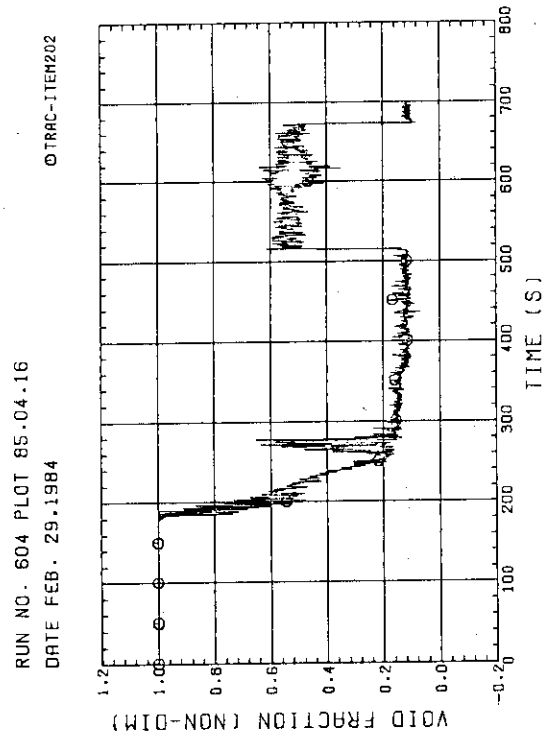

Fig. E-89 VOID FRACTION (BUNDLE 4)

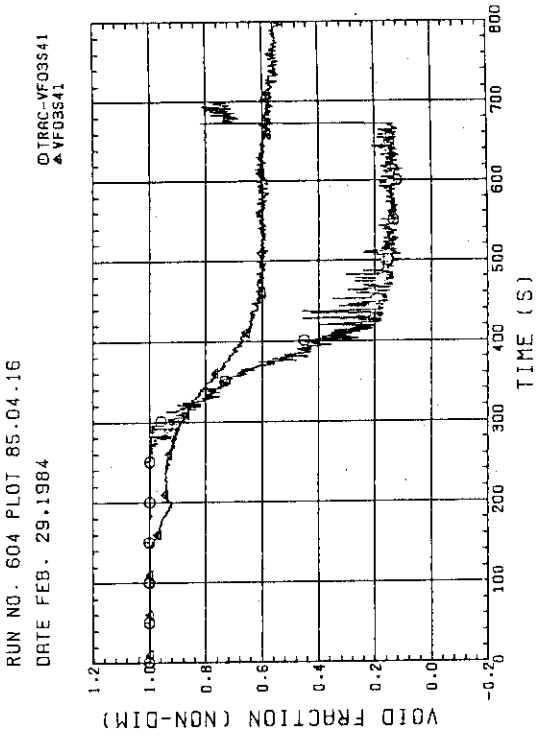

Fig. E-92 VOID FRACTION (BUNDLE 4)

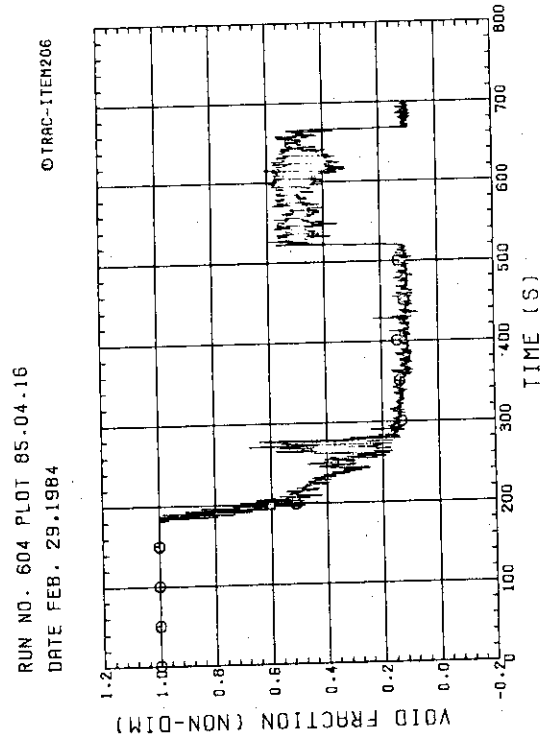

Fig. E-90 VOID FRACTION (BUNDLE 8)

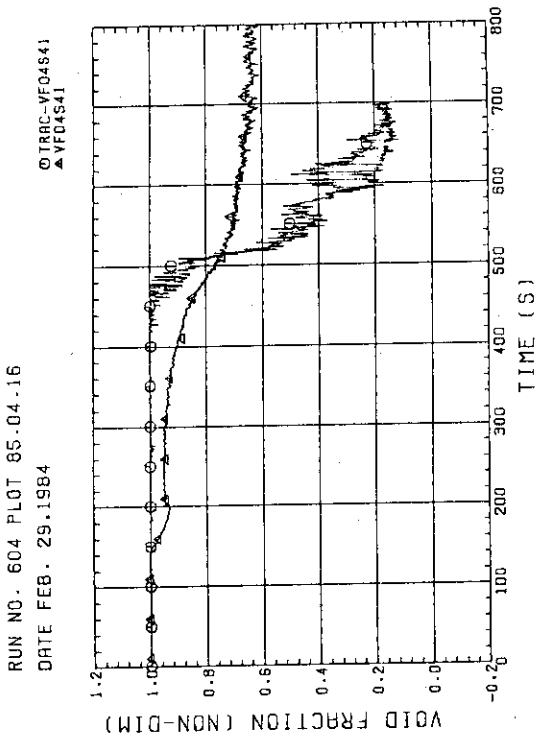

Fig. E-93 VOID FRACTION (BUNDLE 8)

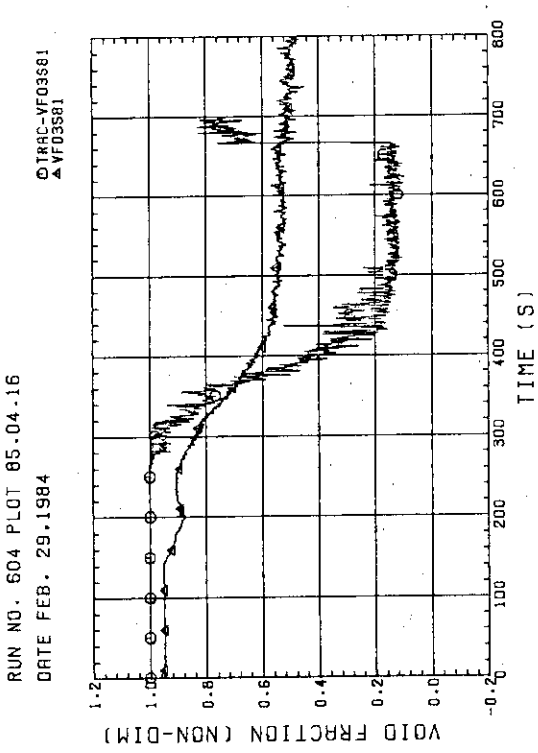

Fig. E-95 VOID FRACTION (BUNDLE 4)

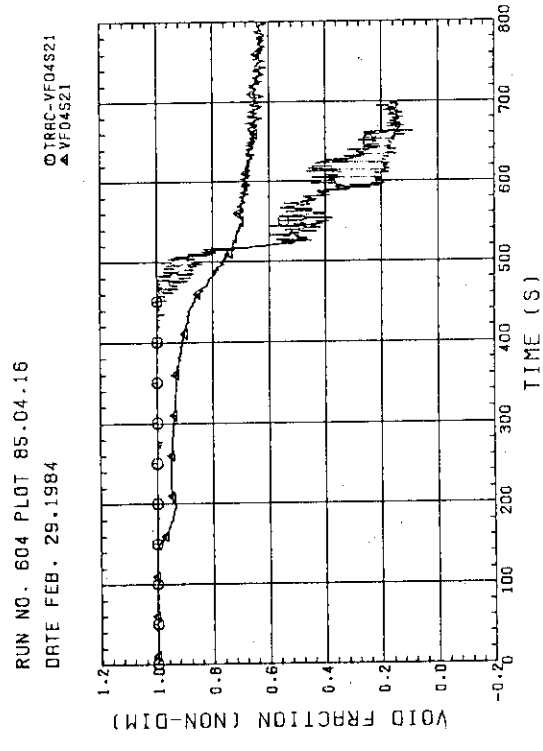

Fig. E-94 VOID FRACTION (BUNDLE 2)

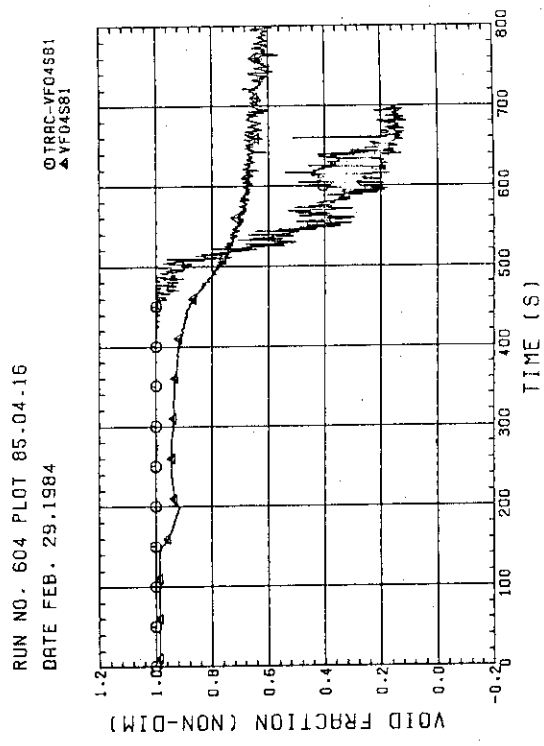

Fig. E-96 VOID FRACTION (BUNDLE 8)

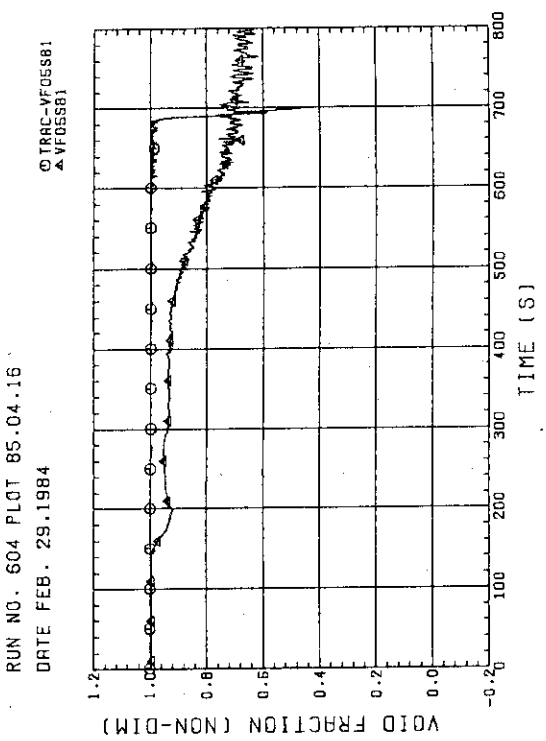

Fig. E-99 VOID FRACTION (BUNDLE 8)

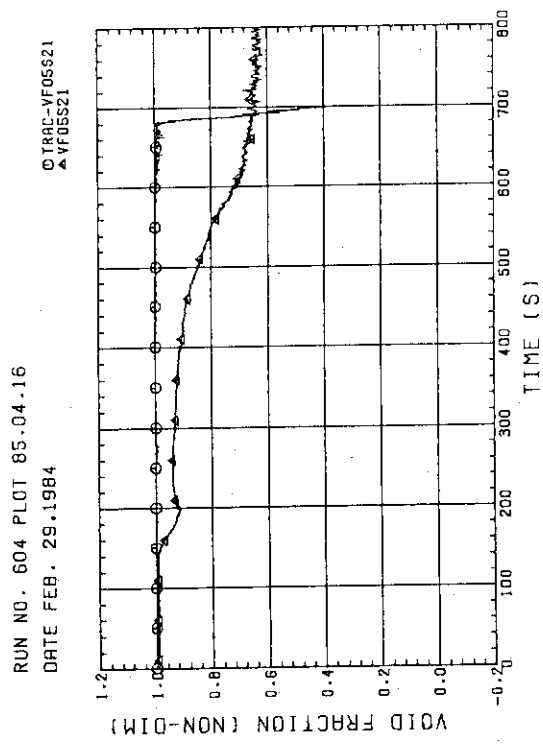

Fig. E-97 VOID FRACTION (BUNDLE 2)

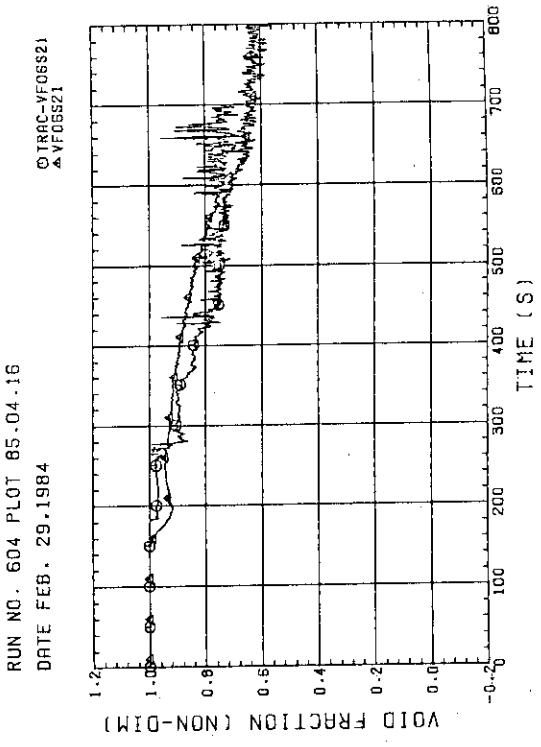

Fig. E-100 VOID FRACTION (BUNDLE 2)

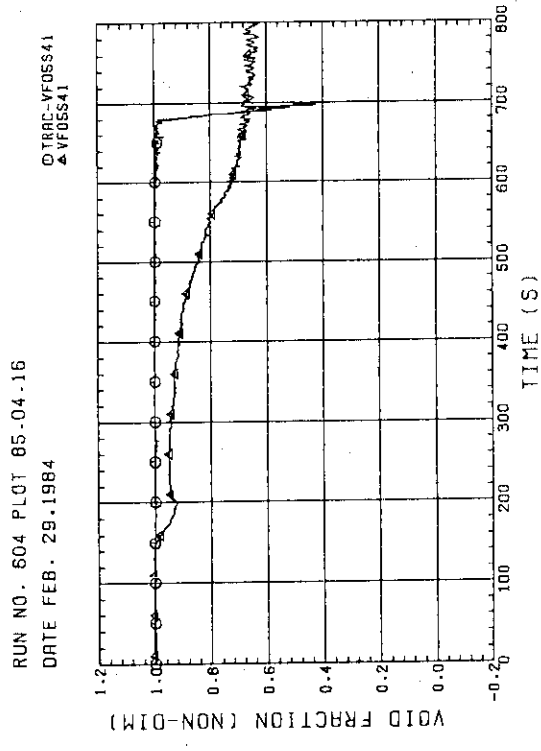

Fig. E-98 VOID FRACTION (BUNDLE 4)

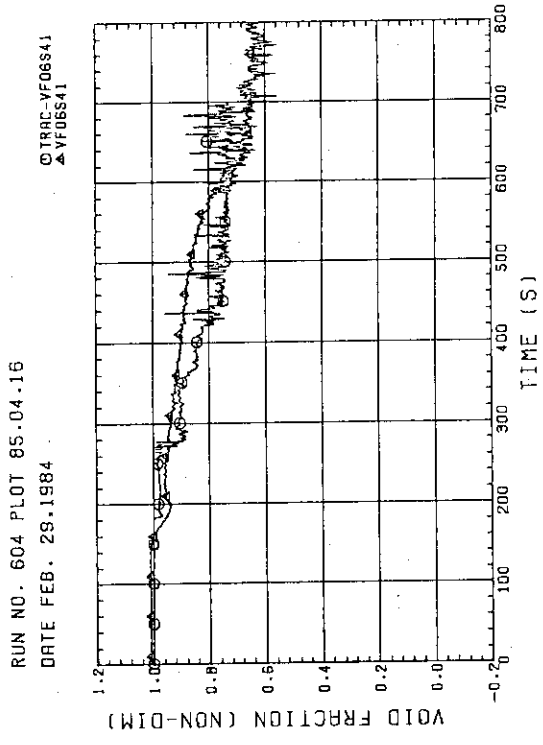

Fig. E-101 VOID FRACTION (BUNDLE 4)

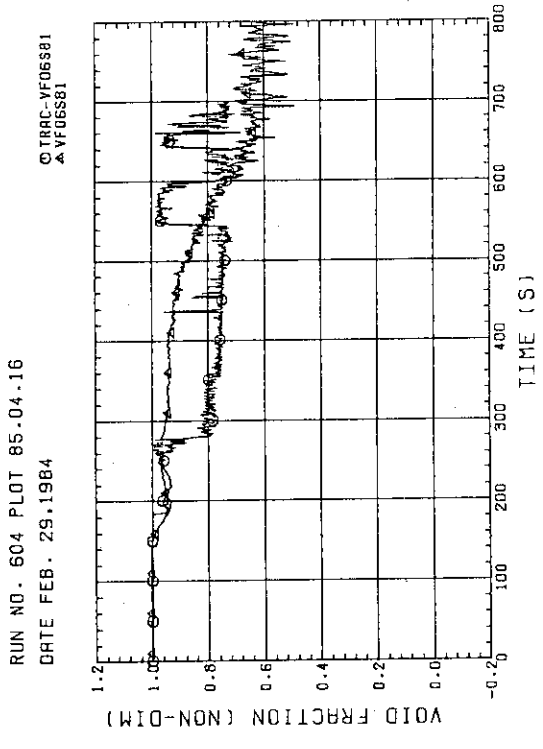

Fig. E-102 VOID FRACTION (BUNDLE 8)

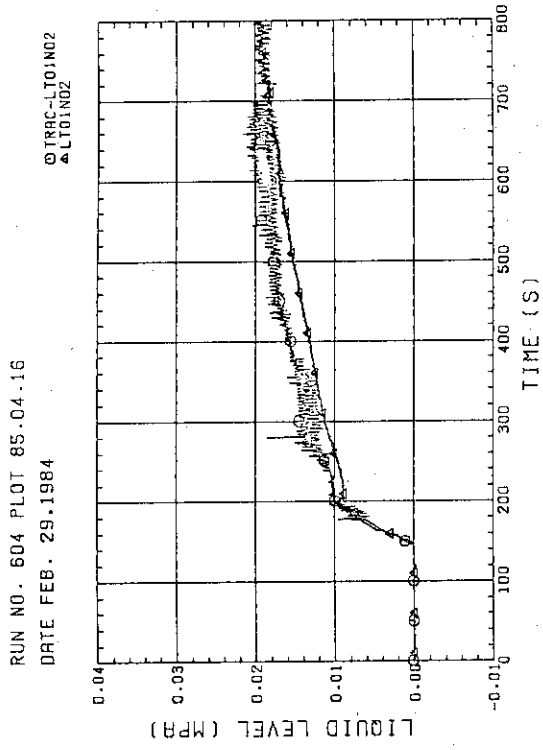

Fig. E-103 CORE BAFFLE FULL HT

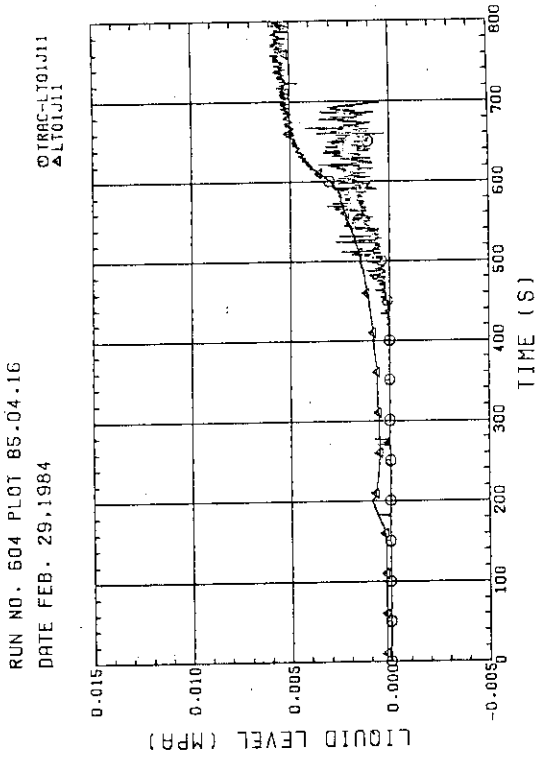

Fig. E-104 UPPER PLENUM LIQUID LEVEL (BUNDLE 1)

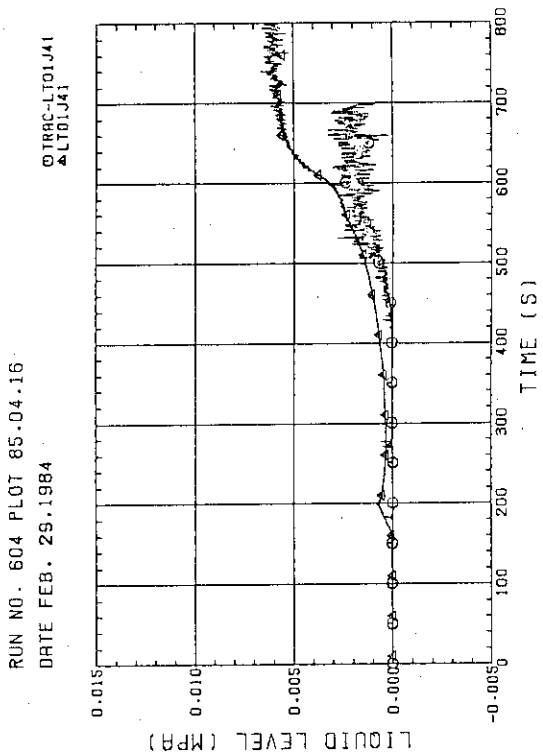

Fig. E-105 UPPER PLENUM LIQUID LEVEL (BUNDLE 2)

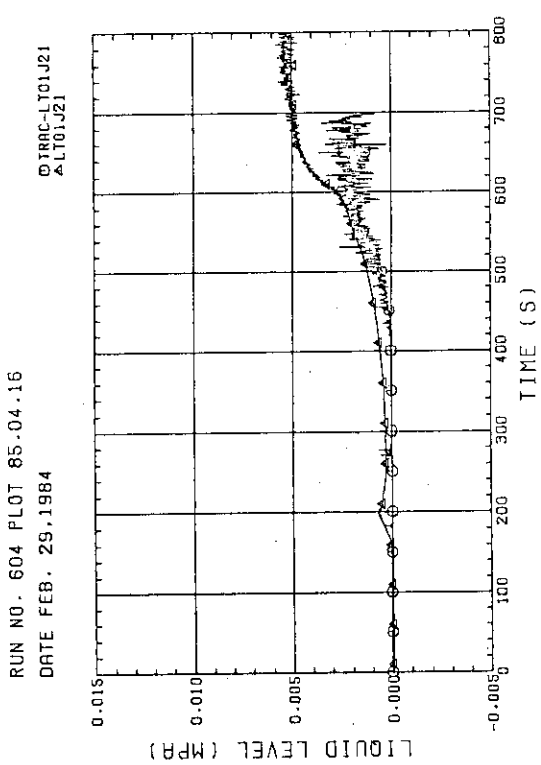

Fig. E-106 UPPER PLENUM LIQUID LEVEL (BUNDLE 3)

Fig. E-107 UPPER PLENUM LIQUID LEVEL (BUNDLE 4)

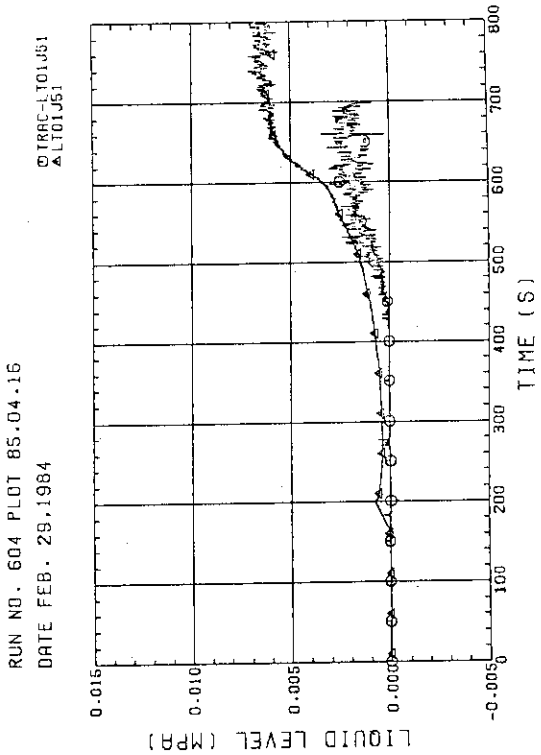

Fig. E-108 UPPER PLENUM LIQUID LEVEL (BUNDLE 5)

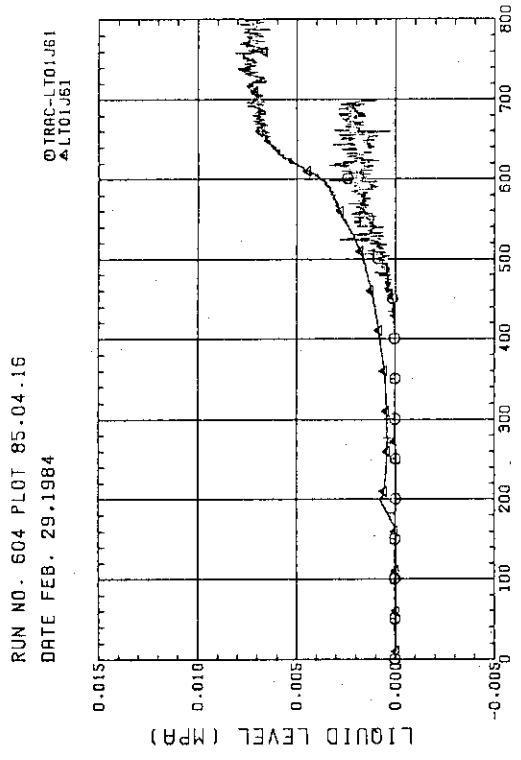

Fig. E-109 UPPER PLENUM LIQUID LEVEL (BUNDLE 6)

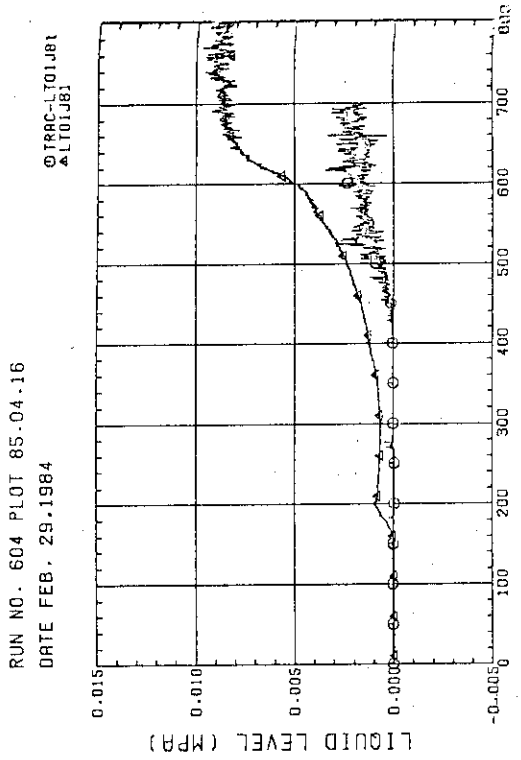

Fig. E-111 UPPER PLENUM LIQUID LEVEL (BUNDLE 8)

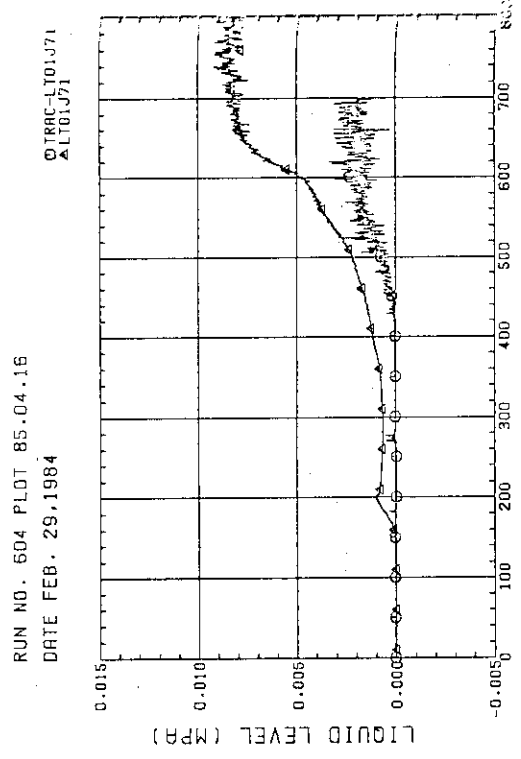

Fig. E-110 UPPER PLENUM LIQUID LEVEL (BUNDLE 7)

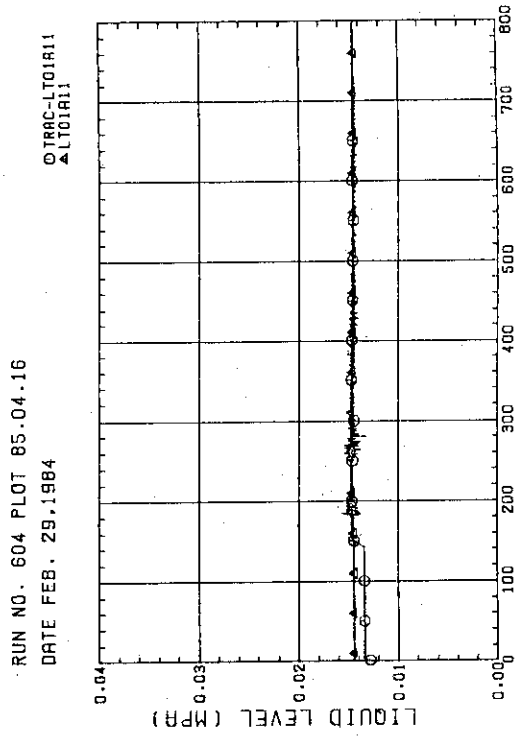

Fig. E-112 LOWER PLENUM LIQUID LEVEL (TOTAL)

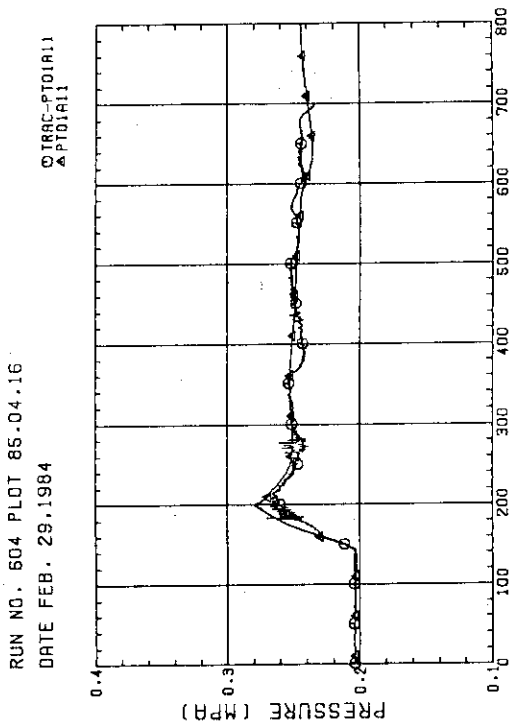

Fig. E-115 PRESSURE (LOWER PLENUM)

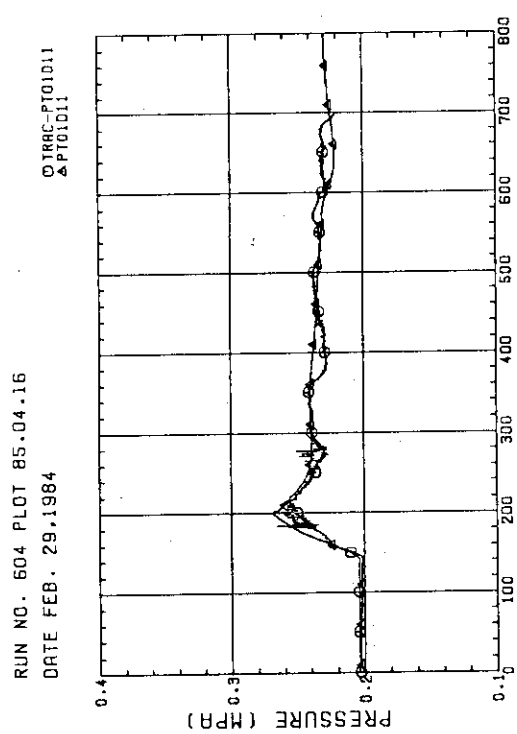

Fig. E-113 PRESSURE (CORE)

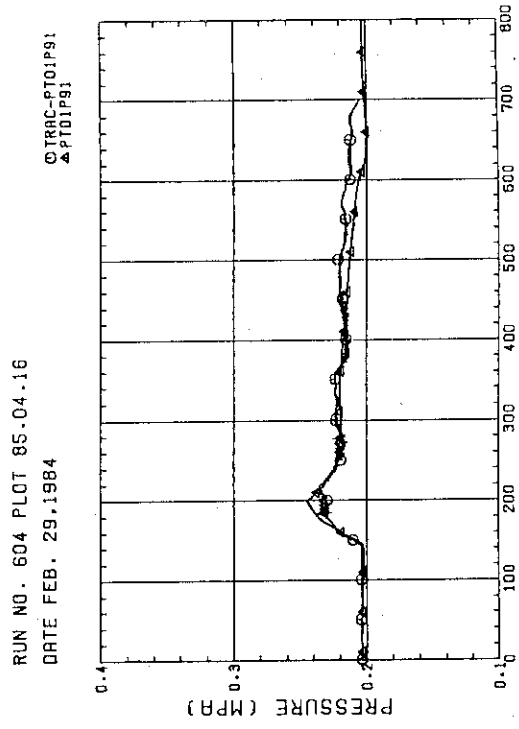

Fig. E-116 PRESSURE (DOWNCOMER)

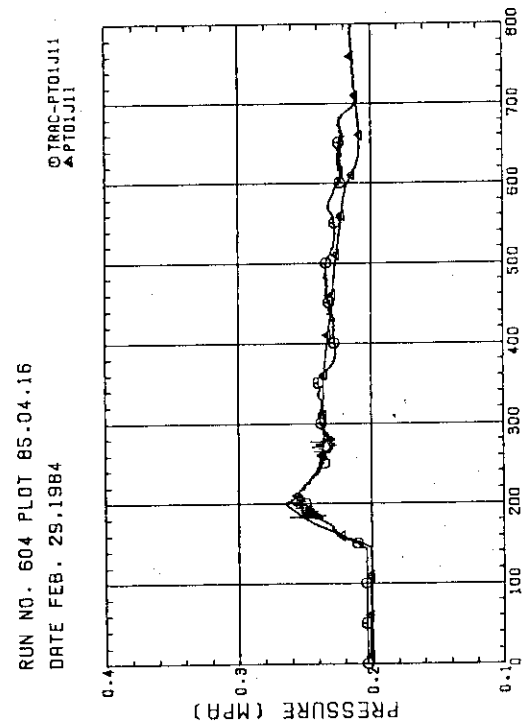

Fig. E-114 PRESSURE (UPPER PLENUM)

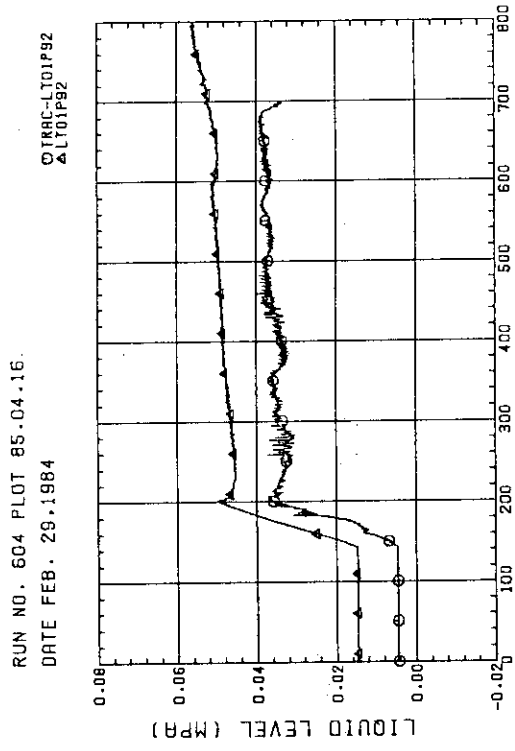

Fig. E-117 LIQUID LEVEL IN DC

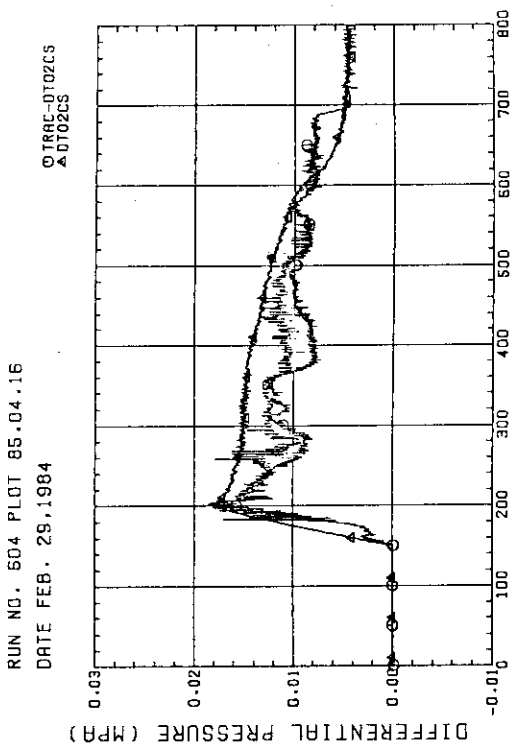

Fig. E-119 DIFFERENTIAL PRESSURE (S/W SEP. - DC)

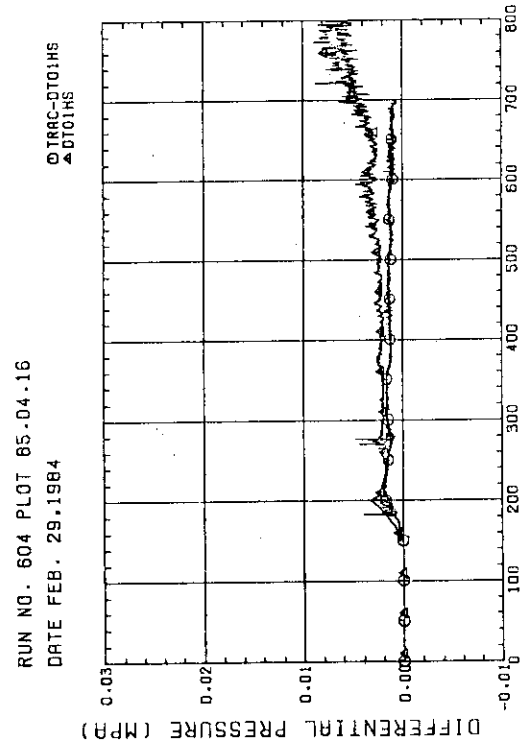

Fig. E-118 DIFFERENTIAL PRESSURE (UP - S/W SEP.)

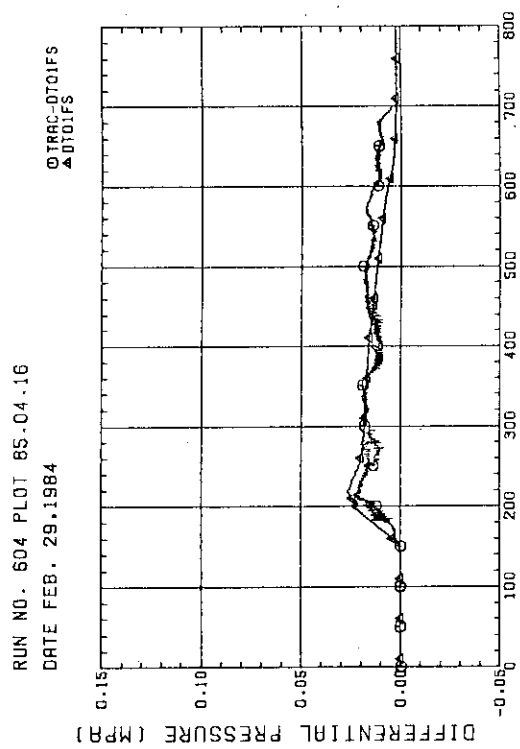

Fig. E-120 DIFFERENTIAL PRESSURE (DC - CT1)

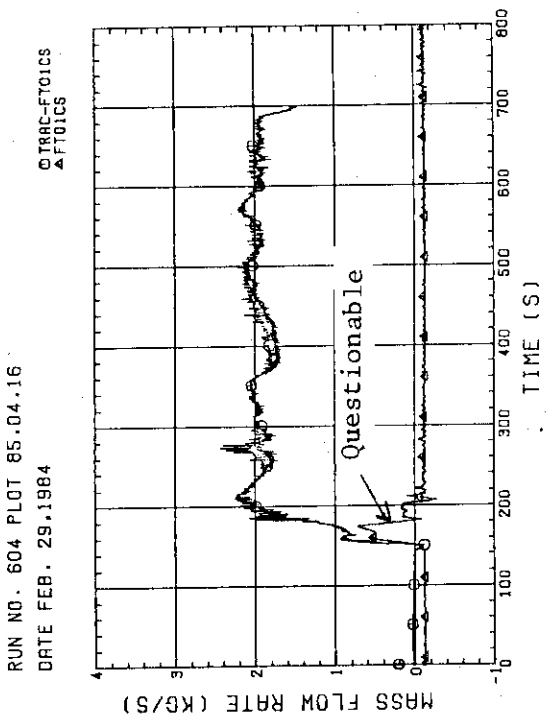

Fig. E-123 MASS FLOW RATE (ICL - ECC TO S/W)

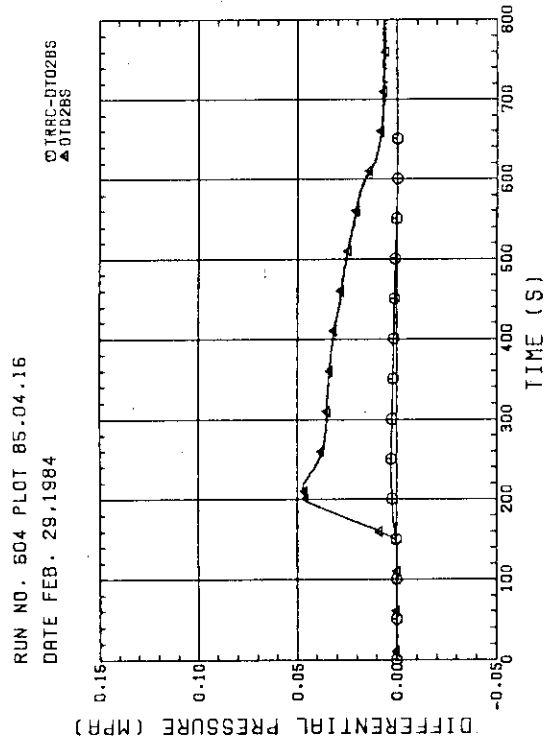

Fig. E-121 DIFFERENTIAL PRESSURE (S/W SEP. - CT2)

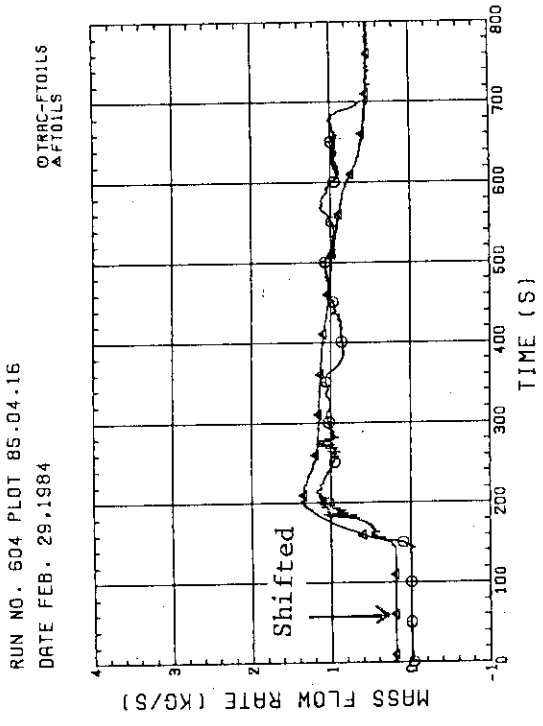

Fig. E-124 MASS FLOW RATE (BCL - S/W SIDE)

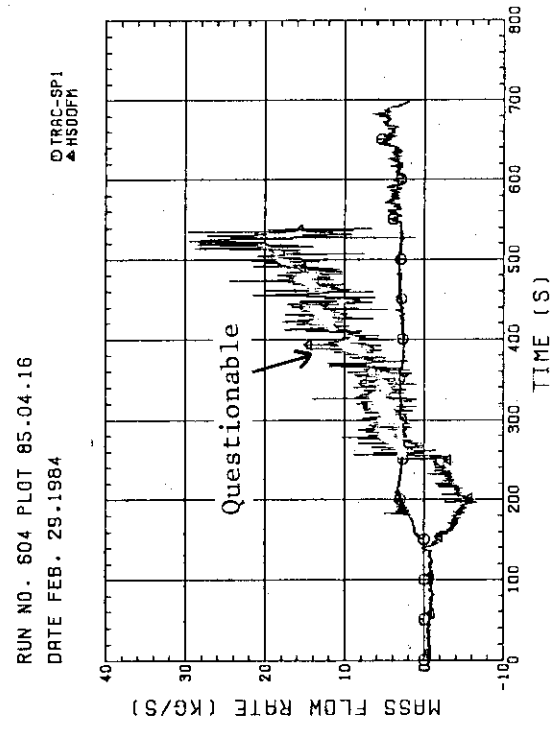

Fig. E-122 MASS FLOW RATE (HOT LEG)

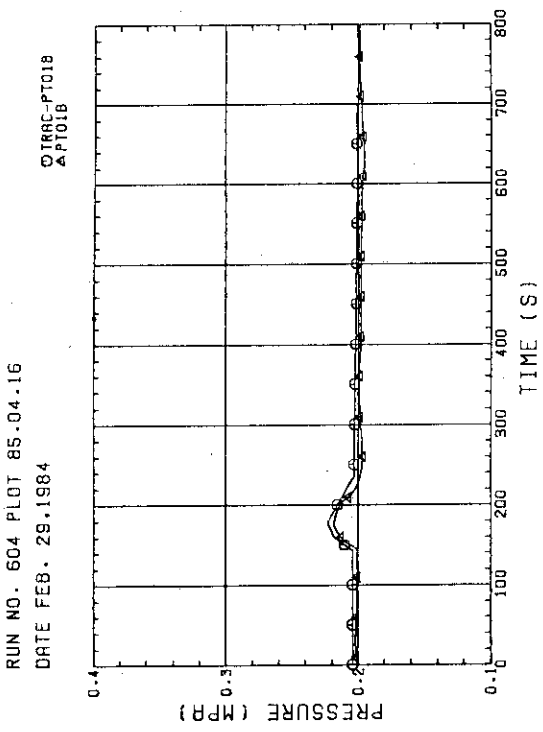

Fig. E-127 PRESSURE (CT2)

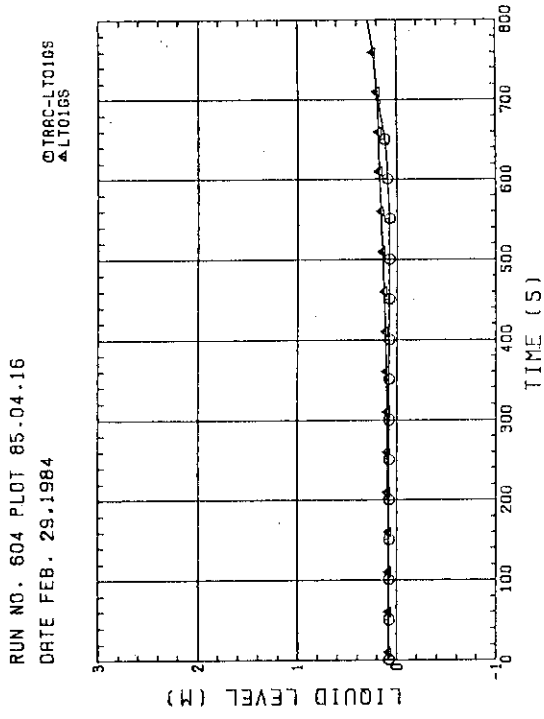

Fig. E-128 LIQUID LEVEL (S/W SEPARATOR)

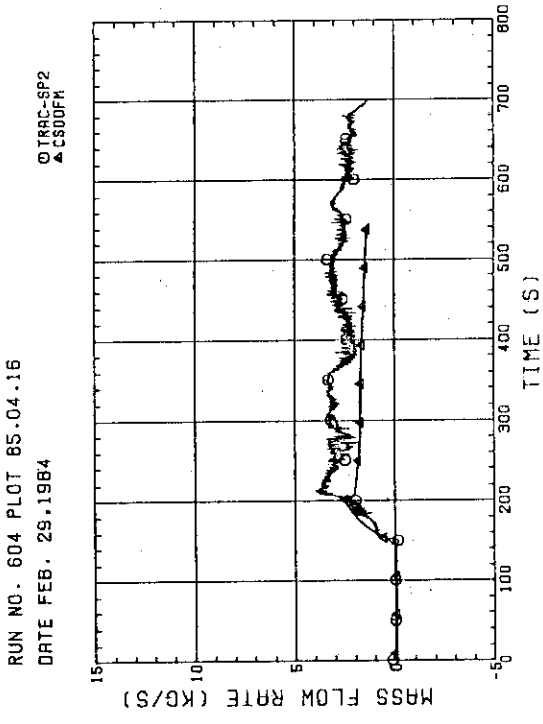

Fig. E-125 MASS FLOW RATE (BCL - PV SIDE)

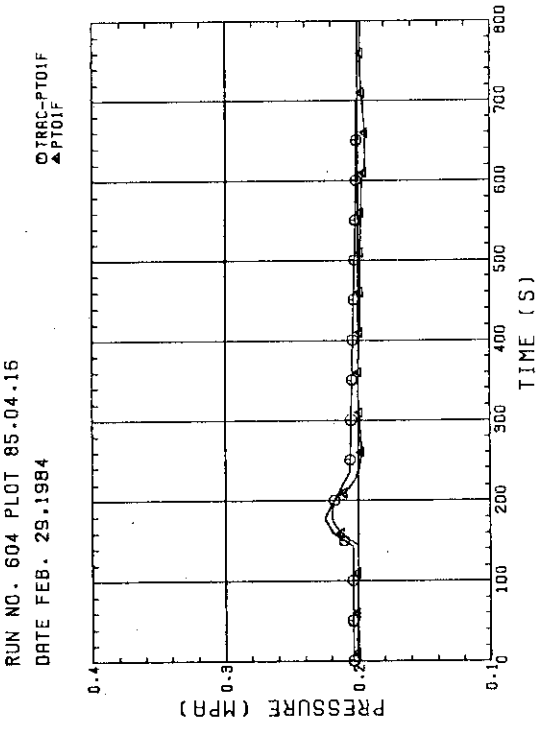

Fig. E-126 PRESSURE (CT1)

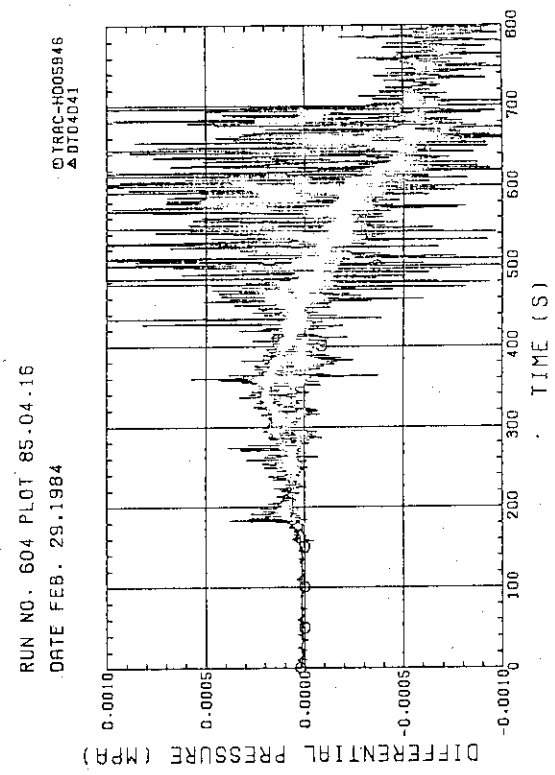

Fig. E-131 HORIZONTAL DIFFERENTIAL PRESSURE (ELEV. 1.905M , BUNDLE 4 - 6)

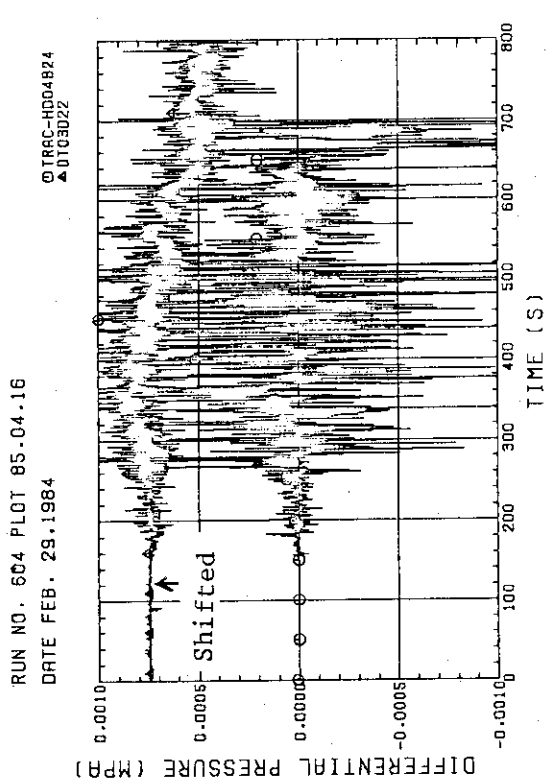

Fig. E-129 HORIZONTAL DIFFERENTIAL PRESSURE (ELEV. 1.365M , BUNDLE 2 - 4)

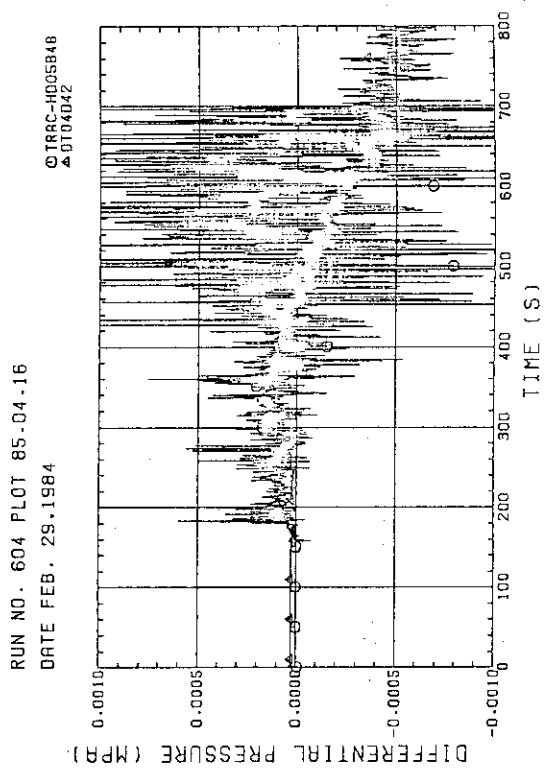

Fig. E-132 HORIZONTAL DIFFERENTIAL PRESSURE (ELEV. 1.905M , BUNDLE 4 - 8)

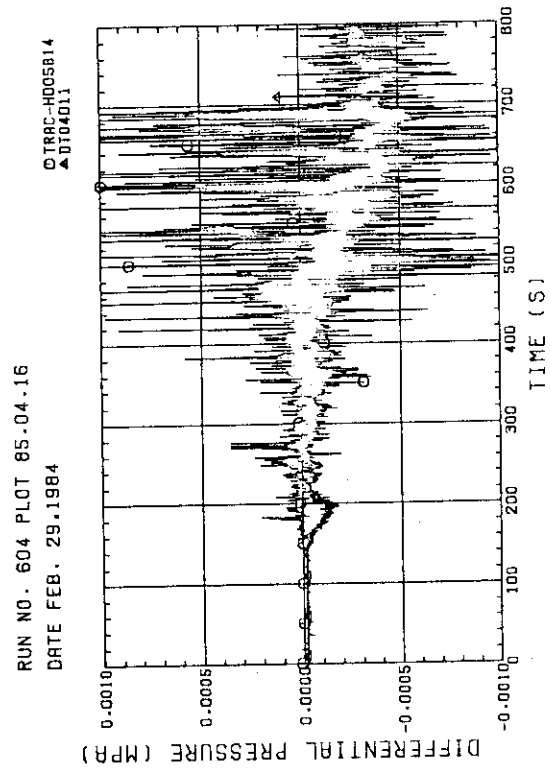

Fig. E-130 HORIZONTAL DIFFERENTIAL PRESSURE (ELEV. 1.905M , BUNDLE 1 - 4)

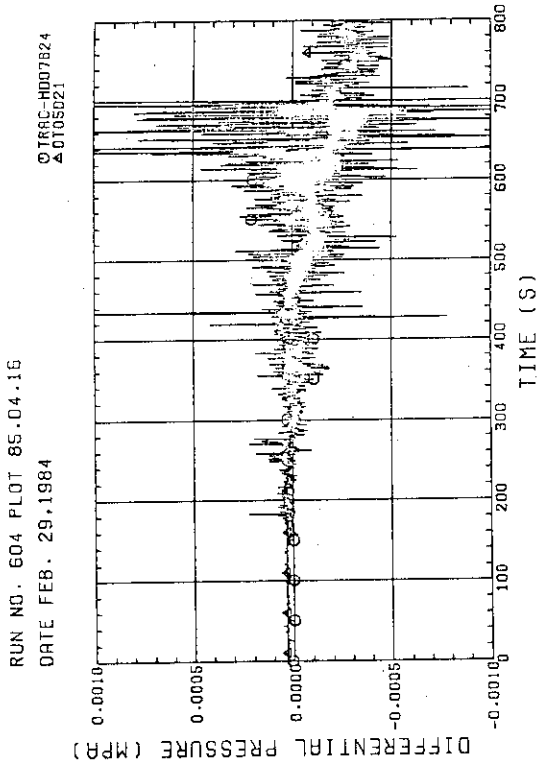

Fig. E-133 HORIZONTAL DIFFERENTIAL PRESSURE (ELEV. 2.57M , BUNDLE 2 - 4)

Appendix F Comparison between TRAC Post-test Analysis and Test Data of Test S2-SH2

List of figures in Appendix F

Fig. F-1 - F-40	Heater rod temperatures
Fig. F-41 - F-64	Water temperatures in core
Fig. F-65 - F-72	Steam temperature in core
Fig. F-73 - F-76	Vertical differential pressures across core lower half
Fig. F-77 - F-80	Vertical differential pressures across core upper half
Fig. F-81 - F-84	Vertical differential pressures across core full height
Fig. F-85 - F-102	Void fractions in core
Fig. F-103	Liquid level in core baffle
Fig. F-104 - F-111	Liquid levels in upper plenum
Fig. F-112	Liquid level in lower plenum
Fig. F-113 - F-116	Pressures in pressure vessel
Fig. F-117	Liquid level in downcomer
Fig. F-118 - F-121	Differential pressures in primary loops
Fig. F-122 - F-125	Mass flow rates in primary loops
Fig. F-126 - F-127	Pressures in containment tanks
Fig. F-128	Liquid level in S/W separator
Fig. F-129 - F-133	Horizontal differential pressures in core

TRAC-PF1 post-test analysis results obtained by the Los Alamos National Laboratory (LANL) based on the 2D/3D Agreement are compared with the test results of Test S2-SH2. For the comparison plots in this Appendix, the TRAC results are identified by circle symbols and the SCTF results by triangular symbols. Comments on the comparison results are presented as follows :

(1) Heater rod temperature (Figs. F-1 - F-40)

The heater rod temperatures predicted by TRAC qualitatively agree with the SCTF results except at the upper part of the core. TRAC overpredicts the turnaround temperature at the lower half of the core and

at the top of the core except in Bundle 6 while underpredicts at elevations from 3622 to 4907 mm from the bottom of pressure vessel (1905 to 3190 mm from the bottom of heated part) in all bundles. The calculated quench time is longer than the test data at almost all elevations. The top quench sometimes observed in the test results is not predicted by TRAC. The beginning of heat up is delayed by about 20 to 40 s in Bundle 6 probably due to an error in the input data.

(2) Water temperatures in core (Figs. F-41 - F-64)

The water temperatures in the core predicted by TRAC exhibit the saturation temperature, while the measured temperatures are affected by the superheated steam temperatures except at the bottom of heated part. At the later period, the measured water temperatures wall agree with the calculated temperatures.

(3) Steam temperatures in core (Fig. F-65 - F-72)

The measured steam temperature sometimes shows much lower temperature than the calculated temperature as shown in Figs. E-66 and E-68 and the measured temperature decreases to the saturation temperature at much earlier time than the calculated temperature. These are due to the fact that the superheated steam probes used for the steam temperature measurement might be wetted by water droplets. Superheat data before the quench of the probes show almost reasonable agreement with the TRAC calculattion as shown in Figs. F-65, F-67 and F-70.

(4) Vertical differential pressures in core (Figs. F-73 - F-84)

TRAC overpredicts the differential pressure across the lower half of the core and underpredicts the differential pressure across the upper half of the core. The calculated differential pressures across the core full height well agree with the test data except during the initial 60 s after the beginning of bottom reflood. During that period, TRAC underpredicts the differential pressure. In general, the calculated vertical differential pressures in the core show oscillatory behavior, whereas no significant oscillations are observed in the SCTF results.

(5) Void fractions in core (Figs. F-85 - F-102)

The calculated void fraction remains almost unity before the occurrence of quench and then decreases repidly, while the measured void fraction gradually decreases with time from the beginning of reflood.

(6) Liquid level in core baffle (Fig. F-103)

The initial increasing of the liquid level in the core baffle is well predicted by TRAC. Thereafter, TRAC slightly overpredicts the

liquid level.

(7) Liquid levels in upper plenum (Figs. F-104 - F-111)

TRAC underpredicts the liquid level in the upper plenum above all bundles. The measured liquid levels in the upper plenum begin to increase just after the beginning of reflood, while the predicted values indicate no increases until about 300 s after the beginning of reflood. In addition, the measured liquid level in the upper plenum is higher at the Bundle 8 side than at the Bundle 1 side at the later period. However, TRAC cannot predict the nonuniform water accumulation in the upper plenum.

(8) Liquid level in lower plenum (Fig. F-112)

The initial liquid level in the TRAC calculation is lower than the measured initial value. There may be an input error for the initial liquid level in the caculation.

(9) Pressures in presure vessel (Fig. F-113 - F-116)

TRAC slightly underestimates the pressure in the core, the upper plenum, the lower plenum and the downcomer during the initial 60 s after the beginning of reflood. After that time, the predicted pressures well agree with the test data. TRAC tends to overpredict the pressures at the later period.

(10) Liquid level in downcomer (Fig. F-117)

The initial liquid level in the TRAC calculation is shifted lower. If the shift of the initial liquid level is corrected, the calculated result well agrees with the test data.

(11) Differential pressures in primary loop (Fig. F-118 - F-121)

The differential pressure between the upper plenum and the steam/water separator predicted by TRAC is much smaller than the SCTF result especially at the later period. The differential pressures between the steam/water separator and the downcomer and between the downcomer and the containment tank-I are also underpredicted by TRAC at the initial 400 and 300 s, respectively. After these times, TRAC overpredicts these differential pressures. The calculated differential pressure between the steam/water separator and the containment tank-II is much lower than the test result.

(12) Mass flow rate in primary loops (Fig. F-122 - F-125)

TRAC underpredicts the mass flow rate in the hot leg. The mass flow rate in the intact cold leg were not measured correctly and the comparison has no meaning in Fig. F-123. The measured mass flow rate in

the steam/water separator side broken cold leg is higher than the TRAC result for about 300 s from the beginning of reflood and then lower than the TRAC result. TRAC overpredicts the mass flow rate in the pressure vessel side broken cold leg.

(13) Pressures in containment tanks (Figs. F-126 and F-127)

Since the measured pressure transients in the containment tank-I were used in the TRAC analysis as the boundary condition, the TRAC and SCTF results should agree well with each other. However, the TRAC input data are slightly higher than the test result.

(14) Liquid level in steam/water separator (Fig. F-128)

The increasing rate of the liquid level in the steam/water separator is well predicted by TRAC.

(15) Horizontal differential pressures in core (Figs. F-129 - F-133)

The average values of the horizontal differential pressures calculated by TRAC are almost zero while the measured horizontal differential pressures become negative at the later period. Therefore TRAC cannot correctly predict the two-dimensional flow behavior in the core.

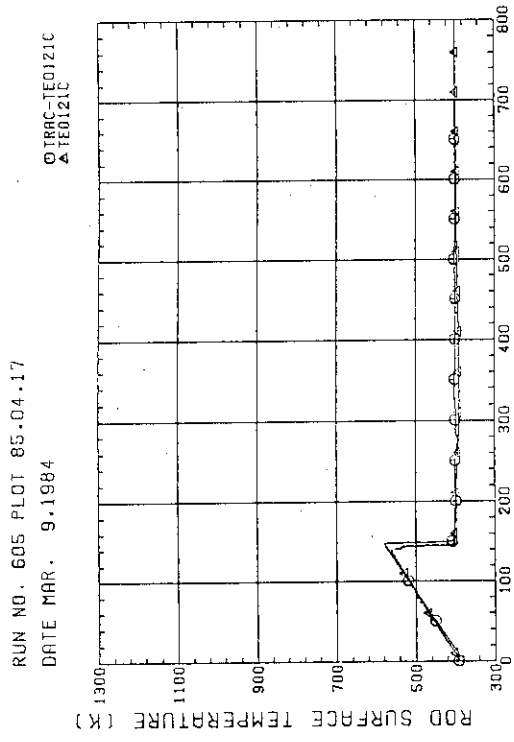

Fig. F-1 HEATER ROD TEMPERATURE (BUNDLE 2 H=1827MM)

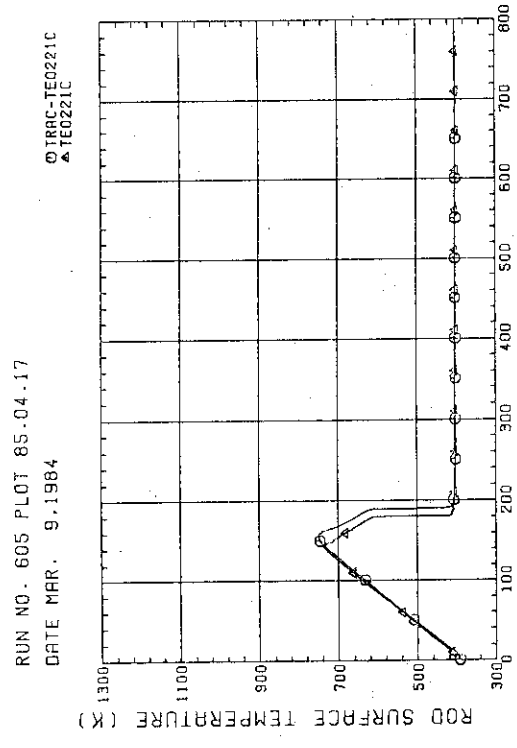

Fig. F-2 HEATER ROD TEMPERATURE (BUNDLE 2 H=2237MM)

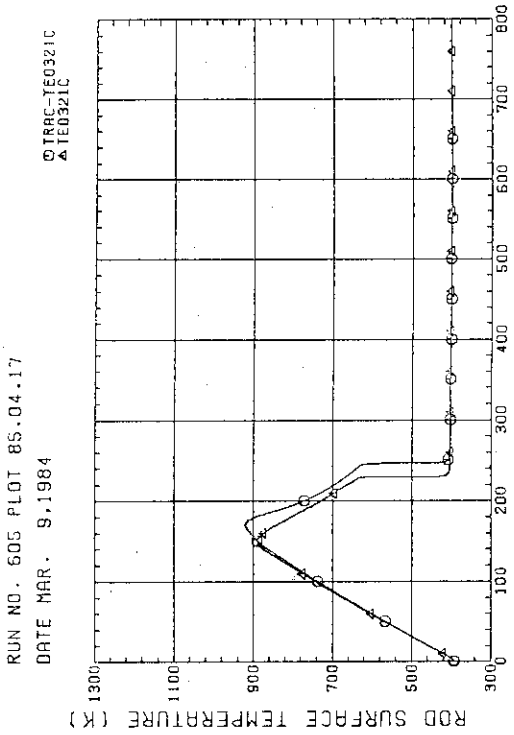

Fig. F-3 HEATER ROD TEMPERATURE (BUNDLE 2 H=2667MM)

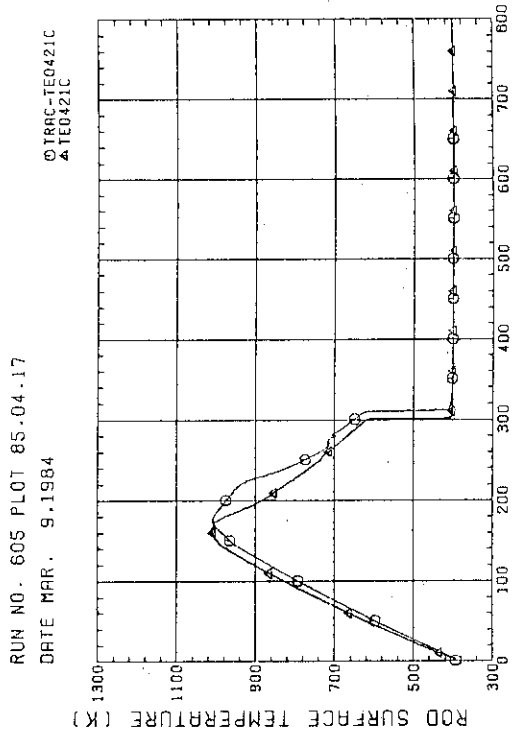

Fig. F-4 HEATER ROD TEMPERATURE (BUNDLE 2 H=3097MM)

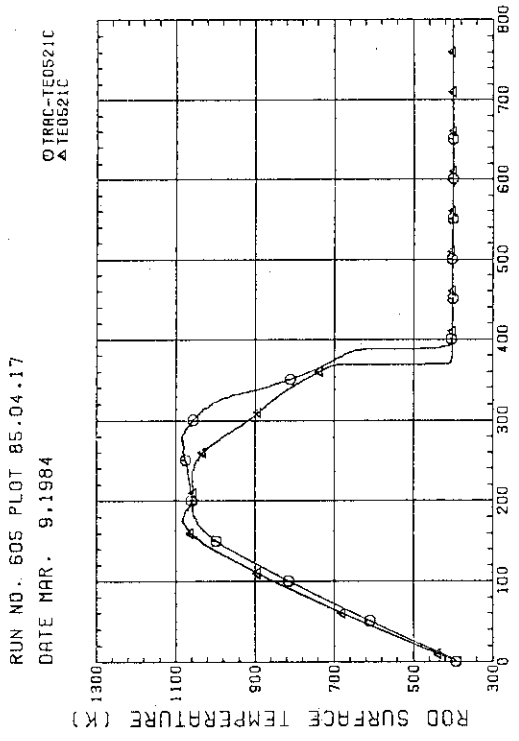

Fig. F-5 HEATER ROD TEMPERATURE (BUNDLE 2 H=3452MM)

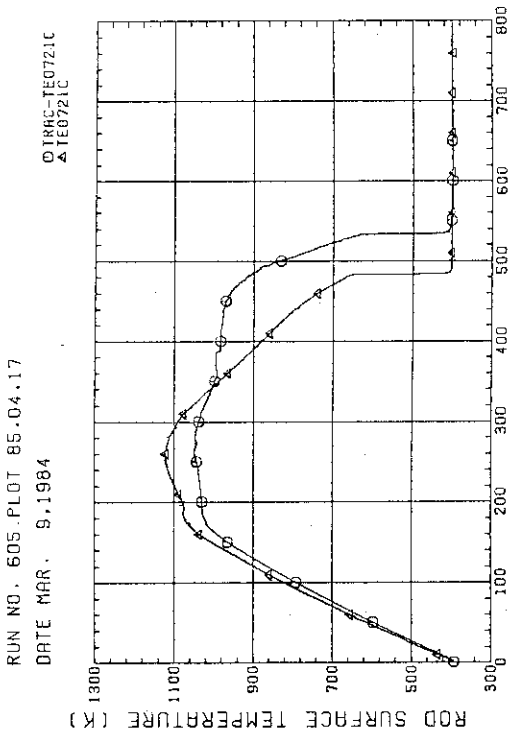

Fig. F-7 HEATER ROD TEMPERATURE (BUNDLE 2 H=4047MM)

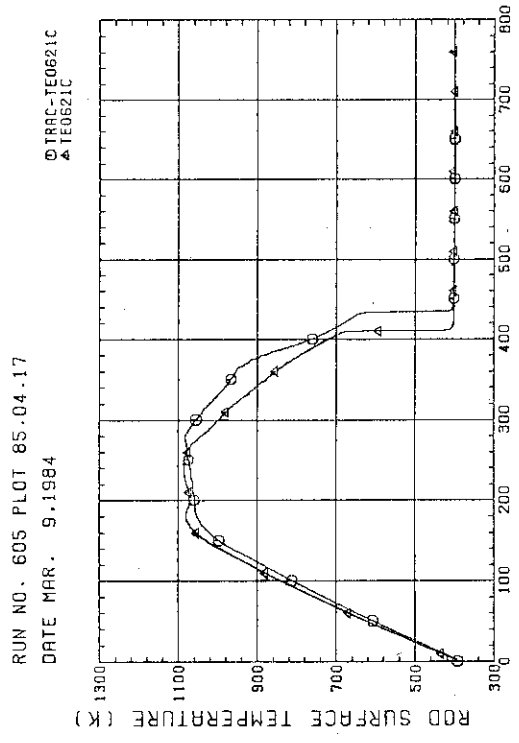

Fig. F-6 HEATER ROD TEMPERATURE (BUNDLE 2 H=3622MM)

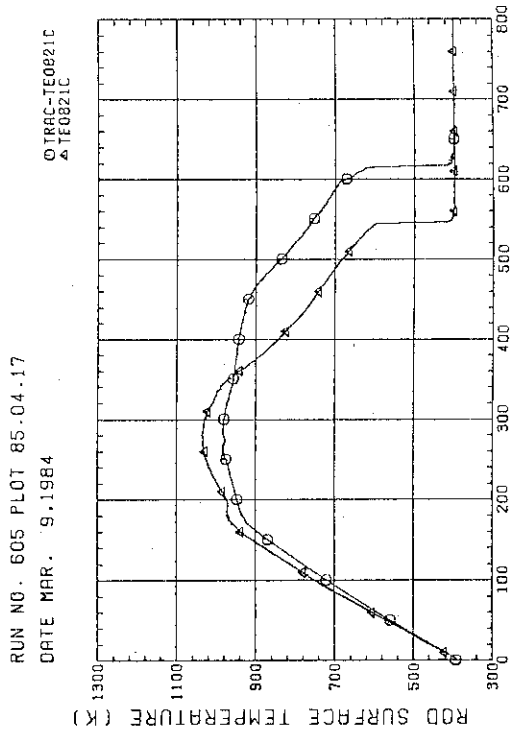

Fig. F-8 HEATER ROD TEMPERATURE (BUNDLE 2 H=4477MM)

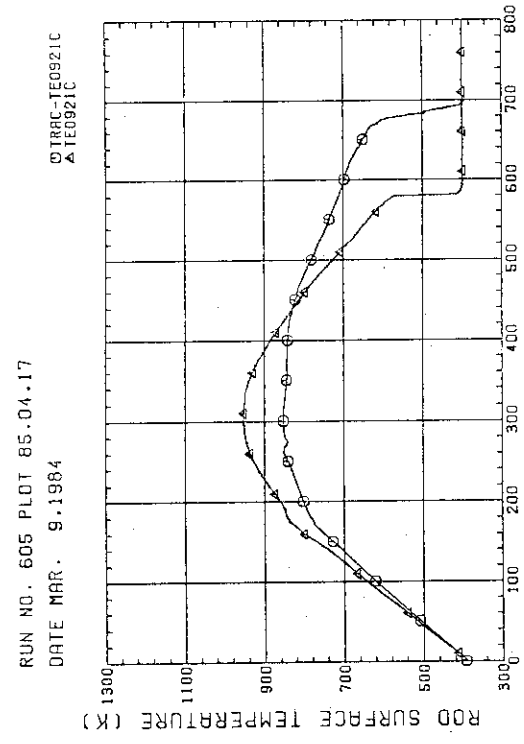

Fig. F-9 HEATER ROD TEMPERATURE (BUNDLE 2 H=4907MM)

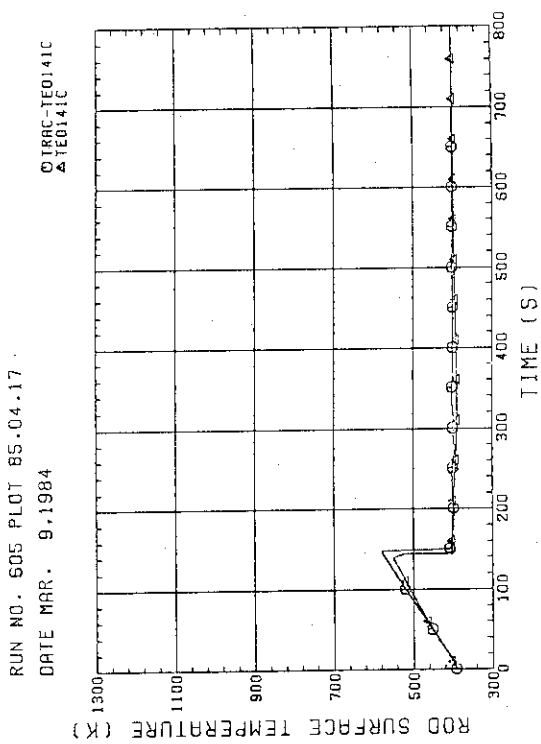

Fig. F-11 HEATER ROD TEMPERATURE (BUNDLE 4 H=1827MM)

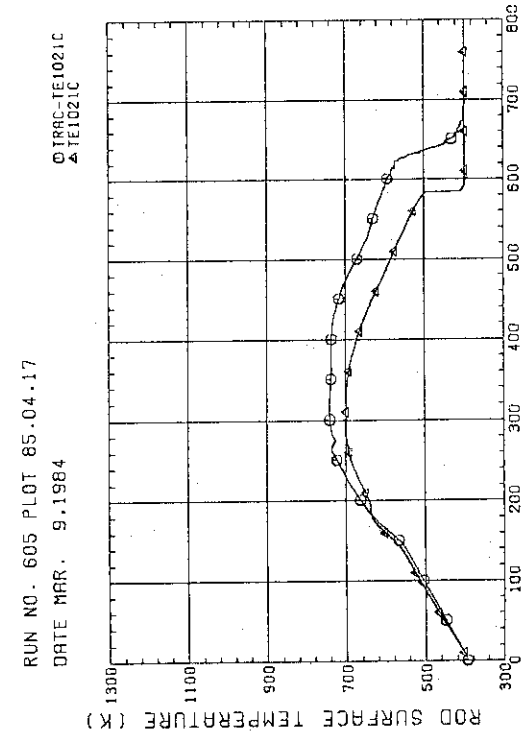

Fig. F-10 HEATER ROD TEMPERATURE (BUNDLE 2 H=5337MM)

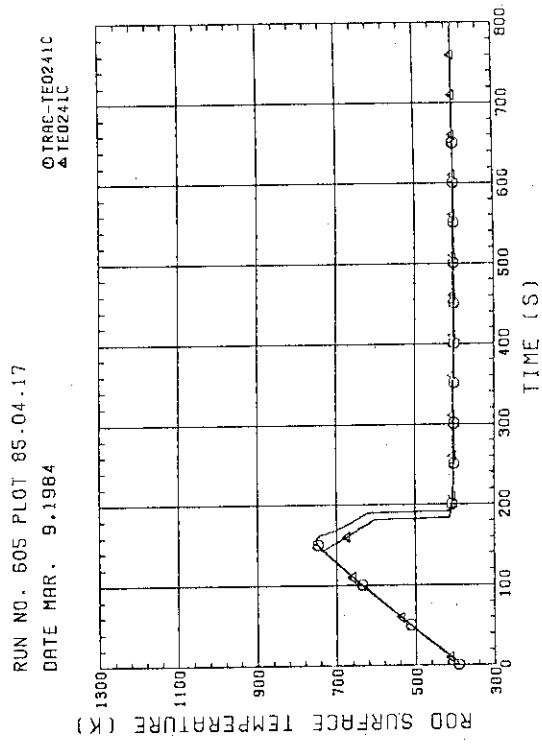

Fig. F-12 HEATER ROD TEMPERATURE (BUNDLE 4 H=2237MM)

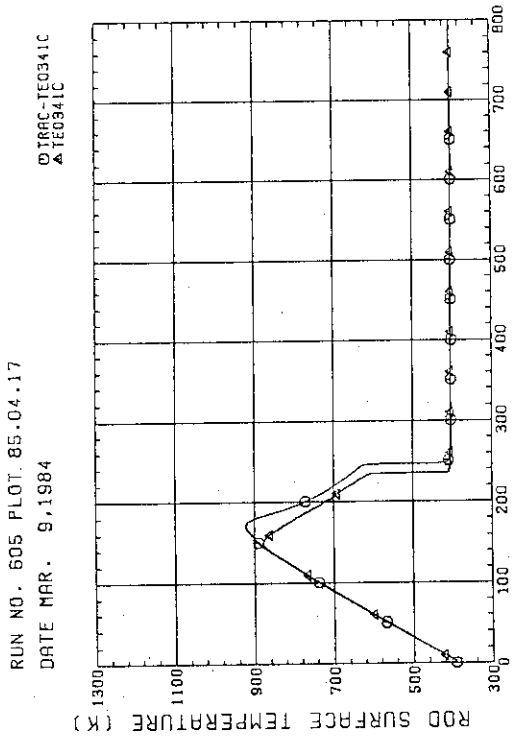

Fig. F-13 HEATER ROD TEMPERATURE (BUNDLE 4 H=2667MM)

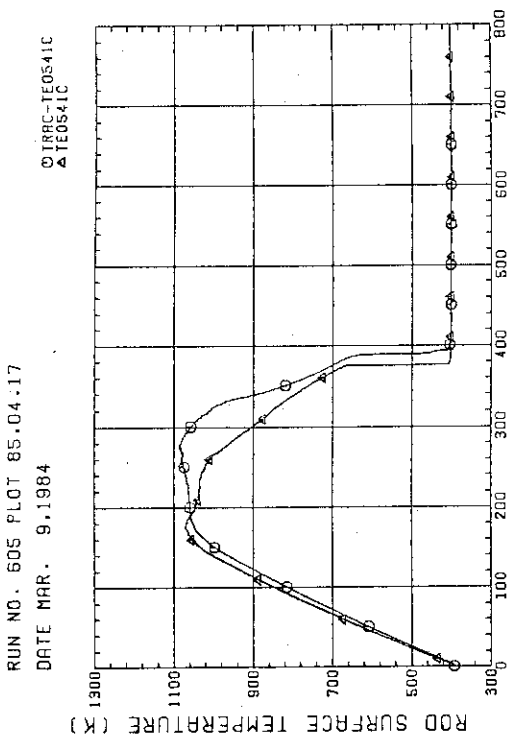

Fig. F-15 HEATER ROD TEMPERATURE (BUNDLE 4 H=3452MM)

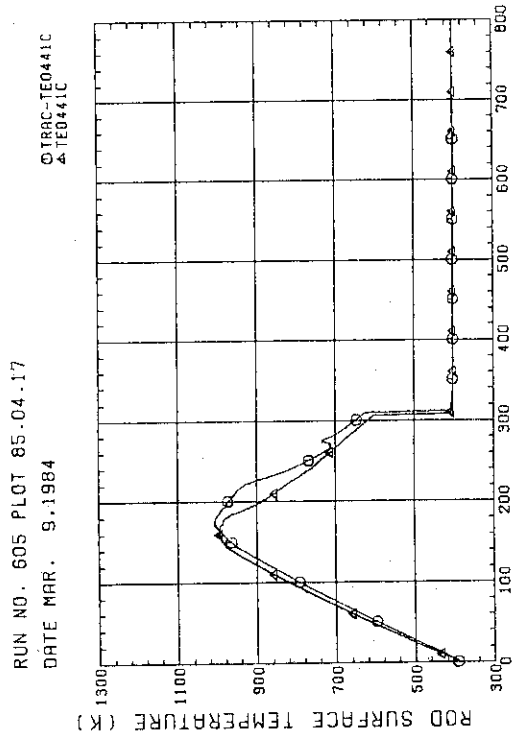

Fig. F-14 HEATER ROD TEMPERATURE (BUNDLE 4 H=3097MM)

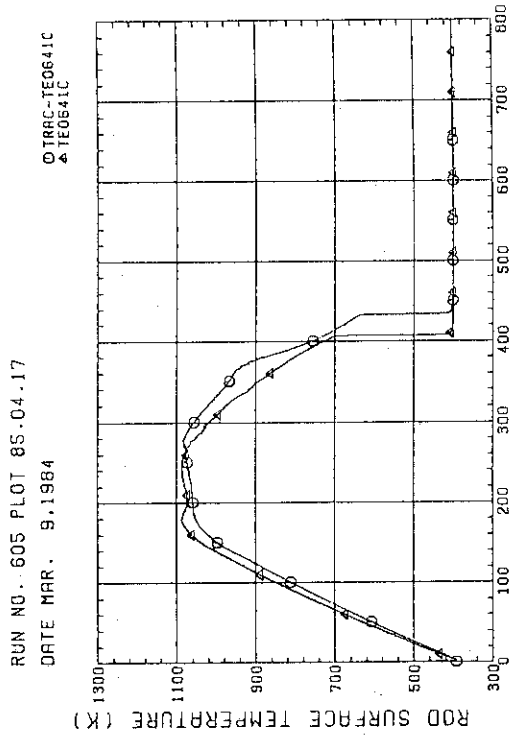

Fig. F-16 HEATER ROD TEMPERATURE (BUNDLE 4 H=3622MM)

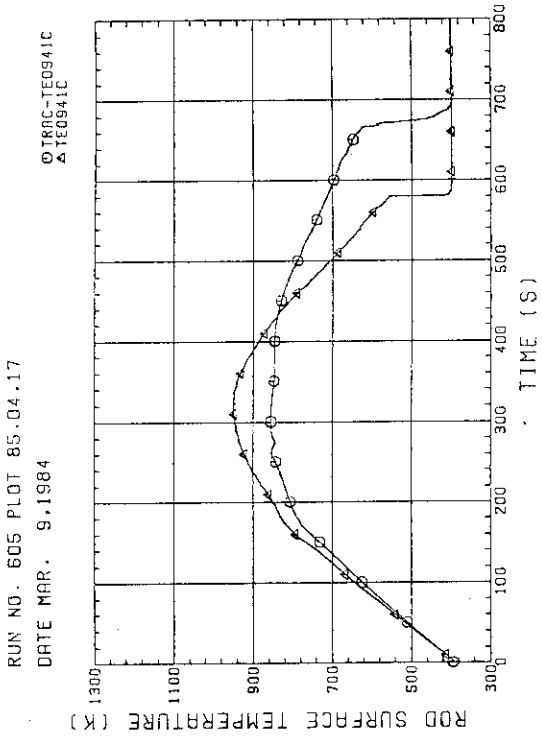

Fig. F-19 HEATER ROD TEMPERATURE (BUNDLE 4 H=4907MM)

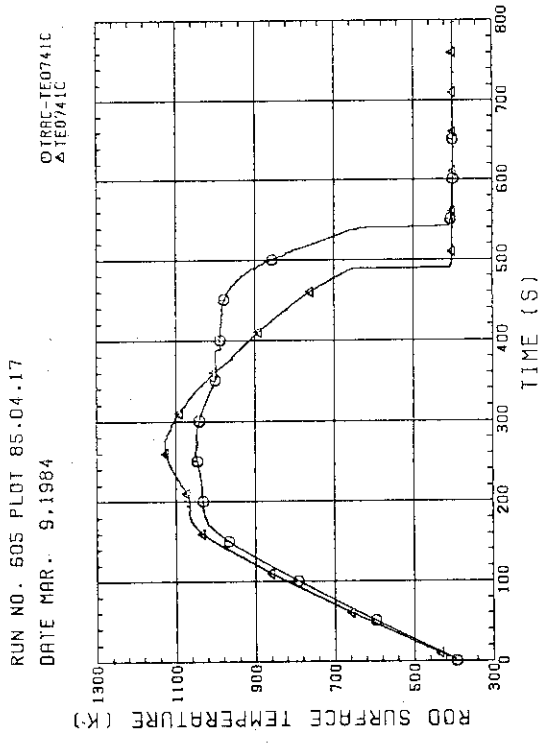

Fig. F-17 HEATER ROD TEMPERATURE (BUNDLE 4 H=4047MM)

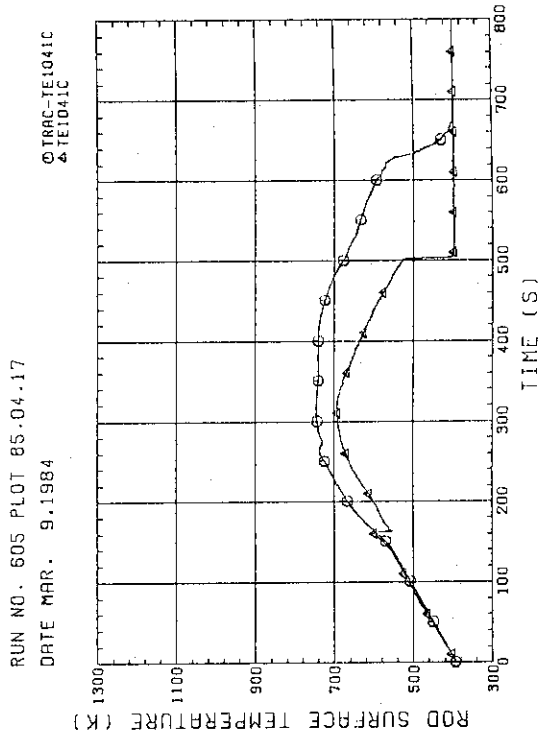

Fig. F-20 HEATER ROD TEMPERATURE (BUNDLE 4 H=5337MM)

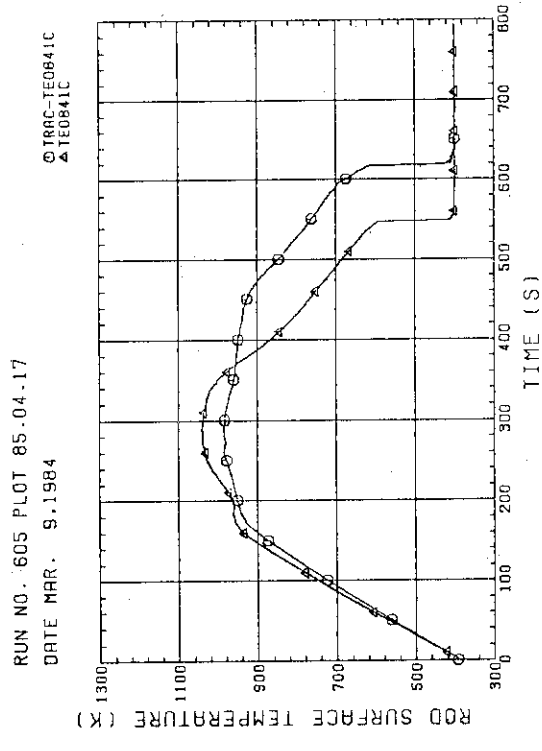

Fig. F-18 HEATER ROD TEMPERATURE (BUNDLE 4 H=4477MM)

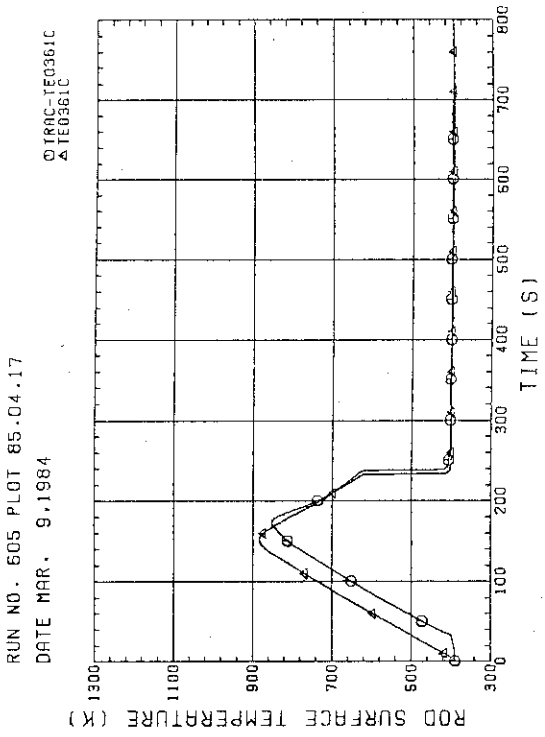

Fig. F-21 HEATER ROD TEMPERATURE (BUNDLE 6 H=1827MM)

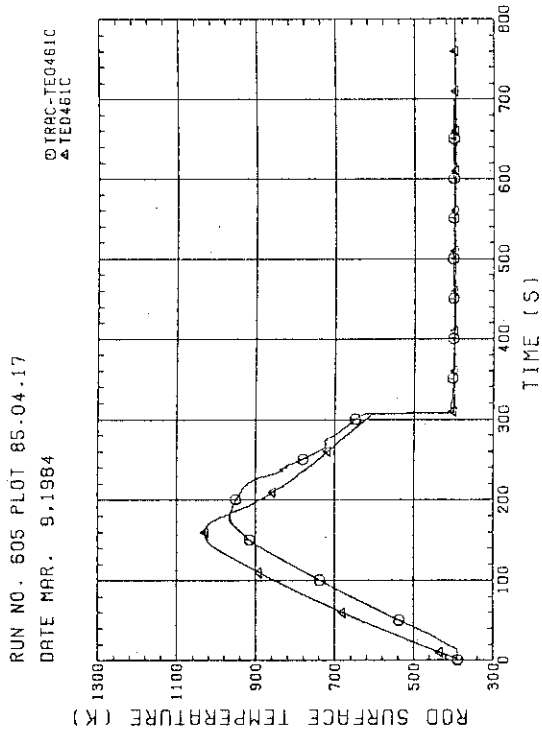

Fig. F-22 HEATER ROD TEMPERATURE (BUNDLE 6 H=2237MM)

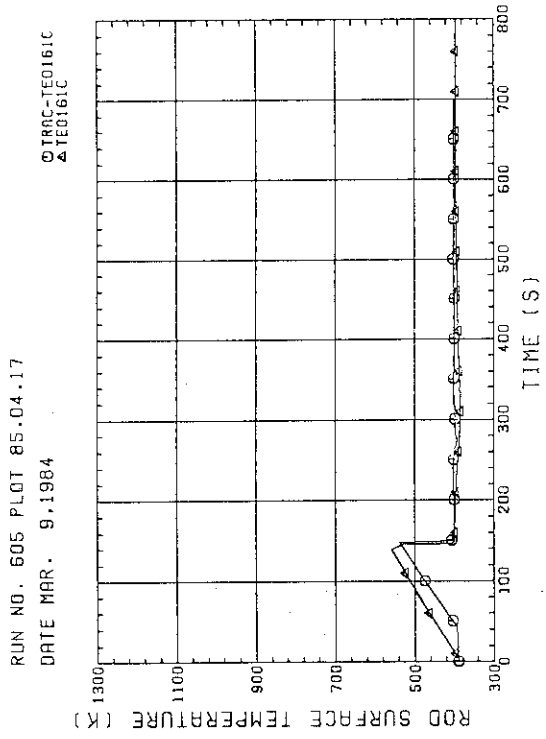

Fig. F-23 HEATER ROD TEMPERATURE (BUNDLE 6 H=2667MM)

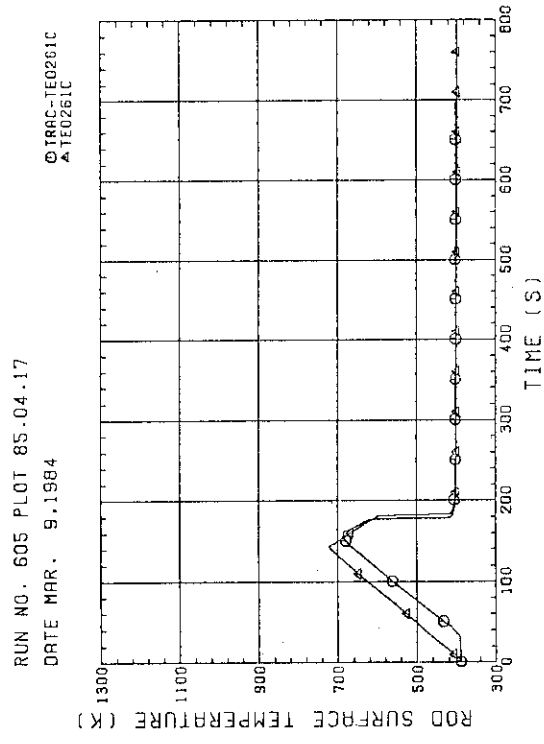

Fig. F-24 HEATER ROD TEMPERATURE (BUNDLE 6 H=3097MM)

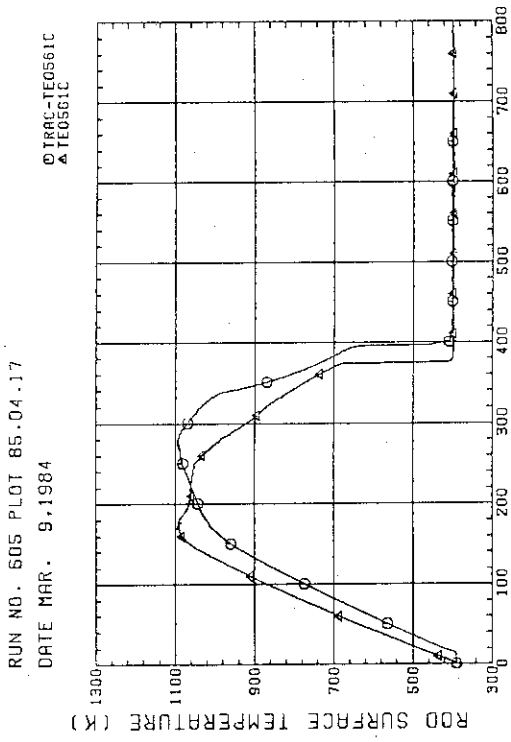

Fig. F-25 HEATER ROD TEMPERATURE (BUNDLE 6 H=3452MM)

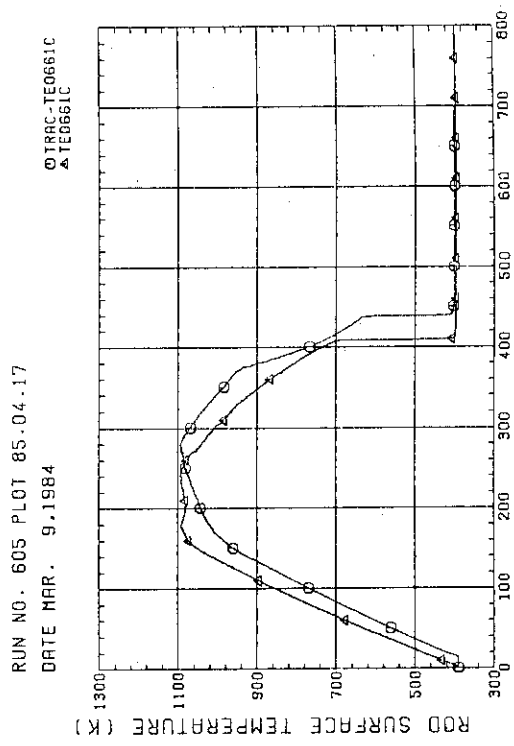

Fig. F-26 HEATER ROD TEMPERATURE (BUNDLE 6 H=3622MM)

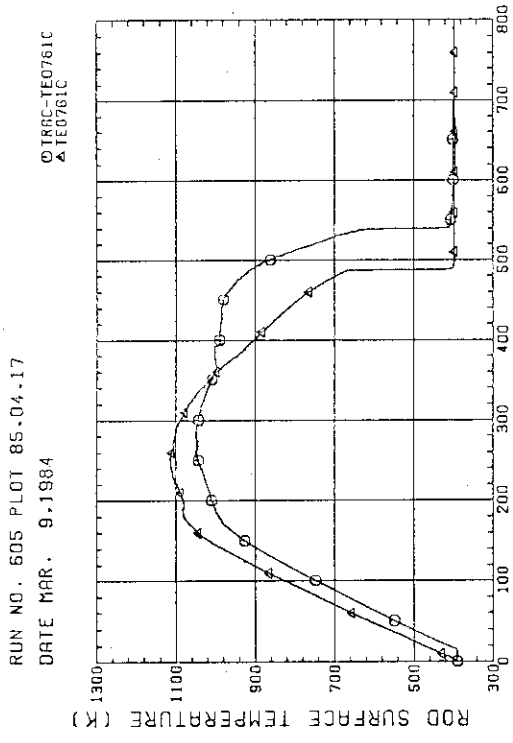

Fig. F-27 HEATER ROD TEMPERATURE (BUNDLE 6 H=4047MM)

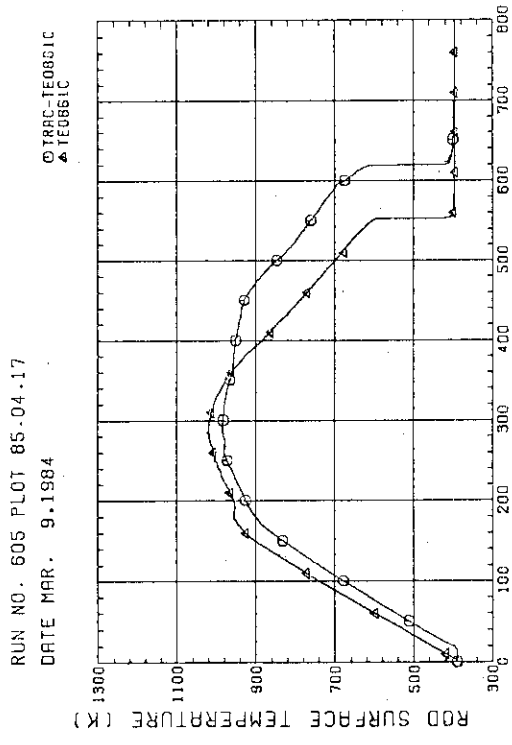

Fig. F-28 HEATER ROD TEMPERATURE (BUNDLE 6 H=4477MM)

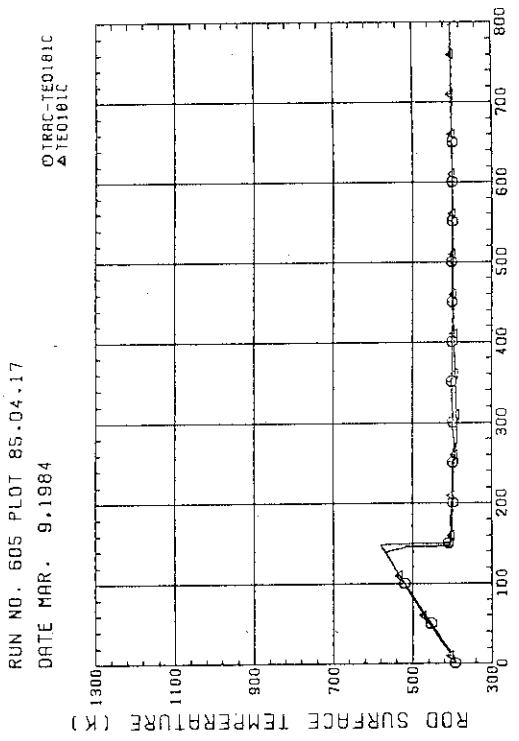

Fig. F-31 HEATER ROD TEMPERATURE (BUNDLE 8 H=1827MM)

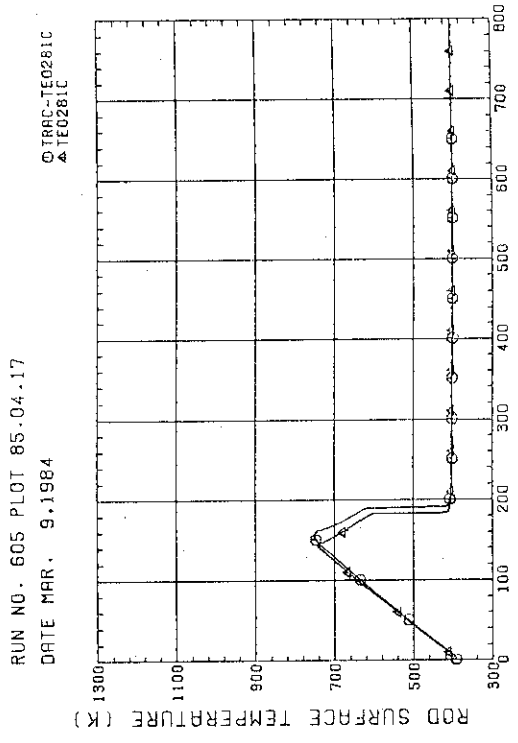

Fig. F-32 HEATER ROD TEMPERATURE (BUNDLE 8 H=2237MM)

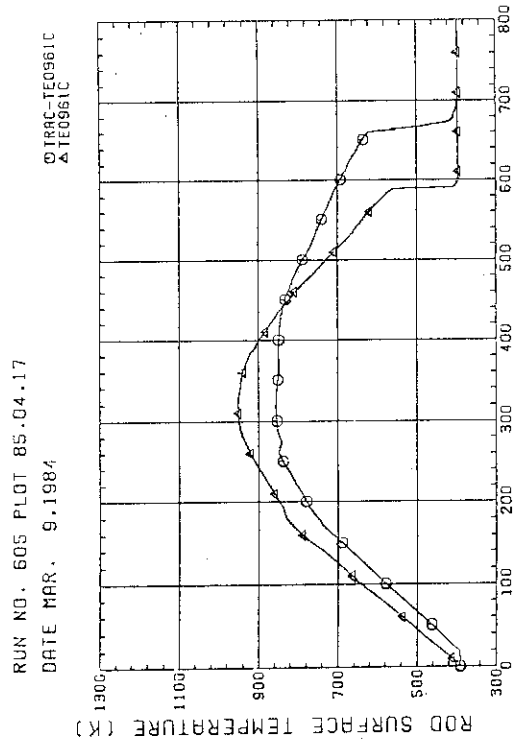

Fig. F-29 HEATER ROD TEMPERATURE (BUNDLE 6 H=4907MM)

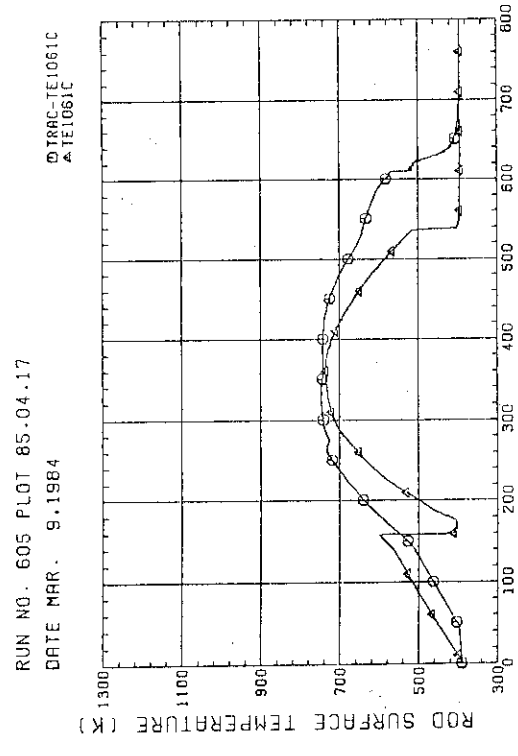

Fig. F-30 HEATER ROD TEMPERATURE (BUNDLE 6 H=5337MM)

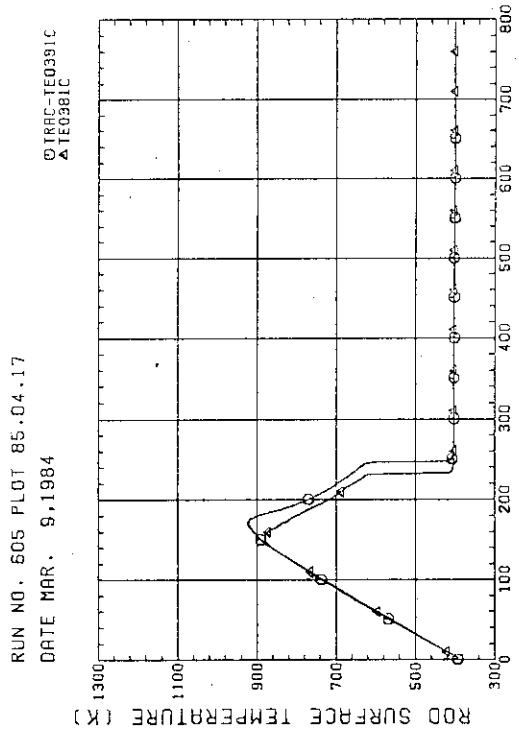

Fig. F-33 HEATER ROD TEMPERATURE (BUNDLE 8 H=2667MM)

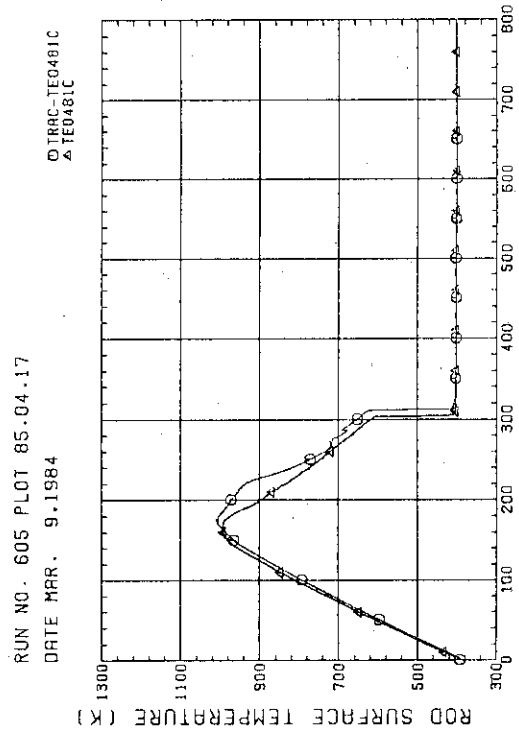

Fig. F-34 HEATER ROD TEMPERATURE (BUNDLE 8 H=3097MM)

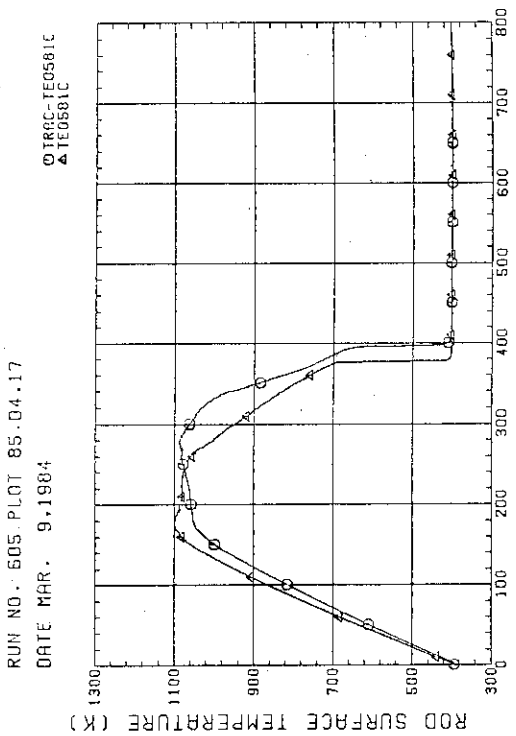

Fig. F-35 HEATER ROD TEMPERATURE (BUNDLE 8 H=3452MM)

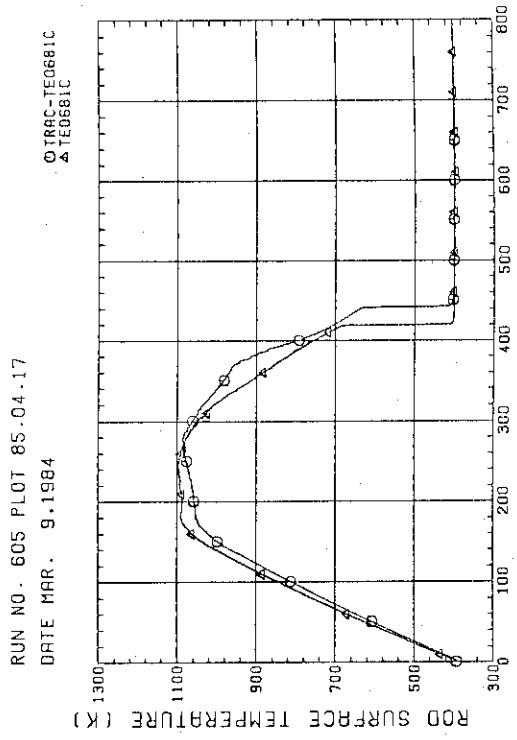

Fig. F-36 HEATER ROD TEMPERATURE (BUNDLE 8 H=3622MM)

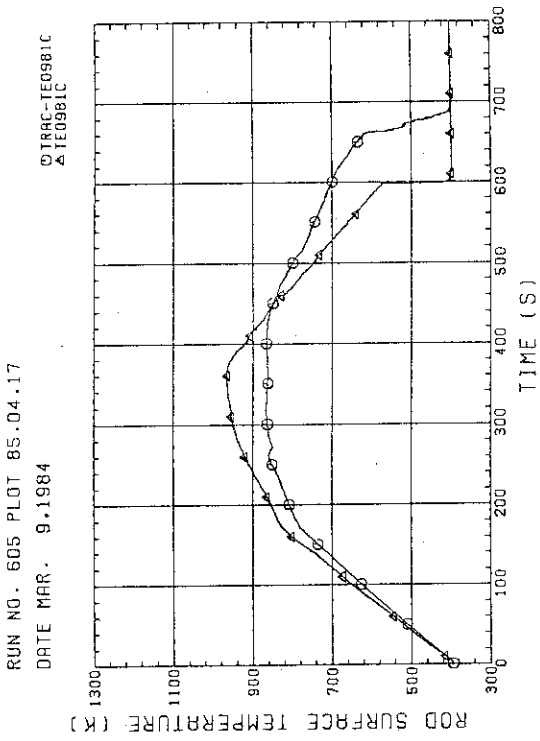

Fig. F-39 HEATER ROD TEMPERATURE (BUNDLE 8 H=4907MM)

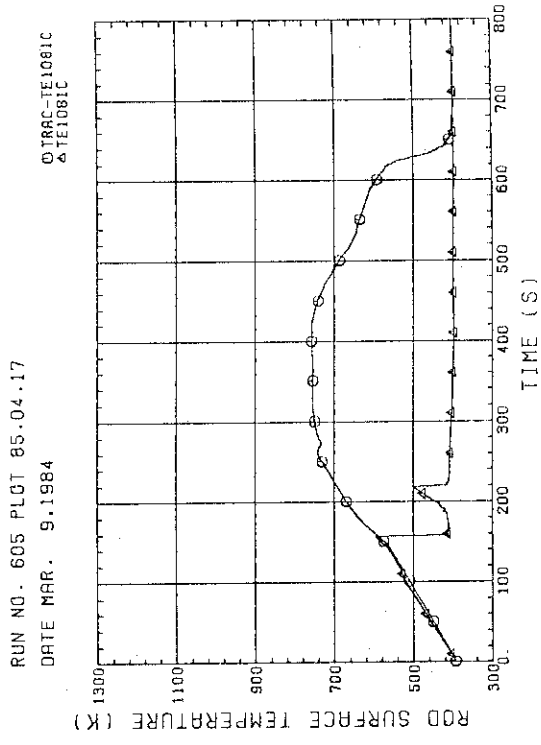

Fig. F-40 HEATER ROD TEMPERATURE (BUNDLE 8 H=5337MM)

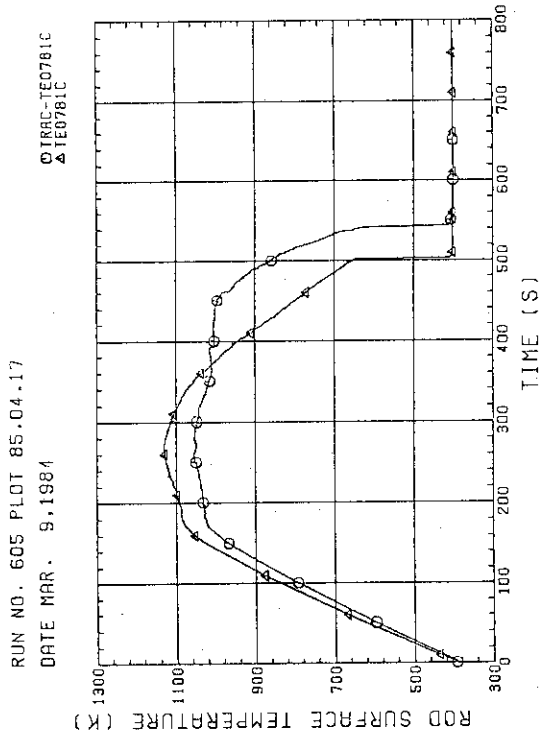

Fig. F-37 HEATER ROD TEMPERATURE (BUNDLE 8 H=4047MM)

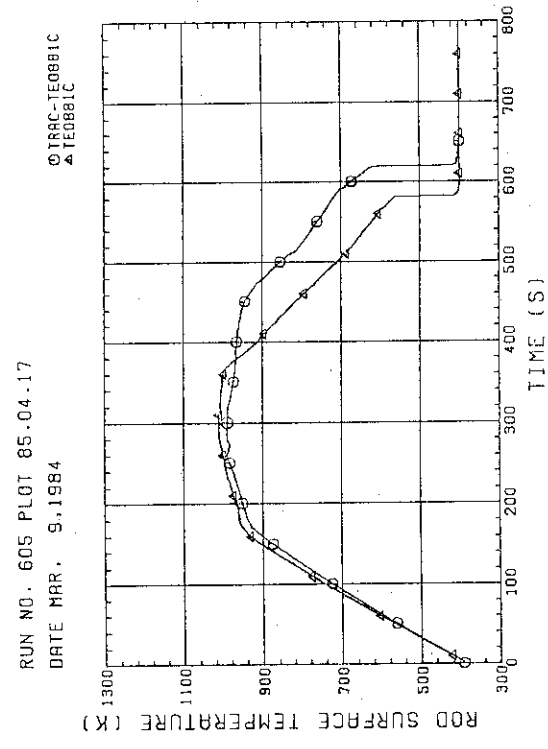

Fig. F-38 HEATER ROD TEMPERATURE (BUNDLE 8 H=4477MM)

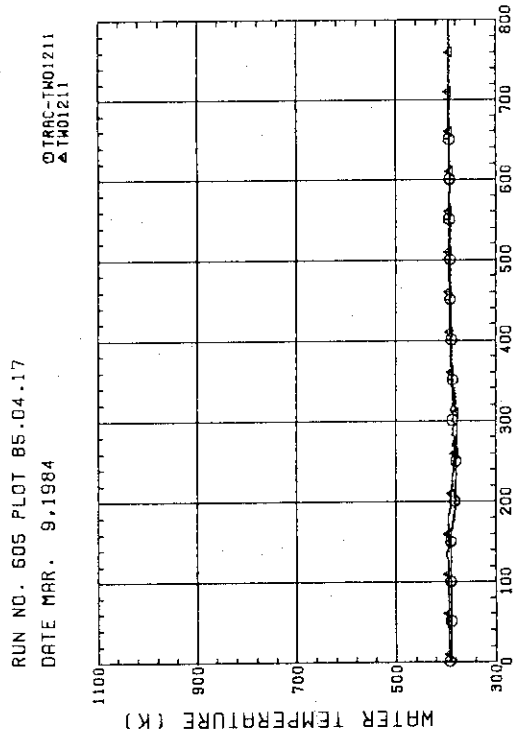

FIG. F-41 WATER TEMPERATURE (BUNDLE 2 H= 0MM)

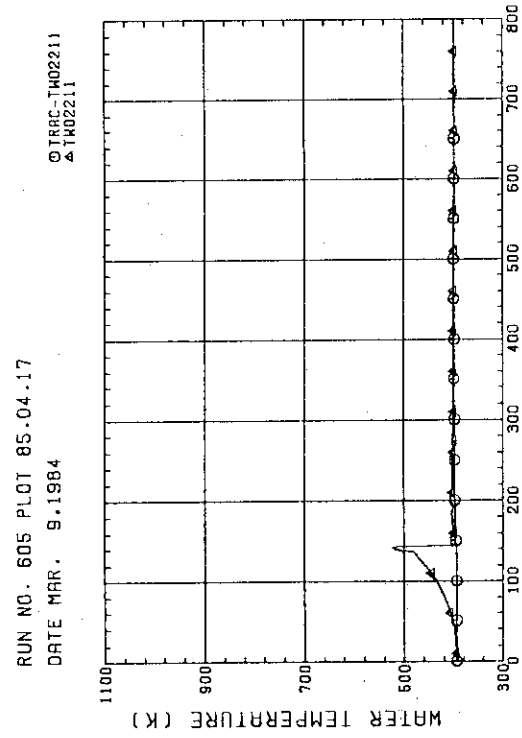

Fig. F-42 WATER TEMPERATURE (BUNDLE 2 H= 950MM)

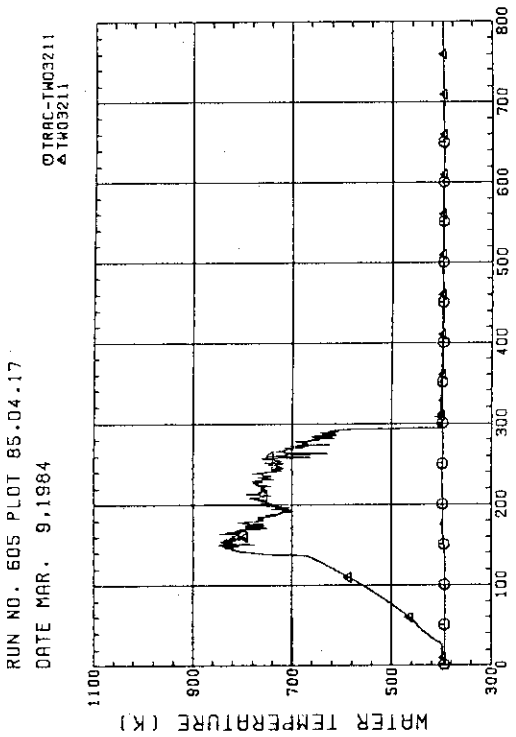

Fig. F-43 WATER TEMPERATURE (BUNDLE 2 H=1735MM)

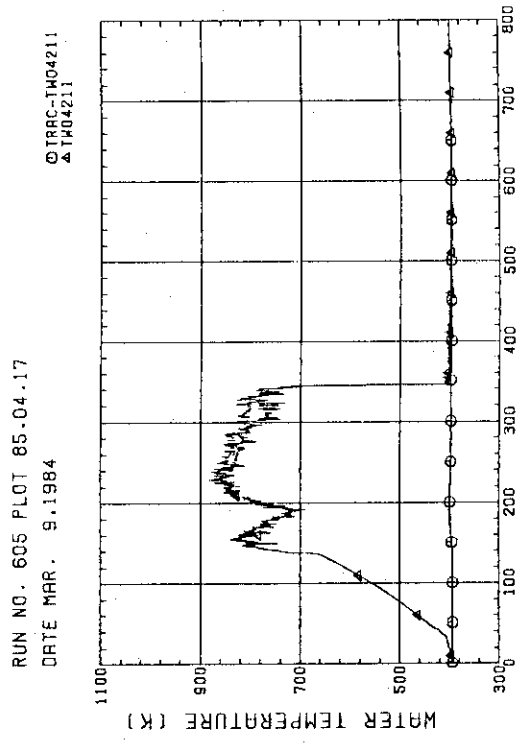

Fig. F-44 WATER TEMPERATURE (BUNDLE 2 H=1905MM)

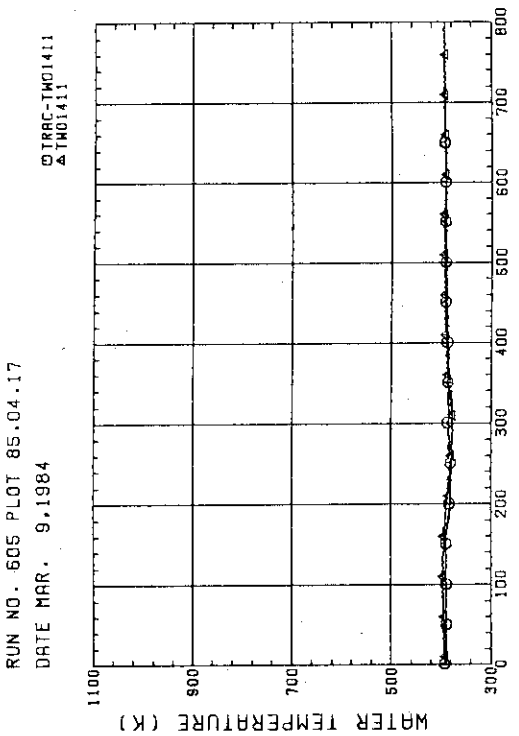

Fig. F-45 WATER TEMPERATURE (BUNDLE 2 H=2760MM)

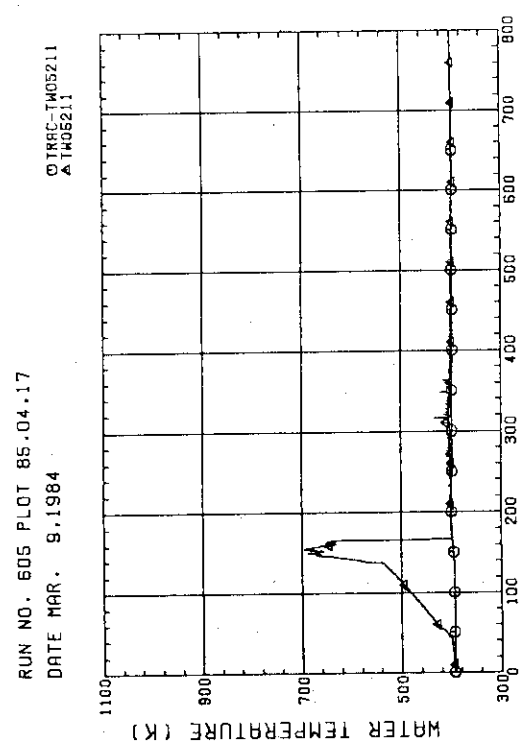

Fig. F-46 WATER TEMPERATURE (BUNDLE 2 H=3660MM)

Fig. F-47 WATER TEMPERATURE (BUNDLE 4 H= 0MM)

Fig. F-48 WATER TEMPERATURE (BUNDLE 4 H= 950MM)

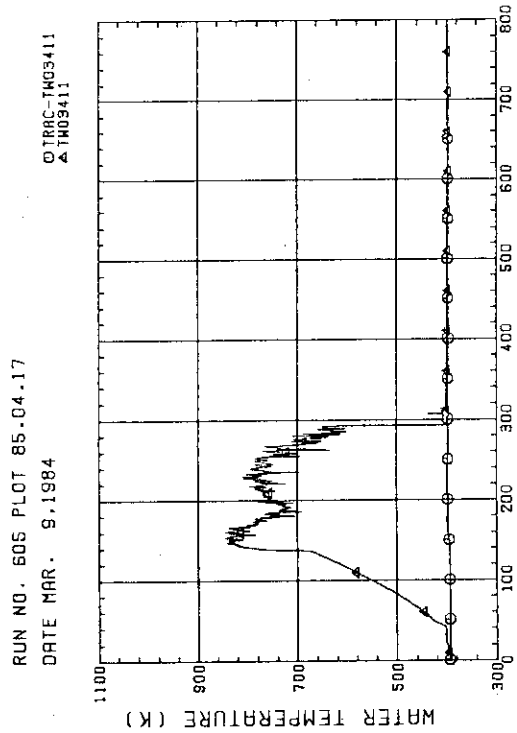

Fig. F-49 WATER TEMPERATURE (BUNDLE 4 H=1735MM)

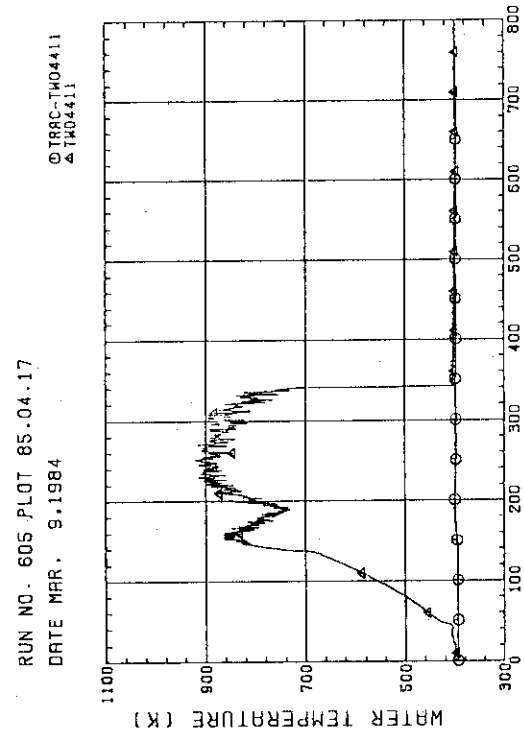

Fig. F-50 WATER TEMPERATURE (BUNDLE 4 H=1905MM)

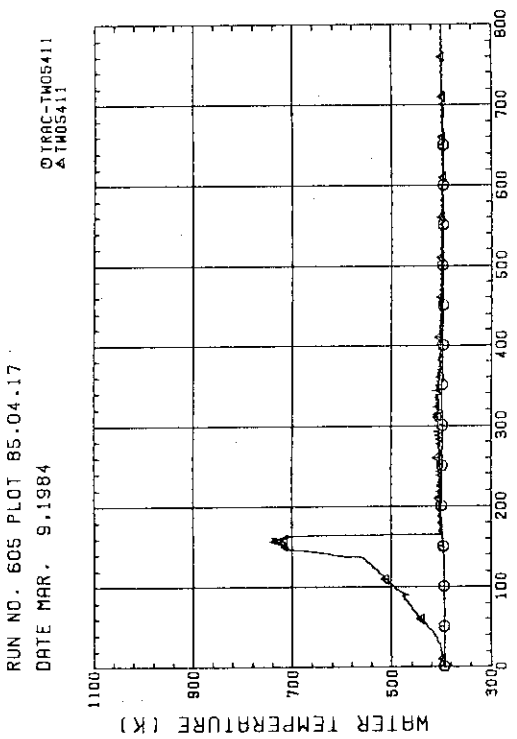

Fig. F-51 WATER TEMPERATURE (BUNDLE 4 H=2760MM)

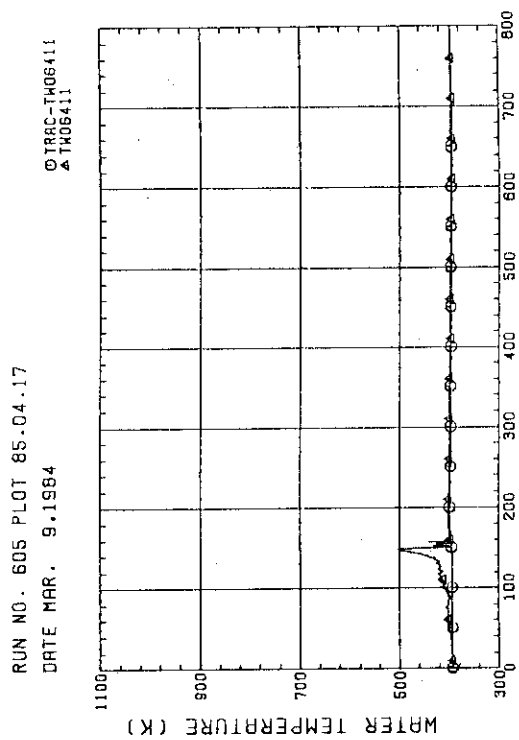

Fig. F-52 WATER TEMPERATURE (BUNDLE 4 H=3660MM)

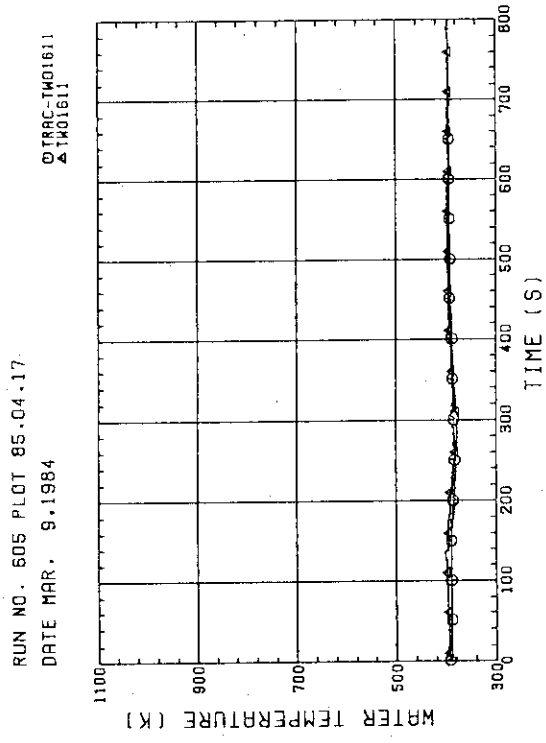

Fig. F-53 WATER TEMPERATURE (BUNDLE 6 H= 0MM)

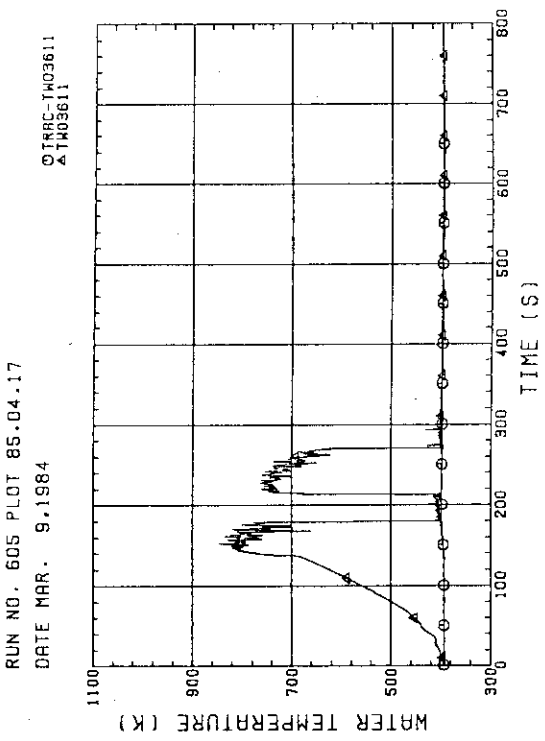

Fig. F-55 WATER TEMPERATURE (BUNDLE 6 H=1735MM)

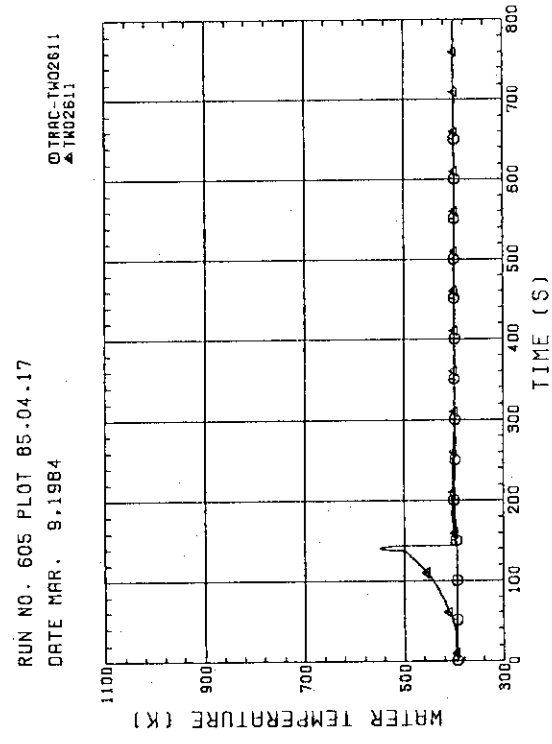

Fig. F-54 WATER TEMPERATURE (BUNDLE 6 H= 950MM)

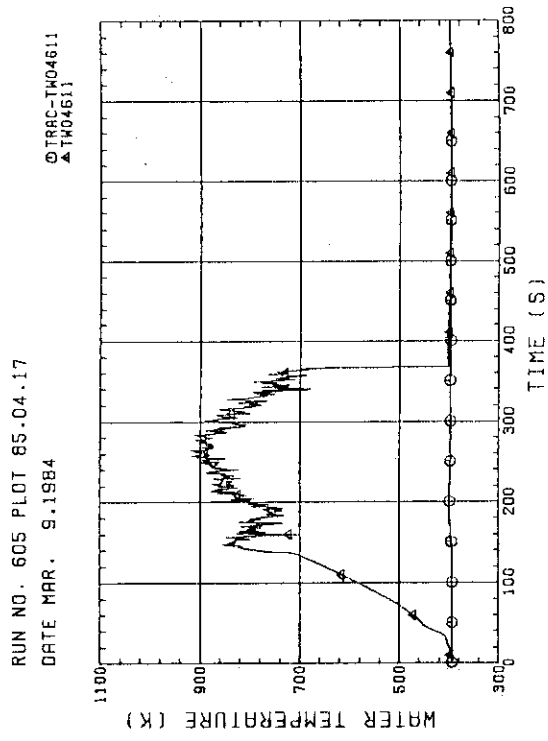

Fig. F-56 WATER TEMPERATURE (BUNDLE 6 H=1905MM)

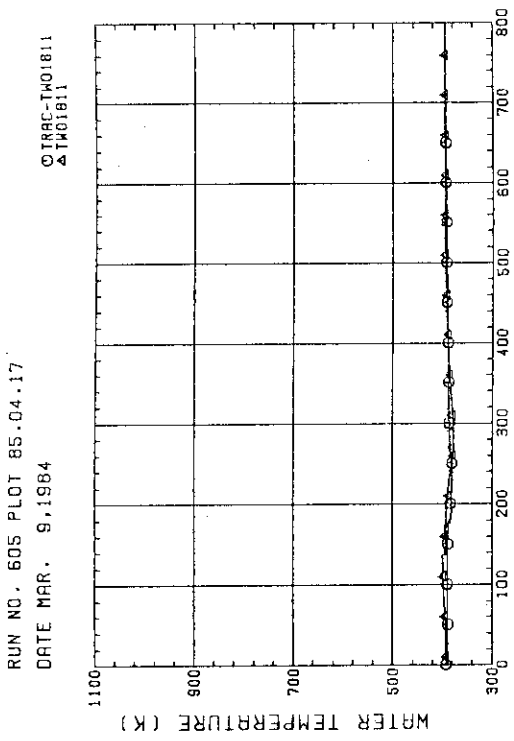

Fig. F-57 WATER TEMPERATURE (BUNDLE 6 H=2760MM)

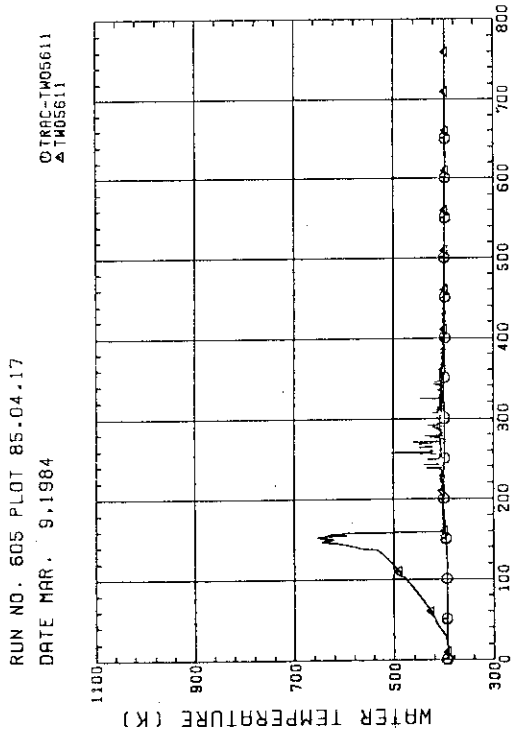

Fig. F-58 WATER TEMPERATURE (BUNDLE 6 H=3660MM)

Fig. F-59 WATER TEMPERATURE (BUNDLE 8 H= 0MM)

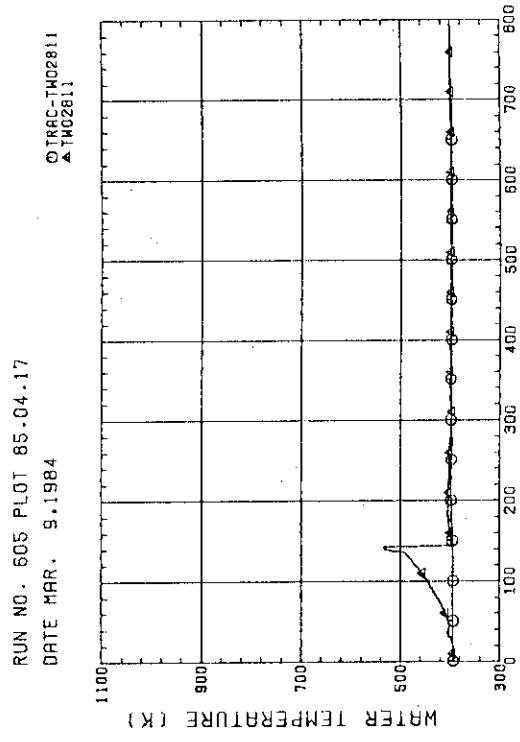

Fig. F-60 WATER TEMPERATURE (BUNDLE 8 H= 950MM)

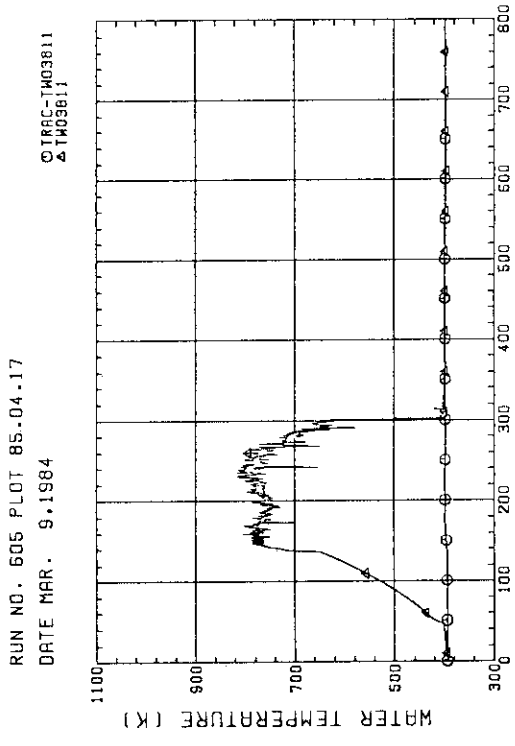

Fig. F-61 WATER TEMPERATURE (BUNDLE 8 H=1735MM)

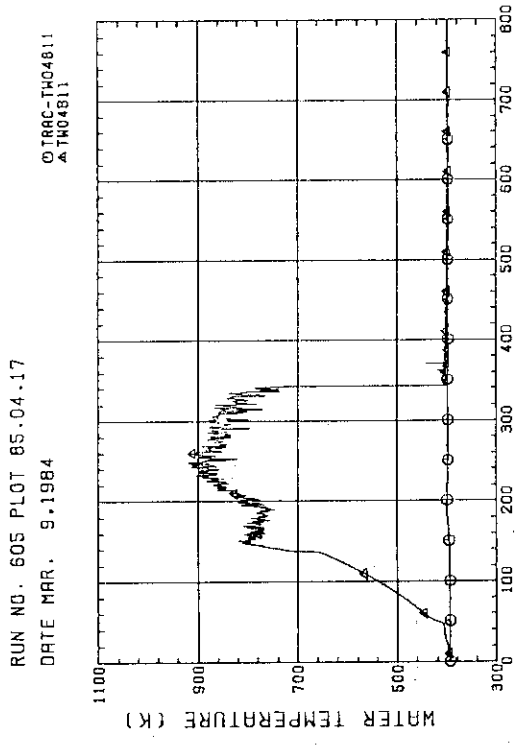

Fig. F-62 WATER TEMPERATURE (BUNDLE 8 H=1905MM)

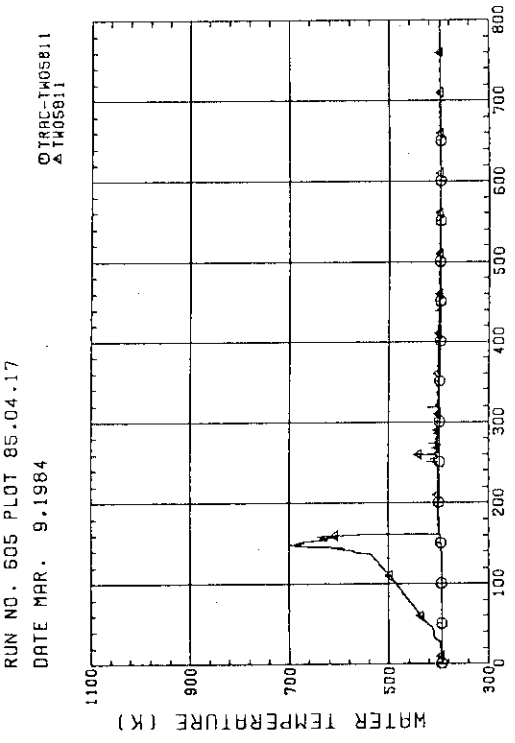

Fig. F-63 WATER TEMPERATURE (BUNDLE 8 H=2760MM)

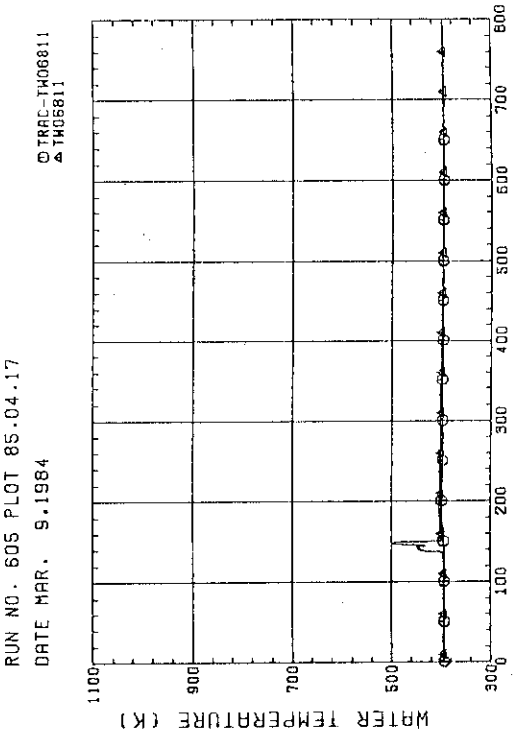

Fig. F-64 WATER TEMPERATURE (BUNDLE 8 H=3660MM)

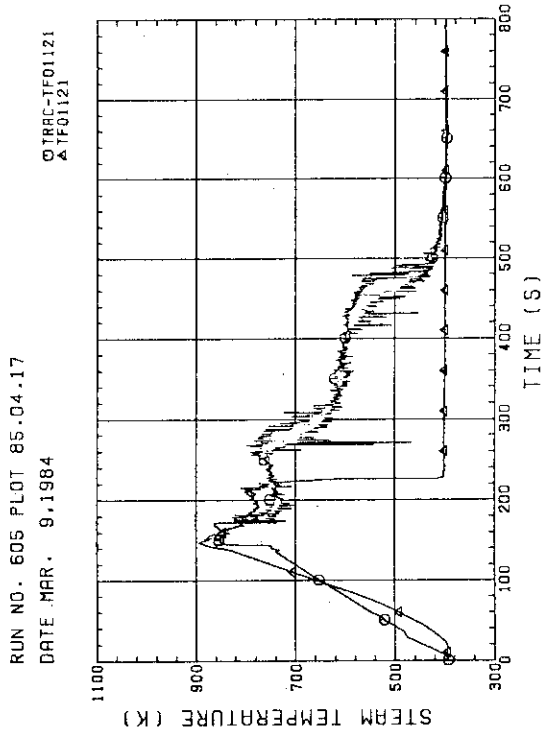

Fig. F-65 STEAM TEMPERATURE (BUNDLE 1 H=1915MM)

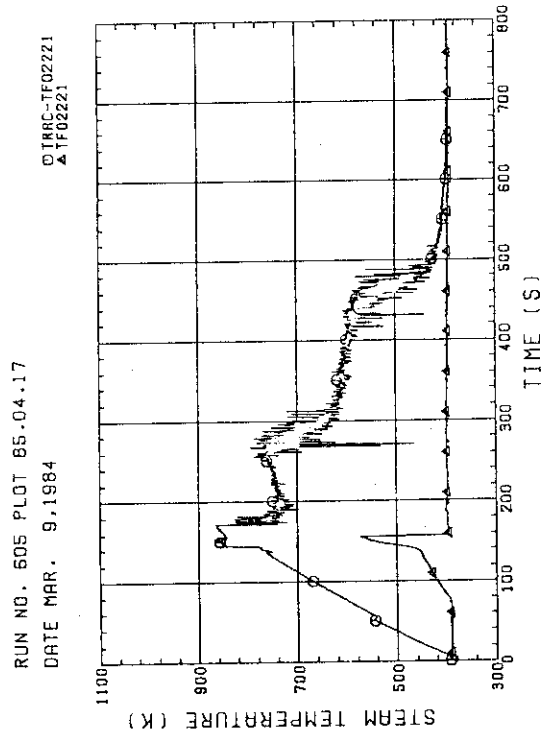

Fig. F-66 STEAM TEMPERATURE (BUNDLE 2 H=1915MM)

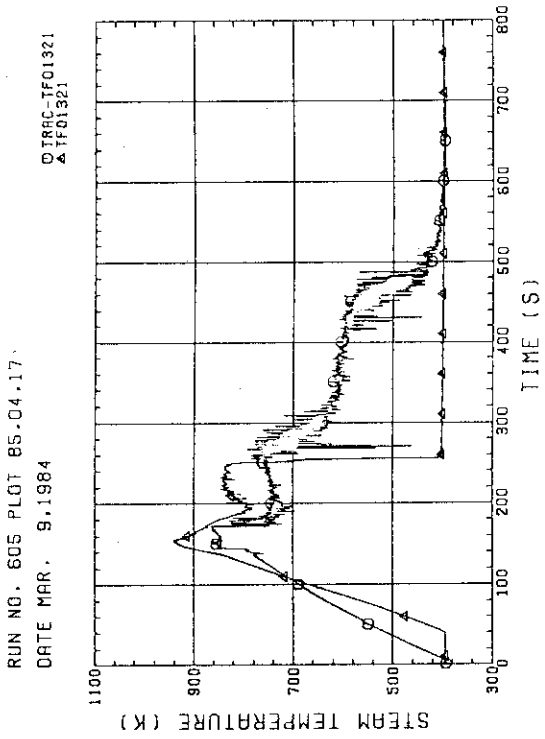

Fig. F-67 STEAM TEMPERATURE (BUNDLE 3 H=1915MM)

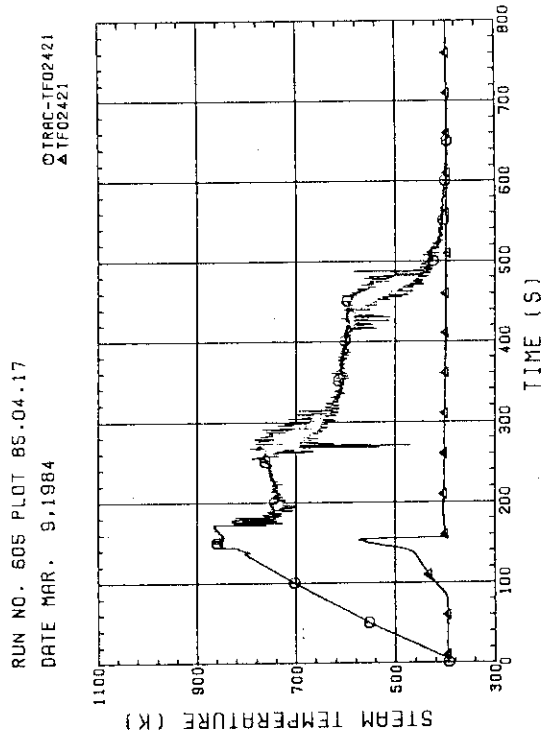

Fig. F-68 STEAM TEMPERATURE (BUNDLE 4 H=1915MM)

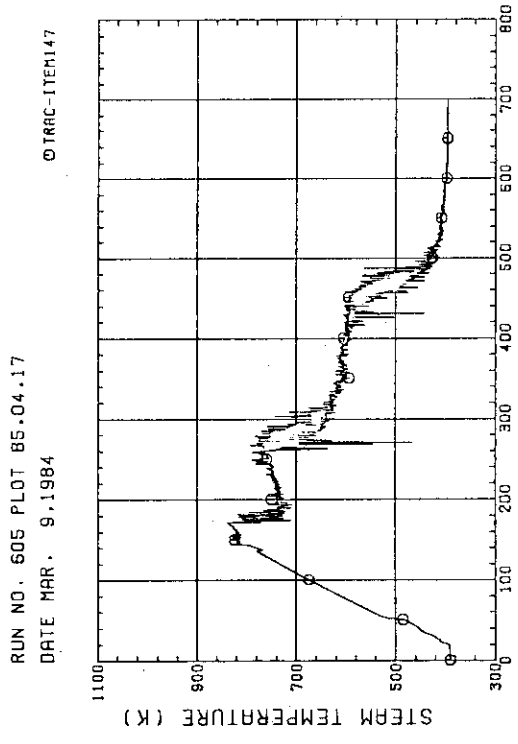

Fig. F-69 STEAM TEMPERATURE (BUNDLE 5 H=1915MM)

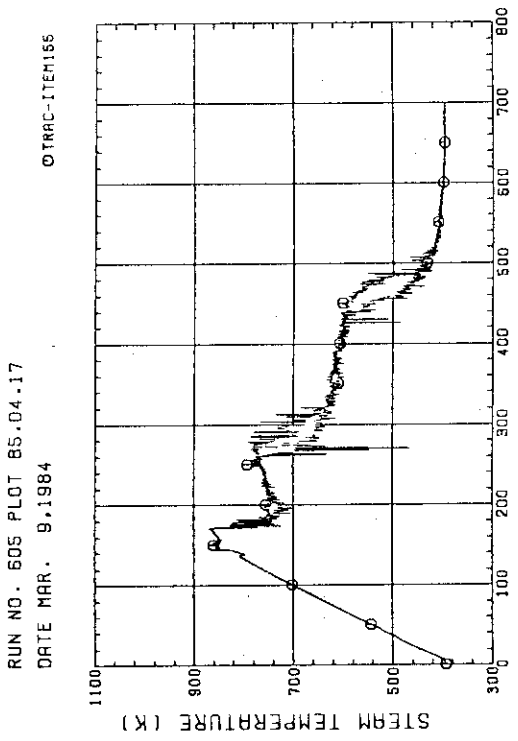

Fig. F-71 STEAM TEMPERATURE (BUNDLE 7 H=1915MM)

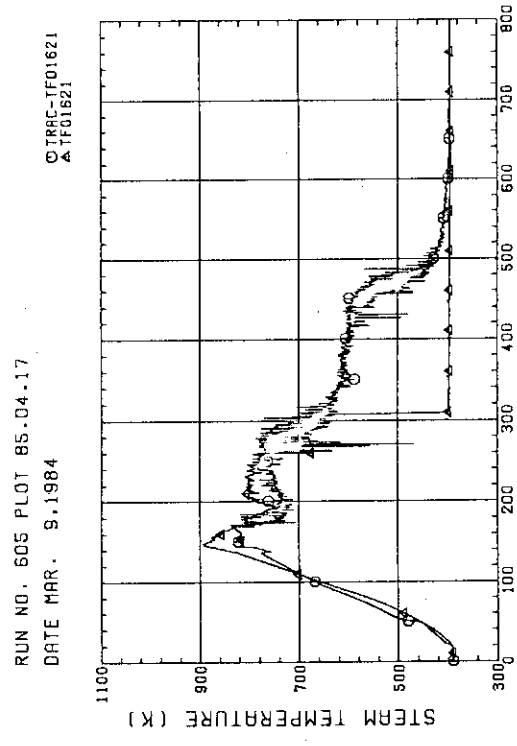

Fig. F-70 STEAM TEMPERATURE (BUNDLE 6 H=1915MM)

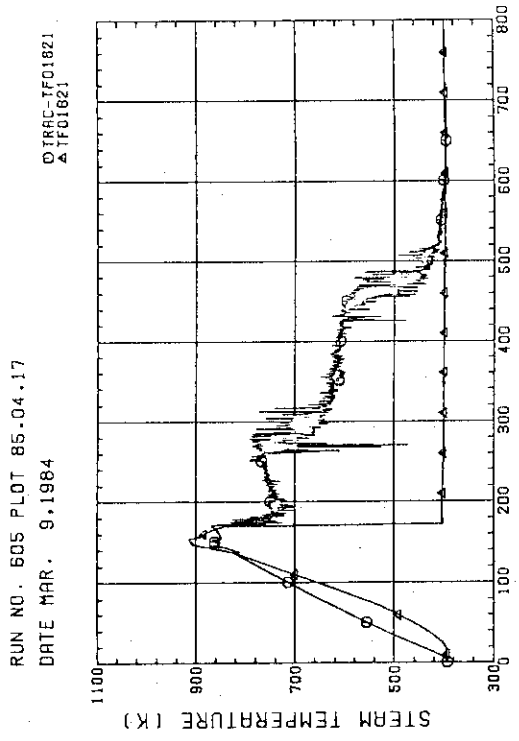

Fig. F-72 STEAM TEMPERATURE (BUNDLE 8 H=1915MM)

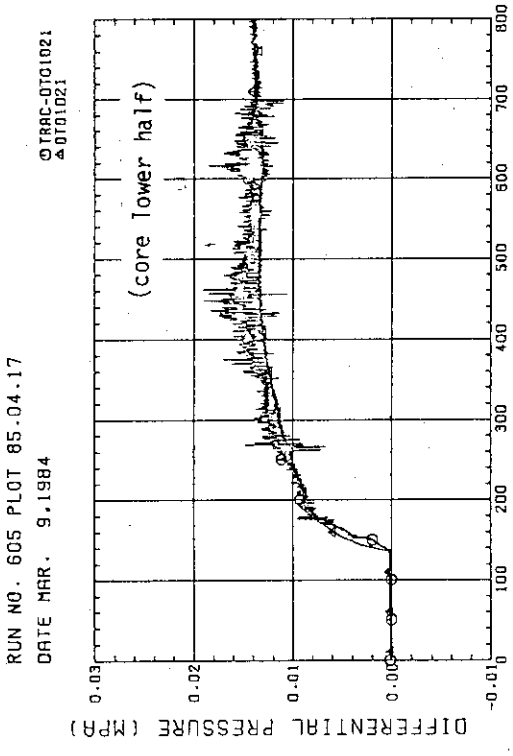

Fig. F-73 VERTICAL DIFFERENTIAL PRESSURE (BUNDLE 2)

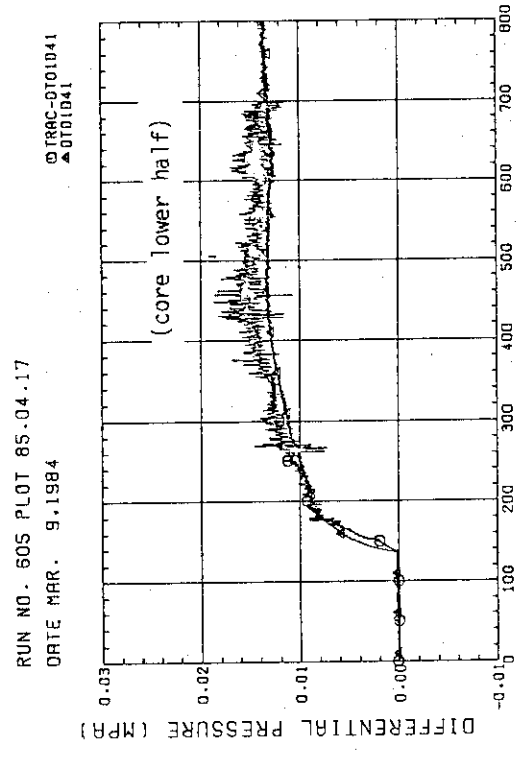

Fig. F-74 VERTICAL DIFFERENTIAL PRESSURE (BUNDLE 4)

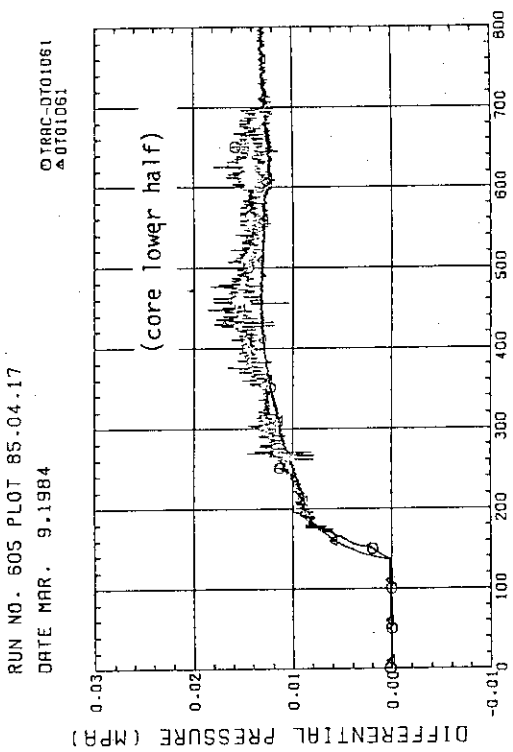

Fig. F-75 VERTICAL DIFFERENTIAL PRESSURE (BUNDLE 6)

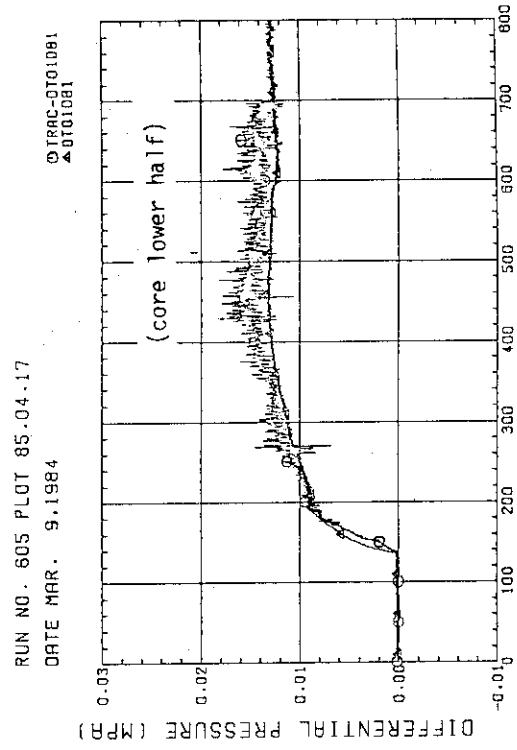

Fig. F-76 VERTICAL DIFFERENTIAL PRESSURE (BUNDLE 8)

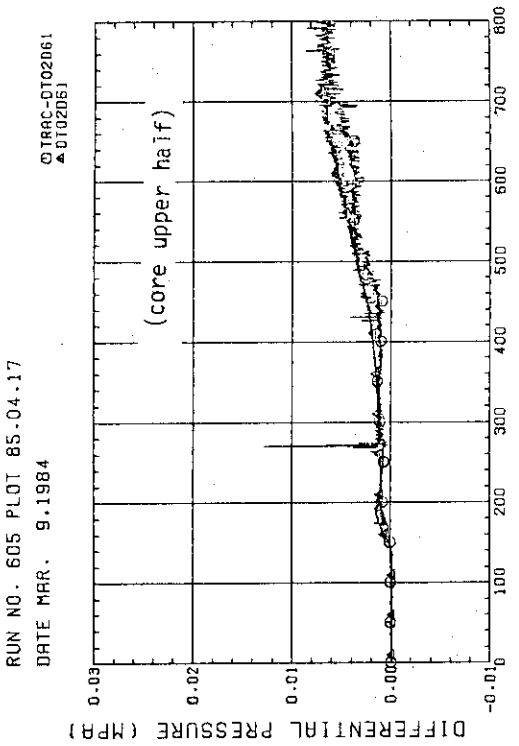

Fig. F-79 VERTICAL DIFFERENTIAL PRESSURE (BUNDLE 6)

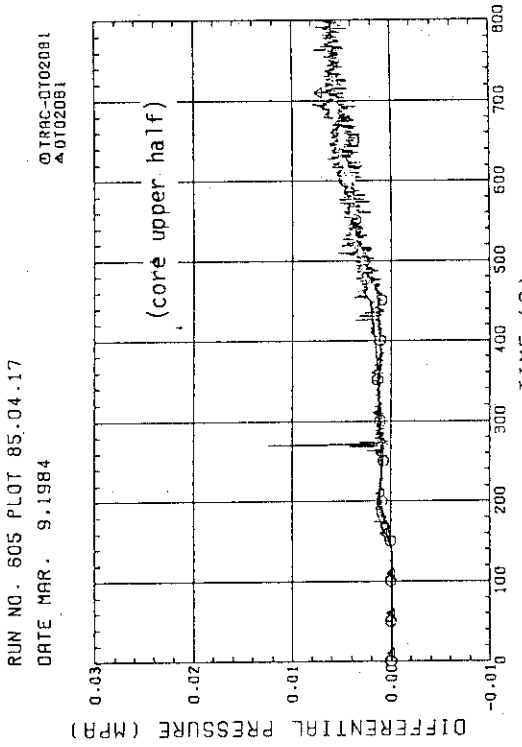

Fig. F-80 VERTICAL DIFFERENTIAL PRESSURE (BUNDLE 8)

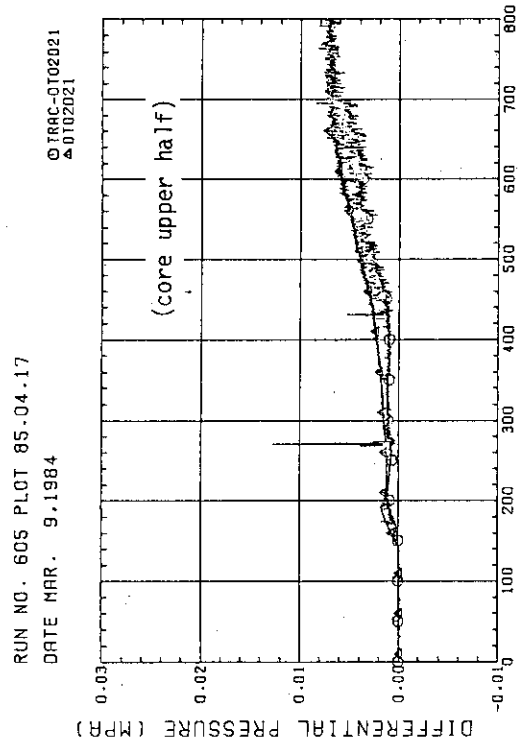

Fig. F-77 VERTICAL DIFFERENTIAL PRESSURE (BUNDLE 2)

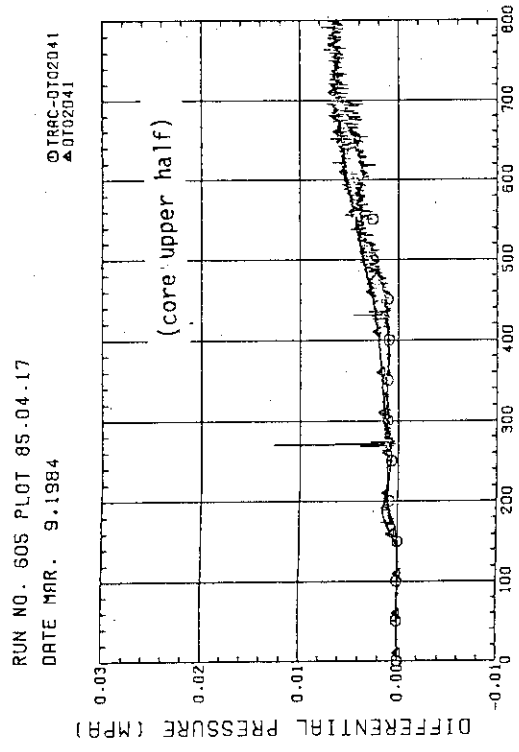

Fig. F-78 VERTICAL DIFFERENTIAL PRESSURE (BUNDLE 4)

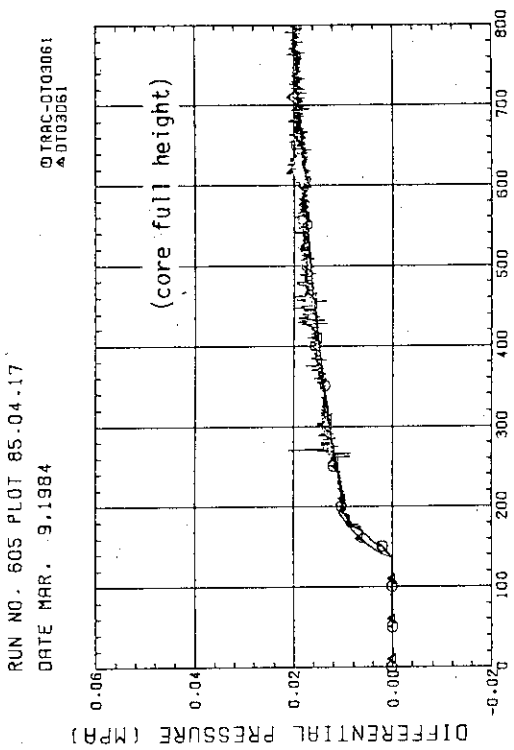

Fig. F-83 VERTICAL DIFFERENTIAL PRESSURE (BUNDLE 6)

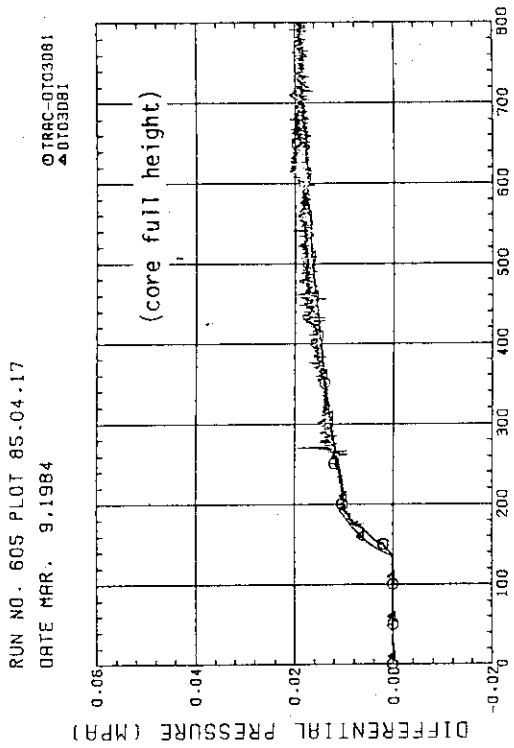

Fig. F-84 VERTICAL DIFFERENTIAL PRESSURE (BUNDLE 8)

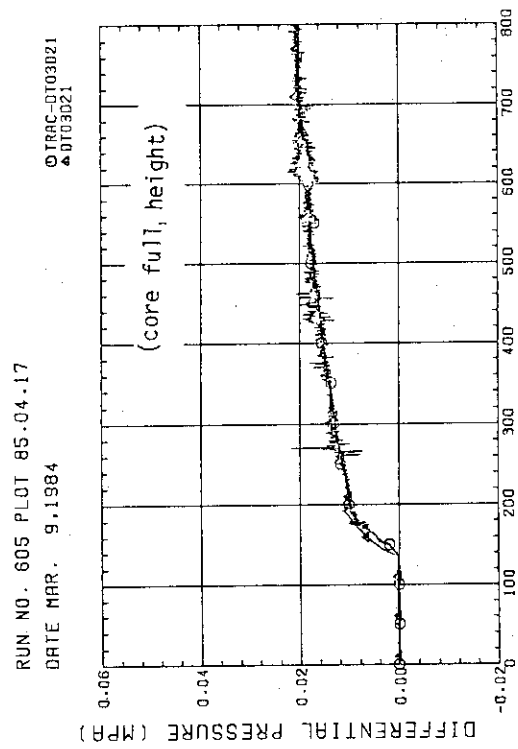

Fig. F-81 VERTICAL DIFFERENTIAL PRESSURE (BUNDLE 2)

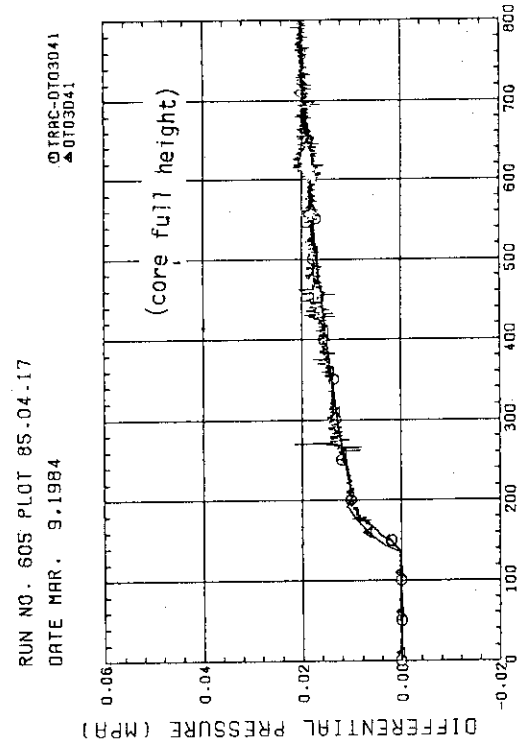

Fig. F-82 VERTICAL DIFFERENTIAL PRESSURE (BUNDLE 4)

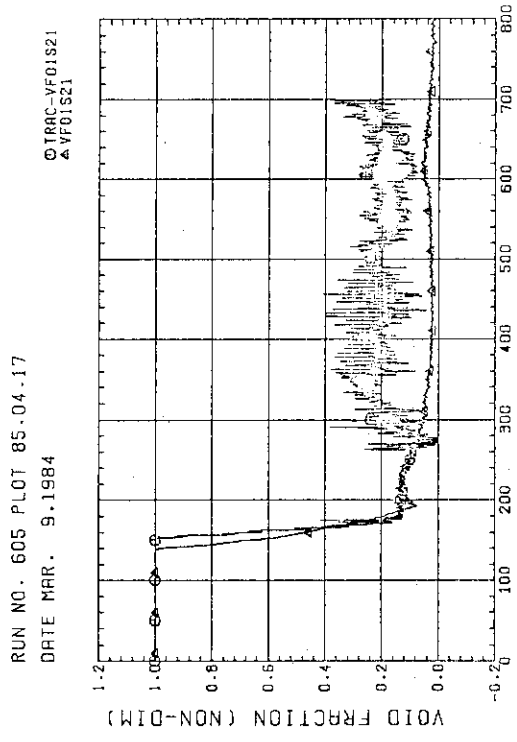

Fig. F-85 VOID FRACTION (BUNDLE 2)

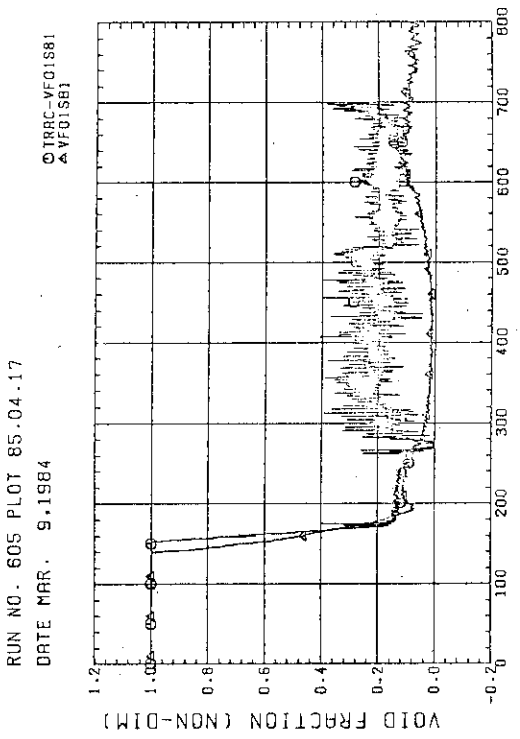

Fig. F-87 VOID FRACTION (BUNDLE 8)

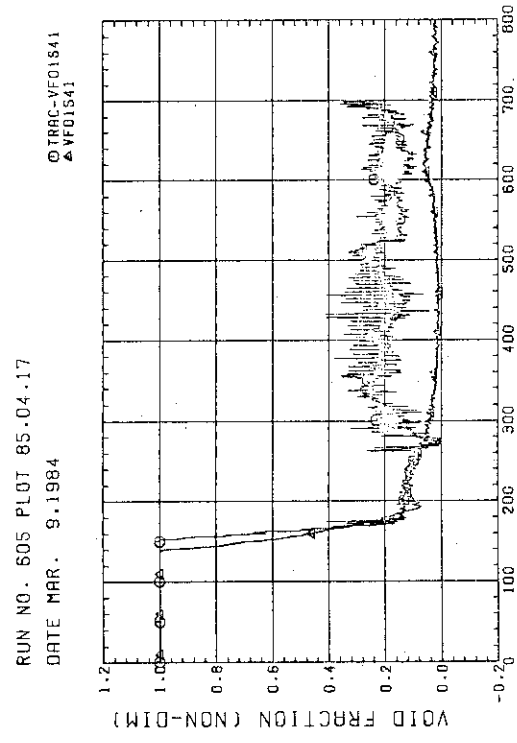

Fig. F-86 VOID FRACTION (BUNDLE 4)

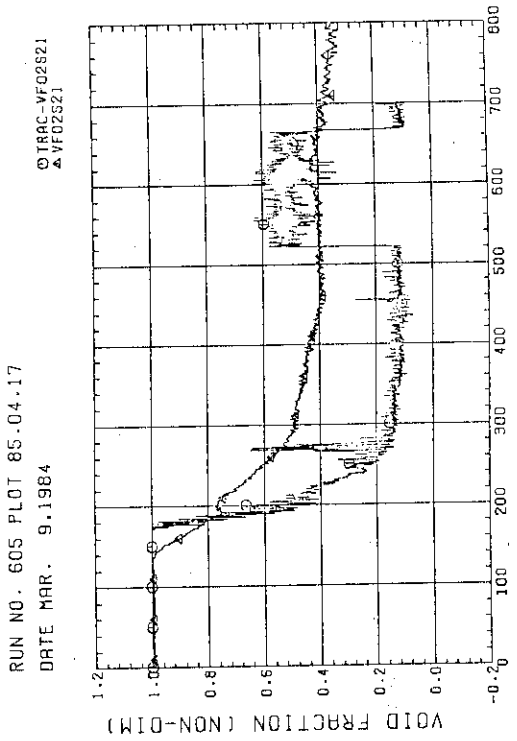

Fig. F-88 VOID FRACTION (BUNDLE 2)

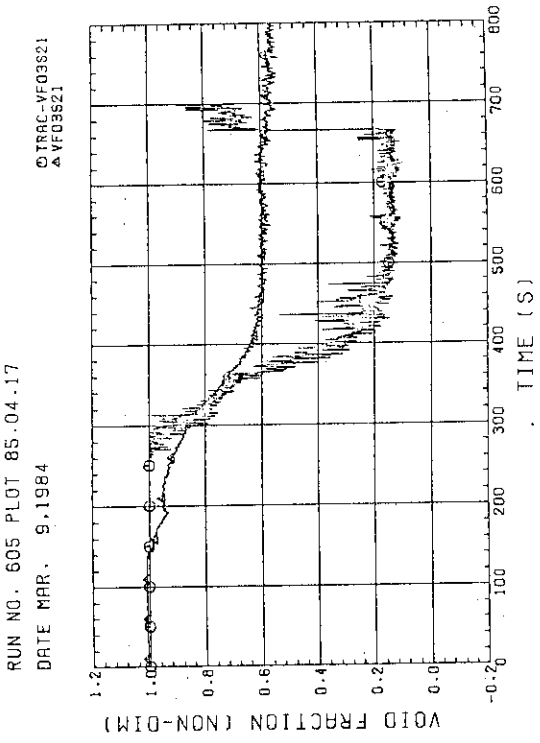

Fig. F-91 VOID FRACTION (BUNDLE 2)

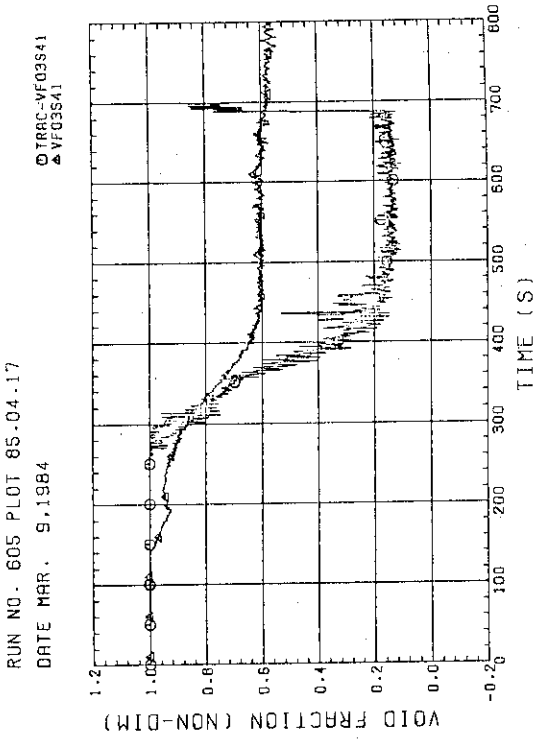

Fig. F-92 VOID FRACTION (BUNDLE 4)

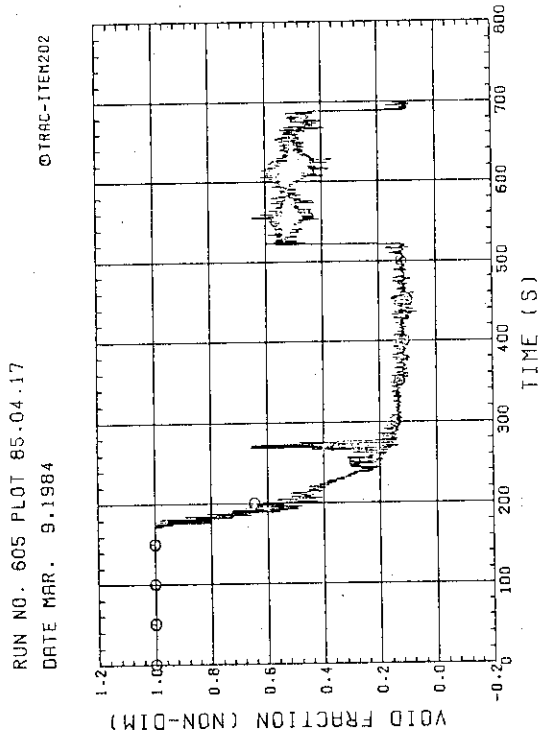

Fig. F-89 VOID FRTACTION (BUNDLE 4)

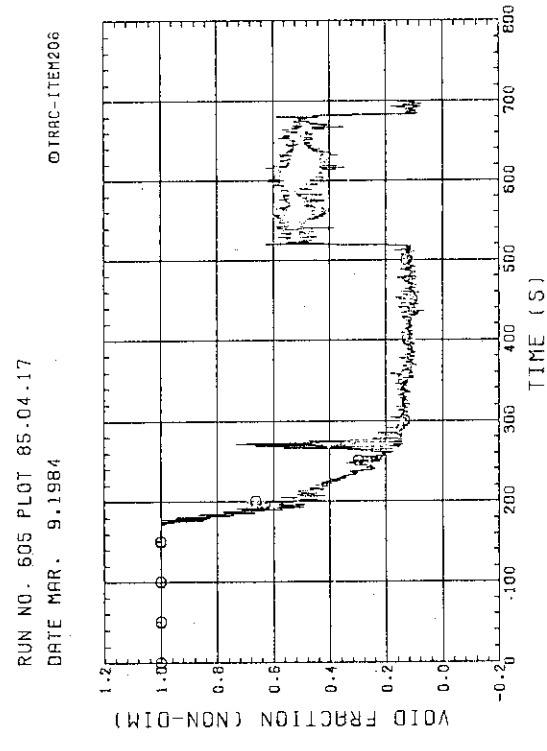

Fig. F-90 VOID FRACTION (BUNDLE 8)

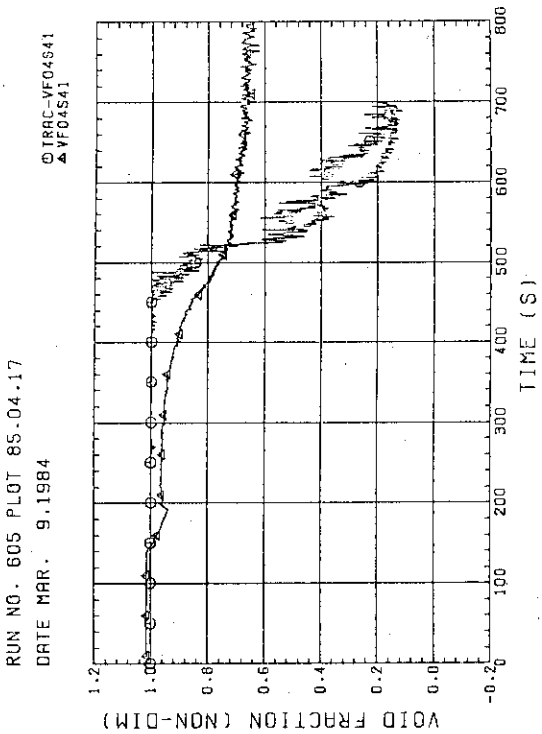

Fig. F-93 VOID FRACTION (BUNDLE 8)

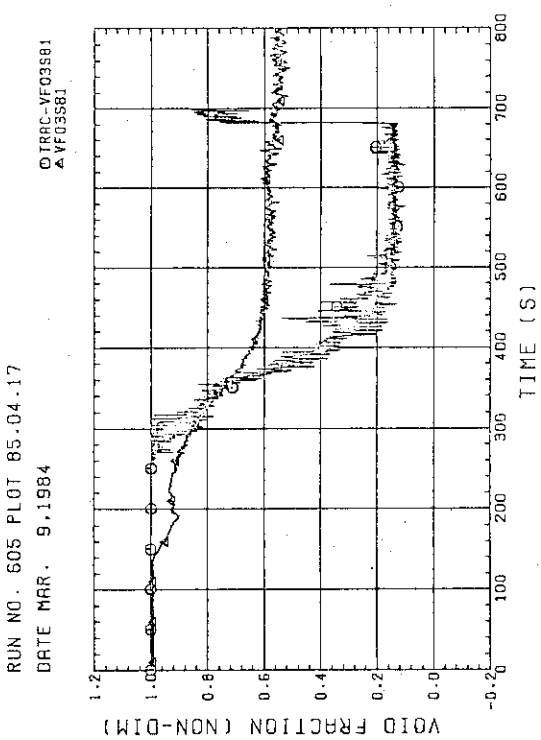

Fig. F-95 VOID FRACTION (BUNDLE 4)

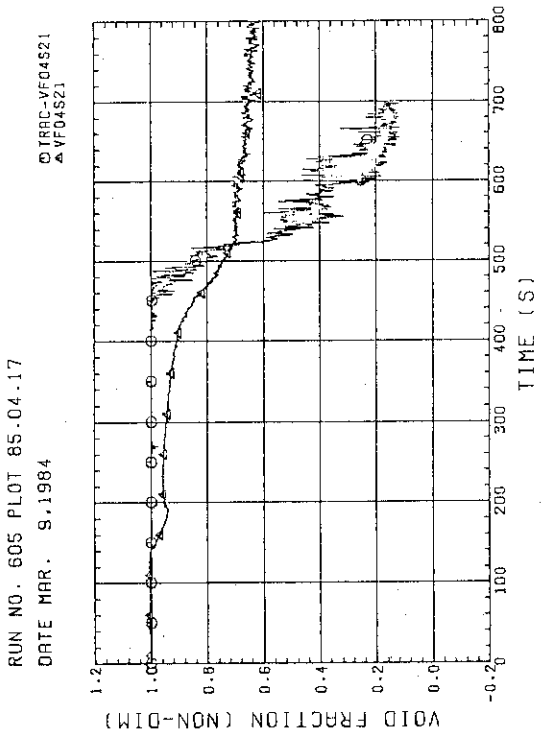

Fig. F-94 VOID FRACTION (BUNDLE 2)

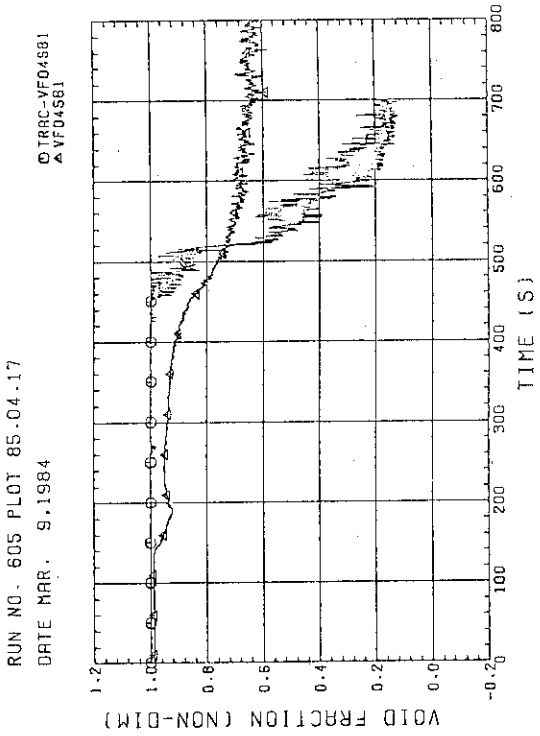

Fig. F-96 VOID FRACTION (BUNDLE 8)

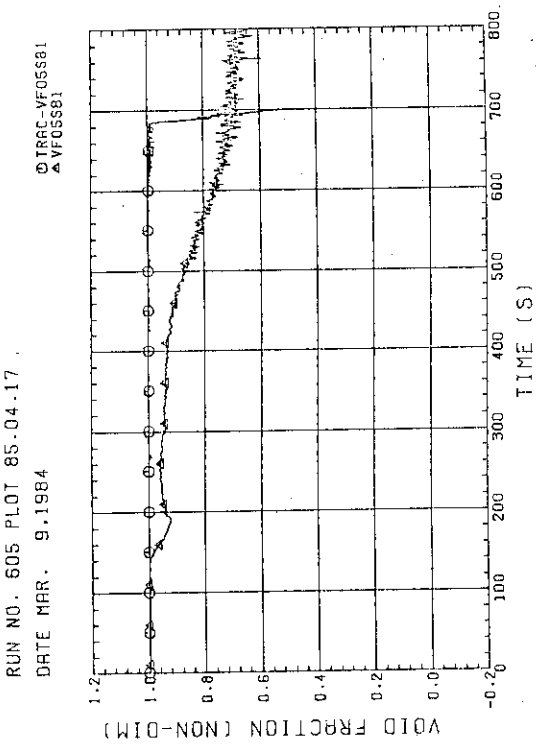

Fig. F-97 VOID FRACTION (BUNDLE 2)

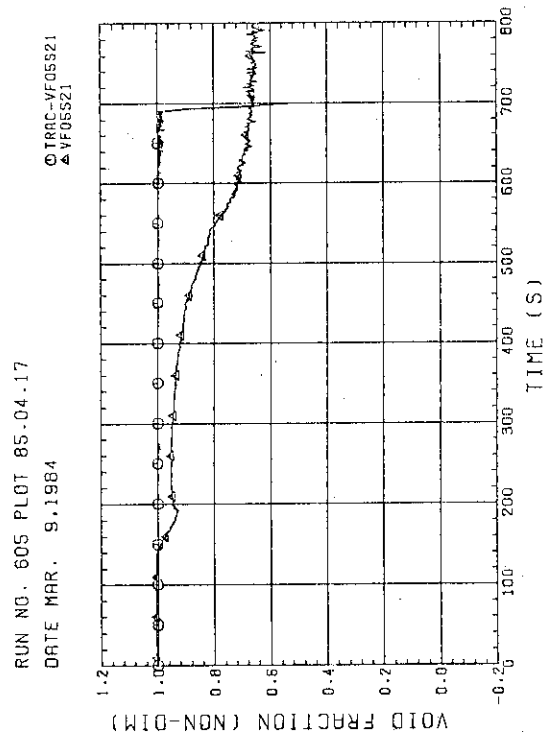

Fig. F-98 VOID FRACTION (BUNDLE 4)

Fig. F-99 VOID FRACTION (BUNDLE 8)

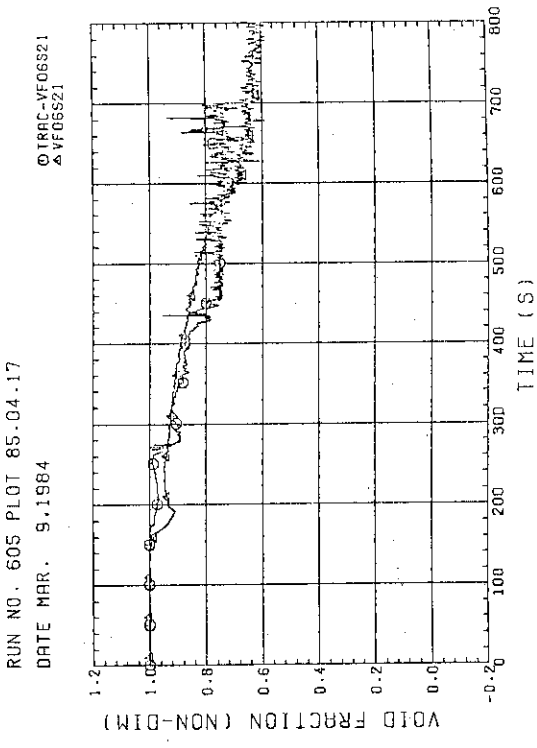

Fig. F-100 VOID FRACTION (BUNDLE 2)

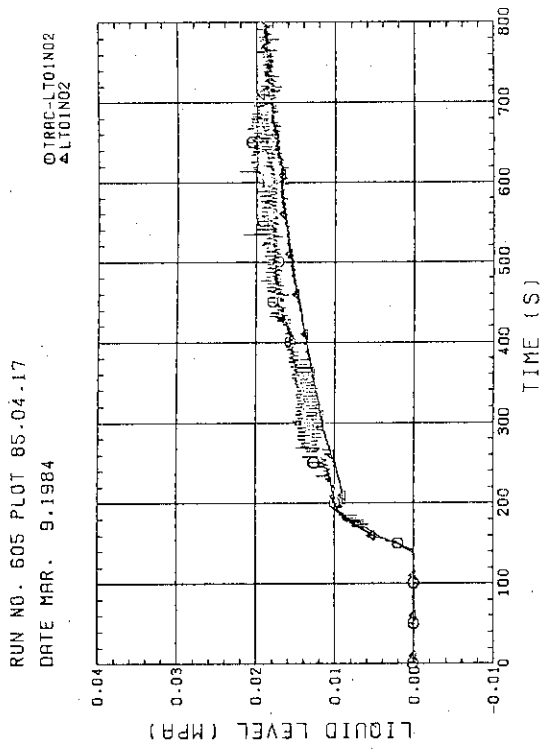

Fig. F-103 CORE BAFFLE. FULL HT

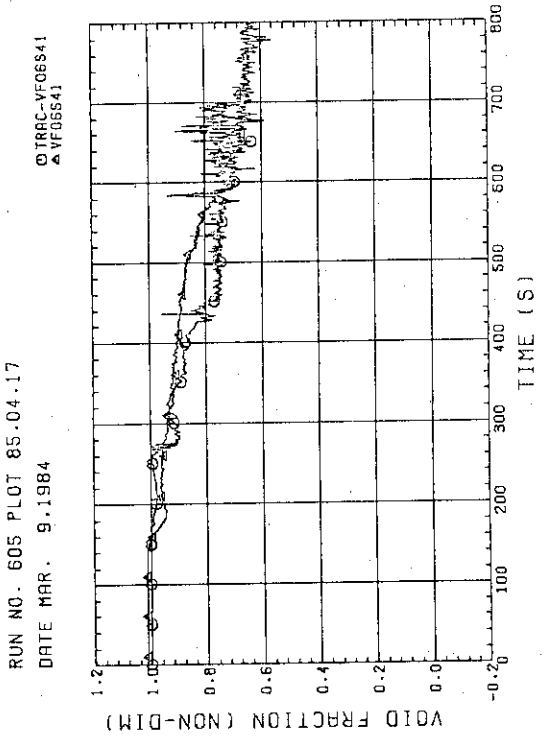

Fig. F-101 VOID FRACTION (BUNDLE 4)

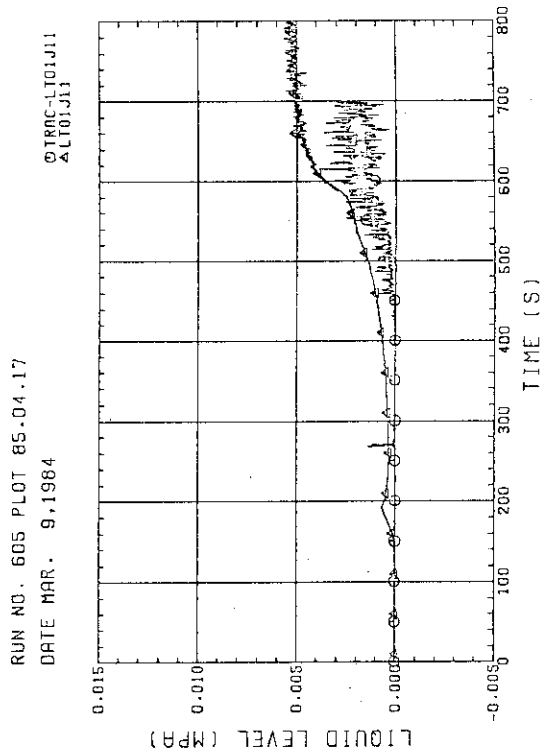

Fig. F-104 UPPER PLENUM LIQUID LEVEL (BUNDLE 1)

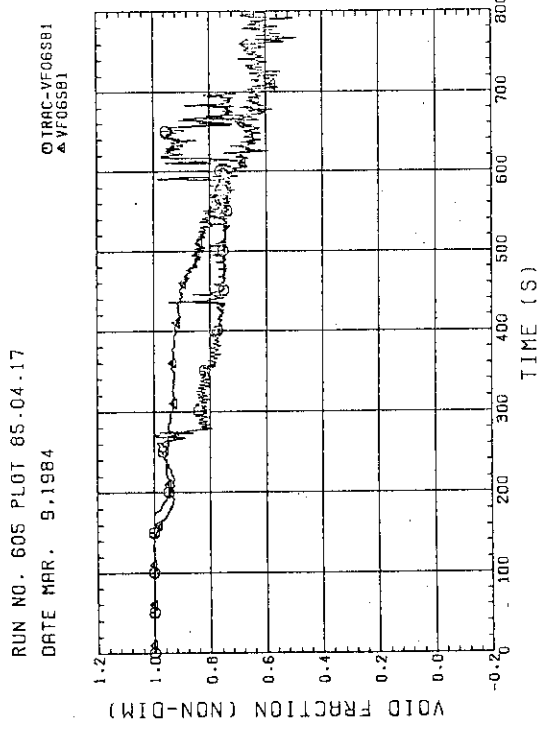

Fig. F-102 VOID FRACTION (BUNDLE 8)

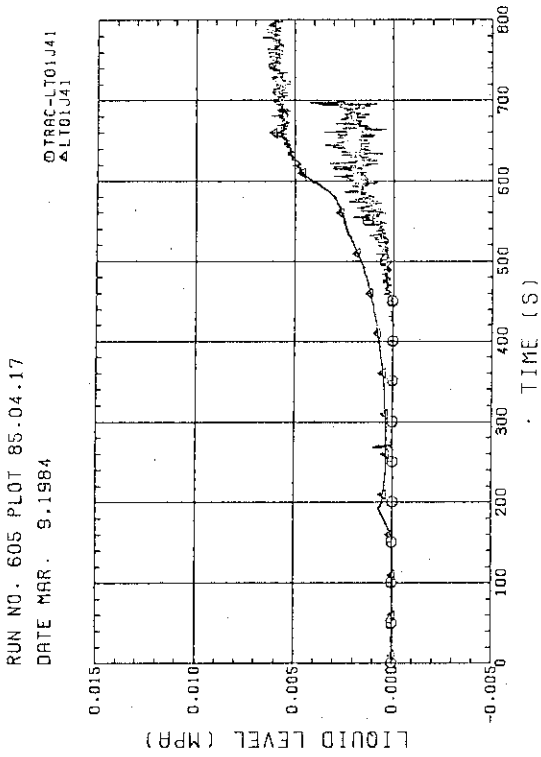

Fig. F-107 UPPER PLENUM LIQUID LEVEL (BUNDLE 4)

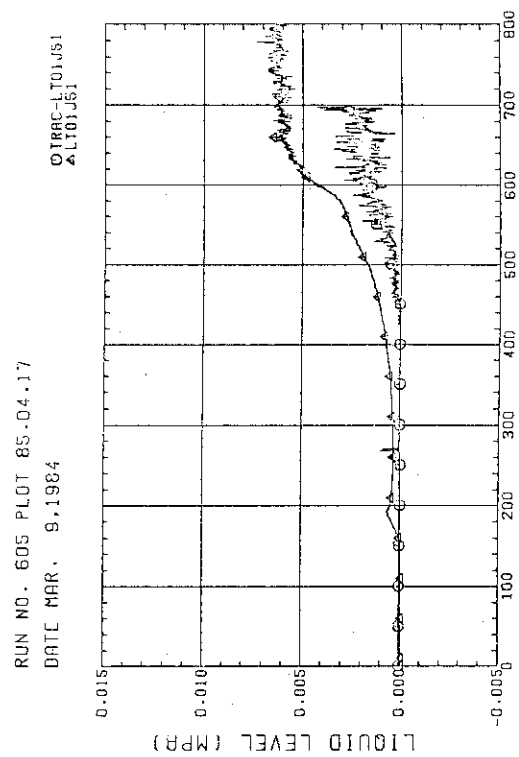

Fig. F-108 UPPER PLENUM LIQUID LEVEL (BUNDLE 5)

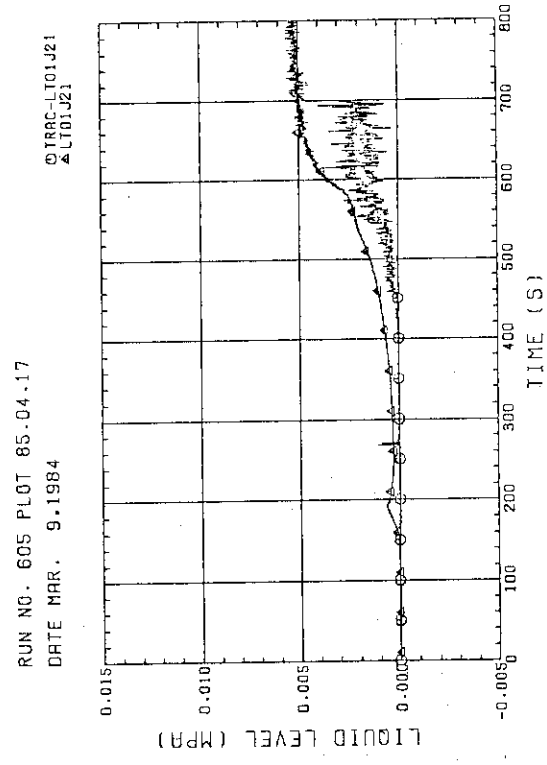

Fig. F-105 UPPER PLENUM LIQUID LEVEL (BUNDLE 2)

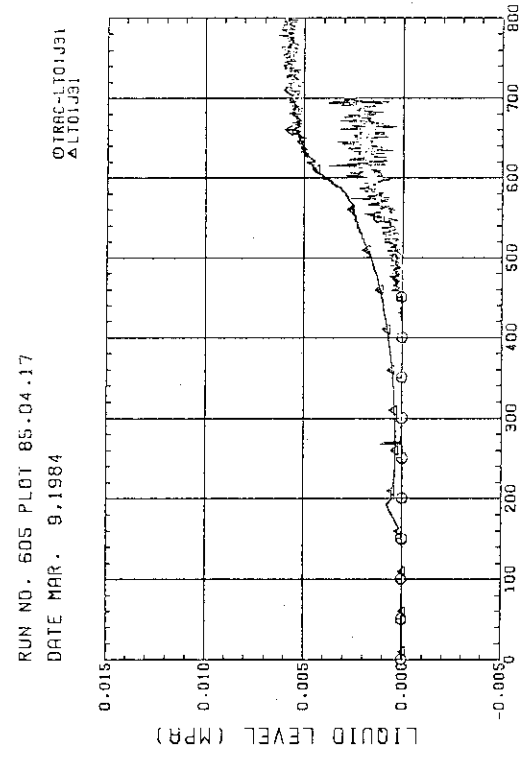

Fig. F-106 UPPER PLENUM LIQUID LEVEL (BUNDLE 3)

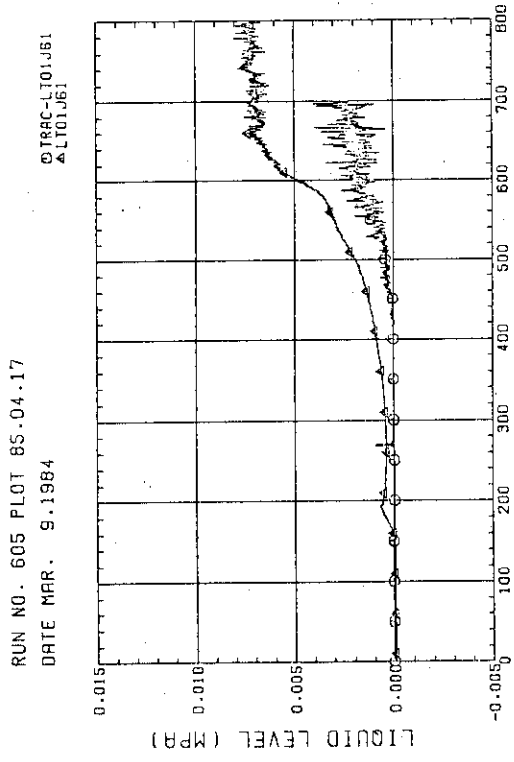

Fig. F-109 UPPER PLENUM LIQUID LEVEL (BUNDLE 6)

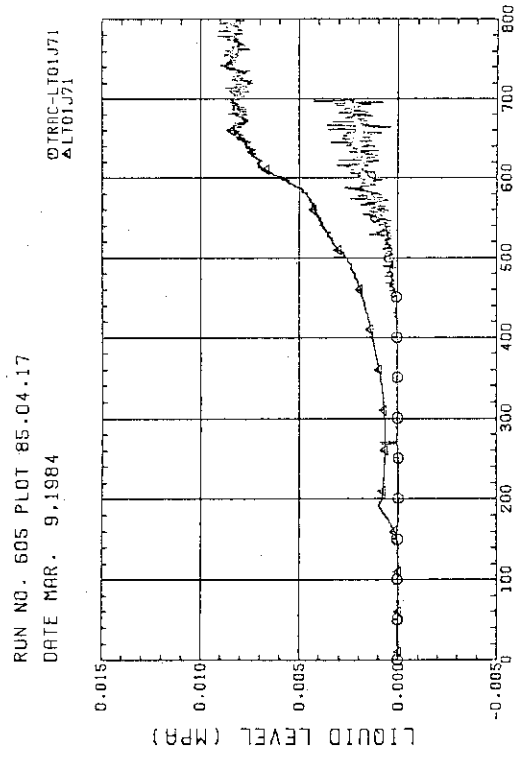

Fig. F-110 UPPER PLENUM LIQUID LEVEL (BUNDLE 7)

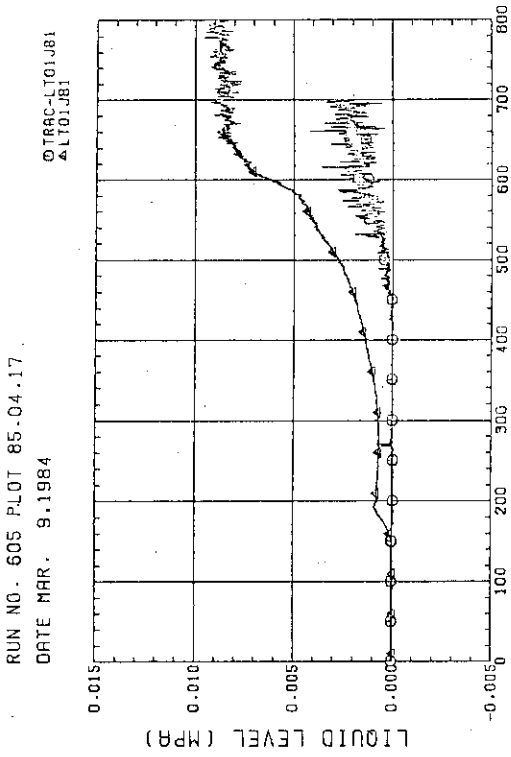

Fig. F-111 UPPER PLENUM LIQUID LEVEL (BUNDLE 8)

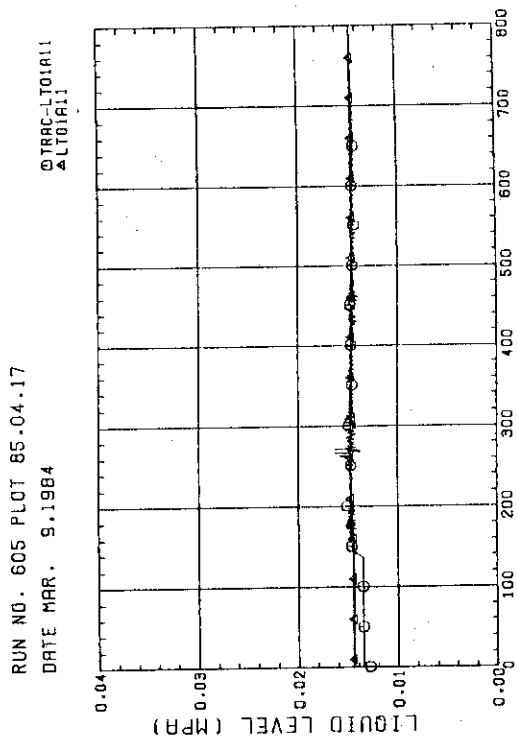

Fig. F-112 LOWER PLENUM LIQUID LEVEL (TOTAL)

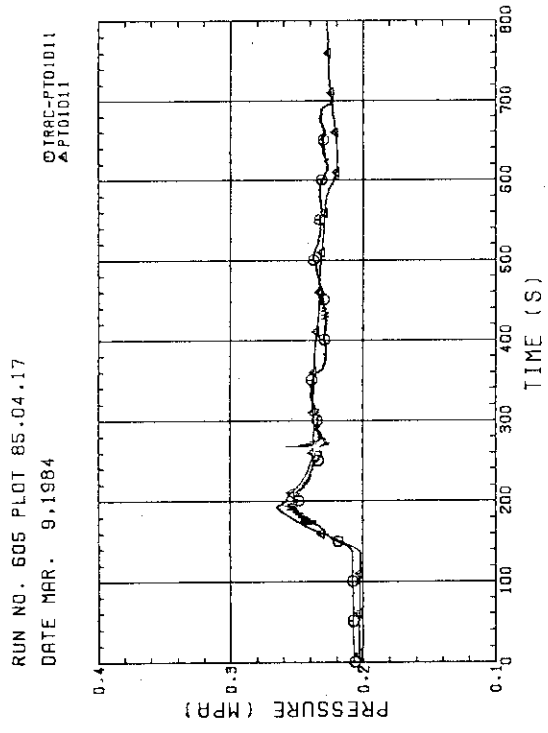

Fig. F-113 PRESSURE (CORE)

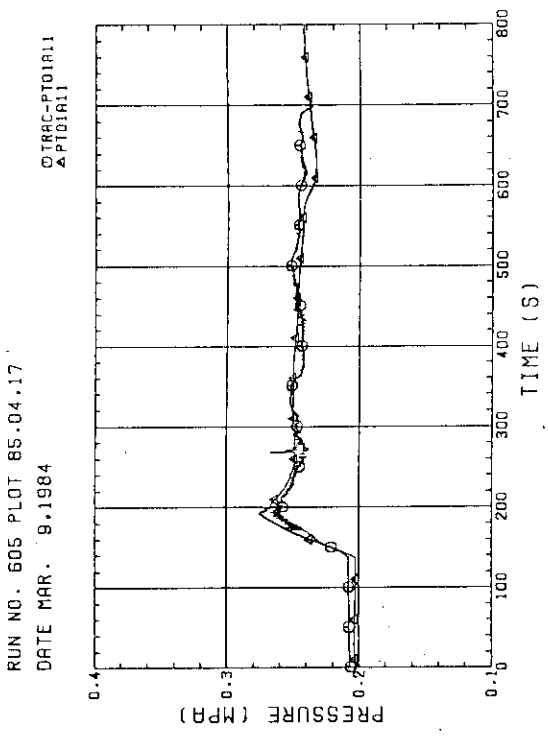

Fig. F-115 PRESSURE (LOWER PLENUM)

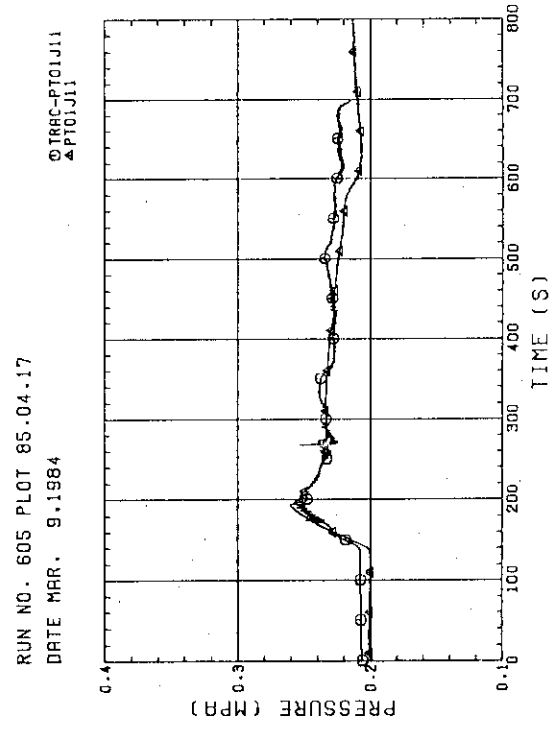

Fig. F-114 PRESSURE (UPPER PLENUM)

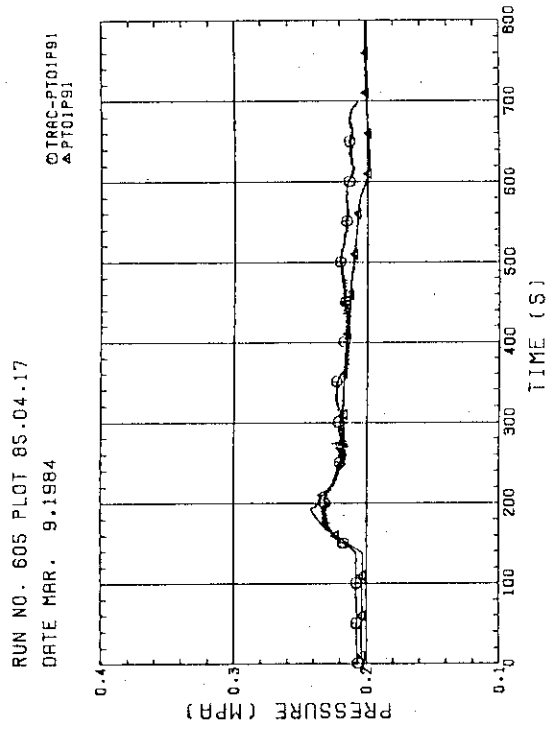

Fig. F-116 PRESSURE (DOWNCOMER)

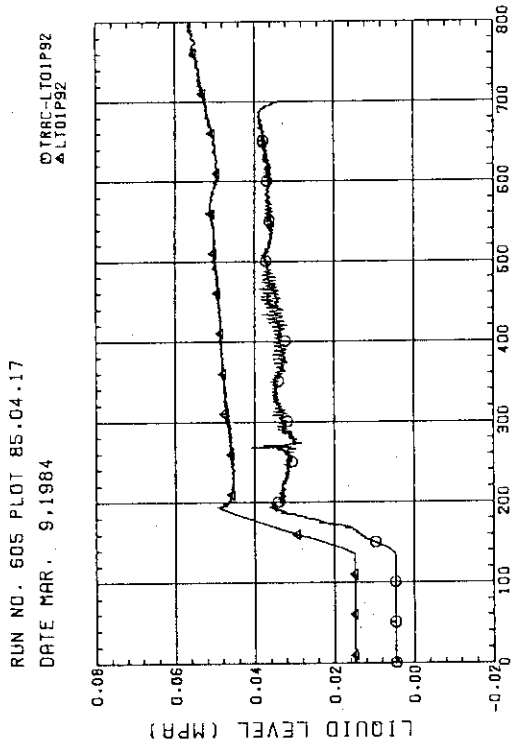

Fig. F-117 LIQUID LEVEL IN DC

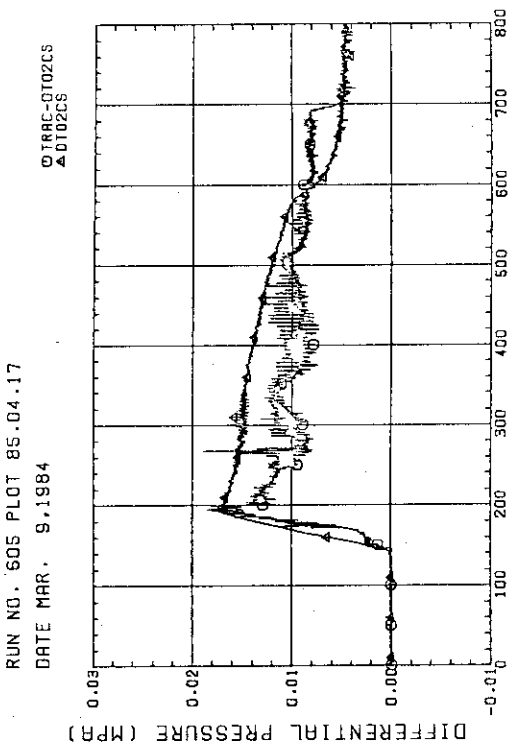

Fig. F-119 DIFFERENTIAL PRESSURE (S/W SEP. - DC)

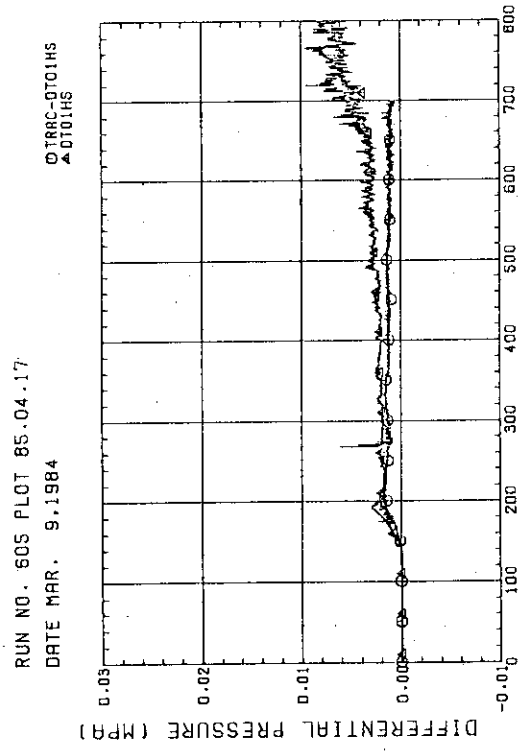

Fig. F-118 DIFFERENTIAL PRESSURE (UP - S/W SEP.)

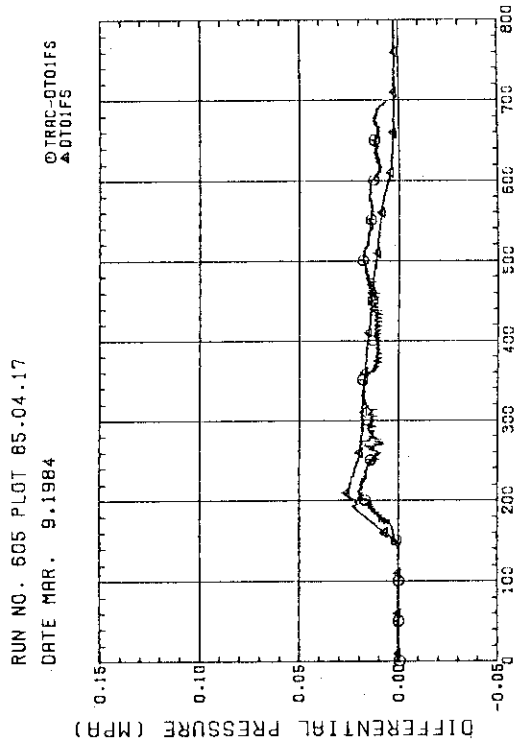

Fig. F-120 DIFFERENTIAL PRESSURE (DC - CT1)

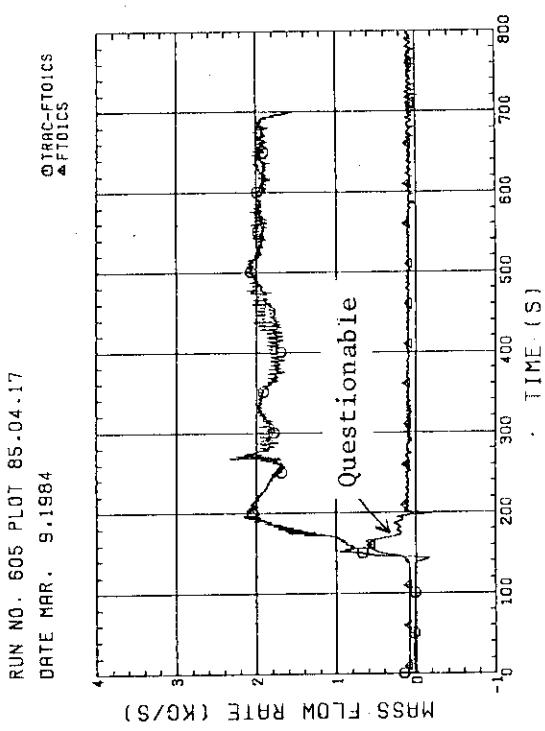

Fig. F-123 MASS FLOW RATE (ICL - ECC TO S/W)

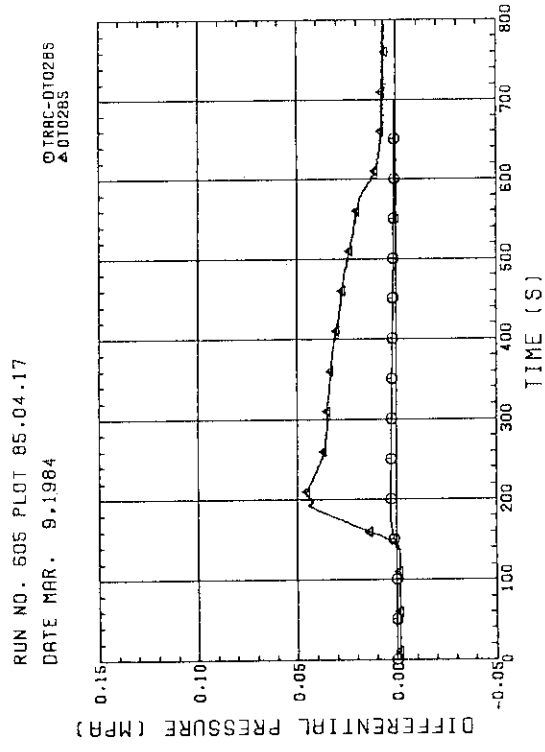

Fig. F-121 DIFFERENTIAL PRESSURE (S/W SEP. - CT2)

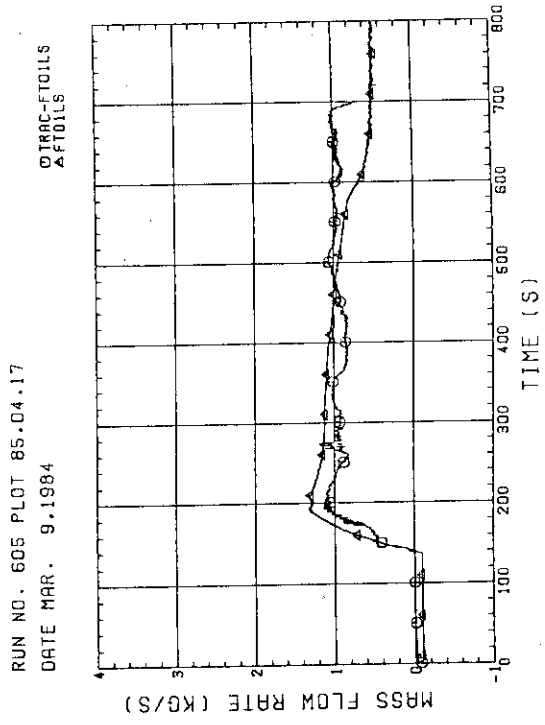

Fig. F-124 MASS FLOW RATE (BCL - S/W SIDE)

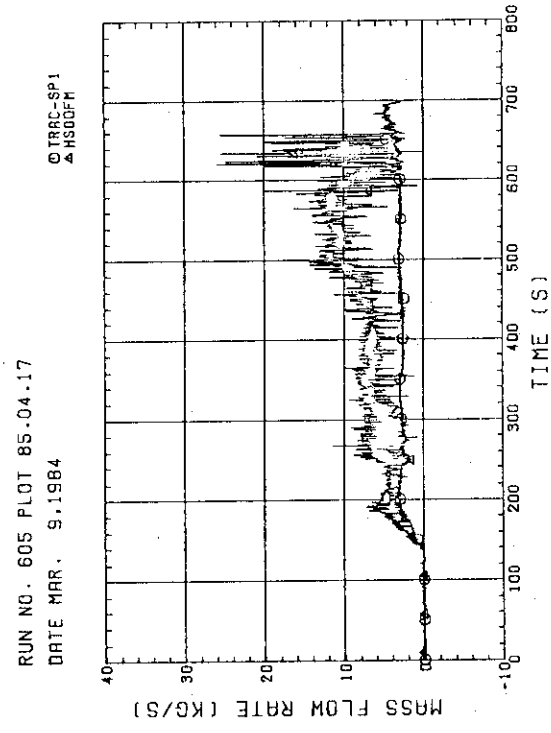

Fig. F-122 MASS FLOW RATE (HOT LEG)

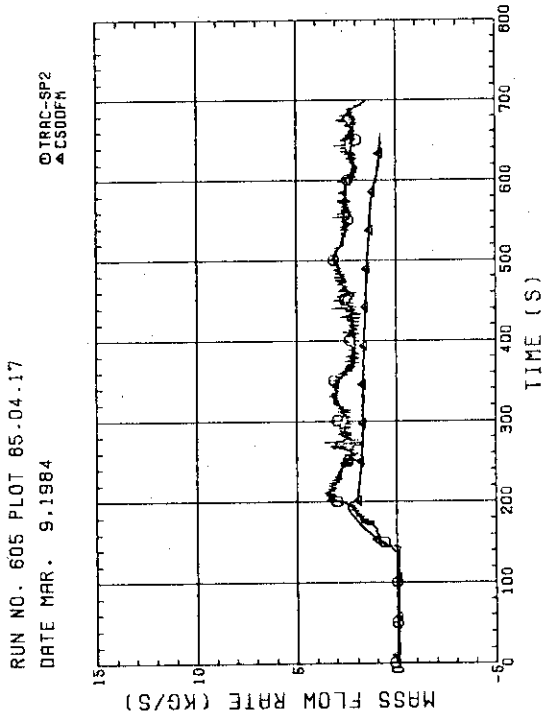

Fig. F-125 MASS FLOW RATE (BCL - PV SIDE)

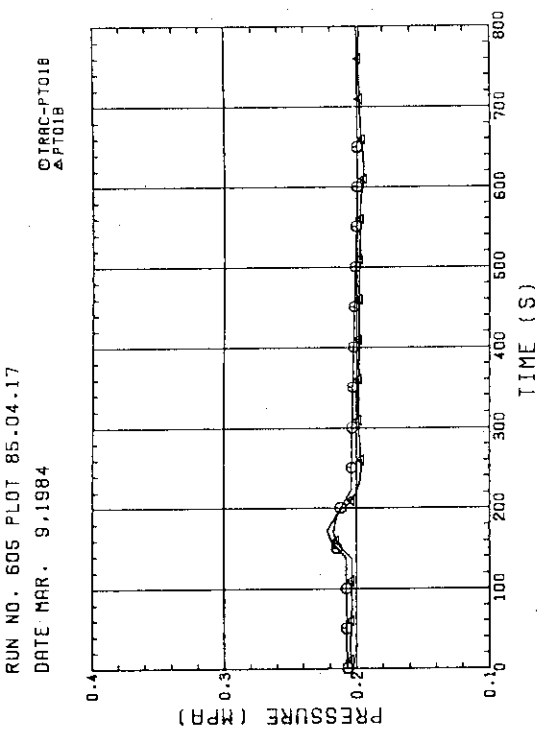

Fig. F-127 PRESSURE (CT2)

Fig. F-126 PRESSURE (CT1)

Fig. F-128 LIQUID LEVEL (S/W SEPARATOR)

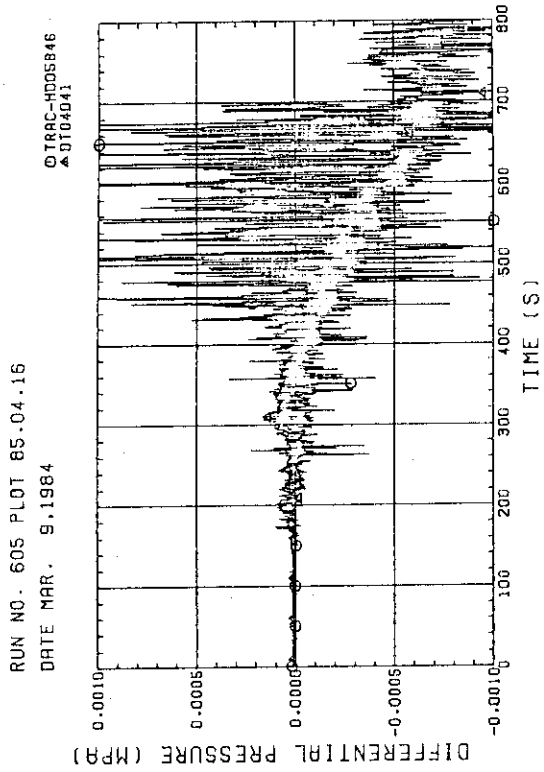

Fig. F-131 HORIZONTAL DIFFERENTIAL PRESSURE (ELEV. 1.905M , BUNDLE 4 - 6)

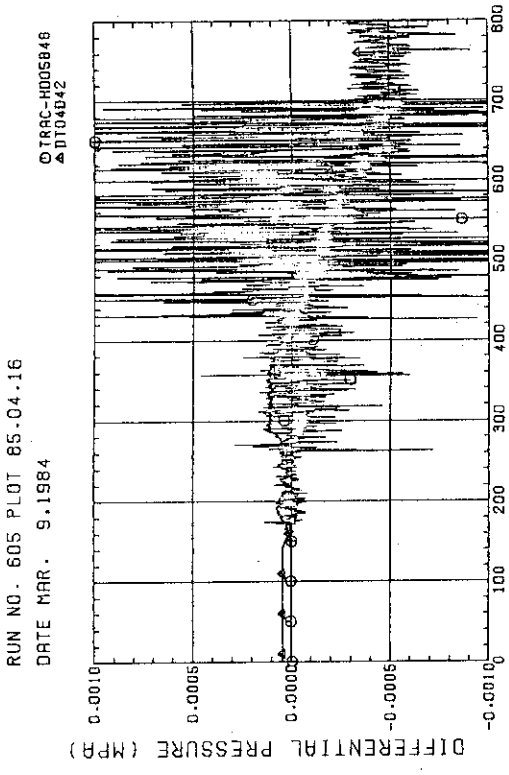

Fig. F-132 HORIZONTAL DIFFERENTIAL PRESSURE (ELEV. 1.905M , BUNDLE 4 - 8)

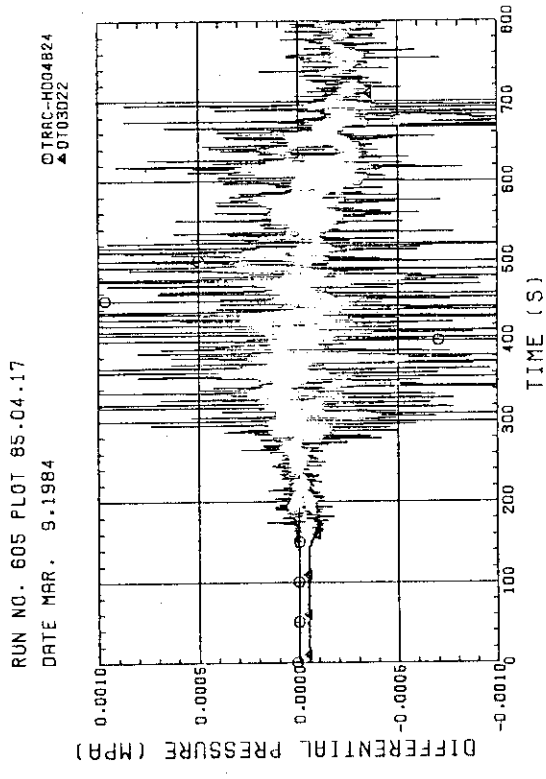

Fig. F-129 HORIZONTAL DIFFERENTIAL PRESSURE (ELEV. 1.365M , BUNDLE 2 - 4)

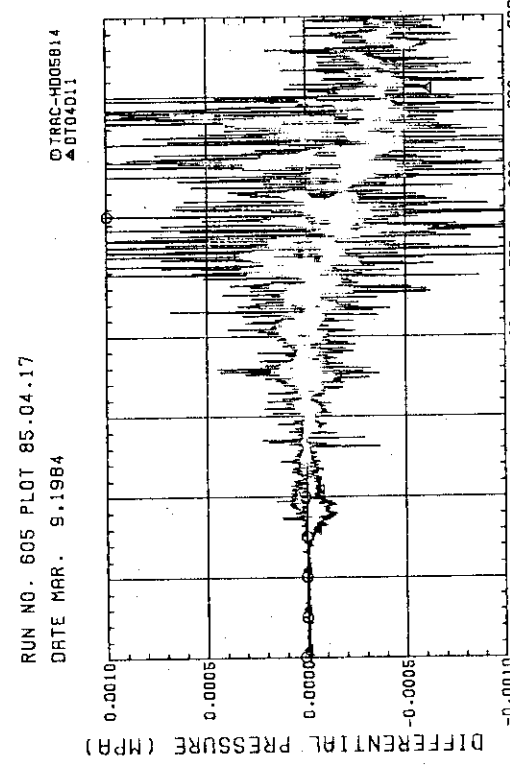

Fig. F-130 HORIZONTAL DIFFERENTIAL PRESSURE (ELEV. 1.905M , BUNDLE 1 - 4)

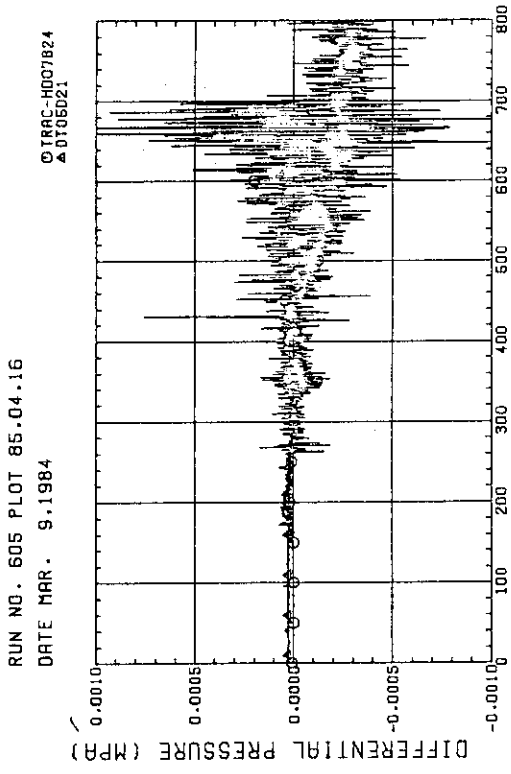

Fig. F-133 HORIZONTAL DIFFERENTIAL PRESSURE (ELEV. 2.57M , BUNDLE 2 - 4)